Geology, geochemistry and geometallurgy of the Productora Cu-Au-Mo deposit, Chile

by

Angela Jane Escolme

MEarthSci (Hons)

Submitted in fulfilment of the requirements for the degree of

Doctor of Philosophy

December 2016

UNIVERSITY OF TASMANIA

CODES

TMVC

TRANSFORMING THE MINING VALUE CHAIN

blank page

Declaration of Originality

This thesis contains no material which has been accepted for a degree or diploma by the University or any other institution, except by way of background information and duly acknowledged in the thesis, and to the best of my knowledge and belief no material previously published or written by another person except where due acknowledgement is made in the text of the thesis, nor does the thesis contain any material that infringes copyright.

Signature:

Date: 21.12.16

Authority of Access

This thesis is not to be made available for loan or copying for eighteen months following the date this statement was signed. Following that time the thesis may be made available for loan and limited copying and communication in accordance with the Copyright Act 1968.

Signature:

Date: 21.12.16

blank page

Abstract

The Productora Cu-Au-Mo deposit is hosted by a hydrothermal breccia complex in the Coastal Cordillara of Region III, northern Chile. Mineralisation at Productora extends discontinuously over 8 km in a northeast-oriented corridor. The current resource, which includes the neighbouring Alice porphyry Cu-Mo deposit, is estimated at 236.6 Mt grading 0.48 % Cu, 0.10 g/t Au and 135 ppm Mo.

The district is characterised by hydrothermal mineralisation associated with Mesozoic arc magmatism along the convergent South American plate margin. The Andean tectonic cycle led to the formation of orogen-parallel metallogenic belts, each representing discrete epochs of mineralisation characterised by distinctive deposit styles and a stepped eastward younging of the deposits. During the Mesozoic, a range of deposit styles formed under extensional conditions in central and northern Chile, including small porphyry Cu, large iron oxide-Cu-Au (IOCG), magnetite-apatite, manto-Cu and precious metal epithermal deposits.

The Mesozoic mineral systems in Northern Chile formed within a convergent tectonic regime where evolving subduction style, magmatic arcs and associated back-arc basin stratigraphy, plutonic complexes and the crustal scale syn-arc strike-slip Atacama Fault Zone (AFZ) evolved in response to changes in the prevailing geodynamic conditions. The Productora deposit is hosted within a thick sequence of broadly coeval rhyolite to rhyodacite lappili tuffs (128.67 ± 1.29 Ma; U-Pb_{zircon}) and breccias between two major intrusions; the Cachiyuyito tonalite (129.8 ± 0.1 Ma) and Ruta Cinco granodiorite batholith (92.05 ± 1 Ma; U-Pb_{zircon}). Several phases of intermediate- and mafic-dykes cross cut the deposit. The deposit is hosted in a domain of structural complexity defined by major northwest-striking faults (normal oblique-slip with dextral strike-slip and northeast side up dip-slip) that crosscut major north to northeast-striking faults (normal oblique-slip with sinistral strike-slip, and east-side up dip-slip movement).

Hydrothermal breccias, tectonic breccias, veins and alteration assemblages observed on two cross sections at Productora have been separated into five paragenetic stages. Stage 1 produced quartz - pyrite-cemented hydrothermal breccia with muscovite alteration. Stage 2 formed a chaotic matrix-supported tectonic breccia with kaolinite - muscovite – pyrite alteration. Stage 3 tourmaline – pyrite – chalcopyrite ± magnetite ± biotite-cemented hydrothermal breccias are associated with K-feldspar ± albite alteration. Stage 4 veins contain chalcopyrite ± pyrite ± sericite, illite, epidote and chlorite, and stage 5 veins contain calcite. The stage 3 breccias have been further subdivided into five facies based on their mineralogy. The Productora hydrothermal system crosscuts earlier-formed sodic-calcic alteration and magnetite-apatite mineralisation associated with the Cachiyuyito stock.

The breccia complex formed as a result of at least two stages of hydraulic fragmentation (stage 1 and stage 3) and one tectonic breccia event (stage 2), which shows evidence of multiple episodes of reactivation. Alteration minerals are consistent with moderate temperature (<300°–400°C) weakly acidic fluids during stage 1, and moderate to high temperature (>300°C) alkaline fluids during stage 3. Lower temperature (<300°C), weakly acidic fluids prevailed during stages 4B and 4C, and alkaline fluids predominated during stages 4A, 4D and 5.

Main stage mineralisation is associated with the stage 3 hydrothermal breccia (average grade 0.34–0.62 % Cu, 0.8–0.14 g/t Au, 66–128 ppm Mo) and stage 2 tectonic breccia (average grade 0.8 % Cu, 0.21 g/t Au, 141 ppm Mo). Chalcopyrite is the dominant hypogene Cu-sulphide mineral and occurs predominantly as stage 3 breccia cement and syn-breccia veins with pyrite in equal proportion. Chalcopyrite and pyrite are disseminated in the stage 2 breccias. Pyrite is elevated in the south compared to the north, and chalcopyrite:pyrite ratios are ~1.00 and <0.25 respectively. Gold and Cu are strongly associated spatially, and synchrotron XRF and LA-ICP-MS analyses indicate that Au occurs as micron to sub-micron grains on pyrite and chalcopyrite grain boundaries. In this study, mineralisation at Productora was dated using Re-Os on stage 3 molybdenite at 130.1 ± 0.6 Ma.

The Alice Cu-Mo porphyry deposit is situated 400 m to the west of Productora. Mineralisation occurs as disseminated chalcopyrite and quartz – pyrite – chalcopyrite ± molybdenite vein stockwork hosted by a granodiorite porphyry stock (121.1 ± 2.1 Ma). Potassic alteration (biotite ± actinolite replacing hornblende) is associated with quartz – sulphide veins. Mineralisation was dated by Re-Os on molybdenite at 124.1 ± 0.6 Ma (within error of the porphyry stock). The margins and deeper parts of the system are overprinted by albite ± epidote ± sericite alteration, which locally caused destruction of biotite and chalcopyrite. The Alice porphyry is spatially associated with the Silica Ridge lithocap, which is characterised by massive textureless quartz-altered rock above domains of alunite, pyrophyllite and dickite.

At Productora, $\delta^{34}S_{sulphide}$ values range between -8.5 and +2.2 ‰. This is consistent with a magmatic sulphur source and fluids evolving under oxidising conditions with no significant input from evaporate- or seawater-sourced fluids. Stage 3 tourmalines (n = 8) have average initial Sr of 0.70397, consistent with Cretaceous intrusive rocks and mantle-derived Sr. One stage 4 epidote sample returned a more radiogenic initial Sr value of 0.70525, indicating fluid mixing or fluid- wall rock interaction. An εNd value of +5.2 (n = 1, tourmaline) is consistent with the Cretaceous and Jurassic igneous rocks of the region. LA-ICP-MS analysis on stage 3 pyrite (n = 8) for Pb isotopes and trace elements indicate low Pb content (<5 ppm) with significant thorogenic and uranogenic Pb isotope contamination. Early pyrite

grains have elevated Pb (4.6 ppm), Cu (47 ppm), U (4.0 ppm), Th (2.6 ppm) and Au (0.06 ppm) which also all co-vary. Late-stage pyrite that has replaced chalcopyrite does not contain significant Pb, U, Th, As or Au, but does have elevated Cu (>530 ppm).

Supergene mineralisation in the north of Productora (chrysocolla, malahcite and Cu-wad) is indicative of a geochemically mature weathering environment developed under near neutral to alkaline pH. In the south, the supergene assemblage is less mature (chalcocite/digenite) and indicates in-situ weathering of chalcopyrite.

Quantitative and predictive geometallurgical models have been developed to integrate geological findings with geometallurgical data in order to advance ore body knowledge at Productora. To improve the understanding of mineralogical variability across the deposit, whole rock geochemistry (33-element ICP-MS) has been converted to mineral proportions through calculated mineralogy using linear programming for each assay interval in the deposit. Calculated mineralogy results for major minerals, including quartz, K-feldspar, albite, pyrite, iron oxides, chalcopyrite and molybdenite, are excellent (R^2 > 0.8) when compared with the measured mineralogy by quantitative X-ray diffraction. A new sample classification scheme for dominant Cu-species (oxide, transitional-oxide, transitional-sulphide, sulphide or insoluble) was also developed based on sequential leach data and S wt%. The new scheme enabled domains of weak acid insoluble Cu-wad to be identified. Machine learning algorithms were used to predict Cu-species class using a series of nine proxies (sample depth in drill hole, Ca %, Cu %, Fe %, K %, Mn ppm, S %, Ln(Cu/S) and the logged regolith term). The optimum algorithm was Bagging-REPTree with five iterations. Applied to the training set with ten-fold cross validation, the model is 67.6 % accurate. The model is most successful at recognising sulphide, transitional-sulphide and insoluble samples with accuracy of 70.2 %, 87.5 % and 67.8 % respectively against the training set.

Based on textural, mineralogical, stable and radiogenic isotope data, the Productora breccia complex is inferred to be a magmatic-hydrothermal breccia complex formed as a result of explosive volatile fluid release at depths causing brecciation and alteration of the overlying rock mass. Metal-bearing fluids were of magmatic affinity and evolved under oxidising conditions. Despite sharing many similarities with the Andean IOCG clan (strong structural control, regional sodic-calcic alteration, local U), fluid evolution at the Productora Cu-Au-Mo deposit is consistent with that of a porphyry magmatic hydrothermal breccia (sulphur-rich, acid alteration assemblages and relatively low magnetite, <5 wt%). The Productora camp provides an excellent example of the close spatial association of Mesozoic magnetite-apatite, porphyry (Alice) and a magmatic-hydrothermal breccia mineralisation styles, a relationship seen throughout the Coastal Cordillera of northern Chile.

Acknowledgements

This thesis is the result of significant technical and moral support from many individuals. I have benefited greatly from the advice, help and friendship that have been extended to me over the past few years and would like to acknowledge all those who have been a part of my PhD experience.

Firstly, I would like to thank my supervisors Prof. David Cooke, Assoc. Prof. Ron Berry and Dr. Julie Hunt for all their endless support, teaching, patience and enthusiasm throughout this project. It's been an honour to work with you all. I'd especially like to thank Dave, from whom I have learnt so much, for all the opportunities that have enabled me to develop as a geologist — my photo and rock library have grown significantly! Your zealous use of red pen has greatly enhanced both my writing skills and this thesis. I would like to thank Ron for always being available to provide honest advice and help to solve problems in his retirement - I'm extremely grateful for all that you contributed. I am thankful to Julie for always being very supportive, even from afar, and especially for the help you provided during my second field season in Chile.

This project would not have been possible without the vision and generosity of Hot Chili Ltd, whom sponsored this innovative project and made me feel part of their team. In particular I would like to thank Warren Potma for his enthusiasm setting the project up, and for his insightful ideas and discussions. The project also benefited greatly from the inputs of John Beeson and Scott Halley, I am fortunate to have had the opportunity to learn from you both during our time at Productora. Geologists Bruce Hunter, Cristian Vasquez, Antonio Muñoz Algobia, Ana Centeno and Pablo Torres all provided logistical support and friendship throughout my field seasons - muchas gracias! Thanks also go to Christian Easterday, Melanie Leighton, Sam Kemp and Lachy MacDonald for their input and help along the way.

I am extremely grateful to CSIRO, SEG, AusIMM and Australian Synchrotron for their generous contributions and ongoing support to this project. I am particularly grateful to Dr. Louise Fisher, Dr. Mark Pearce and Dr. James Cleverley whom facilitated collaboration with CSIRO and access to 'machines that go ping'! I'd especially like to thank Louise and Mark, as well as David Patterson, for their expertise, time and enthusiasm whilst working at the Australian Synchrotron.

It has been a tremendous experience to work with the world-class research group at CODES and Earth Sciences Department, University of Tasmania, and it will be an honour to join the ranks of CODES graduates. I would like to acknowledge all those who have provided advice, ideas and enlightening discussions along the way including Garry Davidson, Jocelyn McPhie, Leonid Danyushevsky, Sarah Gilbert, Nathan Fox, Anya Reading and Jay Thompson. Sebastian Meffre has been a surrogate supervisor, providing helpful advice on a wide range of analytical processes and data interpretation, always delivered with a smile — huge thanks! Thank you also to Al Cuison and Michele Chapple-Smith for working magic on my samples in the lapidary. Huge thanks also go to Martin Gal for helping me write my first Python programs. I am exceptionally grateful to Karsten Goemann and Sandrin Feig at Central Sciences Laboratory for their advice, help and attention to detail. I would also like to acknowledge all the staff who work behind the scenes and have contributed to a fantastic experience, in particular Jane Higgins, Helen Scott and Deborah Macklin.

I have shared my PhD years with a group of inspirational scientists whom I am fortunate to call my close friends. Erin Lawlis, Evan Orovan, Stephanie Sykora, Marc Rinne, Nic Jansen, Nathan Steeves, Emily Smyke, Ayesha Ahmed and Shawn Hood — thank you all for technical advice, smiles, kind words, beers and dance parties! Extra thanks go to Ayesha Ahmed for helping to keep me sane over the past few months by literally running up a mountain with me — high five! Massive thank you also to Evan for helping with a Christmas miracle.

Final words go to my family and friends beyond the department who have all been incredibly supportive, encouraging and understanding throughout. Thank you to Barbara and John Escolme (Mum and Dad) for instilling in me the ethics of hard work and dedication that have helped me achieve this goal, and always supporting my choice to live 'down under'. Finally, words can not express my gratitude to my partner Josh Phillips, an exceptional geologist who has been with me on this PhD journey from day one. Thank you Josh for all your insightful discussion, help, moral support, enthusiasm, optimism, patience, humour, kind words and love. You are the best!

Table of Contents

Digital Appendices

Digital appendices available from:

Helen Scott

ARC Industrial Transformation Research Hub Manager – Transforming the Mining Value Chain (TMVC)

CODES | School of Physical Sciences

University of Tasmania

Helen.Scott@utas.edu.au

or

Angela Escolme

Angela.Escolme@utas.edu.au

List of Appendices

D6 Linear programming calculated mineralogy example (Excel)

D7 Analysis of cluster groups

D8 Discriminant projection analysis

D9 Global modal constraints

D10 Calculated mineralogy vs. WLSQ - compositional groups

D11 Calculated mineralogy vs WLSQ - difference by cross section

D12 Global vs. compositional calculated mineralogy comparison

D13 Leapfrog interpolation explanation

D14 Flotation problem minerals

Appendix E

E1 SEM data from Cu-wad (Excel)

E2 Sequential leach classification example (Excel)

E3 Machine learning algorithm descriptions

E4 Python code

E5 Sequential leach classification - version 2 example (Excel)

Appendix F

F1 Etched pyrite photos

F2 Gold solubility in pyrite

List of Figures

List of Tables

blank page

Chapter 1: Introduction

1.1 Preamble

The Coastal Cordillera of northern Chile is host to a range of deposit types, including iron oxide-copper-gold (IOCG), porphyry Cu-Au, magnetite-apatite, manto-Cu and precious metal epithermal systems. They define the orogen-parallel Mesozoic metallogenic belt. The Mesozoic mineral systems in northern Chile formed within a convergent tectonic regime where evolving subduction style, magmatic arcs and associated back-arc basin stratigraphy, plutonic complexes and the crustal scale syn-arc strike-slip Atacama Fault Zone evolved in response to prevailing geodynamic conditions (Figure 1.1). Relationships between Andean IOCGs, magnetite-apatite, manto-Cu and porphyry-Cu deposits, which all share a close temporal and spatial association in the Chilean Coastal Cordillera, have been the subject of much research and controversy (e.g. Hitzman et al., 1992; Barton and Johnson, 1996; Marschik and Fontboté, 1996; Williams et al., 2005; Chen, 2010; Tornos et al., 2010 and Tornos 2011).

The Productora Cu-Au-Mo deposit is an enigmatic breccia complex that presents characteristics consistent with both the porphyry and IOCG models. Further intrigue arises from the neighbouring magnetite-apatite and porphyry-Cu-Au-Mo mineralisation, making Productora a deposit of significance in the ongoing debate over possible relationships between these mineralisation styles. In addition, important deposit, camp and regional scale exploration implications arise from understanding the genesis and evolution of the Productora deposit.

Northern Chile is one of the most productive IOCG provinces globally, owing to the major Cu-rich IOCG deposits, La Candelaria (470 Mt grading 0.95 %Cu; Marschik and Sollner, 2006) and Mantoverde (400 Mt @ 0.52 %Cu; Benavides et al., 2007). The only porphyry deposit currently being mined in the Coastal Cordillera is Andacollo (476.6 Mt grading 0.34 %Cu and 0.12 g/t Au (Teck Resources Limited, 2013). Porphyry and IOCG deposits share some common alteration types, for example sodic-calcic, potassic and phyllic assemblages which are typically zoned upward and outward. Acid alteration and

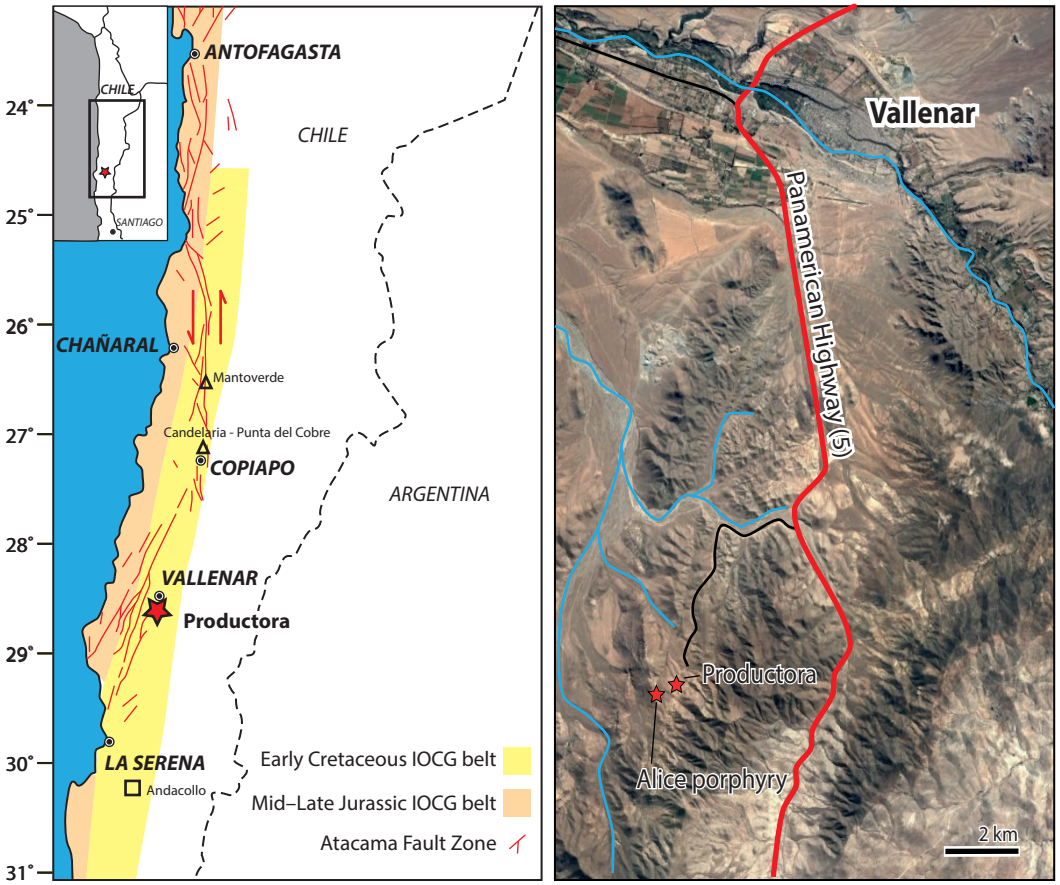

Figure 1.1 Location of Productora in Coastal Cordillera of northern Chile, within the Early Cretaceous IOCG, Pacific Porphyry belt and Chilean Iron Belt associated with the Atacama Fault Zone. Aerial photo from www.Google.com.

advanced argillic assemblages are not common or voluminous in IOCG deposits — although chlorite and muscovite bearing assemblages are widespread, particularly in the shallower parts of IOCG systems (sensu stricto; Barton and Johnson 2000, Barton, 2014). Mineralisation in Andean IOCG deposits occurs in a range of styles including veins and stockworks, hydrothermal breccias, calcic skarns, replacement horizon (mantos) and 'composite' styles, which generally include veins and a combination of other styles (Silltoe, 2003). Copper (± Au) in IOCG deposits is typically associated with abundant iron-oxides, either magnetite or hematite (15–25 wt% Fe in Cu ores; Williams et al. 2005), and suite of anomalous minor elements including various combinations of F, P, Co, Ni, As, Mo, Ag, Ba, LREE, and U (Williams et al., 2005). Porphyry mineralisation typically occurs as distinctive quartz-bearing stockwork veinlets and as disseminations in the wall rock (Sillitoe, 2010). Mineralised magmatic hydrothermal breccias and calcic-skarns are also commonly associated with porphyry systems (e.g. Meinert et al., 2005). Intimately associated porphyritic intrusions are a key characteristic in porphyry systems. Sulphide assemblages are typically zoned upward and outward from chalcopyrite ± bornite-rich core, chalcopyrite ± pyrite zone to outer pyrite halo. There are three porphyry end-members in terms of metal content: Cu-Mo, Cu-Au and Cu-Au-Mo (Kesler et al., 1973). Complex and variable alteration assemblages, mineralisation styles and their spatial distributions impact on bulk mineralogy and processing considerations for economic ore zones in both deposit types.

Geometallurgical considerations are paramount to the success and risk mitigation of low grade mining projects. Typically during scoping and project definition studies, predictions of mine performance are made from the extrapolation of limited datasets. The most important and risk prone decisions are made during project infancy when the least amount of metallurgy data is available (Lamberg, 2011). Mineralogy is a fundamental characteristic for a given rock mass throughout the mining chain, from blasting, through valuable phase extraction to waste management (Hoal, 2008). Current methods for estimating bulk mineralogy are slow and expensive, particularly where mineralogy is complex and variable. Predictions of mine performance can be improved where estimates of mineral abundance are extensive (Hunt et al., 2008). The collection of multi-element geochemical data has become routine for many companies in the minerals industry. This geochemical information can be translated into mineral proportions through calculated mineralogy. Mineral proportions are more accessible and amenable to metallurgists and mining engineers who are interested in understanding rock properties and mineralogical variability across a deposit (Hoal, 2008).

Knowledge about the proportions of Cu-oxides and Cu-sulphides is important when considering the most appropriate processing route (leach versus flotation) for ore, and for estimating valuable phase recovery and ultimately resource value. Weathering and supergene mineralisation are variably developed at deposits within the Chilean Mesozoic metallogenic belt. For example, at Mantoverde, production is entirely from supergene oxide ore (Benavides et al., 2007), whereas supergene oxidation and enrichment are only poorly developed at Candelaria (Sillitoe and Clark, 1969). Current industry practice is to characterise samples in the weathering zone through sequential, or diagnostic, leaching. This is usually only carried out on a suite of samples selected to be representative based on geological logging, which is often inconsistent between loggers. Extrapolation of sequential leach data, using more readily available data such as multi-element geochemical assays, has the potential to dramatically increase the number of samples used for geometallurgical characterisation of oxide and sulphide ore domains by several orders of magnitude.

1.2 Thesis aims and objectives

The primary objectives of this thesis are two-fold: 1) increase the geological understanding of the Productora deposit and revise the genetic model. 2) advance the knowledge of deposit-wide mineralogy and Cu-speciation for the purposes of understanding processing characteristics. Within this framework, key aims of this study include:

1. Describe major lithologies and interpret their distribution on key sections in order to develop a revised geological model for the Productora Cu-Au-Mo deposit

2. Describe the hydrothermal breccias, alteration assemblages, veins and mineralisation at Productora, establish timing relationships and determine the absolute age of mineralisation

3. Constrain the physiochemical environment of hydrothermal breccias, alteration, veins and related ore deposition, and fluid source(s)

4. Determine the deportment of Au

5. Calculate modal mineralogy from multi-element geochemical assays in order to constrain mineralogical variability across each study section and the whole deposit

6. Extrapolate Cu-speciation classification, in terms of oxide, transitional or sulphide, using multi-element geochemical data in order to define geometallurgical domains on each study section and within the broader deposit

7. Synthesise results into a genetic model for Productora and highlight aspects that may aid exploration at the Productora camp and regional scales within the Mesozoic mineralisation belt

1.3 Approach and methods

The objectives outlined in section 1.2 have been achieved through a combination of literature review, field work, laboratory analyses and numerical modelling. Geological observations and interpretations are largely limited to two study sections (at 6,822,215 mN and 6,820,850 mN) due to the availability of drill core. The study sections provide geological control sections upon which geometallurgical studies have been based.

1.3.1 Field work

Two field seasons were undertaken in Chile totalling ten weeks (February 2014 and November 2014). The principal objective of the field work was to construct two representative cross sections through the deposit at 6,822,215 mN and 6,820,850 mN and document the breccias, hydrothermal alteration and mineralisation, and their spatial distribution. Limited drill core was available as a result of Hot Chili Ltd's whole core assay protocols. Since geometallurgical core was stored in cold storage in Santiago, field time was split between Productora and Santiago. A total of 16 drill holes (2,797 m) were graphically logged following the methods of McPhie et al. (1993) and Blackwell (2010) in order to consistently

record the salient features. Six days of reconnaissance mapping were undertaken in order to familiarise with the outcropping geology. A total of 218 samples were collected from drill core (n = 177), reverse circulation cuttings (n = 2), laboratory rejects (n = 17) and surface rock chips (n = 22).

1.3.2 Laboratory work

Laboratory work was conducted on samples in order to further characterise lithotypes, hydrothermal breccias, alteration and veins. Detailed method statements are provided in later chapters, but are summarised briefly here. A total of 49 polished thin sections were prepared at the University of Tasmania's lapidary facility. Polished thin sections were examined in transmitted and reflected light in order to identify alteration minerals, breccia cement and vein assemblages, and their cross cutting relationships. The author also reviewed 27 ground slabs, 19 polished blocks and 218 hand specimens. Staining for K-feldspar (n = 16) and Ca-feldspars (n = 30) was conducted at University of Tasmania on selected thins section offcuts, rock chips and drill core samples. A total of 37 short-wave infrared (SWIR) spectra were measured using the ASD Terraspec instrument at CODES, University of Tasmania. Spectra were interpreted using The Spectral Geologist Professional© (TSG) version 5.03.002 software by comparison to a reference database. Samples were characterised using the electron microprobe (EMPA) and scanning electron microscope (SEM) at the Central Sciences Laboratory (CSL), University of Tasmania. A total of seven samples were analysed by EMPA in order to determine mineral compositions. Five samples were analysed using scanning SEM to characterise Cu-wad (n = 1) and biotite-chlorite (n = 4) relationships.

In order to characterise intensely altered rocks, hand specimen samples, including core slabs and thin section off cuts, were mapped using the Bruker M4 Tornado micro-XRF element mapper at the CSIRO Mineral Resources Flagship, Perth, Australia. Data were post-processed using Bruker M4 Tornado analysis software. Ten samples were also mapped using the synchrotron XRF at the XFM beamline, Australian Synchrotron, Melbourne, in order to determine Au deportment. Synchrotron data were processed using the GeoPIXE software suite by Dr Louise Fisher and Dr Mark Pearce of CSIRO Mineral Resources Flagship, Perth.

Stable (S) and radiogenic (Pb, Sr and Nd) isotopes for hydrothermal minerals were analysed in order to constrain fluid source(s) at Productora. A total of 48 paragenetically constrained mineral samples were submitted to Christine Cook at the CSL, University of Tasmania, Australia, for sulphur isotope analyses. Mineral separates of tourmaline (n = 8) and epidote (n = 1) were submitted to Dr. Roland Maas at University of Melbourne for Sr (n = 9) and Nd analyses (n = 1). Eight paragenetically constrained samples of pyrite were prepared as polished 25 mm diameter mounts for Pb isotope analyses by laser ablation inductively coupled plasma mass spectrometry (LA-ICP-MS) at CODES, University of Tasmania.

Geochronology studies were undertaken in order to constrain the absolute ages of magmatism, volcanism and mineralisation at Productora and the neighbouring Alice porphyry. Five samples were submitted for U-Pb dating of zircon at CODES, University of Tasmania. Two samples were submitted to Dr Robert Creaser, University of Alberta for Re-Os dating of molybdenite.

1.3.3 Numerical modelling and machine learning

Numerical modelling was conducted using the following data sets provided by Hot Chili Ltd and detailed below: semi-quantitative X-ray diffraction (QXRD), multi-element geochemistry by inductively coupled plasma atomic emission spectrometry and mass spectrometry (ICP-AES and ICP-MS), and sequential leach. Numerical models were generated in Microsoft Excel® (2010) using the Solver add-in. Machine learning on was conducted using open source machine learning Java software Waikato Environment for Knowledge Analysis© (WEKA) version 3.6.11. Machine learning algorithms were applied to unseen data using code written in Python™.

1.3.3.1 Data sets

Hot Chili Ltd provided access to all geological and metallurgical data during the course of the study including geological logging, existing alteration models and classification, 33-element geochemical assay data, hardness testing and recovery data. A sampling program was devised early in the project, in consultation with Hot Chili Ltd, to collect additional multi-element (48-elements by ICP-AES/MS), sequential leach and QXRD data to support the current study (Table 1.1). A total of 1720 sample intervals were selected from two study cross sections through the deposit at 6,822,215 mN and 6,820,850 mN. Laboratory coarse rejects from the selected intervals were retrieved from site storage and submitted to ALS Global Ltd, La Serena, Chile where a 250 g split was taken and pulverised. A 20 g scoop of the pulverised split was taken and dispatched to Genalysis Laboratory Services Pty Ltd, Perth, Australia, for QXRD analysis. Analyses by ICP-AES/MS and sequential Cu leach were performed on the remainder at ALS Global Ltd (Figure 1.2).

Table 1.1 Analytical program provided by Hot Chili Ltd to support this research.

Method	Laboratory	Material	Sample interval	n (6,822,215 mN)	n (6,820,850 mN)
48-element ICP-AES/MS	ALS Global Ltd (La Serena, Chile)	Coarse reject	1 in 4	880	767
Sequential Cu-leach	ALS Global Ltd (La Serena, Chile)	Coarse reject	1 in 4	137	222
QXRD	Genalysis Laboratory Services Pty Ltd (Perth, Australia)	Pulp	1 in 8	349	276

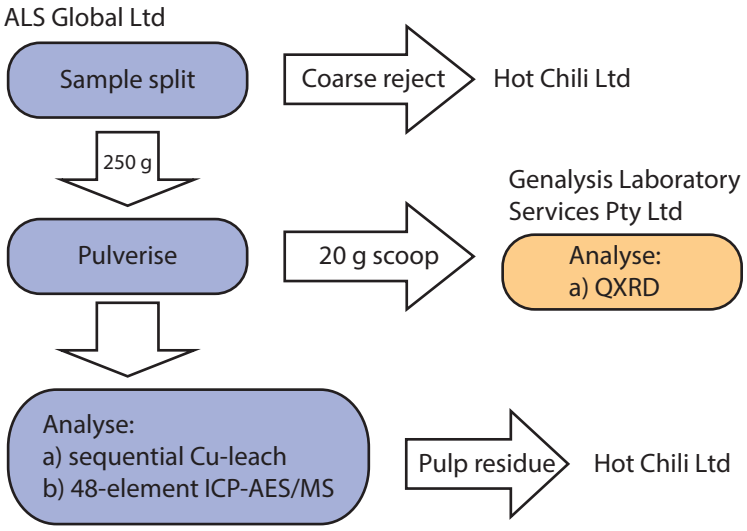

Figure 1.2 Preparation and analysis of coarse reject samples selected from section 6,822,215 mN and 6,820,850 mN.

Whole rock multi-element geochemistry

Hot Chili Ltd assay protocols include analysis of 33-elements by ICP-AES as standard on every 1 m assay interval, method description provided in Appendix A1. Additional multi-element data was required to conduct immobile element litho-geochemical discrimination on the study sections. Specifically Hf, Nb, Sc and Zr were required elements that were missing from the pre-existing assay suite. A total of 1642 samples, from every fourth 1 m interval down hole, were submitted to ALS Global Ltd for 48-element analysis by ICP-AES/MS (method description in Appendix A2).

Sequential Cu leach

An additional 359 samples from section 6,822,215 mN and 6,820,850 mN were analysed by sequential Cu leach in order to a) provide a training set for extrapolation and b) constrain Cu-speciation on the two control sections. Method description provided in Appendix A3. Samples were selected from every fourth meter between surface and the top of sulphide (as indicated by logged weathering) from selected drill holes on section 6,822,218 mN and 6,820,850 mN.

QXRD data

A training set of measured model mineralogy by QXRD was acquired from 625 laboratory pulp reject samples submitted to Genalysis Laboratory Services Pty Ltd, Perth, Australia. Samples were selected from every eighth 1 m interval of the selected drill holes on sections 6,822,215 mN and 6,820,850 mN. Detailed method description accompanies application of the data set in section 5.4.1.

1.4 Thesis organisation

Following this introduction, there are seven chapters that describe and interpret the Productora Cu-Au-Mo deposit and present novel approaches to geometallurgical modelling in order to characterise mineralogical variability and advance ore body knowledge at the Productora Cu-Au-Mo deposit:

- Chapter 2 reviews the Mesozoic geology and metallogeny of northern Chile, with emphasis on the current understanding of the relationship between magnetite-apatite, IOCG and porphyry deposit types
- Chapter 3 describes the local geology at Productora based on observations from two cross sections through the deposit at 6,822,215 mN and 6,820,850 mN. The geology is presented in the context of deposit-scale observations by previous workers
- Chapter 4 describes the hydrothermal breccias and associated alteration, and mineralisation observed on the two study sections. Breccias are classified based on texture and mineralogy. Discussion is focussed around breccia genesis, physiochemical conditions inferred from the observed mineralogy, and gold deposition
- Chapter 5 presents numerical models of deposit wide modal mineralogy calculated from 33-element ICP-AES geochemical data
- Chapter 6 presents a novel approach to predicting Cu-speciation (in terms of oxide, transitional and sulphide) for every assay interval using geochemical data and machine learning algorithms
- Chapter 7 presents new stable (S) and radiogenic (Pb, Sr and Nd) isotope data for hydrothermal minerals from the Productora deposit. These data sets are used to inform interpretations of fluid sources and to constrain physiochemical conditions and depositional mechanisms at Productora
- Chapter 8 concludes the thesis by presenting a revised genetic model for the formation of the Productora Cu-Au-Mo deposit with exploration and processing implications. The genetic model is discussed in the context of current models for Andean IOCG and porphyry-Cu deposits.

1.5 Location and access

The Productora deposit is located in the Coastal Cordillera of Region III, northern Chile at latitude 28°42'S and longitude 70°48'W or WGS84 (zone 19) 6,822,500 mN, 323,500 mE (Figure 1.1). The nearest township is Vallenar, 17 km to the north. The deposit is situated in the Productora basin, partially covered by Quaternary gravels. Elevations range between 600 m and 900 m above sea level. Productora is accessible by four-wheel drive vehicle year-round via the Ruta Cinco Highway south of Vallenar and a well maintained gravel road.

The Productora project is 100% owned by a Chilean incorporated company named Sociedad Minera El Águila Ltd (SMEA). SMEA is a joint venture company, 80 % owned by Sociedad Minera El Corazón Ltd (a 100% subsidiary of Hot Chili Limited), and 20 % owned by CMP Productora (a 100% subsidiary of Compañía Minera del Pacífico S.A (CMP).

1.6 Productora exploration and mining history

The Productora camp has a long mining history for Fe, Cu and Au extending back to pre-Hispanic times. Hot Chili Ltd, completed acquisition of the main tenement package in 2010. Historical Fe mining has occurred at the La Chulula, La Bandera, Mariposa, Carmen, and La Negra mines. Copper mining in the past century has occurred regionally and locally at the Productora and Santa Innes mines (operated by Playa Brava), Remolina, and Montserrat mines. In addition, there are more than 80 smaller pits, workings, or mineralised outcrops in the project area containing Fe, Cu or Au mineralisation (Hot Chili Ltd, pers. comm., 2016). Exploration activities at Productora prior to 2010 are summarised in Table 1.2.

Following acquisition of the tenement package in 2010, Hot Chili Ltd commenced an extensive 80 x 40 m drill out. Approximately 160,000 m of drilling was completed over four years. A resource of 214.3 Mt grading 0.48 % Cu, 0.1 g/t Au and 138 ppm Mo was announced in March 2014 (Hot Chili Ltd, 2014). A scoping study was completed in 2013 and pre-feasibility study completed in early 2016 with an upgraded resource of 236.6 Mt grading 0.48 % Cu, 0.10 g/t Au and 135 ppm Mo (Hot Chili Ltd, 2016) which included the Alice porphyry discovery made in late 2014. Recent discoveries at the deposit include a series of Au-bearing veins located south of the Productora Cu-Au-Mo deposit. At the time of writing, exploration was focussed on delineating the Au-bearing veins and exploring further porphyry-Cu potential at the camp scale.

Table 1.2 Summary of exploration activities and research at Productora. Compiled from Fox (2000) and Hot Chili Ltd pers. comm. (2014).

Date	Activity
Chilean Commission for Nuclear Energy (CCHEN)	
1980s	Uranium exploration focused on near-surface secondary-U potential: 10 diamond drill holes (35-100 m) — minor uranium oxide discovered, mapping, surface geochemical sampling, ground spectrometry and magnetometry, trenching, drilling (28 shallow percussion holes) and resource estimation Cu-Mo-U anomalies defined by soil sampling, trench assays returned 7 m @ 1820 ppm U Near-surface U mineralisation defined over 2km within a zone of hydrothermal alteration 3km long by 500m to 800m wide, trending 010°
General Minerals Corporation (GMC)	
1995-1999	Candelaria-style IOCG exploration
1996	Mapping of original tenement package (75 hectare, 1300 m x 500 m)
1997	Reconnaissance mapping 1:10,000 scale; 8 reverse circulation drill holes (PR-1 to PR-8) for 2028 m in original tenement package close to the Productora and Santa Innes mines; intercepts of 30-70 m at 0.3-0.6 %Cu with elevated Au, Mo, Co, U and REE; reflected light and SEM analyses
1997-'98	Trench 1 - 1.6 km south-southwest of Productora Mine: 110m trench, no sulfides or oxides. Trench 2 - 100m northwest of trench 1: 120m long, high Cu values returned locally (4.9 % Cu, 263 ppb Au and 83 ppm La) Trench 3 - West of Productora Mine (down slope): 140m long, averaged 0.36 % Cu (maximum 1.3 % Cu), >300ppb Au (maximum 721 ppb Au) and >100ppm La (maximum 563 ppm La)
1998	Detailed mapping 1:10,000 and 1:5,000
General Minerals Corporation (GMC) and Teck Corporation joint venture	
1999	Targeted secondary Cu mineralisation in south of property and Productora basin; induced polarisation (IP) survey indicated 6.1km long by 2km wide linear anomaly; 11 reverse circulation drill holes for 2848 m (PR-9 to PR-19); highest grade intercepts from hypogene chalcopyrite and only minor secondary Cu; Cu-Au-Mo-U mineralisation was found to be associated with iron oxides and strong potassic (K-feldspar) alteration
Playa Brava	
2008-2013	Small underground Cu-mine; pre-mining resource estimate 2.5 Mt at 1.5–2 % Cu and 0.3–0.5 g/t Au
Hot Chili Ltd	
2010	Tenement consolidation; historical data compilation and validation, mapping and soil sampling, aero-magnetic and radiometric surveys; surface mapping (Beeson et al., 2012); systematic 80x40 m drill out
2011	First resource estimate (central lease only):
2013	JORC compliant resource: 214.3 Mt grading 0.48 % Cu, 0.1 g/t Au and 138 ppm Mo
2014	Systematic 400 m x 400 m soil sampling programme; Alice prophyry discovery
2015	IP and magnetotelluric surveys, Re-$Os_{molybdenite}$ geochronology (Alice mineralisation)
2016	JORC compliant resource 236.6 Mt grading 0.48 % Cu, 0.10 g/t Au and 135 ppm Mo; pre-feasibility study

1.7 Previous research of the Productora deposit

Geology and mineralisation at the Productora deposit were first documented in an MSc study by Fox (2000) titled 'Fe-oxide (Cu-U-Au-REE) mineralisation and alteration at the Productora prospect'. She provided the most comprehensive documentation of the geology of the Productora deposit prior to the current study. Key outcomes included geological map and cross section interpretations, alteration paragenesis and geochronology (^{39}Ar-$^{40}Ar_{K\text{-feldspar}}$ and U-Pb_{zircon}), alteration map and cross section

interpretations, volcanic stratigraphy interpretation, description and dating of the Cachiyuyito and Ruta Cinco intrusions, sulphur isotope analyses, mass balance evaluations, comparison to other regional deposit styles and interpretations of the geological history and genetic model. Fox (2000) concluded that Productora was similar to the Candelaria deposit — a magnetite-dominant IOCG with significant sulphide mineralisation associated with potassic alteration. Magnetite-apatite mineralisation at Productora was interpreted to be part of the Cachiyuyito hydrothermal system, emplaced at 129.8 ± 0.1 Ma ($U\text{-}Pb_{zircon}$). The Ruta Cinco border phase was dated by Fox (2000) at 96.1 ± 0.2 Ma ($U\text{-}Pb_{zircon}$) and hydrothermal K-feldspar associated with Cu mineralisation was dated at 91.4 ± 0.2 Ma ($^{39}Ar\text{-}^{40}Ar_{K\text{-}feldspar}$). Fox (2000) speculated that regional evaporite deposits may be a source of boron for abundant tourmaline and dumortierite but that magmatic fluids were the likely sulphur source.

Ray and Dick (2002) summarised previous work at Productora, including a number of unpublished company reports. They described the lithologies, structure, mineralisation and alteration and presented revised geology and alteration maps and geological history. They acknowledged similarities with Candelaria and the Punta del Cobre district but also highlighted differences including the spatial association of alteration and Fe-oxide mineralisation and lack of garnet - pyroxene - scapolite skarn at Productora. They also noted similarities between alteration at Productora and other Au and magnetite-rich porphyry systems. The genetic model proposed by Ray and Dick (2002) invokes six stages of hydrothermal alteration, with three discrete styles of Fe-oxide mineralisation, associated spatially with the Cachiyuyito stock.

Between July 2009 and May 2012, sampling and detailed mapping (1:2,500 scale) was performed across Productora by Beeson et al. (2012) on behalf of Hot Chili Ltd. Geological observations included systematic documentation of lithology, structure, alteration mineralogy, alteration intensity, strain intensity, scintillometer readings, sample locations and photographs of key geological features. Beeson et al. (2012) presented the most comprehensive mapping campaign to date, with significantly more detailed mapping of lithologies and structure than previous workers. Beeson et al. (2012) also proposed a genetic model for the deposit formation which included a structural interpretation. Beeson et al. (2012) agreed with previous workers regarding the association of magnetite-apatite mineralisation with the Cachiyuyito stock, but explicitly proposed that Cu-Au-Mo mineralisation was genetically associated with the Ruta Cinco intrusion.

In-house studies implemented by Hot Chili Ltd include preparation of polished blocks and thin sections with corresponding petrographic descriptions by Universidad Católica del Norte, alteration geochemistry modelling (S. Halley and W. Potma, pers. comm., 2014), induced polarization surveys and

geochronology (Re-Os on molybdenite from Alice porphyry). Independent consultants including Scott Halley, Greg Hall, John Beeson, John Dilles and Richard Sillitoe have visited the project at Hot Chili's request and provided technical reports. As part of the current study several posters, conference abstracts and extended abstracts have been published (Escolme et al., 2014; 2015a and b; 2016).

1.8 Background information and details

- Throughout this thesis samples are refereed to by sample identification number, drill hole name and sample depth. A compilation of samples numbers, drill hole numbers and UTM coordinates are provided in Appendix A4
- All coordinates are for datum WGS84, UTM zone 19
- Grade shells presented in this thesis were generated from drill hole data using Leapfrog Geo version 3.1.0 interpolant function and are not representative of Hot Chili Ltd resource wireframes or resource grade models
- The term 'ore' is used to refer to mineralised rock and domains of mineralised rock at Productora which may or may not be economic
- The term 'Cu-oxide' is used sensu lato to refer to non-sulphide minerals commonly found in the oxide weathering zone (Chávez, 2000) and encompasses a variety of Cu-bearing silicate and oxide minerals.

Chapter 2: Mesozoic Geology and Metallogeny of Northern Chile

2.1 Introduction

Northern Chile (18°S to 34°S) has a history of mineral exploitation dating back to pre-colonial times, when copper (Cu) was produced by the Incas from native copper and Cu-rich minerals. The Spanish mined Cu and precious metals from 1541-1810. In recent times, Chile has become the world's largest producer of Cu and second largest of molybdenum (Mo), owing to the bulk mining of enormous low grade, high tonnage Cenozoic porphyry deposits such as Rio Blanco-Los Bronces, Chuquicamata and El Teniente (Maksaev et al., 2007).

The Mesozoic and Cenozoic metallogeny of northern Chile is characterized by hydrothermal mineralisation associated with arc magmatism along the convergent South American plate margin. The Andean tectonic cycle has led to the formation of orogen-parallel metallogenic belts, each representing discrete epochs of mineralisation characterised by distinctive deposit styles and a stepped eastward younging of the belts (Sillitoe and Perelló, 2005; Figure 2.1). The Mesozoic saw a range of deposit styles forming under extensional conditions in central and northern Chile, including; small porphyry Cu deposits, manto style Cu (also known as stratabound), iron oxide-Cu-Au (IOCG) and precious metal epithermal systems (Camus, 2002). Cenozoic mineralisation in the same region has been dominated by large porphyry Cu-Mo deposits.

The Mesozoic mineral systems in Northern Chile formed within a convergent tectonic regime where evolving subduction style, magmatic arcs and associated back-arc basin stratigraphy, plutonic complexes and the crustal scale syn-arc strike-slip Atacama Fault System (AFS) evolved in response to prevailing geodynamic conditions. In order to provide background and context to the Mesozoic metallogeny of northern Chile, these major themes are reviewed. Deposit styles that formed during the Mesozoic are discussed, with special consideration to the relationships between deposit styles.

2.2 The Andean tectonic cycle

The evolution of the central Andean Cordillera began with a period of terrane accretion during the Paleozoic when micro-continents, including the Chilenia terrane, were accreted onto the western South American continental margin, which was then part of the Gondwana supercontinent (Mpodozis and Ramos, 1990). At the end of the Paleozoic, lateral growth of the continent by accretion terminated and a subduction zone formed along the western margin of the accreted terrane, marking the beginning of the Andean orogenic cycle (Mpodozis and Ramos, 1990; Coira et al., 1982). The present day Nazca plate, and previously the Aluk (Phoenix) plate (Larson and Pitman, 1972), have been subducted orthogonally under the South American plate, from Panama in the North to Patagonia in the South (Figure 2.2).

2.2.1 Subduction geometry

Present day Chile is characterised by Chilean-style low angle subduction (Mpodozis and Ramos, 1990). There are, however, three segments of flat slab subduction along the present day South American

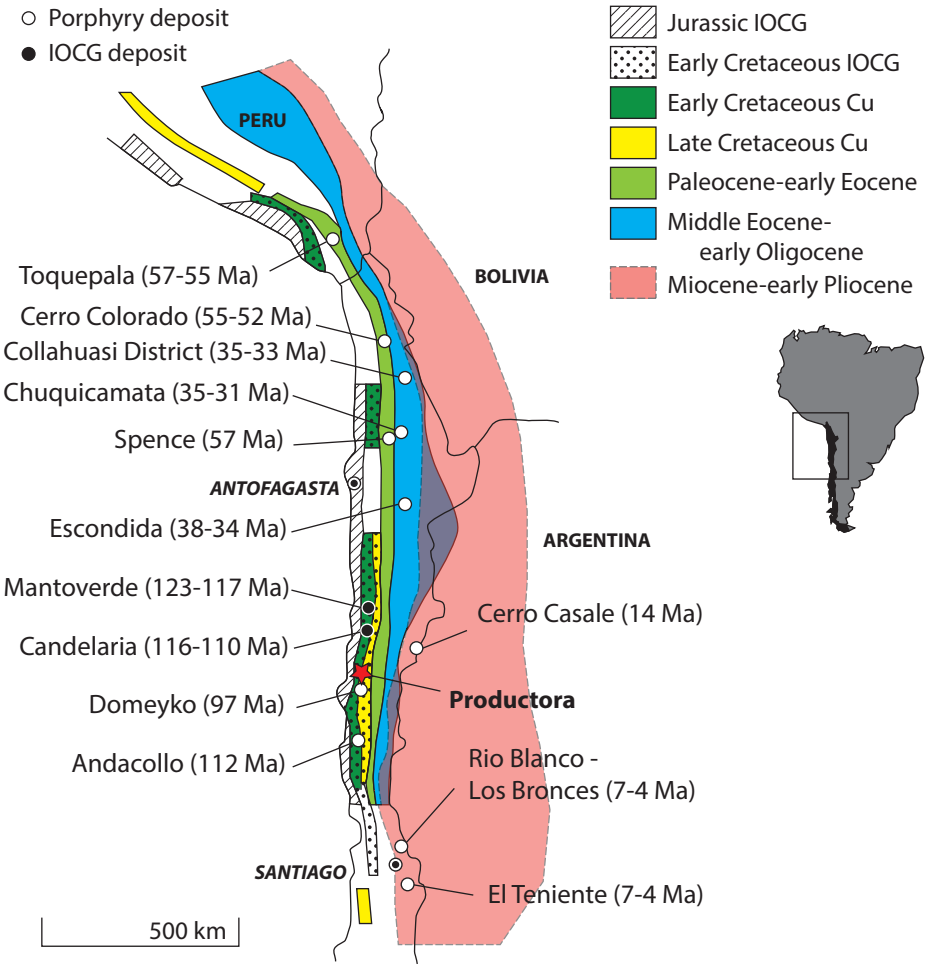

Figure 2.1 Orogen parallel metallogenic belts of the Andes, each representing discrete epochs of Cu mineralization characterized by deposit style and a stepped eastward younging (modified from Sillitoe and Perelló, 2005).

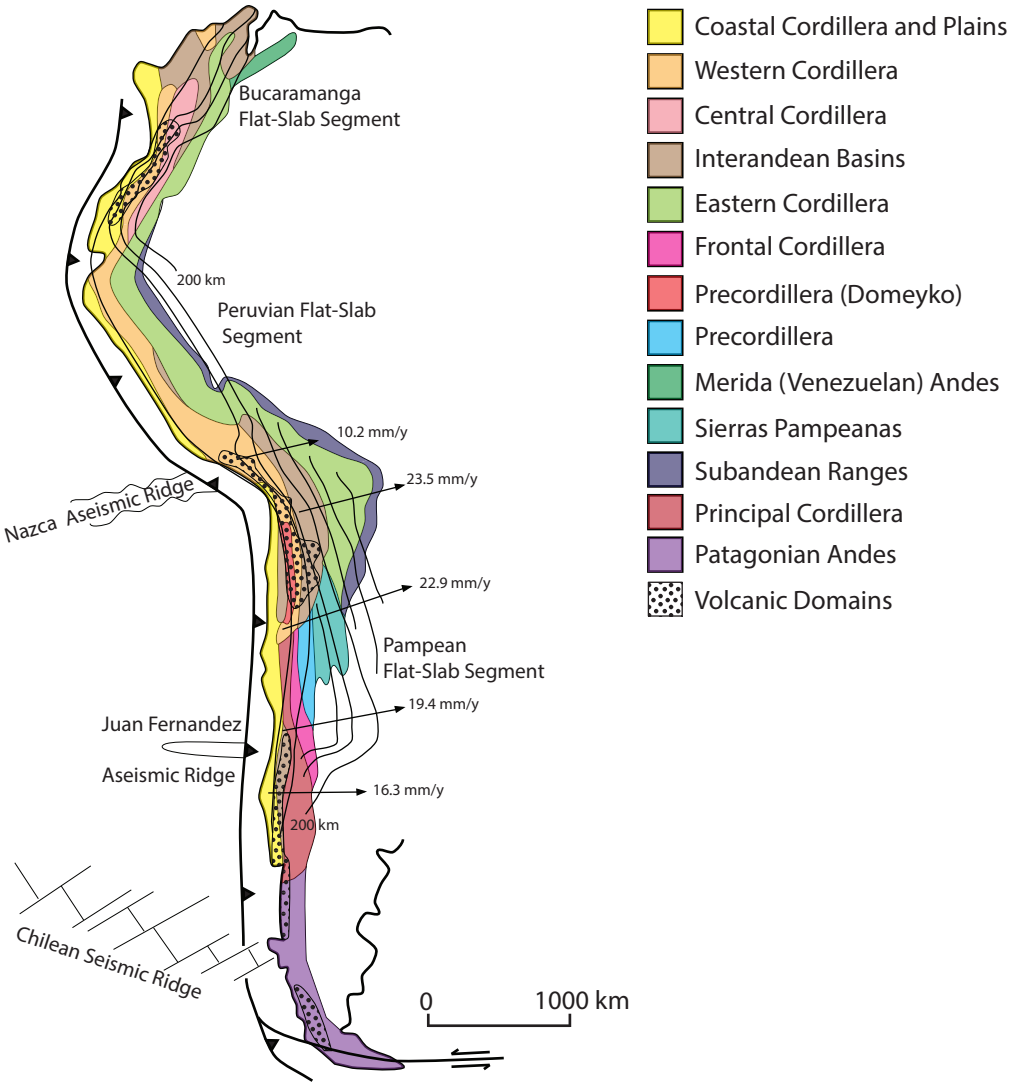

Figure 2.2 Major physiographic provinces and geophysical features along the Andes. Shape of subducted oceanic plate shown by contours in kilometers, zones without volcanism occur above the flat slab segments. Modified from Ramos (1999) and Sillitoe and Perelló (2005).

subduction zone; the Bucaramanga, Peruvian and Pampean flat slab segments (Figure 2.2). The Pampean flat slab segment, extends for a strike length of approximately 300 km below northern Chile (27° to 33°S). The phenomenon of flat slab subduction is thought to be associated with the subduction of thickened buoyant crust, for example oceanic plateaus or ridges such as the Juan Fernandez Ridge (Cross and Pilger, 1982; Gutscher et al., 2000).

Changes in subduction geometry, and subsequent stress regimes, from north to south have been influential in the complex geological and structural architecture of this region (Ramos 1999). Two discrete tectonic segments were recognised in northern Chile by Mpodozis and Ramos (1990): a northern segment (21°S to 27° S) and central-northern segment (27° to 35° S). Although experiencing a broadly similar large scale tectonic evolution the two segments show major geological differences that have influenced the metallogeny of the region (Mpodozis and Ramos, 1990; Sillitoe and Perelló, 2005).

2.2.2 Mesozoic magmatic arc and back arc basins

Following the initiation of subduction in the late Paleozoic, the South American continental margin was characterised by the formation of Mesozoic magmatic arcs with associated backarc basins under extensional-transtensional conditions (Mpodozis and Ramos, 1990; Mpodozis and Allmendinger, 1993; Scheuber and Gonzalez, 1999; Figure 2.3 A). The extensional tectonic regime has been inferred from paleogeography, tectonostratigraphy and ophiolite occurrences (Mpodozis and Ramos, 1990; Flint et al., 1993) with low-angle normal fault structural geometries and top-to-the-northeast kinematics observed in the Sierra Fraga-Puquios region, northern Chile (Mpodozis and Allmendinger, 1993). The driver for extensional geodynamics has been attributed to a high-angle, oblique subduction regime in the Mesozoic (Dallmeyer et al., 1996; Taylor et al., 1998; Scheuber and Gonzalez, 1999; Grocott and Taylor, 2002; Parada et al., 2007).

Paired magmatic arcs and backarc basins formed in what is now the Coastal Range (Coastal Cordillera; Figure 2.2) of northern Chile during Jurassic to Early Cretaceous extension and subsidence (Mpodosiz and Ramos, 1990). At this time, the geothermal gradient and heat flow through the thin (30 km) crust was high (Lucassen and Thirlwall, 1998). Widespread volcanism led to the formation of thick arc volcanic sequences (La Negra Formation; Oliveros et al., 2006). Marine intercalations within the volcanic sequences and limited detritus in the back arc basin sediments suggest the existence of lowland topography (Vergara et al., 1995; Scheuber and Gonzalez, 1999). The Tarapacá Basin in northern Chile is an example of a major extensional ensialic backarc basin, formed to the east of the magmatic arc that filled with both carbonate and clastic sediments (Charrier et al., 2007). Further south, in the central northern tectonic segment, more rapid mantle upwelling under the thin attenuated crust led to the formation of the central Chile aborted marginal basin, where large volumes of andesitic and basaltic volcanics were erupted (Aberg et al., 1984). The aborted marginal basin, which never achieved production of new crust, extends from 27° to 34° S (Mpodozis and Allmendinger, 1993). Eastward, these volcanics are intercalated with carbonate and clastic sediments of the Aconcagua platform, a narrow shelf formed along the stable continental margin (Mpodozis and Ramos, 1990). A range of deposit classes are associated with this Mesozoic extensional period including small porphyry copper, manto-type copper, iron oxide-copper-gold and magnetite-apatite deposits (Sillitoe and Perelló, 2005).

2.2.3 Basin closure and deformation

Severe deformation, beginning during the middle Cretaceous, caused closure of the back arc basins. In the North, the Tarapacá Basin was uplifted to form the Proto-Cordillera de Domeyko, and eastward thrusting across central northern Chile formed the Aconcagua fold and thrust belt (Mpodozis and

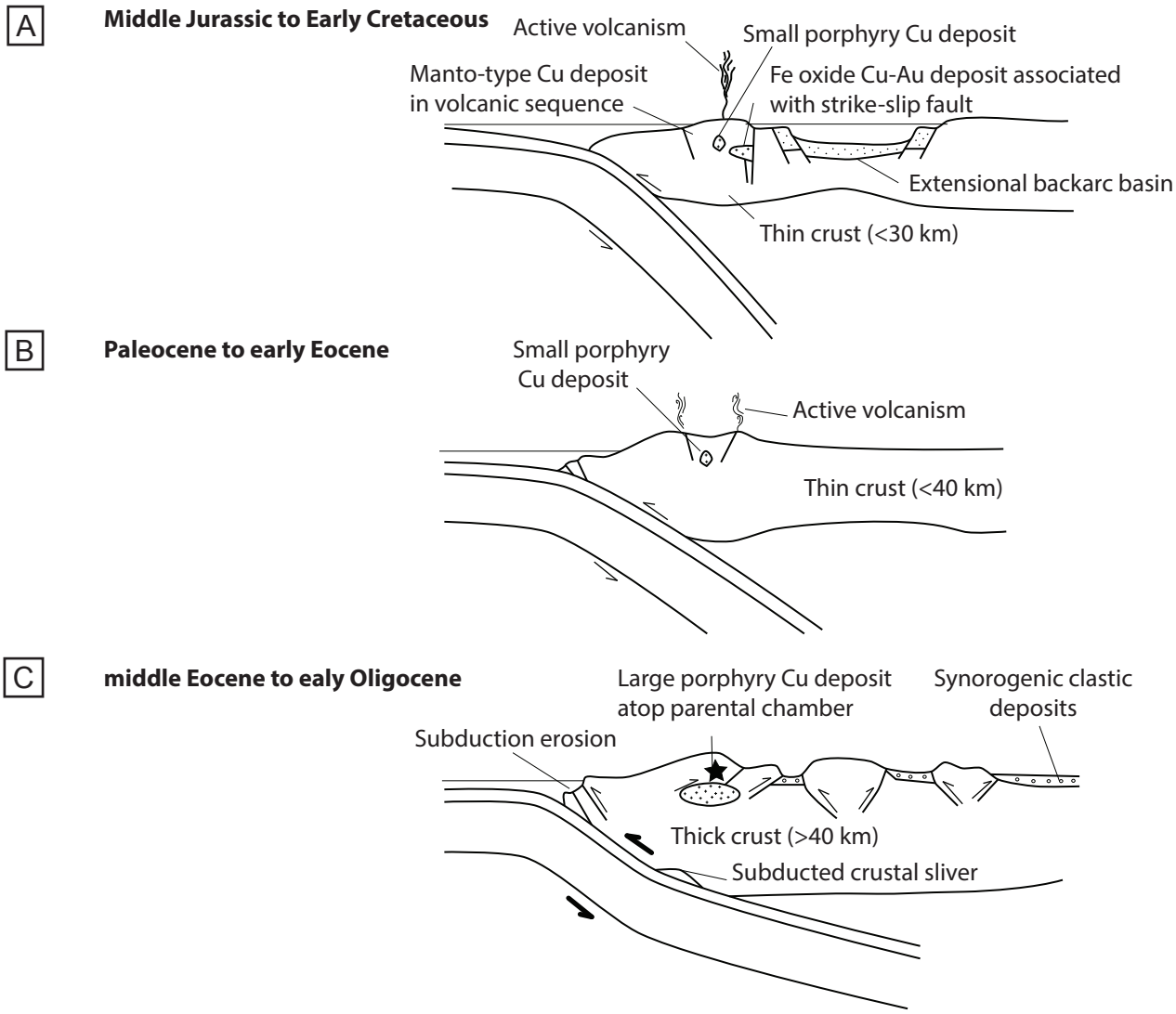

Figure 2.3 Schematic tectonomagmatic sections of the central Andean margin of northern and central Chile showing features relevant to the formation of the major metallogenic belts. A) Middle Jurassic – Early Cretaceous extensional to transtensional magmatic arc, steep subduction, thin crust and high geothermal gradient, abundant volcanism and development of paired magmatic arcs and back arc basins. IOCG, manto-type Cu and small porphyry Cu deposits formed in this environment. B) Paleocene to early Eocene, neutral to mildly extensional conditions with active volcanism and formation of small porphyry Cu deposits. C) Middle Eocene-early Oligocene and Miocene-early Pliocene belts formed under compressional conditions with low-angle subduction, crustal thickening and without significant volcanism — large porphyry Cu deposits formed under these conditions. Modified from Sillitoe and Perelló (2005).

Ramos, 1990). A broad zone of deformation extending 1000 km from the trench above the Pampean flat slab segment suggests that the compressional tectonic regime, prevalent by the mid Tertiary, was caused by shallowing of the subduction angle during the Late Cretaceous (Barazangi and Isacks, 1979; Pilger, 1981; Ramos, 1999; Ramos and Folguera, 2009). It has been estimated that 3 to 5 times more seismic energy is released above flat slab segments (Gutscher et al., 2000) and may be a key driver for significant crustal shortening (up to 320 km across northern Chile and Bolivia) and thickening in the overriding plate (Schmitz, 1994; Kley et al., 1999). Today the thickest Andean crust (70–74 km) is located in northern Chile, approximately 20 °S (Beck et al., 1996). Here uplift of the foreland Sierras Pampeanas (Jordan et al., 1983) has generated the highest mountains of the main Andes – the Aconcagua Massif. Ranging to

over 7,000 m, the central Chilean Andes are the highest mountains in a non-collisional plate margin (Mpodozis and Ramos, 1990).

Crustal thickening and shallowing subduction angle in the Late Cretaceous caused the magmatic arc to migrate eastward from its Jurassic position, in the present day Coastal Cordillera, to its Quaternary position along the Argentina-Chile border (Ramos, 1999). The onset of this compressional tectonic regime caused volcanism to cease (Ramos, 1999) and led to more evolved magmas and diminished formation of IOCG, massive magnetite and manto-type Cu deposits (Sillitoe, 2003). The suppression in volcanism permitted large fluid-rich mantle derived magma chambers to form in relatively shallow crustal levels, producing large porphyry copper deposits during the Tertiary (Sillitoe and Perelló, 2005; Figure 2.3 C).

Since the late Cenozoic, active volcanism has persisted in northern-most Chile along the Western Cordillera, north of the flat slab segment at 26 °S. Strato-volcanoes predominate in this region, generating andesite and dacite lavas (Ramos, 1999; Figure 2.2). The magmas are mantle-derived but underwent extensive geochemical modification on their ascent through the thickened crust (Ramos, 1999).

2.3 Mesozoic tectonostratigraphy

Andean stratigraphy provides an insight into major geodynamic episodes, such as supercontinent breakup and tectonic cycles therein, through regional unconformities and paleogeographic changes (Charrier et al., 2007). The current Andean tectonic cycle began in the Early Jurassic (Coira et al. 1982) when magmatic arcs and back arc basins were constructed along the Gondwana continental margin on a basement of Triassic volcano-sedimentary sequences, Permian granitoids (Charrier et al., 2007) and the Paleozoic subduction complex (Mpodozis and Ramos, 1990). The stratigraphy of the current Andean cycle reflects two phases; an earlier period (Early Jurassic to Late Cretacous) of intense arc activity followed by a Late Cretaceous to Cenozoic eastward migration of the magmatic arc and foreland basin development (Charrier et al., 2007) This review focuses on the Early Jurassic to Late Cretaceous stratigraphy, which host Mesozoic mineralisation in northern Chile.

The geodynamics of the Andean margin in northern Chile during the Early Jurassic to Late Cretaceous were dominated by extensional tectonics leading to intense arc magmatism, thick basin sediment sequences and emplacement of large batholiths (Charrier et al., 2007). Extensive volcanic sequences were deposited; these are comparable in volume to the smaller of the Large Igneous Provinces (LIP). Mesozoic volcanism in Chile therefore represents a major magmatic event in Earth history (Oliveros et al., 2006; Sillitoe, 2003). The stratigraphy of this period has been further divided into two substages

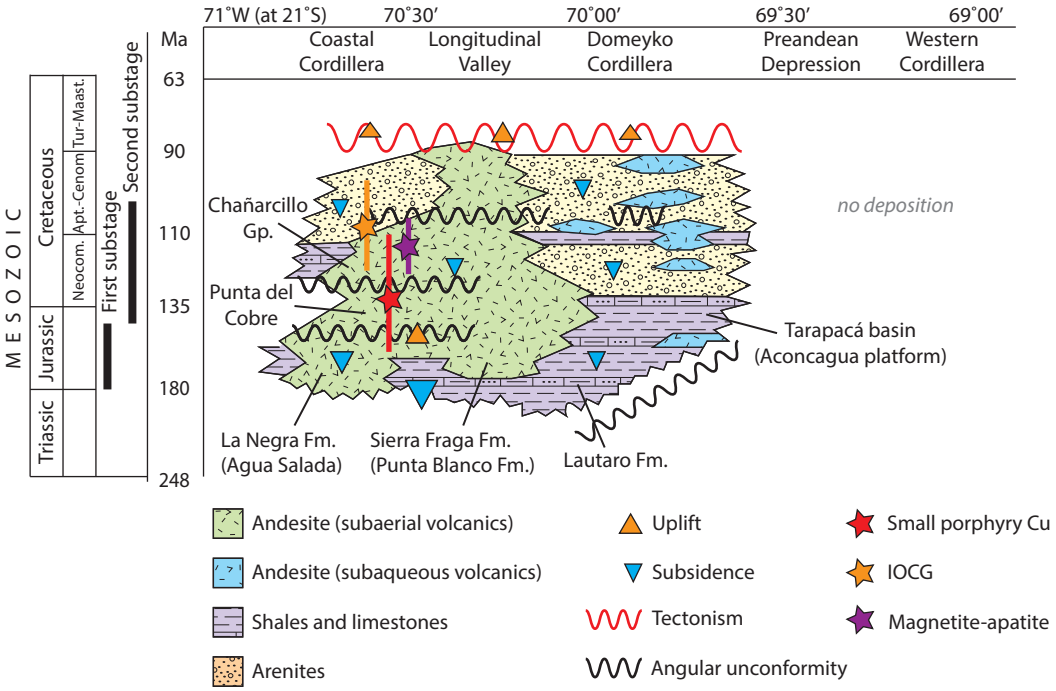

Figure 2.4 Generalised time-space diagram for Mesozoic northern Chile (21°-25°S) showing the relationship between stratigraphic units, tectonic events and mineralization. Southern (~29 °S) stratigraphic equivalents indicated by parentheses. Modified from Ireland (2010). Spatial distribution of magmatic products is based on compilation of radiometric ages by Scheuber et al. (1994). Additional details from Coira et al. (1982), Herve et al. (1988), Bogdanic et al. (1990), Scheuber and Andriessen (1990), Scheuber and Reutter (1992), Charrier and Muñoz (1994), Prinz et al. (1994), Scheuber et al. (1995), Bahlberg and Hervé (1997), Scheuber and Gonzalez (1999), Haschke et al. (2002) and Franz et al. (2006).

by Charrier et al. (2007): (1) a late Early Jurassic to Kimmeridgian phase of intense arc activity with transgressive-regressive marine cycles in the backarc basins; (2) a period of lesser magmatic arc activity in the Kimmeridgian to Aptian-Albian with continued marine cycles (Figure 2.4).

The extensive arc volcanics of the first substage are several thousand meters thick and overlie the Triassic basement (Charrier et al., 2007). In the northern extent of the Coastal Cordillera, the stratigraphy is dominated by the La Negra Formation, a 5,000 to 10,000 m thick pile of sub-aerial to shallow marine volcanic rocks (Mpodozis and Ramos, 1990; Sillitoe., 2003; Sillitoe and Perelló, 2005; Figure 2.4). Along the northern Coastal Cordillera, volcanic units, stratigraphically equivalent to La Negra formation include the Oficina Viz, Caleta Lígate, El Godo, Camaraca and Los Tarros Formations. Near La Serena (~29°S), the arc volcanics of the Coastal Cordillera are represented by the Agua Salada Volcanic Complex which is also dominated by porphyritic andesite lavas and volcaniclastics with calcareous intercalations up to 6,400 m thick (Charrier et al., 2007). For simplicity, Oliveros et al. (2006) collectively grouped these as the Early Andean Magmatic Province (EAMP). Based on $^{40}Ar/^{39}Ar$ dating of primary minerals (plagioclase, amphibole and biotite) Oliveros et al. (2006) interpreted that volcanism was contemporaneous from north to south. The EAMP is characterised by sub-aerial to locally shallow sub-marine porphyritic andesite and basaltic-andesite lavas with minor basalts, dacites, rhyolite (ignimbrites) and other volcaniclastics as well as calcareous shallow marine sedimentary deposits

(Oliveros et al., 2006). The volcanics evolved from tholeiitic to calcalkaline to late alkaline (Losert, 1974; Rogers and Hawkesworth, 1989; Oliveros et al. 2006; Charrier et al., 2007). Sr and Nd isotopic compositions ($^{87}Sr/^{86}Sr$=0.7030–0.7040, $^{143}Nd/^{144}Nd$=0.512850–0.512950) indicate mantle source with limited crustal assimilation (Rogers and Hawkesworth, 1989; Lucassen et al., 2002; Oliveros et al., 2006).

Deposits of the second substage are not widely observed in the North but are seen further south and include the late Jurassic Punta del Cobre Formation (Figure 2.4). The Punta del Cobre Formation consists of basaltic-andesites, andesite and dacite volcanic to volcaniclastic distal arc deposits. The formation's basal contact is transitional with La Negra Formation (Charrier et al., 2007) and is overlain by marine backarc deposits of the Chañarcillo Group, indicating that volcanism was continuous in the area from the Jurassic to the Early Cretaceous (Marschik and Fontboté, 2001). Early Cretaceous arc deposits are represented further south by the Arqueros and Quebrada Marquesa Formations, thick accumulations of volcaniclastic rocks, andesite and minor rhyolite lavas with marine intercalations (Charrier et al., 2007). The intercalations of lavas and marine sediments suggest that the region was a topographic low during the Early Cretaceous (Vergara et al., 1995; Scheuber and Gonzalez, 1999).

Moving eastward, the volcanic arc successions transition into more distal and thinner arc deposits of similar composition. These include the Sierra Fraga Formation, south east of Copiapo, which is the 2000 m thick distal equivalent to the extensive La Negra Fromation (Tomlinson et al., 1999). These distal deposits, represented further south by the Punta Blanca Formation, intercalate with backarc basin deposits (e.g., Lautaro Formation) which transition rapidly to deep marine facies to the east (Charrier et al., 2007).

East of the magmatic arc, the back arc basin sediments, including those of the Tarapacá Basin, unconformably overlie Triassic basement deposits (Charrier et al. 2007). These thick sedimentary sequences, including the Aconcagua platform in the South of Chile, record marine transgression-regression cycles with both marine and continental deposits (Charrier et al., 2007).

Regional alteration/metamorphism has been observed throughout the volcanic sequence of the Coastal Cordillera (Atherton and Aguirre, 1992). Secondary minerals include chlorite, epidote, quartz, calcite, titanate, sericite, actinolite, K-feldspar, zeolites, prehnite and pumpellyite (Oliveros et al., 2006). These secondary assemblages are related to low grade burial metamorphism (prehnite – pumpellyite to greenschist facies) (Aguirre et al., 1989; Atherton and Aguirre, 1992; Sillitoe and Perelló, 2005) and/or hydrothermal alteration related to plutonic intrusions (Losert, 1974; Sato, 1984; Charrier et al., 2007).

2.4 Chilean Coastal Batholith

The Chilean Coastal Batholith is composed of elongate, orogen-parallel plutons. It defines a 1,200 km magmatic belt in the Coastal Cordillera from 18°S to 38°S. Although the batholith is dominated by early S-type magmas of Late Carboniferous to Permian age that intruded the basement, arc magmatism continued through the Mesozoic and into the Cenozoic with eastward migration of increasingly I-type magmatism (Berg et al., 1983).

Major Mesozoic plutonic complexes range in age from 200 to 106 Ma (Oliveros et al., 2007), with two major phases of emplacement c. 200-127 Ma and c. 106-103 Ma (Dallmeyer et al., 1996). These intrusions are typically over 50 km long and were contemporaneous with the volcanic stratigraphy that dominates the region (Sillitoe, 2003). Age determinations indicate that magmas were emplaced episodically in a series of relatively short (3 to 14 m.y.) pulses throughout the Jurassic and Early Cretaceous (Dallmeyer et al., 1996; Sillitoe, 2003; Vásquez et al. 2011). Pulses of plutonic activity occur during periods of activity on the extensional fault systems, whereas volcanism occurs when these faults are dormant (Grocott et al., 1994).

Mesozoic igneous activity in northern Chile was bimodal, with felsic intrusions emplaced into intermediate volcanics (Parada et al., 2007). Mesozoic plutons range in composition from early gabbros and diorites to quartz diorites and monzodiorites to later tonalities and granodiorites with minor granites (Sillitoe, 2003; Parada et al., 2007). There is a broad geochemical homogeneity of calc-alkaline to high-K calc-alkaline affinities, high LILE contents relative to HFSE, Nb, Ta and Ti depletions, LREE/HREE fractionation and enrichment in Pb over Ce (Oliveros, 2007; Vásquez et al., 2011). The geochemical data indicates a depleted asthenosphere source with slab components, metasomatized by slab fluids, without significant assimilation of continental crust (Oliveros, 2007; Parada et al. 1999). Variations between plutonic and volcanic compositions are attributed to increased fractional crystallisation of plagioclase-olivine-clinopyroxene (Oliveros, 2007) and variation toward more mafic compositions through the Mesozoic are attributed to increasing contribution from the granitic crust (Vásquez et al., 2011).

The Mesozoic plutons are characterised by shallow depths of emplacement, as indicated by Al-in-hornblende barometer calculations, and rapid cooling, as indicated by similarities in age data, U-Pb on zircon, $^{40}Ar/^{39}Ar$ on hornblende and Rb-Sr on biotite (Dallmeyer et al., 1996). Emplacement is thought to be controlled by large scale extensional tectonics (Grocott et al. 1994), specifically north and northwest striking faults, with sinistral strike-slip and normal dip-slip movements (Dallmeyer et al., 1996).

2.5 Atacama Fault System

The Atacama Fault System (AFS) is a north-trending, arc parallel fault system extending over 1,000 km from Iquique (20°S) to La Serena (~30°S). It cuts volcanic and intrusive rocks of the Jurassic and Early Cretaceous magmatic arc in the Coastal Cordillera (Sillitoe and Perello, 2005; Brown et al., 1993; Figure 2.5). Development of the AFS was contemporaneous with formation of the Mesozoic arc in the Coastal Cordillera (Brown et al., 1993) and is believed to have provided the structural architecture for magma ascent (Berg et al., 1983; Scheuber and Reutter, 1992; Grocott et al., 1994). The time-space association of arc magmatism with faulting is consistent with a transtensional tectonic environment with arc normal extension and strike-slip displacement (Hervé, 1987; Scheuber and Reutter, 1992; Brown et al., 1993). Based on the orientation of the primary faults that make up the AFS, the northern extents of the system can be divided into three arcuate segments (Brown et al., 1993; Figure 2.5). Most studies focus on the central segment (e.g., Scheuber and Andriessen, 1990; Brown et al., 1993).

The sinistral strike-slip AFS system consists of discontinuous and crosscutting faults that developed in response to oblique subduction of the Phoenix (Aluk) plate. It exhibits both ductile and brittle behaviour

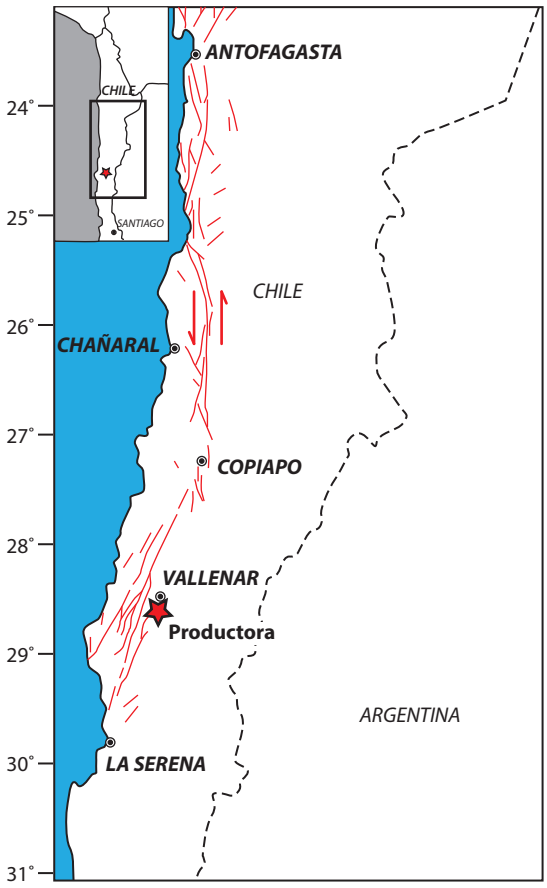

Figure 2.5 Major faults of the southern Atacama Fault System (AFS) in northern Chile with location of Productora for reference. The AFS can be divided into three arcuate segments: La Serena to Chañaral, Chañaral to Antofagasta and Antofagasta to Iquique. Modified from Brown et al. (1993).

(Hervé, 1987; Woodcock and Daly, 1986; Scheuber and Andriessen, 1990; Scheuber and Reutter, 1992; Dallmeyer et al. 1996), with brittle fabrics superimposed over ductile features (Brown et al., 1993). The overlapping faults define asymmetric, fault-bounded slabs interpreted to be sidewall rip-out structures (Brown et al., 1993; Taylor et al., 1998).

Two ductile, sinistral, strike-slip, shear zones have been recognised in the AFS between 23°15'S and 27°S (Scheuber and Andriessen, 1990; Brown et al., 1993). In the western zone, sheared rocks of Jurassic-Early Cretaceous age are interpreted to have formed under amphibolite-facies conditions and show an early dip-slip component, with down-throw of the eastern block (Brown et al., 1993). The eastern zone consists of Cretaceous mylonites, formed under greenschist facies conditions (Scheuber and Andriessen, 1990). Early Cretaceous ductile deformation caused sinistral strike-slip displacements near Antofagasta (Hervé, 1987b; Uribe, 1987; Scheuber and Andriessen, 1990). Ductile deformation is thought to have been facilitated by heating during magma intrusion and can be described as synplutonic (Grocott and Taylor, 2002). This is supported by geochronological data that indicates the plutonic complexes are the same age as the mylonitic wall rocks (Dallmeyer, 1996).

Brittle, sinistral strike-slip displacements have been inferred, through K-Ar dating of associated mineralization, to be of mid-Cretaceous age (Brown et al., 1993). The transition to brittle behaviour is attributed to crustal cooling after shut down of the magmatic arc (Brown et al., 1993), consistent with the timing relationship between the end of peak pluton emplacement and initiation of brittle faulting (Taylor et al. 1998). Intense hydrothermal mineralisation is associated with low-temperature brittle deformation (Hervé, 1987b) as a result of heat transfer into the cool upper crust by hydrothermal fluids through the fault network (Brown et al., 1993). Normal and normal-oblique motions of the AFS were synchronous with mineralisation in the middle to late Mesozoic, and it appears that second order splays of the AFS controlled mineralisation at many Cretaceous Chilean ore deposits (Sillitoe and Perelló, 2005).

2.6 Andean mineralisation epochs

Longitudinal metallogenic belts of the Chilean Andes were first proposed by Domeyko (1876). Little (1926) first gave consideration to deposit type and age of formation. More sophisticated schemes were proposed by Ruiz and Ericksen, (1962), Ruiz et al., (1965) and Clark et al., (1976). With the ever-growing database of geochronological results, a series of eastward-younging belts were delineated by Sillitoe (1988). It is now well established that the Andean Cu province consists of several orogen-parallel metallogenic belts representing restricted epochs of mineralisation (Sillitoe and Perelló, 2005). Within the central Andes, between latitudes 25°S and 36°S, five eastward younging belts are recognized (Figure

2.1); late Paleozoic to early Mesozoic, middle to late Mesozoic, Paleocene to early Eocene, middle Eocene to early Oligocene and Miocene to early Pliocene. Apart from the middle to late Mesozoic belts, porphyry Cu deposits dominate the metallogeny of the Chilean Andes. The shift in mineralisation style from IOCG and magnetite-apatite to porphyry Cu reflects a major change in prevailing tectonic conditions from extensional to compressional during the Late Cretaceous (Sillitoe and Perelló, 2005). The principal mineralisation features of each metallogenic belt, including the prevailing tectonic regime and exemplary deposits are summarized in Table 2.1.

2.7 Mesozoic mineralisation styles

Mesozoic mineralisation is characterized by a range of deposits styles, including porphyry Cu, IOCG, manto-Cu, magnetite-apatite, epithermal precious metal veins and skarn deposits. These deposits formed in an extensional to trantensional tectonic regime in the active magmatic arc of the present day Coastal Cordillera.

2.7.1 Magnetite-apatite

The Chilean Iron Belt (CIB) is a north-trending, 30-40 km wide belt containing over 40 economic, predominantly intrusion-related, Kiruna-type iron deposits. It extends for over 500 km from 25°S to 31°S and is situated to the east of the Coastal Cordillera (Oyarzun et al., 2003; Ménard, 1995), Figure 2.6. Deposits have been dated between 128 and 102 Ma (Oyarzun et al. 2003; Table 2) and are hosted in complexes of iron-rich volcanic and subvolcanic andesites that were intruded by diorites (Ménard 1995; Oyarzun et al., 2003). Deposits of the CIB show similarities in their mineralogy, texture and geochemistry (Chen, 2010). The typical paragenesis consists of magnetite ± tremolite ± apatite followed by albite/oligoclase ± clinozoisite ± chlorite ± sphene ± scapolite ± tourmaline ± pyrite, and pyrophyllite (Ménard, 1995). Magnetite is the ore mineral and forms veins and veinlets, breccias, disseminations and massive replacements (Bookstrom, 1977; Ménard, 1995; Oyarzun et al., 2003). The largest deposits of the CIB deposits include Boquerón Chañar, Los Colorados, El Algarrobo, Cristales and El Romeral with total reserves approximately 2,000 Mt (60 % Fe; Oyarzun et al. 2003). Spatially, deposits are associated with the southern segment of the AFS, which is believed to have provided structural pathways for dioritic magmas and fluids (Berg et al., 1983; Scheuber and Reutter, 1992; Grocott et al., 1994; Figure 2.6) when the tectonic regime evolved from extensional to compressional during the Cretaceous (Oyarzun et al., 2003).

Table 2.1 Summary of Andean epochs of mineralisation. Compiled from Sillitoe and Perelló (2005).

Age	Epoch	Tectonic Regime	Location	Dominant Mineri-sation Style	Deposits	Characteristics
12-4.3 Ma	Miocene to Early Pliocene	Compressional	Principal Cordillera	Porphyry Cu-Mo	El Teniente Los Pelambres Los Bronces-Rio Blanco	Multiphase stocks and hydrothermal breccia complexes; pervasive hydrothermal alteration shells; biotite- and tourmaline-rich breccia complexes emplaced in a variety of country rocks including volcanic sequences; mineralisation hosted by both veinlet stockworks and breccia matrix through large rock volumes; large scale regional tectonics and structural controls focussed magma accent and fluid flow, particularly at fault intersections
43-31 Ma	Middle Eocene to Early Oligocene	Compressional magmatic arc	Principal Cordillera	Porphyry Cu-Mo-Au	Chuquicamata Escondida Radiomiro Tomic	Major supergene oxidized and enriched zones; examples of exotic Cu deposits; related to small epizonal stocks, often associated with the Domeyko fault system; deposits occur in clusters or alignments of three or more; important structural control; deposits formed over very a brief time interval
60-50 Ma	Paleocene to Early Eocene	Neutral to mildly extensional magmatic arc	Principal Cordillera	Porphyry Cu-Mo	Cerro Colorado Spence Sierra Gorda deposits	Poorly mineralised; only those with supergene enrichment are economic; characterized by potassic, sericitic, intermediate argillic and advanced argillic alteration; typical supergene minerals include atacamite, chalcocite and chrysocolla; commonly have associated tourmaline breccia, which can also host Cu-Mo and locally Au and/or W mineralisation within matrix
132-97 Ma	Early Cretaceous	Extensional to transtentional	Coastal Cordillera	IOCG	Manto Verde Candelaria-Punta del Cobre Tocopilla	Youngest known IOCG province; hosted within volcano-sedimentary magmatic arc sequences; occur as veins and stockworks, hydrothermal breccias, calcic skarns, replacement horizon (mantos) and 'composite' styles; characterised by low Ti hydrothermal magnetite ± specular hematite with chalcopyrite plus Au and anomalous Co, U, REE, Mo, Zn, Ag; alteration typically complex and varied; generalised upward and outward zonation observed from deep magnetite-actinolite-apatite transitions to shallow specular hematite-chlorite-sericite

Table 2.1 continued.

Age	Epoch	Tectonic Regime	Location	Dominant Mineri-sation Style	Deposits	Characteristics
				Porphyry Cu-Mo and Cu-Au	Andacollo Dos Amigos	Generally small <300 Mt, low grade (up to 0.4 % Cu) and mostly uneconomic; small porphyry stocks of quartz diorite to granodiorite emplaced in the contemporaneous volcano-plutonic arc; associated with potassic (biotite, K-feldspar) alteration and intermediate argillic overprints of chlorite, sericite, illite and/or smectite assemblages; contain Mo but are relatively poor in Au (except Andacollo)
				Manto-Cu	Mantos Blancos Michilla District Lo Aguirre	Hosted in Mesozoic basaltic and andesitic, volcanic and volcano-sedimentary rocks; associated with coeval dioritic to granodioritic plutons; mineralisation occurs in stratabound disseminated bodies and steeply dipping hydrothermal breccias surrounding barren diorite intrusions with associated veins; dominant hypogene sulphide phases are bornite, chalcopyrite, chalcocite and pyrite ± covellite and digenite; hypogene mineral zonation has been observed at a number of deposits; most deposits have an upper oxidized zone but supergene enrichment only occurs at the larger deposits
				Magnetite -apatite	Boqueron Chanar Los Colorados El Algarrobo El Romeral	Intrusion related, Kiruna-type iron deposits; typical paragenesis consists of magnetite ± tremolite ± apatite followed by albite/oligoclase ± clinozoisite ± chlorite ± sphene ± scapolite ± tourmaline ± pyrite, and pyrophyllite; form veins and veinlets, breccias, disseminations
298-230 Ma	Late Paleozoic to Triassic	Extensional magmatic arc	Principal Cordillera of North western Argentina	Porphyry Cu-Mo	San Jorge deposits La Voluntad Cerro Samenta Lila	Deposits are poorly mineralised, generally <0.2 % Cu; none currently economic; suggests conditions were unfavourable for significant mineralisation; occur in less eroded parts of volcanoplutonic arc

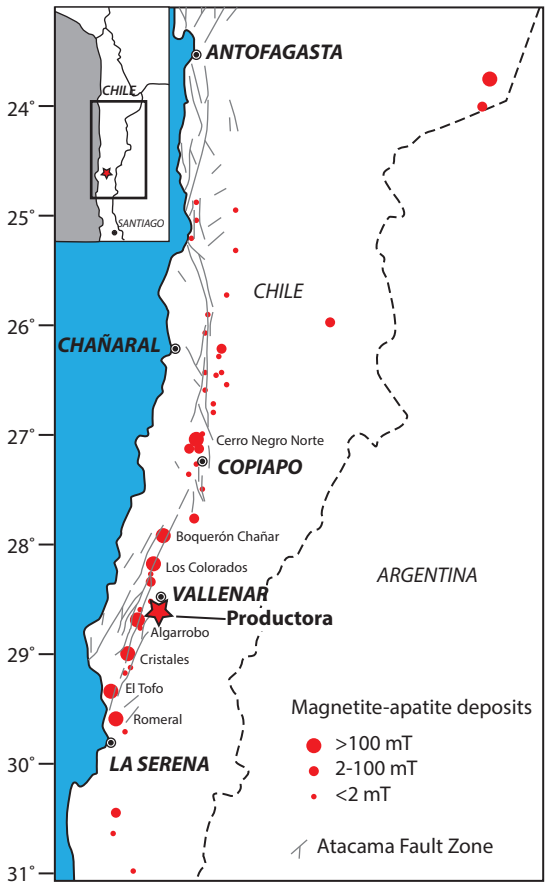

Figure 2.6 Magnetite-apatite ore deposits of the Chilean Iron Belt with the location of Productora for reference. Modified from Naslund et al., 2002.

2.7.1.1 Magnetite-apatite genetic model

The current literature regarding deposits within the CIB is centred around two main hypotheses (1) a metasomatic model associated with granodiorite pluton intrusions (Ruiz et al. 1965; Park, 1972; Bookstrom, 1977; Ménard, 1995) and (2) immiscible iron derived from magmatic differentiation and melt crystallisation (Kiruna type; Park, 1961; Travisany et al., 1995; Naslund et al., 2002, Nyström and Henríquez, 1994). More recently a magnetite froth flotation model has also been proposed (Knipping et al. 2015a and b).

In a study of the El Romeral iron mine, Bookstrom (1977) proposed that iron was remobilised from sediments in contact with the El Romeral diorite pluton. Hydrothermal deposition of magnetite and actinolite occurred at temperatures between 550°C and 475°C. At El Algarrobo, Ménard (1995) also favoured a metasomatic model but suggested iron was sourced from the clinopyroxene and orthopyroxene-bearing diorite intrusions through leaching by a supercritical saline fluid exsolved from the pluton. Deposition is proposed to have occurred with decreasing pressure and temperature along fractures.

Table 2.2 Summary of significant deposits in the Chilean Iron Belt, compiled from Naslund et al., 2002 and Oyarzun et al., 2003.

Deposit	Tonnage (Mt)	Mineralisation age (Ma)	References
Boqueron Chanar	>100	128 ± 4	Zentilli (1974)
Los Colorados	491	110 – 115	Pichon (1981), Oyarzún and Frutos (1984), Knipping et al. (2015a), Reich et al. (2016)
El Algarrobo	>100	99.6 ± 5 115.6 ± 5.8 128 ± 6.4	Montecinos (1985)
Cristales	>100		
El Romeral	451	110 ± 3 118 ± 0.2	Munizaga et al. (1985) Rojas et al. (2015)
El Tofo	>100		
Cerro Iman		102 ± 3	Zentilli (1974)
Carmen	20-100	131 ± 1.0	Gelcich et al. (2005), Gálvez (2013)
Bandurrias	20-100		
El Dorado	20-100		

Travisany et al. (1995) argued for the involvement of iron-rich magma in the formation of CIB in the Pleito-Melón district, 75 km north of La Serena. They likened the deposits to those of Kiirunavaara, Sweden (type locality for magnetite-apatite Kiruna deposits; Frietsch, 1978), and the Cenozoic deposits of El Laco, Incahuasi and Magnetita Pedernales in the Principal Cordillera, which some have argued formed through iron-rich magma injection at subvolcanic-volcanic levels (e.g. Nyström and Henríquez, 1994). The magnetite lava model remains controversial, however with Hildebrand (1986) and Hitzman et al. (1992) questioning the theoretical existence of Fe oxide-dominated magma under hypabassal conditions. Rhodes et al. (1999) argue that field, petrographic and REE evidence at El Laco indicate magnetite is associated with hydrothermal activity, which supports a metasomatic-hydrothermal origin. Sillitoe and Burrows (2002) also note textures in the El Laco Sur open pit support a replacement origin by hot, hypersaline brine. However, Knipping et al. (2015a and b) propose that textures and chemical zoning of magnetite crystals in ores from Los Colorados are consistent with magnetite crystallised from a silicate melt followed by magmatic-hydrothermal magnetite overgrowth. They propose a model of that involves crystallization of magnetite microlites from a silicate melt, nucleation of aqueous fluid bubbles on magnetite surfaces, and formation and ascent of buoyant fluid bubble-magnetite aggregates.

Barton and Johnson (1996, 2000) summerised the variety of hypotheses concerning magnetite-apatite deposits into three distinct genetic models: 1) magmatic-hydrothermal wherein key fluids are of magmatic origin, 2) terrestrial-hydrothermal wherein key fluids are basinal or surficial or nonmagmatic brines circulated by igneous or crustal heat, 3) direct crystallisation from immiscible Fe-rich melt. These models can also be invoked for IOCG deposit genesis.

2.7.2 Iron oxide-copper-gold

The Mesozoic IOCGs of the Coastal Cordillera are the youngest known IOCG province globally. They are the most economically significant Cu deposits of the Mesozoic belt of northern Chile, owing to the large reserves of the Candelaria - Punta del Cobre district and Manto Verde, which were discovered in 1986 and 1988 respectively (Maksaev et al., 2007).

The IOCG deposits of the Mesozoic can be divided into two sub-belts based on their age (Figure 2.7 and Table 2.3). The Middle-Late Jurassic (170-150 Ma) sub-belt includes Tocopilla, Guanillos, Maguayán, Montecristo-Julia, Las Animas, and an Early Cretaceous (130-110 Ma) sub-belt includes the major copper-rich deposits Candelaria, Mantoverde, Panulcillo and El Espino (Sillitoe, 2003; Chen 2010). The Early Jurassic deposits formed in a dominantly extensional environment whereas the major Early Cretaceous Cu-rich deposits formed under a transtensional to compressional regime (Sillitoe, 2003).
At the regional scale, deposits are hosted within contemporaneous volcano-sedimentary magmatic arc sequences and occur within 2 km of pluton contacts in association with faults and splays of the AFS (Sillitoe, 2003; Figure 2.7). The Late Jurassic deposits are associated with normal faults displaying

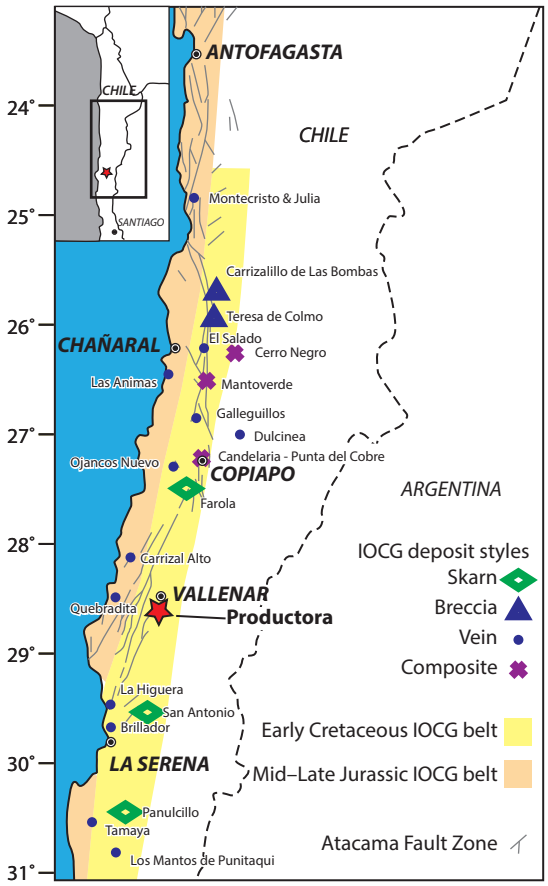

Figure 2.7 Subdivision of the Chilean IOCG province into western Middle-Late Jurassic and eastern Early Cretaceous belts showing distribution of deposit styles. Modified from Sillitoe (2003).

Table 2.3 Selected Mesozoic IOCG deposits with tonnage, grade and ages. Modified from Chen et al., 2013. Minzn = mineralisation

Sub-belt	Deposit	Tonnage (Mt)	Fe (%)	Cu (%)	Au (%)	Ag (g/t)	Minzn. age (Ma)	References
Middle-Late Jurassic	Guaillos						~167	Boric et al. (1990)
	Tocopilla	2.4	ne	3.1	trace		~165	Ruiz and Peebles (1988)
	Julia						~164	Boric et al. (1990)
	Las Animas						~162	Sillitoe (2003)
Early Cretaceous	Mantoverde	400	ne	0.52	0.11		117-128	Benavides et al. (2007)
	Candelaria	470	ne	0.95	0.22	3.1	110-116	Marschik and Fontboté (2001)
	Punta del Cobre	>120	ne	1.5	0.2-0.6		110-117	Marschik and Fontboté (2001)
	Panulcillo	~15	ne	~1.45	≤0.1		~115	Hopper and Correa (2000)
	El Espino	30	ne	1.2	0.15		~108	Sillitoe (2003)
	El Soldado	>200	ne	1.4			~108	Boric et al. (2002)
	Teresa de Colmo	70	ne	0.8	trace			Hopper and Correa (2000)
	Cerro Negro	249	ne	0.4	0.15			Sillitoe (2003)

east-side–down displacement. The Early Cretaceous deposits are localised on sinistral transtensional structures (Grocott and Taylor, 2002; Sillitoe, 2003; Figure 2.7). Candelaria is hosted by the La Negra Formation and is cut by the Lar Fault, of the southeast-verging El Bronce fold-thrust system (Marschik et al., 2000). Manto Verde was localised by the Manto Verde fault, a north-northwest splay between two north trending regional faults (Benavides et al. 2007). The structural localisation of deposits suggests that ore fluids may have been have been channelled, potentially from magma bodies, by the major fault systems, possibly up to several kilometres laterally or vertically (Sillitoe, 2003). The occurrence of pre-mineral mafic dykes in the same fault systems provide an indication that the deposits may have a genetic association with mafic magmas, either entire plutons or mafic magma underplating, which may have also contributed Cu-Au-Co-Ni-As-Mo-U that are typically anomalous (Sillitoe, 2003).

2.7.2.1 Iron oxide-copper-gold deposits — characteristic features

A variety of IOCG mineralisation styles have been documented including veins and stockworks (hosted by intrusive rocks, particularly equigranular gabbrodiorite and diorite), hydrothermal breccias, calcic skarns, replacement horizon (mantos) and 'composite' styles, which generally include veins and a combination of other styles (Silltoe, 2003). Composite deposits hosted within volcano-sedimentary sequences, such as Candelaria, tend to be the largest and have the most complicated alteration assemblages and over printing relationships (Sillitoe, 2003).

The Chilean IOCG deposits are characterised by low titanium hydrothermal magnetite, and/or specular hematite, which occur together with chalcopyrite as the dominant hypogene Cu phase, plus Au and

anomalous concentrations of Co, U, REE, Mo, Zn, Ag and other elements (Hitzman et al., 1992; Barton and Johnson, 1996). The iron oxides are typically post-dated by pyrite and Cu-bearing sulphides (Ruiz et al. 1965). Candelaria is an example of a magnetite-dominated deposit where magnetite-rich veins also contain significant actinolite, biotite and quartz with local apatite, clinopyroxene, garnet, hematite and K-feldspar. Examples of specular hematite dominant deposits include the vein breccia at Mantoverde and veins, breccia and mantos in the Punta del Cobre district deposits (Marschik et al., 2000; Benavides et al. 2007). Hematite-rich veins typically contain sericite and/or chlorite ± K-feldspar or albite. In many cases, these shallow hematite veins transition downwards to magnetite (e.g., Ruiz et al., 1965) suggesting that although distinction of the two deposit styles is reasonable, separation into different geological systems is debatable.

Alteration in the IOCG deposits is typically complex and varied. A generalised upward and outward zonation is typically observed in deposits that have sodic, calcic and/or potassic alteration, deep magnetite-actinolite-apatite transitions to shallow specular hematite-chlorite-sericite (e.g., Candelaria-Punta del Cobre; Hitzman et al. 1992). At Candelaria-Punta del Cobre, widespread, early sodic or sodic-calcic alteration, characterised by albite ± actinolite and a pervasive biotite-quartz-magnetite ± K-feldspa, preceded Cu mineralisation. At Manto Verde, Cu-mineralisation is associated with sericite, K-feldspar and chlorite but not biotite. Generally tourmaline is common and quartz is sparse, although not totally absent (Sillitoe, 2003).

2.7.2.2 Iron oxide-copper-gold genetic model

There are two main genetic models for IOCG deposit formation, reflecting alternative fluid sources, which continue to be debated: (1) metal-bearing magmatic brine (Hitzman et al. 1992; Ullrich and Clark, 1999; Pollard, 2001; Pollard, 2006) and (2) external 'basinal' brine heated by intrusions (Eugster and Chou, 1979; Haynes et al., 1995; Barton and Johnson, 1996; Williams et al., 2005). Hitzman et al. (1992) argued that variations in deposit mineralogy and geochemistry can be largely attributed to the influence of pressure, temperature and oxygen fugacity on hydrothermal fluids controlled by depth in the shallow crustal environment (<4-6 km), similarly to other magmatic-hydrothermal systems. Sodic alteration at deep levels are interpreted to result from interaction of hyrothermal fluids with heat sources; potassic alteration at high levels result from cooling hydrothermal fluids by interaction with cool country rock or meteoric water (Hitzman et al., 1992). A recent review of Andean IOCG deposits by Sillitoe (2003) also favoured the magmatic–hydrothermal model owing to the presence of Mesozoic porphyry copper-(gold) deposits in the Cretaceous arc, which provide evidence for a magmatic-hydrothermal source of Cu in the belt. Additional supporting evidence includes sulphur isotopes near 0 ‰, consistent with a magmatic source of sulphur, volumetrically large alteration zones indicating deep hydrothermal

sources and elevated CO_2 also indicating a deep fluid source (Pollard, 2001). Sillitoe (2003) proposed a model where mineralizing fluids are exsolved from deeper, more primitive portions of cooling plutons during final consolidation. Mafic dyke magmas may have also been derived from this source (Sillitoe, 2003). Metalliferous fluids and mafic magmas ascended to ore-forming levels, guided by second and lower order fault splays, intrusive contacts and stratigraphic horizons in an environment with an elevated geothermal gradient, which may have favoured prolonged ascent and lateral flow before ore deposition (Sillitoe, 2003).

An alternative genetic model for IOCG formation invoking chloride-rich basinal-brines from evaporite dissolution was proposed Barton and Johnson (1996). Site specific and anecdotal evidence of this model have also been proposed by a number of other authors including Chou and Eugster (1979), Haynes et al. (1995) and Hitzman (2000). The evaporitic brine model is contested by Sillitoe (2003) who argued that the occurrence of deposits within large plutonic complexes, subdued paleo-topography, later age, spatial distribution of evaporites and evidence of fluid ascent as opposed to descent, all suggest that a basinal brine model in isolation is implausible, and that magmas must have been involved as a heat ± fluid source. Overall there is agreement in the literature that deposits formed from fluids on a cooling path, that magmatic heat is the typical driver, and that various fluids penetrate well into large intrusive complexes.

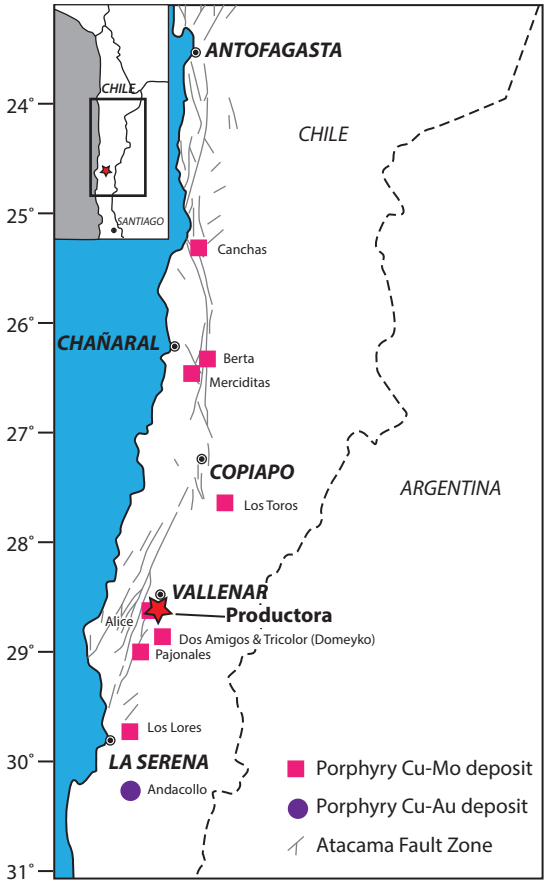

Figure 2.8 Pacific porphyry Cu belt with Productora for reference. Modified from Maksaev et al. (2007).

2.7.3 Porphyry Cu-(Mo-Au)

The 'Pacific Porphyry Cu Belt' defined by Llaumett et al. (1975) encompasses of a number of Early Cretaceous (132-97 Ma) porphyry deposits in the Coastal Cordillera, including Andacollo (the only deposit currently being exploited), Galenosa, Puntillas, Antucoya-Buey Muerto, Dos Amigos at Domeyko, Pajonales and Colliguay (Maksaev et al. 2007; Figure 2.8). The deposits are generally small, <300 Mt, and low grade (up to 0.4 % Cu) making most of them uneconomic (Sillitoe, 2003). Cu mineralisation is related to small porphyry stocks of quartz diorite to granodiorite emplaced in the contemporaneous volcano-plutonic arc with associated potassic (biotite, K-feldspar) alteration and intermediate argillic overprints of chlorite, sericite, illite and/or smectite assemblages (Sillitoe and Perrelló, 2005). The porphyry prospects contain Mo but are relatively poor in Au, with the exception of Andacollo (Sillitoe and Perrelló, 2005).

The Andacollo district includes the Andacollo porphyry and peripheral epithermal gold veins and manto-replacement deposits (Reyes, 1991). The Andacollo porphyry is the only currently economic Mesozoic porphyry deposit of the Pacific Porphyry Cu belt owing to its supergene enrichment blanket and anomalously high gold grades. Current probable reserves are 276.6 Mt grading 0.33% copper and 0.12 g/t gold (Teck Resources Limited, 2016). Gold grades in Chilean porphyries are typically only on the order of 0.1 g/t or less (Sillitoe, 1981; Camus, 2002). Andacollo, described by Llaumett et al. (1975) and summarised by Reyes (1991), is hosted by small stocks and dykes of K-rich tonalitic porphyry and andesite and dacite volcanic rocks. Mineralisation occurs in a core of biotite-K-feldspar potassic alteration within a large, 5 km long, trend of bleached quartz-sericite alteration with a weak propylitic halo. Hypogene mineralisation is low grade (0.3-0.8 % Cu) and characterised by chalcopyrite, pyrite, specular hematite, molybdenum and trace gold, occurring to depths of approximately 200m below a supergene blanket. Three hypogene zones are recognised; an internal zone of pyrite-chalcopyrite-specular hematite with the highest copper and molybdenum concentration and low pyrite to chalcopyrite ratios, a central zone with lower copper and molybdenum and an elevated pyrite to chalcopyrite ratio, and an external zone with high pyrite and only trace chalcopyrite. The overlying supergene enriched blanket is 40 m thick, dominated by chalcocite which rims chalcopyrite and pyrite with grades between 0.6 and 1.7 % Cu (Reyes, 1991). The system has a barren, 0.07 % Cu, leached cap of 30m thickness with limited copper oxide minerals.

The Andacollo porphyry deposit has been dated at 112 ± 10 Ma and 105 ± 3 Ma using biotite K-Ar and 104 ± 3 Ma and 98 ± 2 Ma from whole rock K-Ar (Munizaga et al. 1985; Reyes, 1991) indicating an Early Cretaceous age. This is comparable with radiometric dating of other altered and unaltered rocks in

the district (Sillitoe, 1981; Munizaga et al., 1985; Reyes 1991). The similar ages suggest that alteration and mineralisation occurred concurrently with development of the Cretaceous volcano-plutonic arc (Reyes, 1991). The extensional, as opposed to compressive, stress regime still prevalent during the Early Cretaceous is thought to be a major factor responsible for the small sizes and low hypogene grades of these deposits compared to those of the Tertiary (Sillitoe 2003).

2.7.4 Manto-type copper deposits

The Chilean manto-type Cu deposits, also known as stratabound, are currently the third largest source of Cu production in Chile. They can be divided into two groups based on their age and location: (1) Jurassic volcanic-hosted deposits, including Mantos Blancos and the Michilla District which occur in northern Chile between 21°30'S and 26°S and (2) Lower Cretaceous volcanic hosted deposits, including El Soldado and Lo Aguirre which occur in the intra-arc basin of central Chile from 30°S and 34°S (Maksaev et al., 2007; Figure 2.9). The manto-type deposits are considered a distinctive class which is relatively uncommon outside of the Coastal Cordillera of northern and central Chile (Sillitoe, 2003). Comprehensive reviews of the Chilean manto-type deposits are given by Maksaev and Zentilli (2002) and Maksaev (2007).

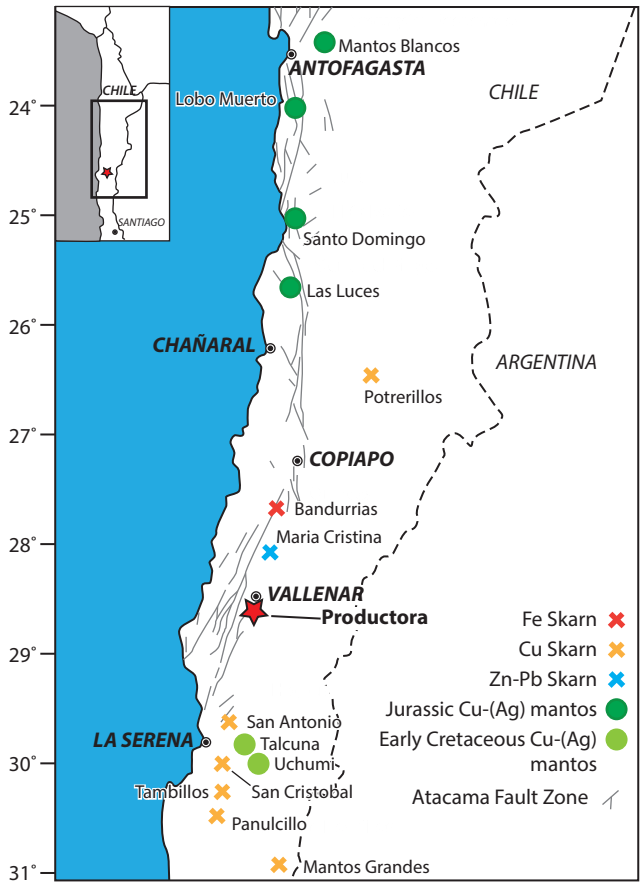

Figure 2.9 Mesozoic manto-type Cu and skarn deposits with Productora for reference. Modified from Maksaev et al. (2002).

Manto deposits are generally hosted in Mesozoic basaltic and andesitic, volcanic and volcano-sedimentary rocks in distal, peripheral locations to coeval dioritic to granodioritic plutons (Maksaev and Zentilli, 2002; Sillitoe and Perrelló, 2005). Mineralisation occurs in stratabound disseminated bodies and steeply dipping hydrothermal breccias surrounding barren diorite intrusions with associated veins (Sillitoe and Perrelló, 2005). The highest grades are typically found in zones of high permeability, such as permeable faults, hydrothermal breccia, dike contacts, vesicular flow tops and flow breccia. The dominant hypogene sulphide phases are bornite, chalcopyrite, chalcocite and pyrite plus occasional covellite and digenite, with additional minor sphalerite and galena identified in the Early Cretaceous deposits (Maksaev and Zentilli, 2002). Hypogene gangue minerals include quartz, hematite, pyrite, chlorite, albite, calcite and local magnetite as well as zeolites, epidote and bitumen in the Early Cretaceous deposits (Maksaev and Zentilli, 2002). Hypogene mineral zonation has been observed at a number of deposits, including Mantos Blancos, Santo Domingo, Lo Aquirre and El Soldado, with high grade cores centred on redox fronts in the host stratigraphy (Sillitoe, 1992; Sillitoe and Perrelló, 2005). The deposits are characterised by a core of Cu-rich minerals (chalcocite – bornite ± digentite), surrounded by successive zones of chalcopyrite ± bornite, chalcopyrite - pyrite and pyrite (Maksaev and Zentilli, 2002; Sillitoe and Perrelló, 2005). Mineralisation is commonly rich in silver, and lacks gold (Sillitoe and Perelló, 2005).

Most of the manto-type deposits are weathered, and have an upper oxidized zone. However supergene enrichment has only occurred at some of the larger deposits. This is probably due to low pyrite abundance, which limited acid production, and abundant calcite gangue which neutralised acid fluids (Maksaev et al., 2007). Cu-oxide minerals include atacamite, minor chrysocolla, malachite, Cu-sulphate and rare cuprite and native Cu (Maksaev et al., 2007).

Mantos Blancos is the largest of the Chilean manto-type deposits with pre-mining reserves of 500 Mt at 1% Cu (Ramírez et al., 2006). The other Jurassic manto deposits are smaller, with reserves of several millions of tonnes of ore at 1 to 3.8 % Cu and 8 to 25 g/t Ag (Maksaev and Zentilli, 2002). Unlike other manto-type deposits, Mantos Blancos is partly hosted in a rhyolitic dome and diorite and granodiorite intrusions (Ramírez et al., 2006).

Opinions are divided regarding the fluid sources for this enigmatic deposit class, which is now widely accepted as epigenetic. The two main schools of thought are (1) magmatic-hydrothermal (Wolf et al., 1990) and (2) metamorphic (Sato, 1984; Sillitoe, 1992). A magmatic-hydrothermal origin related to sub-volcanic stocks and dykes is the most popular model (Palacios, 1990; Wolf et al., 1990; Espinoza et al., 1996; Maksaev et al., 2007) although other authors have also suggested underlying batholiths act as hydrothermal fluid sources (Losert, 1974; Maksaev et al., 2007) or as heat sources to mobilize fluids of

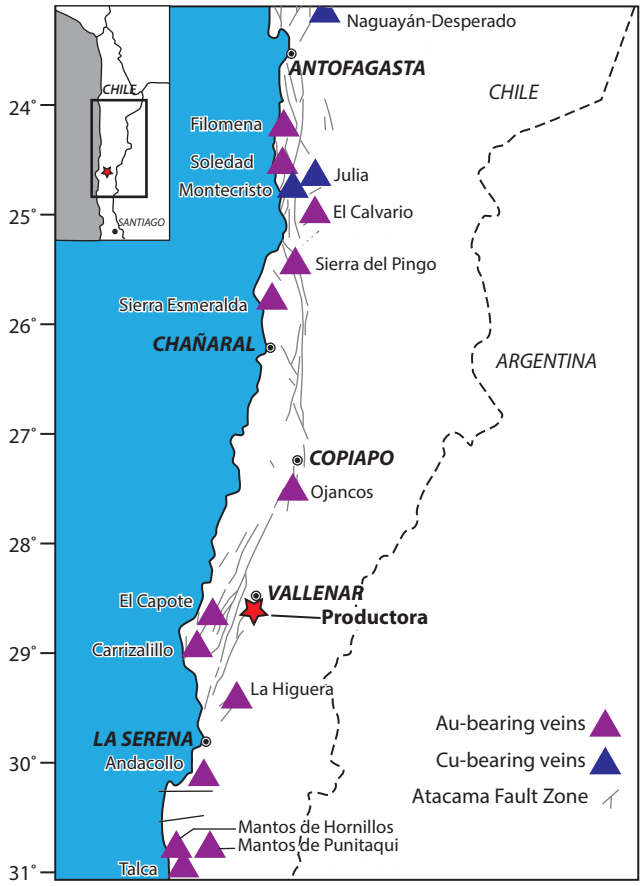

Figure 2.10 Districts with mesothermal vein deposits in northern Chile, with Productora for reference. Modified from Maksaev et al. (2002).

mixed origin which later cooled or mixed with meteoric waters, causing Cu precipitation (Maksaev and Zentilli, 2002).

2.7.5 Other mineralisation styles

The geological setting of the Coastal Cordillera was amenable to the formation of a variety of small Cu, Au and Ag deposit styles during the Mesozoic, either in association with the major deposit classes discussed or discretely. These include Cu-, Ag and Au-bearing metal veins and skarns (Figure 2.9 and Figure 2.10).

The most common type of hydrothermal gold deposits found in Chile, are Late Jurassic to Early Tertiary volcanic-hosted epithermal vein deposits associated with volcanic centres and porphyry systems (Camus, 1990; Sillitoe, 1991). The Mesozoic epithermal deposits are mostly low/intermediate sulphidation type (Hedenquist, 1987; Hedenquist et al., 2000) with a typical mineral assemblages of quartz-pyrite-chalcopyrite-galena-sphalerite and minor carbonates, barite, hematite and sulphosalts (Camus, 1990). These deposits tend to be smaller than the Miocene high sulphidation deposits. A review of 20 significant

Table 2.4 Mesozoic epithermal gold deposits. Compiled from Camus (1990). [1]Lepeltier (1964), [2]Flores (1943), [3]Flores and Ruiz (1946), [4]Flores (1948), [5]Swayne (1949), [6]Villarroel (1972), [7]Galay (1974), [8]Salinas (1975), [9]Camus and Drummond (1979), [10]Llaumett (1980), [11]Camus (1981), [12]Camus and Duhalde (1981), [13]Camus (1982), [14]Rivera (1984), [15]Frank et al. (1985), [16]Camus et al. (1986), [18]Camus and Reichhard (1987), [19]Lowell and Aspillaga (1987). anh = anhydrite, ank = ankerite, apy = arsenopyrite, bar = barite, cal = calcite, cpy = chalcopyrite, gn = galena, hem = hematite, py = pyrite, qtz = quartz, rds = rhodochrosite, sd = siderite, sp = sphalerite, spc = specularite, stb = stibnite, tet/ten = tetrahedrite/tennantite.

Ton (x10^6)*	Au (g/t)	Ag (g/t)	Au/ Ag	% Cu + Pb + Zn	Setting	Age	Host Rock	Major minerals	Minor minerals	Rare mins.	Alteration	Ref.
Faride												
1.50	2.80	240	0.012	2.5	Marginal to porphyry system	Upper Cretaceous	Granodiorite	Ag - Au - gn bar - qtz - hem - Mn-oxides	Ag-sulfides - sp - cpy - py - cal - sd - rds - Mn-silicates	Tet/ ten	Argillic, propylitic	16
San Cristobal												
Disseminated												
15.90	1.58	NP	>1	NP	Volcanic complex	Upper Cretaceous	Quartz porphyry	qtz - py - Au	-	-	Argillic	14, 19
Vein												
0.15	4.00	50	0.08	2.0 %Cu				qtz - py - Au cpy - cal - bar	gn - sp - hem - anh	-	Argillic	
Inca de Oro												
0.20	4.00	NP	>1	Traces	E-trending structure within magmatic arc	Lower Cretaceous	Andesite, granodiorite	qtz - py - Au	Au tellurides - cal - cpy	-	Argillic	3, 6
Cachiyuyo de Oro												
0.30	12.00	NP	>1	NP	Magmatic arc; mineralization along N to NE-trending structures	Upper Cretaceous	Granodiorite	qtz - py - Au	hem - cpy	bn - gn	Argillic	8
El Capote												
0.50	9.00	NP	>1	NP	Magmatic arc; Mineralization along N15-40W-trending structures	Upper Jurassic-Lower Cretaceous	Granodiorite, tonalite	Au - qtz - apy	cpy - py - cal - hem - bar	cov - pyr	Argillic	2, 15
Andacollo (porphyry related)												
10.00	1.50	NP	>1	NP	Radial fractures marginal to porphyry Cu system	Upper Cretaceous	Rhyolite, dacite				Propylitic zone	10
Los Mantos de Punitaqui												

*Ton = production + reserves

Ton (x10^6)*	Au (g/t)	Ag (g/t)	Au/ Ag	% Cu + Pb + Zn	Setting	Age	Host Rock	Major minerals	Minor minerals	Rare mins.	Alteration	Ref.
2.50	9.00	NP	>1	0.5 %Cu	N-S to NE-trending shear zone	Lower Cretaceous	Meta-andesite	qtz - spc - py - cpy - cal - Au	mt		Argillic	7, 1
Las Vacas												
0.25	12.50	NP	>1	NP	Magmatic arc; with mineralization along N-trending structures	Lower Cretaceous	Granodiorite	qtz - py - Au	cal - hem		Argillic	5, 18
El Bronce												
4.30	5.00	20	0.25	2.2	Structures marginal to caldera	Upper retaceous-Lower Tertiary	Andesite, breccia, tuff	qtz - py - Au - sp - cpy - cal - sd - ank	Ag - gn - ten - hem - bn	po - apy	Argillic, propylitic	13, 16
Alhue												
0.50	5.00	20	0.25	0.1 %Cu	Subvolcanic system associated with magmatic arc; mineralization along N-trending structures	Upper Cretaceous	Andesite, breccia, granodiorite, tuff	qtz - py - Au	cpy - sp	-	Argillic	4
Chancon												
0.55	5.00	10	0.5	1.5	Subvolcanic system associated with magmatic arc; mineralization hosted by N-trending shear zones	Upper Cretaceous-Lower Tertiary	Andesite, breccia	qtz - py - Au	cpy - sp	bn - mt	Argillic	12
El Tigre												
0.25	8.00	50	0.16	1.5	Subvolcanic system associated with magmatic arc; mineralization controlled by N-trending structures	Upper Cretaceous	Andesite, breccia	qtz - py - Au - apy	gn - sp - cpy - stb	-	Argillic	11
El Chivato												
0.20	7.50	NP	>1	NP	Magmatic arc; mineralization along N-trending structures and N-trending shear zones	Lower Cretaceous	Granodiorite, monzonite				Argillic	9

*Ton = production + reserves

Table 2.5 Significant skarn deposits. Compiled from Maksaev et al. (2007). Data from [1]Mosocoso et al. (1982); [2]Ardila (1993); [3]Ardila et al. (1993); [4]Rivano et al. (1993); [5]Lieben et al. (2000); [6]Sugaki et al. (2000); [7]Parada and Larrondo (1999). Fm. = Formation, Gp. = Group, Ref. = reference

Name	Host	Production	Hypogene ore mineral	Skarn Assemblage	Mineralisation	Geochronology	Ref.
Cu-Skarns							
Cabildo district	Lower Cretaceous Lo Prado Fm.; limestone, sandstone, marl, tuff and conglomerates adjacent to diorite, tonalite, granodiorite batholith		Hypogene: chalcopyrite with minor pyrrhotite and pyrite; supergene: chalcocite	Garnet, clinopyroxene, amphibole, epidote, calcite, scapolite, quartz, chlorite and titanite	Stratabound, vein type and irregular Cu-bearing ore bodies hosted within the skarn units	Batholith: 106 ± 3 – 96 ± 3 Ma (K-Ar)	4
San Antonio district	Lower Cretaceous Arqueros Fm.; carbonate and volcanic rocks; Santa Gracia granite	Historically 200 Kt @ 1.5–2.2 % Cu, 1–2 g/t Au	Magnetite, pyrite, hematite, chalcopyrite, minor galena, sphalerite, arsenopyrite, pyrrhotite and bornite	Garnet, clinopyroxene, scapolite, epidote, amphibole, calcite, biotite, phlogopite, K-feldspar, quartz, chlorite, illite, prehnite and laumonite	Stratabound and strataform (4-6 m thick, 75-120m strike, 20-90m down dip)	Batholith: 98 – 89 ± 0.6 Ma (K-Ar)	1, 2, 3
Panulcillo mine	Lower Cretaceous; carbonate rocks; dioritic stock	500 Kt @ 2.75–3.50 % Cu, 0.5–1.0 g/t Au	chalcopyrite with pyrrhotite, pyrite, sphalerite, arsenopyrite, galena, magnetite, hematite and minor molybdenite	Gandite garnet, phlogopite, clinopyroxene, scapolite, pargasite, calcite, plagioclase, epidote, clinozoisite, chlorite, illite, K-feldspar and axinite	Irregular orebodies occur within garnet zone, 20-50 m thick, up to 160 m strike and 60 m down dip	Mineralisation: 115 ± 3Ma (K-Ar); intrusive: 132 ± 7 Ma (K-Ar)	2, 6
La Campana district	Lower Cretaceous Lo Prado Fm.; limestone; Caleu Pluton gabbro	Opositora mine 68.5 Kt @ 1.5 % Cu, 25 g/t Ag	chalcopyrite, pyrite, pyrrhotite, bornite, molybdenite, sphalerite, magnetite; minor galena, arsenopyrite, marcasite, hematite	Garnet (grossularite-andradite), pyroxene (diopside-salite), calcite, quartz	Ore bodies are up to 20m thick, 200m strike, 100m down dip	Intrusion: 117-94 Ma and 130 ± 1.5 Ma ($^{40}Ar/^{39}Ar$)	7
Zn-Pb skarn							
Maria Cristina	Lower Cretaceous Chañarcillo Gp.; carbonate rocks; diorite porphyry		sphalerite, pyrite, galena, minor marcasite and magnetite and trace chalcopyrite and tetrahedrite	Garnet (andradite), pyroxene (diopside), magentite, epidote	Coarse-grained, pyrite rich massive sulfide within carbonates, massive sulfides retrograde skarn	Intrusion: 93.6 ± 0.4 Ma ($^{40}Ar/^{39}Ar$)	5
Fe Skarn							
Cerro Bandurrias	Lower Cretaceous Chañarcillo Gp.		magnetite (partially martized)	Garnet, scapolite	Ore horizon is 7 m thick, 1.7 km strike		
Cu-Au Skarn							
Mina Lar (Candelaria)	Lower Cretaceous Chañacillo Gp.	200 Kt					

hydrothermal gold deposits by Camus (1990; Table 2.4), identified a number of other common features. Host rocks to the hydrothermal gold deposits include andesites, volcanic breccias, ignimbrites, tuffs, rhyolites and dacites, as well as diorite to granodiorite stocks. Many gold-bearing veins deposits contain accessory metals, including Ag, Cu, Pb, Zn, As and Hg, although typically only Au and Ag is recovered. Mineralization is structurally controlled, and in many cases is related to volcanic centres. Veins range from 100 m to 8 km in length with ore shoots of lengths between 50 – 600 m, widths between 0.20 – 23 m and vertical extent up to 400 m. Vertical and lateral metal zonation patterns have also been noted in vein deposits; an upper precious-metal-bearing zone, intermediate base-metal-bearing zone and lower root zone (Camus, 1990). Multiple alteration stages are common, Table 2.4, with quartz-sericite and argillic assemblages predominant. Propylitic assemblages, chlorite and tourmaline are also observed.

Only a few skarn deposits are currently being exploited in Chile. These include the Cabildo district, north of Santiago, and El Toqui district in Patagonia (Figure 2.9). A summary of several skarn districts is provided in Table 2.5. Within the Lower Cretaceous intercalated carbonates and volcano-sedimentary sequences of Coastal Cordillera, 13 skarn deposits have been recognized, although none are being mined (Maksaev et al., 2007; Figure 2.9). Cu skarns are most prevalent, although Zn-Pb (e.g., Maria Cristina) and Fe skarns (e.g., Bandurrias) have also been documented.

2.8 Relationships between deposit styles

In addition to debate over the genetic models for individual deposit classes, there has been much discussion regarding the genetic relationships between the deposit classes, particularly between magnetite-apatite and IOCG, and also between IOCG and porphyry deposits (Hitzman et al., 1992; Barton and Johnson, 1996; Marschik and Fontboté, 1996; Williams et al., 2005; Chen, 2010; Tornos et al., 2010). The Punta del Cobre district has been proposed as an example of transition between magnetite-apatite and porphyry-Cu deposits (Marschik and Fontboté, 1996).

2.8.1 Magnetite-apatite and IOCG deposit relationships

Although having both a temporal and a broad spatial association, no transitions have been documented between Chilean magnetite-apatite and IOCG deposits. A crude zonal relationship has been suggested where deposits are adjacent (e.g., Manto Verde and Manto Ruso; Rieger et al., 2012). Sillitoe (2003) proposed that magnetite-apatite deposits may occur at depth below magnetite-dominated IOCGs, and that a transition may occur where Cu content of the IOCG ores decreases with depth. Magnetite-apatite deposits of the Coastal Cordillera are mostly 128 to 102 Ma (Oyarzun et al., 2003) whereas the IOCGs are between 170 and 110 Ma (Sillitoe, 2003; Chen, 2010). This temporal gap suggests different

processes influenced formation (Chen, 2010). Hitzman et al. (1992), Barton and Johnson (1996) and Barton (2014) included the magnetite-apatite deposits as end-members of the IOCG class based on the abundance of late-stage pyrite, chalcopyrite and gold in and proximal to some massive magnetite deposits (e.g., Marcona, El Romeral and Cerro Negro Norte) as well as similarities in alteration and gangue mineralogy, especially actinolite and apatite. Comparison of Re-Os signatures in IOCGs and magnetite-apatite deposits have shown they are either distinctly different, indicating different fluid-rock interactions during deposit formation (Mathur et al., 2002), or overlapping — suggesting similar fluid-rock interactions (Barra et al., 2017). Williams et al. (2005) highlight the independent distribution pattern of deposits, i.e. clustering of deposits, and the typically younger Cu-Au mineralization age, which suggests they are not part of a continuum (Table 2.3 and Table 2.3). It remains unclear why magnetite-dominated deposits did not evolve to economically significant Cu ±Au deposits (Chen, 2010). Despite being forming in the same general environment and sharing an association with diorite intrusions (Ménard, 1995), magnetite-apatite deposits and IOCGs have different genetic models including different fluid sources (Williams et al., 2005; Chen, 2010), although these sources are not thought to be radically different by some (e.g., Sillitoe, 2003).

2.8.2 IOCG and porphyry deposit relationships

There are a number of similarities between IOCG and porphyry deposits, including the presence of hydrothermal magnetite and/or hematite and potassic, potassic-calcic and/or sodic alteration assemblages (Hitzman, 1992; Sillitoe, 2003). Sodic-calcic alteration associated with porphyry deposits has been interpreted to be unrelated to magmatic fluids in a number of deposits — most notably at Yerington, Nevada (Dilles et al., 1995). Au-rich porphyry-Cu deposits may also display strong albitization, have associated REE-enriched Cu-Au-magnetite skarns and can be spatially associated both with diorite intrusions and magnetite-apatite deposits (Meinert, 1984; Sillitoe, 1997; Williams et al., 2005). Distinguishing features include the intrusion-centred alteration and mineralisation zonation patterns of porphyry deposits, which contrast with the district-scale asymmetric alteration patterns of IOCGs, which lack an obvious intrusive centre. There is an intimate and clear association of porphyry deposits with contemporaneous igneous intrusions, whereas IOCGs have no clear spatial and/or temporal association (Williams et al., 2005). Porphyry deposits are major sources of Cu, Mo, Au and Ag and locally Pb and Zn, whereas IOCGs are rich in Fe with subordinate Cu ± Au (Hitzman, 1992). In porphyry deposits, abundant sulphide minerals and sulphates (e.g. anhydrite) indicate an excess of sulphur in the hydrothermal fluids, this leads to sulphide minerals being more abundant than iron oxides and also enables acid alteration of wall rocks to kaolinite or pyrophyllite - alunite (argillic alteration). Although anhydrite is common in some IOCG deposits (e.g. Candelaria), typically IOCGs have lower sulphur abundances and are more oxidized thus iron oxides dominate the mineral parageneses (Williams et al., 2005).

Porphyry deposits tend to be preserved in less deeply eroded, younger metallogenic belts than IOCGs (Andean, Proterozoic and minor Mesozoic). This suggests that the depth of formation may be influential in the respective deposit genesis. Porphyry deposits are poorly preserved in the Coastal Cordillera whereas IOCGs, which are interpreted to form at greater depths (Marschik et al. 2003; Tornos et al., 2010), are widespread. This raises the question whether shallower-formed porphyries in the Coastal Cordillera have been eroded away and whether the IOCGs and magnetite-apatite deposits could in fact represent the root zones of such systems.

Tornos et al. (2010) argued that the Tropezón Cu-Mo-(Au) deposit in northern Chile is an IOCG with porphyry features, and used this as evidence for a genetic relationship between the deposit classes. Tropezón is hosted by a quartz diorite with similar mineralogy and Cu-(Au) and Mo mineralisation to porphyry systems but shows a much simpler hydrothermal evolution. Magmatic exsolution produced a single pulse of alkaline Fe- and Ca-rich fluids resulting in Ca-Fe-K alteration with associated chalcopyrite, molybdenite, bornite and gold forming a zoned ore body, this was later overprinted by hematite from low-temperature basinal brine circulation. This genetic model is consistent with the hybrid model of Barton and Johnson (2000). Hydrothermal alteration at Tropezón is similar to Candelaria (Tornos et al., 2010).

2.8.3 Summary of deposit relationships

The association of a number of deposits styles in the Mesozoic suggests that they share common fundamental drivers for formation. Although deposits are temporally and spatially discrete, their occurrence within a short epoch in geological time and space suggests that they have more similarities than differences. Mineral deposits can be viewed as an expression of the prevailing geological environment at the time of formation which in turn dictates available fluid sources, fluid evolution and depositional sites. The abundance of iron-rich deposits in the Mesozoic indicates that a fundamental driver either promoted iron mobilisation and deposition or inhibited copper and sulphur transport. The younger ages of magnetite-apatite deposits suggests that this was particularly prevalent toward the end of the Early Cretaceous. The similarities in mineralisation style (e.g., veins and breccia), textures and alteration assemblages between porphyry and IOCG deposits suggest that these deposits form by similar magmatic-hydrothermal processes. It is the expression of these processes in the local geology which results in the suite of characteristics on which a deposit classification is made. A fundamental difference between these two deposit classes is their association with an intrusive body. In the case of porphyry systems the intrusive body provides both a source and a trap, resulting in many similarities within the deposit class. The evolution and genesis of an IOCG deposits is less constrained, as a result deposits can present a wide range of features which reflect many different processes that can occur such as mixing with basinal brines

or metasomatism of the country rock. It would seem that the prevailing geological environment in the portion of the Mesozoic magmatic arc preserved in the modern Coastal Cordillera did not favour the formation of porphyry deposits but hydrothermal systems were active and generated the range deposits seen today.

2.9 Concluding remarks

The Mesozoic mineral systems of Northern Chile formed within a convergent tectonic environment with subduction styles and tectonic regimes evolving from extensional (high-angle) to compressional (low-angle subduction). Extensive magmatic arc with associated back-arc basin stratigraphy and plutonic complexes of the Coastal Batholith developed under Cretaceous extensional conditions. The crustal scale, syn-arc, strike-slip, Atacama Fault System (AFS) provided the architecture for magma ascent and fluid pathways, and is strongly associated with Mesozoic mineralisation. Dominant mineralisation styles of the Mesozoic include magnetite-apatite, IOCG, manto-Cu and small porphyry-Cu. Low sulphidation, epithermal Au and skarns deposits are also common.

The geology and metallogeny presented in this review are an overview in terms of the far field and local forces governing ore deposit formation in northern Chile. There is no doubt the tectonic and structural history is far more complicated than simply a transition from extensional to compressional regimes. The interplay of the major processes discussed here is likely to be extremely complex over geological timescales. The impact of evolving subduction regime on development of large and small scale structures and relative fault movement is influential on magma and fluid pathways. Changing fault behaviour, as faults are heated by batholith emplacement and then cooled, may have modified such fluid pathways. There are also additional processes to consider that have not been discussed in this review including slab roll back, foreland erosion and subduction of positive topographic features on the down going slab, which may also have been important to mineralisation. The geological history of the Andes is protracted and complex, to fully understand the Mesozoic environment requires reconstruction of many events. The ever increasing availability of geochronological data and developments on our understanding of the structural evolution of the region will continue to help unravel the complexities of this geological puzzle.

Our understanding of the ore deposits in northern Chile remains incomplete. For the most part deposit models are interpreted based on deposit scale features which are put into a regional framework. Perhaps this is a backwards approach? Developing an understanding of the regional and far field processes that led to metallogenic epochs in time and space, and how these pertain to the local processes which contributed to the catastrophic events forming an ore deposit, may provide a greater understanding of deposit genesis and the relationship between deposits.

Chapter 3: Deposit Geology

3.1 Introduction

This chapter summarises the major geological characteristics of Productora. Geological data have been compiled from the literature, predominantly from Fox (2000) and various unpublished company reports, and supplemented with new observations and interpretations from this study. Detailed descriptions are provided for each of the lithologies encountered during graphic core logging. Lithological descriptions are augmented by new geochronological data. Extrapolation of core observations to construct two cross sections at 6,822,215 mN and 6,820,850 mN, has been achieved with the aid of immobile element lithogeochemistry. Major features of the local geology at Productora include the Jurassic volcanic stratigraphy, two major intrusive bodies, a hydrothermal breccia complex and a complex fault network. The hydrothermal breccias are described in detail in Chapter 4. Structural geology is summarised from previous workers and presented in a regional context.

3.2 Previous work

Fox (2000) provided the most comprehensive documentation of the geology of Productora prior to the current study. Key geological outcomes included a geological map, cross section interpretations, volcanic stratigraphy interpretation, description and dating of the Cachiyuyito and Ruta Cinco intrusions, and a proposed geological history. Her lithological descriptions were augmented by approximately 70 whole rock major and trace element analyses. Ray and Dick (2002) summarised previous work at Productora, including a number of unpublished company reports. Heavily drawing on the work of Fox (2000), they described the lithologies and structure with a revised geological map and geological history.

Figure 3.1 Regional geological map of the district around Productora showing major stratigraphic units, regional faults and infrastructure. Map modified from Arévalo et al. (2009), legend modified from Arévalo et al.(2009), Moscoso et al. (1982) and Gana et al.(2003)

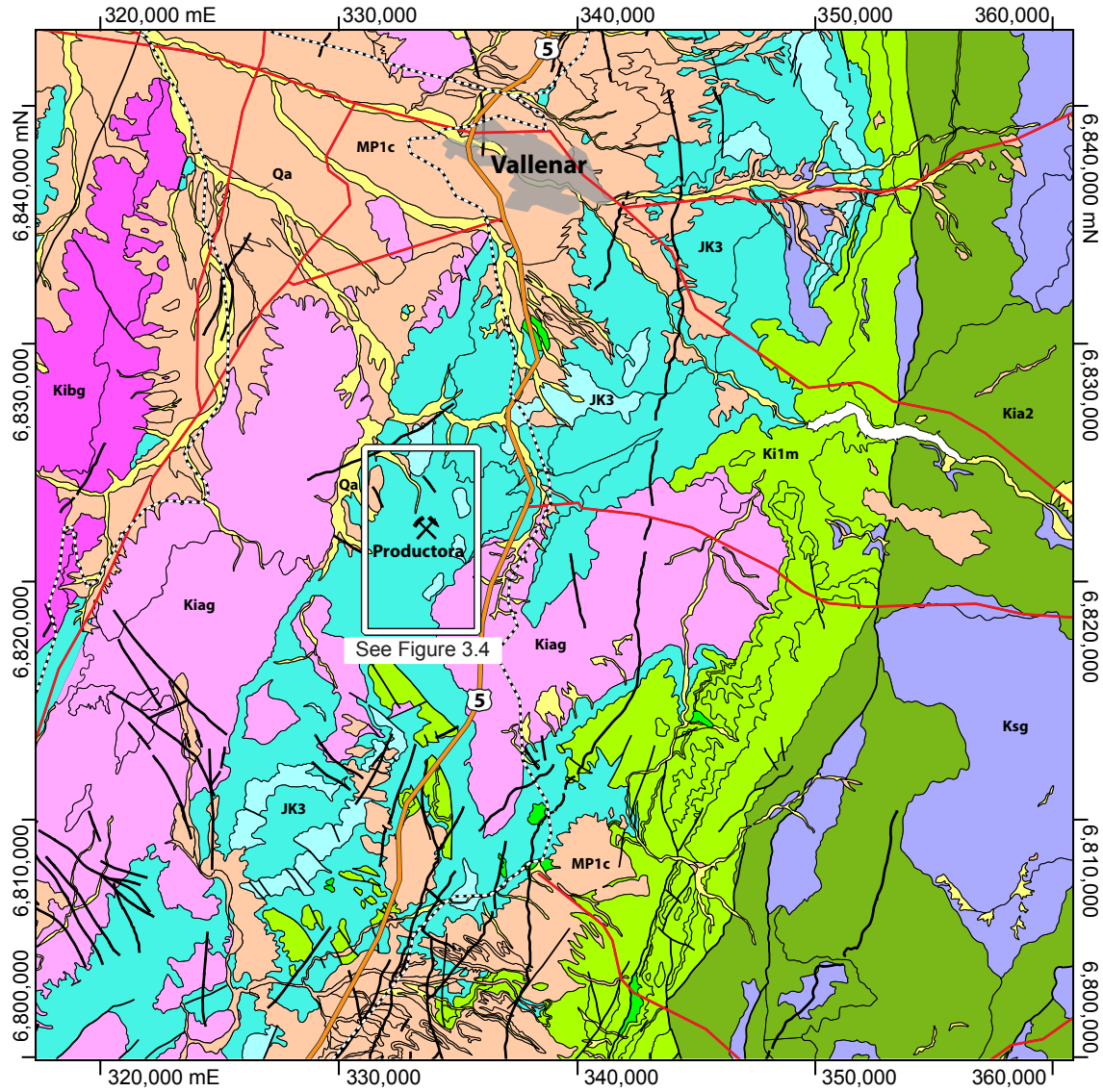

Cenozoic
- Quarternary
- Tertiary

Mesozoic
- Cretaceous
  - Late
  - Early
- Jurassic

Qa: Pleistocene-Holocene
Alluvial, subordinate colluvial or lacustrine deposits: gravels, sands, silts and alluvial fans

MP1c: Late Miocene-Pliocene
Clastic sedimentary sequences of alluvial, colluvial or fluvial: conglomerates, sandstone and siltstone

Ksg: Late Cretaceous (90-65 Ma)
Monzodiorites, granodiorites, gabbros and pyroxene, biotite and hornblende diorites; andesitic and diorite porphyry

Kia2: upper Early Cretaceous - lower Late Cretaceous Cerrillos Group
Sedimentary and volcanic sequences: epiclastic and pyroclastic rocks, andesitic lavas and basalts with intercalated of lacustrine and locally marine sediments

Ki1m
Early Cretaceous (Neocomian)
Chañarcillo Group. Coastal marine sedimentary sequences: limestones, calcarenitas, sandstone, marl and cockles

JK3: Late Jurassic-Cretaceous Bandurrias Group

Volcanic sequences: basaltic to rhyolitic lavas, domes, breccias and andesitic, dacitic agglomerates

Continental and marin clastic intercalations

Major road

Pan American Highway

Railway

Urban area

Kiag : upper Early Cretaceous - lower Late Cretaceous (123-85 Ma)
Diorites and pyroxene-hornblende-monzodiorites, granodiorite, hornblende-biotite-monzogranites. East of Atacama - El Romeral Fault system and associated with mineralization of Fe-Cu-Au (Candelaria) and Cu-Au (Andacollo)

Kibg
Lower Early Cretaceous (144-124 Ma)
Monzodiorites and diorite pyroxene, hornblende and biotite granodiorite and tonalite. Associated with the Atacama-El Romeral fault system and Fe mineralization (Cerro Iman, Algarrobo)

Between July 2009 and May 2012, sampling and detailed mapping (1:2,500 scale) was performed across Productora by Beeson et al. (2012). A total of 843 rock chip samples were collected. Geological observations included systematic documentation of lithology, structure, alteration mineralogy, alteration intensity, strain intensity, scintillometer readings, sample locations and photographs of key geological features. Beeson et al. (2012) presented the most comprehensive mapping campaign to date, with significantly more detailed mapping of lithologies and structure than previous workers.

Despite >160,000 m of close spaced drilling (80 m x 40 m) being completed across the deposit between 2010 to 2013, only limited geological interpretations were conducted due in part to intense alteration and hydrothermal brecciation, and in part due to assaying of whole drill core by Hot Chili Ltd. No detailed documentation of the breccia facies were conducted prior to the current study.

3.3 Methods

Geological descriptions in this study are based largely on observations from diamond drill core logging and six days of reconnaissance mapping in key areas. Cross sections have been constructed at 6,822,215 mN and 6,820,850 mN based on graphic logging, core photography and immobile element lithogeochemistry.

3.3.1 Graphic logging

A total of 16 drill holes were examined in this work, predominantly from two key cross sections at 6,822,215 mN and 6,820,850 mN (Figure 3.4; Appendix B1). Available core was extremely limited due to Hot Chili Ltd's whole core assay protocols, although photographs were available for most diamond

Figure 3.2 Core logging at a cold storage facility in Santiago where geometallurgical core was being stored. Make-shift core racks were set up in the loading bay.

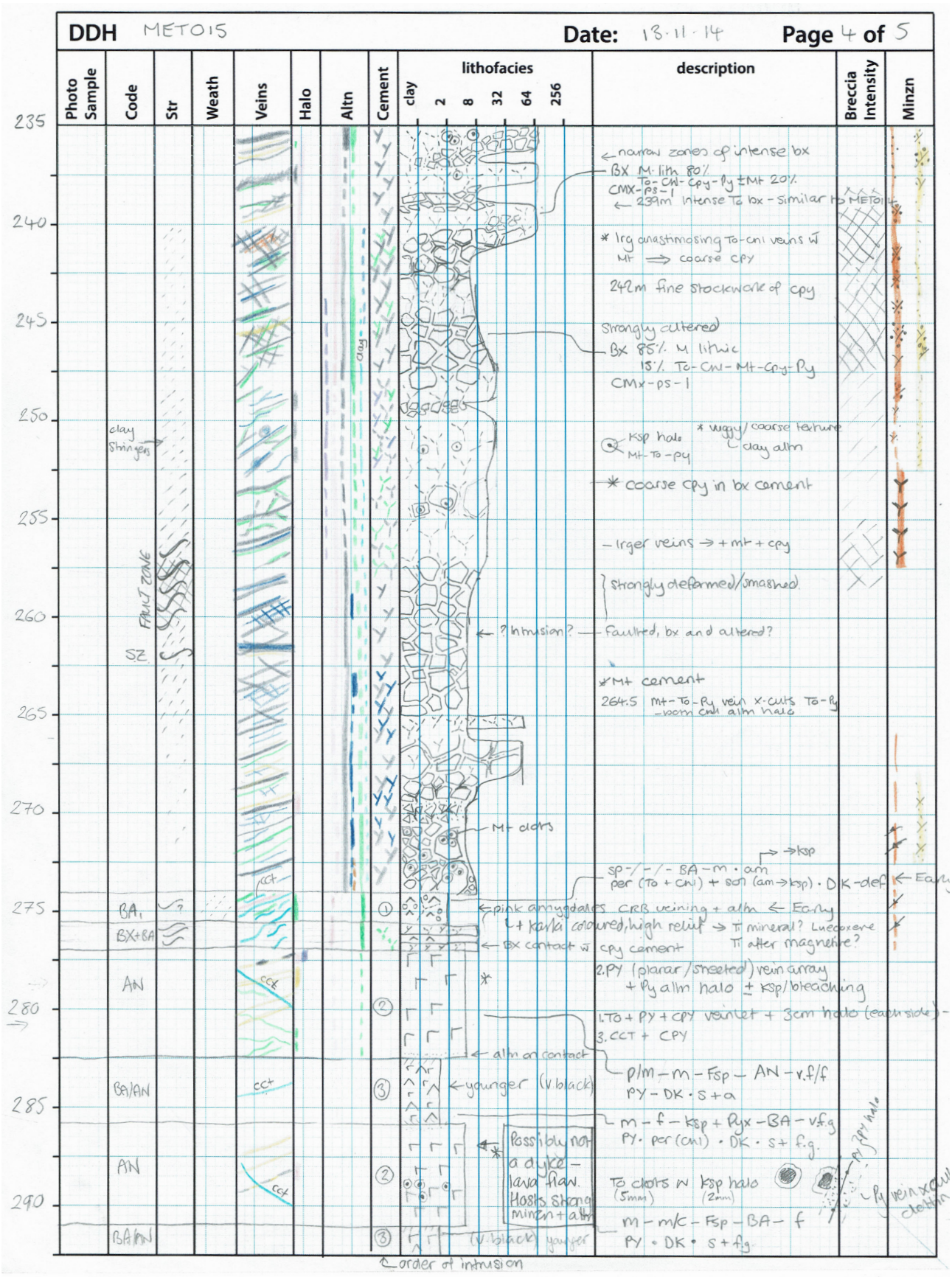

Figure 3.3 Example of graphic log from hole MET015 239–292.5 m. Graphic logging followed the method of Blackwell (2010; Appendix B2). Lithofacies size recorded as average clast, phenocryt or grain size, with pattern fill to reflect rock texture. Annotations detail breccia texture and composition (see for legend). Mineralogy of cement, mineralisation, veins and alteration were recorded by colour. Breccia intensity and weathering both recorded by cross hatching.

core, and chip trays have been retained from all reverse circulation (RC) drill holes. Most of the available core was HQ core, drilled for geometallurgy purposes - consequently this was kept in cold storage in Santiago. Of the 25 available drill holes, there were commonly missing intervals that had been sampled previously. Core was graphically logged on make-shift core racks in a loading bay at the cold storage facility (Figure 3.2).

A total of 2,797 m of core was graphically logged at a scale of 1:250 or 1:1,000 following the methods of McPhie et al. (1993) and Blackwell (2010) in order to record the salient features of the geology. An example of the graphic logging style employed is provided in Figure 3.3. The graphic logging legend of Blackwell (2010) is provided in Appendix B2. All graphic logs completed during this study are provided digitally in Appendix B3.

3.3.2 Logging from core photo library

In order to make cross section interpretations, additional drill core was photo-logged from the core photography library using prior knowledge of rock types and textures from graphic core logging. A total of 19 holes, containing 6083 m of core were logged from photographs (Appendix B4; Figure 3.5 and Figure 3.6).

3.3.3 U-Pb geochronology

Five samples were submitted to CODES, University of Tasmania for geochronological analysis by U-Pb method through the laser ablation inductively coupled mass spectrometry (LA-ICP-MS) method on zircons. Samples were crushed to <400 μm and zircons hand picked from a non magnetic heavy mineral separate. Zircon grains were mounted in epoxy resin, and reviewed under cathode luminescence at the Central Sciences Laboratory, University of Tasmania in order to check for inheritance. Analysis of U-Pb was performed on suitable grains using an Agilent 7900 quadrupole ICP-MS with 193 mm coherent Ar-F excimer laser and Resonetics S155 ablation cell. Further method details are provided in Appendix B5. In most cases little to no inheritance was observed in the data and results plotted on concordia. Analyses which showed evidence of Pb loss or common lead were excluded from the age calculations. Results are presented in the following text, supporting data provided in Appendix B6 and B7.

3.3.4 Immobile-element lithogeochemistry

The rocks at Productora have undergone brecciation, pervasive, intense hydrothermal alteration and are locally offset by numerous faults. Primary features are largely obscured by these events. This has led to

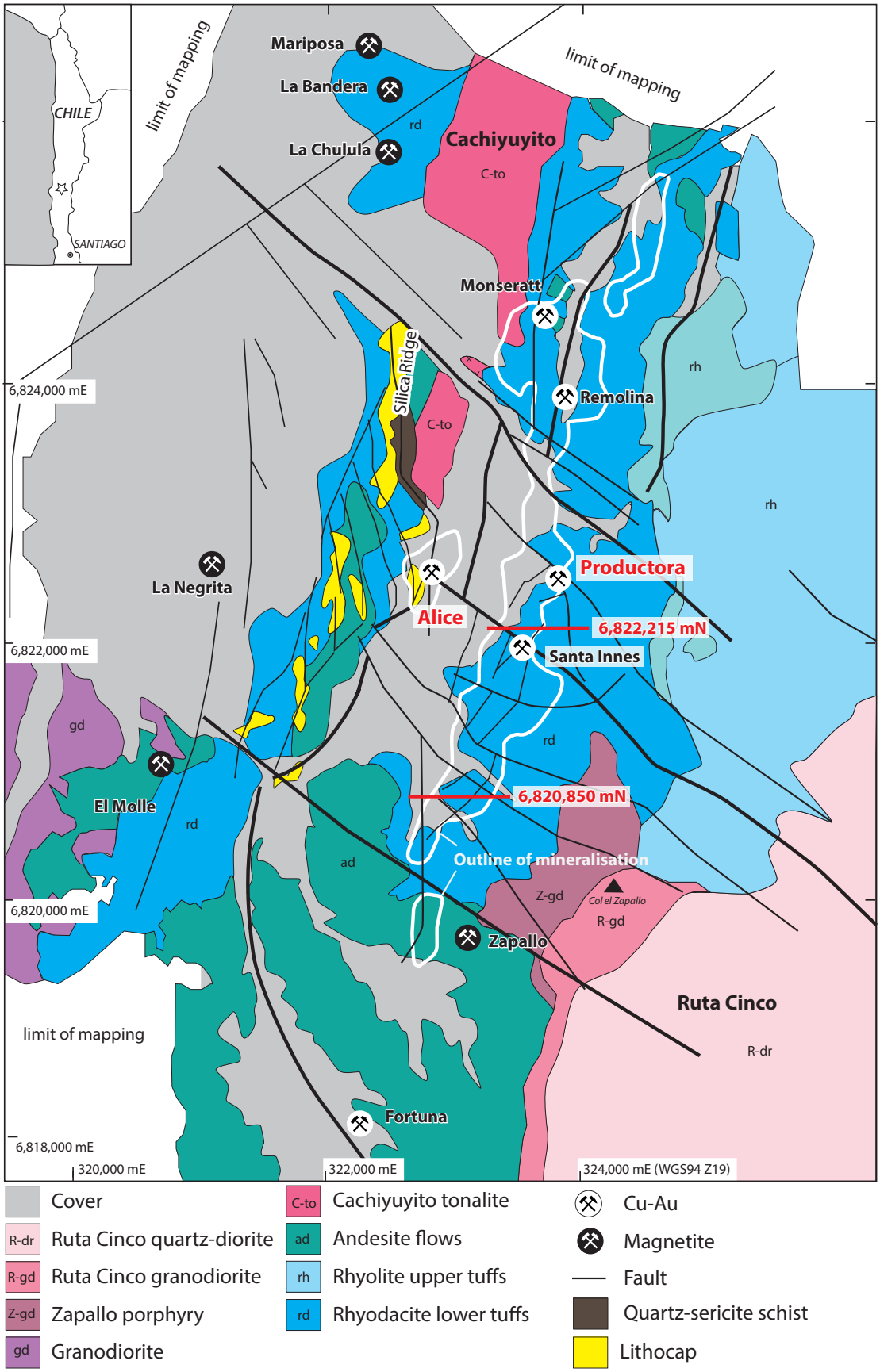

Figure 3.4 Map showing local geology and major structures from surface mapping. Also shown are local mineralisation occurrences, outline of mineralisation (defined as Hot Chili Ltd drilling intervals >0.1 %Cu projected to surface) and location of study sections at 6,822,215 mN and 6,820,850 mN. Modified from Ray and Dick (2002), Beeson (2012) and J. Beeson pers. comm. (2015).

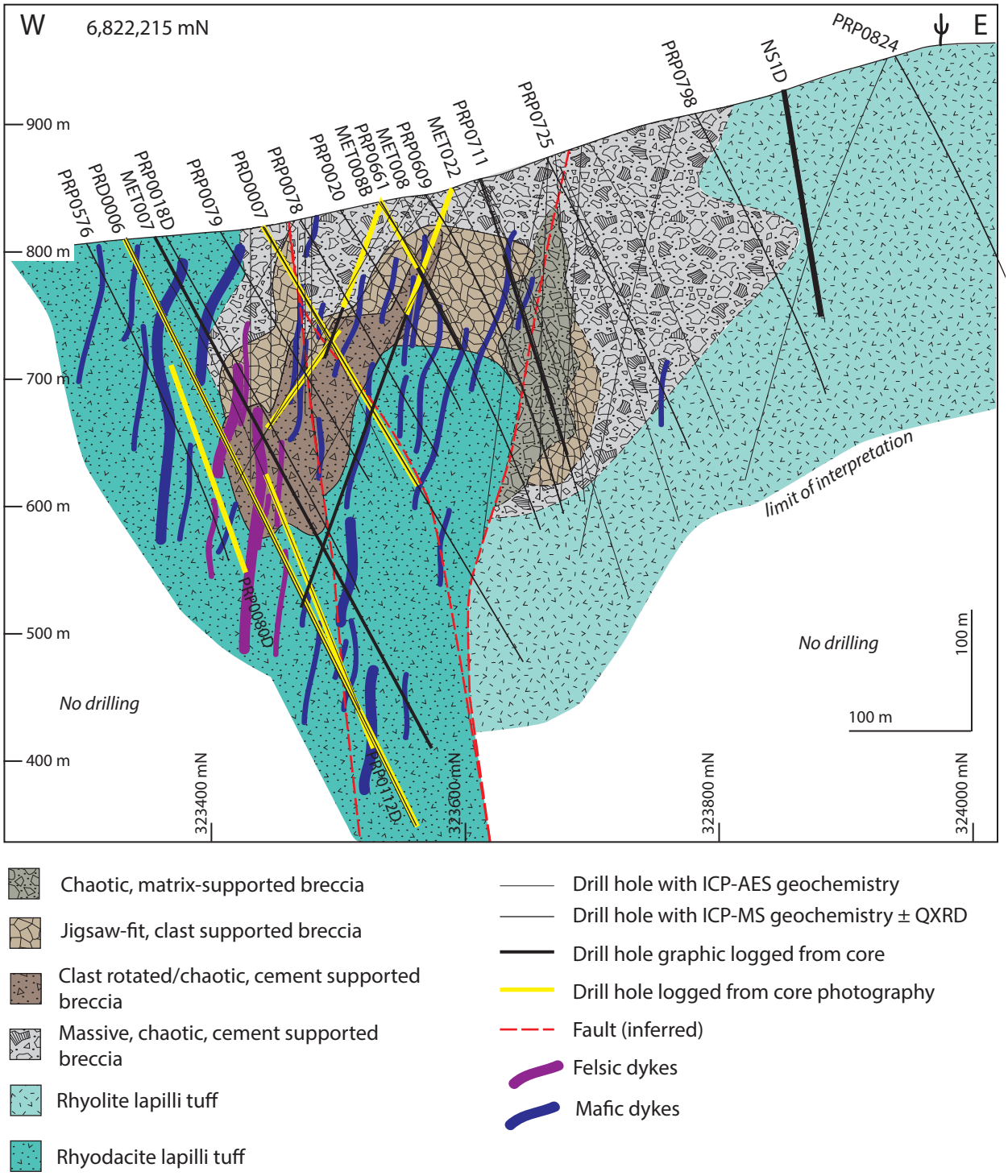

Chaotic, matrix-supported breccia

Jigsaw-fit, clast supported breccia

Clast rotated/chaotic, cement supported breccia

Massive, chaotic, cement supported breccia

Rhyolite lapilli tuff

Rhyodacite lapilli tuff

Drill hole with ICP-AES geochemistry

Drill hole with ICP-MS geochemistry ± QXRD

Drill hole graphic logged from core

Drill hole logged from core photography

Fault (inferred)

Felsic dykes

Mafic dykes

Figure 3.5 Cross section at 6,822,215 mN showing geology interpreted from graphic core logging, photo logging and immobile element lithogeochemistry. Breccia domains reflect variations in texture and internal clast organisation — protolith textures were largely obscured by alteration and brecciation in these domains. Unusual contact relationships between the rhyodacite lapilli tuff and breccia complex on this section reflect movement on unconstrained faults and the three dimensional shape of the breccia complex.

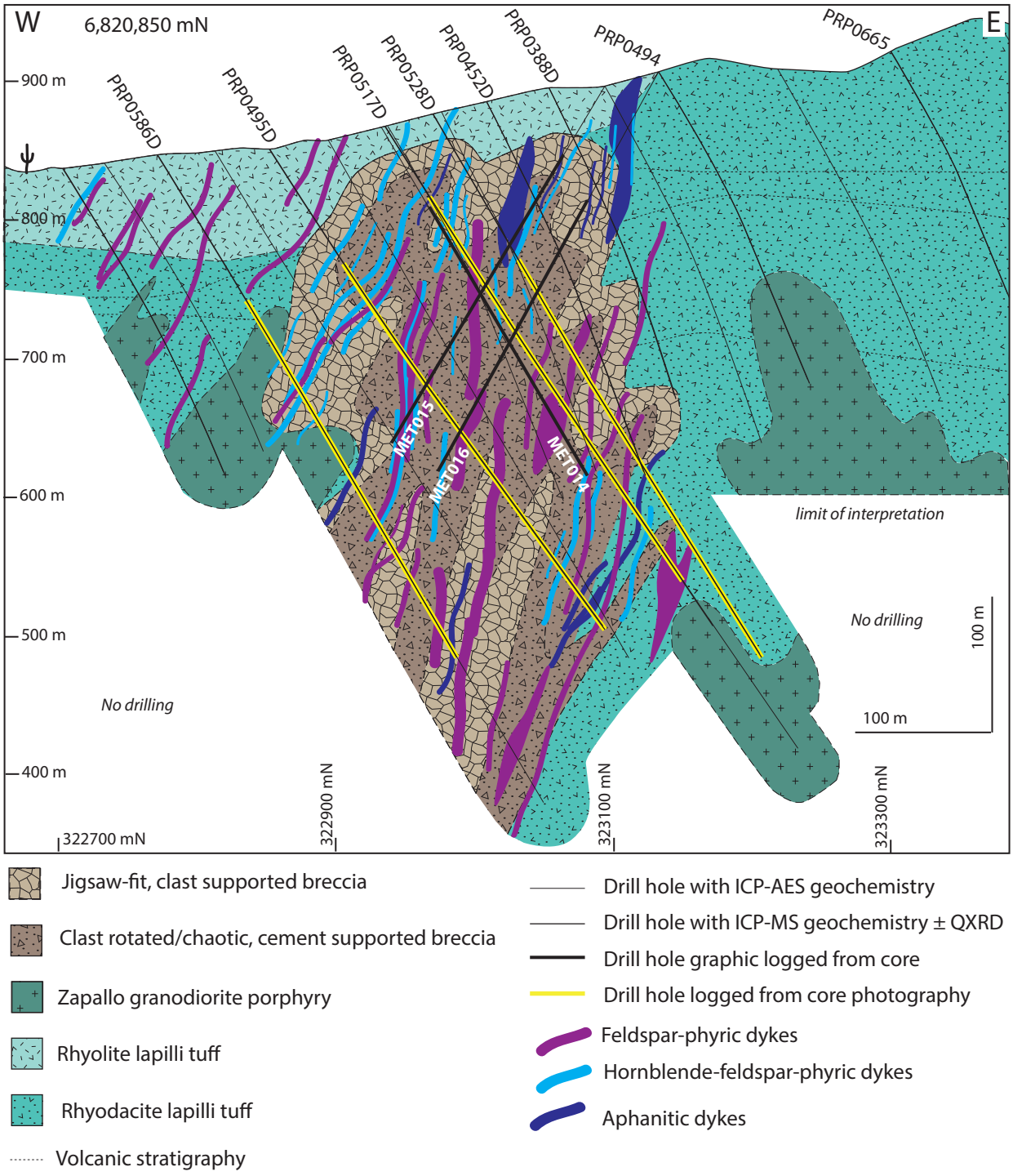

Figure 3.6 Cross section at 6,820,850 mN showing geology interpreted from graphic core logging, photo logging and immobile element lithogeochemistry. Breccia domains reflect variations in texture and internal clast organisation — protolith textures were largely obscured by alteration and brecciation in these domains.

inconsistent geological logging throughout the drill hole database, rendering interpretation of primary geology unreliable. In order to overcome this issue and develop a new geological model at Productora immobile element lithogeochemistry using a whole rock multi-element ICP-MS geochemistry (1.3.3.1) database has been employed. Lithologies have been discriminated using a series of bivariate plots between the following elements available in the dataset: Al, Cr, Hf, Nb, Sc, Ti, Tl, V, and Zr. Productora data were compared to a dataset compiled from Andean arc rocks from northern Chile (21–25°S) acquired from Georoc online database (provided in Appendix B8). Intrusive rocks were discriminated based on Hf:Zr ratios, which diverge from the ratio of volcanic rocks due to fractional crystallisation. Mafic lithologies were selected based on Cr content (mafic - A >50 ppm, mafic - B >400 ppm). Scandium was used as a proxy for Fe in order to discriminate rhyolite, rhyodacite and dacite. A combination of bivariate plots were used to validate compositional groups and further subdivide where appropriate (Appendix B9). Results were validated against graphic logging, core photos, petrography, classification diagrams (e.g. TAS; least altered samples only) and typical Andean arc rock compositions.

3.4 Volcanic rocks

Productora is hosted by the Bandurrias Formation (Segerstrom 1960; Moscoco et al., 1982), part of the Jurassic-early Cretaceous magmatic arc (Charrier et al., 2007; Figure 3.7). The Bandurrias Formation was deposited during a 40–55 million year period of extension and basin formation punctuated by shorter

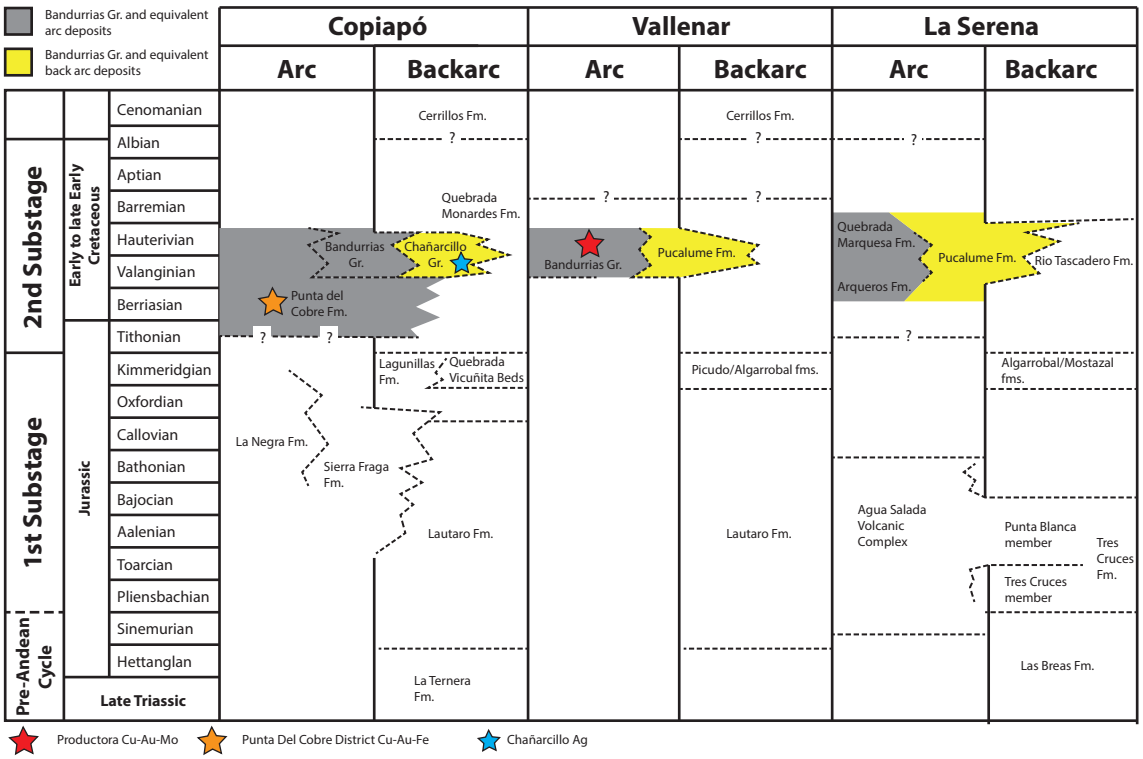

Figure 3.7 Chronostratigraphic relationships between arc and backarc stratigraphy, during the first stage of Andean tectonic cycle in Copiapó, Vallenar and La Serena regions, and major regional mineral deposits (modified from Charrier et al., 2007). Fm. = formation, Gr. = group

contractional episodes of basin inversion (Charrier et al., 2007). The cyclical evolution of the Andean margin in this region resulted in several cycles of transgression and regression during the formation of the Jurassic and Early Cretaceous marine backarc basins. The Bandurrias Group is a thick package of predominantly andesite volcanic rocks with intercalations of clastic volcanic rocks (tuff and breccia), siliclastic and calcareous marine rocks, which are lateral facies variations of the backarc Chañacillo Group limestones (Moscoco et al., 1982).

Locally, the Bandurrias Group consists of a range of felsic and intermediate-mafic volcanic sequences, and is characterised by rapid lateral facies variations (Moscoso et al., 1982). Fox (2000) described a gentle southeast-dipping stratigraphy of volcaniclastic rocks and flows at Productora with early andesitic volcanics succeeded by three dacitic tuffs and unconformably overlain by basalt and basalt-andesite flows (Figure 3.8; Table 3.1). The volcanic stratigraphy sequence proposed by Fox (2000) was supported by the results of field mapping by Beeson et al. (2012). Both authors commented on the challenge of determining whether or not the 'siliceous appearance' of felsic volcanic rocks in the field is due to the rhyolitic primary composition of the stratigraphy, or a reflection of intense hydrothermal alteration.

During this study, four major volcanic lithologies have been identified at Productora. From oldest to youngest they are; rhyodacite lapilli tuff, rhyodacite monomict breccia, rhyolite welded lapilli tuff and rhyolite lapilli tuff. The relationship between these lithologies and those proposed by Fox (2000) is presented in Figure 3.8. Whilst the term rhyodacite is not commonly used in recent literature, the term

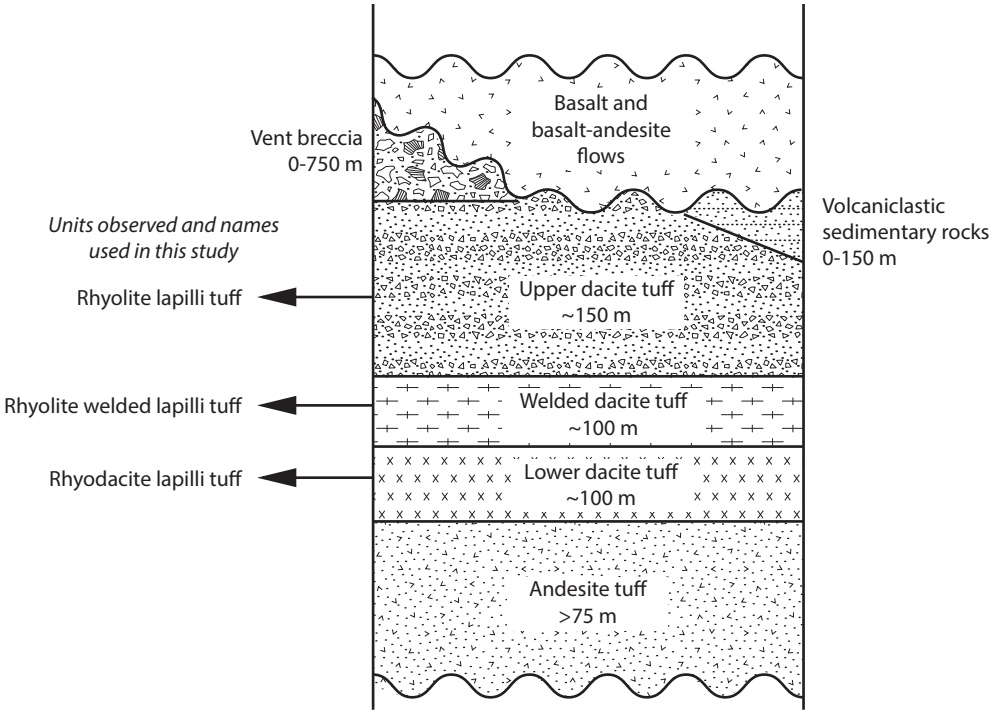

Figure 3.8 Stratigraphic column for volcanic rocks at the Productora deposit. Modified from Fox (2000).

Table 3.1 Summary of lithology descriptions from Fox (2000).

Name	Distribution	Thickness	Composition	Description	Other comments
Basaltic-andesite flows	Southeast; strike of 025° for 2.5 km	Approximately 150 m	Basaltic andesite	Phenocrysts of cpx (altered to chl + act) and pl (bimodal size, 0.4 and 1.0 mm) in groundmass of pl (0.4 mm), finely disseminated mt (0.02 - 0.2 mm), fine grained, felted am (act after cpx?)	Overlies vent breccia, volcaniclastic sedimentary rocks and dacite ash-flow tuff; relationship to basalt flow unknown
Basalt flows	West; outcrop at base of silica ridge over 2.5 km by 1-1.5 km	Max. 150 m; pinch out at margins	Basalt	Subhedral phenocrysts (40%) of ol, pl, cpx (1–2 mm) and secondary hmt, in groundmass of pl (0.04–0.1 mm), cpx (0.03 mm) and fine disseminated secondary hmt (0.02–0.04 mm), ol phenocrysts are altered to bow	Unconformable lower contact with ash-flow units
Dacite breccia	Southeast; outcropping 1 km by 0.3 km	Max. 75 m	Dacite	Polymictic (andesite-dacite ash-flow tuff), angular to subrounded blocks (up to 0.5 m), white qtz-phyric groundmass	Interpreted as a vent breccia by Fox (2000)
Volcaniclastic sedimentary rocks	Southeast; outcropping 1 km by 0.1–0.3 km	Approximately 150 m		Monomineralic layers (0.02–3 cm thick) of qtz, hmt, mgt, chl, ep or tur, thicker layers have anastomosing boundaries and some form boudin-like shapes, generally sub-horizontal (dip 15° southeast)	Layering interpreted as hydrothermally replaced bedding
Upper dacite ash-flow tuff	East; strike of 030° for 3 km with outcropping width of 0.3–1 km	Approximately 250 m	Dacite	Qtz, pl and kfs phyric with lithic clasts of andesite and devitrified pumice (0.5–2 cm) in matrix of fine grained plag, ksp and rounded qtz eyes (0.01mm); large, rounded-elliptical pumice fragments observed locally at base of unit (2–6 cm, max. 15cm) in matrix of chl, qtz and pl	Distinguished from lower dacite unit by more abundant qtz phenocrysts (5%); large pumice fragments thought to be autobreccia; composition toward rhyolite
Dacite welded ash-flow tuff	Central and north-east; strike of 030° for 3 km; 0.5–1 km wide (narrows to 0.1 km in south); truncated by northeast trending fault	Approximately 100 m	Dacite	Abundant subhedral, broken pl (1–2 mm) and rounded qtz eyes (0.5 mm) with resorption textures in matrix of fine grained pl and qtz, eutaxitic textures with no remaining pore space, devitrified, groundmass is generally pale purple-dark maroon)	Eutaxitic textured interpreted as complete welding
Lower dacite ash-flow tuff	Central; strike of 030° for 4 km; 0.5 km wide	Approximately 100 m	Dacite	Qtz + fsp phyric, lithic clasts (0.5–2 cm) of andesite and pumice (devitrified to qtz + fsp), devitrified matrix of tr, qtz and pl, primary texture obliterated by devitrification and alteration	Eutaxitic texture and qtz resorption textures distinguish it from dacite ash–flow tuff
Andesitic ash-flow tuff	Discontinuous throughout but best exposed in north	Min. 75 m	Andesite - no qtz and abundant chl + act (after hbl)	Broken pl phenocrysts 1 mm (up to 4 mm), rounded devitrified pumice fragments of qtz + fsp (up to 4cm), primary texture obliterated by devitrification and alteration	In hand specimen difficult to determine between tuff and flow due to euhedral appearance of pl phenocrysts

act = actinolite, am = amphibole, bow = bowlingite, chl = chlorite, cpx = clinopyroxene, ep = epidote, fsp = feldspar, hbl = hornblende, hmt = hematite, kfs = K-feldspar, mt = magnetite, ol = olivine, pl = plagioclase, qtz = quartz, tr = tremolite, tur = tourmaline etc.

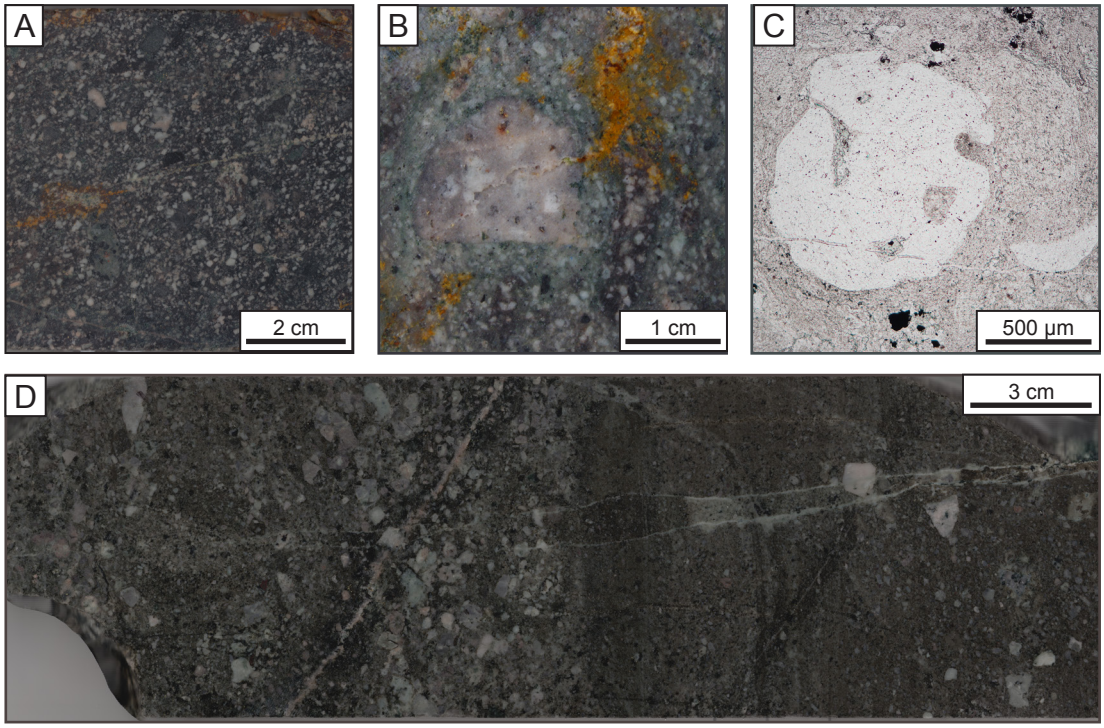

Figure 3.9 Representative core and thin section photos from rhyodacite lapilli tuff. A) Crystal-rich lapilli tuff (PR14AE015; MET007 409 m). B) Feldspar-phyric clast (MET007 406 m). C) Plane-polarised transmitted light photo showing volcanic quartz with resorption texture (PR14AE017; MET007 406.3 m). D) Crystal-poor interbed with polymict lapilli, some showing strong K-feldspar alteration and normal graded bedding (PR14AE047; MET007 376.5 m).

has been included in this study to enable clear differentiation between the more felsic rhyolite units and more mafic rhyodacites following the volcanic rock classification scheme of Streckeisen (1984).

3.4.1 Rhyodacite lapilli tuff

Age: 128.67 ± 1.29 Ma (Table 3.3)

The oldest and most abundant volcanic rocks encountered in drill core from Productora are variably altered, massive, moderately sorted, leucocratic, polymict lithic- and crystal rich volcanic sandstones (Table 3.2; Figure 3.9 A). Lithic clasts are angular, typically granule to pebble size, with oversize cobbles, and vary from aphanitic quartz-felspathic to feldspar-phyric, commonly showing intense hydrothermal K-feldspar alteration (Figure 3.9 B). Feldspar crystal fragments range from complete euhedra to chips and splinters. Quartz crystals typically show resorption textures (Figure 3.9 C). Although the sandstones are predominantly massive, examples of graded bedding with increased clast rounding (Figure 3.9 D) and interbeds of massive, poorly sorted, lithic pebble-rich sandstone and fiamme-bearing volcanic mudstones have been observed in drill core and core photos. Intense hydrothermal alteration and overprinting breccia events pose challenges to the recognition of the volcanic sandstones, which can easily be misidentified as a porphyritic coherent unit. Careful attention needed to be paid to the recognition of lithic clasts and the crowded uneven crystal distribution, as these provide convincing evidence for a clastic origin for the

Table 3.2 Characteristics of volcanic lithologies from Productora.

Grainsize	Components (clasts, matrix, cement)	Lithofacies (fabric, clast organisation, geometry)	Apparent thickness and distribution	Interpretation	Classification
Rhyodacite lapilli tuff					
Sandstone-gravel breccia (1/16-4 mm)	40-80% lithics, quartz and feldspar crystals - lithics: polymictic, 5 %, 1-5 mm with oversized >64 mm, aphanitic quartz-feldspathic ± feldspar phenocrysts, angular - quartz crystals, 5 %, resorption textures, 0.2-1 mm - feldspar: 25 % plagioclase, 0.2-2 mm, commonly broken crystals fragments and 5 % K-feldspar (0.2-0.4 mm), commonly sericite altered 20-60 % fine grained, massive matrix	Matrix supported, moderately sorted, chaotic, stratified, local graded bedding, concordant with gradational contacts	> 166 m (MET007); 81 m (MET018); 142 m (MET022); 97 m (PRP0027D) Major lithology in drill core from south and central-west in north	Pyroclastic	Rhyodacite
Rhyodacite monomict breccia					
Very fine grained (<20 µm)	Phenocrysts: <5 % feldspar phenocysts, 0.2-1 mm, euhedral, commonly sericite altered? Groundmass: microcrystalline quartz-feldspar	Massive, ± flow alignment of prismatic groundmass crystals (trachytic texture)	120 m (PRP0018D) Drill core in central north	Lava (sub-aerial?)	Rhyodacite
Rhyolite welded lapilli tuff					
Sandstone (1-2 mm)	40-60 % lithics, quartz, feldspar, shards - lithics: polymictic, 10 %, 1-10 mm, aphanitic quartz-feldspathic ± feldspar phenocrysts, sub-angular - quartz crystals, 3-5 %, 0.2-1.2 mm - feldspar: 25 % plagioclase, 0.2-1.5 mm,<3% K-feldspar, 0.2-0.4 mm, commonly sericite altered - pervasively muscovite altered glass shards define welded fiamme texture 40-60 % fine grained, massive matrix	Clast-matrix supported; chaotic, welded	189 m (NS1D) Drill core and surface in north east	Welded pyroclastic	Rhyolite
Rhyolite lapilli tuff (hand specimen only)					
Sandstone (1-2 mm)	40-60 % lithics, quartz, feldspar - lithics: polymictic, 10 %, 1-20 mm with oversized >256 mm, angular, aphanitic quartz-feldspathic ± feldspar phenocrysts - quartz crystals, 5 %, 0.5-1 mm - feldspar: 25 % K-feldspar after plagioclase(?), 1-1.5 mm 40-60 % fine grained, massive matrix	Matrix supported; poorly sorted; chaotic	Outcropping on hillside in north east	Pyroclastic	Unknown

lapilli tuff (Figure 3.9 B). The composition is interpreted to be rhyodacite based on the abundance of feldspars and quartz. The rhyodacite lapilli tuff is equivalent to the lower dacite tuff of Fox (2000).
No upper or basal contacts for the rhyodacite lapilli tuff were observed in drill core or mapping. Fox (2000) described the upper contacts with overlying basalt and basalt-andesite flows to the south as unconformable (Figure 3.4).

3.4.1.1 Interpretation

Based on the presence of abundant crystal fragments in a fine grained matrix and a variety of lithic fragments that show aphanitic to porphyritic textures, combined with the generally massive nature of the lithology, the rhyodacite lapilli tuff is interpreted to be a lithified pyroclastic flow deposit resulting from explosive magmatic or phreatomagmatic eruptions combined with a turbulent flow regime (e.g., McPhie et al., 1993). Further detailed graphic logging of volcanic textures, in order to determine facies associations, would be required to constrain the genesis of the pyroclastic flow, such as by vertical column collapse to form ignimbrite. Minor units with graded bedding are interpreted to represent intervening episodes of sedimentation from mass flow or suspension.

3.4.2 Monomict rhyodacitic breccia

Monomict rhyodacitic breccia has been intersected in drill core in the northern section where the unit is overprinted by later hydrothermal breccias (Figure 3.5; MET007 and MET008B). This unit is a pervasively K-feldspar altered, massive, clast-supported, moderately well sorted, in-situ to clast-rotated, monomict lithic, variably chlorite-rutile and K-feldspar cemented, granule- to pebble-sized breccia (Figure 3.10 A and H). Clasts consist of sparsely, fine-medium, feldspar-phyric, aphanitic, massive coherent rhyodacite (Figure 3.10 B and G). The rhyodacite clasts have primary plagioclase and K-feldspar phenocrysts and have undergone secondary K-feldspar replacements of plagioclase where

Table 3.3 Geochronology for major lithologies at Productora. Age error quoted as 2 sigma.

Lithology	Sample ID	Age (Ma)	Dating method	Number of zircon analyses	Reference
Rhyodacite lapilli tuff	PR14AE177	128.67 ± 1.28	U-Pb (zircon)	12	This study
Rhyolite welded lapilli tuff	PR14AE143	127.99 ± 1.28	U-Pb (zircon)	11	This study
Cachiyuyito	KF-78	129.8 ± 0.1	U-Pb (zircon)	6	Fox (2000)
Zapallo porphyry	PR14AE175	118.87 ± 1.19	U-Pb (zircon)	15	This study
Ruta Cinco border	KF-417	96.1 ± 0.2	U-Pb (zircon)	3	Fox (2000)
Ruta Cinco core	PR14AE120	92.05 ± 1.00	U-Pb (zircon)	12	This study
Alice porphyry	PR14AE210	121.1 ± 2.1 Ma	U-Pb (zircon)	16	This study

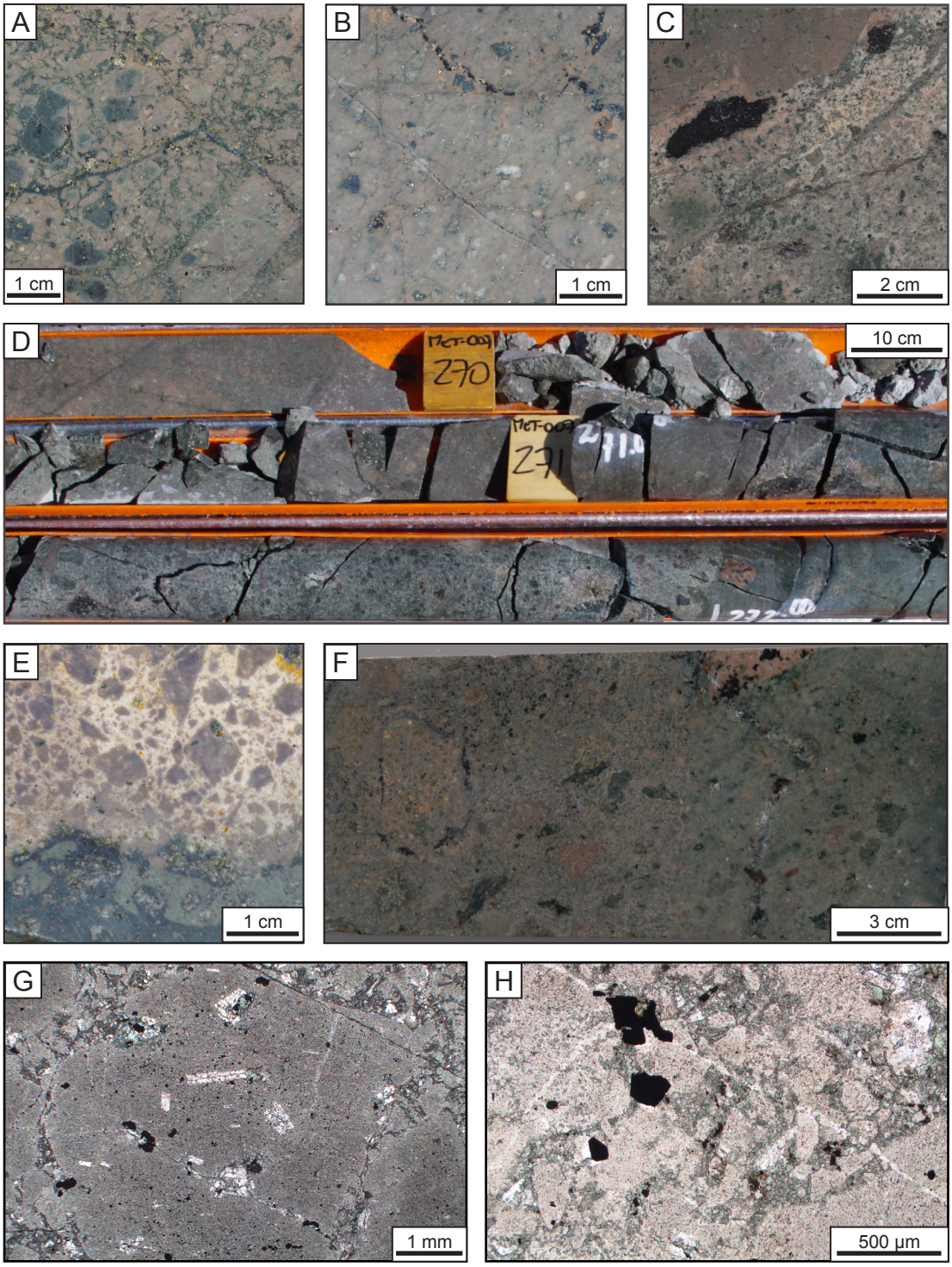

Figure 3.10 Representative core photos from rhyodacite monomict breccia. A) Monomictic pebble-sized breccia now cemented by chlorite with pervasive–patchy K-feldspar alteration of clasts (MET007 197.70 m). B) Coherent feldspar-phyric rhyodacite-oversized clast hosted in rhyodacite monomict breccia (MET007 252 m). C) Contact between rhyodacite monomict breccia and hydroclastic breccia (PR14AE065; MET007 272.25 m). D) Basal contact between rhyodacite monomict breccia and rhyodacite lapilli tuff, hydroclastic textures and vesicles preserved in tuff (MET007 269.70–272.20 m). E) Hydroclastic contact between rhyodacite monomict breccia and rhyodacite lapilli tuff (MET007 275.50 m). F) Vesicles preserved in rhyodacite lapilli tuff (PR14AE192; MET007 271.95 m). G) Plane-polarised transmitted light photo showing clast with feldspar phenocrysts in aphanitic groundmass (PR14AE021; MET008B 103.90 m). H) Plane-polarised transmitted light photo showing breccia cemented by chlorite and rutile with cross cutting quartz veinlets and disseminated sulphides (PR14AE022; MET008B 104.20 m).

hydrothermal alteration is most intensely developed. The clastic groundmass consists of microcrystalline quartz-feldspar. A trachytic texture has been observed in some thin sections. In general the breccia is pale pink to light maroon, reflecting a dusting of fine grained hematite in the feldspars (Figure 3.10 B). The composition is inferred to be rhyodacite based on the abundance of primary feldspars and quartz.

The monomict rhyodacitic breccias are inherently variable in texture and have typically been subjected to intense texturally destructive K-feldspar alteration, and locally overprinted by hydrothermal brecciation, which have locally obscured contact relationships. A sharp basal contact with rhyodacite lapilli tuff was noted in drill core (MET007 272.25 m; Figure 3.10 C and D, Appendix B3). Within 1 m of the contact, the rhyodacite lapilli tuff contains a higher proportion of variably altered, angular, monomict rhyodacite lithic granules, which grade to pebbles 10 cm further away from the contact (Figure 3.10 D and E), implying that intense brecciation occurred at the contact. The matrix to the contact zone breccia and lapilli tuff is vesicular within 90 cm of the contact, suggesting steam involvement (hydroclastic breccia; Figure 3.10 F).

3.4.2.1 Interpretation

The coherent characteristics of the clasts (massive, even distribution and narrow size range of feldspar phenocrysts in aphanitic groundmass with trachytic texture), jigsaw fit breccia texture and monomict nature suggest autobrecciation of a lava (eg. McPhie et al., 1993) . The sharp basal contact and the vesicular texture of the immediate underlying sedimentary rocks suggests interaction with water (hydroclastic) — most likely from wet sediments as no other evidence of subaqueous emplacement is noted. As no large intervals of massive coherent rhyodacite have been intersected, it is assumed that either only the edge of the body has been observed in the northern section (Figure 3.5), or the entire body has experienced autobrecciation. It is not possible to determine the mode of emplacement for the rhyodacite breccia without more information on associated facies, but given the available evidence, a subaerial flow-dome or shallow crypto dome are considered the most likely scenarios (e.g. McPhie et al., 1993). Texturally destructive alteration and the lack of key contact and related facies information, limits the confidence in these genetic interpretations.

3.4.3 Rhyolite welded lapilli tuff

Age: 127.99 ± 1.28 Ma (Table 3.3)

A variably altered, matrix- and clast-supported, moderately sorted, massive, fiamme bearing, crystal-, shard- and polymictic lithic- rich sandstone is observed in drill core from the eastern hillside (Figure 3.5;

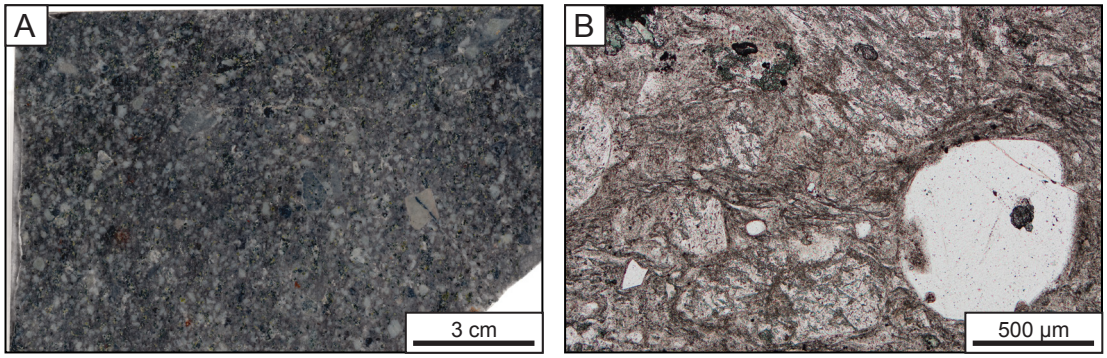

Figure 3.11 Representative core and thin section photos from welded rhyolite lapilli tuff. A) Core showing crystal-rich composition with polymict lapilli (PR14AE143; NS1 143.60 m). B) Plane-polarised transmitted light photo showing welded groundmass mantling quartz and feldspar crystals (PR14AE143; NS1 143.60 m).

Figure 1.1; NS1D). In hand specimen this unit appears similar to the rhyodacite lapilli tuff described above but differs in thin section where a fiamme welded shard (eutaxitic) texture is apparent (Figure 3.11). Clasts range from granule to small pebbles, and are subangular, dominated by aphanitic quartz-feldspathic and commonly feldspar phyric lithic fragments. Crystals include a range of broken to complete plagioclase feldspars, subordinate K-feldspar and quartz crystals with resorption textures. The composition is inferred to be rhyolite based on the composition of feldspar and relatively higher quartz abundance compared to the rhyodacitic lithologies. No upper or basal contacts for the rhyolite welded lapilli tuff were observed in this study but unit thickness is estimated to be in excess of 190 m based on core observations (Figure 3.5). In cross section, the unit is interpreted to be juxtaposed against the rhyodacite lapilli tuffs (Figure 3.5) due to east side down dip-slip fault movement. This interpretation is supported by the juxtaposition of contrasting high and low temperature alteration assemblages and pathfinder elements (Escolme et al., 2015). The rhyolite welded lapilli tuff corresponds with the welded dacite tuff of Fox (2000).

3.4.3.1 Interpretation

The platey shards that define the fiamme texture (Figure 3.11) are interpreted to be former glass shards indicating explosive fragmentation of magma or lava (McPhie et al., 1993). The absence of delicate spines and bubble walls amongst the shards indicate welding has occurred (McPhie et al., 1993). The unit is interpreted to be a welded pyroclastic flow deposit on the basis of the fiamme texture, shards and abundant crystal and lithic fragments with no internal organisation (McPhie et al., 1993). The unit is interpreted to be a welded ignimbrite.

3.4.4 Rhyolite lapilli tuff

This unit is exposed high on the eastern hillside (Figure 3.4 and Figure 1.1). It is a pervasively K-feldspar

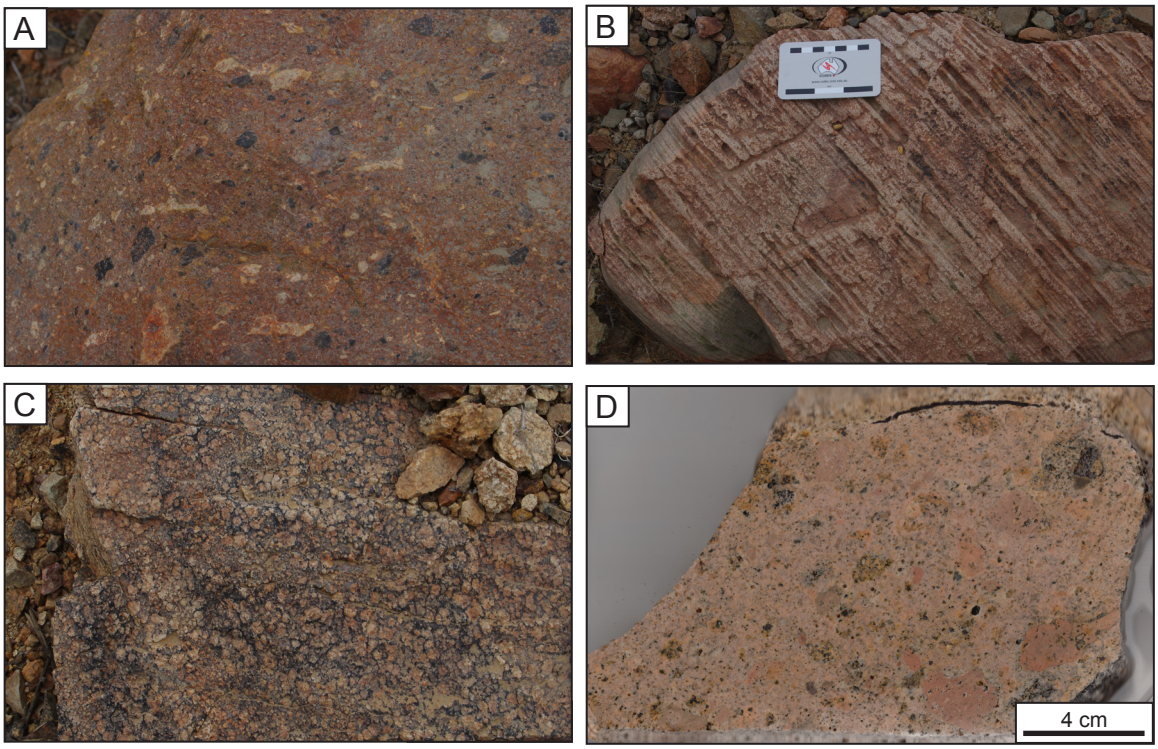

Figure 3.12 Photos of rhyolite lapilli tuff. A) Reconnaissance mapping photos showing juvenile clasts and B) flow banded rhyolite in float (324425 mE, 6824217 mN. C) Spherulites 323430 mE, 6821044 mN. D) Photo of hand specimen with abundant polymict lapilli (PR14AE197; 6,821,850 mN, 324450 mE).

altered, blocky, matrix supported, poorly sorted, massive, crystal- and lithic-rich sandstone with oversized lithic cobble clasts (Table 3.2; Figure 3.12). Examples of rhyolitic flow banding, cobble conglomerates, juvenile clasts and spherulites were observed during two reconnaissance mapping trips and by other workers (Figure 3.12; this work; Beeson et al. 2012).

Hand specimen observations from an outcrop of this unit indicate lithic clasts are polymict, angular and range broadly in size, with a number of oversized clasts observed (Figure 3.12 D). Similar to the other volcanic units, the clasts are typically either aphantitic quartz-feldspathic or feldspar-phyric. Pervasive alteration masks much of the matrix but plagioclase ghosts and round quartz eyes have been observed. Hand specimen observations (leucocratic, quartz eyes) suggest a rhyolite composition. The rhyolite lapillic tuff corresponds to the upper dacite tuff of Fox (2000).

3.4.4.1 Interpretation

Spherulites indicate quenching of high temperature lava, to form natural glass, and subsequent devitrification at high temperature (400-700 °C; McPhie et al., 1993). This unit is interpreted to be a sequence of felsic volcanic facies consisting of both flows and pyroclastic deposits.

3.5 Intrusive rocks

3.5.1 Cachiyuyito

Age: 129.8 ± 0.1 Ma (Fox, 2000; Table 3.3)

The Cachiyuyito stock outcrops as an elongate, 2.5 km long body in the north of the deposit (Figure 3.4), the El Molle stock is believed to be a fault displaced extension of this intrusion (Dick and Ray, 2000). The Cahciyuyito was described as an equigranular-weakly feldspar-phyric, concentrically zoned intrusion with a tonalite core and diorite border phase. Free quartz is only observed in the tonalite core (Table 3.4; Fox, 2000; Beeson et al., 2012). The Cachiyuyito was not observed during this study. The absolute age of the Cachiyuyito stock indicates it is broadly coeval with the host volcanic stratigraphy (within analytical error; Table 3.3). This is consistent with contemporaneous emplacement of plutons and volcanism (Sillitoe, 2003). Further geochronology would be beneficial to better constrain the relative ages.

3.5.2 Alice porphyry

Age: 121.1 ± 2.1 Ma (Table 3.3)

The Alice porphyry does not crop out at surface but was observed in drill core from two holes (PRP0874D and PRX0001D) during this study. Several phases of intrusion are documented including: equigranular tonalite, feldspar-crowded porphyry, quartz-feldspar porphyry with the possibility of additional phases (Beeson, 2015). This is supported by graphic logging of PXP0001D, where abrupt changes in vein

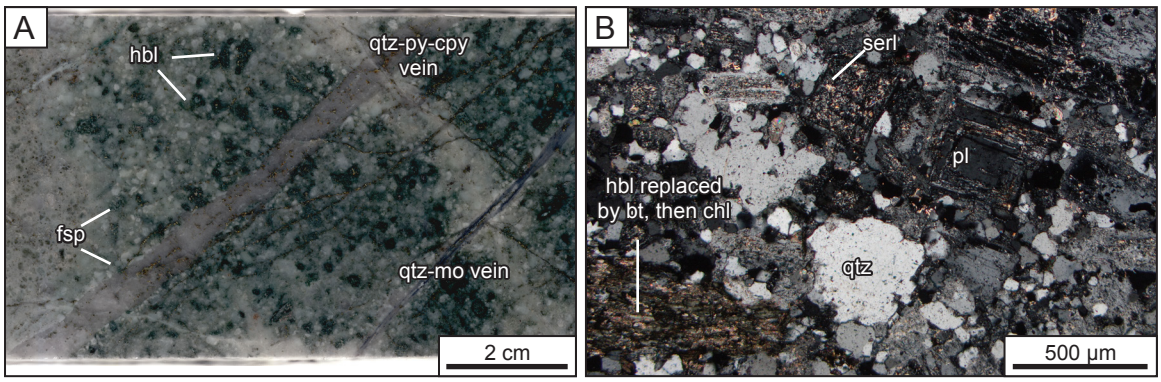

Figure 3.13 Representative photos of Alice granodiorite porphyry. A) Photo of half core showing feldspar- and hornblende-phyric texture (PR14AE215, PXP0001D 217.5 m). B) Cross polarised, transmitted light photomicrograph showing plagioclase, quartz and hornblende phenocrysts (PR14AE214, PXP0001D 195.7 m). bt = biotite, chl = chlorite, cpy = chalcopyrite, fsp = feldspar, hbl = hornblende, mo = molybdenite, py = pyrite, qtz = quartz

Table 3.4 Summary of intrusive lithology descriptions from Fox (2000) and Ray and Dick (2002).

Name	Age (Ma)	Distribution	Composition	Description
Cachiyuyito	129.8 ± 0.1	Elongate, north–northeast oriented body; cropping out over 2.5 km with maximum width 800 m	Concentrically zoned; tonalite core and diorite border	Equigranular to weakly porphyritic, abundant plagioclase (72 %), hornblende and augite, quartz only in core, accessory zircon, ilmentite, apatite, zoisite and carbonate
Ruta Cinco	96.1 ± 0.2 (border phase)	Southeast	Composite batholith; coarse-grained, leucocratic granodiorite core and quartz monzodiorite border	Core: medium-coarse grained (average 2–3 mm), equigranular, abundant rounded xenoliths of diorite (long axis 15–20 cm) Border: weakly magnetic, medium grained (ave. 1 mm), irregular interstitial quartz (0.5 mm), sub-anhedral biotite and hornblende (1–2 mm), anhedral clinopyroxene (0.5–1 mm), abundant (up to 1 %) subhedral to euhedral apatite (0.1 x 0.08 mm), locally kaolinite altered with biotite ± garnet ± cordierite hornfels contact aureole
Andesite dykes		Abundant on eastern ridge proximal to Ruta Cinco contact; outcrop typically 1 m x 5–10 m length; strike 310°–320°; cross cut Cachiyuyito and volcanic rock but not Ruta Cinco, interpreted to be related to early stages of Ruta Cinco intrusion (Fox, 2000)	Andesite	Phaneritic: fine grained, equigranular, plagioclase (subhedral, 0.04–0.4 mm) and clinopyroxene (0.2–0.4 mm), rare plagioclase and pyroxene phenocrysts (1–2 mm), alteration to actinolite, magnetite (0.1 mm), chlorite and epidote Porphyritic: phenocrysts of plagioclase (20 %) and clinopyroxene (both 1–3 mm) ± hornblende (max. 2 cm), very fine groundmass dominated by plag (0.1–0.02 mm) intergrown with clinopyroxene and anhedral primary and secondary magnetite (0.02 mm), rare disseminated chalcopyrite and pyrite

abundances imply the presence of a younger intrusion (Appendix B3 - PXP0001D 225 m and 262 m). Samples of Alice porphyry collected in this study are all texturally and compositionally similar, therefore they are described collectively. All samples show alteration of feldspars to muscovite and mafic phases to chlorite.

Thin sections from five samples of the Alice porphyry reveal a feldspar- ± quartz-phyric to crystal-crowded granodiorite (Appendix B10). Phenocrysts of plagioclase and subordinate K-feldspar make up 15-40 % of the rock and are typically between 0.4-2.5 mm (Figure 3.13). Quartz and hornblende locally occur as minor phenocrysts (<5 % total phenocrysts), up to 3 and 6 mm in size respectively. Oscillatory zoning of large plagioclase crystals is noted, and has been enhanced by muscovite alteration. The groundmass is composed of interlocking, anhedral fine grained (0.2–0.6 mm) quartz and feldspar crystals. Chlorite has locally replaced secondary biotite after hornblende phenocrysts. Minor phases include zircon and secondary rutile. An upper contact with host volcanic rocks was observed in PRX0001D. Adjacent to the contact the Alice porphyry is strongly muscovite altered with strong foliation developed locally.

3.5.3 Zapallo Porphyry

Age: 118.87 ± 1.19 Ma (Table 3.3)

The Zapallo porphyry intrusion has been mapped over a 0.8 km^2 area to the east of Productora (Beeson et al., 2012; Figure 3.4) on the western flank of El Zapallo hill, after which it is named. The intrusion has not been described previously in any detail. It was identified in drill core from the southern study section during graphic logging. It is a medium grained, crystal crowded, feldspar - hornblende-phyric, medium grained granodiorite (Figure 3.14 A; Appendix B10) containing subhedral phenocrysts of feldspar and hornblende up to 2 mm in size.

The intrusion is massive, with abundant mafic xenoliths (Figure 3.14 A) of sparsely, medium, feldspar phyric, fine grained diorite. The groundmass fines toward sharp, discordant contacts with a narrow breccia zone between it and the dacite-rhyodacite lapilli tuff. The contact breccia has an apparent thickness of approximately 1 m in drill core (Appendix B3, MET018 at 284 m and 291 m). It is a polymict, lithic, clast-matrix supported, poorly sorted, chaotic, massive, pebble-sized breccia. The breccia is composed of 80 % subangular, tabular-subequant, lithic clasts. Clasts include volcanic sandstone and lithic breccia (Figure 3.14 B) which are variably altered (intense chlorite, clay or quartz alteration). A matrix of <4 mm lithic fragments and rock flour comprises 15 %, and pyrite, quartz and clay make up 5 % cement.

The results of U-Pb geochronology (Table 3.3) indicate that the feldspar porphyry is approximately 22

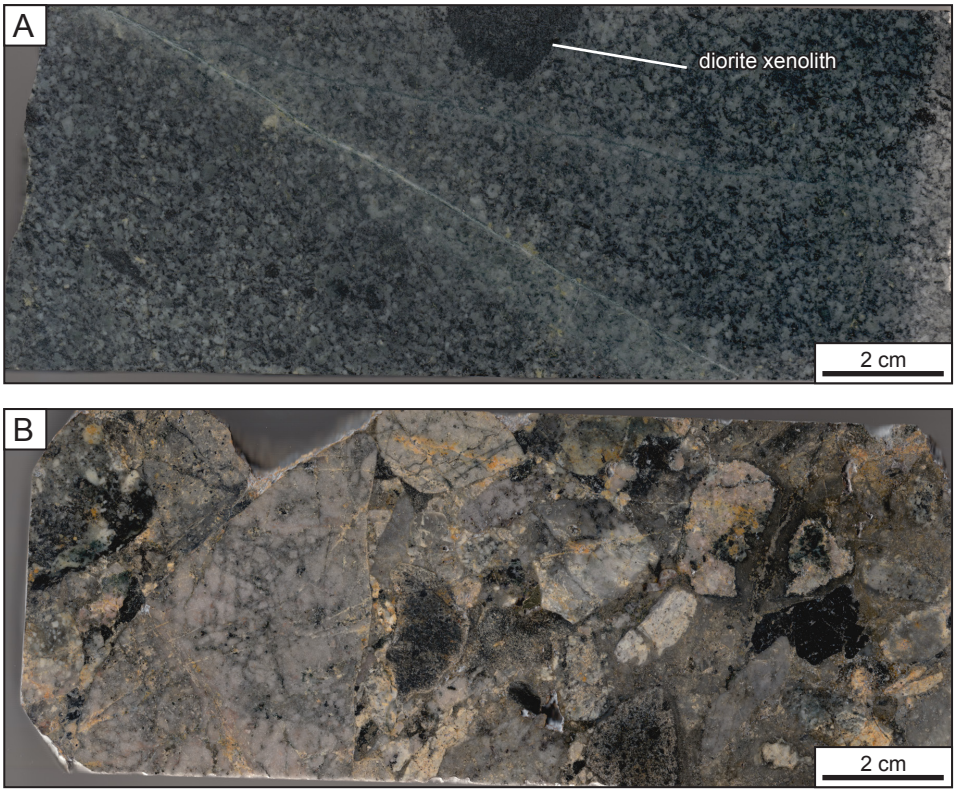

Figure 3.14 Half core photos of A) Zapallo medium-grained, granodiorite porphyry with diorite xenolith (PR14AE175, MET016 328.5 m) and B) polymict contact breccia (PR14AE186, MET0168 291.2 m).

m.y. older than the Ruta Cinco phases that crosscut it. The contact breccia is likely to be a cataclasite that has been hydrothermally cemented with quartz and pyrite. The presence of breccia fragments indicates that the breccia is polyphase.

3.5.4 Ruta Cinco

The Ruta Cinco intrusion (named after the Pan-America highway that crosses it) crops out to the southeast of the deposit (Figure 3.4). It is part of the Camarones plutonic complex (Figure 3.1) which crops out over 100 km^2 and forms part of the vast Chilean coastal batholith (Moscoco et al., 1982).

The intrusion is a composite batholith, with a coarse grained, leucocratic granodiorite core and quartz-monzonite border phase (Table 3.4; Fox, 2000). During this study, only the granodiorite core was observed in a quarry located 4.7 km to the south east of the Productora deposit, adjacent to the Ruta Cinco highway (Figure 3.15 A).

3.5.4.1 Ruta Cinco granodiorite core

Age: 92.05 ± 1 Ma (Table 3.3)

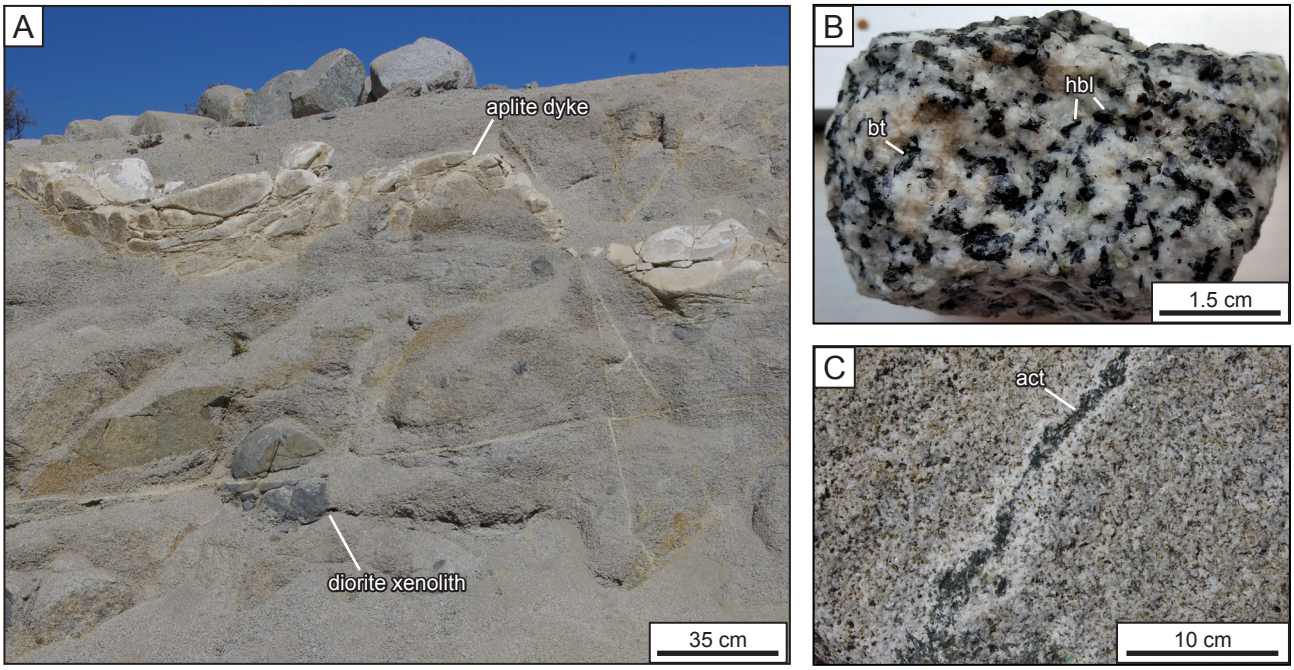

Figure 3.15 Representative photos of Ruta Cinco core phase outcrop in a small quarry at 326,322 mN 6,828,807 mN. A) Quarry outcrop showing aplite dykes and round diorite xenoliths, B) Hand specimen showing medium grained quartz, feldspar, hornblende and biotite (PR14AE120). C) Actinolite vein with bleached selvage in outcrop. act = actinolite, bt = biotite, hb = hornblende

In outcrop, the granodiorite has been strongly weathered but several notable features were observed; abundant mafic xenoliths, aplite dykes, goethite (after pyrite)-chrysocolla veins, amphibole-feldspar-quartz veins, and clasts of megacrystic hornblende phyric andesite (Figure 3.15). The amphibole occurs as dark green radiating prismatic crystals (Figure 3.15 C). These veins appear to be cut by aplite dykes. Well rounded, mafic xenoliths between 5 and 60 cm in size, comprise approximately 2 % of the outcrop. These have been cross cut by aplite dykes, which range from 1-20 cm in width. In hand specimen the rock is medium grained (average 1-2 mm grain size) and equigranular (Figure 3.15 B). The rock typically consists of 5 % biotite, 10 % hornblende, 20 % quartz and 65 % feldspar.

3.5.4.2 Ruta Cinco quartz-monzodiorite border phase

Age: 96.1 ± 0.2 Ma (Fox, 2000; Table 3.3)

The Ruta Cinco border phase was mapped by Fox (2000) and Beeson et al. (2012) on the El Zapallo hill top (>1150 m elevation) to the southeast of the deposit (Figure 3.4). It forms a 300-600 m thick border to the Ruta Cinco core. The intrusion is described as a medium grained quartz-monzodorite which is weakly magnetic and contains 20 % biotite and hornblende with abundant apatite (Fox, 2000; Table 3.4).

Table 3.5 Summary of dykes observed during core logging.

Type	Description	Cross cutting relationships	Timing
Ovoid feldspar-phyric basalt	Very dark green-black; poor-moderately, ovoid, fine-medium, fsp-phyric; ± pyroxene ghosts; aphanitic groundmass; weakly magnetic	Intensely chl altered; abundant veins of py, cpy and cct; brecciated by tur-cemented breccia; locally deformed	Pre-mineralisation
Basaltic-andeiste	Massive; fsp-phyric; dark green; magnetic; aphanitic groundmass	Crosscuts tur-cemented breccias	Post-main mineralisation
Feldspar-phyric basaltic-andesite	Dark green; aphanitic-locally weak fsp ± pyx ± hbl phyric; unaltered; undefromed;	Cross cuts dacite dykes and tur-cemented breccias; weakly veined by py-kfs ± tur with kfsp vein halo	Post-main mineralisation
Fine feldspar-phyric dacite	Pale grey; fine fsp-phyric;	Crosscuts coarse fsp-phyric dacite dyke and tur-cemented breccias; local propylitic alteration	Post-main mineralisation
Coarse feldspar-phyric dacite	Grey, medium-coarse fsp-phyric;	Cross cuts tur-cemented breccias; locally crosscut by tur-kfs-cpy veins and propylitic alteration	Post-main mineralisation

cct = calcite, cpy = chalcopyrite, fsp = feldspar, kfs = K-feldspar, hbl = hornblende, py = pyrite, pyx = pyroxene, tur = tourmaline

3.5.5 Minor intrusions

Several phases of dykes were recognised at Productora during core logging, summarised in Table 3.5. Compositions ranged from basalt, to basaltic-andesite to dacite (Figure 3.16). Pre- and post mineralisation dykes were observed. In general, dykes were more commonly observed and over larger intervals in core from the southern study section, 6,820,850 mN. The dominant dyke orientation is northwest to north-northwest with mostly steep (>75°) to subvertical dip (W. Potma, pers. comm., 2014). Dykes with west-northwest strike and steep to sub-vertical dip were also noted. Previous authors have mapped dykes crosscutting the Cachiyiyto stock but not the Ruta Cinco intrusion (Fox, 2000; Beeson et al. 2012). Based on this, dykes have been inferred to be associated with the emplacement of the Ruta Cinco intrusion (Fox, 2000).

3.6 Distribution of geological units interpreted from immobile element lithogeochemistry

Samples were classified into eight different rock types and a further three sub-types were determined using immobile-element lithogeochemistry: basaltic-andesite, basalt, dacite, rhyodacite (A, B and C), rhyolite, granodiorite, tonalite and monzodiorite. Lithological groups were determined on the basis of natural breaks and populations in the dataset (Table 3.6; Appendix B9). In order to validate interpreted

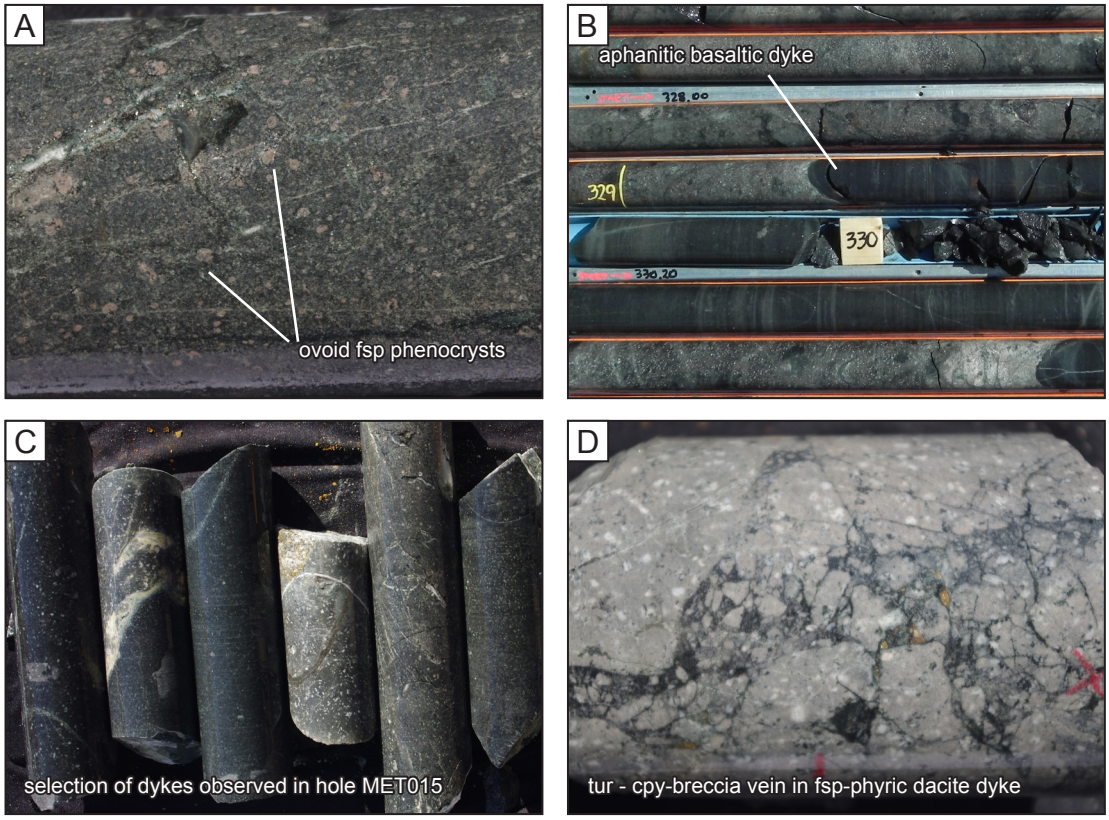

Figure 3.16 Selection of photos to show dykes observed during core logging. A) Ovoid feldpar-phyric basalt dyke (PR14AE166, MET015 275.30 m). B) Aphanitic basalt dyke (NS8D, 325.46–332.70 m). C) Selection of dykes from hole MET015. D) Coarse feldspar-phyric dacite dyke cross cut by tourmaline - chalcopyrite-cemented breccis vein (PR14AE172, MET016 290.80 m) . cpy = chalcopyrite, fsp = feldspar, tur = tourmaline.

lithologies, classified data were plotted on cross section and compared to graphic logging, core photos, the Hot Chili Ltd geological logging database, petrographic observations and major element classification diagrams (for least altered samples; Figure 3.17 and Figure 3.18). Validation of lithogeochemistry was limited to areas where metallurgical core (drill holes with MET prefix) had been graphically logged (Figure 3.5 and Figure 3.6) or diamond drill holes which had core photos. The majority of drill holes at Productora were drilled by reverse circulation and it was not possible to make another field trip to access chip trays.

3.6.1 Discussion

On section 6,822,215 mN lithogeochemistry interpretations indicate volcanic rocks to the east are more felsic in composition. This is consistent with observations of welded rhyolite lapilli tuff and rhyolite lapilli tuff in drill core (sections 3.4.3 and 3.4.1). Three discrete rhyodacite compositions were identified, rhyodacite A, B and C. Rhyodacite A and B are most prevalent across section 6,822,215 mN whereas rhyodacite C is sporadically distributed. Since geochemical data is from 1 m whole rock intervals, rhyodacite C may reflect intervals of mixed lithology. Alternatively rhyodacite C may be a type of dyke. It was not possible to confirm either as no core or core photos were available for intervals of rhyodacite

Table 3.6 Rock types discriminated using immobile element lithogeochemistry. Characteristics are approximate, rock types classified with respect to natural populations in the data and validated against logging data, rock compositions from the Georoc database, petrography, QAP-diagrams and core photography.

Rock Type	Geochemical characteristics	Validation
Basaltic-andesite	50–400 ppm Cr, >0.25 % Ti	Logging - database, core photos
Basalt	>400 ppm Cr, >0.25 % Ti	Logging - database, core photos
Dacite	> 12 ppm Sc, high Ti:Nb	Georoc database[1], QAP-diagram (volcanic)
Rhyodacite A	7–12 ppm Sc, >110 ppm Zr	Georoc database[1], QAP-diagram (volcanic)
Rhyodacite B	7–12 ppm Sc, 60–110 ppm Zr	Georoc database[1], QAP-diagram (volcanic)
Rhyodacite C	7–12 ppm Sc, low Ti:Nb	Georoc database[1], QAP-diagram (volcanic)
Rhyolite	< 7 ppm Sc, < 80 ppm Zr	Logging - graphic, QAP-diagram (volcanic)
Tonalite	High Hf:Zr, >20 ppm Sc	Petrography, QAP-diagram, core photos, plutonic classificaton diagram[2] (Debon amd Le Font, 1983)
Granodiorite	High Hf:Zr, ~10–15 ppm Sc	Petrography, QAP-diagram, core photos, TAS plutonic classification diagram[2] (Middlemost, 1994)
Monzodiorite	High Hf:Zr, ~5 ppm Sc	Petrography, QAP-diagram, core photos, TAS plutonic classification diagram[2] (Middlemost, 1994)

[1]Appendix B8, [2]for least altered rocks

C. In addition to the challenges of potentially mixed intervals, ICP-MS geochemical data was only available for every 1 in 4 meters, which limits the resolution of interpretation. Features smaller than 4 m may be missed or overestimated is they repeat at the same interval as sampled.

Where graphic logging coincides with rhyodacite A, monomict rhyodacite breccias were observed. The monomict rhyodacite breccias are interpreted to have been emplaced as a subaerial volcanic flow or dome. The distribution of rhyodacite A, which is interpreted to relate to the rhyodacite dome, is shown in Figure 3.17. The distribution of rhyodacite B on section 6,822,215 mN suggests that rhyodacite A was intruded into it.

Lithogeochemistry on section 6,820,850 mN indicates more variable geology than the northern section. Several intervals of tonalite and granodiorite intrusions are indicated and have been validated using core photography and graphic logs (Figure 3.18). The eastern intervals are inferred to be the Zapallo porphyry however, it is unknown whether the eastern intervals are part of the same intrusive complex. A small interval of monzodiorite also occurs in the west of section 6,822,215 mN and was confirmed

Figure 3.17 Cross section at 6,822,215 mN showing lithologies interpreted from immobile element lithogeochemistry on each assay interval with ICP-MS geochemisrty. Interpretations were validated by comparison to graphic logging and core photographs (where available), for example A) monzodiorite intrusion and B) basaltic-andesite dyke. Rhyodacite - A (shaded orange) is locally associated with monomict rhyodacite breccias identified in graphic logging (section 3.4.2). The monomict rhyodacite breccias are inferred to have been emplaced as a subaerial dome or flow, and modified by hydothermal brecciation. Due to intense alteration and brecciation the domain of rhyoodacite-A (shown in orange) was not previously recognised in core logging.

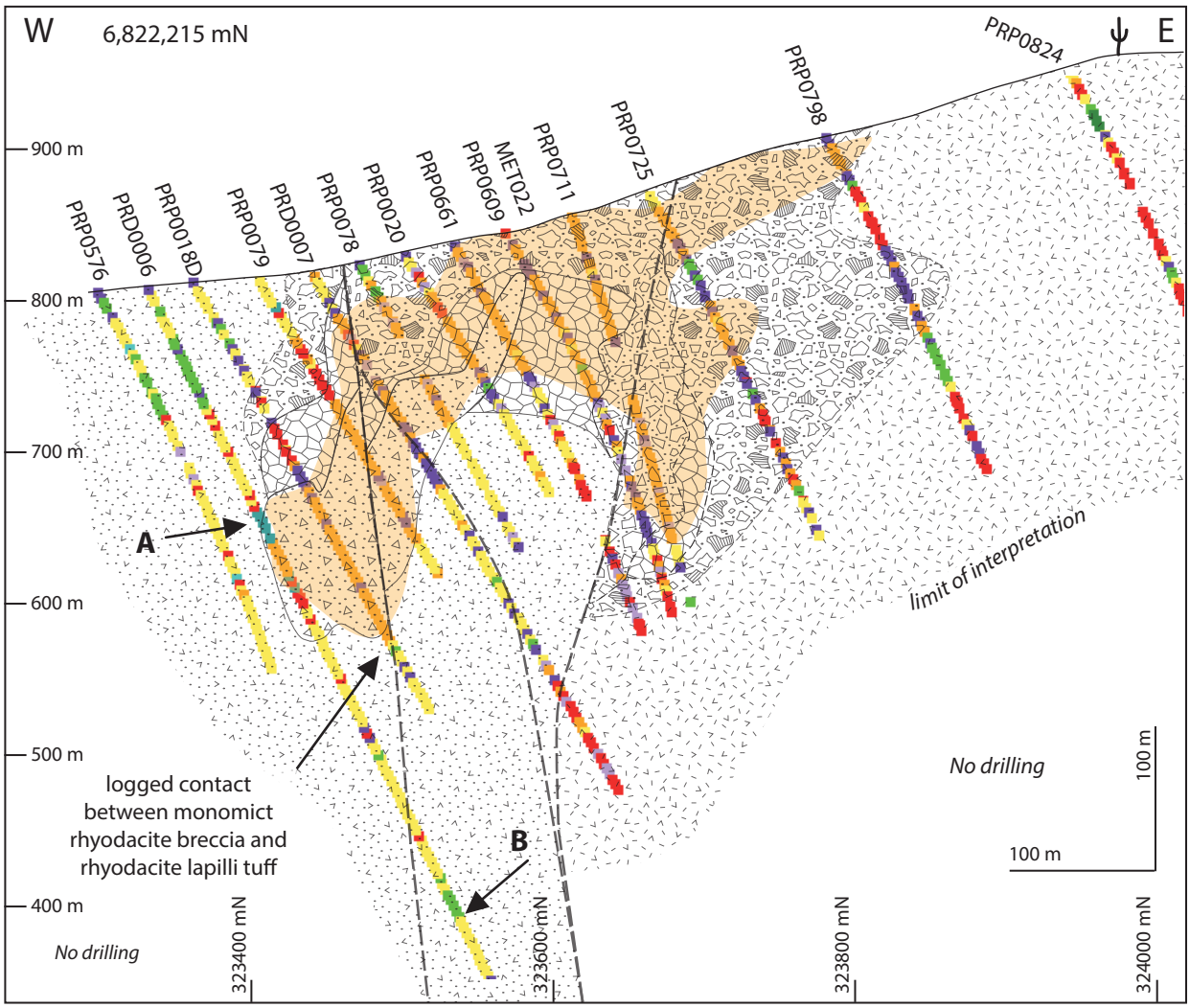

Jigsaw-fit, clast supported breccia

Clast rotated/chaotic, cement supported breccia

Rhyolite lapilli tuff

Rhyodacite lapilli tuff

Monomict rhyodacite breccia/rhyodacite dome (?)

Lithology - interpreted from immobile element lithogeochemistry

- Basaltic-andesite
- Basalt
- Rhyodacite A
- Rhyodacite B
- Rhyodacite C
- Dacite
- Rhyolite
- Tonalite
- Granodiorite
- Monzodiorite

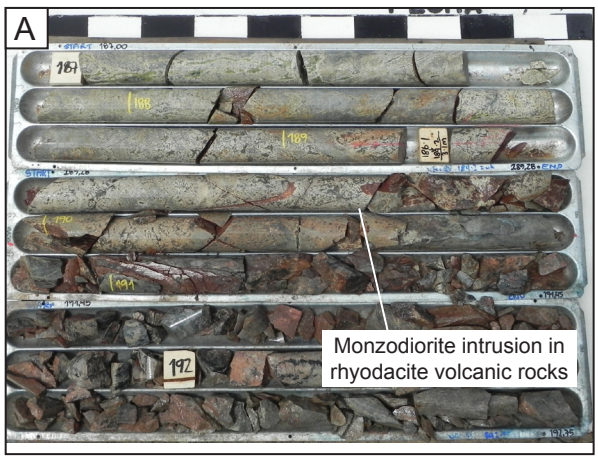

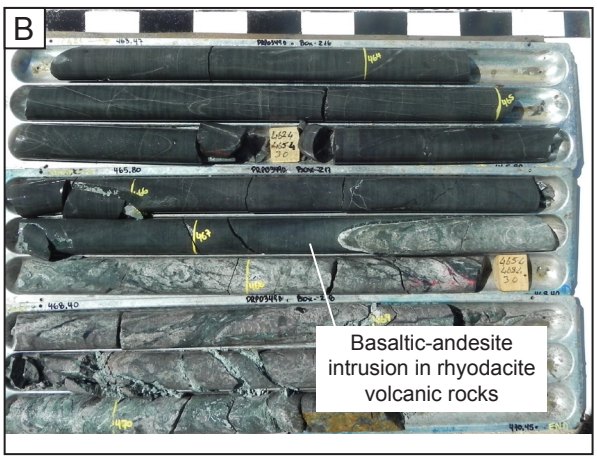

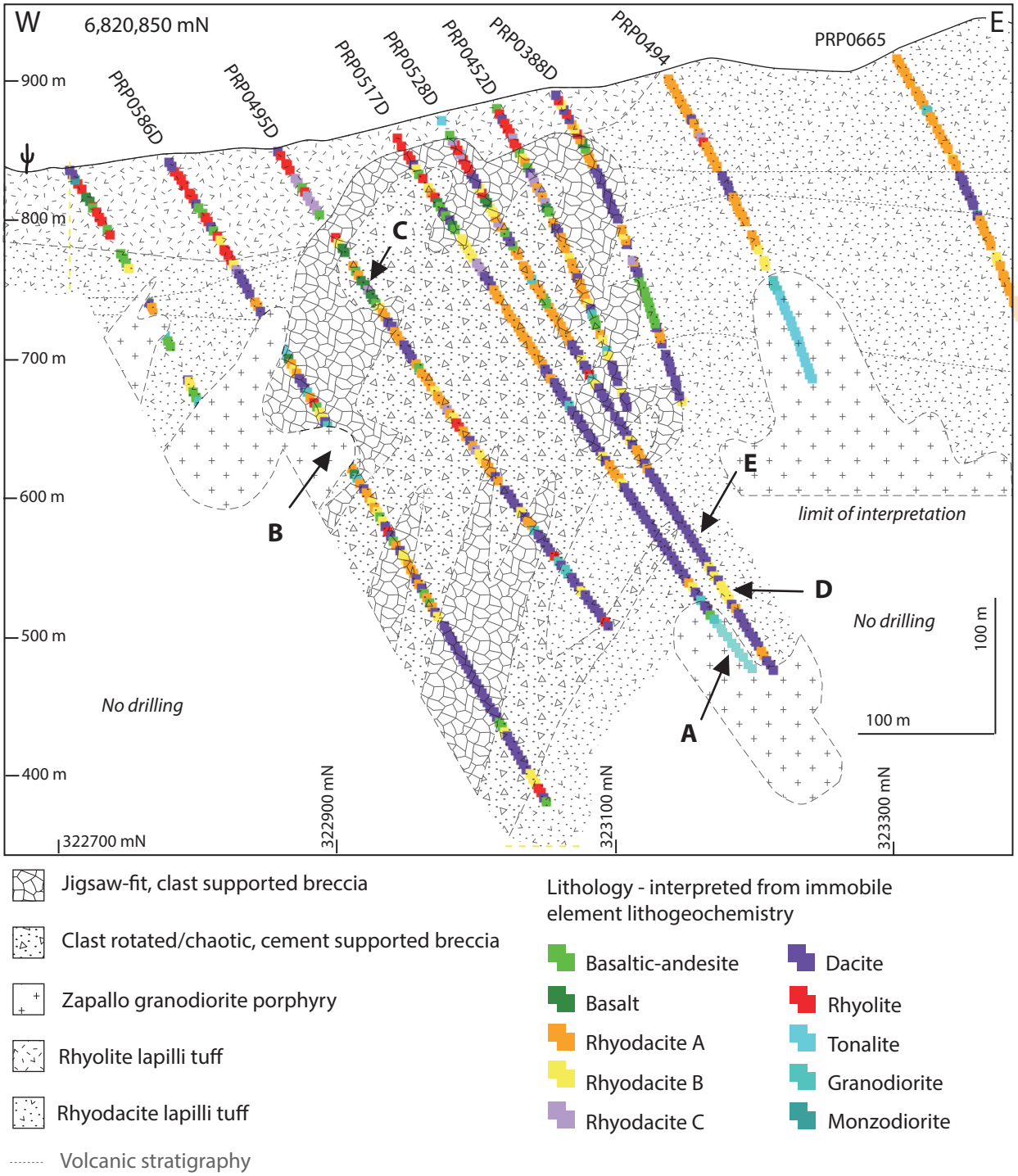

Figure 3.18 Cross section at 6,820,850 mN showing lithologies interpreted from immobile element lithogeochemistry on each assay interval with ICP-MS geochemistry. Interpretations were validated by comparison to graphic logging and core photographs (where available). Examples provided in Figure 3.19.

in core photos. Approximately 50–100 m of rhyolite volcanic rocks are indicated across the shallow portion of the deposit. Rhyodacite A transitions to dacite at depth. A 25–50 m dacite bed (or flow) is also inferred in the east. The dacite is likely to correspond with the andesite tuff of Fox (2000; Table 3.1 and Figure 3.8). Significantly more mafic dyke intervals are predicted on the southern section, this is consistent with core observations and photo logging.

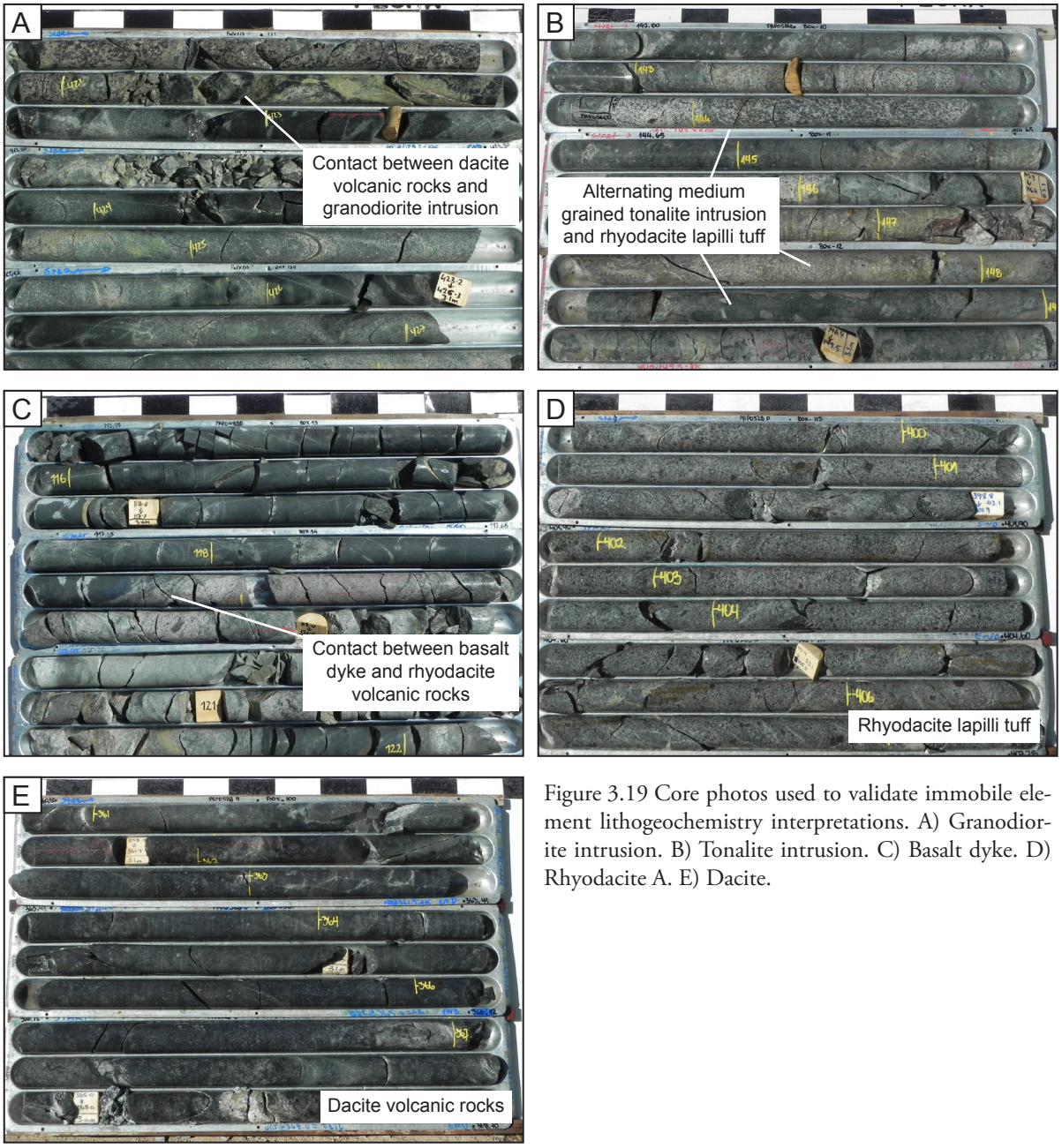

Figure 3.19 Core photos used to validate immobile element lithogeochemistry interpretations. A) Granodiorite intrusion. B) Tonalite intrusion. C) Basalt dyke. D) Rhyodacite A. E) Dacite.

The distribution of rhyodacite A on section 6,822,215 mN, partly relates to the rhyodacite dome, but is also partially coincident with the breccia complex. This could indicate a significant component of rhyodacite A in the breccia complex either as juvenile or wallrock clasts, or coherent bodies. Without being able to validate this interpretation with visual observation, this raises the question as to whether the assumed immobile elements are truly immobile or at least in part reflect alteration during brecciation. Textural observations from section 6,822,215 mN and the broad distribution of rhyodacite A to the east on section 6,820,850 mN support the former. However, mass balance calculations would be beneficial to improve confidence in this assumption in the absence of core to log.

3.7 Structure

At Productora, several major faults and numerous minor faults define a domain of structural complexity. These features have been mapped and interpreted most comprehensively by Beeson et al. (2012). As no structural mapping was completed during this study, this section is primarily a summary of the observations of previous workers, drawing heavily on the work of Beeson et al. (2012) and J. Beeson pers. comm. (2015).

3.7.1 Regional structure

The Productora deposit is located approximately 10 km to the east of the major arc-parallel, crustal scale Atacama Fault System (AFS; section 2.5, Figure 2.5). The sinistral strike-slip AFS system consists of many discontinuous and cross cutting faults. Overlapping faults define asymmetric, fault-bounded slabs interpreted to be sidewall rip-out structures (Brown et al., 1993; Taylor et al., 1998), jogs and duplexes (Cembrano et al., 2005). At Productora, local structures are inferred to be subsidiary to the AFS (Fox, 2000; Ray and Dick, 2002; Beeson et al., 2012).

3.7.2 Local structure

At Productora, there are three major north-northwest striking faults and three major northwest striking structures (Figure 3.20). There are also numerous examples of minor northwest-, west- and northeast-oriented faults that locally host diorite and porphyritic dacite dykes (Beeson et al., 2012; Fox, 2000; Ray and Dick, 2002). Northeast-striking faults are also more common to the north of the deposit. The north-striking faults generally dip 60-80° to the west and have normal oblique-slip with sinistral strike-slip, and east-side up dip-slip movement (Fox, 2000). The northwest-striking faults, which are numerous, have normal oblique-slip with dextral strike-slip and northeast side up dip-slip movement. The northwest-striking faults crosscut the north-striking fault set (Figure 3.20; Fox, 2000; Ray and Dick, 2002; Beeson et al., 2012).

Interpretation of major faults was made for section 6,822,215 mN based on information available in the Hot Chili Ltd drill hole database, including rock quality index (RQD), fracture frequency, weathering and observations from core photographs. No fault orientations were recorded for the drill holes on section 6,822,215 mN. Two intersecting faults were interpreted in 3D (Figure 3.21; fault A 70° → 050° and fault B 80°→ 070°) and one in 2D only (apparent dip → dip direction, 80° → 270°) — due to a lack of diamond drill core on adjacent sections. The fault orientations are consistent with

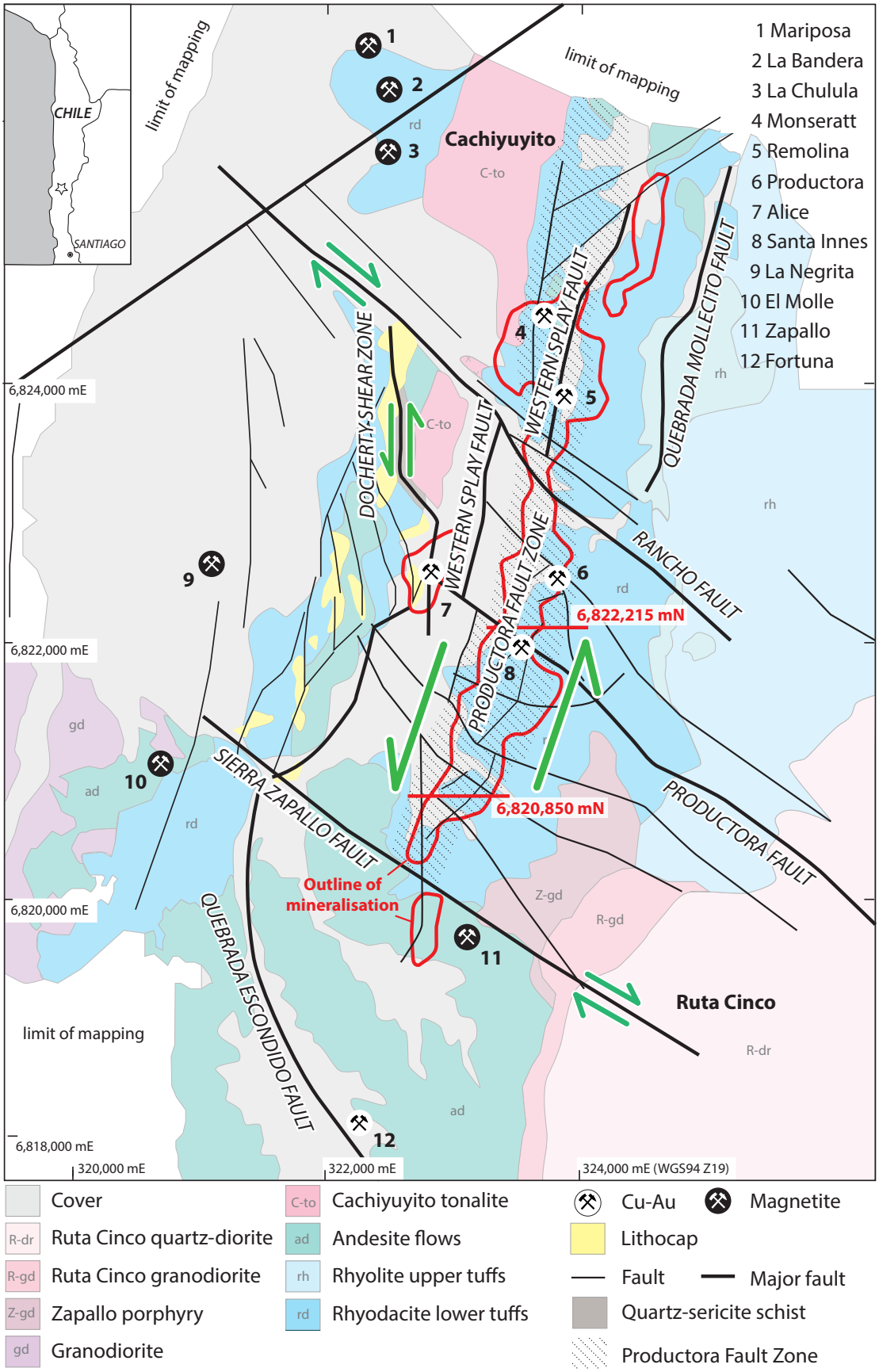

Figure 3.20 Map of local structures mapped at Productora. Compiled from Ray and Dick (2002) and Beeson (2015). The Productora breccia complex is situated in the north-northeast oriented Productora Fault Zone (PFZ). The PFZ is inferred to be sinistral and is crosscut by three major dextral faults. Also show are local mineralisation occurrences and outline of mineralisation (defined as Hot Chili Ltd drilling intervals >0.1 %Cu projected to surface)

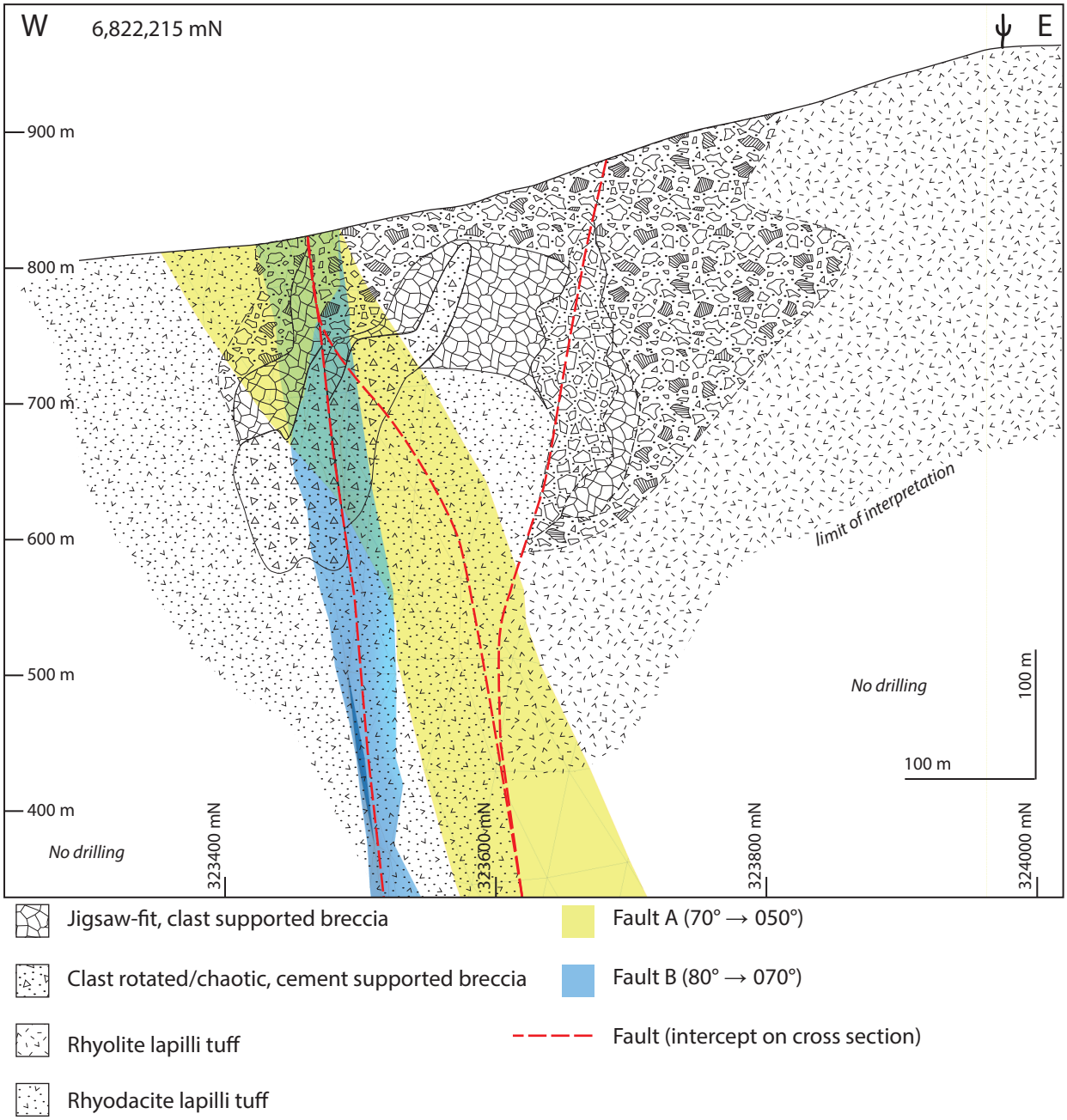

Figure 3.21 Cross section at 6,822,215 mN showing 3D models of fault planes (±75 m window) and intersection of faults on cross section (red line). Faults inferred from logged rock quality index, fracture frequency and core photography.

the northwest-striking fault set mapped at surface (Beeson et al., 2012), Fault A is consistent with the mapped Productora fault (Figure 3.20).

North-striking faults

Productora fault zone

The Productora fault zone (PFZ) should not to be confused with the Productora fault of Ray and Dick (2002), which is a northwest-striking fault that cross cuts the PFZ (Figure 3.20). The PFZ is a major

north to north-northeast oriented fault zone which passes through the historic Productora mine and extends several kilometres to the north and south (Beeson et al. 2012; Figure 3.20). It is expressed as a series of damage zones and fault segments. The Productora fault zone is inferred to be sinistral with minor reverse movement, west block up, based on the asymmetric fault plane structures (Beeson et al. 2012). Multiple orientations of fault-slip lineations indicate a protracted movement history with multiple fault-slip events.

Western splay fault

The Western Splay fault, also known as the Quebrada Verde fault (Ray and Dick, 2002), was named after its apparent splay relationship relative to the PFZ (Figure 3.20). It is located to the west of the deposit and strikes north-northeast, joining the PFZ approximately 2 km north of the historic Productora mine. The Western Splay fault and Quebrada Mollecito fault are reported to have both dip-slip and sub-horizontal sinistral strike-slip movement with multiple reactivations (Ray and Dick, 2002). The faults are thought to have controlled the intrusion of the Cachiyuyito stock.

Docherty shear zone

The Docherty Shear Zone is a major ductile structure located to the west of Productora (Ray and Dick, 2002; Beeson et al., 2012;; Figure 3.20). It is oriented sub-parallel to the PFZ and offset by a number of north-west striking faults (Figure 3.20). Asymmetric fabrics within a mylonitic zone indicate predominantly sinistral movement(s). Rootless isoclinal, intrafolial folds are locally preserved within the mylonitic fabric also suggest accommodation of high strain in this structure (Beeson et al., 2012).

3.7.2.1 Northwest-striking faults

Rancho fault

The Rancho fault strikes northwest from north of the historic Productora mine, extending past a small ranch from which it takes its name (Ray and Dick, 2002; Beeson et al., 2012; Figure 3.20). It has been described as a 100 m wide fault corridor defined by numerous small scale structures (Beeson et al., 2012). Movement is inferred to be predominantly normal, southwest block up, from the juxstaposition of higher temperature alteration assemblages, of K-feldspar - tourmaline - chlorite - epidote in the southwest block, against lower temperature assemblages of chlorite - epidote - calcite in the north east block (Beeson et al., 2012). Stratigraphic displacements also indicate apparent dextral offset.

Sierra Zapallo Fault

The Sierra Zapallo fault zone is a major regional structure located south of the deposit adjacent to the El Zapallo hilltop. It hosts the historic Zapallo magnetite deposit (Figure 3.20). The fault zone is a 2 km wide corridor comprised of numerous small scale (< 5 m) fault segments. The Sierra Zapallo fault shows apparent normal, southwest block down, dextral oblique slip displacement (Beeson et al. 2012). Several hundred meters normal displacement have been inferred from stratigraphic relations - specifically the upper andesite unit exposed south of the fault occurs as a hilltop overlying felsic volcanic deposits to the north of the fault (322,450mE and 6,820,500mN; Beeson et al., 2012).

3.7.2.2 Interpretation

Fault activity at Productora is long lived with evidence for multiple reactivation events. Major faults are thought to have locally controlled pathways for pre-mineralisation magma ascent (Ray and Dick, 2002) and later post-mineralisation reactivation juxtaposed alteration types. The arrangement of north-west striking faults (normal oblique-slip with dextral strike-slip and northeast side up dip-slip) and

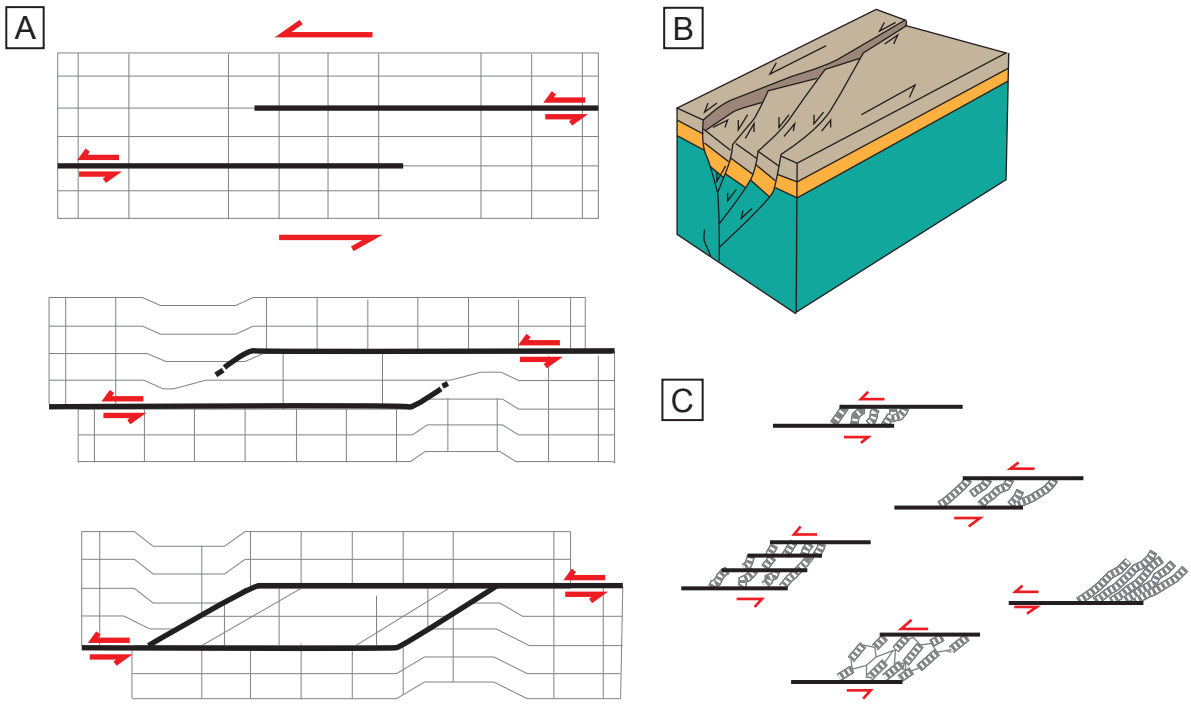

Figure 3.22 Geometry and structural development of strike-slip duplexes. A) Plan view showing extensional duplexe formation by propagation of splay faults inward from overstepping straight master faults. B) Three-dimensional architecture of extensional duplexes showing oblique-slip faults and bulk non-plane strain. C) Internal structure of dilational jogs forming duplex like structures. Modified from Cembrano et al. (2005).

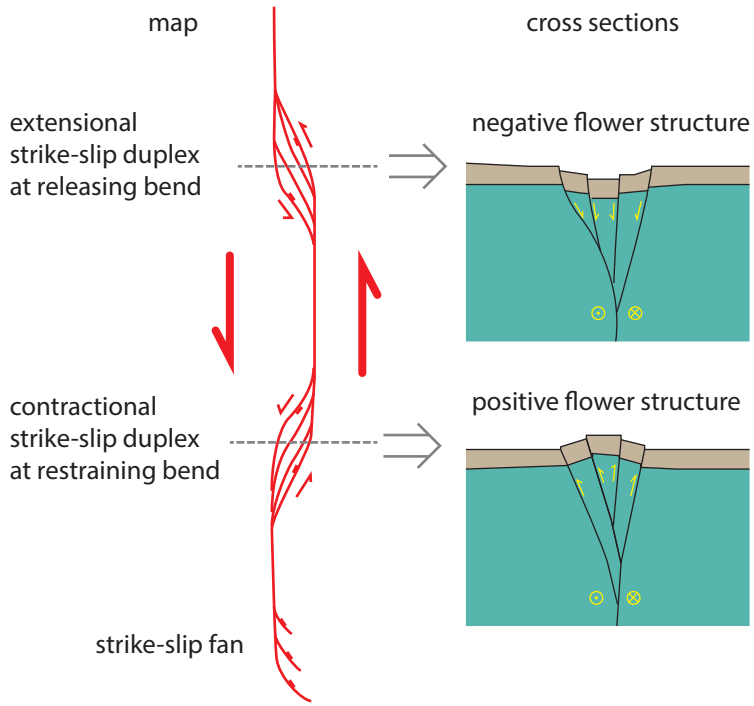

Figure 3.23 Map and cross-sections of a generic strike-slip fault system, showing flower structures and duplexes developed at bends. Modified from Woodcock and Richards (2003).

north–northeast striking faults (normal oblique-slip with sinistral strike-slip, and east-side up dip-slip movement) at Productora suggests formation as a result of step-over between two strike-slip faults (Figure 3.22). This interpretation was first proposed by Beeson et al. (2012). The major faults define an uplifted block between the Rancho fault and Sierra Zapallo fault with flanking half-graben blocks down thrown on either side (Beeson et al. 2012). The Productora deposit is hosted within the uplifted block. The current structural model is a strike-slip duplex (Figure 3.22 and Figure 3.23). However, the uplifted block suggests a positive flower structure which is inconsistent with the observed fault arrangement — contraction at a restraining bend on a sinistral stike-slip system should result in predominantly northeast oriented faults (Figure 3.23). More detailed reconciliation of regional structures and local structural mapping beyond the scope of the current study are required to confidently characterise the structural setting of Productora.

3.8 Conclusions

Two geological cross sections have been constructed across the Productora deposit based largely on interpretations of graphic logs, core photo logs and lithogeochemistry.

- Four major volcanic lithologies have been identified. From oldest to youngest, they are: rhyodacite lapilli tuff, rhyodacite monomict breccia, rhyolite welded lapilli tuff and rhyolite lapilli tuff

- New U-Pb_{zircon} geochronology reveal that the rhyodacite lapilli tuff was deposited at 128.67 ± 1.2 Ma and rhyolite welded lapilli tuff is 127.99 ± 1.28 Ma (Table 3.3, Appendix B6 and B7). These data indicate that the volcanic sequence was broadly coeval (almost within error) with the emplacement of the Cachiyuyito intrusion (129.8 ± 0.1 Ma (Fox, 2000; Table 3.3)

- Volcanic textures are consistent with an explosive sub-aerial magmatic arc environment that generated thick pyroclastic deposits and lavas flows and/or domes

- Four significant intrusions have been recognised, from oldest to youngest they are: Cachiyuyito tonalite-diorite, Alice granodiorite porphyry, Zapallo porphyry and Ruta Cinco batholith

- New U-Pb_{zircon} geochronology data indicate that the Alice porphyry was emplaced at 121.1 ± 2.1 Ma. The Zapallo porphyry was emplaced at 118.87 ± 1.19 Ma and the Ruta Cinco core phase at 92.05 ± 1 Ma

- Several phases of predominantly northwest to north-northwest striking, steep to subvertical, basalt and dacite dykes were recognised. All but one were emplaced after main stage mineralisation

- Immobile element lithogeochemistry was used to extrapolate geological interpretations across both study sections at 6,822,215 mN and 6,820,850 mN. Ten discrete rock types were recognised; basalt, basaltic-andesite, dacite, rhyodacite A, B and C, rhyolite, tonalite, granodiorite and monzodiorite. Distribution of rock types was interpreted on cross section as follows:

    - » Rhyolite lapilli tuff occurs as a thick sequence in the east on section 6,822,215 mN and as a 50–100 m thick unit on section 6,820,850 mN

    - » Rhyodacite A occurs in the centre of section 6,822,215 mN where it is inferred to have been emplaced as a sub-aerial dome or flow. Rhyodacite A is distributed more widely to the east on section 6,820,850 mN

    - » Rhyodacite B occurs in the west on section 6,822,215 mN.

    - » Dacite composition volcanics, which were not encountered in core logging, occur predominantly at depth on section 6,820,850 mN. The dacite is interpreted to be equivalent to the andesite tuff of Fox (2000)

    - » Granodiorite intervals on section 6,820,850 mN are inferred to be part of the Zapallo

porphyry.

- Fault architecture at Productora is dominated by north-west striking faults (normal oblique-slip with dextral strike-slip and northeast side up dip-slip) and north–northeast striking faults (normal oblique-slip with sinistral strike-slip, and east-side up dip-slip movement).

Chapter 4: Alteration and mineralisation

4.1 Introduction

This chapter documents the breccias and associated alteration and mineralisation features from the Productora Cu-Au-Mo hydrothermal breccia complex and neighbouring Alice Cu-Au-Mo porphyry prospect (Figure 4.1). Two detailed cross sections were constructed through the Productora breccia complex at 6,822,215 mN and 6,820,850 mN, based on observations made during this study. The chapter is focussed on paragenetic and geochemical relationships between breccias, alteration assemblages and veins, within the framework of the two study sections. Breccias have been classified based on texture and mineralogy. Mineralisation is described with respect to that observed on the study sections, with emphasis on Au deportment. Supergene mineralisation across the deposit is described briefly. Timing relationships have been established by cross cutting relationships and Re-Os geochronology. Discussion is focussed around breccia genesis, physiochemical conditions inferred from the observed mineralogy and gold deposition.

4.2 Previous work

Alteration and mineralisation at the Productora deposit was previously described by Fox (2000) and Ray and Dick (2002). The amount of geological information available has increased markedly since the extensive 80 x 40 m drill out by Hot Chili Ltd between September 2010 and June 2013. The previous work was largely based on surface mapping and was completed before the current resource of 236.6 Mt grading 0.48 % Cu, 0.10 g/t Au and 135 ppm Mo (including Alice porphyry; Hot Chili Ltd, 2016) was realised.

Fox (2000) argued that three hydrothermal systems were responsible for the observed alteration and mineralisation at Productora; the Cachiyuyito system, the Productora system and the Ruta Cinco system (Table 4.2). Ray and Dick (2002) proposed six stages to the hydrothermal system (Table 4.1) and inferred that they were all related to the Cachiyuyito stock based on a mapped alteration pattern centred

on the intrusion. Ray and Dick (2002) did note, however, that the Cu-mineralisation was not centred on the stock but on its flank. Both Fox (2000) and Ray and Dick (2002) described two major discrete styles of mineralisation, magnetite-apatite and Cu-sulphide dominant, as well as minor distal magnetite-hematite veins and mantos, and gold veins. The tourmaline breccia complex had not been discovered at this time, although tourmaline veins associated with mineralisation were observed by both authors. The Productora hydrothermal breccia complex and breccia facies have not been previously described in the literature, other than via conference presentations related to the current study (Escolme et al., 2015a and b, 2016).

Mineralisation was first dated at 91.4 ± 0.2 Ma using ^{39}Ar-^{40}Ar dating methods on hydrothermal K-feldspar (Fox, 2000). This age was be inferred to indicate association with the Ruta Cinco intrusion, which was dated at 96.1 ± 0.2 Ma using U-Pb_{zircon} dating (Fox, 2000), by Beeson et al. (2012). More recently molybdenite samples from both Prodcutora and the Alice porphyry were dated using Re-Os methods by Marquardt et al. (2015) and Hot Chili Ltd (unpublished) respectively. Results gave absolute ages of 128.9 ± 0.6 Ma (Productora) and 122.8 ± 0.6 Ma (Alice). These data indicate that Productora and Alice mineralisation are significantly older than the Ruta Cinco intrusion and are therefore unrelated.

4.3 Methods

4.3.1 Terminology

This work uses non-genetic descriptive terminology to describe lithofacies at Productora based on the methods of McPhie et al. (1993) and Davies (2002). A summary of terminology used for breccia descriptions is provided in Table 4.3.

Table 4.1 Alteration stages identified across the Productora project by Ray and Dick (2002).

Zone	Mineral assemblage	Mineralisation	Location
I	Albite ± actinolite, magnetite and epidote veins		Cachiyuyito stock
II	Magnetite-actinolite-apatite veins and breccias; retrograde epidote, chlorite and coarse calcite; remnant albite	Magnetite mineralisation	Adjacent to Cachiyuyito and El Molle stocks
III	K-feldspar ± tourmaline ± quartz; magnetite-hematite veins; local retrograde epidote-chlorite, secondary biotite, chalcopyrite and pyrite	Productora and Santa Innes mineralisation; numerous Cu ± Au ± U ± REE occurrences	Eastern side of valley
IV	Albite and quartz ± epidote ± hematite		Eastern slopes
V	quartz ± white sericite ± specular hematite ± pyrite ± green sericite-muscovite veins		Western slopes (Silica Ridge)
VI	epidote, chlorite ± quartz ± albite ± jasper veins	Small magnetite and/or hematite veins and mantos with anomalous Cu, Au, Zn, Pb, Ag, Co, and Mn	Distal and/or high elevation areas

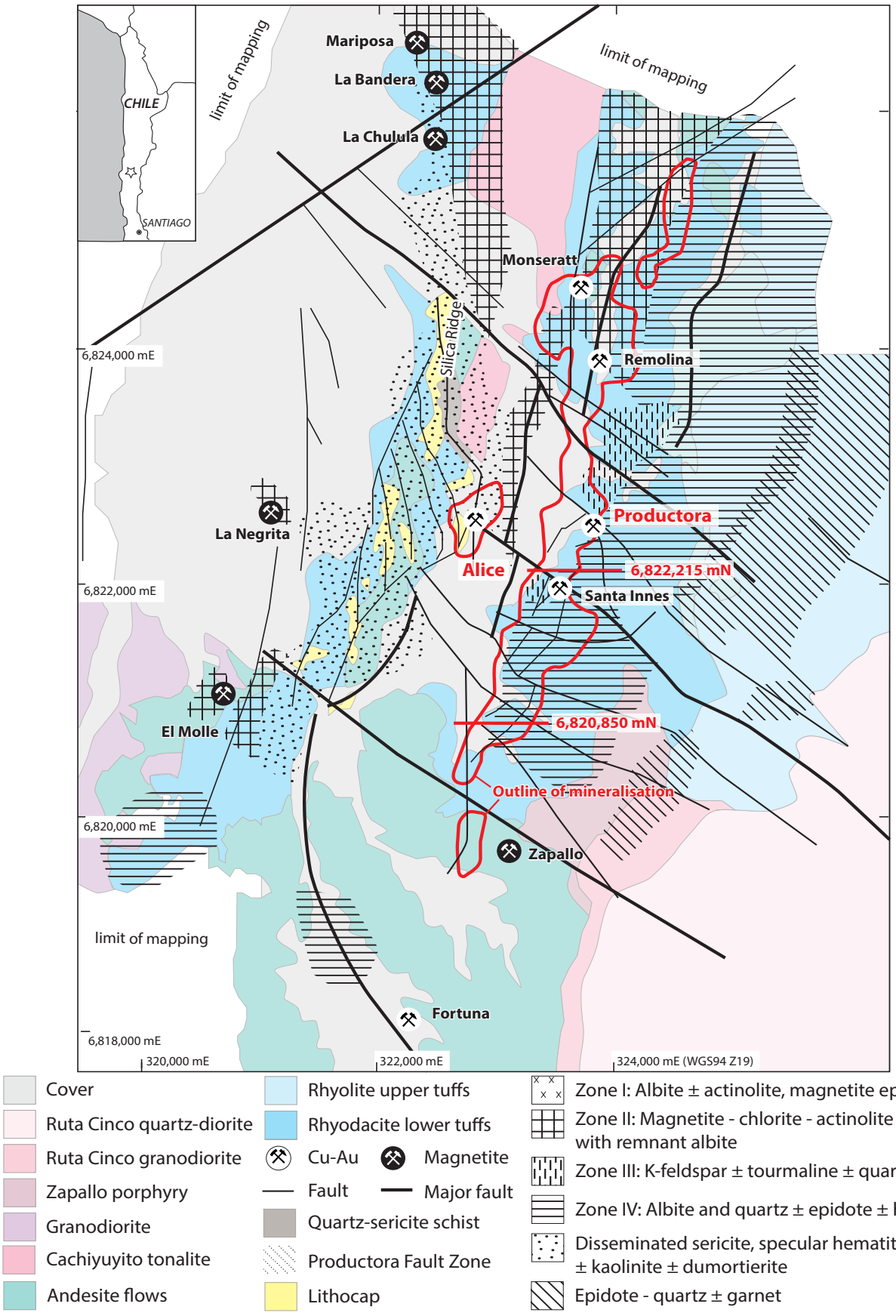

Figure 4.1 Map showing local geology, with alteration and major structures from surface mapping. Also shown are local mineralisation occurrences, outline of mineralisation (defined as Hot Chili Ltd drilling intervals >0.1 %Cu projected to surface) and location of study section lines 6,822,215 mN and 6,820,850 mN. Modified from Ray and Dick (2002), Beeson (2012) and J. Beeson pers. comm. (2015).

Table 4.2 Summary of three major alteration stages as presented by Fox (2000).

Alteration	Mineral assemblage	Alteration	Mineralization	Timing
Cachiyuyito System				
Sodic (albite)	Albite, calcite, epidote, chlorite, actinolite, magnetite, and hematite	Chachiyuyito stock; disseminations, replacements and veins	None associated	Pre-Cu
Sodic-calcic and magnetite-apatite	Albite, epidote, chlorite, actinolite, magnetite, hematite Magnetite, apatite, actinolite	Lower dacite ash-flow tuff adjacent to Cachiyuyito stock	Hosted in andesite tuff adjacent to Cachiyuyito stock; massive magnetite veins intergrown with apatite and actinolite; barren of sulphide; historic mines at Mariposa, La Bandera, La Chulula, La Negrita and Carmen	Pre-Cu
Productora System				
Early silicification	Quartz, pyrite, specularite, sericite, alunite	Moderate-strong quartz - muscovite ± pyrite replacement (Silica Ridge); associated with N-striking faults; proximal to foliated quartz-alunite rocks; texturally destructive	Fe-sulphides associated with silicification in the South	Early; overprints Cachiyuyito system in north
K-Fe metasomatism	Chlorite, magnetite, K-feldspar, tourmaline	Alteration of andesitic and lower dacitic ash-flow tuffs; weakly developed in Cachiyuyito intrusion;	Pyrite and chalcopyrite veins; strike N; smaller veins strike NW; post mineralisation movement on NW-striking faults; pyrite dominant in S; Cu-sulfides dominant in N	Syn-Cu; overprints Cachiyuyito system; crosscuts early silicification
Stage I	Biotite - pyrite minor K-feldspar	Observed in andesite and lower dacite ashflow tuffs; biotite replaced by chlotite in stage II	Pyrite (up to 10%) intergrown with biotite	Syn-Cu
Stage II	K-feldspar - chlorite - magnetite - pyrite - chalcopyrite ± biotite ± sericite ± epidote ± quartz	Variable depending on host lithology; K-feldspar alteration ranges from moderate to intense flooding; minor quartz alteration;	Extensive in andesite ash-flow tuff; disseminated chalcopyrite, pyrite and magnetite veins; pyrite cross-cut by chalcopyrite; supergene Cu-outcrops at Remolina, Productora and Santa Innes mines	Syn-Cu; overprints stage I, K-feldspar dated at 91.4 ± 0.2 Ma
Stage III	Epidote - chlorite - specularite ± tourmaline ± muscovite	Veins and disseminations; thick tourmaline veins abundant in central zone and Eastern ridge; extensive muscovite alteration occurs in NW	Chalcopyrite-tourmaline veins cross-cuts K-feldspar alteration; chalcopyrite intergrown with chlorite, specularite, epidote, ± tourmaline	Syn-Cu; occurs in all lithologies; cuts all previous alteration
Ruta Cinco System				
Propylitic	Actinolite, magnetite, epidote, chlorite, quartz, chalcedony, pyrite	Affects southeast of property; epidote ± pyrite veins, rare chalcopyrite; chalcedony and quartz veins common	Associated earthy hematite - gold - quartz ± barite-pyrite veins, Ruta Cinco hosts several generations of quartz veins and minor pyrite veins with Cu-oxides	Post-Cu; gold veins crosscut earlier alteration

4.3.2 Graphic logging

Observations from detailed graphic logging are used to define and describe breccia facies and their timing relationships. Graphic logging methodology is describe in section 3.3.1 and logs are provided in Appendix B3.

4.3.3 Petrography

A total of 49 polished thin sections were prepared at the University of Tasmania's lapidary facility. Polished thin sections were examined in transmitted and reflected light in order to identify alteration minerals, breccia cement and vein assemblages, and their cross cutting relationships. The author also reviewed 27 ground slabs, 19 polished blocks and 218 hand specimens collected during field work.

4.3.4 Feldspar staining

Feldspar staining was performed on selected samples at CODES, University of Tasmania, in order to assist with the identification and modal abundance estimation of plagioclase and K-feldspar. As many of the protolith rocks at Productora are quartz-feldspar dominant and have undergone intense alteration it is commonly difficult to gauge variations in hydrothermal feldspar and quartz alteration intensity. Each sample was etched with hydrofluoric acid and then gently brushed with barium chloride solution, followed by a treatment of potassium rhodizonate, which stains Ca-plagioclase red. The sample was then treated with sodium cobaltinitrate, $Na_3Co(NO_2)_6$, which stains K-feldspar yellow. Pure Na-feldspar (An <3) does not stain using either technique.

4.3.5 SWIR

A total of 37 short wavelength infrared spectra were collected from hand specimens using the ASD Terraspec instrument at CODES, University of Tasmania. Three analyses were performed on each sample and a record kept of the analysis position and target, e.g. vein halo or alteration. Spectra were interpreted using The Spectral Geologist Professional© (TSG) version 5.03.002 software by comparison to a reference database. SWIR data are provide in Appendix C1.

4.3.6 Scanning electron microscope

Scanning electron microscope (SEM) data were collected using the Hitachi SU-70 field emission SEM fitted with an Oxford AZtec XMax80 EDS system at the Central Sciences Laboratory, University of Tasmania. Data were collected from five thin sections in order to (a) identify unknown small (< 20 μm)

Table 4.3 Terminology for the non-genetic description of breccia lithofacies at Productora.

Term	Definition	Reference
Coherent rock	Formed from cooling and solidification of magma or molten lava; characteristically porphyritic, equigranular or aphanitic textures	McPhie et al. (1993)
Clastic rock	Rock forming as a result of fragmentation or dissolution processes, distinguished on the basis of their fragmental character	McPhie et al. (1993)
Volcaniclastic	Descriptive term for lithofacies composed of predominantly volcanic particles	Fisher (1961)
Breccia	Clastic aggregate of sub-rounded to angular casts which can be described in terms of clasts, matrix, cement and open space	Davies (2002), Simpson et al. (2007)
Conglomerate	Clastic rocks of dominantly rounded clasts >2 mm	Wentworth (1922), Bryner (1986)
Infill	Interstitial material between clasts - this may be matrix, cement, open space or a combination of any or all of the above	Pass (2010)
Matrix	Clastic interstitial material < 2 mm in diameter, may include small rock fragments or crystals, also known as 'rock flour'	Sillitoe (1985), Taylor and Pollard (1993), Davies (2002)
Cement	Chemical precipitate, either mineral or crystalline igneous rock (e.g. diorite cemented breccia)	Davies (2002), Simpson et al., (2007), Davies et al., (2008)
Jig-saw fit breccia	Angular clasts which have undergone limited or no movement Also known as: Shatter breccia Crackle breccia Mosaic breccia	Pass (2010) Baker et al. (1986), Taylor and Pollard (1993), Laznicka (1988), Corbett and Leach (1998), Mort and Woodcock (2008)
Rotated clast breccia	An extension of jig-saw fit breccia where clasts are still angular to sub-angular but show evident minor rotation from their original positions	Davies (2002), Pass (2010)
Chaotic breccia	Randomly oriented clasts that have undergone considerable transport and attrition resulting in sub-angular-rounded clasts.	Laznicka (1988), Pass (2010)
Breccia vein	Hydrothermally cemented breccia with vein-like dimensions, up to 20 cm wide	this study
Breccia dyke	Hydrothermally cemented breccia with dyke-like dimensions, 20 cm to 3 m wide	this study
Lobate and globular	Delicate, irregular or fluidal clast shapes	Pass (2010)

minerals, including uranium bearing phases, (b) image ambiguous biotite-chlorite relationships, (c) image tourmaline zoning and measure compositional variations.

4.3.7 Model mineralogy estimates

A substantial data set of estimated model mineralogy, based on quantitative X-ray diffraction (QXRD) data combined with geochemical assay through a weighted least squares correction (WLSQ), was generated across sections 6,822,215 mN and 6,820,850 mN primarily to support the geometallurgy aspects of this study. This data set is described in detail in section 5.5. In this chapter, interpretations are presented that are in part based on this estimated model mineralogy data set, which will henceforth be referred to as WLSQ-QXRD data.

4.3.8 Micro-XRF mapping

Hand specimen samples, including core slabs and thin section off cuts, were mapped using the Bruker M4 Tornado micro-XRF element mapper at the CSIRO Mineral Resources Flagship, Perth, Australia. Samples were mapped using a 25 µm beam size, 40 µm step width and 4 ms dwell time. At these conditions, large core samples up to 60 cm^2 can be mapped in several hours. Data were post-processed using Bruker M4 Tornado© analysis software version 1.3. Full element maps and individual area selections were validated by review of the sum spectra. Maps of individual elements and red-green-blue (RGB) combination maps were generated as required to explore alteration mineralogy and texture.

4.3.9 Synchrotron analysis

Ten polished thin sections were prepared at CSIRO Mineral Resources Flagship, Australia Resources Research Centre, Perth as petrographic thin sections of 110–150 µm thickness mounted on pure quartz glass slides to avoid potential trace element contamination from normal glass slides (Fisher et al., 2015). The thin sections were analysed by X-ray fluorescence (XRF) microscopy performed using the XFM beamline at the Australian Synchrotron (Figure 4.2; Paterson et al. 2011) using the Kirkpatrick-Baez mirror microprobe end-station following the methods of Fisher et al. (2015). This end-station provides a monochromatic 2 µm beam spot size for energies in the range 4–20 keV. The XFM beamline is equipped with a Maia 384 detector array which can acquire full spectral X-ray data for each detector at step sizes down to 2 µm over areas of several square centimetres (Kirkham et al. 2010; Ryan et al. 2010a) with count rates of ~4–10 M/s and energy resolution of 300–400 eV (recent upgrades to Maia 384C provide 240 eV resolution; Ryan et al. 2014). The XFM beamline is able to collect full spectral data across an entire thin section volume in a relatively short time frame (6–8 hours) at high resolution (2–4 µm) to

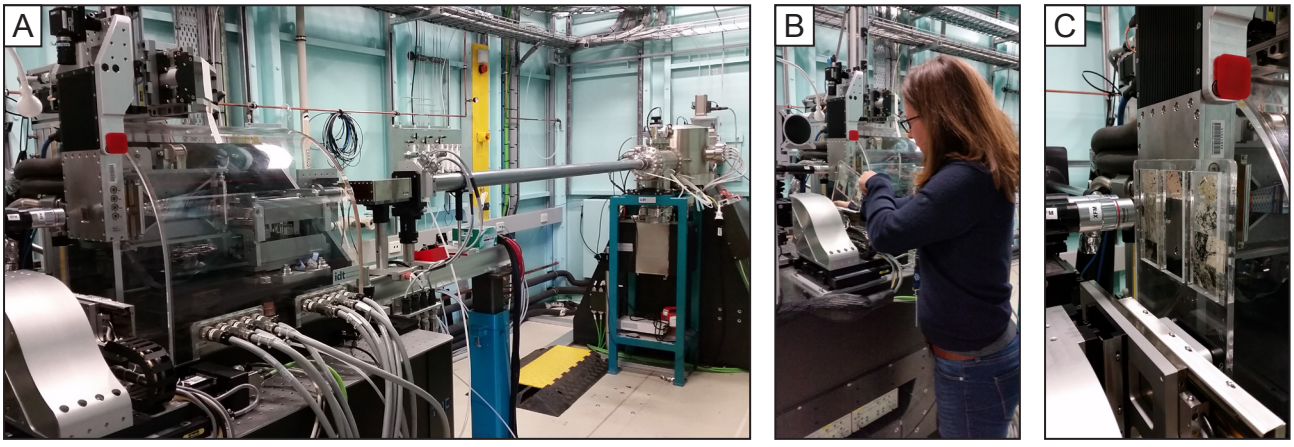

Figure 4.2 The Australian Synchrotron XFM beamline, Melboune. A) Inside the XFM beamline lead lined 'hutch'. B) Loading the sample holder, which is held in position by magnets. C) Sample holder positioned between 384-element Maia detector and camera.

generate quantitative multi-element images up to 100 Mpixels (Paterson et al. 2011; Ryan et al. 2010a, b). This has the advantage of enabling Au anywhere within the thin section volume to be detected, as opposed to just gold exposed at the surface of the section.

Synchrotron data were processed using the GeoPIXE software suite by Dr Louise Fisher and Dr Mark Pearce of CSIRO Mineral Resources Flagship, Perth. The GeoPIXE software employs a fundamental parameters approach of spectral deconvolution and imaging using the dynamic analysis method (Ryan 2000; Ryan et al. 2010b). This method generates a matrix transformation which can be used to project full spectral data both in real-time and off-line. The method is based on fitting a representative total spectrum and a detailed model of Maia detector array efficiency (Ryan et al. 2010a). Spectra are fitted to X-ray line intensities that reflect integration of yields and X-ray self-absorption effects for the given matrix or mineral phase, identified by the user, and the contrasting efficiency characteristics across the detector array (Ryan et al. 2010a, b). Whole thin section maps were initially produced by fitting the bulk spectra for the sample. Trace element quantification for specific mineral phases were then refined by extraction and refitting of the spectra using an appropriate matrix for the mineral phase of interest following the methods of Fisher et al. (2015). Due to the high energy of the X-ray incident beam, the X-ray penetration is not limited to the upper few microns of the sample. Therefore each image pixel represents an average of the whole volume sampled (Ryan et al. 2014; Dyl et al. 2014).

4.4 Productora — hydrothermal breccias, veins and altered rocks

4.4.1 Paragenesis

The evolution of the Productora hydrothermal system produced a sequence of hydrothermal breccias, tectonic breccias, veins and alteration assemblages that have been separated into five paragenetic stages. The relationship of these five stages with the broader camp scale parageneses is outlined in Figure 4.3. Camp scale events at Productora include the Cachiyuyito hydrothermal system, which generated sodic-calcic assemblages and magnetite-apatite mineralisation; the Ruta Cinco system, which produced propylitic alteration and gold-bearing veins (Fox, 2000 and Ray and Dick, 2002; Table 4.1 and Table 4.2); and the Alice porphyry intrusion with associated alteration and Cu-Mo mineralisation. The Alice porphyry system is briefly described in this chapter whereas the Cachiyuyito and Ruta Cinco systems are beyond the scope of this work. Their features are summarised in Table 4.1, Table 4.2 and Appendix C2.

The Productora breccia complex formed due to at least three brecciation events. Associated breccia facies have been identified based on the proportions of clasts to matrix and cement. Timing relationships between events have been established through cross cutting relationships. Where applicable, breccias

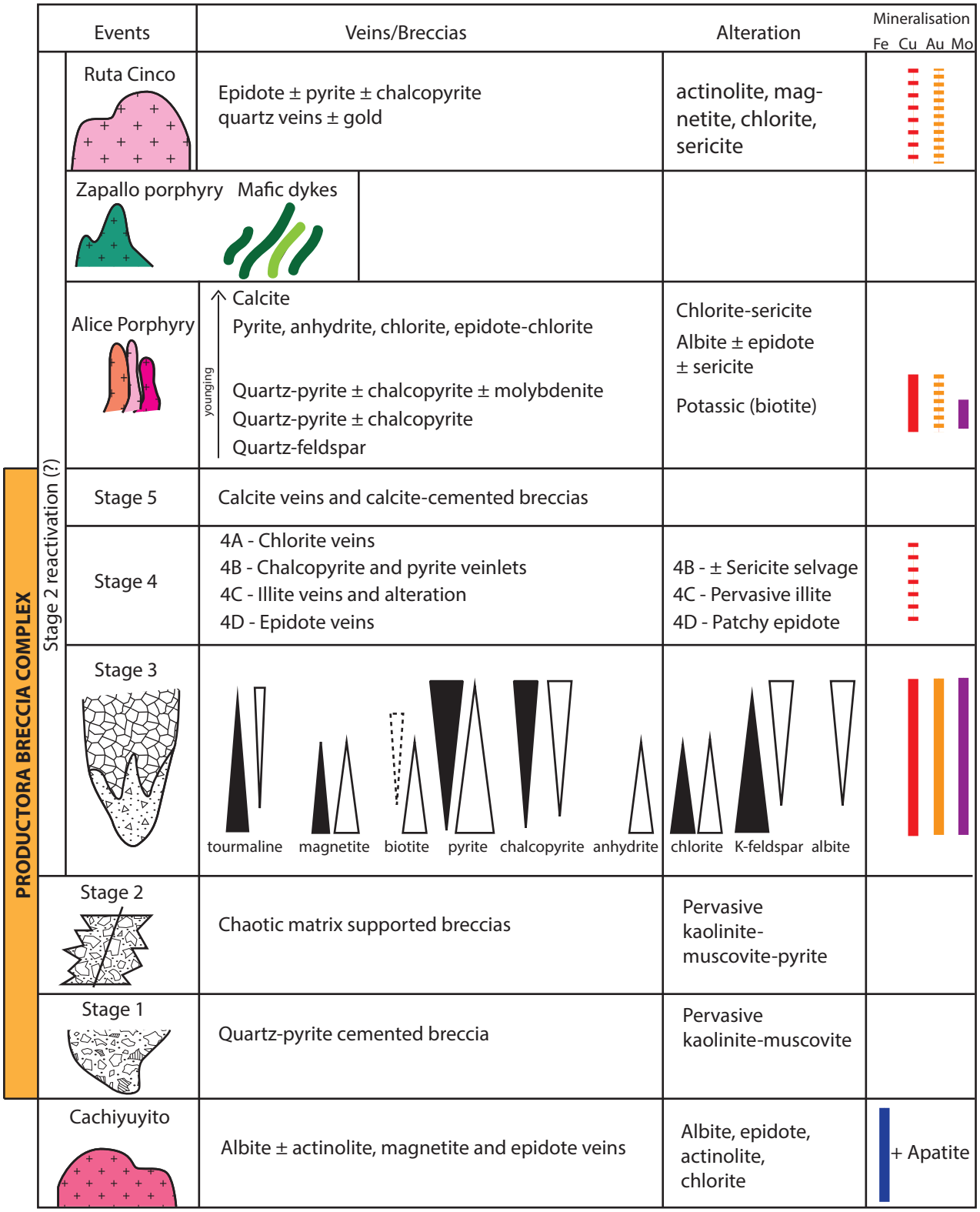

Figure 4.3 Summary of the Productora camp scale paragenesis for major minerals. Paragenesis of the Productora breccia complex is separated into five stages. Reactivation of stage 2 is shown on the left of the diagram. Vertical variations in stage 3 breccia cement mineralogy are shown by triangles whose width is proportional to mineral abundance, strike variation is shown by triangle colour (black = section 6,822,215 mN, white = 6,820,850 mN). Relative intensity of mineralisation is shown by continuous (strong) or dashed (weak) lines. Ruta Cinco and Cachiyuyito events summarised from Fox (2000) and Ray and Dick (2002).

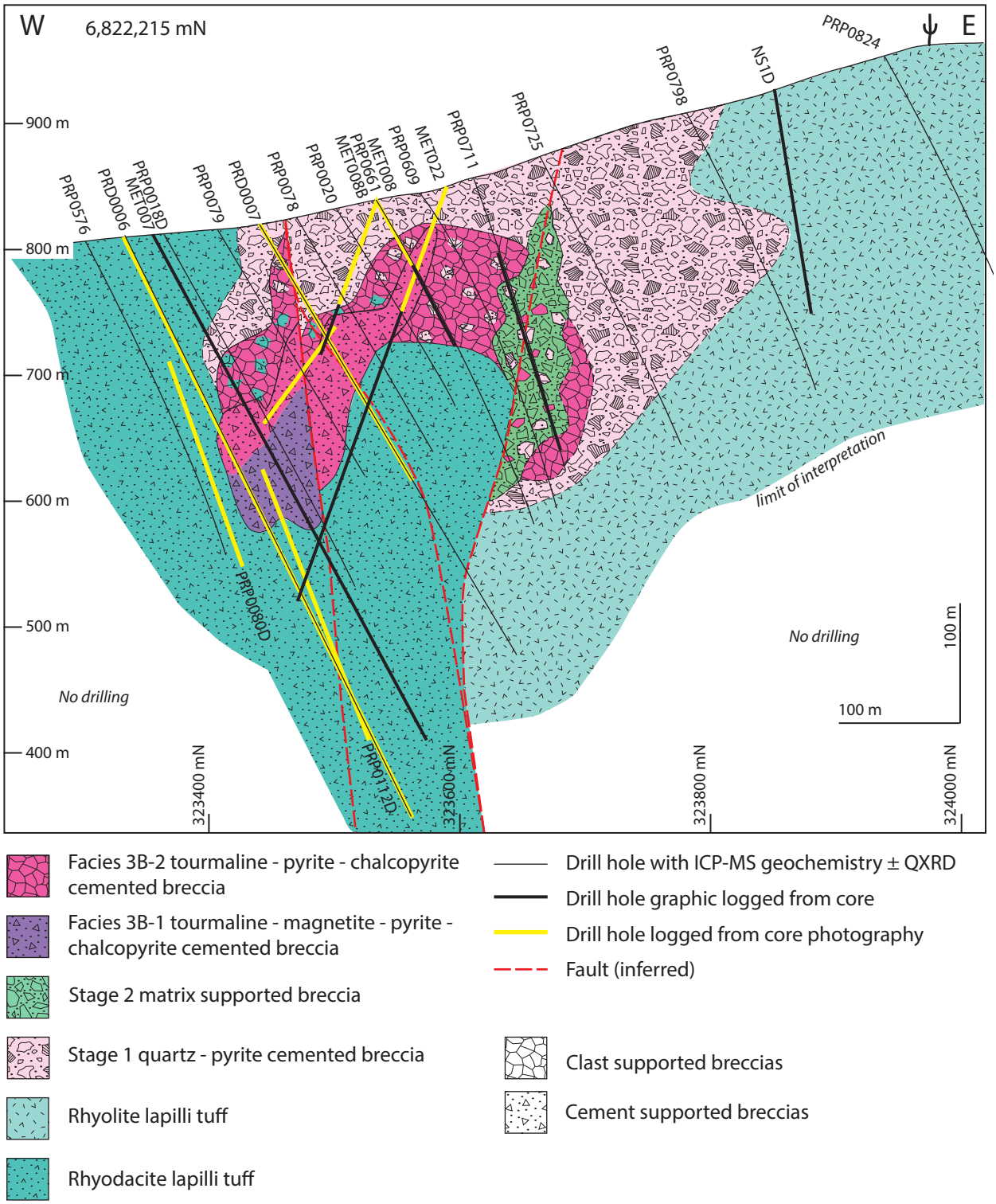

Figure 4.4 Cross section at 6,822,215 mN showing interpreted distribution of breccia facies. Interpretation is based on graphic core logging, core photo library, drill hole data base (provided by Hot Chil Ltd), detailed hand specimen and thin section observations and WLSQ-QXRD data. Breccia cross-cutting relationships are indicated by the inclusion of clasts of earlier breccia stages. Stage 2 breccias are cross cut by stage 3 and also overprint stage 3 due to later fault reactivation. Variable breccia morphology (clast supported vs. cement supported) in stage 3 breccias are shown by fill pattern.

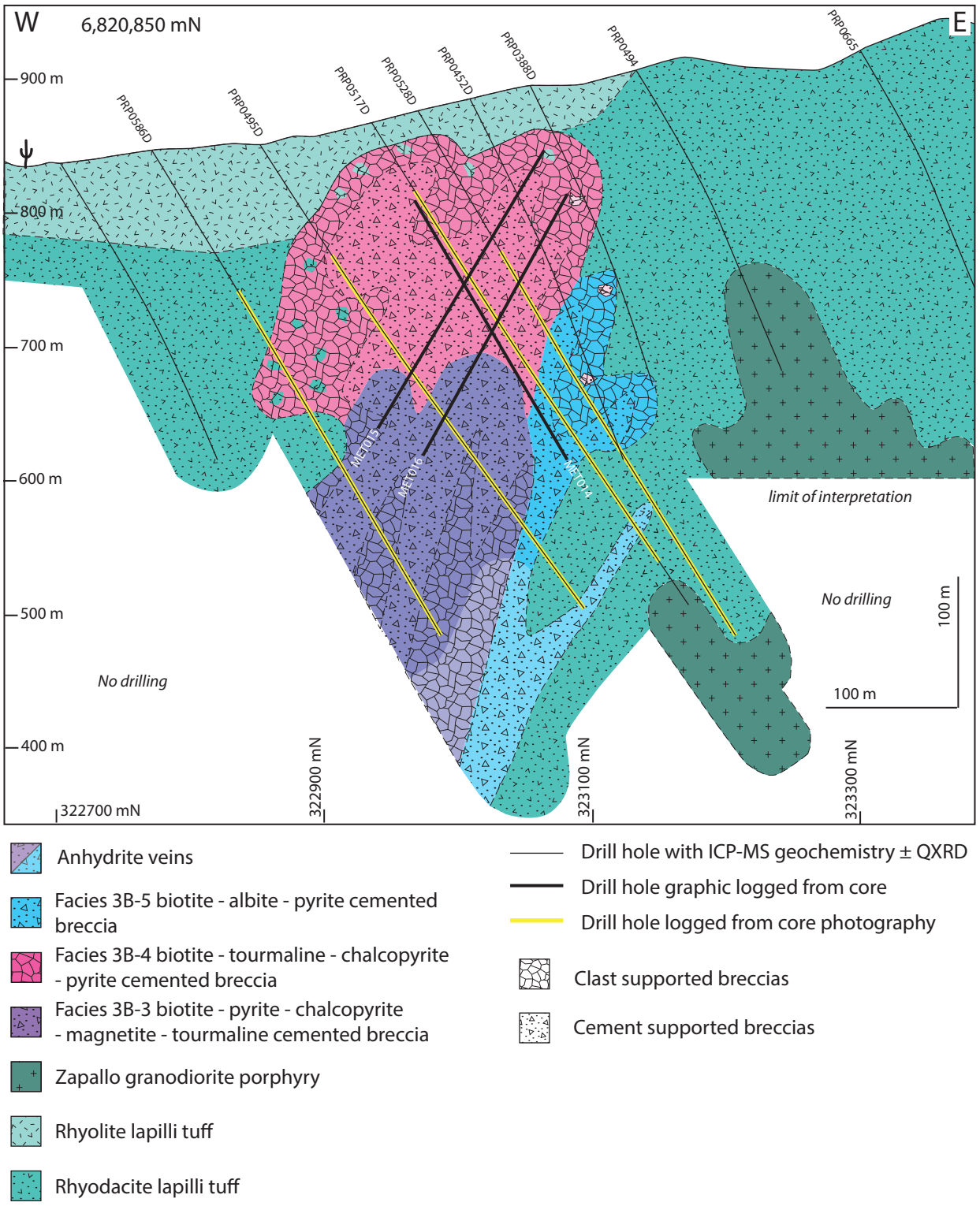

Figure 4.5 Cross section at 6,820,850 mN showing interpreted distribution of breccia facies. Interpretation is based on graphic core logging, core photo library, drill hole data base (provided by Hot Chili Ltd), detailed hand specimen and thin section observations and WLSQ-QXRD data. Variable breccia morphology (clast supported vs. cement supported) in stage 3 breccias are shown by fill pattern.

Table 4.4 Breccia facies identified in this study at the Productora deposit. anh = anhydrite, ab = albite, ap = apatite, bt = biotite, bn = bornite, brn = brannerite, cc = chalcocite, chl = chlorite, CLs = clast-supported, CMx = cement-supported, cpy = chalcopyrite, cv = covellite, ep = epidote, fsp = feldspar, hem = hematite, ilm = ilmenite, kfs = K-feldspar, kln = kaolinite, mnz = monazite, mo = molybdenite, mt = magnetite, ms = muscovite, MXs = matrix-supported, py = pyrite, qtz = quartz, rt = rutile,tnt = titanite, tur = tourmaline, urn = uraninite, U = unknown uranium bearing minerals.

Clast abundance, size and shape	Matrix	Cement	Major cement	Minor cement	Open space	Fabric
Stage 1 qtz-py cemented						
60–80 % lithic; granule–cobble; out-sized boulders; equant; angular–rounded; polymict lithic (fine grained, fsp-phyric or aphanitic, qtz-fsp rich lithic fragments and clastic lithic fragments	5–20 % lithic; angular; moderately sorted; medium sand–granule size	10–15 % massive, micro-crystalline (qtz) and disseminated py (0.05–0.3 mm)	qtz-ms-py	rt-tur ± cc ± ab	na	CLs-MXs
Stage 2 matrix supported breccia						
30–60 % lithic; coarse sand–pebble; sub-angular–well rounded; polymict (variable intense altered clasts, qtz; ksp; py)	15–50 % lithic and rock flour; medium sand–granule size	0%	na	na	na	MXs
Sub-stage 3B: Main stage breccias						
Facies 3B-1 tur-mt-chl-py-cpy						
70–90 % lithic; typically pebble size; range from granule–cobble size; angular; locally monomict lithic (fsp-phyric pebble-sized breccia, fsp-phyric coherent and lapilli tuff)	0–15% lithic; angular; moderately sorted; medium sand–granule size	10–30 % massive	tur-chl-mt-cpy-py ± ep	kfs-ep-qtz-rt	na	CLs with narrow zones of CMx
Facies 3B-2 to-py-cpy						
70–80 % lithic; typically 64 mm; oversize clasts up to 1 m; angular; monomict lithic (fsp-phyric coherent and clastic rock)	0–10 % lithic; angular; moderately sorted; medium sand–granule size	10–20 % massive	tur-py-cpy ± chl	rt ± mo ± mt ± cv ± hem ± ilm ± U[2]	na	CLs, locally CMx
Facies 3B-3 bt-py-cpy-mt-tur						
80–95 % lithic; granule-cobble size; angular–sub-rounded; monomict (lapilli tuff)	0–5 % lithic; angular; poorly sorted; medium-sand–granule size	5–20 % massive	bt (-chl) -py-cpy-mt	ms-tur ± anh ± ab ± ap ± tnt ± ilm ± urn ± brn ± mnz	0–3%	CLs and minor CMx domains
Facies 3-B4 bt-tur-cpy-py						
85–95 % lithic; pebble–cobble; angular; tabluar; locally monomict (lapilli tuff and polymict lithic — possibly Stage 1 breccia)	0-2 %; angular; moderately sorted; medium sand size	5–15 % massive	bt (chl)-tur-cpy-py	rt ± ab ± mo ± ms ± ap	na	CLs
Facies 3B-5 tur-bt-py-cpy						
80–90 % lithic; granule–cobble; sub-angular–rounded; polymict (crystal rich lapilli tuff, feldspar phyric coherent clasts, polymict qtz cemented breccia)	0–7 %	10–30 % massive	bt (chl)-to-py-cpy	± mt ± ab	na	CLs, locally CMx

[1]photo logging only, [2]uranium-rich minerals identified in hand specimen only by the red stained damage zone

Internal clast organisation	Alteration	Examples	Comments
Very poorly sorted; chaotic; massive; medium–thick graded bedding	Pervasive kln-ms alteration; py also sparsely disseminated through clasts; post-breccia qtz ± py ± ep ± chl and ms veins; locally intense qtz alteration	Outcrops at 323990 mE and 6822050 mN, 323697 mE and 6822288 mN; drill intersections PRD00071 59–84 m; PRD00091 81–145 m; sample PR14AE119, PR14AE183–184, PR14AE188–189	Distinguished by poorly sorted, chaotic, matrix rich texture and pale bleached colouration; commonly goethite stained where weathered
Poorly sorted; chaotic; massive; thick, diffuse bedded	Intense kln–ms; pyrite flooding;	MET023 82.5–105 m; samples PR14AE126–139	Cross cuts Stage 1; cross cut and mineralisaed by Stage 3; multiple phases of reactivation
Very poorly–moderately sorted; jigsaw fit; narrow zones of chaotic, massive, locally stratified 50 cm beds	Variable; pervasive qtz proximal to fractures and in discrete zones replacing tourmaline; pervasive kfs with weak to moderate hematite dusting; locally texturally destructive	MET007 200–227 m; PRD00061 190–219 m; PRD0011 114–157 m; samples PR14AE060–062 and PR14AE065	Cross cuts 3A (kfs flooding); bleached to pale pink; characterised by texturally destructive kfs
Moderately sorted; jigsaw fit–rotated; massive	Patchy to pervasive kfs alteration and tur clots	MET008B 101–131 m; samples PR14AE019–038, PR14AE054–59, PR14AE177–178, PR14AE180	Overprints stage 1 breccia
Poorly–well sorted; jigsaw fit	Patchy pervasive pink kfs alteration, biot (-chl) clots w/ kfs halos; patchy bleaching; patchy clay alteration; anh-tur-cpy-py veins	MET015 227–274 m; MET016 298–316.5 m; samples PR14AE162–165, PR14AE171, PR14AE172, PR14AE174	Localised tectonic breccia domains (?)
Poorly–well sorted; jigsaw fit–rotated; massive	Most bt retrogressed to chl; diagnostic feldspar staining indicates patchy kfs with minor albite alteration; pink kfs veins and halos associated with breccia cement and veins; chl rich clots	MET014 100–124 m[1] and 132–152 m; samples PR14AE146–148	Cross cuts polymict, massive, poorly sorted breccia — inferred to be stage 1 breccia (MET0014 145–148.5 m)
Very poorly sorted; rotated–chaotic	Intense, mottled and patchy alteration obscures rock texture;	MET014 267–289 m; sample PR14AE153	Overprinting of stage 1 qtz-py breccia

have been further subdivided based on cement mineralogy, which varies laterally and vertically (Figure 4.4 and Figure 4.5). Some modification of breccia mineralogy was caused by syn-breccia alteration, but domains altered by this phenomenon have been constrained spatially.

4.4.2 Stage 1: Quartz-pyrite cemented breccia

The earliest recognised hydrothermal feature at Productora is a massive, matrix supported, chaotic, poorly sorted, quartz-pyrite cemented, polymict lithic breccia (Figure 4.5 and Figure 4.6 A). It is composed of 60–80 % clasts, 5–20 % matrix and 10–15 % cement. Clasts are equant, angular–rounded, polymict lithic and typically of pebble size, although in outcrop, domains with boulder-sized clasts were noted (Figure 4.6 B). On section 8,622,215 mN, this breccia is 400 m wide and extends more than 300 m vertically. The stage 1 breccia is broadly distributed across the northern portion of Productora where it has been identified in drill core and during reconnaissance mapping on the eastern hillside (Figure 4.6 A and B). The stage 1 breccia was also observed over 1,300 m to the south, on section 6,820,850 mN, where it has been overprinted by stage 3 breccias and alteration assemblages.

Clasts in the quartz-pyrite cemented breccia have been pervasively altered to kaolinite-muscovite with a characteristic pale bleached colour. Locally there is also intense quartz-pyrite alteration of both clasts and infill. Despite intense alteration, it is possible to identify textures within individual clasts, including phenocrysts in a fine grained groundmass (Figure 4.6 C and D) and clastic textures, which suggest a volcanic protolith and multiple brecciation events. The matrix comprises angular, moderately sorted, medium sand to granule size lithic clasts (Figure 4.6 D and E). The quartz cement is massive and microcrystalline with disseminated pyrite (0.05–0.3 mm; Figure 4.6 F and G). No significant Cu, Au or Mo mineralisation is associated with the stage 1 breccia. Pyrite contents are typically 1–2 % but can vary between <1–6 %, in part due to later alteration events and weathering.

Although no contacts were observed, the overall breccia geometry is inferred from photo logs and mapping as a discordant dyke-like body, tapering from approximately 400 m wide near surface to 100 m at 300 m depth and extending at least 1,300 m in length. Further mapping and core logging is required to better constrain the geometry of the quartz-pyrite cemented breccia.

4.4.3 Stage 2: Matrix-supported breccia

The stage 2 facies was intersected over a 75 m interval in drill core (MET023) from the east of section 6,822,215 mN at depths greater than 100 m from surface (Figure 4.4). Stage 2 occurs as a domain of intense brecciation and kaolinite-muscovite alteration with apparent dimensions, constrained from

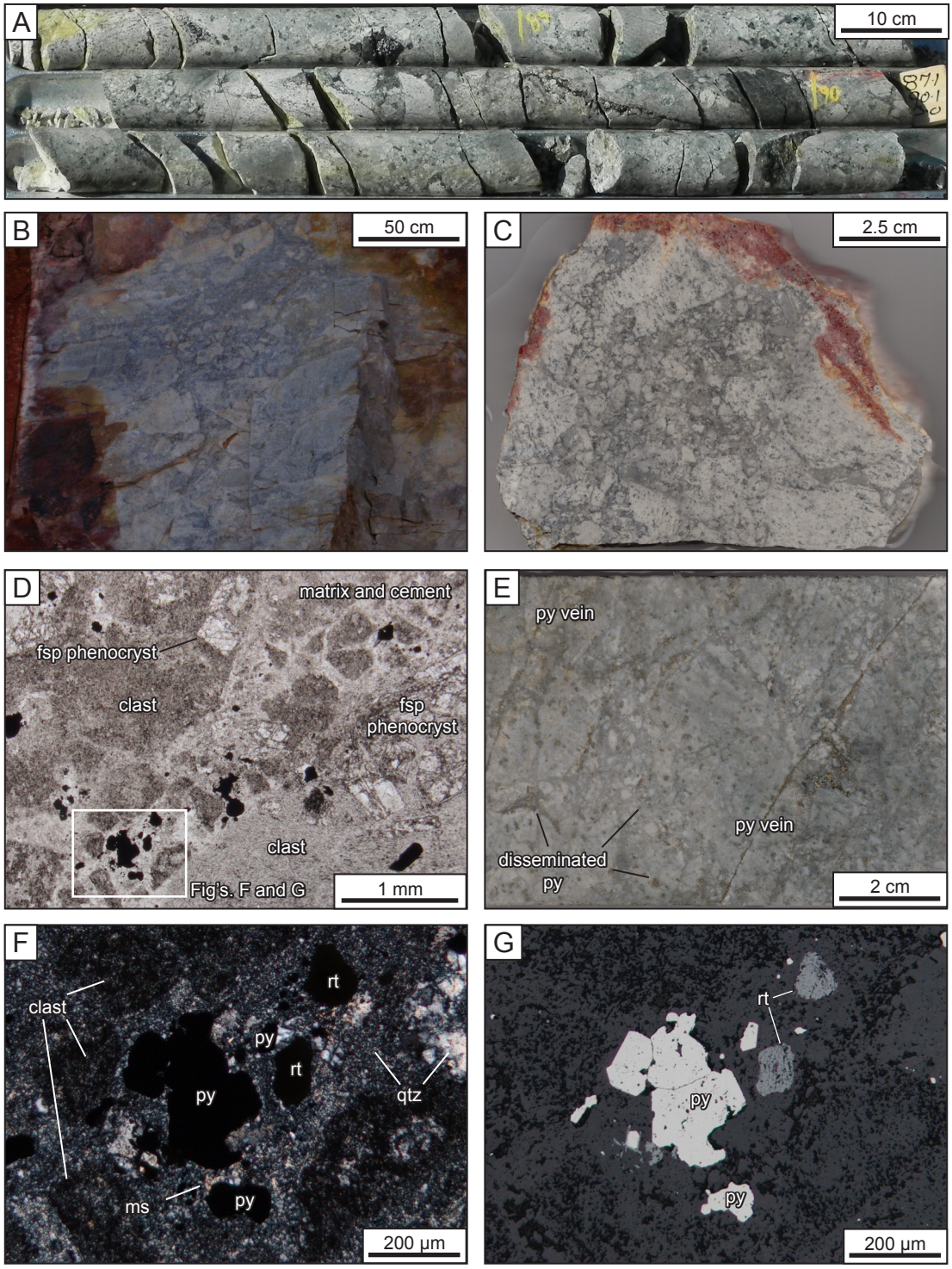

Figure 4.6 Examples of stage 1 quartz-pyrite cemented breccia. A) Chaotic, polymictic textures in drill core (PRD0009 87.3–91.1 m). B) Chaotic, matrix-supported, poorly sorted texture exposed in drill pad outcrop, clasts range from pebble to boulder size. C) Surface hand specimen (PR14AE119) showing matrix-supported texture with matrix of angular lithic fragments in quartz-pyrite cement, lithic clasts and matrix are intensely kaolinite-muscovite altered. D) Plane-polarized, transmitted light image of feldspar-phyric, kaolinite-muscovite altered clasts with infill of quartz-pyrite cement and angular lithic matrix (PR14AE119). E) Photo of cut core showing matrix-rich infill with pyrite disseminated throughout infill and clasts with post-brecciation pyrite veins (PR14AE188, MET018 285 m). F) Cross-polarized, transmitted light image of part of (D; insert) showing cement of disseminated pyrite grains with micro-crystalline quartz and muscovite and kaolinite-muscovite altered lithic fragments. G) Plane-polarised reflected light image of part of (D; insert) showing pyrite and rutile in cement. fsp = feldspar, ms = muscovite, py = pyrite, qtz = quartz, rt = rutile

drilling data, of 30–50 m width, 160 m vertical extent and >150 m length. The stage 2 breccia cross cuts stage 1 (Figure 4.4) and is itself cross cut by stage 4-C (Figure 4.7 A). The breccia also cross cuts, and is cross cut by facies 3B-2 (Figure 4.7 A).

The stage 2 breccia is characterised by massive, matrix-supported, chaotic, very-poorly sorted polymict lithic breccias (Table 4.4). They are typically composed of 30–60 % clasts and 15–50 % lithic and rock flour matrix. Clast shape varies from sub-angular to well-rounded (Figure 4.7 B), and clasts range in size from coarse-sand to pebble-size. Clast types include massive quartz, feldspar-phyric coherent rock and clasts of chaotic, polymict breccia (Figure 4.7 C) and quartz-cemented breccia (Figure 4.7 D). Stage 2 breccias have a high proportion of massive matrix that is dominated by rock flour and angular lithic fragments (Figure 4.7 D). The matrix has the same composition as clasts, and ranges from medium-sand to granule-sized.

Stage 2 is associated with intense kaolinite-muscovite alteration and local pyrite flooding, some of which may also relate to earlier (stage 1) and later (stage 4) alteration events. Kaolinite-muscovite alteration is texturally destructive and affected both clasts and matrix. Alteration intensity increases with breccia intensity. The most intense example of stage 2 brecciation was intersected in hole MET023 at 129–153 m, where the drill core is unconsolidated and consists of alternating clay-sulphide, and quartz-sulphide assemblages (Figure 4.7 E). Hand specimen and petrographic observations with SWIR analysis indicate that the mineralogy of this zone is dominated by kaolinite (Appendix C1) with lesser muscovite - pyrite - chalcopyrite - covellite. Pyrite flooding is observed locally with kaolinite alteration in the intensely brecciated zones (Figure 4.7 F). Chalcopyrite has locally cemented quartz-rich domains (Figure 4.7 G). The domain of intense brecciation and alteration also corresponds with high grade intervals of both Cu and Au (181m @ 1.0 %Cu, 0.3 g/t Au, 173 ppm Mo including 71 m @ 1.6 %Cu, 0.4 g/t Au, 229 ppm Mo, PRP0711; Hot Chili Ltd, 2013). Mineralisation is interpreted to be due to overprinting by stage 3.

Where drill core is coherent, chalcopyrite is observed predominately in veins with tourmaline (Figure 4.8 A) that are inferred to be facies 3B-2. Chalcopyrite also occurs as disseminated grains within the strongly brecciated zones. Chalcopyrite is commonly replaced by covellite at grain boundaries (Figure 4.8 B). Molybdenite grains are rare but were observed with chalcopyrite and tourmaline (Figure 4.8 C). Pyrite is strongly associated with kaolinite alteration and occurs as disseminated, round grains (10–50 μm; Figure 4.8 D and E). Pyrite also occurs with muscovite-illite in veins and locally with illite as breccia cement (Figure 4.8 F) — this association is inferred to be stage 4 overprint. Muscovite - kaolinite - quartz alteration is observed either side of the intense kaolinite-rich domain. Muscovite crystallinity, calculated using TSG software (AlOH feature depth divided by depth of water feature at ~1900 nm), increases with depth.

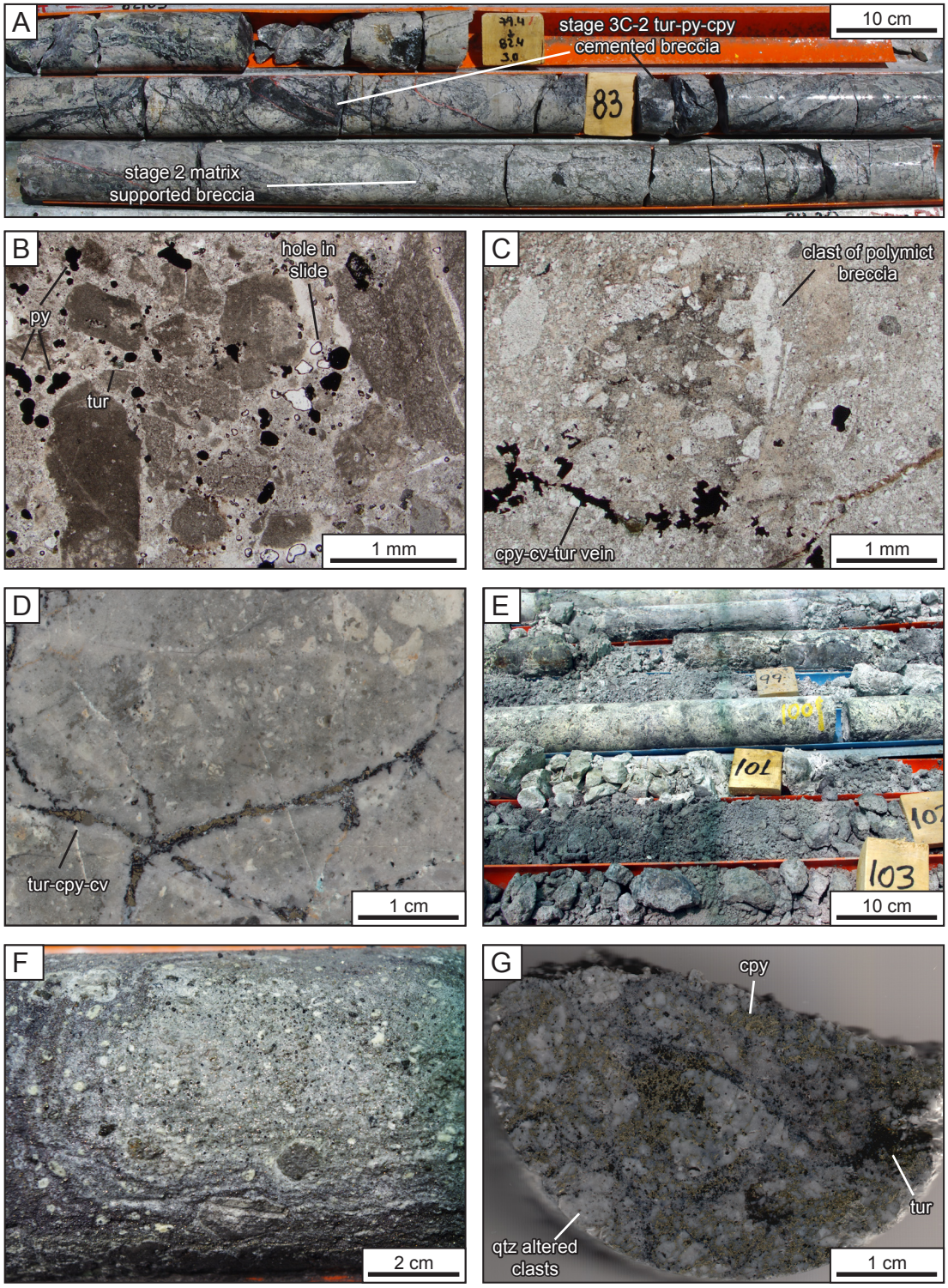

Figure 4.7 Representative photos of stage 2 breccia. A) Core photo showing stage 3, facies 3B-2 breccia overprinting stage 2 massive, chaotic, matrix supported breccia (MET023 82–84.50 m). B) Transmitted light photomicrograph showing clay altered, polymict clasts in matrix of lithic fragments and rock flour with disseminated pyrite and tourmaline (PR14AE124, MET023 81.50 m). C) Transmitted light photomicrograph showing a polymict breccia clast in matrix-rich breccia with crosscutting chalcopyrite - covellite - tourmaline vein (PR14AE125, MET023 84.10 m). D) Core photo showing polymict lithic fragments in matrix of rock flour and lithic fragments (PR14AE125). E) Photo of weakly cemented, broken drill core, typical of the most intensely brecciated domains of stage 2 (MET023 97–103 m). F) Core photo showing kaolinite - pyrite-rich, fine-grained breccia (MET023 96 m). G) Hand specimen photo of quartz - chalcopyrite - tourmaline-cemented breccia with monomict clasts of a quartz-altered clastic rock (PR14AE126, MET023 102.20 m). cpy = chalcopyrite, cv = covellite, py = pyrite, qtz = quartz, tur = tourmaline.

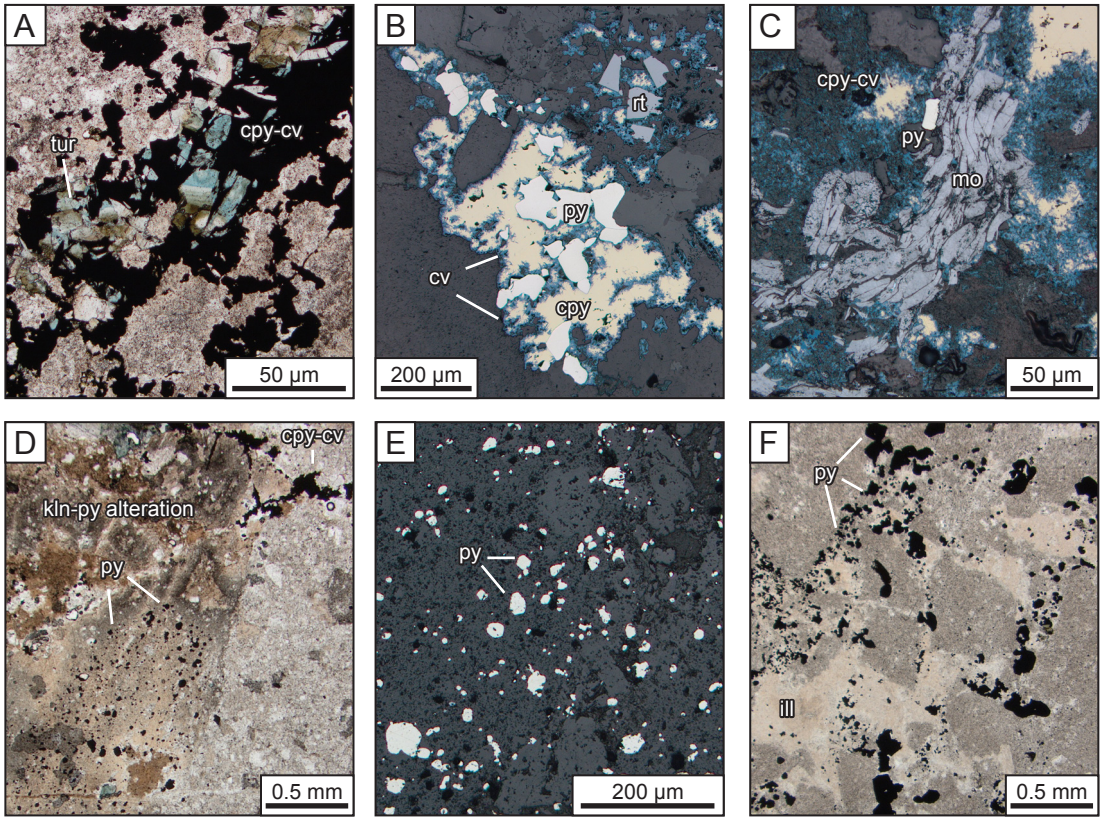

Figure 4.8 Representative photomicrograph from stage 2. A) Transmitted light photo showing facies 3B-2 vein of zoned tourmaline with chalcopyrite, facies 3B-2 cross cuts stage 2 (PR14AE125, MET023 84.10 m). B) Reflected light photo showing chalcopyrite with covelite replacement at grain boundaries (PR14AE123, MET023 79.20 m). C) Reflected light photo showing molybdenite in association with chalcopyrite-covellite (PR14AE125). D) Transmitted light photo showing kaolinite-pyrite alteration of matrix supported breccia (PR14AE125). E) Reflected light photo showing disseminated pyrite, typically associated with kaolinite alteration (PR14AE125). F) Transmitted light photo showing pyrite - muscovite cement and kaolinite-altered clasts (PR14AE127, MET023 167.70 m). cpy = chalcopyrite, cv = covelllite, ill = illite, kln = kaolinite, mo = molybdenite, py = pyrite, tur = tourmaline, rt = rutile

4.4.4 Stage 3: Potassic alteration, tourmaline breccias and main stage mineralisation

The tourmaline-cemented breccias and associated alteration are the most abundant and widely developed paragenetic stage in the ore zones at the Productora deposit. Most of the Cu-Au-Mo mineralisation is associated with the Stage 3 hydrothermal breccia complex, with sulphide precipitated as cement along with tourmaline, magnetite, biotite and other minor phases in varying proportions. In addition to occurrences as breccia cement, sulphides also occur in syn-brecciation veins and as disseminations in altered clasts. Based on hand specimen observations during this study, stage 3 has been subdivided into two sub-stages; sub-stage 3A — K-feldspar alteration and related veins, and sub-stage 3B — tourmaline-cemented breccias and related veins. The tourmaline breccias are further subdivided in five facies based on their predominant cement mineralogies and textures (Table 4.4, Figure 4.4 and Figure 4.5), which vary laterally and vertically throughout the breccia complex. Boundaries between breccia facies are inferred to be gradational. Interpretations of the breccia sub-stages have been determined through a combination of graphic logging from available drill core, logging from core photography, detailed hand specimen and

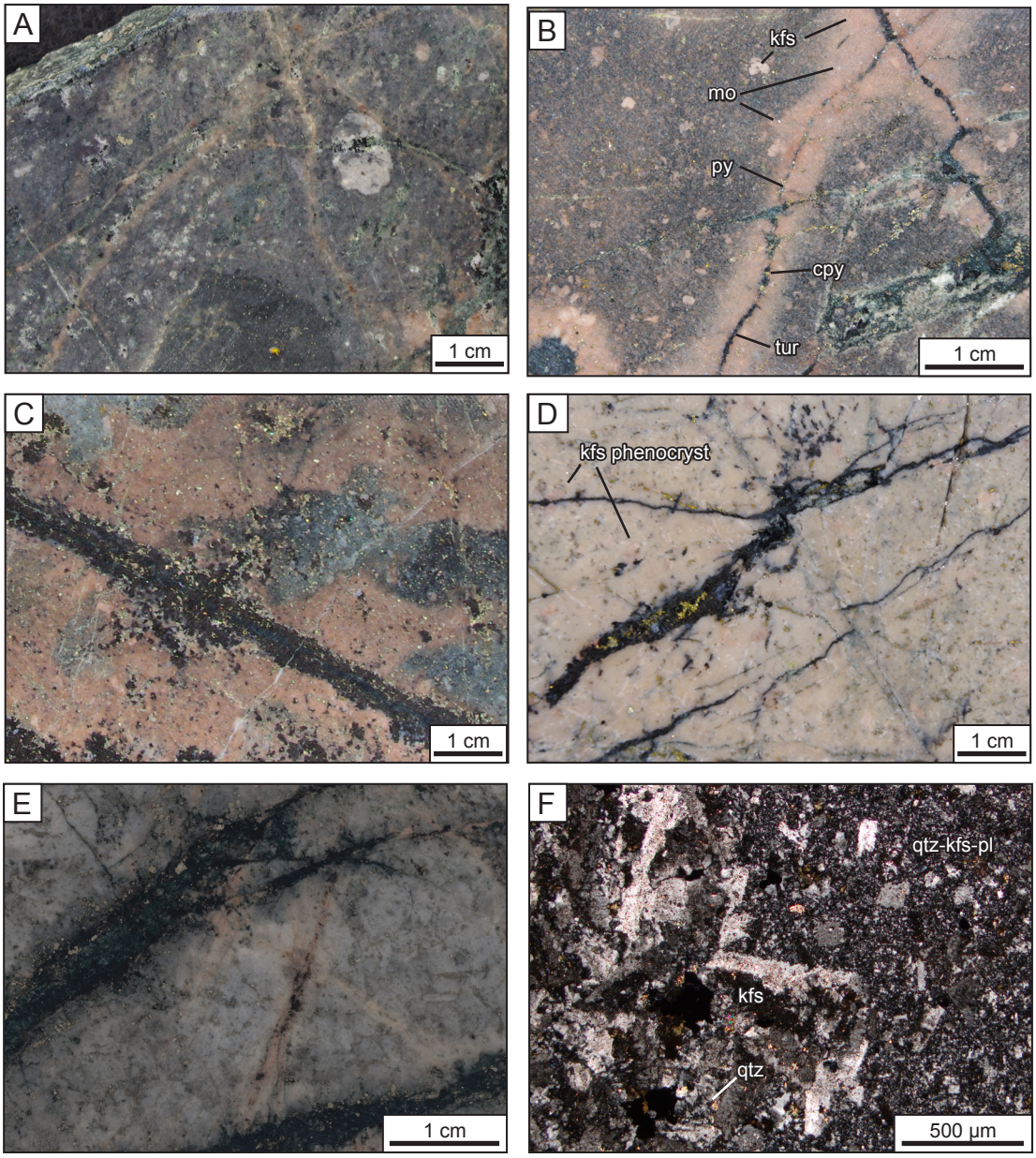

Figure 4.9 Representative photos of sub-stage 3A K-feldspar alteration. A) Core photo showing K-feldspar veinlets in rhyodacite lapilli tuff from the margin of the breccia complex (PR14AE002, MET007 459.43 m). B) Core photo showing K-feldspar alteration halos to tourmaline-pyrite-chalcopyrite veins. Disseminated molybdenite occurs in vein halo (PR14AE113, PRP0066D 181.35 m). C) Core photo showing K-feldspar alteration front in rhyodacite lappilli tuff (PR14AE114, PRP0066D, 188.60 m) D) Core photo showing texturally destructive K-feldspar flooding with tourmaline-chalcopyrite veins (PRP0066D 171.80 m). E) Core photo showing K-feldspar veinlets cross cutting stage 1 breccia and overprinted by facies 3B-3 breccia (PR14AE147, MET014 148.25 m). F) Crossed polarised transmitted light photomicrograph showing K-feldspar alteration front (left) in microcrystalline quartz-K-feldspar-plagioclase groundmass of rhyodacite lapilli tuff (PR14AE114, above). cpy = chalcopyrite, kfs = K-feldpar, mo = molybdenite, pl = plagioclase, py = pyrite, qtz = quartz, tur = tourmaline.

polished thin section observations supplemented by a QXRD data set (discussed in 4.3.7). Due to a lack of available drill core through the mineralised domain on the southern section, interpretations of breccia facies are less confident in that area. No cross-cutting relationships were observed between the stage 3 facies, implying that stage 3 was potentially one catastrophic brecciation event.

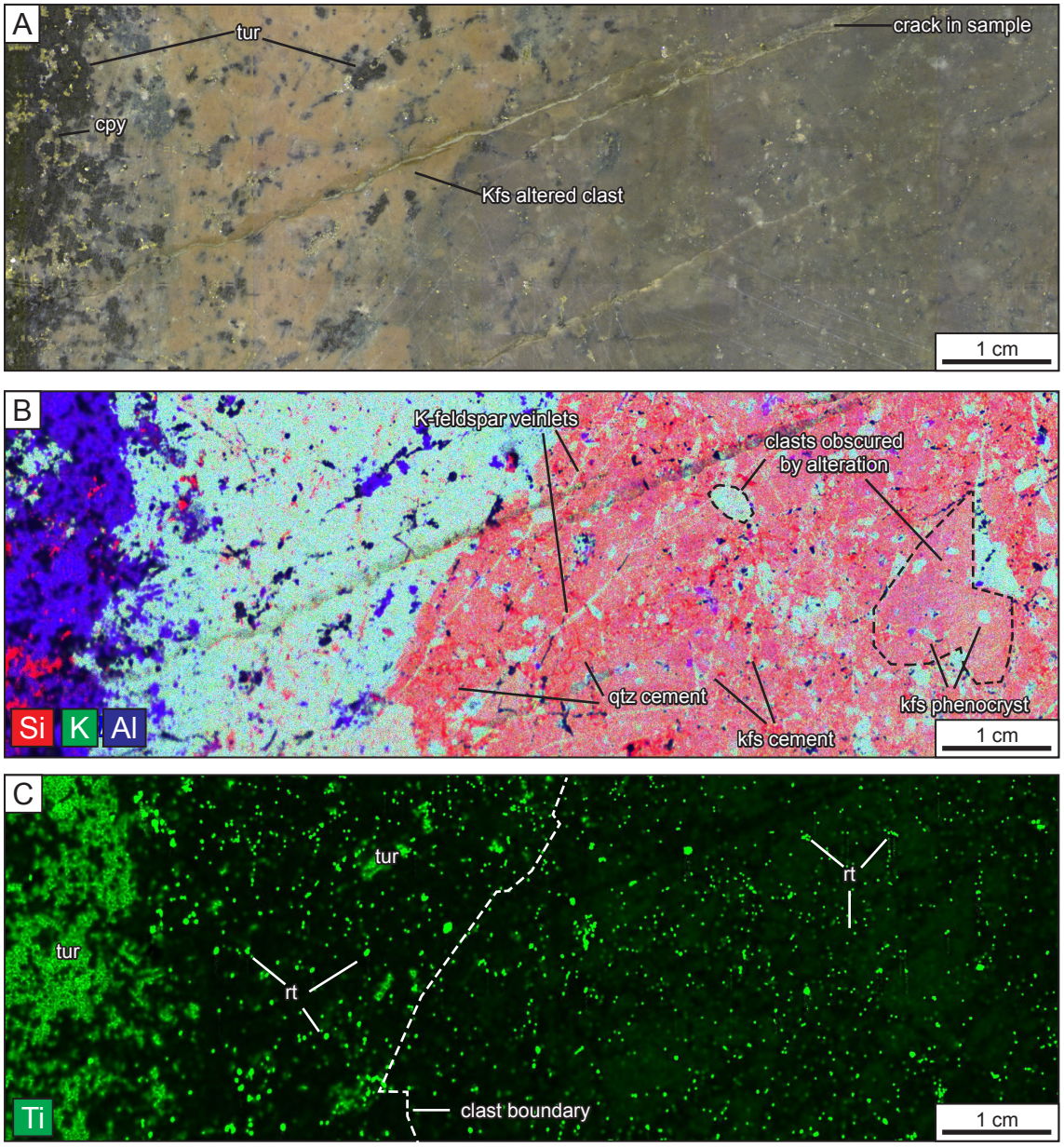

Figure 4.10 Micro-XRF element maps for sample PR14AE062 exhibiting intense sub-stage 3A K-feldspar alteration. A) Photograph of mapped sample area showing intense K-feldspar alteration obscuring relic textures. A domain of intensely K-feldspar alteration surrounds a tourmaline-chalcopyrite alteration clot (left) but it is not clear if this is an alteration halo or clast . B) RGB-image showing Si, K and Al maps across sample. High K and Al domains (turquoise) indicate K-feldspar-rich areas, Si-rich areas (red) contain higher quartz. Blue areas are tourmaline or chlorite. Element maps highlight a complex breccia texture. The sample is a chaotic, quartz cemented, matrix supported polymict breccia with large, intensely K-feldspar altered clast. Two types of clasts can be see — one K-feldspar rich (turquoise) type and the other K-feldspar and quartz rich with K-feldspar phenocrysts (red-turquoise). The matrix-supported breccia is variably cemented by quartz (red) and K-feldspar. C) Element map for Ti showing high Ti in rutile and low Ti with tourmaline, possibly small rutile inclusions. Distribution and size of rutile grains varied in different clast types. Also, closer to the tourmaline-chalcopyrite alteration clot grains are fewer but larger suggesting cm-scale Ti mobility with increased alteration.

4.4.4.1 Sub-stage 3A: Syn-breccia K-feldspar alteration and veins

Syn-breccia K-feldspar alteration occurs as halos around K-feldspar veins (Figure 4.9 A and B) and as domains of intense K-feldspar flooding (Figure 4.9 C and D). K-feldspar veinlets and tourmaline veins

with K-feldspar selvages (0.5 – >2cm wide) are observed distal (>100 m) to the breccia complex. The overprinting of K-feldspar veinlets by sub-stage 3B tourmaline-cemented breccias suggests that sub-stage 3A K-feldspar veins were a precursor to the brecciation event (Figure 4.9 E). K-feldspar alteration intensity ranges from moderate to strong. Where moderate, relict textures of the volcanic protoliths are observed, including phenocrysts and crystal fragments now replaced by K-feldspar. Where strong, the alteration is texturally destructive and complete replacement of the groundmass has occurred, obscuring clast boundaries (Figure 4.9 C, D and F), although K-feldspar phenocrysts are commonly preserved (Figure 4.9 D). Micro-XRF mapping reveals complex textures obscured by the pervasive K-feldspar alteration (Figure 4.10). Titanium, hosted by rutile grains, not visible to the naked eye can be used to distinguish clasts versus alteration (Figure 4.10 C). Where K-feldspar alteration is more intense, rutile grains are coarser, suggesting Ti-mobility on the scale of centimetres occurred.

4.4.4.2 Sub-stage 3B: Tourmaline breccias and veins

Facies 3B-1: Tourmaline - magnetite - chlorite - pyrite - chalcopyrite-cemented breccia

Breccia facies 3B-1 was observed in drill core from the northern study section (6,822,215 mN; MET007; Figure 4.4 and Figure 4.11 A) where it overprinted the monomict rhyodacite breccia lithology (section 3.4.2) and stage 1 quartz - pyrite cemented breccia (Figure 4.11 B and C). The 3B-1 breccia is a massive monomict lithic breccia. It is predominantly clast-supported, varies from jigsaw fit to chaotic, is very-poorly–moderately sorted and has a tourmaline - magnetite - chlorite - pyrite - chalcopyrite cement (Table 4.4). It is typically composed of 70-90 % clasts, 0–15 % matrix and 10-30 % cement. Clasts are angular and typically pebble sized but range up to cobble size locally. Where facies 3B-1 was observed in drill core, the clasts were predominantly monomict with lithic fragments either of monomict rhyodacite breccia and/or feldspar-phyric rhyodacite (Figure 4.11 B and D) transitioning to rhyodacite lapilli tuff downhole — concordant with the down hole change in host lithology. Discrete domains of chaotic, matrix and cement rich breccias were also observed locally, with some stratification noted (Figure 4.11 E). Massive tourmaline cement was observed over intervals of 75 cm in hole PRD0011 (at 156 m). Later replacement of massive tourmaline by quartz has created what is inferred to be a quartz-cemented tourmaline pseudo-breccia (Figure 4.11 F). Narrow ductile strain zones have also been observed within the breccia body (Figure 4.11 G). The structures are composed of anastomosing veins of tourmaline, K-feldspar, quartz and chlorite.

Accessory quartz, rutile and epidote occur in addition to the major cement mineralogy in facies 3B-1 breccias. Epidote and quartz are locally major cement components. Tourmaline habit ranges from large (100-200 μm) equant crystals to small (<100 μm) prismatic crystals. The larger crystals commonly show colour zoning in plane-polarized transmitted light (Figure 4.12 A). Tourmaline is commonly intergrown

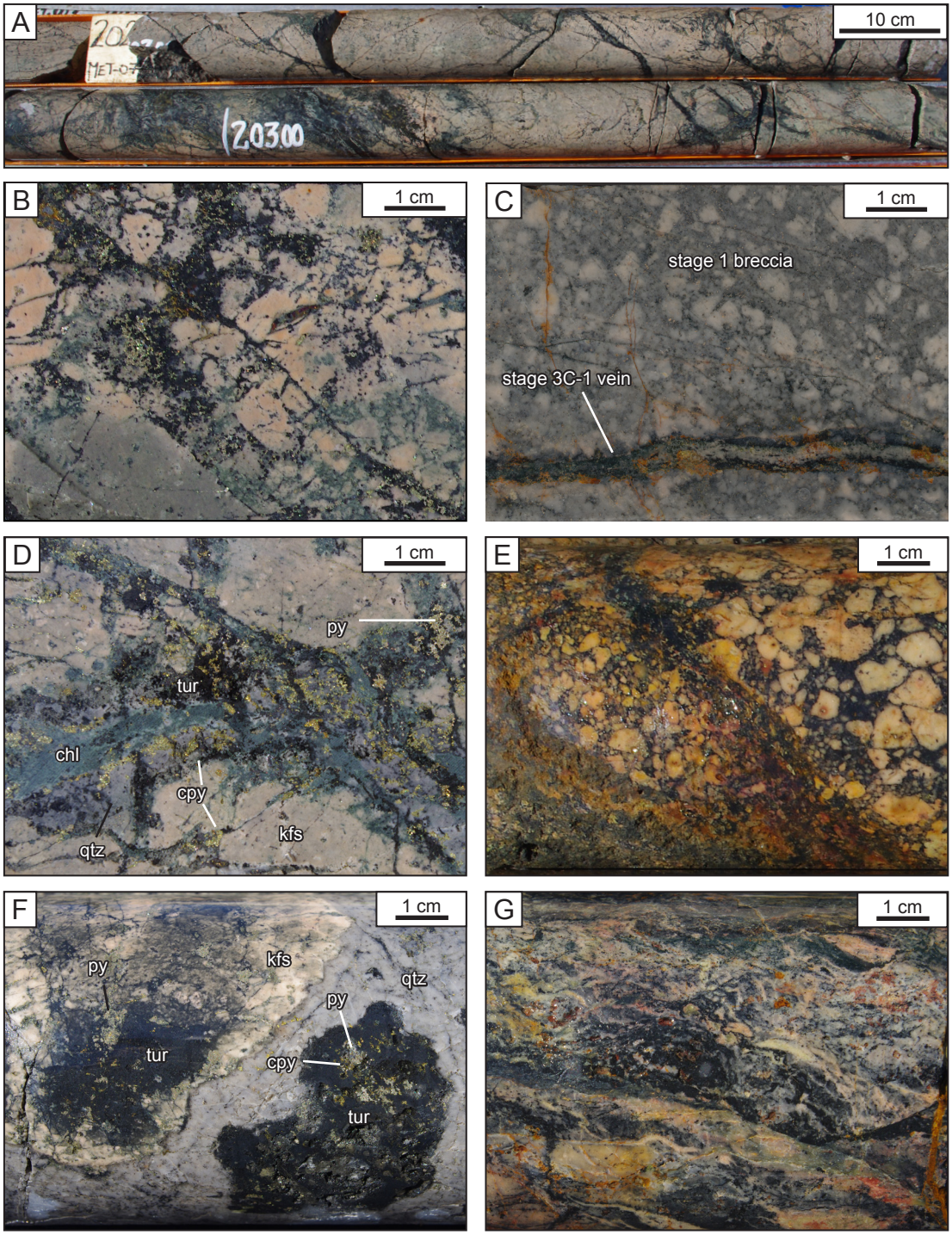

Figure 4.11 Representative hand specimen scale photos of facies 3B-1 breccias. A) Photo of drill core showing jigsaw fit tourmaline-cemented breccia with intense, texturally destructive K-feldspar alteration (MET007 201–204 m). B) Tourmaline-chalcopyrite cemented breccia with associated K-feldspar alteration cross cutting relic monomict rhyodacite breccia (PR14AE183, MET007 200 m). C) Facies 3B-1 K-feldspar vein with tourmaline halo cross cutting stage 1 breccia. D) Tourmaline-chlorite-quartz-chalcopyrite cemented breccia with feldspar phyric coherent clasts (MET007 199 m). E) Domain of chaotic and stratified breccia (PRD0011 102.10 m). F) Core sample showing quartz alteration of tourmaline cement to create a pseudo-breccia texture with tourmaline and K-feldspar - tourmaline altered apparent clasts (PR14AE095, PRD0011 126.50 m). G) Core sample with anastomosing tourmaline-K-feldspar - quartz vein showing apparent ductile texture (PRD0011 49.50 m). kfs = K-feldspar, cpy = chalcopyrite, chl = chlorite, py = pyrite, qtz = quartz, tur = tourmaline, rt = rutile

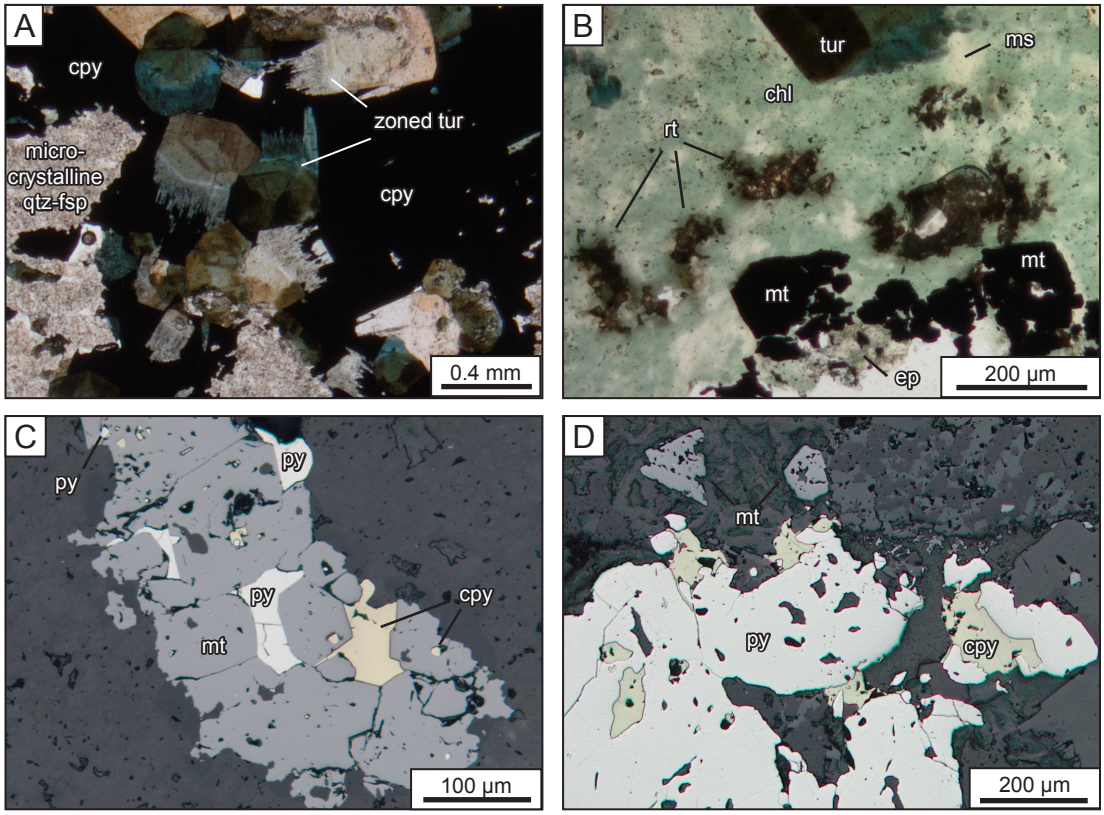

Figure 4.12 Representative photomicrographs of facies 3B-1 breccias. A) Transmitted light photo of zoned tourmaline intergrown with chalcopyrite (PR14AE060, MET007 188.25). B) Transmitted light photo showing chlorite aggregate with rutile, magnetite and tourmaline (PR14AE060). C) Reflected light photo showing subhedral magnetite with inclusions of, and interstitial, chalcopyrite and pyrite (PR14AE062, MET007 218.45 m). D) Reflected light photo showing concave grain boundaries of both chalcopyrite and pyrite indicating they are intergrown and possibly in equilibrium (PR14AE060) cpy = chalcopyrite, chl = =chlorite, fsp = feldspar, ms = muscovite qtz = quartz, py = pyrite, rt = rutile, tur = tourmaline.

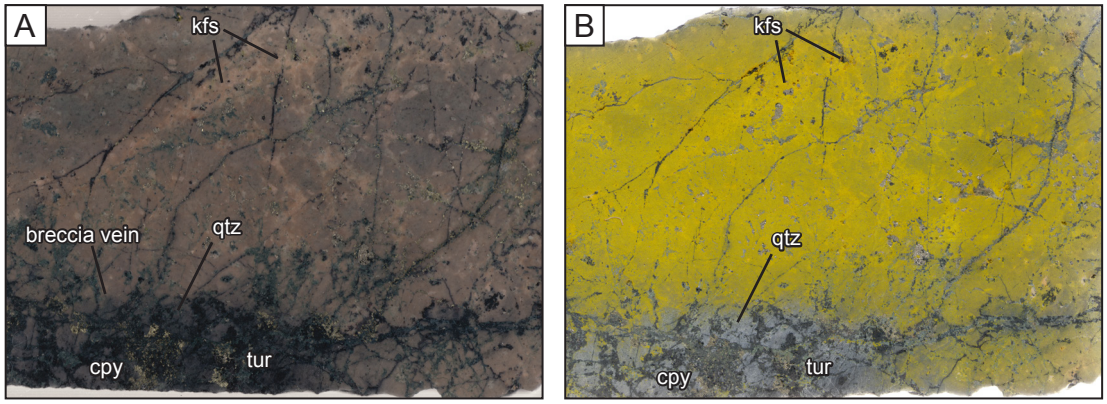

Figure 4.13 A) Example of 3B-1 breccia vein with quartz altered selvage and intense K-feldspar alteration of host monomict rhyodacite breccia with replacement of protolith breccia infill by K-feldspar (PR14AE061, MET007 191.80 m). B) Feldspar staining of sample in image A showing pervasive K-feldspar alteration of relict clasts and infill, and quartz alteration proximal to breccia vein. cpy = chalcopyrite, kfs = K-feldspar, qtz = quartz, tur = tourmaline.

with pyrite and chalcopyrite and some tourmaline grains have abundant small inclusions of rutile. Chlorite occurs as massive aggregates or fibrous rosettes, commonly in association with tourmaline. The massive aggregates of chlorite commonly contain clusters of rutile (Figure 4.12 B). Although little evidence of relict biotite was observed from this breccia facies, the consistent association of chlorite and rutile is interpreted to indicate that chlorite formed, in part, by retrograde alteration of Ti-bearing biotite. Where abundant in the breccia cement, epidote occurs as euhedral 100-500 μm grains, locally pseudomorphing relict feldspar phenocrysts. Epidote has also enclosed small crystals of magnetite and chalcopyrite. Magnetite occurs as aggregates of smaller grains (20–100 μm), commonly associated with chlorite (Figure 4.12 B). Its habit varies from anhedral to euhedral. Magnetite is more commonly associated with chalcopyrite than pyrite. Pyrite and chalcopyrite both occur intergrown with subhedral magnetite grains, and also occur as small inclusions within magnetite grains (Figure 4.12 C). Chalcopyrite occurs on pyrite grain edges, infilling cracks and also as inclusions in pyrite. Concave grain boundaries with pyrite suggest that chalcopyrite may have been partially replaced by pyrite, however, the opposite relationship has also been observed (Figure 4.12 D), suggesting that conditions varied between pyrite and chalcopyrite stability. Pyrite commonly occurs as large grains, typically with abundant inclusions of K-feldspar and quartz, and locally with inclusions of chalcopyrite, and rarely pyrrhotite.

Breccia facies 3B-1 is succeeded by 3B-1 veinlets and patchy alteration. Veinlets have 0.5-2 cm wide halos of K-feldspar-tourmaline alteration. In clastic protoliths, such as the monomict rhyodacite breccia, the matrix has been selectively altered. Where alteration is more advanced, clots of tourmaline with K-feldspar halos are observed. Disseminated grains of pyrite range from 5–600 μm, chalcopyrite from 10–300 μm and magnetite from 20–600 μm.

Facies 3B-1 is associated with intense K-feldspar alteration (sub-stage 3A) that modified the mineralogy of the monomict rhyodacite breccias to K-feldspar-dominant (Figure 4.13). K-feldspar alteration was, in most cases, intense and texturally destructive. Facies 3B-1 breccias are also locally associated with syn-breccia K-feldspar veins and quartz-rich alteration (PRD0011, 115–127 m; Figure 4.11 F).

Facies 3B-2: Tourmaline - pyrite - chalcopyrite-cemented breccia

The 3B-2 breccia facies and related veins were observed in drill core on the northern section (6,822,215 mN; Figure 4.4) where they occur at depths shallower than the 3B-1 breccia. The 3B-2 breccia typically occurs in narrow (<5 m) domains and also as 0.1–2 m thick breccia dykes and veins that cross cut the monomict rhyodacite volcanic breccia (Figure 4.14 A and B), stage 1 breccia and stage 2 breccias. The 3B-2 breccia and veins are associated with syn-breccia K-feldspar and quartz alteration.

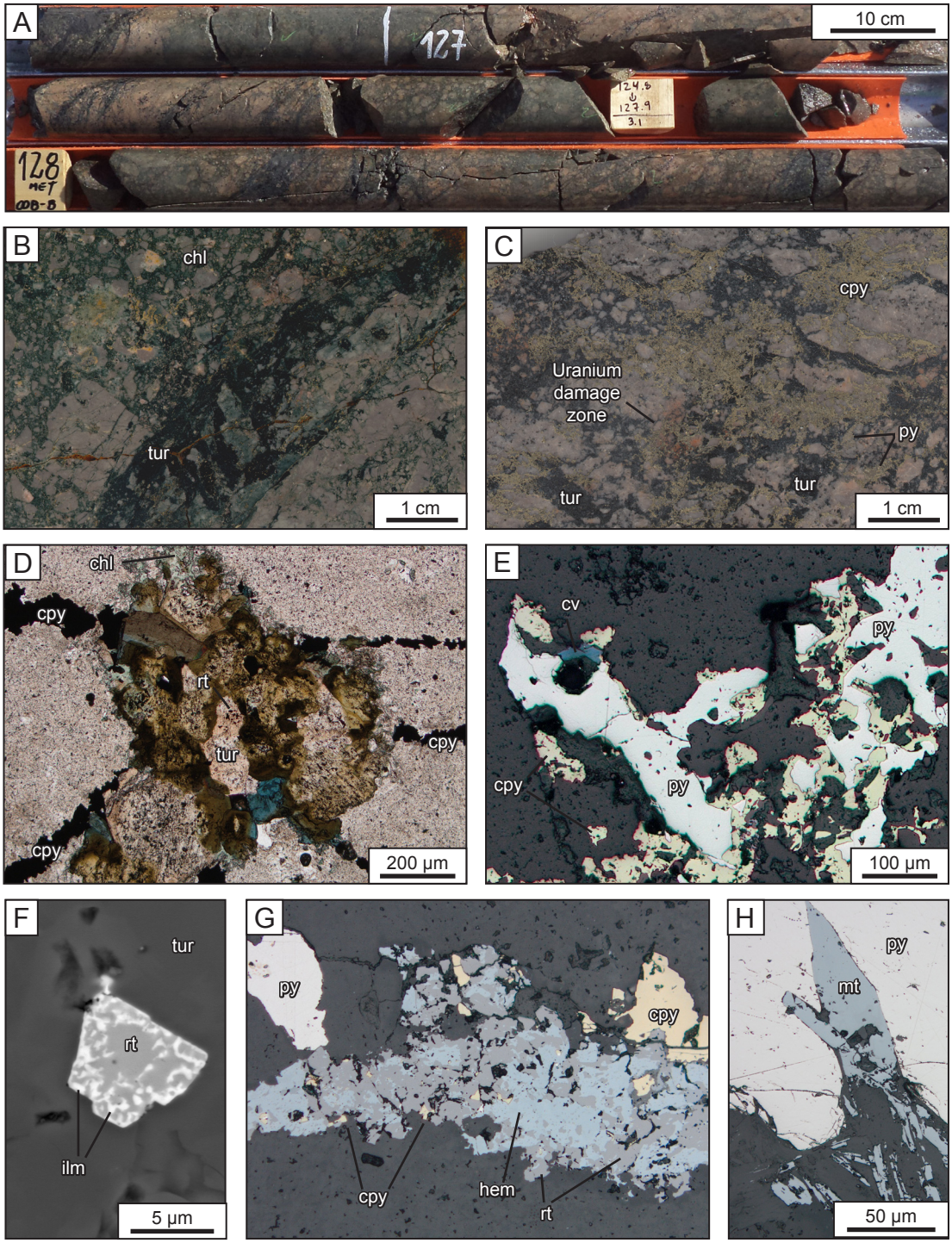

Figure 4.14 Representative photographs of facies 3B-2 breccias. A) Photo of drill core showing 3B-2 tourmaline veins with K-feldspar halos cross cutting massive, monomict rhyodacite breccia (MET008B 126.65–128.80 m). B) Drill core sample showing replacement of monomict rhyodacite breccia chlorite infill by tourmaline from facies 3B-2 (PR14AE022, MET008B 104.20 m). C) Tourmaline - chalcopyrite - pyrite cemented breccia with ragged clast boundaries, suggesting chemical corrosion of clasts, and lithic matrix. Also note discolouration of damage zone around uranium-rich phase (PR14AE180, MET022 117.15 m). D) Tourmaline - chalcopyrite - chlorite - rutile clot in quartz - feldspathic rock (PR14AE027, MET008B 118.10 m). E) Chalcopyrite after pyrite with covelite (PR14AE027). F) SEM electron backscatter image showing rutile grain with ilmenite replacement (PR14AE027). G) Vein of hematite and rutile with chalcopyrite and pyrite inclusions (PR14AE059, MET007 170.95 m). H) Magnetite pseudomorph of hematite (mushketovite; PR14AE027). chl = chlorite, cpy = chalcopyrite, cv = covellite, hem = hematite, ilm = ilmenite, mt = magnetite, py = pyrite, rt = rutile, tur = tourmaline

The 3B-2 facies is characterised by massive, clast-supported and locally cement-supported, jigsaw-fit to clast rotated, moderately sorted, tourmaline - chalcopyrite - pyrite cemented, lithic breccias (Table 4.4). They are typically composed of 70–80 % lithic clasts, 0–10 % lithic matrix and 10–20 % cement. Clasts have angular to ragged shapes (Figure 4.14 C) and are typically pebble-sized, although oversized clasts up to 1 m in diameter were recognised from drill core intersects. Intense K-feldspar alteration has precluded the identification of clast protolith in many instances. Where alteration was less intensely developed, clasts of the monomict rhyodacite breccia and stage 1 breccia have been noted. Distinguishing between the two becomes increasingly challenging with increased intensity of alteration. Where present, the matrix is composed of medium sand to granule size, moderately sorted, angular lithic fragments (Figure 4.14 C). The cement is dominated by tourmaline, with varying amounts of chlorite, chalcopyrite and pyrite. These minerals have also replaced chlorite breccia cement in the monomict rhyocdacite breccia, have filled 3B-2 veins that cut the cement, and occur as alteration clots in clasts (Figure 4.14 A, B and D). Inclusions of rutile with ilmenite replacement lamellae are common in the equant, zoned tourmaline grains. Pyrite and chalcopyrite are inferred to have formed synchronously, as both examples of chalcopyrite overgrowing pyrite (Figure 4.14 E) and pyrite overgrowing chalcopyrite are observed. Typically they occur in veins and as breccia cement. Pyrite also commonly occurs as fine (5-10 μm) disseminated grains in the clasts and cement. Covellite, inferred to be supergene, was observed as individual grains and as partial replacements of chalcopyrite grain boundaries (Figure 4.14 E). Where facies 3B-2 overprinted the stage 2 matrix-supported breccia, pyrite and chalcopyrite are significantly more abundant, >7 % and >6 % respectively. Pyrite and chalcopyrite occur both with and without tourmaline as disseminations within the stage 2 matrix. Rare veins of hematite-rutile-chalcopyrite and magnetite were also observed (Figure 4.14 G). Laths of magnetite noted in one sample were interpreted to be pseudomorphs of hematite (mushketovite; Figure 4.14 H).

Facies 3B-3: Biotite - pyrite - magnetite - tourmaline-cemented breccia

The facies 3B-3 breccia was observed in drill core (MET015 and MET016) from section 6,820,850 mN at depths greater than 100 m from surface. The cement-supported breccia is predominantly hosted by lapilli tuff and is surrounded by a halo of 3B-3 veins with biotite-K-feldspar alteration halos up to 3 cm wide.

In general, facies 3B-3 is characterised by massive, clast-supported, jigsaw fit, poorly–well sorted biotite-pyrite - chalcopyrite - magnetite - tourmaline-cemented, monomict lithic breccias (Table 4.4, Figure 4.15 A). They contain 80–95 % lithic clasts, 0–5 % lithic matrix, 5–20 % cement and 0–3 % open space. Clasts are angular to sub-rounded and range from granule to cobble size. Although intensely altered

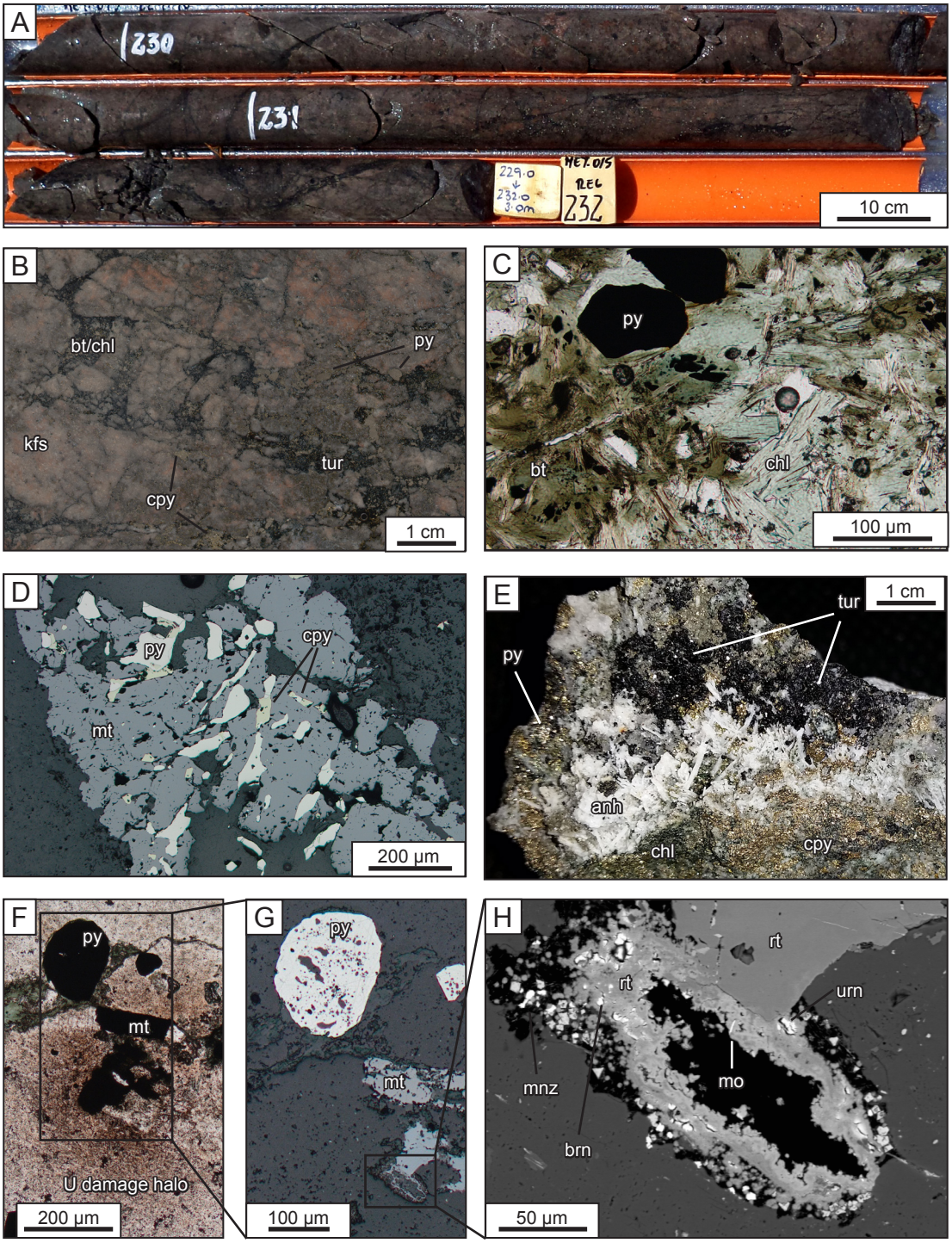

Figure 4.15 Representative photos of breccia facies 3B-3. A) Photo of drill core showing jigsaw fit breccia and associated K-feldspar alteration (MET 015, 229.90-232 m). B) Intense K-feldspar alteration is texturally destructive and locally obscures lapilli tuff protolith textures (PR14AE162, MET015 239.60 m). C) Chlorite replacing biotite-dominant cement (PR14AE162). D) Reflected light photo showing magnetite vein with pyrite and chalcopyrite inclusions (PR14AE162). E) Hand specimen photo of anhydrite - chalcopyrite - tourmaline - pyrite vein (PR14AE174, MET016 316.40 m). F) Plane polarised transmitted light photo showing red stained damage halo around uranium rich phases (PR14AE163, MET015 250.70). G) Reflected light photo of uranium-rich phase with rutile, magnetite and pyrite. Pyrite contains abundant inclusions of K-feldspar (PR14AE163). H) SEM backscattered electron image showing a variety of <5µm diameter, uranium rich minerals hosted in an amorphous TiO_2 phase (PR14AE163). ahn = anhydrite, bt = biotite, brn = brannerite, chl = chlorite, cpy = chalcopyrite, mnz = monazite, mo = molybdenite, mt = magnetite, py = pyrite, rt = rutile, tur = tourmaline, urn = uraninite

(Figure 4.15 B), relict textures suggest clasts are monomict, consisting of lapilli tuff. Matrix abundance varies with the intensity of brecciation. Where present, the matrix consists of angular, poorly sorted, medium-sand–granule size lithic fragments range from 0.25–4 mm. The cement has massive texture and contains abundant biotite, pyrite, chalcopyrite and magnetite. Biotite has largely been altered to chlorite, but relict biotite has been observed thin sections (Figure 4.15 C). Pyrite occurs as large grains (40–1500 μm), commonly with inclusions of silicate minerals, and chalcopyrite occurs as finer (5–20 μm), anhedral, angular grains that are interstitial to biotite and chlorite. Chalcopyrite has commonly overgrown and surrounded pyrite grains, and also occurs as inclusions within pyrite. Magnetite occurs both as large euhedral grains (100–250 μm) and finer anhedral grains that are interstitial to biotite. Magnetite also occurs in facies 3B-3 veins with pyrite and chalcopyrite. The sulphides also occur as inclusions in magnetite, and intergrowths between magnetite grains (Figure 4.15 D). Tourmaline is only a minor phase in the 3B-3 facies. It occurs as 10–200 μm, equant, euhedral grains (Figure 4.15 E). The breccia contains open spaces that are inferred to have formed via dissolution of gypsum (after anhydrite). Fibrous anhydrite was observed with chalcopyrite, tourmaline, pyrite and chlorite in a massive facies 3B-3 vein (PR14AE174; Figure 4.15 E). Uranium-rich phases have been identified in hand specimen by the red stained radiation-induced damage halo in the K-feldspar altered rocks. Scanning electron microscope analyses have revealed a range of uranium minerals including uraninite and brannerite together with monazite and a lead-rich phase in an amorphous TiO_2 phase clustered in the centre of the damage halo (Figure 4.15 F–H).

Facies 3B-4: Biotite - tourmaline - chalcopyrite - pyrite-cemented breccia

The 3B-4 breccia was observed in drill core (MET014) from shallower portions of the southern section (6,820,850 mN), approximately 140 m below the surface. The breccia has overprinted massive, polymict stage 1 breccia (Figure 4.16 A), in which protolith textures have largely been obscured by intense K-feldspar and albite alteration (Figure 4.16 B and C).

Facies 3B-4 is characterised by massive, clast supported, jigsaw fit–rotated; poorly sorted, biotite - tourmaline - chalcopyrite - pyrite-cemented, monomict breccias (Table 4.4, Figure 4.16 B and D). They are composed of 85–95 % lithic clasts, 0–2 % lithic matrix and 5–15 % cement. The clasts are angular and range from pebble to cobble size. Although obscured by alteration, the lithic clasts have textures consistent with lapilli tuff and locally massive polymict breccia protoliths. Matrix is sparse, and only occurs where the intensity of brecciation and proportions of cement are higher (Figure 4.16 D). In these domains the matrix is angular, moderately sorted, medium sand–granule sized lithic fragments. The massive cement is dominated by biotite, which has mostly retrogressed to chlorite (Figure 4.16 E). Biotite was not readily identified in hand specimen but is observed as olive-green, tabular–flakey fibrous

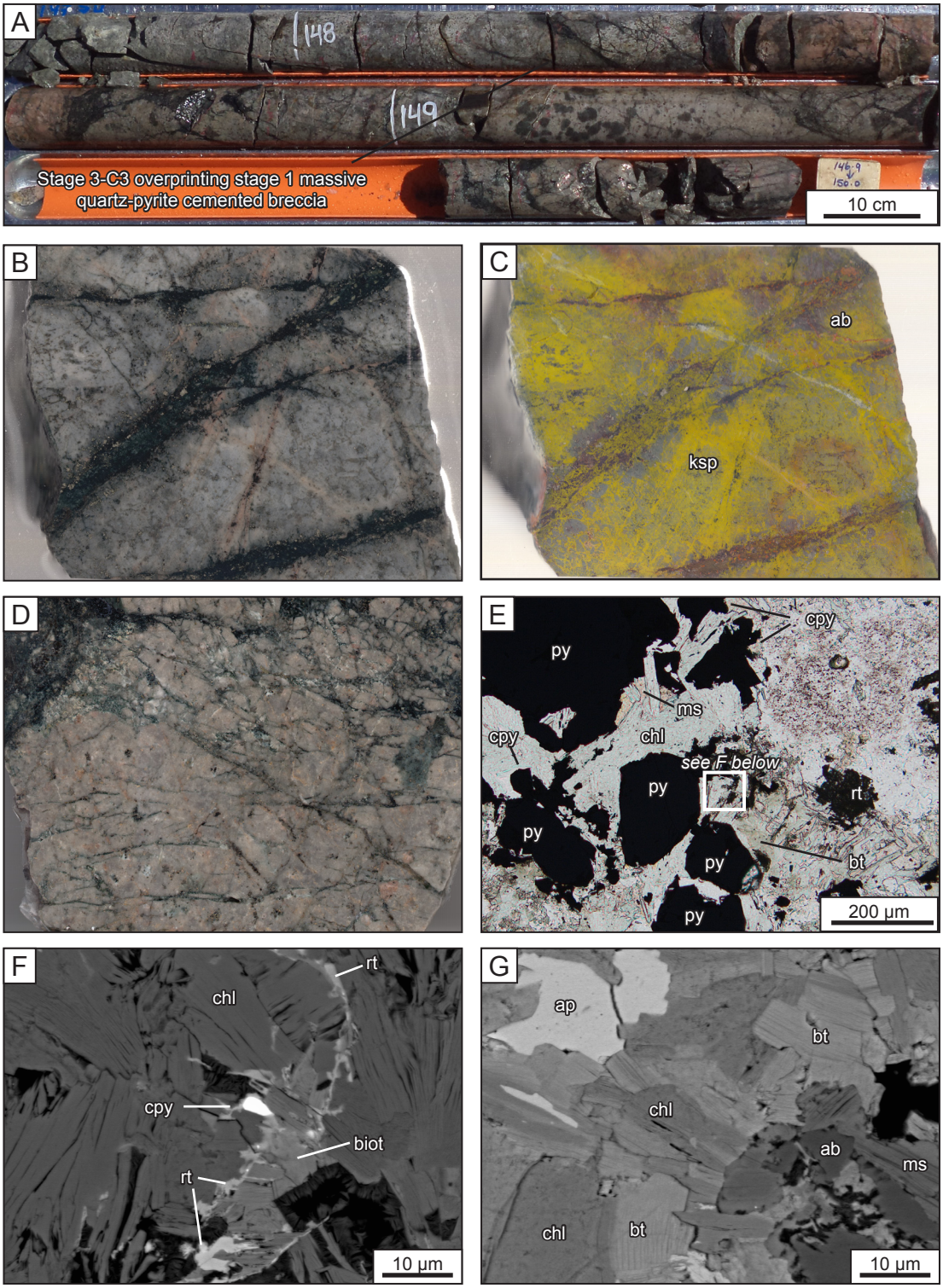

Figure 4.16 Representative photos of breccias facies 3B-4. A) Drill core showing 3B-4 breccia overprinting stage 1 breccia (MET014 147.74–150 m). B) Jigsaw fit breccia 3B-4 breccia overprinting stage 1 quartz-pyrite cemented breccia (PR14AE147, MET014 148.25 m). C) Sample shown in B with feldspar staining to show intense K-feldspar alteration (yellow) of clasts and veins, and albite (red) association with breccia cement. D) Jigsaw fit–clast rotated, biotite-cemented breccia overprinting lapilli tuff (PR14AE148, MET014 148.70). E) Transmitted light photomicrograph showing cement mineralogy; chlorite after biotite, pyrite, chalcopyrite, rutile and muscovite (PR14AE148). F) SEM backscattered electron image of chlorite and rutile replacing biotite, rutile occurs on grain boundaries (PR14AE148). G) SEM backscattered electron image of chlorite replacing tabular biotite crystals with associated apatite, muscovite and albite (PR14AE148). alb = albite, ap = apatite, bt = biotite, chl = chlorite, cpy = chalcopyrite, ms = muscovite, kfs = K-feldspar, py = pyrite, rt = rutile.

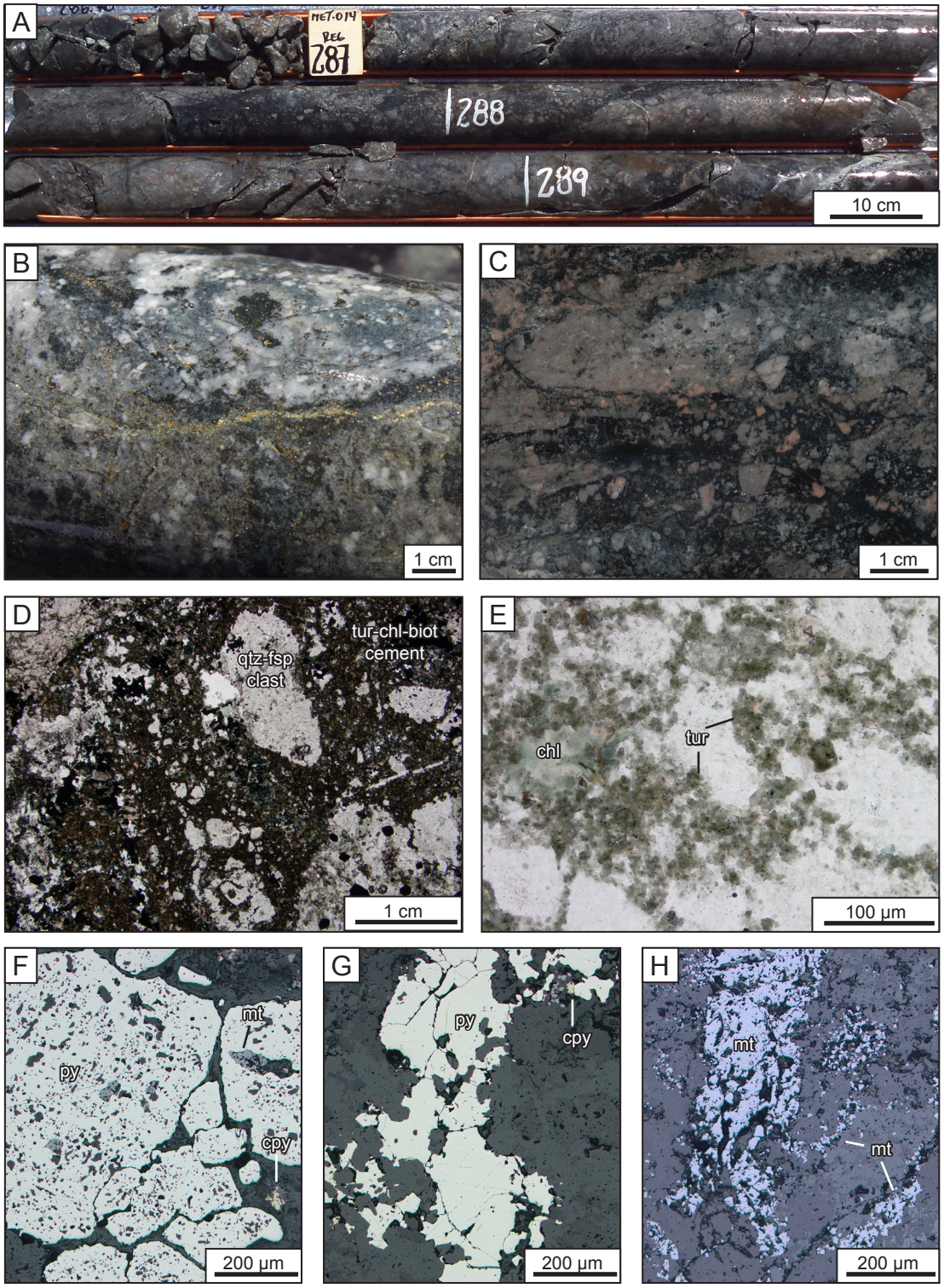

Figure 4.17 Representative photos of breccia facies 3B-5. A) Photo of drill core showing example of intense, cement-supported, chaotic breccia domain (MET 014, 286.70-289.45 m). B) Drill core photo showing feldspar-phyric clast (MET014 274.30 m). C) Half-core photo showing tourmaline - biotite-rich, cement-supported and matrix-rich breccia with intense, texturally destructive K-feldspar alteration of clasts (PR14AE153, MET014 287.80 m). D) Transmitted light photomicrograph showing tourmaline - biotite-rich cement and poorly-sorted lithic matrix (PR14AE151, MET014 248 m). E) Transmitted light photomicrograph showing cement aggregate of fine (approximately 10 µm), equigranular, equant tourmaline grains (PR14AE153). F) Reflected light photomicrograph showing large pyrite grain with abundant inclusions of silicate minerals and minor magnetite (PR14AE151). G) Reflected light photomicrograph showing pyrite vein (PR14AE151). H) Reflected light photomicrograph showing late magnetite vein and fine grained disseminated magnetite occurring with breccia cement (PR14AE151). chl = chlorite, cpy = chalcopyrite, fsp = feldspar, mt = magnetite, qtz = quartz, tur = tourmaline.

crystals in plane-polarised light (Figure 4.16 E). SEM analyses have confirmed that biotite has been partially to totally altered to chlorite and rutile (Figure 4.16 F and G). Chlorite is pale green, and locally anomalous blue in crossed-polarised light (Figure 4.16 E). Tourmaline cement is less abundant in 3B-4 facies than breccias from the northern study section. Tourmaline typically occurs as equant, euhedral grains between 20–100 μm, commonly as aggregates, and also exhibits colour zoning from shades of brown to blue. Rutile is commonly intergrown with chlorite, where it occurs in clusters of 10–30 μm grains. Chalcopyrite is more abundant than pyrite and occurs as anhedral, angular grains, commonly interstitial to biotite and chlorite. The range of chalcopyrite grain sizes is large, typically 5–200 μm, with abundant smaller grains. Large equant grains of pyrite, typically 80–250 μm, occur in the breccia cement with smaller grains (5–10 μm) sparsely disseminated throughout the clasts. Molybdenite is associated with tourmaline in breccia cement and occurs as blades and laths with prominent basal cleavage.

Facies 3B-5: Tourmaline - biotite - pyrite - chalcopyrite-cemented breccia

The 3B-5 breccia facies is located on the eastern margin of the 3B-4 and 3B-3 breccia facies (Figure 4.5) and was observed in drill core from the southern section. Distribution of the 3B-5 facies was interpreted from WLSQ-QXRD data. Only two samples were collected from the 3B-5 breccia facies in the current study. Facies 3B-5 is a cement-rich breccia associated with intense, pervasive albite and K-feldspar alteration, which locally obscured protolith textures.

Facies 3B-5 is typified by massive, clast supported and locally cement supported, jigsaw–chaotic, poorly–well sorted tourmaline, biotite, pyrite, chalcopyrite-cemented, polymict lithic breccias (Table 4.4, Figure 4.17 A). The 3B-5 breccias contain 80–90 % lithic clasts, 0–7 % lithic matrix and 10–30 % massive cement. Compared to the other stage 3 breccia facies, 3B-5 appears to be more chaotic and cement-rich. Clasts are predominantly sub-angular and range from granule to cobble size, generally finer and more rounded where cement is most abundant. Clast types include lapilli tuff and feldspar-phyric coherent felsic rocks (Figure 4.17 B). Where brecciation is more intense, the abundance of cement and angular, coarse sand-sized matrix is higher (Figure 4.17 C and D). The matrix is composed of lithic fragments. The breccia cement is dominated by tourmaline, which occurs predominantly as aggregates of fine (approximately 10 μm), equigranular equant grains (Figure 4.17 E). Biotite occurs with tourmaline, but is largely retrogressed to chlorite. Pyrite occurs as both large round, inclusion rich disseminated grains and in syn-breccia veins (Figure 4.17 F and G). Magnetite was observed in one of the two samples as cross cutting veins and cement replacements, these observations suggest magnetite is an overprint — most likely introduced as part of the 3B-3 facies.

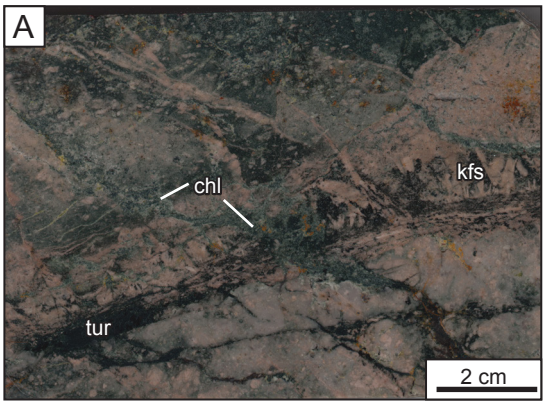

Figure 4.18 Half-core photo showing sub-stage 4A chlorite vein cross cutting tourmaline-K-feldspar veins and K-feldspar alteration of rhyodacite lapilli tuff (PR14AE048, MET007 441.33 m). chl = chlorite, kfs = K-feldspar, tur = tourmaline

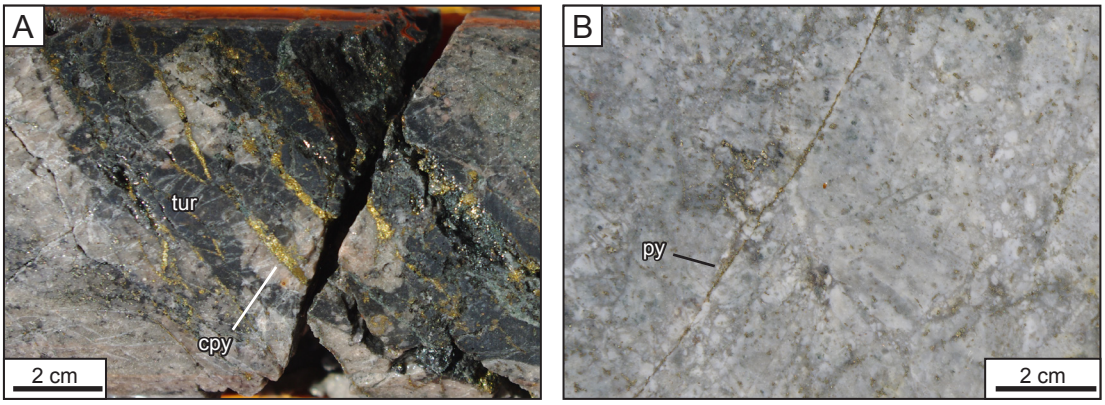

Figure 4.19 Representative photos of sub-stage 4B. A) Core photo showing late chalcopyrite veins cross cutting stage 3 tourmaline-cemented breccia (MET015 257 m). B) Half-core photo showing pyrite veinlet, with a narrow bleached selvage, cross cutting stage 1 breccia (PR14AE188, MET018 285.20 m).

4.4.4.3 Stage 4: Post-breccia veins and alteration

Sub-stage 4A: Chlorite veins

Chlorite occurs ubiquitously throughout the host volcanic sequence as pervasive alteration. In the stage 3 breccia facies, chlorite also occurs as cement and in syn-breccia veins with tourmaline and sulphides. These occurrences within the stage 3 breccias are inferred to be largely a product of retrograde stage 4 chlorite alteration of stage 3 biotite. Late chlorite veins attributed to stage 4 cross-cut stage 3 breccias and veins (Figure 4.18), and the volcanic stratigraphy on section 6,822,215 mN and 6,820,850 mN.

Sub-stage 4B: Chalcopyrite and pyrite veinlets

Thin veinlets of sub-stage 4B chalcopyrite and pyrite, occurring both together and separately, were observed in drill core from both section 8,622,215 mN and 6,820,850 mN. Veinlets cross cut all earlier breccias, veins and alteration assemblages. Sub-stage 4B veinlets are typically planar, <1-3 mm thick,

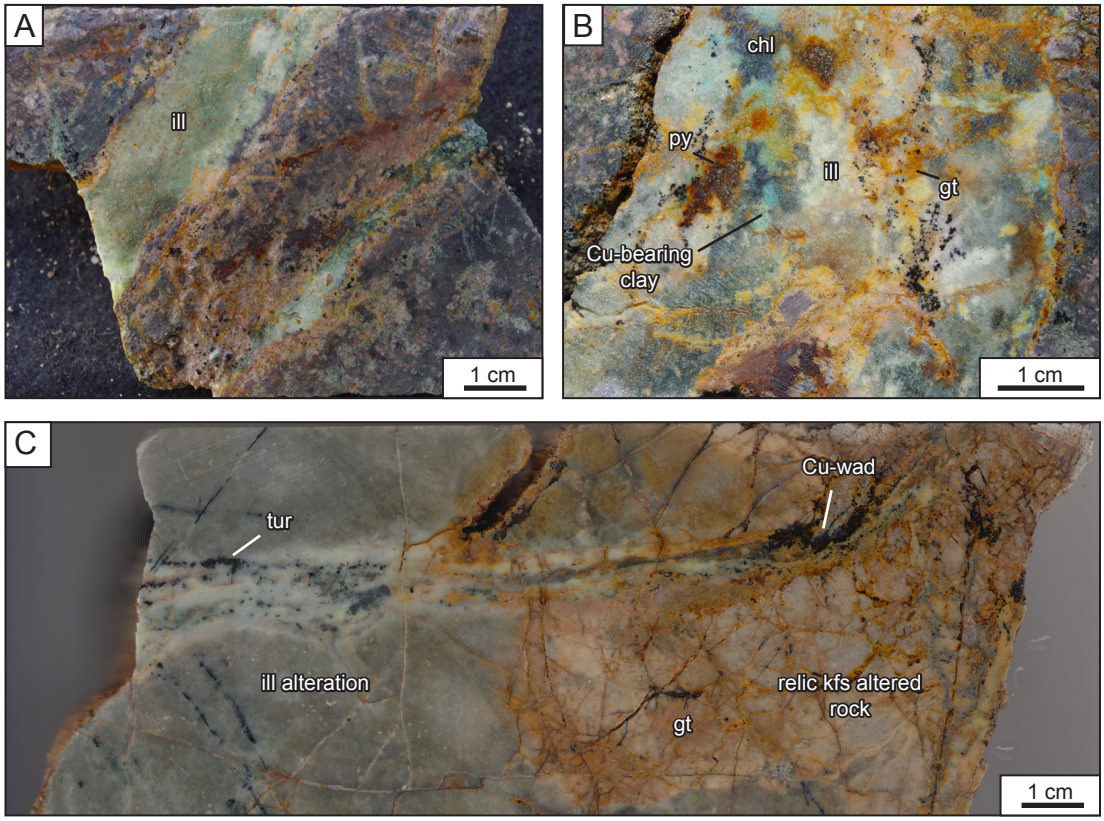

Figure 4.20 Representative photos of sub-stage 4C. A) Core photo of pale green illite vein cross cutting rhyodacite lapilli tuff, confirmed by SWIR analysis (PR14AE010, MET007 432.30 m). B) Core photo showing weathered illite-chlorite-Cu-bearing clay-pyrite-goethite vein (PR14AE053, MET007 400.73 m). C) Core photo showing pervasive illite alteration of K-feldspar altered rock with goethite after pyrite (PR14AE156, MET014 112.15 m). chl = chlorite, gt = goethite, kfs = K-feldspar, illite = illite, py = pyrite, tur = tourmaline.

and occur both sparsely and in sheeted arrays (Figure 4.19 A). Pyrite veinlets commonly have bleached muscovite selvages from 1–10 mm (Figure 4.19 B).

Sub-stage 4C: Illite veins and alteration

Massive illite veins were observed cross cutting all earlier alteration stages in drill core from both 6,822,215 mN and 6,820,850 mN. Veins of green, massive illite ± pyrite range from 5 mm to 5 cm wide. Illite mineralogy was confirmed by SWIR (Figure 4.20 A; Appendix C1). Where intersected in drill core, illite veins are either monomineralic or complex mixtures of illite with chlorite, pyrite. Weathering has produced low temperature Cu-bearing clays and goethite. Pyrite occurs in clusters of grains, clusters are 0.5–2 cm (Figure 4.20 B). Illite also commonly occurs in the centre of tourmaline - K-feldspar veins, replacing chlorite after biotite and sub-stage 4A chlorite. Pervasive illite alteration was also observed in the shallower portions of section 6,820,850 mN (< 100 m depth; Figure 4.20 C).

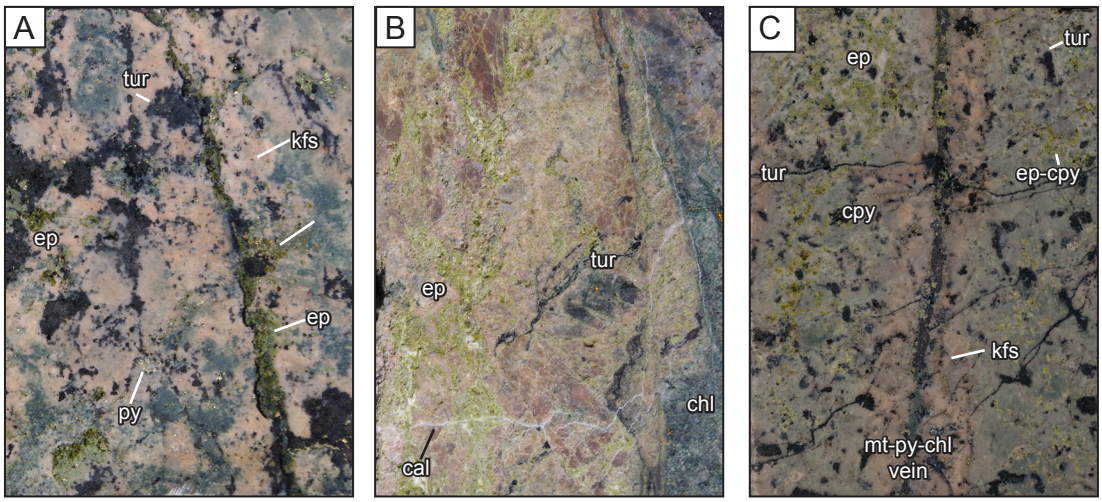

Figure 4.21 Representative photos of sub-stage 4D epidote alteration and veins. A) Half-core photo showing epidote vein cross cutting stage 3C-1 tourmaline-K-feldspar-chalcopyrite clots (PR14AE060, MET007 188.25 m). B) Half-core photo showing epidote-cemented breccia with cross cutting calcite veinlets (PR14AE100, PRP0064D 343.50 m). C) Half-core photo showing patchy epidote alteration over magnetite-tourmaline-K-feldspar veins (PR14AE038, MET007 162.20 m).

Sub-stage 4D: Epidote

Late stage epidote was commonly observed in drill core from the west of section 6,822,215 mN, where it occurs in narrow veinlets (<2 mm), veins (2-4 mm), stockworks, disseminated grains and feldspar-phenocryst replacements (Figure 4.21). Disseminated occurrences are commonly associated with disseminated chalcopyrite. Sub-stage 4D epidote veins typically contain a combination of chlorite, chalcopyrite pyrite and/or magnetite. Epidote was most commonly observed overprinting facies 3B-1 and 3B-2 breccias (Figure 4.21 A), and has locally altered the rhyodacite lapilli tuff. Epidote - K-feldspar ± chalcopyrite alteration has locally overprinted late dacite dykes. This could be sub-stage 4D epidote or a later event.

4.4.4.4 Stage 5: Calcite veins and breccias

Stage 5 veins and breccias with calcite infill were observed in drill core (PRP0064D and PRP0066D) from the northeast of the deposit, between 6,822,040 and 6,822,150 mN. Stage 5 calcite veins range from hairline veinlets to massive breccia veins that cross cut earlier assemblages, including sub-stage 4D epidote veins and stockworks (Figure 4.21 B). Hairline veins are ubiquitous across the deposit (Figure 4.22). Distinctive stage 5 comb-textured veins and calcite cemented breccias were only observed peripheral to the mineralised breccia complex at depths >150 m below surface. Further constraints on the distribution of stage 5 comb-textured veins and calcite breccias could not be made due to the limited core availability. These distinctive stage 5 veins are dominated by calcite with sparse chalcopyrite and/or pyrite. Veins (>5-10 mm) consist of comb textured calcite (Figure 4.23 A) with chalcopyrite in the centre. The (10–40 mm wide) calcite-cemented breccia veins were observed with open space vugs cross

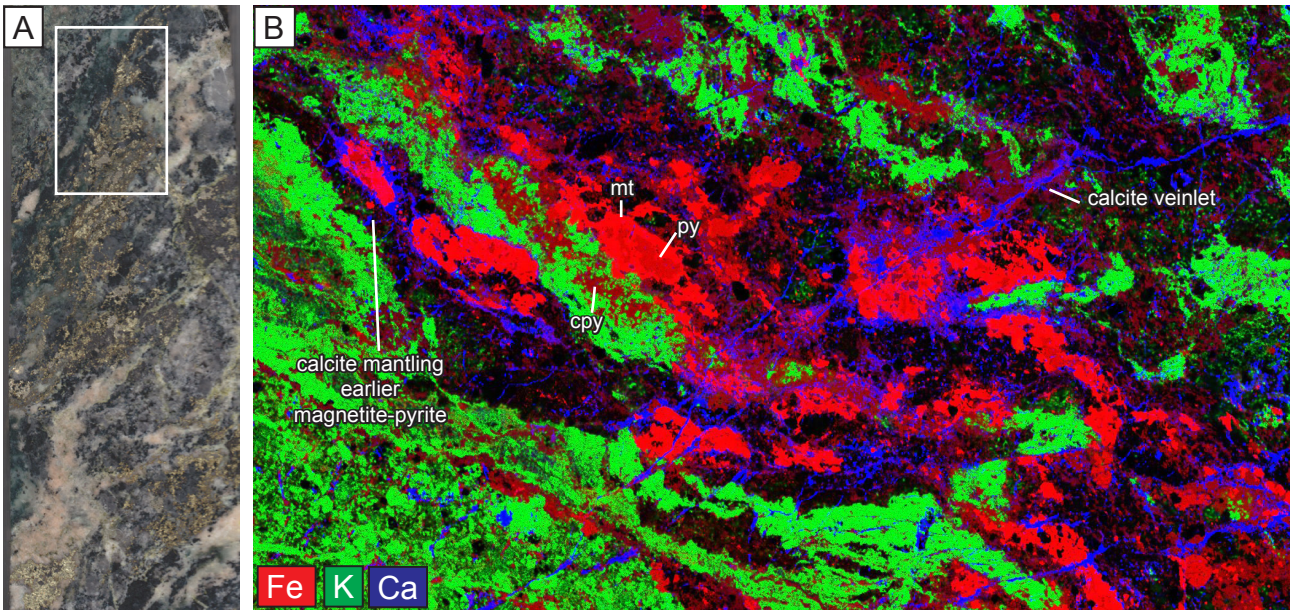

Figure 4.22 Example of stage 5 calcite veinlets. A) Photograph of sample showing location of detailed element map in (B). B) Micro XRF element map of sample PR14AE098 (PRP0064D 265.9 m) showing Fe (red), K (green) and Ca (blue). Ca indicates calcite veins, which can be seen to cross cut and overprint earlier features. Reds domains indicate magnetite, pyrite, chalcopyrite and tourmaline in order of decreasing intensity. Green areas indicate K-feldspar. cpy = chalcopyrite, mt = magnetite, py = pyrite.

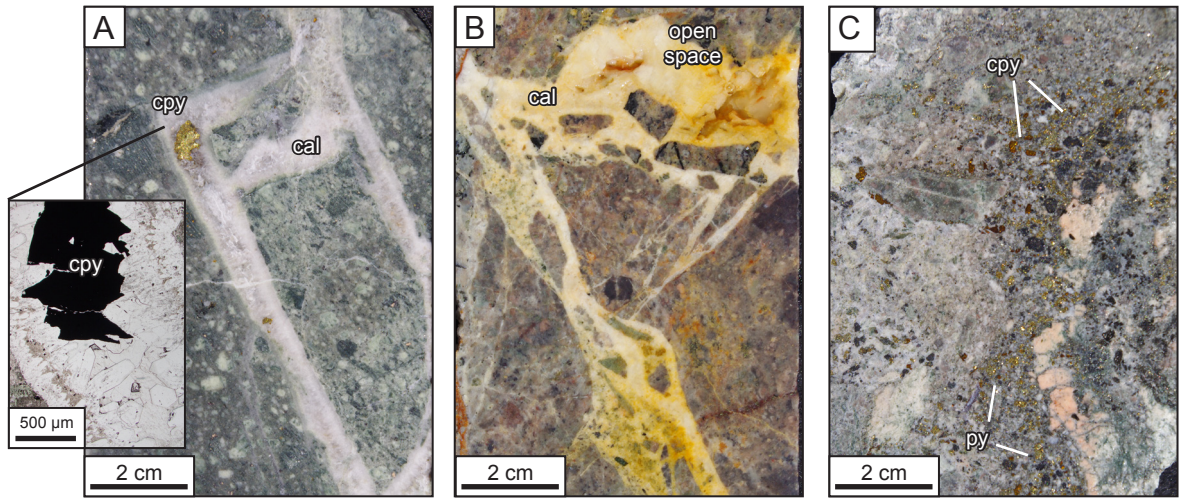

Figure 4.23 Representative core photos of stage 5. A) Half-core photo showing late calcite-chalcopyrite vein with comb-texture in dacite-porphyry. *Insert:* Transmitted light photomicrograph showing two generations of calcite with comb texture growing in from vein margins with chalcopyrite in the centre (PR14AE117, PRP0066D 206.88 m). B) Half-core photo showing calcite-cemented breccia vein in rhyodacite lapilli tuff (PR14AE099, PRP0064D 2335.06 m). C) Half-core photo of calcite-cemented, sulphide breccia. Chalcopyrite and pyrite clasts are stratified in a sulphide rich layer (PR14AE097, PRP0064D 265.90 m). cal = calcite, cpy = chalcopyrite, py = pyrite.

cutting rhyodacite lapilli tuff (Figure 4.23 B). A narrow calcite-cemented breccia zone, 20 cm wide, was also observed (Figure 4.23 C). The breccia zone consists of abundant chalcopyrite and pyrite clasts which appear stratified in a subhorizontal layer.

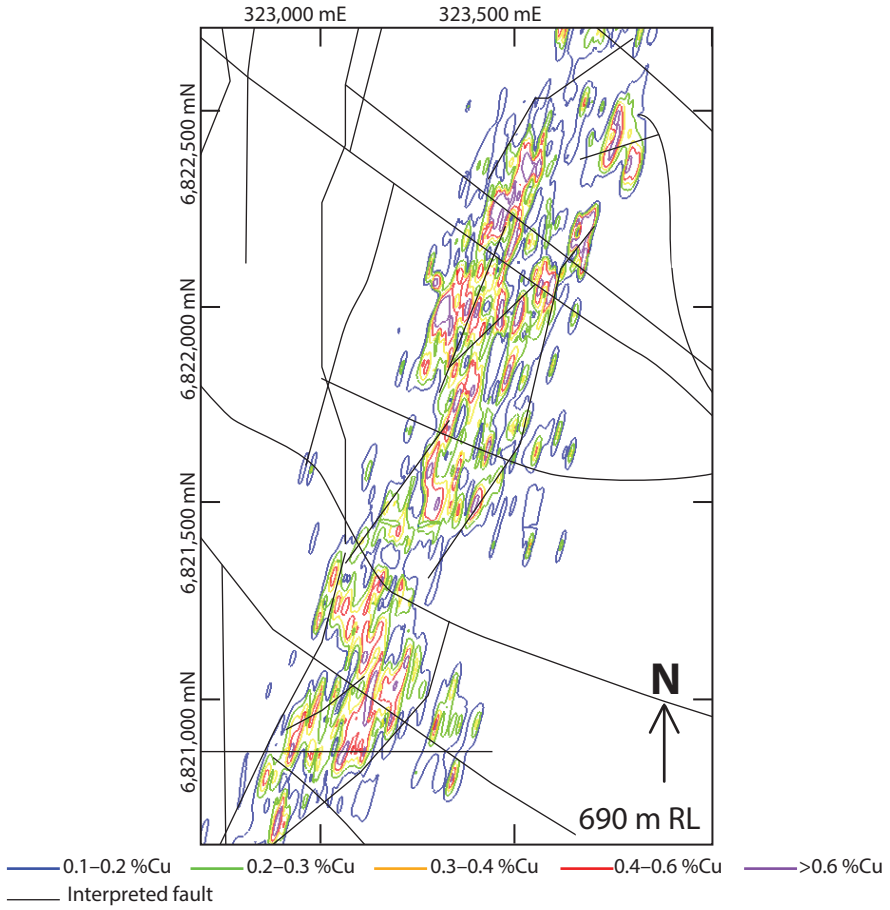

Figure 4.24 Plan slice at 690 m RL showing grade shells and fault interpretation. Mineralisation is situated in a northeast oriented structural corridor of intersecting northeast and northwest faults. Mineralisation is offset by northwest oriented faults. Cu grade shells modelled in 3D from Hot Chili Ltd whole rock assay database using Leapfrog Geo 3.1.0 (spheroidal interpolant; global trend with dip 75, dip azimuth 285, pitch 0; ellipsoid ratios maximum 3, intermediate 3, minimum 0; adaptive resolution 20). Note Leapfrog model is not representative of Hot Chili Ltd resource wireframes. Fault interpretation from J. Beeson pers. comm. (2015).

4.4.5 Structural controls on brecciation

The influence of local structure on hydrothermal alteration and mineralised zones at Productora has been discussed by previous workers (Fox, 2000; Ray and Dick, 2002; Beeson et al., 2012). Fox (2000) highlighted the general north-strike orientation of mineralisation and the typically northwest strike of mineralised veins. Abrupt changes in alteration mineralogy and intensity of Cu mineralisation are attributed to post-mineralisation movement on northwest trending faults (Fox, 2000). These relationships are demonstrated well at the deposit scale when Cu grade shells are compared with major mapped faults (Figure 4.24). At the camp scale there is a clear association of mineralisation occurrences with major intersecting structures (e.g. Alice porphyry Cu-Au-Mo deposit; Figure 4.1). The Santa Innes, Productora, Remolina and Monsoratt sites of historic Cu-Au mining are all situated within a northeast striking structural corridor.

4.5 Alice porphyry

The Alice Cu-Au-Mo porphyry deposit was discovered in late 2014 by Hot Chili Ltd approximately 400 m to the west of the Productora deposit (Hot Chili Ltd, 2014). During this study the Alice porphyry Cu-Au-Mo deposit was observed in drill core from two holes, PXP0001D and PRP0874D, which intercept the mineralised granodiorite porphyry stock (section 3.5.2). A total of seven samples were collected from the available drill core. Brief descriptions of the Alice vein paragenesis and alteration, based predominantly on hand specimen observations and the unpublished work of previous authors (pers. comm. Beeson, 2015 and Sillitoe, 2015), are outlined in this section. Mineralisation is also described here briefly. More detailed deposit description and characterisation falls beyond the scope of the current study, which is focused on the neighbouring Productora Cu-Au-Mo breccia complex.

4.5.1 Vein paragenesis

Vein paragenesis at the Alice porphyry has been determined from observations of drill core from hole PXP0001D (Figure 4.25 and Figure 4.26). Early veins include granular quartz-K-feldspar veins (Figure 4.26 D) and quartz - pyrite ± chalcopyrite veins which lack internal symmetry (Figure 4.26 A). Early anhydrite veins are also observed locally. Planar quartz veins with central seams and variable pyrite, chalcopyrite and molybdenite cross cut earlier veins (Figure 4.26 B, C and D). Late veins include pyrite veins and anhydrite veins (Figure 4.26 E and F). Dark chlorite veins overprint earlier veins but are themselves locally overprinted by anhydrite (Figure 4.26 F). Epidote ± chlorite and calcite veins overprint all other vein types (Figure 4.26 G). Main stage quartz veins, with central pyrite ± chalcopyrite ± molybdenite seam, are typically offset by chlorite filled fractures, which typically have a bleached muscovite-rich selvage (<2 mm width; Figure 4.26 B). Dark chlorite veins locally transition to breccia veins up to 30 cm wide (Figure 4.26 F). Late anhydrite veins locally exploit existing fractures (earlier veins) and overprint chlorite veins and breccias (Figure 4.26 F), and pyrite veins.

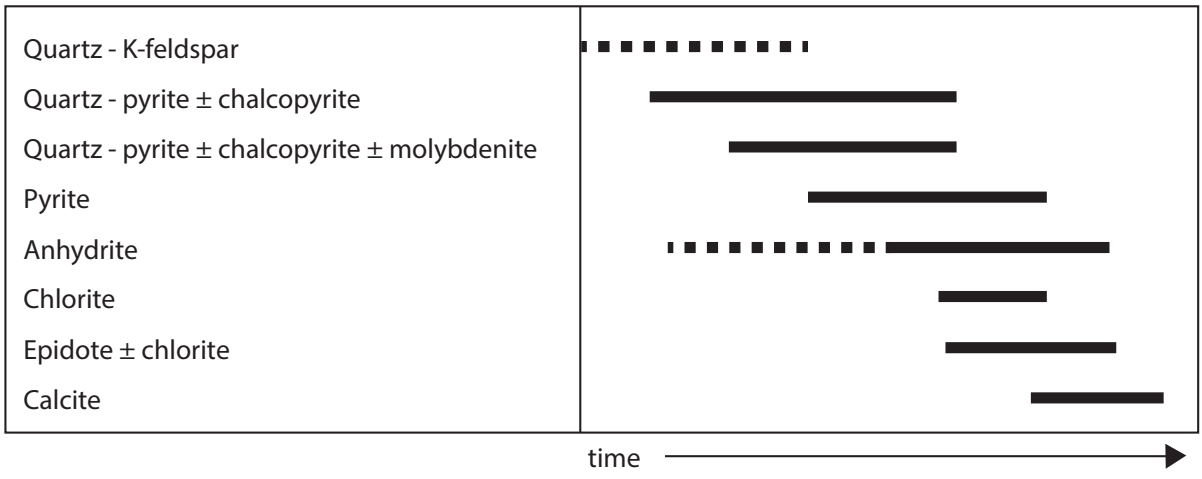

Figure 4.25 Paragenesis for veins observed at Alice based on hand specimen observations.

Table 4.5 Descriptions of major vein types identified at Alice. Veins are listed in order of earliest to latest based on majority of observations, some mutual cross cutting relationships were also observed.

Vein	Width	Selvage	Morphology	Dip[1]	Dip-direction[1]
Qtz±Kfs	<1–3 mm	± Kfs (<10 mm)	Discontinuous, wispy, irregular; locally define stockwork	70–95	280
Qtz-py±cpy	<3 mm		Massive, irregular	-	-
Qtz-py ± cpy ± mo	10–20 mm	± ms (1 mm)	Symmetrical with central seam; multiple generations; planar; typically sheeted	80–90	270
Py ± qtz	<1–3 mm	± ms (<5 mm)	Massive	60–80	340
Chl ± py	1–5 mm	± Kfs ± ms (<1 mm)	Anastomosing, laminated; stockwork to breccia	95	290
Anh ± cal	1–5 mm		Massive, irregular–anastomosing, stepped, variable width	Irregular	Irregular
Cal	<1–3 mm	None	Planar, massive	-	-

[1]pers. comm. Beeson (2015)
anh = anhydrite, cal = caclite, chl = chlorite, cpy = chalcopyrite, Kfs = K-feldspar, mo = molybdenite, py = pyrite, qtz = quartz.

4.5.2 Alteration

Potassic alteration is associated with the early quartz - pyrite ± chalcopyrite veins and main stage quartz - pyrite ± chacopyrite ± molybdenite veins. Potassic alteration is manifested as biotite ± actinolite replacement of hornblende (Figure 4.28 and Figure 4.27). Quartz - actinolite - chlorite - magnetite alteration has locally overprinted potassic alteration (Sillitoe, 2015). The margins and deeper parts of the porphyry stock were overprinted by albite ± epidote ± sericite alteration which also caused destruction of biotite and chalcopyrite (Sillitoe, 2015). This is evidenced by elevated Na and depleted Cu (<0.1 % Cu) in assay intervals. Late stage chlorite-sericite alteration is ubiquitous, causing replacement of biotite by chlorite (Figure 4.27) and sericite alteration of plagioclase.

4.5.3 Mineralization

The Alice porphyry deposit has a total high grade resource of 17.9 Mt at 0.41 % Cu, 0.04 g/t Au and 39 ppm Mo (Hot Chili Ltd, 2016). Mineralisation primarily occurs as fine grained, disseminated chalcopyrite and pyrite, plus sulphide stringers and quartz-sulphide veins (Table 4.5), associated with potassic alteration. Molybdenite was only observed in quartz veins, both early massive and main stage symmetrical varieties. Quartz - actinolite - chlorite - magnetite alteration is associated with higher grade mineralisation, whereas late albite ± epidote ± sericite alteration is grade-destructive (Sillitoe, 2015). The highest Cu grades occur in the centre of the porphyry stock (approximately 0.5 % Cu) and decrease outwards to approximately 0.1 % Cu on the margins (Figure 4.28). Significant intercepts include 151 m @ 0.4 % Cu, 48 ppm Mo (including 54 m @ 0.5 % Cu, 0.1 g/t Au, 60 ppm Mo; Hot Chili Ltd, 2015).

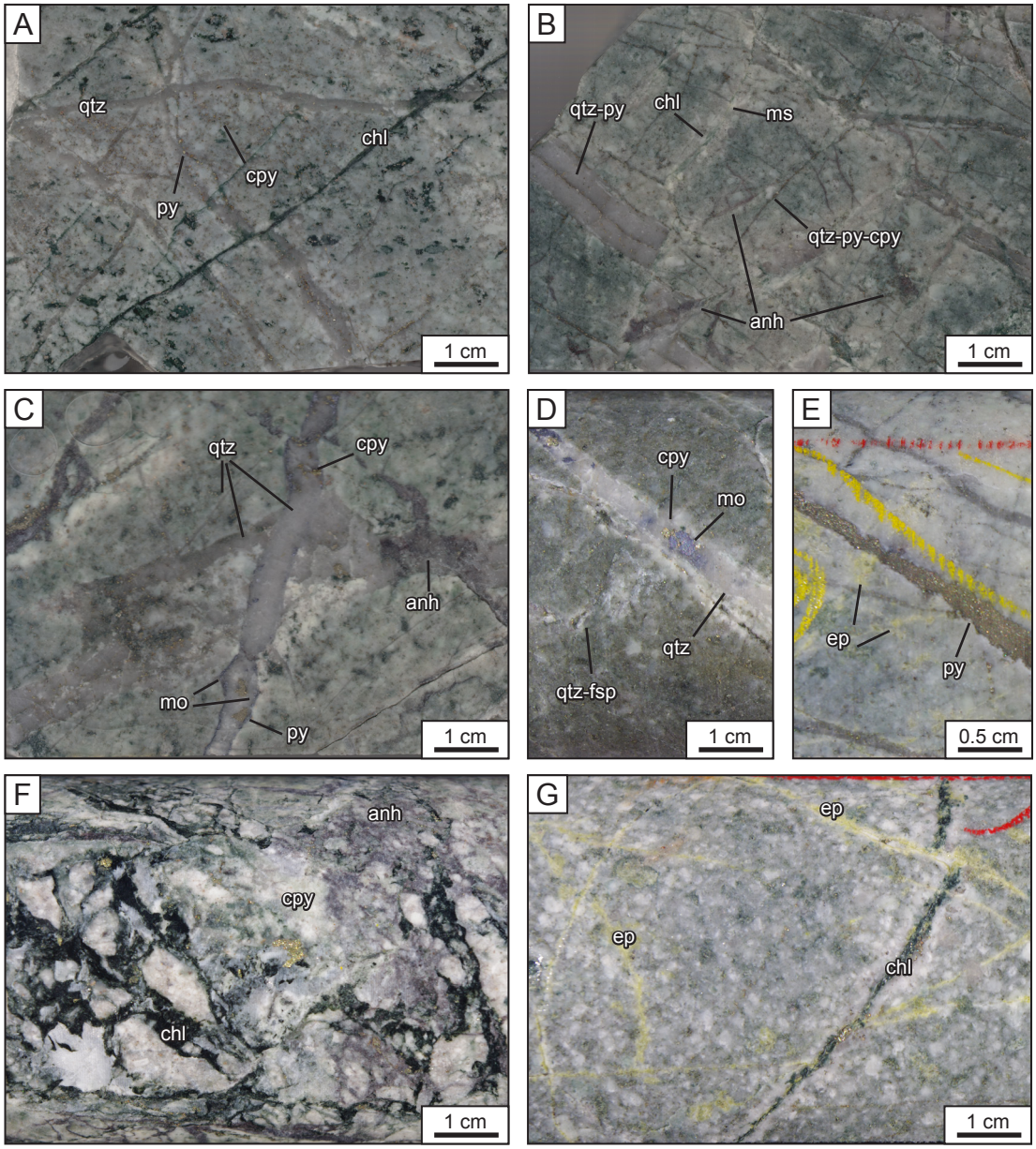

Figure 4.26 Representative photos of core specimens of major Alice Cu-Mo porphyry vein paragenetic relationships. A) Irregular, discontinuous early quartz - pyrite - chalcopyrite veins cross cut by later chlorite veins (PR14AE214, PXP0001D 195.7 m). B) Quartz veins with pyrite seam cross cuts earlier quartz - pyrite - chalcopyrite veinlets and is itself cross cut by anhydrite. Both are cross cut and displaced by chlorite-cemented fractures with muscovite selvages (PR14AE212, PXP0001D 175.8m). C) Quartz vein with central pyrite-chalcopyrite seam cross cut by massive quartz vein with molybdenite margins and grains of pyrite and chalcopyrite. Cross cut by irregular anhydrite vein (PR14AE213, PXP0001D 185.45m). D) Massive quartz - molybdenite - chalcopyrite vein cross cutting early quartz - K-feldspar vein and disseminated chalcopyrite (PXP0001D 154m). E) Massive pyrite vein cross cutting earlier quartz veinlets (PXP0001D 259m). F) Chlorite - chalcopyrite-cemented breccia with anhydrite overprint (PXP0001D 195m). G) Chlorite vein cross cut by epidote veinlets (PXP0001D 232m).

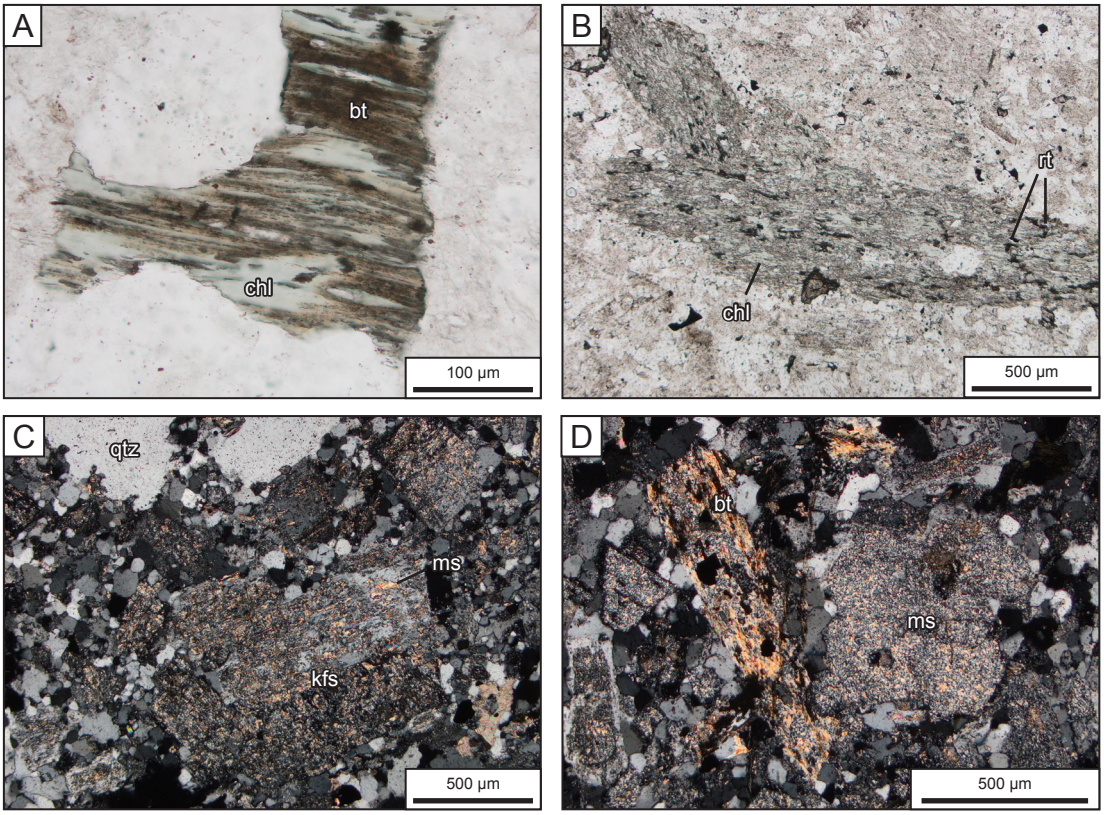

Figure 4.27 Representative photomicrographs of alteration minerals from Alice porphyry. A) Chlorite replacing biotite (PR14AE212). B) Hornblende now replaced by chlorite and rutile after biotite (PR14AE214). C) Muscovite alteration of K-feldspar phenocryst (PR14AE215). D) Pervasive muscovite alteration of feldspars and biotite after hornblende (PR14AE213). bt = biotite, chl = chlorite, kfs = K-feldspar, ms = muscovite, qtz = quartz, rt = rutile.

4.6 Silica Ridge lithocap

Lithocaps are defined as lithologically controlled zones of pervasive advanced argillic alteration with structurally controlled components, including their subvertical root zones (Sillitoe, 1995). Remnants of a lithocap crop out on a ridgeline (known as Silica Ridge) immediately above the Alice porphyry deposit (Figure 4.28). It forms resistant high points along a north striking ridgeline that extends over 6 km (Figure 4.29 A). The ridge is disjointed and offset by several faults in the south (Figure 4.1). The lithocap consists predominantly of massive, textureless quartz altered rocks (Figure 4.29 B and C). Locally there is evidence of chaotic, poorly sorted pebble to cobble-sized, quartz-cemented lithic breccias (Figure 4.29 B). Narrow breccia veins with botryoidal chalcedony cement and open space, and tourmaline-cemented breccias were also observed locally (Figure 4.29 C). Previous authors have also noted occurrences of the borosilicate dumortierite (Fox, 2000, Sillitoe, 2015). Directly beneath the lithocap, alunite is observed on the hillsides and road cuttings as well as in drill cuttings from holes adjacent to the lithocap. Pyrophyllite and dickite are observed down slope from the alunite and massive quartz, and in drill cuttings from >178 m depth. Similar massive, pervasive quartz alteration is observed 1.5 km to the east in drill pads excavated on the eastern flank of the Productora deposit. No associated alunite or pyropyllite were observed in the eastern outcrops.

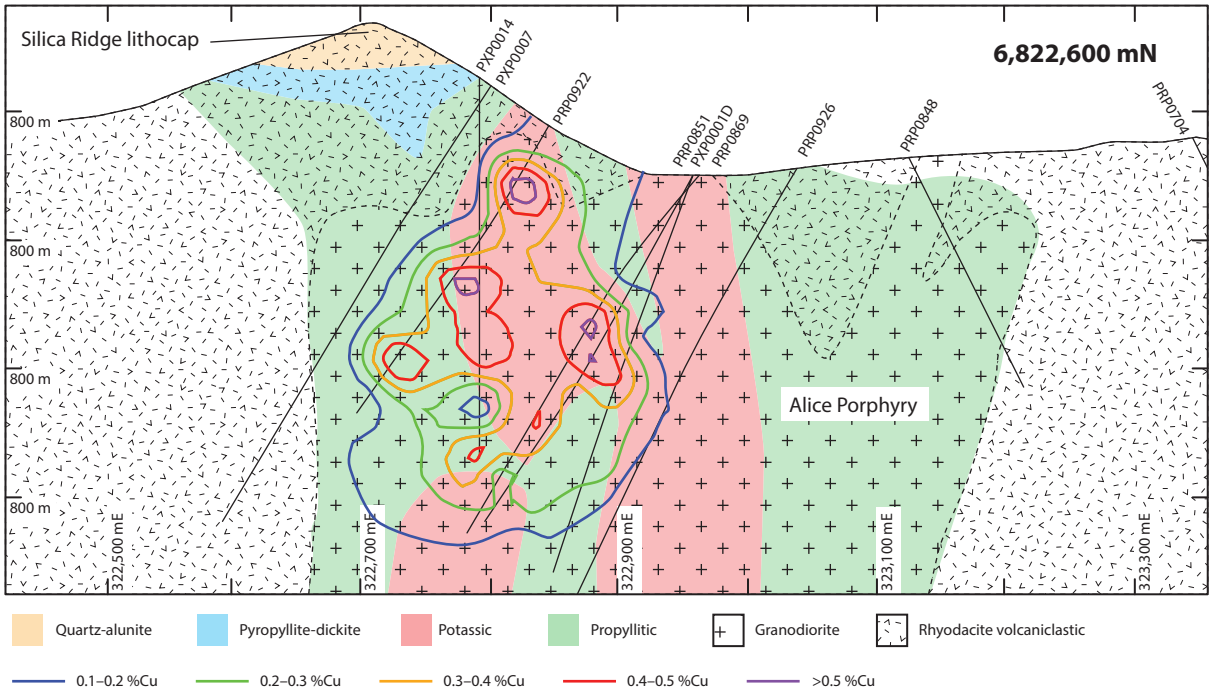

Figure 4.28 Cross section at 6,822,600 mN showing Alice porphyry granodiorite stock, alterations assemblages and Silica Ridge lithocap with Cu grade shells. Grade shells created from down hole assay database provided by Hot Chili Ltd using Leapfrog Geo 3.1.0 interpolant function with spheroidal model and adaptive resolution at 20. Mineralisation is associated with potassic alteration. Geology and alteration modified from Beeson (2015).

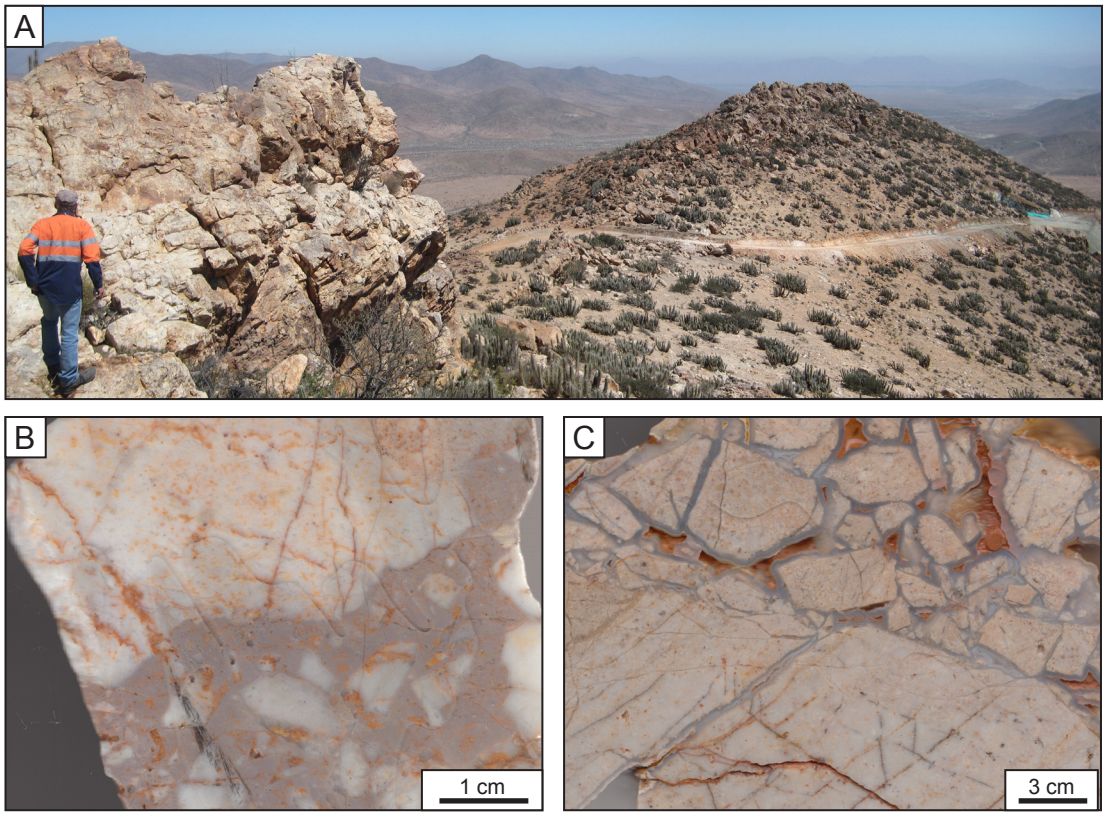

Figure 4.29 Photos from Silica Ridge lithocap. A) Photo looking north along the northern segment of the disjointed lithocap. B) Hand specimen photo of chaotic, quartz-cement-supported, lithic breccia (PR14AE194, 322744 mE 6,822,481 mN, 826 m). C) Hand specimen photo of botryoidal chalcedony-cemented, lithic breccia with open space fill (PR14AE193, 322,746 mE 6,822,481 mN, 825 m).

4.7 Supergene mineralisation

Depths of weathering, as recorded in the drill hole data base, are variable across the deposit but typically range between 80–100 m. Domains of deep weathering, 200–350 m depth and locally up to 535 m depth, occur in narrow domains throughout the deposit. These domains potentially represent the draw-down of meteoric waters along faults and fractures to cause weathering at depth (e.g. Chávez, 2000). Economic mineralisation at Productora is predominantly composed of Cu-sulphides (Hot Chili Ltd, 2014). In the north (> 6,821,735 mN) the oxide-transitional zone is mostly barren or low grade (<0.2% Cu) with discrete zones (10–45 m down hole intercepts) of higher Cu grade (>0.2% Cu, locally up to 1% Cu) and perched domains of sulphide-transitional material. To the south, two major domains of oxide mineralisation (0.2 – >1% Cu) occur; between 6,820,475 to 6,821,535 mN, and from 6,821,255 to 6,821,655 mN (Figure 4.30). More detailed modelling and characterisation of supergene mineralogy is provided in Chapter 6.

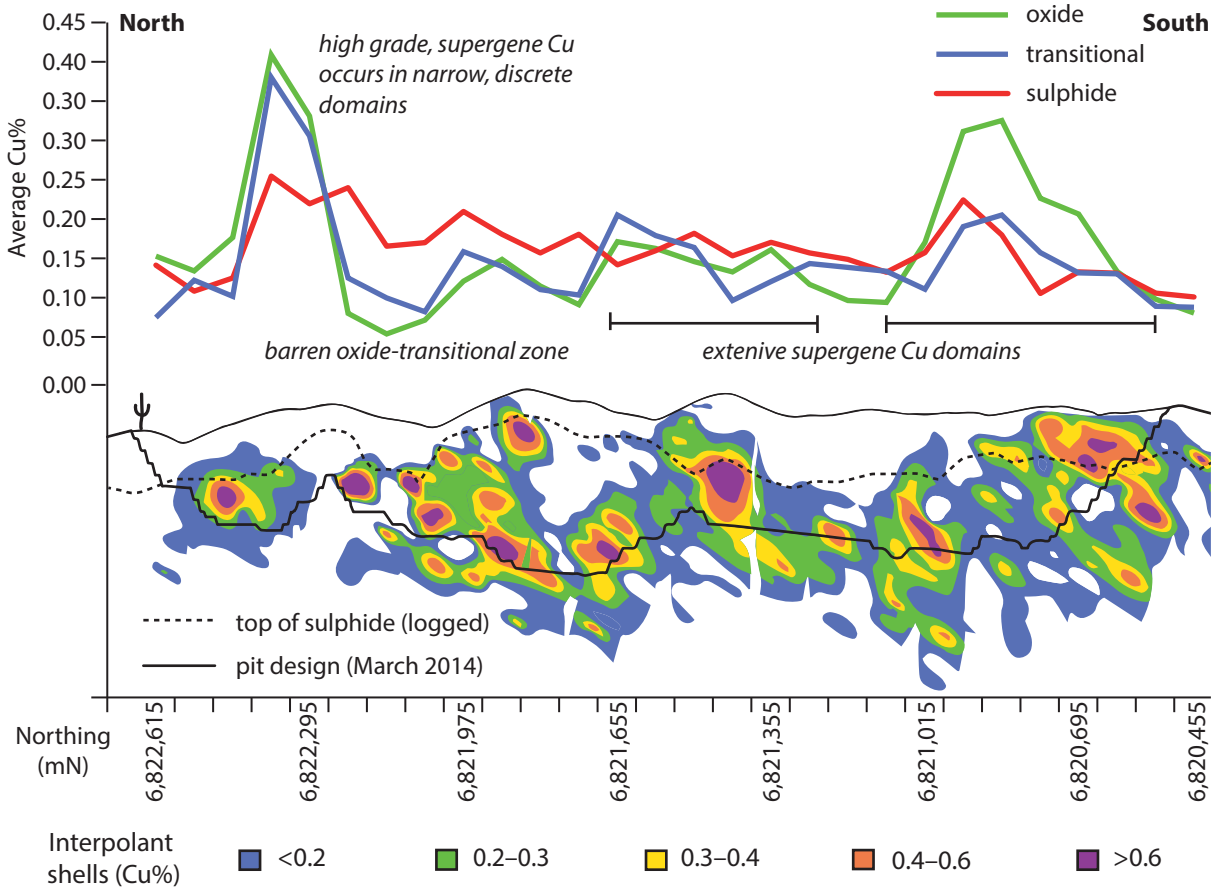

Figure 4.30 Plot showing average Cu grade (Cu%) of oxide, transitional and sulphide samples (as defined by Hot Chili Ltd logging) for each 80 m cross section and long section showing slice through Cu grade shells modelled in 3D from Hot Chili Ltd whole rock assay database using Leapfrog Geo 3.1.0 (spheroidal interpolant; global trend with dip 75, dip azimuth 285, pitch 0; ellipsoid ratios maximum 3, intermediate 3, minimum 0; adaptive resolution 20). Note leapfrog model is not representative of Hot Chili Ltd resource wireframes. Long section is scaled to the plot. Supergene mineralisation is indicated on long section where Cu grade shells extend above top of sulphide surface. These domains broadly correspond with areas of higher average Cu% in the oxide and transitional samples - note some mismatch occurs as a result of the long section being a slice only and the plot presenting the average of each cross section.

4.7.1 Supergene mineralogy

Fox (2000) described supergene mineralisation at Productora as consisting of chrysocolla and tenorite with minor pseudomalachite, chalcocite, digenite, covellite, and other unidentified blue and green copper oxides, carbonates, and silicates. Native gold grains, of undisclosed size, were also reported as occurring with tenorite in the historic Productora mine (Fox, 2000). Supergene uranium mineralisation was identified by CCHEN during an exploration campaign during the late 1980's (Beeson, 2012). They observed torbenite to be commonly intergrown with tenorite.

The drill core available for the current study was predominantly from the sulphide domain of the deposit and contained little supergene mineralisation. In order to better understand the supergene mineral assemblage, both on sections 6,822,215 mN and 6,820,850 mN and deposit-wide, logged mineralisation (from the drill hole database provided by Hot Chili Ltd) and QEMSCAN data (provided by Hot Chili Ltd) were reviewed.

4.7.2 Logged supergene minerals

A review of the logged mineralisation in the drill hole database provided by Hot Chili Ltd indicates that overall Cu-bearing oxide minerals have not been identified or recorded as frequently as sulphide minerals (Table 4.6). The most commonly recorded oxide minerals in the company database are Cu-bearing

Table 4.6 Summary of mineralisation codes logged in drill hole database provided by Hot Chili Ltd.

Mineralisation Code	Mineral	Count Min1	Count Min2	Range
Hypogene				
py	pyrite	18006	3047	0–40 %
mt	magnetite	2064	1005	0–80 %
cp	chalcopyrite	1989	10623	0–10 %
mo	molybdenite	23	175	0–2 %
Supergene				
lu	Cu-bearing limonite	441	97	0–4.5 %
co	chrysocolla	242	67	0–5 %
ne	neotocite	135	68	0–10 %
oc	copper oxide	91	24	0–5 %
hm	hematite	40	17	0–10 %
ccu	clay with Cu-oxide	33	18	0–4 %
cu	cuprite	23	12	0–2 %
cc	chalcocite	20	33	0–3 %
ma	malachite	12	6	0–10 %

CountMin1 indicated the number of occasions the mineral has been recorded as the primary mineral under mineralisation. Count Min2 indicates number of occasions the mineral was recorded as a secondary mineral. Range indicates the percentage range recorded in the data base by the logger for each mineral.

limonite, chrysocolla and neotocite. A generic term 'copper oxide' was also commonly used by loggers. Cuprite, chalcocite and malachite were recorded less commonly.

Chrysocolla and black Cu-wad were the most common Cu-oxide minerals reported during graphic core logging in the current study. As black Cu-wad is not a mineral option in the Hot Chili Ltd logging code it is assumed that the neoticite, and possibly Cu-bearing limonite are equivalent terms.

4.7.3 QEMSCAN data review

Observations from graphic core logging were supplemented by the results of a mineralogy characterisation study performed by ALS Metallurgy, Perth, Australia on behalf of Hot Chili Ltd. Eighteen contiguous composite crushed (10#, -2 mm) samples from the oxide zone were analysed using QEMSCAN (quantitative evaluation of minerals by scanning electron microscopy) to determine oxide mineralogy. Analysis was performed in field scan mode with 7.25 µm X-ray acquisition spacing, detailed method description is provided in Appendix C3. The QEMSCAN results indicate that the oxide mineralogy

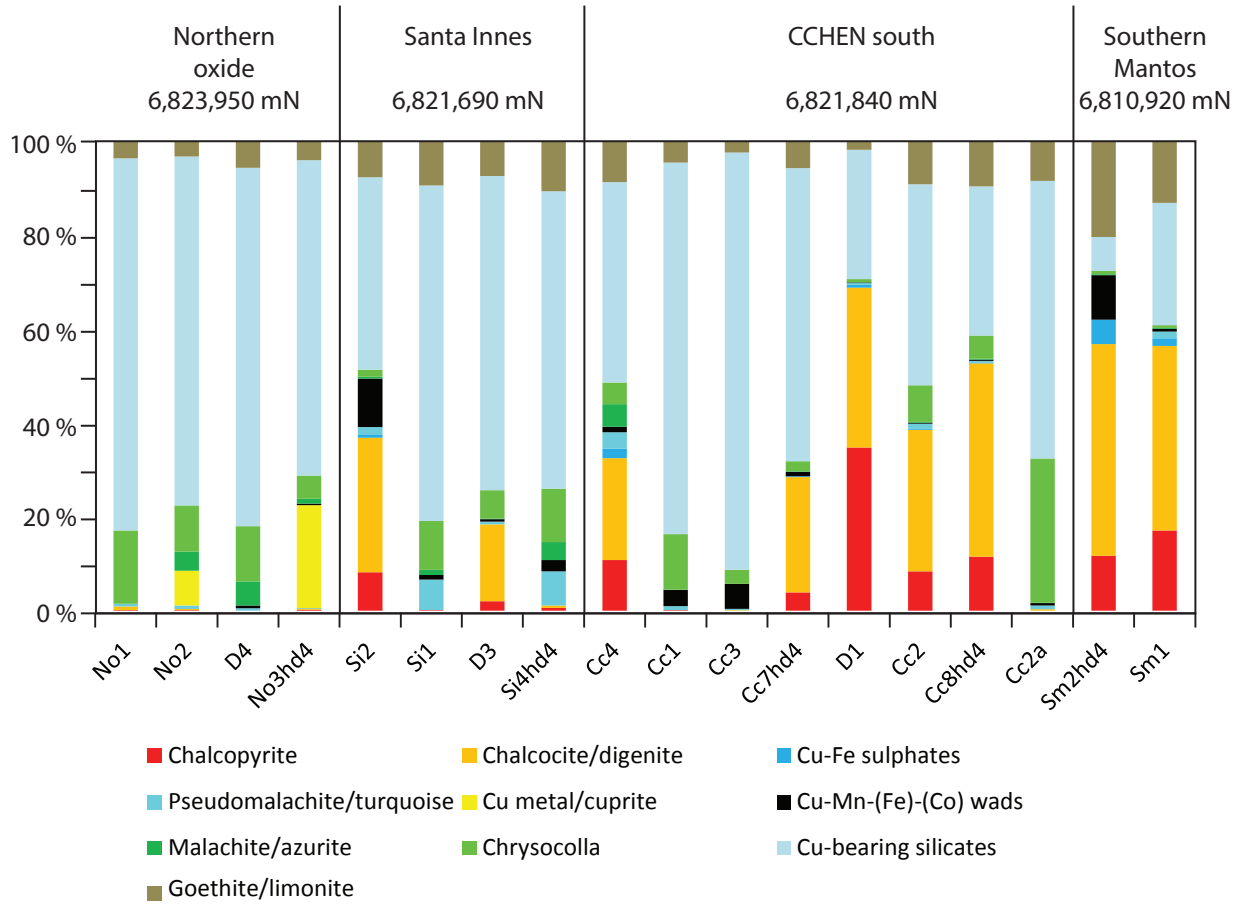

Figure 4.31 Results from QEMSCAN mineralogy study performed by ALS Metallurgy, Perth, Australia on behalf of Hot Chili Ltd. Results indicate that oxide-Cu mineralogy varies significantly from north to south and a large proportion of Cu occurs as Cu-bearing silicates. In the south, sulphides are much more abundant, particularly chalcocite. In the north, mineralogy is dominated by Cu-bearing silicates, chrysocolla and cuprite.

predominantly consists of Cu-bearing silicates, chalcocite, chrysocolla, limonite and malachite with variable cuprite/native-Cu, Cu-Mn-(Fe)-(Co)-wads and pseudomalachite/turquoise (Figure 4.31). Cu-bearing silicates are the most abundant Cu-bearing phases. It was reported that at the scan conditions used, it was not possible to determine whether the Cu-bearing silicates were a discrete Cu-silicate mineral (e.g. similar to chrysocolla), silicate mineral/s with structurally bound Cu, such as biotite, muscovite, chlorite and clays, or a fine intergrowth of Cu-silicates with other silicate minerals (ALS, 2015b). Limonite was reported to contain variable Cu (between 1 and 13 wt%). The QEMSCAN results indicate that the oxide mineralogy varies from north to south. In the north, mineralogy is dominated by Cu-bearing silicates, chrysocolla and cuprite. In the south, weathering appears to be less extensive and the proportion of the sulphide phases chalcopyrite and chalcocite is much higher. There is also a lower proportion of Cu-bearing silicates in the south.

4.8 Mineralisation

The current total resource at Productora and Alice is 236.6 Mt grading 0.48 % Cu, 0.10 g/t Au and 135 ppm Mo, of which 218.7 Mt at 0.48 % Cu, 0.10 g/t Au and 142 ppm Mo is from the Productora breccia complex (Hot Chili Ltd, 2016). For the purposes of this study, ore zones are discussed primarily in relation to spatial domains that each represent different paragenetic breccia facies of the Productora main stage mineralisation (stage 3) interpreted on sections 6,822,215 mN and 6,820,850 mN and described in section 4.4.4.2. Data from multiple drill hole intervals intersecting the spatial domains were compiled in Appendix C4. Three sulphide ore zones are discussed from the northern section representing mineralisation from facies 3B-1, facies 3B-2, and stage 2 overprinted by facies 3B-2 (Figure 4.32). Although stage 2 was not a mineralising event, significant mineralisation is associated with a domain where the stage 2 breccia is overprinted by facies 3B-2. This ore domain is known as the Habanero ore zone (Hot Chili Ltd, 2013). The ore zones from the southern section are discussed in relation to three domains that each represent stage 3 breccia facies; 3B-3, 3B-4 and 3B-5 (Figure 4.33). The oxide and sulphide metal content of the 3B-4 domain are also presented.

Elevated Cu, Au and Mo grades at the Productora deposit spatially and paragenetically coincide primarily with the stage 3 tourmaline -cemented breccia complex (Figure 4.32, Figure 4.33 and Figure 4.34). Discrete zones of high grade mineralisation have also been observed within the stage 2 breccia, also known as the Habanero ore zone (Figure 4.32). Mineralised intervals from within the 0.2 % Cu grade shell (as modelled using Leapfrog Geo) across the two sections were compiled in order to analyse metal content and associations for each of the major ore zones included in this study (intervals shown in Figure 4.32 and Figure 4.33).

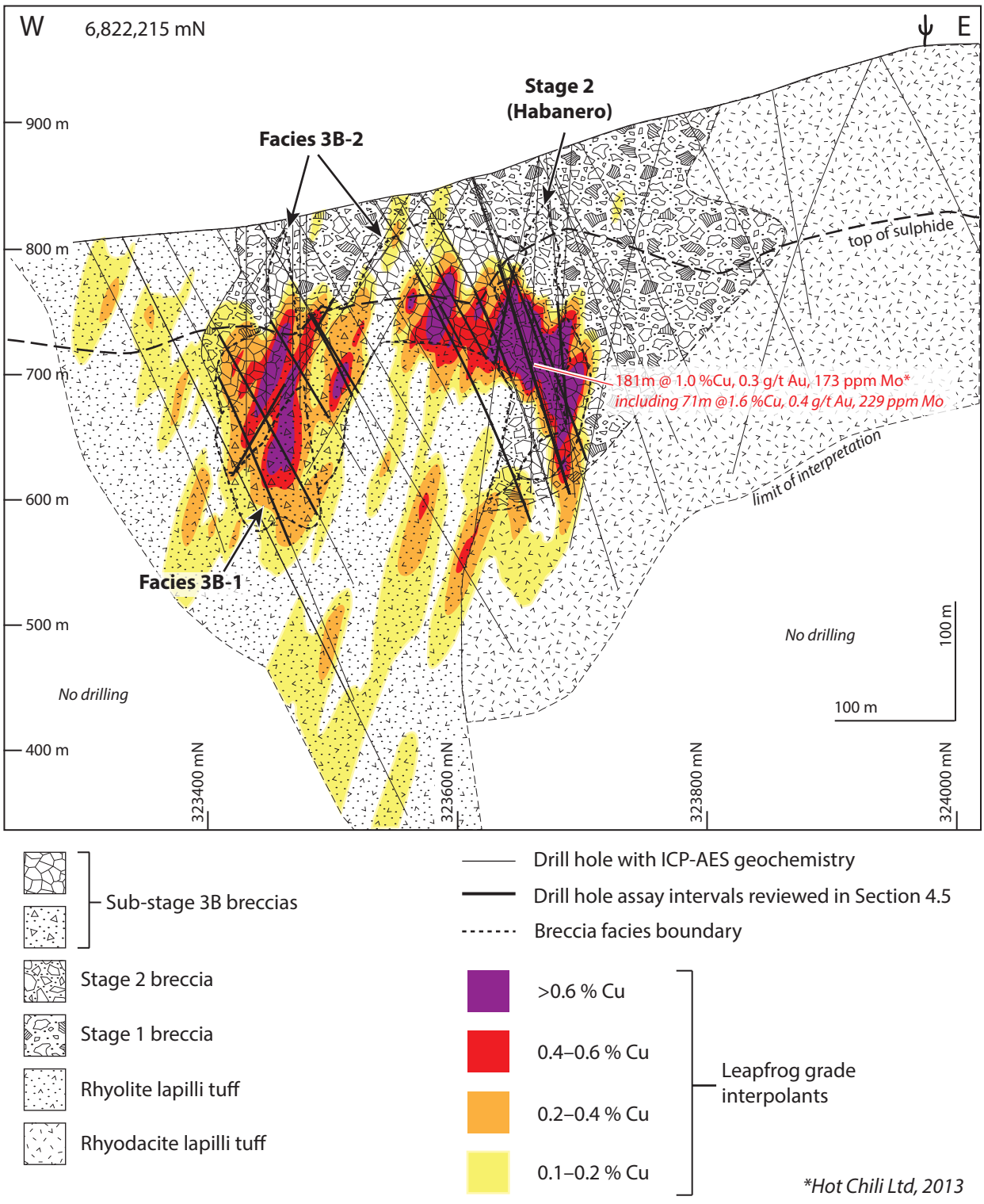

Figure 4.32 Cross section at 6,822,215 mN (+/- 40 m window) with Cu grade shells modelled in 3D from Hot Chili Ltd whole rock assay database using Leapfrog Geo 3.1.0 (spheroidal interpolant; global trend with dip 75°, dip azimuth 285°, pitch 0; ellipsoid ratios maximum 3, intermediate 3, minimum 0; adaptive resolution 20). Simplified geology and mineralised breccia facies also shown with drill holes from assay database and intervals used for metal comparison.

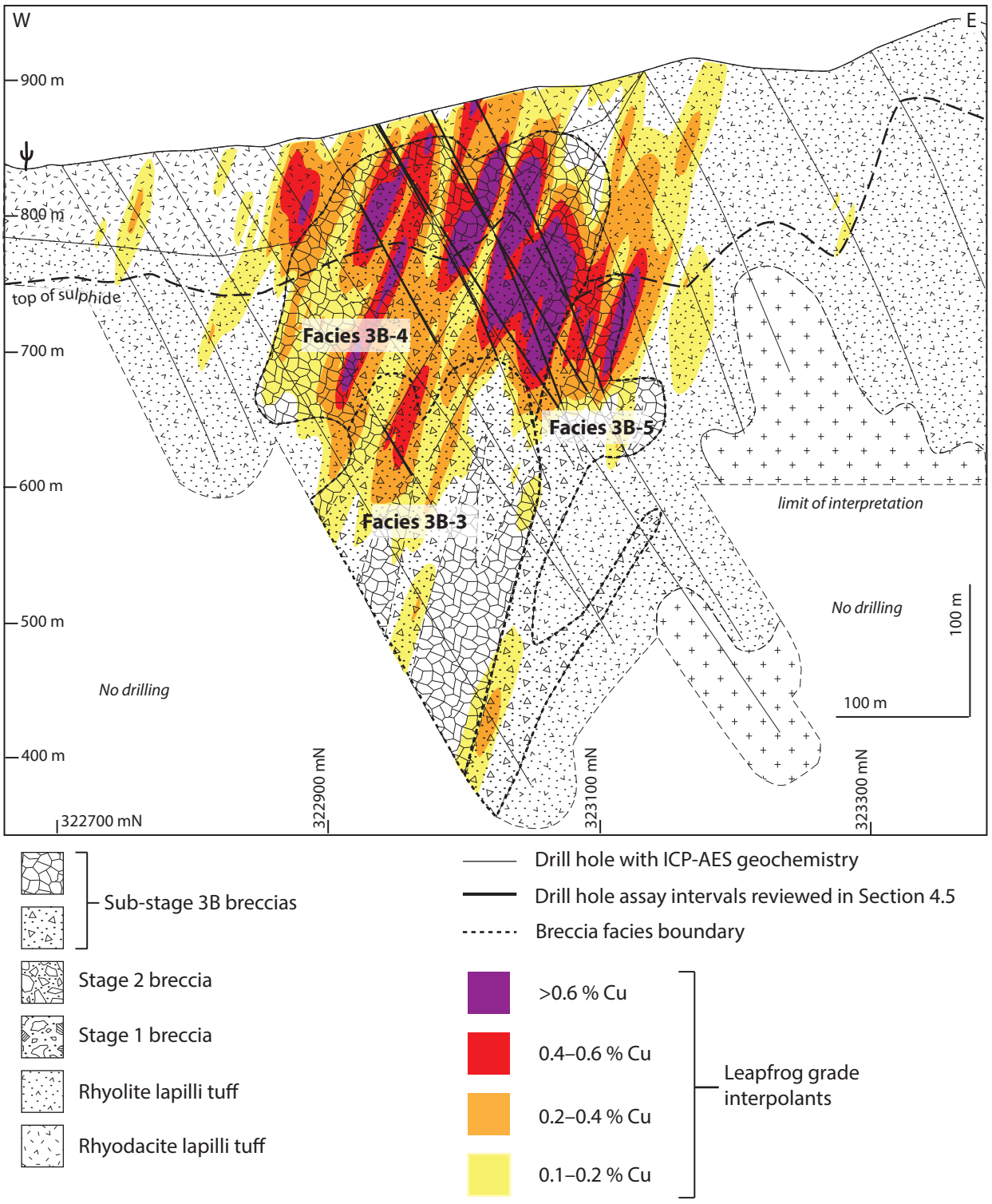

Figure 4.33 Cross section at 6,820,850 mN (+/- 40 m window) with Cu grade shells modelled in 3D from Hot Chili Ltd whole rock assay database using Leapfrog Geo 3.1.0 (spheroidal interpolant; global trend with dip 75, dip azimuth 285, pitch 0; ellipsoid ratios maximum 3, intermediate 3, minimum 0; adaptive resolution 20). Simplified geology and mineralised breccia facies also shown with drill holes from assay database and intervals used for metal comparison.

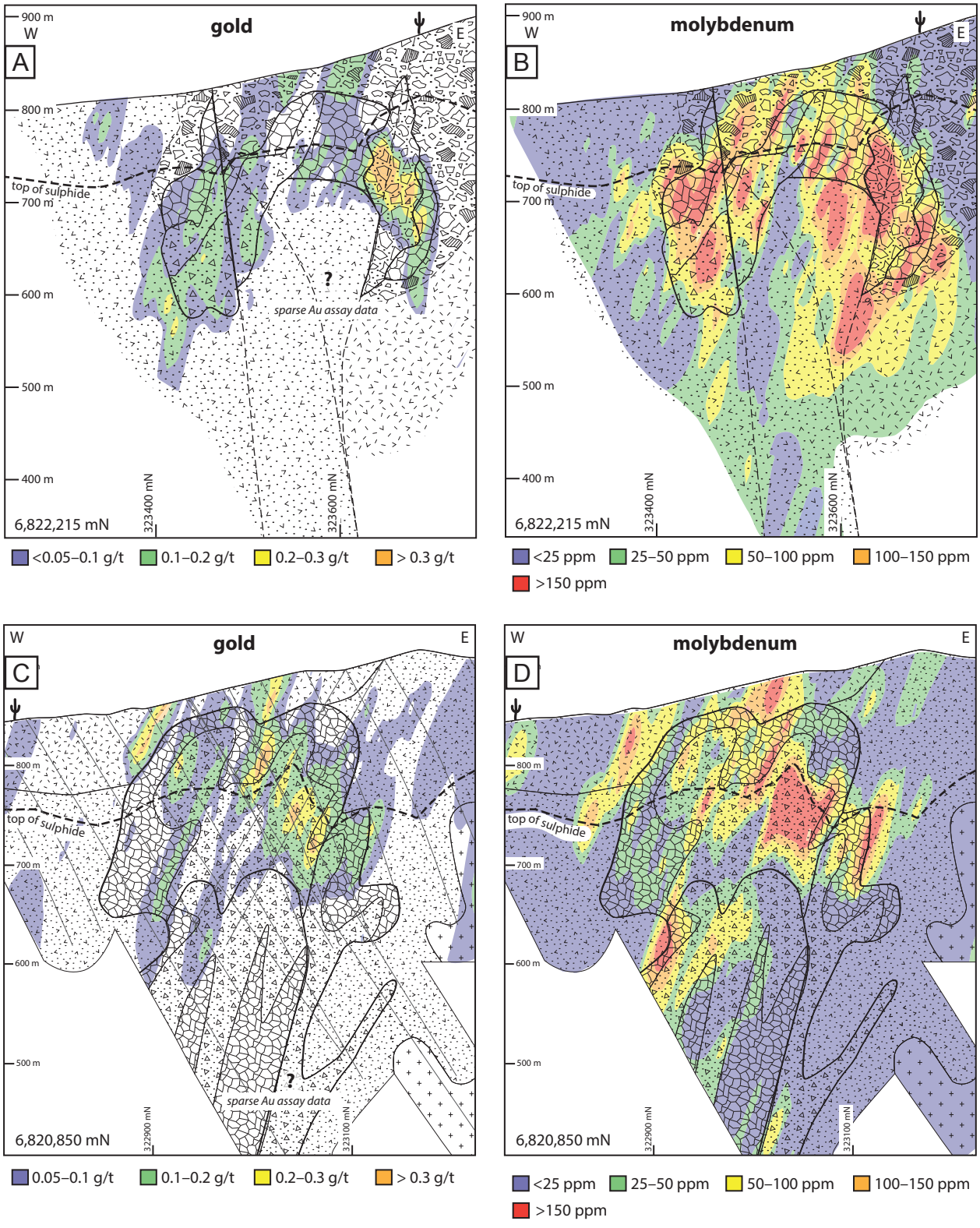

Figure 4.34 Cross sections at 6,822,215 mN (A and B) and 6,822,215 mN (C and D) showing interpolants of gold and molybdenum. Assay data from drill hole database provided by Hot Chili Ltd. Note gold assay data was only collected on samples with >0.1% Cu. Interpolants generated in Leapfrog Geo version 3.1.0 (spheroidal interpolant; global trend with dip 75°, dip azimuth 285°, pitch 0; ellipsoid ratios maximum 3, intermediate 3, minimum 0; adaptive resolution 20). cpy = chalcopyrite, py = pyrite.

4.8.1 Metal distribution

Metals grades are variable across the ore domains described in this study. On average, the Habanero zone has the highest grades of Cu (average 0.8 %, locally up to 5.81 %), Au (average 0.2 g/t, maximum of 1.44 g/t) and Mo (average 141 ppm, up to 2340 ppm; Figure 4.35, Appendix C5). Published intercepts from the Habanero ore zone include 72 m @ 0.7 % Cu from 120 m (PRP0609) and 102 m @ 1.0 % Cu and 0.2 g/t Au from 124m (PRP0611; Hot Chili Ltd, 2013; Figure 4.32). High grades are likely to have resulted from the interaction of mineralising fluids with brecciated host rocks that were a favourable site for ore deposition. The sub-stage 3B breccias with a component of magnetite-cement (3B-1 and 3B-3) are lower in Cu (average of 0.34 % Cu), Au (average of 0.1 g/t and 0.08 g/t respectively) and Mo (average of 121 ppm and 66 ppm respectively) than the more tourmaline-rich breccia facies (3B-2 and 3B-4). The breccia facies observed on section 6,822,215 mN (stage 2, 3B-1 and 3B-2) contain more Mo than those on section 6,820,850 mN (Figure 4.35).

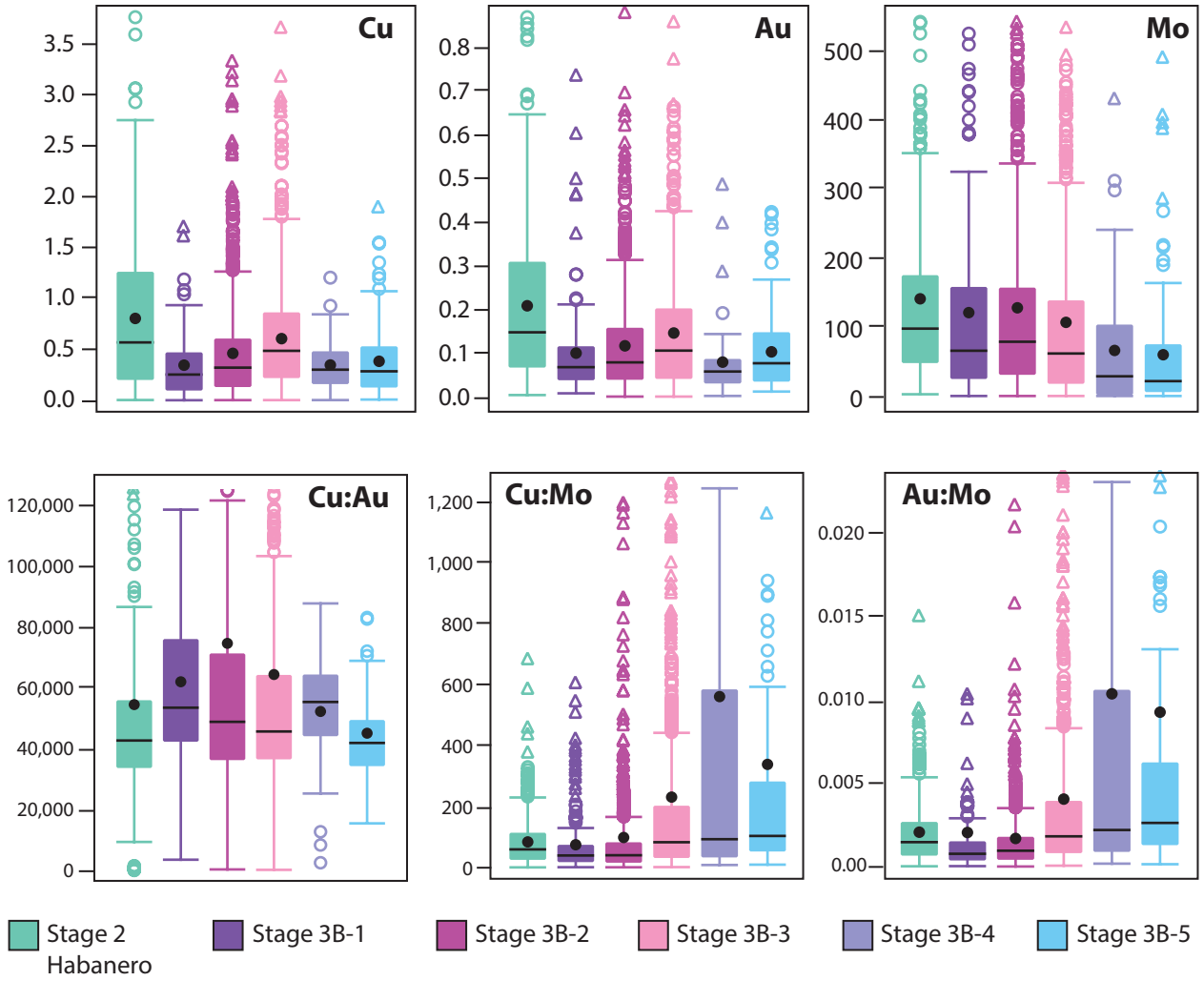

Figure 4.35 Top) Tukey plots scaled for outlier data showing i) Cu, ii) Au and iii) Mo content by breccia facies/ore zone. Bottom) Tukey plots scaled to regular data showing i) Cu:Au, ii) Cu:Mo and iii) Au:Mo ratios by breccia facies/ore zone.

Table 4.7 Metal contents, ratios and Spearman correlation coefficients for each breccia facies.

	Average Cu %	Average Au g/t	Average Mo ppm	Cu:Au	Cu:Mo	Au:Mo	Correlation coefficients		
							Cu-Au	Cu-Mo	Au-Mo
All	0.55	0.14	117	64,143	164	0.0033	0.77	0.46	0.51
Stage 2 (Habanero)	0.8	0.21	141	54,487	84	0.0021	0.82	0.53	0.50
Facies 3B-1	0.34	0.1	121	61,961	74	0.002	0.75	0.64	0.43
Facies 3B-2	0.45	0.17	128	74,547	98	0.0017	0.69	0.45	0.50
Facies 3B-3	0.34	0.08	66	52,232	560	0.0103	0.84	0.52	0.52
Facies 3B-4	0.6	0.14	107	64,341	231	0.004	0.77	0.41	0.57
Oxide	0.58	0.14	82	82,799	284	0.0039	0.57	0.14	0.56
Sulphide	0.62	0.14	129	47,500	182	0.0042	0.94	0.59	0.56
Facies 3B-5	0.38	0.1	60	45,117	338	0.0092	0.92	0.69	0.56

On section 6,820,850 mN, the 3B-4 breccia facies has been weathered, generally to less than 100 m below surface (Figure 4.33). Comparison of the oxide and sulphide material shows that, on average, the oxide material is slightly lower in Cu (0.62% Cu in sulphide, 0.58% Cu in oxide) and Mo (129 ppm Mo in sulphide, 82 ppm Mo in oxide) but similar in Au (0.14 g/t Au; Table 4.7).

Productora has typical Cu/Au ratios of 64,000 within ore zones (Table 4.7). Average ratios of Cu:Au are lowest within the Habanero ore zone and breccia facies 3B-3 and 3B-5 (Table 4.7, Figure 4.35; Appendix C5). The tourmaline-rich 3B-2 breccia facies has the highest Cu:Au (74,547) and lowest Au:Mo ratios (0.0017; Table 4.7). Facies 3B-3 and 3B-5 have higher Cu:Mo and Au:Mo ratios, reflecting their low Mo content. Oxide material associated with facies 3B-4 has significantly higher Cu:Au and Cu:Mo ratios compared to the 3B-4 sulphide material (Table 4.7). Gold-rich porphyry systems are defined as those with Cu/Au ratios <40,000 (Kesler et al., 2002). Although facies 3B-4 sulphide and 3B-5 are close to the cut-off at 47,500 and 45,117 respectively, Productora is not classified as Au-rich compared to porphyry Cu-Au systems using Kesler et al.'s (2002) criterion.

Overall Cu and Au are strongly correlated with each other in each breccia facies (Spearman correlation coefficients between 0.75–0.94), but have poorer correlations with Mo (Spearman correlation coefficients between 0.43–0.69; Table 4.7). The Cu-Au correlation varies somewhat between ore zones but more significantly with the weathering profile. The Cu-Au correlation is strongest within the sulphide component of facies 3B-4, with a Spearman correlation coefficient of 0.94. However, this correlation breaks down within the overlying weathering zone, where Cu-Au only has a correlation coefficient of 0.57 (Table 4.7).

4.8.2 Sulphide zonation

Chalcopyrite is the principal hypogene Cu-sulphide mineral at Productora. It predominantly occurs

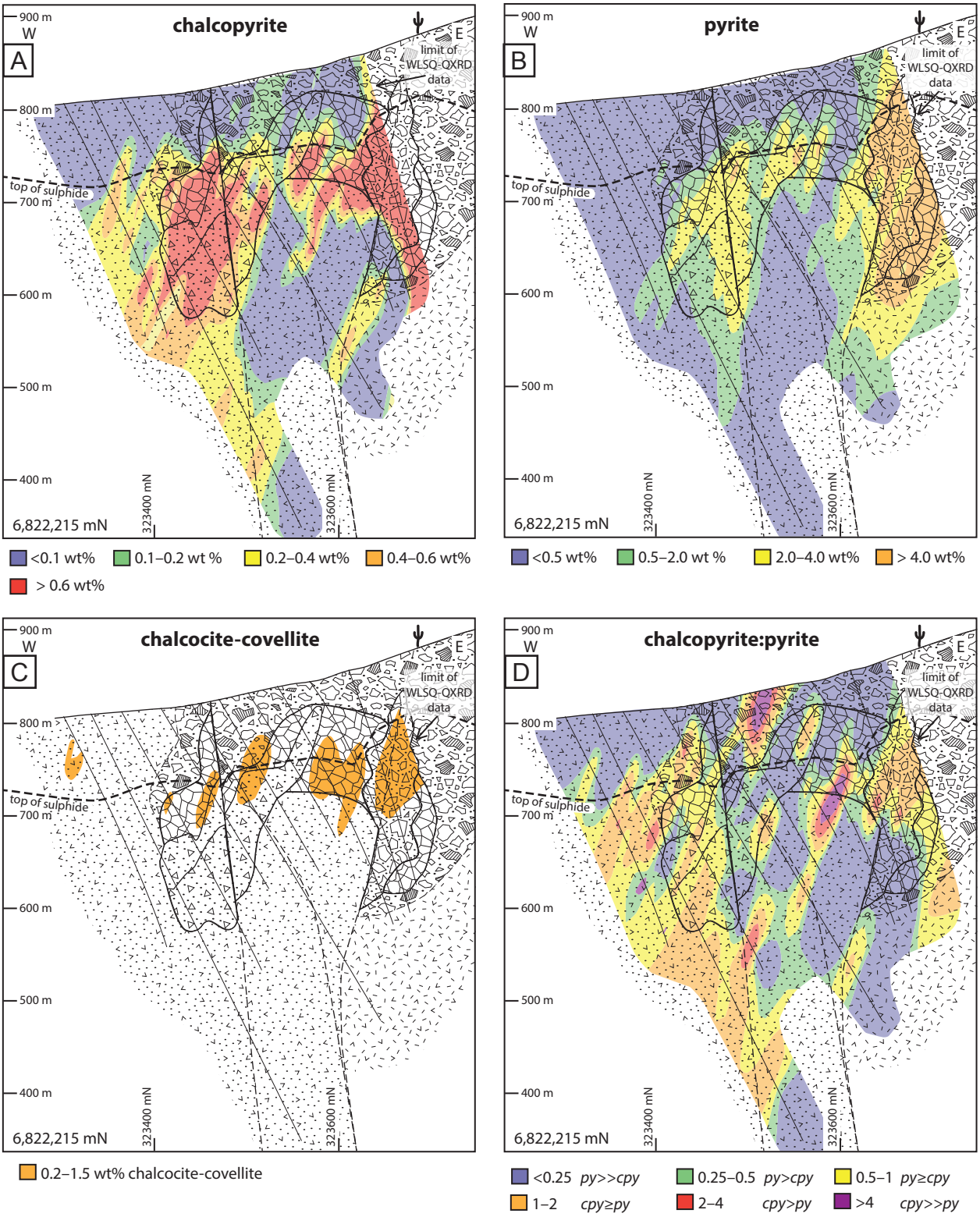

Figure 4.36 Cross section at 6,822,215 mN showing interpolant of estimated abundance of A) chalcopyrite B) pyrite C) chalcocite-covellite and D) chalcopyrite:pyrite ratio from WLSQ-QXRD data. Interpolants generated in Leapfrog Geo version 3.1.0 (spheroidal interpolant; global trend with dip 75°, dip azimuth 285°, pitch 0; ellipsoid ratios maximum 3, intermediate 3, minimum 0; adaptive resolution 20). cpy = chalcopyrite, py = pyrite.

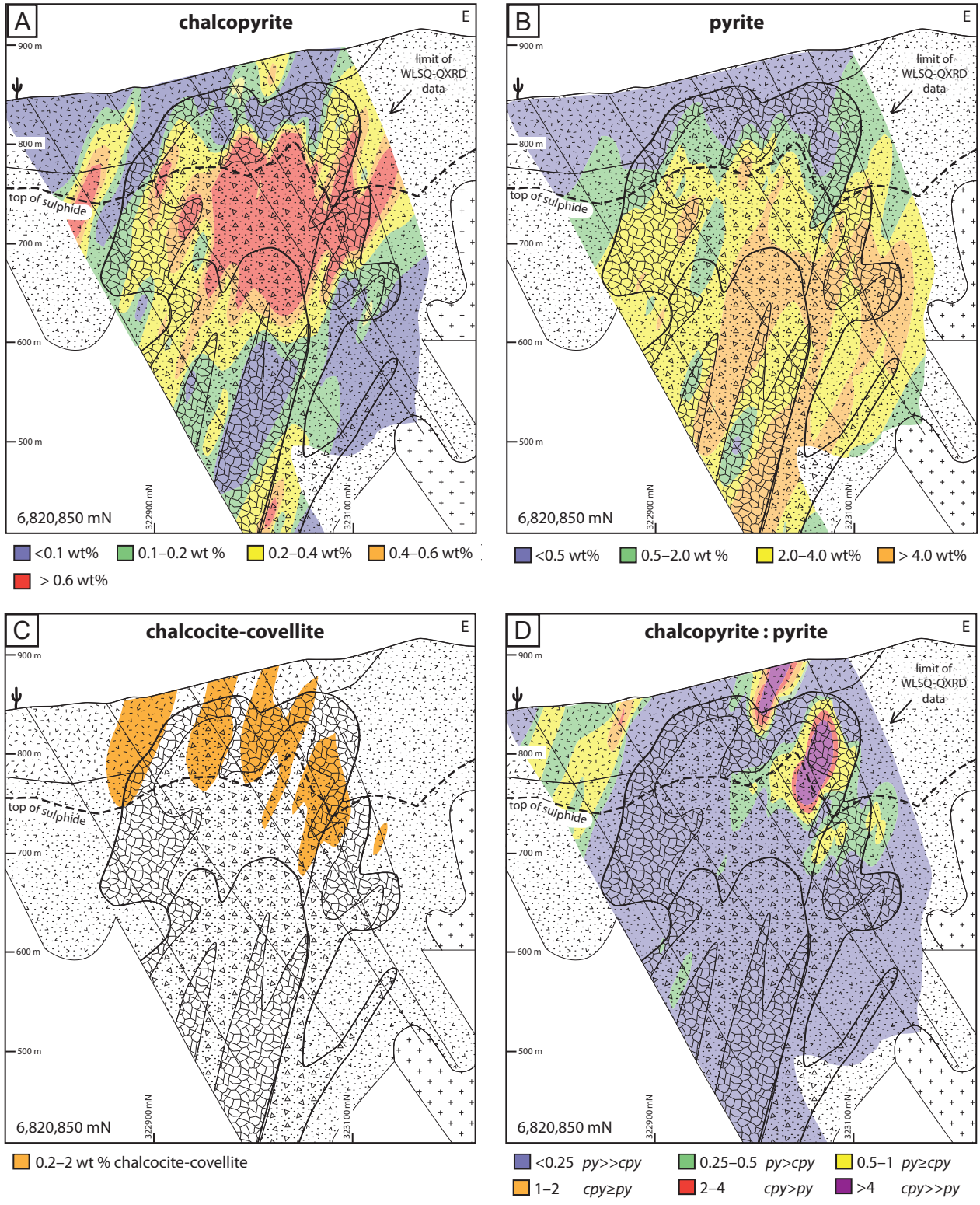

Figure 4.37 Cross section at 6,820,850 mN showing interpolant of estimated abundance of A) chalcopyrite B) pyrite C) chalcocite-covellite and D) chalcopyrite:pyrite ratio from WLSQ-QXRD data. Interpolants generated in Leapfrog Geo version 3.1.0 (spheroidal interpolant; global trend with dip 75°, dip azimuth 285°, pitch 0; ellipsoid ratios maximum 3, intermediate 3, minimum 0; adaptive resolution 20). cpy = chalcopyrite, py = pyrite.

with pyrite as stage 3 breccia cement and syn-breccia veins (Figure 4.36 A and B, and Figure 4.37 A and B). Pyrite and chalcopyrite are largely absent from the upper 100 m of the deposit, which is in part due to weathering and in part the distribution of breccia facies. Section 6,822,215 mN has high pyrite abundance associated with the stage 2 breccia domain, but pyrite diminishes with depth (Figure 4.36 B). Pyrite abundance increases with depth on section 6,820,850 mN (Figure 4.37 B). Covellite and minor chalcocite occur in the upper parts of the sulphide domain, and the lower parts of the weathered zone (Figure 4.36 C and Figure 4.37 C). Petrographic observations of covellite replacing chalcopyrite along grain boundaries indicate that covellite is supergene (section 4.4.3 and 4.4.4). Estimates of model chalcopyrite and pyrite abundance (from WLSQ-QXRD) show that the ratio of chalcopyrite to pyrite is much higher within the breccia complex on section 6,822,215 mN (Figure 4.36 D) compared to the breccias complex on section 6,820,850 mN (Figure 4.37 D). Pyrite and chalcopyrite occur in approximately equal proportions across section 6,822,215 mN whereas pyrite is predominates over chalcopyrite on section 6,820,850 mN.

4.8.3 Gold deportment

Gold is a valuable by-product of many porphyry Cu deposits globally (e.g. Kesler et al., 2002). Despite its common occurrence in porphyry Cu systems, Au distribution and chemistry remain poorly understood. At Productora, low gold grades preclude the observation of any potential free gold. Large grains should be extremely rare, small grains will be too small to see with the naked eye or by reflected light petrography,

Table 4.8 Samples analyses by synchrotron XRF.

Sample ID	Hole ID	Depth (m)	Alteration Stage	Description	Au[1] (g/t)	Number of grains	Size (μm)
PR14AE127	MET023	164.7	3B-2/Stage 2	Ill altered tur - py-cemented chaotic breccia	0.34	0	-
PR14AE129	MET023	119	3B-2/Stage 2	Kln - ms altered matrix rich chaotic breccia	0.3	1	<4
PR14AE133	MET023	132	3B-2/Stage 2	Kln - ms altered matrix rich chaotic breccia	0.8	1	4
PR14AE139	MET023	223.4	3B-2/Stage 2	Ill vein cross cutting ill - tur - py-cemented chaotic breccia	0.2	3	<4
PR14AE098	PRP0064D	283.2	Cachiyuyito	mt - cpy - py - qtz vein	0.3	1	<4
PR14AE055	MET008	101.90	3B-2	tur - cemented breccia vein	0.3	2	<4
PR14AE031	MET008B	124.20	3B-2	tur - cemented breccia vein	0.1-0.2	0	-
PR14AE062	MET007	218.45	3B-1	tur - py - cpy - kfs alteration clot	0.1-0.2	1	6.8
PR14AE168	MET016	145.5	3B-4	weathered py in tur - kfs altered rock	0.1-0.5	0	-
PR14AE162	MET015	239.6	3B-3	Tur - chl-cemented breccia	<0.1	1	5

[1]estimate based on assay interval of nearest neighbour hole in assay data base as no assay data was available for the samples. cpy = chalcopyrite, ill = illite, kfs = K-feldspar, kln = kaolinite, ms = muscovite, py = pyrite, qtz = quartz, tur = tourmaline

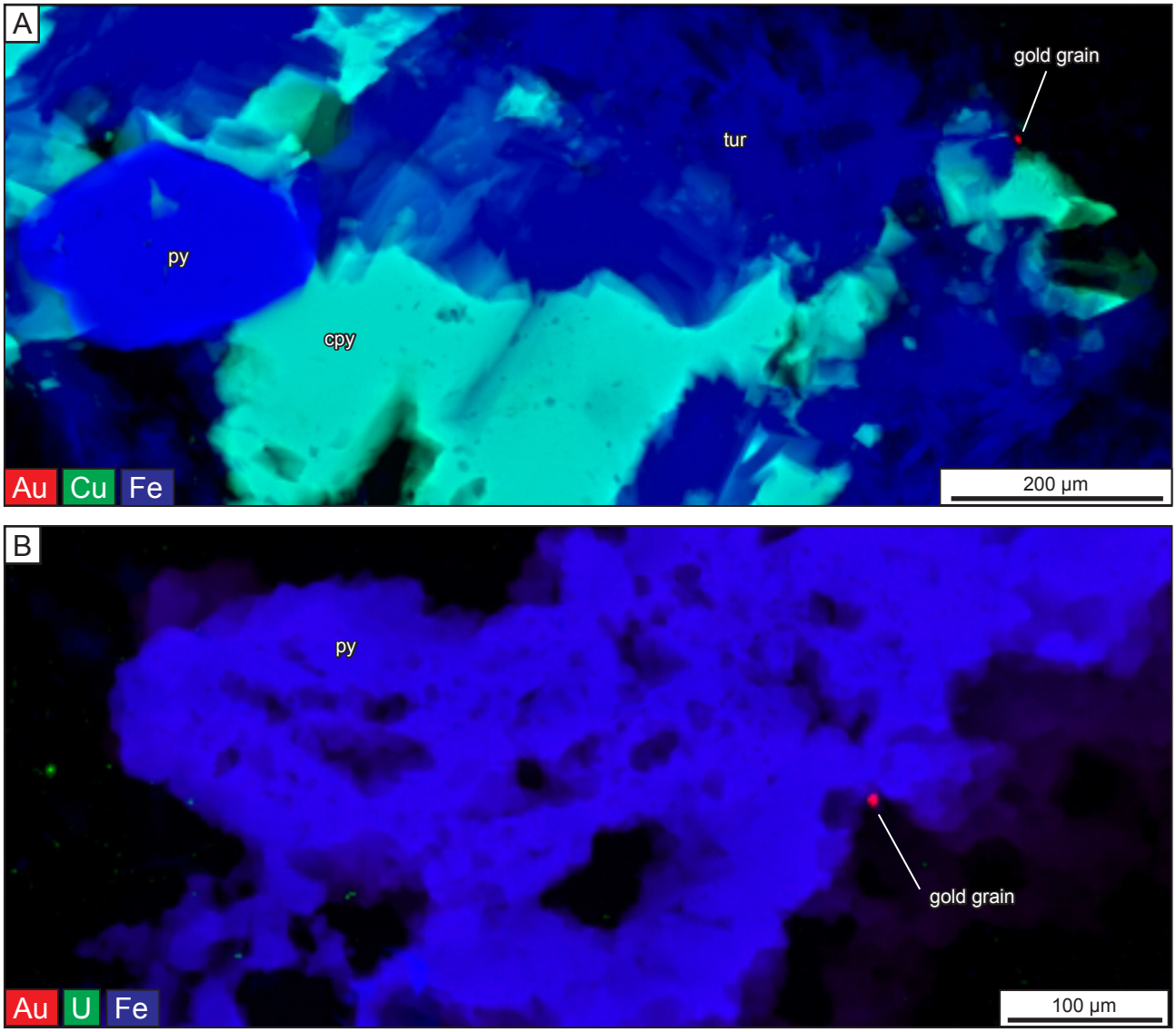

Figure 4.38 Gold and trace element deportment determined by synchrotron XFM. A) RGB element map showing Au, Cu and Fe in facies 3B-3 tourmaline-chalcopyrite-pyrite breccia cement with Au grain (5 µm) situated at tourmaline - chalcopyrite grain boundary (PR14AE162, MET015 239.60 m). B) RGB element map showing Au, U and Fe in facies 3B-1 tourmaline - pyrite - K-feldspar - chalcopyrite alteration clot with Au grain (6.8 µm) situated on pyrite grain boundary (PR14AE062, MET007 218.45 m). cpy = chalcopyrite = pyrite, tur = tourmaline.

and solid solution Au is invisible. To overcome this challenge and to help determine gold deportment at Productora, ten polished sections were analysed by XRF microscopy performed using the XFM beamline at the Australian Synchrotron. Full spectral data were collected across the entire thin section volume.

A total of ten large area maps were collected at a 4 µm step size in order to provide the broadest coverage for the Au deportment study. Ten higher resolution maps were collected over smaller areas using a 2 µm step size. Gold grains on the order of 4 µm were detected in seven of the ten large area maps, at the scan resolution this equates to one pixel per grain. Three high resolution scans included a gold grain, PR14AE062, PR14AE162 (Figure 4.38) and PR14AE133 (Figure 4.39; Table 4.8). Gold grains in the high resolution scans were measured at 4–6.8 µm in size (average radius). Grains are located on grain boundaries with chalcopyrite and pyrite. No evidence for solid solution, also known as invisible gold,

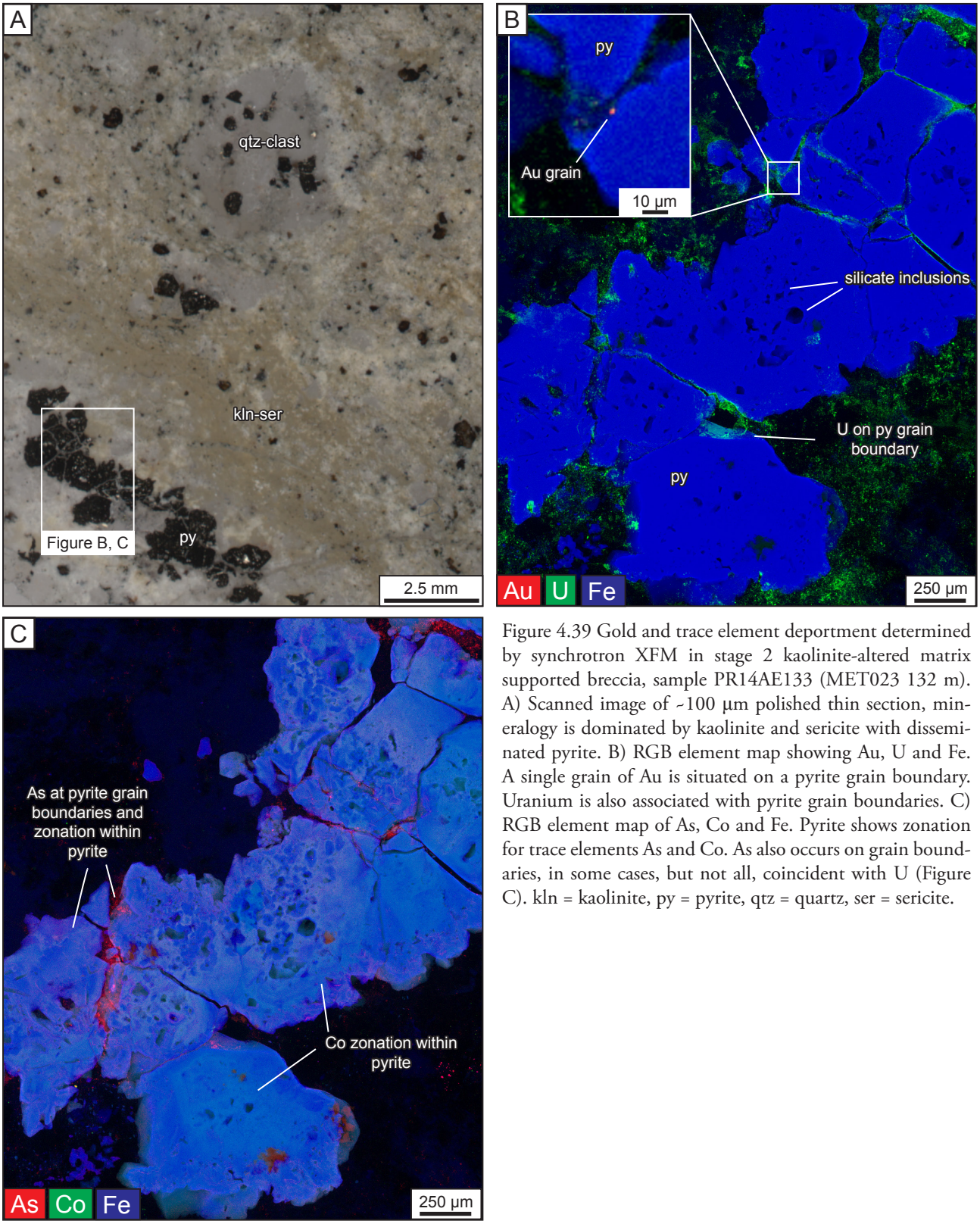

Figure 4.39 Gold and trace element deportment determined by synchrotron XFM in stage 2 kaolinite-altered matrix supported breccia, sample PR14AE133 (MET023 132 m). A) Scanned image of ~100 µm polished thin section, mineralogy is dominated by kaolinite and sericite with disseminated pyrite. B) RGB element map showing Au, U and Fe. A single grain of Au is situated on a pyrite grain boundary. Uranium is also associated with pyrite grain boundaries. C) RGB element map of As, Co and Fe. Pyrite shows zonation for trace elements As and Co. As also occurs on grain boundaries, in some cases, but not all, coincident with U (Figure C). kln = kaolinite, py = pyrite, qtz = quartz, ser = sericite.

was found at the scan conditions.

As full spectra data were obtained during analyses, deportment of other trace elements can also be visualised in the processed images, particularly those captured at high resolution. Uranium minerals

are finely disseminated in gangue and on pyrite grain boundaries in sample PR14AE133 (Figure 4.39) whereas samples from the stage 3 breccia show no U-bearing phases. Trace element zonation is also observed within pyrite grains for Co, As (Figure 4.39) and Ni. Cobalt and As show weak oscillatory zoning around silicate inclusions and with crystal faces. Arsenic is also associated with grain boundaries (Figure 4.39 C). Further investigation using SEM is required to fully characterise the micron scale mineralogy in order to determine the mineralogy of the U- and As-bearing phases. Further investigation is also required to determine whether U associated with pyrite in the Habanero ore zone is likely to be concentrated during processing, as U is a deleterious element.

4.9 Geochronology

Paragenetic relationships demonstrate the sequence of breccia and alteration events detailed in section 4.4. The absolute age of the Productora main stage mineralisation was proposed to be 91.4 ± 0.2 – 90.7 ± 0.7 Ma by Fox (2000; Table 4.9) based on hydrothermal K-feldspar. More recently Re-Os dating on molybdenite yielded an age of 128.9 ± 0.6 Ma (Marquardt et al., 2015; Table 4.9). During the current study, the absolute timing of mineralisation at Productora and the Alice porphyry was determined by Re-Os geochronological analyses of molybdenite.

4.9.1 Method

Two drill core samples were submitted to Dr Robert Creaser at University of Alberta Radiogenic Isotope Facility for mineral separation and Re-Os dating. For each sample, a molybdenite mineral separate was made by metal-free crushing followed by gravity and magnetic concentration methods described in detail by Selby and Creaser (2004). The concentrations of ^{187}Re and ^{187}Os in molybdenite were determined by isotope dilution mass spectrometry using Carius-tube, solvent extraction, anion chromatography and negative thermal ionization mass spectrometry techniques. A mixed double spike containing known amounts of isotopically enriched ^{185}Re, ^{190}Os, and ^{188}Os analysis was used (Markey et al. 2007). Isotopic

Table 4.9 Previous and new geochronology results for main stage mineralisation at the Productora project.

Age (Ma)	Method	Mineral	Reference
Productora			
90.7 ± 0.7	^{39}Ar-^{40}Ar	K-feldspar	Fox (2000)
91.4 ± 0.2	^{39}Ar-^{40}Ar	K-feldspar	Fox (2000)
128.0 ± 0.6	Re-Os	Molybdenite	Marquardt et al. (2015)
130.1 ± 0.6	Re-Os	Molybdenite	this study
Alice			
122.8 ± 0.6	Re-Os	Molybdenite	Hot Chili Ltd unpublished
124.1 ± 0.6	Re-Os	Molybdenite	this study

Table 4.10 Re-Os geochronology results for molybdenite samples from Productora and Alice.

Location	Sample	Re (ppm)	±2σ	^{187}Re (ppm)	±2σ	^{187}Os (ppm)	±2σ	Model age	±2σ (Ma)
Productora	PR14AE059	301.6	1.0	189.6	0.6	411.4	0.3	130.1	0.6
Alice	PR14AE213	2980	10	1873	7	3877	3	124.1	0.6

analysis was made using a ThermoScientific Triton mass spectrometer by Faraday collector. Total blanks for Re and Os are less than <3 picograms and 2 picograms, respectively, which are insignificant for the Re and Os concentrations in molybdenite. The molybdenite powder HLP-5 (Markey et al., 1998), was analyzed as a standard. Over a period of two years, the HLP-5 standard has yielded an average Re-Os date of 221.56 ± 0.40 Ma (1SD uncertainty, n=10). This Re-Os age date is identical to that reported by Markey et al. (1998) of 221.0 ± 1.0 Ma.

4.9.2 Results

Results of Re-Os dating are presented in Table 4.9 and Table 4.10. Analysis of molybdenite disseminated in K-feldspar altered rhyodacite lapili tuff from Productora 3B-3 facies returned a ^{187}Re/^{187}Os age of 130.1 ± 0.6 Ma. This is consistent (almost within error) with the data from Marquardt et al. (2015; Table 4.9). Molybdenite from a quartz - molybdenite - chalcopyrite - pyrite vein in the Alice porphyry deposit returned a ^{187}Re/^{187}Os age of 124.1± 0.6 Ma, which is consistent (almost within error) with unpublished data from Hot Chili Ltd (Table 4.9). Absolute ages for mineralisation indicate that the Productora breccia complex is close in age to the Cachiyuyito stock, and is much older than the Ruta Cinco batholith. Alice porphyry mineralisation is between 3.9–7.3 m.y. younger than the Productora breccia complex. Compared to U-Pb$_{zircon}$ dating of the Alice porphyry intrusion (121.1 ± 2.1 Ma; this study), Alice mineralisation (124.1± 0.6 Ma, this study; 122.8 ± 0.6 Hot Chili Ltd, unpublished) is almost within error.

4.10 Discussion

4.10.1 Breccia genesis

The Productora breccia complex formed due to several brecciation events. There are at least two stages of hydraulic fragmentation, stages 1 and 3. Stage 2 is interpreted to be a tectonic breccia and shows evidence of multiple brecciation episodes, suggesting local host-fault reactivation. Variability in the texture and clast organisation of the stage 3 breccia facies (Table 4.4) reflects the interplay of hydraulic and seismic rupture driven fragmentation mechanisms. The relative proportions of vapour and liquid remain undetermined. Angular, monomict, clasts and clast-supported jigsaw-fit textures indicate

Table 4.11 Interpretation and genetic classification of Productora breccia facies. Genetic terminology from Sillitoe et al. (1985) and Davies et al. (2008a and b).

Breccia Facies	Salient Features	Genetic interpretation	Classification
Stage 1	• Quartz-pyrite cement • Angular clasts • Lack of rock flour • Massive, chaotic, poorly sorted	• High energy, hydraulic ± seismic rupture driven fragmentation • Hydrothermal fluids	Hydraulic
Stage 2	• Abundant rock flour and matrix • Lack of hydrothermal cement • Rounded clasts • Stratification of clasts • Evidence of reactivation	• Non-explosive fragmentation by seismic rupture • Attrition by fault movement • Cataclasite	Tectonic
Stage 3	• Abundant cement • Minor matrix • Cemented by high temperature minerals (tourmaline, chalcopyrite, magnetite, biotite) • Clast supported, jigsaw fit • Angular, monomict clasts • No evidence of multiple events	• Non-explosive hydraulic ± seismic rupture driven fragmentation • Magmatic-hydrothermal fluids • Little bulk clast transport • Likely one catastrophic event	Magmatic-hydrothermal (hydraulic)

little clast transport has occurred. This is atypical compared to major Chilean tourmaline-cemented hydrothermal breccias such as at Sur-Sur, La Union and Los Bronces in the Los Bronces-Rio Blanco porphyry Cu-Mo deposit (e.g. Warnaars et al., 1985; Frikken et al., 2005), Spence and Sierra Gorda porphyry Cu-Mo deposits (D. Cooke, pers. comm., 2016).

Contact relationships between the stage 3 breccia and host rocks have not been well established but the distribution of associated mineralisation indicates a downward-tapering dyke-like morphology that ranges from 300 m width near surface to <100 m at depth (Figure 4.32 and Figure 4.33) and strikes north-northeast over 2.5 km. The breccia complex extends to depths greater than 400 m from surface.

4.10.2 Mineralogy as an indicator of paleo-temperature and acidity

The precipitation of alteration minerals in the hydrothermal environment is controlled by a wide number of variables that fall into the following categories: temperature, fluid chemistry (pH, redox, dissolved species concentrations), host rock compositions, kinetics of reactions, duration of hydrothermal activity or degree of equilibrium and permeability (Browne, 1978). Temperature and fluid chemistry are considered the most influential to hydrothermal alteration mineralogy (Corbett and Leach, 1998). Fluid chemistry encompasses a variety of variables including acidity (pH), redox and sulphur concentrations. Experimentally derived phase diagrams based on active geothermal systems and thermodynamic modelling enable paleo-temperatures and pH to be estimated based on observed mineralogy (Browne,

1978; Hemley et al., 1980; Henley and Ellis, 1983; Hedenquist and Houghton 1987; Reyes 1990; Spear, 2003; Cooke et al., 1996; Losada-Calderon and McPhail, 1996; Masterman, 2003; Seedorff et al., 2005). Fluid inclusion studies provide direct information on hydrothermal fluids but where this information is not available, as is the case in the current study, paragenetic mineral assemblages can be used to constrain fluid pH and temperature (e.g., Pass, 2010). The alteration rank scheme of Corbett and Leach (1998), which was derived from a compilation of data from active geothermal systems, experimental and thermodynamic work, provides a useful framework for estimating pH and temperature (Figure 4.41). Although it is noted that chemical changes via processes such as water-rock interaction could also lead to mineralogical variation at constant temperature.

Temperature change is an important aspect in mineral precipitation, as rapid thermal decline can drive hydrothermal fluids to supersaturation with respect to many ore and alteration minerals (Hemley et al., 1980). The temperature window of active magmatic-hydrothermal systems ranges from above the magmatic solidus (~750°–600°C, depending on magma composition) to low temperatures (<200°C;

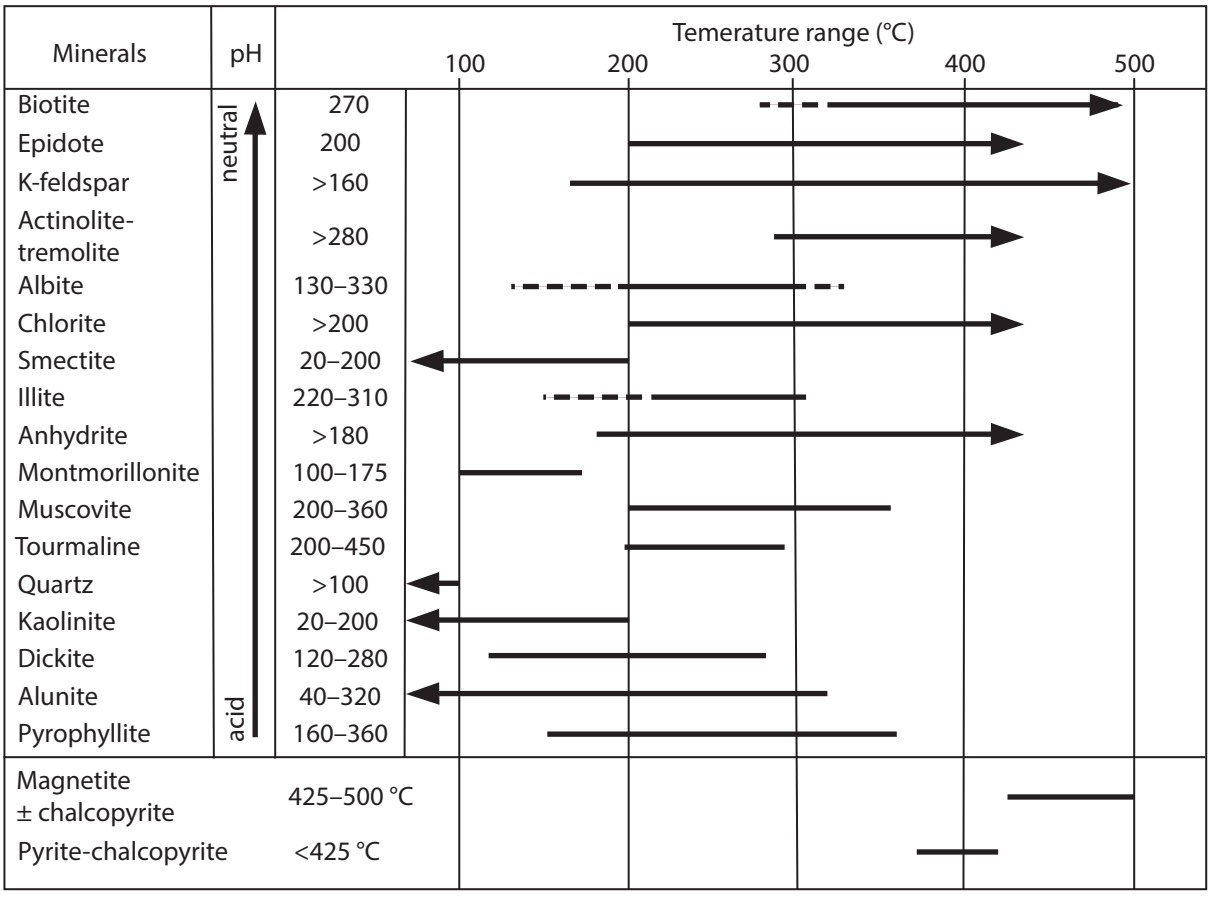

Figure 4.40 Common temperature stability ranges in geothermal systems for hydrothermal minerals observed at Productora. This data can be used as a guide for the mineral stability ranges in hydrothermal systems, however exceptions can occur due to extremes in fluid chemistry. Data deduced empirically from active geothermal systems, experimental modelling and fluid inclusion studies; Hemley et al. (1980); Henley and Ellis, (1983); Hedenquist and Houghton, (1987); Reyes, (1990); Slack, (1996). Minerals have been arranged by their stability with respect to pH. Sulphide and magnetite formation temperatures from experimental studies (Simon et al., 2000). Figure modified from Masterman (2003) and Pass (2010).

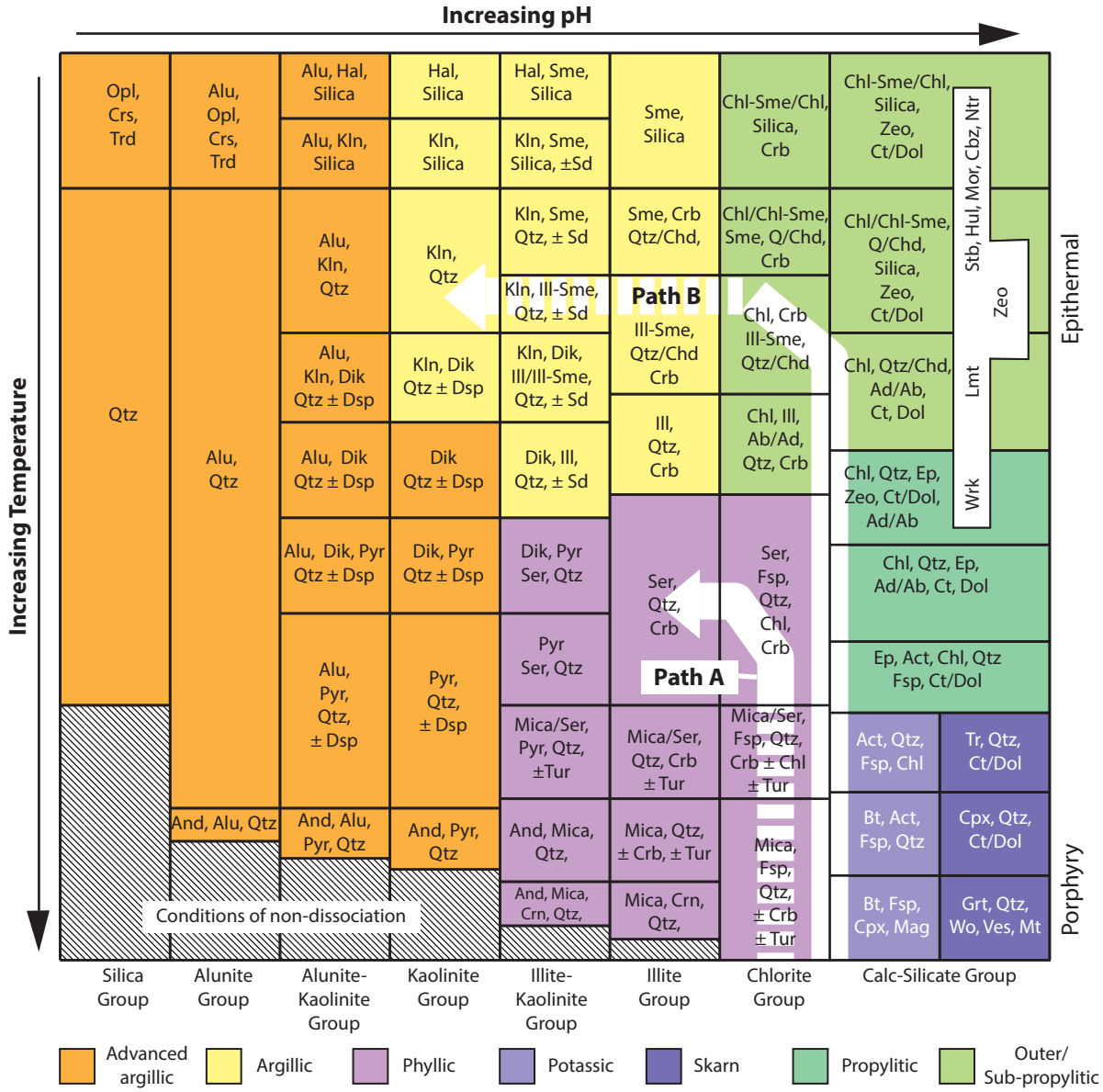

Ab - albite, Act - actinolite, Ad - adularia, Alu - alunite, And - andalusite, Bt - biotite, Crb - carbonate (Ca, Mg, Mn, Fe), Chl - chlorite, Cbz - chabazite, Chd - chalcedony, Chl-Sm - chlorite-smectite, Crn - corundum, Cpx - clinopyroxene, Crs - cristobalite, Ct - calcite, Dol - dolomite, Dik - dickite, Dsp - diaspore, Ep - epidote, Fsp - feldspar, Grt - garnet, Hal - halloysite, Hul - heulandite, Ill - illite, Ill - Sm-illite - smectite, Kln - kaolinite, Lmt - laumontite, Mag - magnetite, Mor - mordenite, Ntr - natrolite, Opl - opaline silica, Pyr - pyrophyllite, Qtz - quartz, Ser - sericite, Sd - siderite, Sme - smectite, Stb - stilbite, Tur - tourmaline, Tr - tremolite, Trd - tridymite, Ves - vesuvianite, Wai - wairakite, Wo - wollastonite, Zeo - zeolite

Figure 4.41 Common alteration minerals in hydrothermal systems modified from Corbett and Leach (1998). Mineralogy indicates relative pH and relative temperature, given similar host rock composition, water-rock ratios, total sulphur and redox state. Tourmaline added (D. Cooke, pers. comm., 2016). Paths A show the possible fluid evolution of stage 1 which formed a quartz - pyrite- muscovite-cemented breccia. Path B shows the possible fluid evolution of stage 3 fluids that formed tourmaline - magnetite - biotite - chalcopyrite - pyrite-cemented breccias then sub-stage 4 chlorite, chalcopyrite - pyrite ± sericite and illite veins. Continued cooling may have generated kaolinite - muscovite - pyrite alteration associated with the stage 2 breccia domain.

Seedorff et al., 2005). The temperature stability ranges for minerals identified at Productora are listed in Figure 4.40. Temperature is discussed in relation to the following ranges: 400° to >600°C is considered high temperature; 300°–400° is moderate temperature, and <300°C is low temperature (after Pass, 2010; Table 4.12).

Alteration mineralogy indicates that early hydrothermal fluids at Productora were low-moderate temperature based on the stage 1 quartz - muscovite assemblage. The main mineralisation stage, tourmaline breccia event and potassic alteration (stage 3) are associated with high temperature fluids, as indicated by tourmaline, biotite and magnetite. Later propylitic and phyllic events (stages 4 and 5) are associated with progressively decreasing low temperature fluids, as indicated by chlorite, epidote and calcite assemblages.

Mineralogy and distribution of the stage 3 breccia facies indicate an upward and outward fluid cooling path from hot magnetite-bearing assemblages (425°–500°C; Figure 4.40) to moderate–high temperature K-feldspar - tourmaline ± biotite assemblages. Thus, it can be inferred that facies 3B-2 is the distal equivalent of 3B-1 and similarly 3B-4 is the distal equivalent of 3B-3. Decreasing proportions of breccia cement and increasing internal clast organisation support this interpretation. On section 6,820,850 mN, chalcopyrite content is much higher in the 3B-4 breccia facies. The high temperature associated with the magnetite-bearing 3B-3 breccia and lower chalcopyrite content suggests that temperatures in this part of the breccia complex were higher than chalcopyrite saturation for this fluid composition. In comparison, the 3B-1 magnetite-bearing facies, on section 6,822,215 mN, has abundant chalcopyrite at a similar depth. It is inferred that the observed mineralogy and breccia facies indicate a temperature gradient

Table 4.12 Summary of mineral assemblage and inferred paleotemperature and acidity associated with each stage of the Productora breccia complex.

Alteration stage	Mineral Assemblage	Temperature	Acidity	Alteration assemblage
Stage 1	quartz - pyrite - muscovite	low-mod	Weakly acidic	Phyllic
Stage 2 alteration	kaolinite - muscovite - pyrite	low	Strongly acidic	Argillic
Facies 3B-1	K-feldspar - tourmaline - magnetite - chlorite - pyrite - chalcopyrite	high	Alkaline	Potassic
Facies 3B-2	K-feldspar - tourmaline - pyrite - chalcopyrite	mod-high	Alkaline	Potassic
Facies 3B-3	K-feldspar- biotite - pyrite - chalcopyrite - magnetite - tourmaline - albite	high	Alkaline	Potassic
Facies 3B-4	K-feldspar - biotite - tourmaline - chalcopyrite - albite	mod-high	Alkaline	Potassic
Facies 3B-5	K-feldspar - biotite - tourmaline - pyrite - chalcopyrite - albite	mod-high	Alkaline	Potassic
Sub-stage 4A	chlorite	low	Weakly acidic to neutral	Propylitic
Sub-stage 4B	chalcopyrite, pyrite ± sericite	low	Weakly acidic	Phyllic
Sub-stage 4C	illite	low	Weakly acidic	Phyllic
Sub-stage 4D	epidote	low	Alkaline	Propylitic
Stage 5	calcite	low	Alkaline	Propylitic

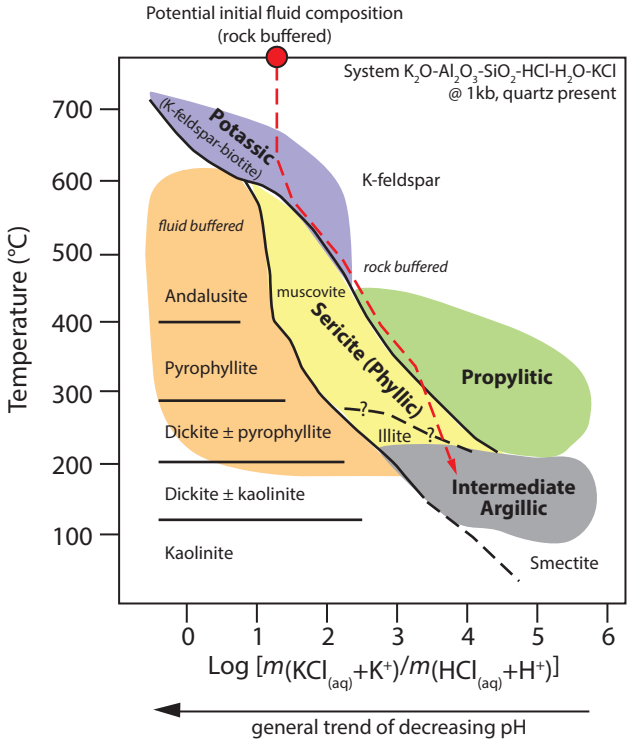

Figure 4.42 Phase diagram for the system K_2O-Al_2O_3-SiO_2-HCl-H_2O-KCl at P_{H2O} = 1 kb, modified from Tosdal (2009) after Seedorff et al., (2005). Red dashed line shows possible initial fluid and evolutionary path for stage 3 to stage 4 fluids at Productora based on the observed alteration mineralogy.

toward higher temperatures in the south. This is suspected to be nearer to the root zone of the breccia complex, and is potentially a target if seeking the progenator intrusion to the magmatic fluids, which could be a porphyry prospect. The mineralogy of stages 4 and 5 are consistent with propylitic (sub-stage 4A, 4D and stage 5; Gustafson and Hunt, 1975) and phyllic (sub-stage 4B and 4C) assemblages. Stages 4 and 5 are interpreted to have formed at lower temperatures, based on the presence of chlorite, epidote or muscovite, in the waning stages of hydrothermal activity (Figure 4.41; Table 4.12).

The salinity of supercritical magmatic-hydrothermal fluids is estimated to be in the range of 2–10 wt % NaCl equiv based on fluid inclusion data (Butte; Rusk et al., 2008). On phase separation to vapour and brine, brine salinity is estimated at 35–70 wt% NaCl equiv (e.g., Roedder, 1971; Nash, 1976; Eastoe, 1978; Bodnar, 1995). The dominant acid species is regarded as $HCl_{(aq)}$ in magmatic-hydrothermal fluids at moderate to high temperature (Losada-Calderon and McPhail, 1996). The dissociation of $HCl_{(aq)}$ is strongly temperature dependant, increasing with decreasing temperature (Sverjensky et al., 1991). Acidity has a non-linear relationship with temperature (i.e., neutral pH = 7 at 25°C = $-\log^{10}[H^+]$). At high temperature and salinity, H^+ is uncommon and so it is essential to combine H^+ and $HCl_{(aq)}$ as $a_{(HCl_{(aq)} + H^+)}$ in order to represent magmatic-hydrothermal fluid acidity across the full temperature range associated with magmatic-hydrothermal deposits. The phase diagram for the K_2O-Al_2O_3-SiO_2-HCl-H_2O-KCl system demonstrates the temperature-acidity stability fields for major

Table 4.13 Alteration types and their implied temperature range and fluid chemistry. Modified from Pass (2010).

Key minerals	Accessory	Temperature[1] (°C)	Fluid Chemistry	Notes / Reference
Potassic				
Bt, kfs, mt		>> 320°C	Neutral to alkaline pH, relatively high aK^+/aH^+	Hendenquist and Houghton (1987)
Bt, kfs, tur, mt, cpy, py		(Figure 4.42)	(Figure 4.42)	Seedorff et al. (2005)
Calc-potassic				
Grt, kfs, bt ± ap ± anh		650°–400°C		Lang et al. (1995b, c)
Sodic				
Ab, di ± chl ± ep		<670° to >350°C		Lang et al. (1995b, c)
Argillic				
Advanced (high T)				
Prl, dsp, and	Qtz, sulfides, tur, en/luz	High to low	<4	Corbett and Leach (1998b)
		250°C (?) and >350°C	Acid pH	Hendenquist and Houghton (1987)
Advanced (low T)				
Kln, alu	Chd, crs, qtz, py	250°–>200°	4–6	Corbett and Leach (1998b)
		180°C	Acid pH	Hendenquist and Houghton (1987)
Intermediate				
Sme or interlayered ill-sme	Sulfides, zeo, qtz, cal	<200°C	Neutral pH, moderate aCa^+/aH^+	Hendenquist and Houghton (1987)
Kln, smec, ill				Meyer and Hemley (1967)
Propylitic				
Inner				
Ep, act	Chl, illite	300°C	Neutral pH, relateivley high aCa^+/aH^+	Hendenquist and Houghton (1987)
		300°–280°C	~5–>7	Corbett and Leach (1998b)
Outer				
Ep	Chl, ill, sulfides	250°C	Neutral pH, relateivley high aCa^+/aH^+	Hendenquist and Houghton (1987)
Cal, chl, py ± ep ± ab		300°–<200°C		Lang et al. (1995b, c)
Sericitic (phyllic)				
Ser (ill), qtz	Sulfides, oxides, (kln)	>220°C	Neutral pH, but increasing high aK^+, aH^+	Hendenquist and Houghton (1987)
Kfs to ser-qtz illite		<550°C 250°–300°C		Seedorff et al., 2005
Silicic				
Qtz, tur(?)	Mo, iltr, zir			Metasomatic addition of Si; Seedorf et al. (2005)

[1]Implied temperature; ab = albite, act = actinolite, ahn = anhydrite, and = andalusite, aln = alunite, ap = apatite, bt = biotite, cal = calcite, chd = chalcedony, chl = chlorite, cpy = chalcopyrite, crs = cristobalite, di = diopside, dsp = diaspore, en = enargite, ep = epidote, grt = garnet, ill = illite, kfs= K-feldsapr, kln = kaolinite, luz = luzonite, ms = muscovite, mt = magnetite, prl = pyrophyllite, py = pyrite, qtz = quartz, sme = smectite, tur = tourmaline, zeo = zeolite.

alteration minerals and alteration types (Figure 4.42). High temperature potassic and advanced argillic assemblages are stable under strongly acid conditions. Moderate temperature potassic, propylitic and low temperature intermediate argillic assemblages are stable under near-neutral to alkaline conditions. Sericitic assemblages can be stable across a range of acidities, from acid to alkaline, and temperature conditions. These relationships are reflected in the alteration rank scheme of Corbett and Leach (1998; Figure 4.41).

Alteration mineral assemblages at Productora have been interpreted to indicate three discrete fluid cooling pathways (Table 4.12; Figure 4.41), however alternative interpretations of fluid chemistry and temperature are also possible. Stage 1 fluids, which formed a quartz-pyrite-cemented breccia with pervasive muscovite alteration, are inferred to have been weakly acidic and cooler than the stage 3 fluids. Stage 3 fluids were more alkaline and higher temperature, stabilising K-feldspar, biotite, tourmaline and magnetite. On cooling, the stage 3 fluids evolved to become weakly acidic and sericite stable, as evidenced by 4B (sulphide-sericite) and 4C veins (illite). Incursion of alkaline fluids is inferred to have formed sub-stage 4A (chlorite), sub-stage 4D (epidote) and stage 5 (calcite) veins. These may have be distal alkaline hydrothermal products of a younger intrusive complex, e.g. Alice or Ruta Cinco, or a non-magmatic (connate?) overprint. Isotopic studies are required to resolve the fluid source(s).

Kaolinite - muscovite - pyrite alteration of the stage 2 breccia (Habanero ore zone), indicates strongly acid, low temperature fluids. The juxtaposition of this strongly acidic, low temperature assemblage (stage 2) against high temperature, alkaline assemblage (stage 3; Figure 4.4) suggests the alteration events were either spatially separated at the time of formation, or the events were separated by considerable time to account for the significant differences in temperature and fluid chemistry. The Habanereo ore zone alteration assemblage is hosted by the stage 2 tectonic breccia (Table 4.11) associated with a major steep fault, and overprints earlier stage 3 tourmaline breccias and veins. It is likely that the fault provided a fluid pathway. The Habanero ore zone assemblage is consistent with argillic alteration (Table 4.13). Acidic fluids associated with the Habanero alteration may have formed as a result of either a cooling brine, where $HCl_{(aq)}$ dissociation is advanced, or vapour condensed into groundwater with disproportionation of contained SO_2 to H_2SO_4 and H_2S, and dissociated HCl and any HF (Giggenbach, 1992; Rye, 1993).

The mineralogy of stage 5 veins (calcite ± chalcopyrite, pyrite) and presence of open space vugs and comb textures indicate formation in a low temperature (220–280°C), shallow environment (300–800 m, <1 km; Hedenquist et al., 2000). These conditions are consistent with the epithermal environment (Hedenquist et al., 2000). The occurrence of epithermal veins adjacent and below the tourmaline-cemented breccias indicates significant exhumation and uplift occurred prior to emplacement of stage 5 veins.

4.10.3 Redox conditions during mineralisation

The redox conditions prevailing in hydrothermal systems can be inferred from the presence or absence of characteristic sulphide, oxide and silicate minerals (Cooke et al., 1996; Cooke et al., 2000). However it should also be noted that, as previously discussed, temperature may also be a key driver for alteration mineralogy changes. At Productora, breccia cement at depth contains magnetite with pyrite and chalcopyrite, whereas in shallower portions of the breccia complex magnetite is only minor (Section 4.4). Fluids in the deeper environment are inferred to have evolved on a path of constant sulphate/sulpide ratio and increasing pH. In the south, chalcopyrite-pyrite (and Au) deposition dominated over magnetite in the shallow breccia facies (Figure 4.33 and Figure 4.34) and the correlation between Cu and Au is high (Table 4.7), indicating co-varying solubility. Fluid evolution in the shallow breccia domains is thus inferred to have been along a trajectory of decreasing SO_4^{2-}/H_2S (i.e., decreasing redox state) and increasing pH (Figure 4.43). Pyrrhotite was only observed as rare blebs in pyrite, therefore the lower limit of fO_2, in the parts of the system observed in this study, is inferred to be at the stability field of pyrrhotite.

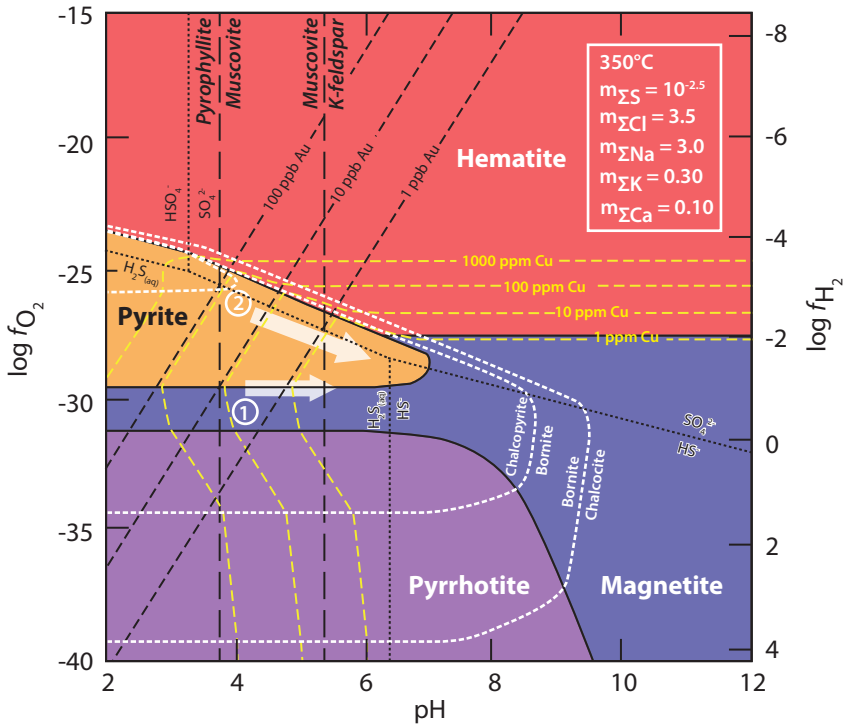

Figure 4.43 fO_2-pH diagram constructed at 350°C (modified from Huston et al. (1993). Mineral stability fields of Fe-oxides and sulphides, K-feldspar, muscovite and pyrophyllite. Gold solubility as $AuCl_2^-$ and Cu solubility as $CuCl^0$. Arrow number one indicates possible evolution of fluids deeper in the breccia complex that precipitated magnetite. Arrow number two indicates evolution of fluids at shallower depth that precipitated chalcopyrite and Au, with only minor magnetite. Calculated from $m_{\Sigma S} = 10^{-2.5}$, $m_{\Sigma Cl} = 3.5$, $m_{\Sigma Na} = 3.0$, $m_{\Sigma K} = 0.30$, $m_{\Sigma Ca} = 0.10$.

4.10.4 Gold deposition

The distribution of Cu and Au at Productora is consistent with porphyry Cu deposits, both in that Cu and Au are closely associated with each other, and that their highest grades occur in the centre of the deposit. In porphyry-Cu deposits, Cu and Au are typically introduced during the earliest stages of alteration and mineralisation (Kesler et al., 2002). Gold in porphyry-Cu deposits, has been observed as 5–100 μm inclusions, overgrowths of electrum and free gold (Baldwin et al., 1978; Cuddy and Kesler, 1982; Tarkian and Koopmann, 1995; Ballantyne et al., 1997; Rubin and Kyle, 1997; Arif and Baker, 2004). Gold occurs in association with sulphide minerals as invisible Au (i.e., within sulphide structure as solid solution), and as inclusions or grains on sulphide grain boundaries, with the latter generally the more common mode of occurence (Kesler et al., 2002). Where bornite is part of the hypogene assemblage, Au shows strong association with bornite (Grasberg, Rubin and Kyle, 1997; Batu Hijau, Arif and Baker, 2004). Where bornite is rare or absent, gold is typically associated with chalcopyrite (Island Copper, Kemess, Pebble and Bajo de Alumbrera; Kesler et al., 2002). At Batu Hijau, invisible Au is less common in chalcopyrite-rich ores, whereas free gold is more common — this is attributed to the lower solubility of Au in chalcopyrite compared to bornite (Arif and Baker, 2004).

Gold deportment in IOCG deposits is less well documented than in porphyry deposits. At the Candelaria-Punta del Cobre district (northern Chile) gold deportment is characterised by tiny inclusions in chalcopyrite, filling of microfractures in pyrite and as Hg-Au-Ag alloys (Ryan et al., 1995; Marschik and Fontbote, 2001). At the Raul-Condestable deposits (southern Peru), gold occurs late in the paragenesis as inclusions in chalcopyrite (Williams et al., 2005). At Ernest Henry (Queensland, Australia) gold was identified primarily as electrum grains with minor solid solution in cobaltite, chalcopyrite and pyrite (Foster et al., 2007). A depositional mechanism of electrochemical deposition of gold as native metal on pyrite was proposed by Foster et al., (2007) for Ernest Henry.

At Productora, gold is predominantly associated with pyrite (e.g., Figure 4.38 and Figure 4.39), with small particles recognised on several pyrite grain boundaries. Only ten individual Au grains were identified by synchrotron XRF analysis, in seven thin sections from Productora. This is insufficient to determine gold's paragenesis. However, the limited results indicate that gold occurs as fine particles on pyrite and chalcopyrite grain boundaries. No evidence of solid solution with pyrite or chalcopyrite was observed. At the synchrotron scan conditions used (section 4.3.9), the detection limit for Au in pyrite was in the order of 60-100 ppm (L. Fisher, pers. comm., 2016).

With regards to depositional mechanisms, the identification of Au grains on the surfaces of pyrite

and chalcopyrite grains indicates two possible scenarios. Either, Au was co-precipitated with sulphide minerals and then subsequently exsolved, or Au was adsorbed directly onto the sulphide mineral surface. Experimental studies and analyses on natural samples indicate that bornite typically contains one order of magnitude more Au in solid solution than chalcopyrite (Simon et al., 2000; Kesler et al., 2002; Arif and Baker, 2004). Gold has been measured in bornite from 0.01–7.99 ppm and chalcopyrite from 0.1–0.5 ppm (Batu Hijau, Kesler et al., 2002; Arif and Baker, 2004). Correlation between average Au content and Cu content for Cu-Fe sulphides is inferred to indicate gold substitutes for Cu in the sulphide (Kesler et al., 2002). Based on the mass balance of average Cu and Au grades in deposits versus Au in solid solution in sulphide minerals, Kesler et al. (2002) concluded that a significant proportion of Au in porphyry Cu deposits must occur as native Au grains.

Adsorbtion-reduction reactions of Au onto sulphide surfaces have also been shown to be an important depositional mechanism under ambient conditions in laboratory studies (Jean and Bancroft 1985; Bancroft and Hyland 1990; Mycroft 1993; Möller and Kerstein 1994; Mycroft et al. 1995; Scaini et al. 1998). Most studies indicate that Au^{3+} in aqueous solution is reduced spontaneously to Au^{1+} on pyrite surfaces, with accompanying oxidation of pyrite, and Au^{1+} reacts with the pyrite again to form metallic gold (Mycroft et al., 1995). Whilst auric species are not proposed at Productora, it has been demonstrated that gold can be deposited in this manner from both bisulphide solutions (Au^{1+}; Scanni et al., 1998) and chloride solutions (Au^{3+}; Mycroft et al., 1995).

The occurrence of Au grains on sulphide grain boundaries has been interpreted to indicate that Au was deposited in solid solution with Cu-Fe sulphides and then exsolved to form grains along grain boundaries (c.f., Cuddy and Kesler, 1982; Gammons and Williams-Jones 1997; Kesler et al., 2002; Arif and Baker, 2004). Experimental studies have shown extensive prograde solid solution of Au at temperatures typical of porphyry Cu deposits (Simmons et al., 2000). Co-precipitation can facilitate Au precipitation from fluids that may have been undersaturated with Au (Gammons and Williams-Jones, 1997). Based on the available data, it is not possible to determine whether Au at Productora was adsorbed onto sulphide surfaces or exsolved following co-precipitation. However, an association with sulphides, both pyrite and chalcopyrite, is evident.

Gammons and Williams-Jones (1997) presented modelling results that support Au being initially transported as $AuCl_2^-$ in high temperature (500 °C, 1 kbar) fluids exsolved from a parent intrusion. Gold solubility in such fluids will decrease steadily on cooling and could lead to precipitation close to source. On cooling to lower temperatures, the dominant metal complex will switch to $Au(HS)_2^-$ if H_2S is present in the hydrothermal fluid, leading to increased Au solubility and therefore dispersion of Au away

from parent intrusion. If H_2S levels are high (pyrite stable) in the initial fluid, the dominant complex will shift to $Au(HS)_2^-$ upon cooling below ~450 °C leading to elevated solubilities throughout the cooling range. This can result in gold being dispersed (Gammons and Williams-Jones, 1997). The correlation of gold and copper with high temperature mineral assemblages at Productora suggests that Au and Cu were precipitated together from chloride complexes (e.g., Figure 4.43). Bisulphide complexed Au would have been deposited distal to the high temperature tourmaline breccia complex.

4.10.5 Supergene environment

Oxide mineralogy at the Productora deposit varies from north to south. In the north, mineralogy is dominated by Cu-bearing silicates, chrysocolla and cuprite. In the south, weathering appears to be less extensive and the proportion of the sulphide phases chalcopyrite and chalcocite is much higher. There is also a lower proportion of Cu-bearing silicates in the south.

The low grade nature of the oxide zone at Productora indicates that significant Cu-leaching has occurred, producing a leached cap at the surface (Figure 4.30). Locally there is evidence for copper addition and in-situ chalcopyrite oxidation. The degree of leaching was largely influenced by the acid-producing sulphides present, neutralizing capacity of host rocks, density of host rock fracturing, and the nature and duration of local and regional weathering conditions (Chávez, 2000). At Productora, pyrite is the most important source of acid solutions responsible for the breakdown of minerals during weathering. The leached cap is evidence that the weathering of pyrite produced fluids that exceeded the neutralising capacity of the host rocks.

The dominant oxide mineral assemblage observed in the north of the deposit, chrysocolla, malachite and Cu-wad (Figure 4.31) is indicative of a geochemically mature system developed under near-neutral to alkaline pH (Chávez, 2000). These conditions are likely the result of depletion of acid-producing pyrite, combined with the buffering capacity of the K-silicate host rocks that neutralised acid solutions by hydrolysis reactions. In the south, the oxide assemblage is less mature (chalcocite-digenite) and indicates in-situ weathering of chalcopyrite. This is consistent with the observed pyrite distribution, as pyrite is more abundant in the south. The high pyrite content of the host rocks resulted in enhanced weathering due to greater acid-forming potential.

4.11 Conclusions

The evolution of the Productora hydrothermal system produced a sequence of hydrothermal breccias, tectonic breccias, veins and alteration assemblages that have been separated into five paragenetic stages: stage 1 quartz-pyrite-cemented breccia, stage 2 chaotic matrix-supported breccia, stage 3 tourmaline breccias, stage 4 phyllic and propylitic veins and stage 5 propylitic veins (Figure 4.3; Table 4.4). Timing relationships have been established by geochronology and cross-cutting relationships.

- The Productora breccia complex has been dated by Re-Os geochronology on molybdenite at 130.1 ± 0.6 Ma (Table 4.10) indicating that the breccia complex is close in age, potentially coeval, with the Cachiyuyito stock (129.8 ± 0.1 Ma; Fox, 2000) and associated sodic-calcic alteration and magnetite-apatite mineralisation. Cross cutting relationships observed by previous authors indicate the Productora system is younger. Further geochronology on the Cachiyuyito stock is recommended

- The new geochronology data indicate that the Productora breccia complex is older (by at least 24 m.y.) than the Ruta Cinco batholith (96.1 ± 0.2 Ma; Fox 2000) and associated propylitic alteration. This disproves the hypothesis that the Productora hydrothermal system is related to the Ruta Cinco batholith (Beeson et al., 2012)

- The Alice porphyry deposit has been dated by Re-Os geochronology on molybdenite at 124.1 ± 0.6 to 122.8 ± 0.6 Ma (Table 4.9 and Table 4.10) and therefore post-dates formation of the Productora breccia complex by approximately 3–7 m.y.

- It is recommended that timing relationships between the Silica Ridge lithocap, Productora breccia complex and Alice porphyry be determined by Ar-Ar dating of alunite.

- Detailed description and interpretation of each breccia stage indicates that the Productora breccia complex consists of at least two stages of hydraulic fragmentation (stage 1 and stage 3) and one tectonic-hydrothermal breccia (stage 2) that shows evidence of multiple episodes of reactivation (Table 4.11). Mineralisation is associated with the stage 3 hydrothermal breccia and stage 2 tectonic-hydrothermal breccia (Habanero).

- Gold deportment studies, by synchrotron XRF, indicate that Au occurs as 4–6.8 μm particles on sulphide grain boundaries (predominantly pyrite; Table 4.8). No solid solution Au was observed at the scan conditions.

- Alteration mineralogy indicates that early hydrothermal fluids at Productora were moderate temperature (<300°–400°C) based on the stage 1 quartz - muscovite assemblage. The

main mineralisation stage, tourmaline breccia event and potassic alteration (stage 3) are associated with high temperature fluids (400°–>600°C), as indicated by tourmaline, biotite and magnetite. Later propylitic and phyllic events (stages 4 and 5) are associated with progressively cooler fluids (<300°C), as indicated by chlorite, epidote and calcite assemblages (Figure 4.40; Figure 4.41; Figure 4.42; Table 4.12).

- Stage 1 fluids, which formed a quartz-pyrite-cemented breccia with pervasive muscovite alteration, are inferred to have been weakly acidic and cooler than the stage 3 fluids. Stage 3 fluids were more alkaline and higher temperature, stabilising K-feldspar, biotite, tourmaline and magnetite. Mineralising fluids then evolved to become weakly acidic (sericite-stable) as evidenced by 4B (sulphide-sericite) and 4C veins (illite). Incursion of alkaline fluids is inferred to have formed sub-stage 4A (chlorite), sub-stage 4D (epidote) and stage 5 (calcite) veins (Figure 4.41; Figure 4.42; Table 4.12).

- The juxtaposition of a strongly acidic, lower temperature assemblage (stage 2, Habanero) and higher temperature, alkaline assemblage (stage 3, tourmaline breccia) suggests the alteration events were either spatially separated at the time of formation, or the events were separated by considerable time to account for the significant temperature and compositional differences.

- The presence or absence of characteristic sulphide, oxide and silicate minerals have been used to infer redox and pH conditions (Figure 4.43). Deep fluids that generated magnetite-pyrite-chalcopyrite assemblages are likely to have evolved at constant sulphate/sulphide ratios and increasing pH. Fluids responsible for chalcopyrite-pyrite (and Au) mineralisation at shallower depths are likely to have evolved along a trajectory of decreasing sulphate/sulphide ratio and increasing pH.

- The dominant supergene mineral assemblage observed in the north of the deposit (chrysocolla, malachite and Cu-wad; Figure 4.31) is indicative of a geochemically mature system developed under near neutral to alkaline pH. In the south the supergene assemblage is less mature (chalcocite/digenite) and indicates in-situ weathering of chalcopyrite.

- Breccia textures and mineralogy as an indicator of paleo-temperature, indicate a temperature gradient and increased intensity of brecciation to the south. This is suspected to be proximal to the root zone of the breccia complex, and is potentially a target if seeking the progenator intrusion to the magmatic fluids, which could be a porphyry prospect.

Chapter 5: Modelling mineralogy

5.1 Introduction

Geometallurgy is an emerging cross-disciplinary activity that can be defined as a quantified and spatially constrained approach to ore characterisation in terms of processing performance (Williams and Richardson, 2004). The term 'geometallurgy' was first referenced in the open-pit mining textbook by McQuiston and Bechaud (1968) who cited the need to understand geology before mine development (Hoal, 2008). Geometallurgy is becoming recognised as a discrete and high value activity where economic optimisation of mining is a key outcome (Walters, 2008). Through integration of a range of existing disciplines, predominantly economic geology, mine engineering and mineral processing, the primary aim of geometallurgy is to provide constrained inputs for resource modelling, reflecting inherent geological variability that impacts on metallurgical performance in order to reduce technical risk (Walters, 2008).

The industrial application of geometallurgy can be described as a 'geometallurgical program' which can be broken down into eight steps (Figure 5.1). A significant weakness in current geometallurgical programs is that only a small number of samples are sent for metallurgical testing. These samples are intended to represent large tonnages of ore, resulting in a dilemma where the full variability of ore, in terms of metallurgical response, must be known to select representative samples, but this information is invariably lacking (Lamberg, 2011).

There has been a focus in recent research on the development of new rock measurement and analysis techniques which can be performed quickly and cheaply (e.g. GeM Comminution Index, JK Rotary Breakage Tester; Kojovic et al., 2010). These techniques fall into three areas: a) techniques measuring physical rock properties, b) techniques of quantitative mineralogy and c) geometallurgical tests. This research aims to advance techniques in quantitative mineralogy through mathematical modelling and machine learning, using commonly available chemical assay and geological logging data.

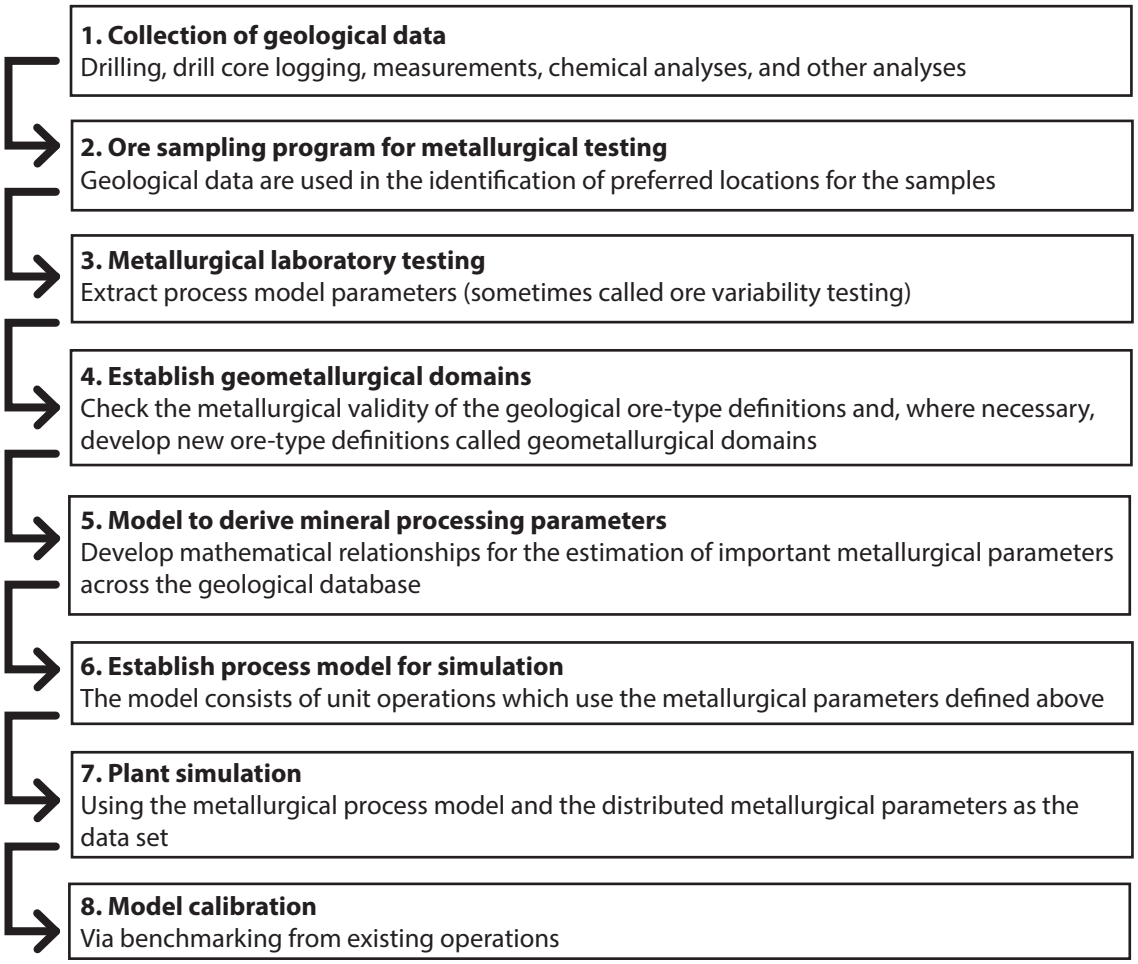

Figure 5.1 Steps of a geometallurgical program, modified from Lamberg (2011).

Mineralogy is a fundamental characteristic for a given rock mass throughout the mining chain, from blasting, through valuable phase extraction to waste management (Hoal, 2008). Understanding mineralogy of the bulk rock, including both the gangue and valuable component (i.e. Cu-bearing minerals of Productora), is critical when making predictions on processing characteristics, such as mill throughput or acid generation/neutralisation potential. These characteristics inform important decisions about processing method, mill flow sheet design, mill sizing and waste management strategies. Throughout the exploration and resource development process, mineralogical data are collected mostly in a qualitative manner through the visual logging of rock types and alteration styles. These datasets are subjective and commonly inconsistent. Current methods for estimating bulk mineralogy are slow and expensive, particularly where mineralogy is complex and variable. Subsequently, quantitative estimates of mineralogy are typically only performed on a small number of 'representative' samples (Lamberg, 2011), chosen to span the range of grade, rock types and alteration styles leading to the dilemma described above. During scoping and project definition studies, predictions of mine performance are made from the extrapolation of this limited dataset. The most important and risk prone decisions are made during project infancy when the least metallurgy data is available. Predictions of mine performance can be

improved where estimates of mineral abundance are extensive (Hunt et al., 2008).

The collection of multi-element geochemical data has become routine for many companies in the minerals industry with 33 element packages by four acid digest and inductively coupled plasma atomic emission spectroscopy (ICP-AES) analysis available in 2015 for as little as $20.95 per sample (excluding sample preparation; ALS, 2015). Large amounts of multi-element geochemical data, commonly on every assay interval, are predominantly used by geologists for exploration and resource development purposes. Translating this geochemical information into mineral proportions through calculated mineralogy can make these data more accessible and amenable to metallurgists and mining engineers who are interested in understanding rock properties and mineralogical variability across a deposit (Hoal, 2008).

In chapters 5 and 6, two strategies for predicting mineralogy amenable to project assessment are presented. In this chapter calculated modal mineralogies are determined from chemical assays. In chapter 6 a new method for predicted Cu species classification (oxide, transitional, sulphide) is presented.

5.2 Data

The work in this chapter draws heavily on multi-element geochemical data (by ICP-AES; provided by Hot Chili Ltd with the Productora drill hole database) and a data set of semi-quantitative X-ray diffraction (QXRD) analyses, collected specifically for the purpose of this study. The acquisition of QXRD data is discussed in this chapter whereas the drill hole data base is discussed in Chapter 1. Through numerical modelling techniques, outlined in sections 5.5 and 5.6, new mineralogical datasets have been developed from the available geochemical and QXRD data in order to understand mineralogical variability at Productora.

5.3 Calculated mineralogy

Traditionally, modal analysis of mineralogy has been done through visual methods such as point counting and image analysis (Leinonen, 1998; Liipo et al., 2004; Donskoi et al., 2007, 2008; Hunt et al., 2008; Lane et al., 2008;). More recently X-ray point counting using SEM-EDS based software has been used widely (Gu, 2003; Fandrich et al., 2007; Lund and Martinsson, 2008; Forrest, 2009; Hoal et al., 2009; Oghazi et al., 2009; Lund et al., 2010). Common commercial packages include Mineral Liberation Analysis (MLA) or Quantitative Evaluation of Minerals by Scanning Electron Microscopy (QEMSCAN). However, these methods are not well suited to the routine analysis of bulk samples at normal assay spacing because they are too slow and expensive. QXRD is a more widely applied method of estimating major minerals (Helle, 2005; Knorr, 2011), particularly in the iron ore industry where

mineralogy is simple and the process is more readily automated. However, with a nominal detection limit of 0.5 % (Omotoso et al., 2006) this method has limited applications when dealing with low abundance minerals. Where mineralogy is complex, the QXRD method is less efficient, as each spectra must be manually interpreted for optimum results (pers. commun., Sharon Ness, 2015).

Calculating mineralogy from chemical assays provides a fast and cost effective alternative method to estimating bulk mineralogy. The resulting large dataset, related to small sample volumes, provides a more effective statistical approach to defining natural variability than a small number of measured data points (Walters, 2008). The element-to-mineral conversion by calculating mineralogy is a mathematical mass process where the bulk chemical composition of a sample is transformed to mineral quantities. In its simplest form, this can be expressed by the equation:

$$A^{*}x = b$$

where A is from a table giving the weight fractions of elements in the minerals (known), the x vector is the weight fractions of the minerals in a sample (unknown) and the b vector is the weight fraction of elements in the sample (known value; Lund et al. 2013; Dephaine and Filippov, 2015).

Mineralogy calculations from assay data are most commonly used in the field of petrology where traditional modal mineralogy methods are not possible, for example due to fine grain size. The MINSQ method of Herrman and Berry (2002) is a simple least squares approach suitable for limited sample numbers where the number of major minerals estimated is less than the number of elements analysed. The method is suitable where samples are few in number and well characterised. Recent examples of the application of MINSQ to petrology include Avchenko (2014), Duan (2014), Galán and Oliveras (2014), Abdioğlu et al. (2015), Denis et al. (2015) and Novoselov and de Souza Filho (2015). Other examples include the work of Gentilii et al. (2015) who presented a comparison of Rietveld X-ray powder diffraction refinement method to results from the MODAN program (Paktunc, 1998) of least squares calculated mineralogy also with respect to petrology applications. Tolosana and Delgado (2011) developed a novel geometric-Bayesian calculated mineralogy approach with a case study to reconstruct the mineralogy of fluvio-glacial sediments and McLemore et al. (2009) applied MODAN (Paktunc, 2001) in a geometallurgy context to samples from a molybdenum mine to assess weathering effects with respect to geotechnical slope stability. Application of calculated mineralogy to iron ore geometallurgy has been presented in combination with QXRD (Parian et al., 2015) and QEMSCAN (Lund et al., 2013). Dephaine and Filippov (2015) attempt quantitative clay mineral analysis using simultaneous linear-equations method of Johnson et al. (1985) in order to estimate kaolin grades for geometallurgical

modelling and assessment of by-product potential. Only one example of the development, and application of a complex deposit-scale calculated mineralogy, for a geometallurgical study at the La Colosa deposit, Colombia (Montoya et al., 2011), was found in the literature at the time of writing.

The current study applies the linear programming and Simplex method (Press et al. 1968), as outlined by Berry et al. (2015) to the Productora Cu-Au-Mo deposit. The method enforces non-negativity and has no practical limit to the number of minerals modelled. A training set of known mineralogy is required. In this case a training set of QXRD data were compiled. To overcome the problems of high detection limits, which limit the representation of low abundance minerals in the training data set, QXRD data have been combined with chemical assay data through a weighted least squares correction, following the methods of Berry et al. (2011).

5.4 Mineralogy by semi-quantitative X-ray diffraction (QXRD)

5.4.1 Method

A total of 625 laboratory pulp reject samples were selected from two cross sections through the Productora Cu-Au-Mo deposit at 6,822,215 mN and 6,820,850 mN (Figure 5.2). Samples were selected from every eighth 1 m interval of the selected drill holes. Samples were submitted to Genalysis Laboratory Services Pty Ltd. (Perth, Australia) for QXRD analysis. Sub-samples of approximately 20 grams were crushed to an average particle size of 4 μm and prepared as un-oriented powder mounts. The X-ray diffraction

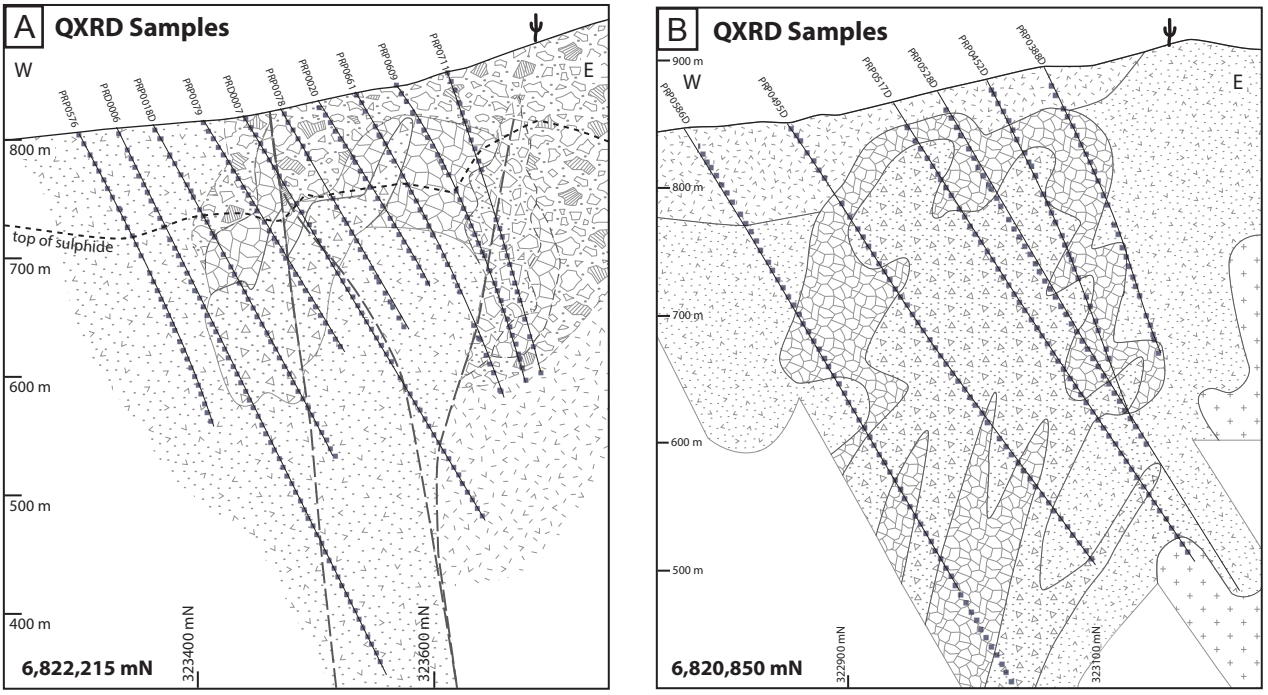

Figure 5.2 Cross sections to show the drill holes from which 625 QXRD samples were collected across study sections A) 6,822,215 mN and B) 6,820,850 mN. Samples were collected every eight meter down hole.

Table 5.1 Absolute error estimates for QXRD analysis (Ness, 2014; Appendix 4.1).

Phase abundance	Absolute Error
50 - 95 wt%	±10 %
10 - 50 wt%	±5 %
3 - 10 wt%	±2 %
0.5 - 3 wt%	Approaching detection limit
0.5 wt%	Typical detection limit (dependent on phase crystallinity)

(XRD) spectra were generated on a PANalytical Cubix3 XRD fitted with a PIXCEL solid state detector and copper radiation (operating at 45 kV and 40 mA). The XRD apparatus was configured with a graphite monochromator in the diffracted beam and fixed slits. Qualitative analysis was performed using the Bruker Diffrac.EVA 3.2 Search/Match software with the ICDD PDF-2 (2011) database. Rietveld quantitative phase analysis, for crystalline phases only, was performed using SIROQUANT® Version 4 software (Ness, 2014; Appendix D1). The detection limit was 0.5 wt %, with absolute errors as in Table 5.1. Clay mineralogy for nine samples was confirmed by clay separation, followed by measurement of oriented clay mounts prepared by air drying, glycolating and heat treatment (Lebedeva, 2014; Appendix D2).

5.4.2 Results

A total of 52 minerals were recognised via individual analysis of each spectra by laboratory staff. Minerals identified in the clay sized fraction (<2 μm) included chlorite, illite-muscovite, kaolinite, montmorillonite, vermiculite and biotite. Of the mineral suite detected (Table 5.1), four minerals were only present below the nominal detection limit of the technique (<0.5 wt%). Nineteen had low abundances, approaching detection limit (0.5–3 wt%). The remaining twenty-nine were present in abundances greater than 3 wt%. Minerals reported at levels below 0.5 wt% were assigned a value of half detection limit (0.25 wt%). Minerals which were not detected in the spectra (i.e. null), were assigned 0 wt%.

A number of rare unusual minerals were also identified in low abundance, and in some cases at low confidence due to low level reflections or overlapping signals (Table 5.1). These were excluded from the mineral list for further work. Several rare minerals were also identified. Of these, only the minerals with significant maximum abundances were included in the results.

It was noted that peak overlap occurred between boehmite and molybdenite (S.Ness, pers. comm., 2015). Molybdenite was observed during core logging, whereas boehmite was not observed. The boehmite and molybdenite values in the raw QXRD results were therefore summed together as ‘molybdenite’.

Table 5.2 Summary statistics of 625 QXRD results listed in order of decreasing number of occurrences greater than 0 wt%.

Mineral	Count >0 wt%	Max wt%	Mean wt%	Range wt%	Standard Deviation	Included in modelling
Major minerals						
Quartz	625	91.00	28.30	91	13.3	Yes
K-feldspar	595	72 .00	23.16	72	17.5	Yes
Illite-muscovite	557	55 .00	11.34	55	11.4	Yes
Albite	519	65 .00	15.45	**65**	17.0	Yes
Chlorite	444	23 .00	3.60	23	3.66	Yes
Pyrite	412	11 .00	1.59	11	2.05	Yes
Magnetite	332	13 .00	0.85	13	1.57	Yes
Tourmaline	281	29 .00	2.41	29	4.16	Yes
Chalcopyrite	264	6 .00	0.36	6	0.69	Yes
Biotite	208	40 .00	3.01	40	5.80	Yes
Kaolinite	206	37 .00	1.70	37	3.81	Yes
Calcite	192	7 .00	0.51	7	1.14	Yes
Mixed clay (illite-montmorillonite)**	169	35 .00	1.05	35	2.60	Yes
Montmorillonite	134	23 .00	0.71	23	2.18	Yes
Molybdenite	122	2 .00	0.09	2	0.24	Yes
Amphibole	113	36 .00	1.08	36	3.88	Yes
Common minerals						
Hematite	91	13 .00	0.22	13	0.83	Yes
Epidote	75	25 .00	0.55	25	1.99	Yes
Ca-Na-plagioclase	63	62 .00	3.32	62	10.90	Yes
Anhydrite	49	7 .00	0.12	7	0.57	Yes
Ankerite	48	2 .00	0.07	2	0.27	Yes
Jarosite	41	6 .00	0.09	6	0.49	Yes
Gypsum	32	5 .00	0.07	5	0.38	Yes
Uncommon minerals						
Pyroxene	23	5 .00	0.08	5	0.43	Yes†
Vermiculite	23	13 .00	0.12	13	0.88	Yes†
Andalusite	21	4 .00	0.06	4	0.40	Yes†
Goethite	21	16 .00	0.09	16	0.77	Yes
Corundum	19	8 .00	0.11	8	0.71	
Apatite	17	3 .00	0.04	3	0.25	Yes
Pyrophyllite	17	11 .00	0.07	11	0.58	Yes†
Rare minerals						
Dolomite	8	2 .00	0.01	2	0.13	Yes
Anthophyllite	7	5 .00	0.03	5	0.34	Yes†
Siderite	6	2 .00	0.01	2	0.12	Yes
Talc	5	14 .00	0.05	14	0.78	Yes†
Perovskite***	4	2 .00	0.01	2	0.10	
Cristobalite	4	3 .00	0.01	3	0.12	
Marcasite	3	1 .00	0.00	1	0.07	

Table 5.2 continued.

Mineral	Count >0 wt%	Max wt%	Mean wt%	Range wt%	Standard Deviation	Included in modelling
Pyrope	3	2 .00	0.01	2	0.14	
Copper (native)	2	0.25	0.00	0.25	0.01	Yes
Alunite	2	1 .00	0.00	1	0.04	
Chrysocolla****	2	0.25	0.00	0.25	0.01	Yes
Obscure minerals						
Dioptase	1	0.25	0.00	0.25	0.01	
Isocubanite	1	1 .00	0.00	1	0.04	
Analcite*	1	1 .00	0.00	1	0.04	
Bassanite*	1	1 .00	0.00	1	0.04	
Lepidocrocite*	1	1 .00	0.00	1	0.04	
Barite	1	1 .00	0.00	1	0.04	
Kinoite	1	1 .00	0.00	1	0.04	
Fayalite	1	1 .00	0.00	1	0.04	
Forsterite	1	3 .00	0.00	3	0.12	
Malachite	1	2 .00	0.00	2	0.08	

* Possibly present due to either low level reflections or overlapping reflections from another phase.** The mixed layer clay varies in composition with a broad major reflection varying from 13.0Å - 10.4Å. *** There is a small peak present at 2.69Å which may be due to perovskite (possibly) or hematite. These samples did not exhibit any red tinge so this reflection has been assigned to the perovskite phase. **** Possibly present but not quantified using Rietveld method due to lack of suitable crystallographic data - estimated concentration only. † included in weighted least squares correction only.

Muscovite and illite could not be distinguished individually with the scan conditions used in this study. They are therefore reported as 'illite-muscovite'. Similarly a broad major reflection varying between 13.0 Å and 10.4 Å is denoted as 'mixed clay', most likely a combination of illite and montmorillonite. Different clinoamphiboles (e.g. tremolite, hornblende) also cannot be distinguished in these scans and are reported as 'amphibole'.

5.4.3 Discussion

The QXRD results indicate that altered volcanic rocks at Productora are dominated by quartz, K-feldspar, albite and illite-muscovite, which all occur in more than 500 of the 625 samples studied (Figure 5.3 and Table 5.1). Quartz content is typically between 20 and 34 wt%, but ranges up to 91 wt%. K-feldspar has the largest interquartile range of 30, from 7 to 37 wt%. Albite is significantly more abundant (detected in 519 samples at 15 wt% on average) than calcic plagioclase, which was only detected in 63 samples at an average at 3 wt%, locally up to 62 wt%. Chlorite, pyrite, magnetite and tourmaline were commonly detected in low abundances (Table 5.1), but with some far outliers. Biotite was regularly detected with a mean of 3 wt% and a number of far outliers up to a maximum of 40 wt%.

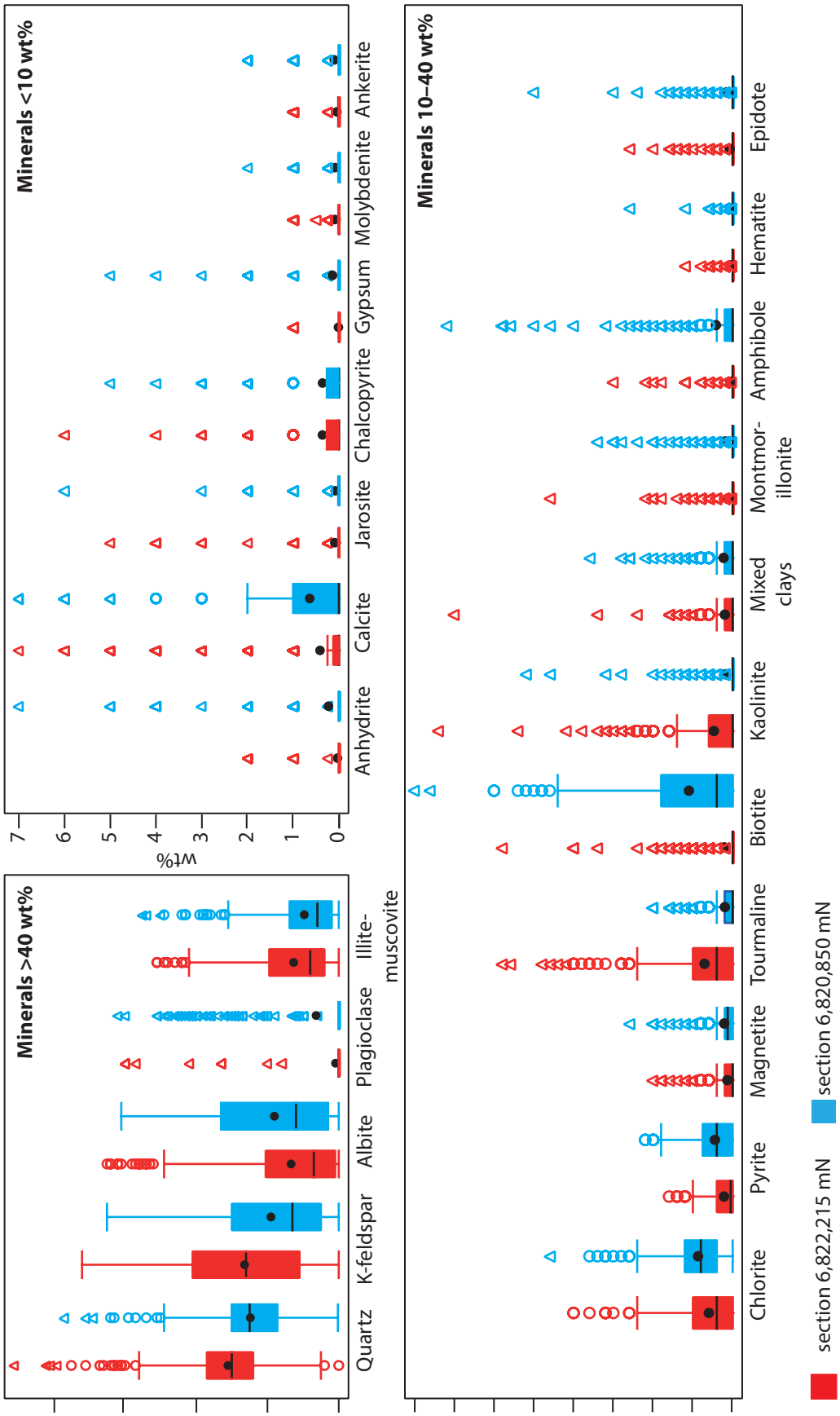

Figure 5.3 Tukey box plots showing wt% minerals measured by QXRD. Plots colour coded by the cross section location of samples (red = 6,822,215 mN, blue = 6,820,850 mN). Mean = black dot, median = black horizontal line.

Pyrite is the most abundant sulphide and chalcopyrite was the most commonly detected Cu-Fe sulphide phase, although it was below detection limit in 401 samples. Molybdenite was detected in 122 samples. Kaolinite is the most common and abundant clay in the sample set, followed by mixed clays and montmorillonite. Vermiculite, a mica-group mineral, is uncommon. Calcite is the most common carbonate mineral, although ankerite was detected in 48 samples. The sulphates anhydrite, jarosite and gypsum were detected in up to 49, 41 and 32 samples respectively (Table 5.1).

The major mineralogy of samples from the northern section (6,822,215 mN) is elevated in quartz, K-feldspar and muscovite relative to the southern section (6,820,850 mN), where there are higher abundances of total plagioclase (albite plus calcic plagioclase; Figure 5.3). The southern section also has significantly higher biotite, chlorite, pyrite, amphibole and calcite abundances. Samples from the northern section contain more tourmaline and kaolinite.

5.5 QXRD data correction by weighted least squares

In order to overcome some of the limitations of QXRD analysis that ensue with low mineral abundances, QXRD data can be combined with chemical assays through a weighted least squares process, as described by Berry et al. (2011). This method aims to find the model mineralogy that is consistent with chemical analysis and is also as close as possible to the QXRD results. It enables a complex and broad range of minerals to be robustly estimated, with high abundance minerals determined by QXRD measurements and low abundance minerals estimated from the chemical assays.

5.5.1 Method

The weighted least squares calculation used here employs the non-linear Solver® routine available in Microsoft Excel®. Estimated mineral abundances are limited to ≥0 wt% (non-negative constraint) and ≤100 wt%, so as to ensure models are physically possible. The calculation incorporates all major and minor elements from the assay data and additional constraints from QXRD analyses. Models are also weighted by an estimate of measurement error on all parameters.

A macro written for Microsoft Excel has enabled the calculation process to be automated for large volumes of samples. The macro copies the input data (measured chemistry and QXRD) from a data sheet into the calculating sheet, activates Solver, and then copies the estimated mineralogy into an answer sheet (Appendix D3). The calculation spreadsheet is set up to perform the following five tasks for each sample:

1) Calculate the predicted error for each chemical analysis and QXRD analysis
   Predicted error = measured value * relative error (%) /100 + absolute error (%)
   Relative error is estimated to be 6 % for QXRD and 3 % for ICP-AES (Table 5.3).

2) Estimate modal mineralogy
   The initial estimate for the solver routine is based largely on the measured QXRD values.

3) Calculate the 'normalised residuals' for mineralogy and chemistry
   Normalised residual is the difference between the mineral estimate and the actual, from chemical analysis or QXRD, normalised by the estimated standard deviation.

4) Calculate the sum of normalised residuals squared (residual SSQ)
   This is the target for Solver which aims to find the minimum value through varying the mineral abundances of the listed phases, between 0 and 100 (unless otherwise indicated).

5) Solver varies the estimated mineralogy repeatedly until the sum of normalised residuals squared (step 4) is minimised.

In order to force the calculation to match the QXRD more closely, particularly for low abundance and or rare minerals that do not have a unique controlling element in their chemistry, such as calcite and anhydrite, the estimate of absolute error of the QXRD measurement was reduced from 0.5 % to 0.1 %. This in turn reduced the calculated standard deviation and ultimately inflated the normalised residual if the estimate did not closely match the measured value. Minerals where this modification was applied include: calcite, ankerite, anhydrite-gypsum, dolomite, anthophyllite, epidote, jarosite, talc, chrysocolla, vermiculite, andalusite, pyrophyllite and pyroxene.

The four acid ICP-AES data does not include Si, CO_2 or H_2O. These have therefore all been included as 'other' analysed elements in the calculations. For each mineral the percentage of non-analysed elements is equal to 100 minus the sum of analyses elements. This then requires an "other minerals" class to be

Table 5.3 Relative and absolute error used in weighted least squares correction calculation (following suggestions in Berry et al., 2011).

Measurement Error	Relative	Absolute
QXRD	6 %	0.50 %
ICP-AES	3 %	0.02 %

included in the analysis. This includes all minerals that have no analysed elements in them. While this could include many trace minerals, the dominant mineral in this class is quartz.

It is assumed that at a 4 μm grain size, the QXRD sample material can be considered homogenous. Sampling error due to the chemical assay being performed on a separate sub-sample to the QXRD was not quantified, but is assumed to be included in the 6% (one sigma) relative error estimate. If the sampling errors were much larger the chi-squared fit to the data should be low and in general this was not the case. About 8 % of sample calculations were rejected with a probability of fit less than 10 % (<10 % arbitrarily indicates unacceptable poor fit whereas >10 % is acceptable). This may be due to underestimating sampling errors, but it could also be that the mineral list was not appropriate for these samples.

5.5.1.1 Mineral compositions for calculations

Mineral compositions used in both the weighted least squares correction of the QXRD data and in the linear programming model were compiled from literature and electron microprobe analyses of available minerals (Table 5.4 and Table 5.5; Appendix D4). Mineral compositions from the electron microprobe were validated by calculating the formula units and comparing them to stoichiometry of the mineral (Table 5.6). To account for minerals which have variable compositions (solid solution), end member compositions were included in the linear programming mineralogy calculations.

5.5.2 Results

A total of 36 minerals were included in the weighted least squares calculation (Appendix D5). Results are robust with over 90 % of samples having a probability of fit of greater than 0.1 (calculated as right-tailed probability of a chi-squared distribution). There were 48 samples (7.8 % of training set) with poor fit, probability of fit <0.1. Most of the samples with low probability of fit were from the southern cross section (6,820,850 mN).

5.5.3 Discussion

Application of the weighted least squares correction to raw QXRD data has provided a robust estimate of mineralogy for both abundant and minor phases (Figure 5.4). Comparison of the weighted least squares corrected data (WLSQ) against the raw QXRD data is used to identify problem areas in both data sets, particularly with regard to phases that have abundances close to QXRD detection limits. Minerals present in high abundance, such as quartz, feldspars, micas and clays show good correlation between

Table 5.4 Mineral compositions used to estimate mineral abundance from assay data and QXRD using weighted least squares method. 'Other' is equal to 100 minus sum of elements listed and is assumed to be largely SiO_2 as well as volatiles such as CO_2 and H_2O. Compiled from Dana and Hurlbut (1971), Deer et al. (1992), stoichiometry and this study.

Mineral	Al %	As %	Ba %	Ca %	Cu %	Fe %	K %	Mg %	Mn %	Mo %	Na %	P %	S %	Ti %	U %	Other %
Actinolite	1.56	0.00	0.00	8.72	0.00	12.71	0.10	8.07	0.09	0.00	0.20	0.00	0.00	0.06	0.00	68.49
Hornblende	5.05	0.00	0.00	8.27	0.00	10.31	0.59	8.23	0.23	0.00	0.83	0.00	0.00	0.41	0.00	66.08
Andalusite	33.30	0.00	0.00	0.00	0.00	0.00	0.00	0.00	0.00	0.00	0.00	0.00	0.00	0.00	0.00	66.70
Anhydrite	0.00	0.00	0.00	29.44	0.00	0.00	0.00	0.00	0.00	0.00	0.00	0.00	23.55	0.00	0.00	47.01
Ankerite	0.00	0.00	0.00	20.02	0.00	12.55	0.00	6.07	0.00	0.00	0.00	0.00	0.00	0.00	0.00	61.36
Anthophyllite	1.12	0.00	0.00	0.69	0.00	11.57	0.04	23.97	0.25	0.00	0.24	0.00	0.00	0.21	0.00	61.91
Apatite	0.00	0.00	0.00	39.06	0.00	0.00	0.00	0.00	0.00	0.00	0.00	18.18	0.00	0.00	0.00	42.77
Arsenopyrite	0.00	46.00	0.00	0.00	0.00	34.30	0.00	0.00	0.00	0.00	0.00	0.00	19.70	0.00	0.00	0.00
Barite	0.00	0.00	58.84	0.00	0.00	0.00	0.00	0.00	0.00	0.00	0.00	0.00	13.74	0.00	0.00	27.42
Biotite	7.37	0.00	0.00	0.14	0.00	13.04	7.35	8.21	0.07	0.00	0.08	0.00	0.00	0.92	0.00	62.82
Calcite	0.00	0.00	0.00	40.04	0.00	0.00	0.00	0.00	0.00	0.00	0.00	0.00	0.00	0.00	0.00	59.96
Chalcocite	0.00	0.00	0.00	0.00	79.85	0.00	0.00	0.00	0.00	0.00	0.00	0.00	20.15	0.00	0.00	0.00
Chalcopyrite	0.00	0.00	0.00	0.00	34.50	30.50	0.00	0.00	0.00	0.00	0.00	0.00	35.00	0.00	0.00	0.00
Chlorite	9.68	0.00	0.00	0.11	0.00	20.33	0.02	9.36	0.08	0.00	0.05	0.00	0.00	0.02	0.00	60.38
Dolomite	0.00	0.00	0.00	21.73	0.00	0.00	0.00	13.18	0.00	0.00	0.00	0.00	0.00	0.00	0.00	65.09
Epidote	12.53	0.00	0.00	16.53	0.00	9.49	0.00	0.02	0.18	0.00	0.00	0.00	0.00	0.00	0.00	61.25
K-feldspar*	9.85	0.00	0.25	0.00	0.00	0.08	13.50	0.00	0.03	0.00	0.31	0.00	0.00	0.03	0.00	75.95
Plagioclase	15.37	0.00	0.00	7.89	0.00	0.20	0.14	0.00	0.00	0.00	3.85	0.00	0.00	0.00	0.00	72.54
Albite (An0)	10.40	0.00	0.00	0.00	0.00	0.04	0.24	0.02	0.00	0.00	8.21	0.00	0.00	0.00	0.00	81.09
Jarosite	0.00	0.00	0.00	0.00	0.00	33.45	7.81	0.00	0.00	0.00	0.00	0.00	12.81	0.00	0.00	45.93
Kaolinite	20.75	0.00	0.00	0.04	0.00	0.16	0.17	0.04	0.00	0.00	0.07	0.00	0.00	0.05	0.00	78.72
Magnetite	0.00	0.00	0.00	0.00	0.00	72.35	0.00	0.00	0.00	0.00	0.00	0.00	0.00	0.00	0.00	27.65
Molybdenite	0.00	0.00	0.00	0.00	0.00	0.00	0.00	0.00	0.00	59.90	0.00	0.00	40.10	0.00	0.00	0.00
Muscovite	19.50	0.00	0.00	0.00	0.00	0.08	8.37	0.05	0.09	0.00	0.47	0.00	0.00	0.00	0.00	71.44
Phengite*	16.46	0.00	0.00	0.00	0.00	3.19	9.14	0.81	0.00	0.00	0.08	0.00	0.00	0.10	0.00	70.22
Chrysocolla	2.05	0.00	0.00	0.00	33.86	0.00	0.00	0.00	0.00	0.00	0.00	0.00	0.00	0.00	0.00	64.09
Pyrite	0.00	0.00	0.00	0.00	0.00	46.59	0.00	0.00	0.00	0.00	0.00	0.00	53.40	0.00	0.00	0.01

*this study

Table 5.4 continued from previous page.

Mineral	Al %	As %	Ba %	Ca %	Cu %	Fe %	K %	Mg %	Mn %	Mo %	Na %	P %	S %	Ti %	U %	Other %
Pyrophyllite	14.98	0.00	0.00	0.00	0.00	0.00	0.00	0.00	0.00	0.00	0.00	0.00	0.00	0.00	0.00	85.02
Pyroxene	0.00	0.00	0.00	17.25	0.00	12.02	0.00	5.23	0.00	0.00	0.00	0.00	0.00	0.00	0.00	65.50
Quartz	0.00	0.00	0.00	0.00	0.00	0.00	0.00	0.00	0.00	0.00	0.00	0.00	0.00	0.00	0.00	100.00
Smectite-montmorillonite	9.44	0.00	0.00	0.49	0.00	2.23	0.37	1.87	0.02	0.00	1.61	0.00	0.00	0.04	0.00	83.93
Titanite	0.00	0.00	0.00	20.44	0.00	0.00	0.00	0.00	0.00	0.00	0.00	0.00	0.00	24.47	0.00	55.09
Talc	0.00	0.00	0.00	0.00	0.00	0.00	0.00	19.23	0.00	0.00	0.00	0.00	0.00	0.00	0.00	80.77
Tourmaline*	13.07	0.00	0.00	1.43	0.00	9.21	0.04	5.23	0.00	0.00	1.26	0.00	0.00	1.51	0.00	68.25
Uraninite	0.00	0.00	0.00	0.00	0.00	0.00	0.00	0.00	0.00	0.00	0.00	0.00	0.00	0.00	88.15	11.85
Vermiculite	8.13	0.00	0.00	0.00	0.00	5.60	0.00	13.62	0.00	0.00	0.00	0.00	0.00	0.00	0.00	72.65

*this study

Table 5.5 Mineral compositions measured on samples from Productora by electron microprobe analysis. Compositional data was used in weighted least squares correction of raw QXRD data, in linear programming models and for mineral stoichiometry calculated from microprobe data.

Mineral	Si	Ti	B	Al	V	Cr	Fe	Ni	Mn	Mg	Ca	Ba	Na	K	Cl	F	O	H	Total
Albite	31.37	<0.02	0.00	10.41	0.03	<0.03	0.05	<0.02	<0.01	0.01	0.38	<0.03	7.80	0.11	0.08	<0.31	47.93	0.00	98.17
K-feldspar[1]	29.42	0.03	0.00	9.85	<0.02	<0.03	0.08	<0.02	0.03	<0.01	<0.07	0.25	0.31	13.50	0.12	<0.32	45.22	0.00	98.70
Muscovite (phlogopite)	22.18	0.10	0.00	16.46	<0.02	<0.03	3.19	<0.02	<0.01	0.81	<0.07	<0.02	0.08	9.14	0.06	<0.38	47.28	0.50	99.79
Muscovite (phengite)	21.83	0.03	0.00	17.66	<0.03	<0.03	1.78	<0.02	<0.01	0.55	<0.07	<0.01	0.11	8.57	<0.03	<0.38	47.29	0.50	98.33
Tourmaline (dravite)	16.80	0.24	3.33	18.03	0.05	<0.03	2.38	0.04	<0.01	5.69	0.45	<0.02	1.46	0.01	<0.04	<0.44	50.96	0.40	99.83
Tourmaline (schorl)	16.13	1.51	3.15	13.07	0.18	<0.04	9.21	<0.02	<0.01	5.23	1.43	<0.02	1.26	0.04	<0.04	<0.45	48.25	0.37	99.83

[1]average K-feldspar value

Table 5.6 Mineral stoichiometry calculated from microprobe data.

Mineral	Pure formula	Microprobe formula estimate
Albite	$NaAlSi_3O_8$	$Ca_{0.05}Na_{0.95}AlSi_3O_8$
K-feldspar (Ba-bearing)	$KAlSi_3O_8$	$K_{0.97}Na_{0.025}Ba_{0.005}AlSi_3O_8$
Phengite	$K(Al,Mg)_2(Si,Al)_4O_{10}(OH,F)_2$	$(K_{0.93}Na_{0.01}4X_{0.53})(Fe_{0.1}Mg_{0.065}Al_{0.835})_2(Si_{0.79}Al_{0.19}X_{0.02})O_{10}(O_{0.5}5H_{0.99},F_{0.39})_2$
Schorl (Fe-Tourmaline)	$NaFe^{2+}{}_3Al_6(BO_3)_3Si_6O_{18}(OH)_4$	$Na_{0.5}Fe_{1.6}Mg_2Al_{4.9}(BO_3)_3Si_6O_{18}(OH)$

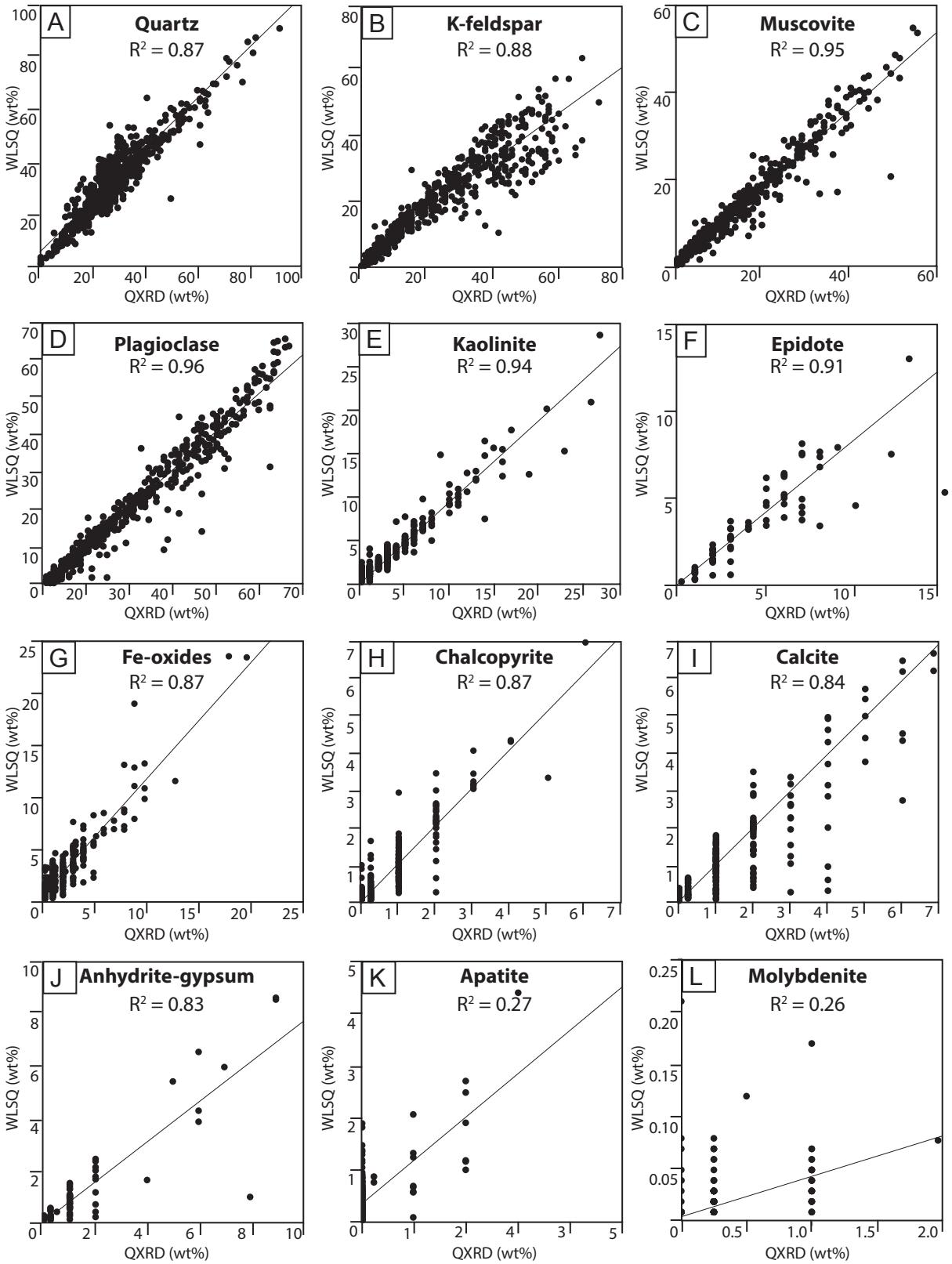

Figure 5.4 Results of weighted least squared correction of QXRD data (WLSQ) plotted against raw QXRD data for a selection of the 36 minerals calculated. A) Quartz. B) K-feldspar. C) Muscovite (including illite). D) Plagioclase (including sodic and calcic plagioclase). E) Kaolinite. F) Epidote. G) Fe-oxides (magnetite, hemetite and goethite). H) Chalcopyrite. I) Calcite. J) Anhydrite and gypsum. K) Apatite. Molybdenite. Minerals with low abundance, such as molybdenite and apatite, are poorly represented by the raw QXRD data which has relatively high detection limit (0.5 wt%), hence the relationship between WLSQ and QXRD is poor.

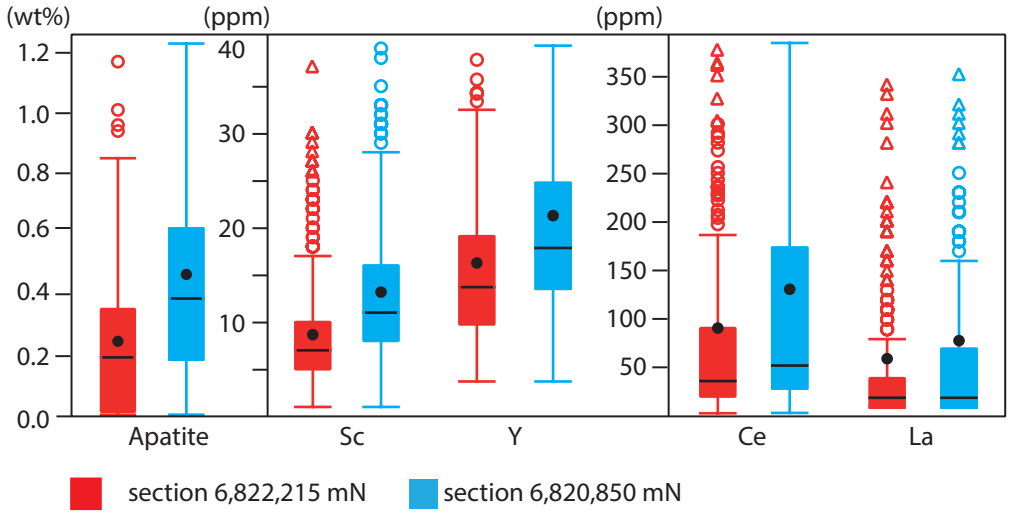

Figure 5.5 Tukey box plot, scaled to regular data, showing WLSQ corrected QXRD apatite data with rare earth elements Sc, Y, Ce, and La (from drill hole database provided by Hot Chili Ltd.) by cross section. Apatite and rare earth elements are more abundant in samples from section 6,820,850 mN. Mean = black dot, median = black horizontal line.

QXRD and WLSQ (Figure 5.4), indicating that the QXRD data are compatible with the chemical analysis of the sample interval.

For lower abundance phases, the correlation between QXRD and WLSQ is poor (Figure 5.4 K and L). This is predominantly due to the high detection limits associated with the QXRD method (Omotoso et al., 2006). For example, molybdenite was commonly not detected by QXRD (Table 5.1), but Mo is present in the chemical analyses (ore reserves include 166.9 Mt @ 138 ppm Mo, Hot Chili Ltd., 2016). Where molybdenite is detected by QXRD, it is predominantly overestimated relative to the concentration of Mo detected by chemical assay. As there is only one known Mo-bearing phase in the deposit, the WLSQ result is a better representation of the abundance of molybdenite at Productora than the QXRD. This is due to the detection limit for Mo in the multi-element geochemical assays (1 ppm or 0.0001 %) being much lower than the QXRD detection limit (0.5 wt%). Similarly apatite is underestimated in QXRD relative to the available P and Ca in chemical assays. In many samples, there is sufficient P to form over 0.5 % apatite, where none was detected by QXRD. Potentially, other rare earth phosphates may also exist, such as anhydrous phosphates, monazite or xenotime. However the available rare earth element (REE) assay data (Ce, La, Sc, Y) suggest REE-phosphates cannot account for majority of the P content. Most of the higher apatite contents come from the southern section and coincide with elevated rare earth element concentrations (Figure 5.5), which suggest a minor component of rare earth phosphates is likely. Without further mineralogical information for minor P-bearing phases, WLSQ data for apatite is considered more accurate than the raw QXRD.

A number of samples (approximately 12 % of data points) have QXRD estimates of K-feldspar higher than can be modelled by K assay values (Figure 5.4 B). Potentially some of the alkali feldspars have

higher Na than the model composition (Table 5.4) and as a result were modelled as albite instead of K-feldspar. This variation is not unreasonable, particular with consideration to the challenges of estimating K-feldspar by QXRD given the variety of potential structural states (adularia, sanidine, orthoclase or microcline).

Approximately 5 % of samples have lower calcite estimates by WLSQ than by QXRD. This is likely to be due to the limitations of QXRD to differentiate between the different carbonate phases. Potentially, there may be more ankerite and dolomite at Productora than suggested by the QXRD results.

5.6 Calculating mineralogy from chemical assay

Modal mineralogy can also be calculated from chemical assay data through linear programming and the Simplex method (Press et al., 1986) using Solver in Microsoft Excel (Berry et al., 2011; Berry et al., 2015). A major benefit of the linear programming method is that there is no practical limit to the number of minerals considered. In addition, non-negativity can be enforced, unlike alternative simple least squares models (Bryan et al., 1969; Le Maitre, 1981; Paktunc, 1999, 2001; Herrman and Berry, 2002) that require more chemical constraints than calculated mineral phases, and in most cases allow negative mineral abundances (Berry et al. 2015). A list of minerals present and their compositions must be provided for linear programming to be applied. A training set is also required, which can be established through QXRD (as in this study) or other independent methods (e.g. SEM point counting).

5.6.1 Linear programming

The linear programming method (also known as linear optimization) aims to maximise a linear objective function based on the proportional sum of a 'property value' of each mineral listed (Berry et al., 2011). This requires user input in order to optimise the property values for each mineral. The property value acts as a proxy for the likelihood of the mineral occurring, with higher values for common minerals and low or negative values for rare minerals. Independent geological information on the mineralogy is required for these property values to be set correctly. In this case the 625 sample QXRD training set corrected against chemical assay by weighted least squares (section 5.5) was used to train the model and establish appropriate property values. Calculated mineral abundances are limited to ≥0 % and ≤100 % in order to ensure results are physically possible. Additional constraints can also be applied to limit upper mineral abundances as required.

The linear program used is from Solver in Microsoft Excel. Using a suitable mineral list and compositions appropriate for the Productora deposit (Table 5.7), an Excel macro enables the program to be automated.

A worked example of the macro-enabled spreadsheet is provided in Appendix D6). The calculation can be broken down into the following process in Solver:

1) Find a feasible solution (i.e. combination of minerals) for which the residuals (i.e. residual element abundances) are zero.

2) Calculate the objective function for the feasible assemblage.
   Objective function = sum product (property value * estimated mineral abundance).

3) Maximise objective function while meeting the restriction that the assemblage is feasible.
   The best estimate of mineralogy is achieved when the objective function is maximised, this is the target for Solver.

Phases modelled are listed in Table 5.7. A number of impossible pure end-members for selected elements (As, Ba, Ca, K, Mg, Na, Mn) were also included in order to ensure that it is always possible to find a feasible solution, including where an unknown phase or solid solution exists.

Phases detected by QXRD but not modelled in this section include corundum, goethite, pyrophyllite, andalusite, and talc. They only occur rarely and have chemical compositions which are not readily distinguished from other phases. For example, andalusite (Al_2SiO_5) and pyrophyllite ($Al_2Si_4O_{10}(OH)_2$) are dominated by Al and Si that are common in most other silicate minerals making it difficult to determine when they do and do not occur as these elements are invariably always present. Other minerals excluded from the model include vermiculite and pyroxene as the chemical composition of these minerals also makes their occurrence difficult to predict and therefore difficult to control in the linear programming calculation.

Minerals that have compositions which cannot be differentiated by the available chemical data were combined. These include:

- Gypsum-anhydrite: gypsum ($CaSO_{4.2}H_2O$) and anhydrite ($CaSO_4$)
- Mixed clay: mixed illite ($(K_{0.6}(H_3O)_{0.4}Al_{1.3}Mg_{0.3}Fe^{2+}_{0.1}Si_{3.5}O_{10}(OH)_2 \cdot (H_2O)$ and montmorillonite ($((Na,Ca)_{0.33}(Al,Mg)_2(Si_4O_{10})(OH)_2 \cdot nH_2O$)
- Fe-oxide: magnetite ($Fe^{3+}_2Fe^{2+}O_4$) and hematite ($Fe^{3+}_2O_3$)

A total of 15 elements (Al, As, Ba, Ca, Cu, Fe, K, Mg, Mn, Mo, Na, P, S, Ti, U) were selected to use in

Table 5.7 Minerals included in the linear programming model and their compositions. Compiled from Dana and Hurlbut (1971), Deer et al. (1992), stoichiometry and this study.

Phase	Al %	As %	Ba %	Ca %	Cu %	Fe %	K %	Mg %	Mn %	Mo %	Na %	P %	S %	Ti %	U %	Other
Other (quartz)	0	-	-	-	-	-	-	-	-	-	-	-	-	-	-	100
Ca-Na-albite	10.41	-	-	0.38	-	0.05	0.11	0.01	-	-	7.80	-	-	-	-	81.24
Na-albite	10.40	-	-	-	-	0.04	0.24	0.02	-	-	8.21	-	-	-	-	81.09
K-feldspar	9.82	-	-	0.12	-	0.10	13.34	-	-	-	0.13	-	-	-	-	76.50
K-feldspar (Ba-bearing)	9.85	-	0.25	-	-	0.08	13.50	-	0.03	-	0.31	-	-	0.03	-	75.95
Plagioclase	15.37	-	-	7.89	-	0.20	0.14	-	0.01	-	3.85	-	-	-	-	72.55
Calcite	-	-	-	40.04	-	-	-	-	-	-	-	-	-	-	-	59.96
Ankerite	-	-	-	20.02	-	12.55	-	6.07	-	-	-	-	-	-	-	61.36
Dolomite	-	-	-	21.73	-	-	-	13.18	-	-	-	-	-	-	-	65.09
Anhydrite-gypsum	-	-	-	29.44	-	-	-	-	-	-	-	-	23.55	-	-	47.01
Chlorite (Fe-rich)	9.68	-	-	0.11	-	20.33	0.02	9.36	0.08	-	0.05	-	-	0.02	-	60.38
Chlorite (Mg-rich)	10.09	-	-	0.04	-	10.52	0.03	14.37	0.04	-	0.03	-	-	0.03	-	64.85
Muscovite	19.50	-	-	-	-	0.08	8.37	0.05	0.09	-	0.47	-	-	-	-	71.44
Muscovite - phengite	16.46	-	-	-	-	3.19	9.14	0.81	-	-	0.08	-	-	0.10	-	70.22
Biotite (Mg-rich)	7.54	-	-	0.02	-	7.91	7.86	11.83	0.05	-	0.07	-	-	1.01	-	63.70
Biotite (Fe-rich)	7.37	-	-	0.14	-	13.04	7.35	8.21	0.07	-	0.08	-	-	0.92	-	62.82
Actinolite	1.56	-	-	8.72	-	12.71	0.10	8.07	0.09	-	0.20	-	-	0.06	-	68.49
Hornblende	3.42	-	-	8.63	-	11.26	0.43	8.03	0.48	-	0.78	-	-	0.53	-	66.44
Tremolite	0.93	-	-	9.32	-	6.38	0.07	11.46	0.12	-	0.21	-	-	0.08	-	71.44
Epidote	12.53	-	-	16.53	-	9.49	-	0.02	0.18	-	-	-	-	-	-	61.25
Epidote (clinozoisite)	17.81	-	-	17.64	-	-	-	-	-	-	-	-	-	-	-	64.55
Magnetite	-	-	-	-	-	72.35	-	-	-	-	-	-	-	-	-	27.65
Apatite	-	-	-	39.06	-	-	-	-	-	-	-	18.18	-	-	-	42.77
Chalcopyrite	-	-	-	-	34.50	30.50	-	-	-	-	-	-	35.00	-	-	-
Pyrite	-	-	-	-	-	46.59	-	-	-	-	-	-	53.40	-	-	0.01
Uraninite	-	-	-	-	-	-	-	-	-	-	-	-	-	-	88.15	11.85
Arsenopyrite	-	46.00	-	-	-	34.30	-	-	-	-	-	-	19.70	-	-	-
Molybdenite	-	-	-	-	-	-	-	-	-	59.90	-	-	40.10	-	-	-

Phase	Al %	As %	Ba %	Ca %	Cu %	Fe %	K %	Mg %	Mn %	Mo %	Na %	P %	S %	Ti %	U %	Other
Chalcocite	-	-	-	-	79.85	-	-	-	-	-	-	-	20.15	-	-	-
Titanite	-	-	-	20.44	-	-	-	-	-	-	-	-	-	24.47	-	55.09
Rutile	-	-	-	-	-	-	-	-	-	-	-	-	-	59.96	-	40.04
Barite	-	-	58.84	-	-	-	-	-	-	-	-	-	13.74	-	-	27.42
Kaolinite	20.75	-	-	0.04	-	0.16	0.17	0.04	-	-	0.07	-	-	0.05	-	78.72
Smectite-montmorillonite	9.44	-	-	0.49	-	2.23	0.37	1.87	0.02	-	1.61	-	-	0.04	-	83.93
Jarosite	-	-	-	-	-	33.45	7.81	-	-	-	-	-	12.81	-	-	45.93
Tourmaline (schorl)	13.07	-	-	1.43	-	9.21	0.04	5.23	-	-	1.26	-	-	1.51	-	68.25
Tourmaline (dravite)	18.03	-	-	0.45	-	2.38	0.01	5.69	-	-	1.46	-	-	0.24	-	71.74
Native-Cu	-	-	-	-	10.00	-	-	-	-	-	-	-	-	-	-	-
Chrysocolla	2.05	-	-	-	33.86	-	-	-	-	-	-	-	-	-	-	64.09

the calculated mineralogy models based on their abundance in the drill hole assay database (Figure 5.6). Only elements that occur at greater than 0.1 wt% in at least one sample, and which can be reconciled against minerals from the QXRD or petrographic reports, were included. Elements that only rarely were detected in abundances greater than 0.1 wt% but were not used in the model include Co, Cr, La, Ni, Pb, Sb, Sc, Sr, Th, V, W and Zn. For example, Ni occurs locally at concentrations up to 0.4 wt% but on average is only 0.004 wt%. Because no obvious Ni-rich phases were identified in the QXRD results, Ni was not included in the model.

5.6.2 Cluster analysis

A significant limitation of the linear programming method used in this study is that each sample has been treated the same regardless of the degree of weathering, or of the composition. This effectively masks variability in the mineralogy, because the linear programming mineralogy calculation applies the same property values and rules to all samples, even where this may not be appropriate, for example weathered samples are generally likely to have more clays than non-weathered samples. Because the modal mineralogy calculations are being used in an attempt to highlight variability, it is desirable to avoid the masking effect of applying a single global model. To remedy this problem, the dataset has been split into discrete groups which can be modelled separately. A number of parameters were available on which the data set could be divided, including logged weathering, lithology, alteration and geochemistry.

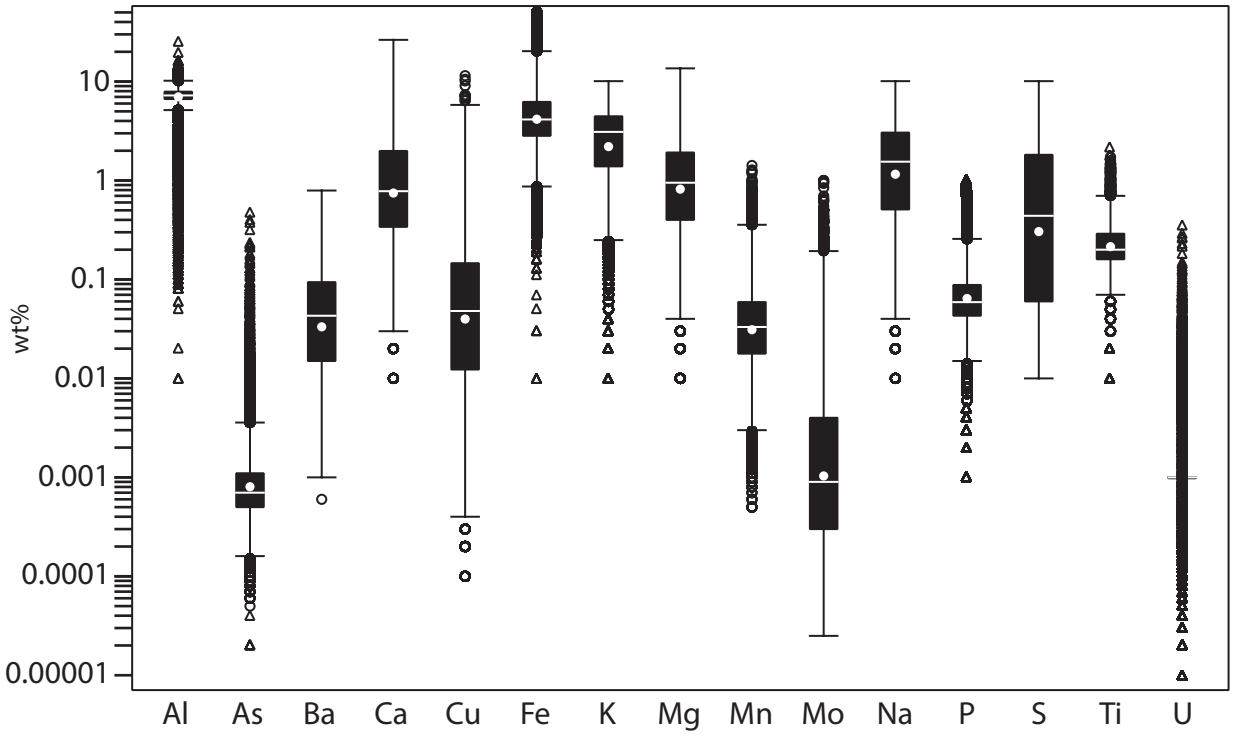

Figure 5.6 Tukey box plot showing most abundant elements from entire drill hole database (data provided by Hot Chili Ltd.). These elements were used in the linear programming modelling. Mean = white dot, median = white horizontal line.

In this study weathering (as recorded by geological logging in the Hot Chili Ltd drill hole database) and geochemistry were used.

A key aim of the calculated modal mineralogy is to identify which samples are likely to have high clay contents, either through weathering or due to hypogene clay alteration. Logged 'weathering' was used to isolate samples suspected of high clay content (kaolinite and smectite) as a result of weathering. This was validated using the available WLSQ data, which indicates that samples logged as oxide or transitional are generally more clay-rich (Figure 5.7).

In order to identify fresh samples rich in hypogene clay (mostly kaolinite) a cluster analysis of the weighted least squares corrected data (WLSQ; 625 samples) was performed using the ioGAS® version 6.1 K-Means clustering tool. Major rock-forming-mineral abundances from WLSQ (total plagioclase, total amphibole, total clay, total muscovite, tourmaline, quartz, chlorite, biotite and K-feldspar) were used for cluster analysis. These generated a good separation in the cluster groups and also enabled the clusters to be rationalised and validated against the logging results and the geology model. Three discrete groups defined on major mineralogical variables were identified (Figure 5.8). These populations were validated using principle component analysis, histograms, box plots and bivariate discrimination plots of WLSQ mineralogy and logged lithology (Appendix D7).

Comparison of the cluster groups against logged lithology and multi-element alteration index indicates that the Group 1 (blue) cluster in Figure 5.8 is predominantly associated with intermediate composition rocks and undifferentiated breccia with sodic-calcic alteration assemblages more typical of distal locations to ore. Least altered samples and smectite-rich samples also plot in this group. The Group 2 (orange) cluster is mostly associated with tourmaline-breccias that have K-feldspar and sericite alteration. The Group 3 (pink) cluster includes some tourmaline breccias together with felsic intrusive rocks and

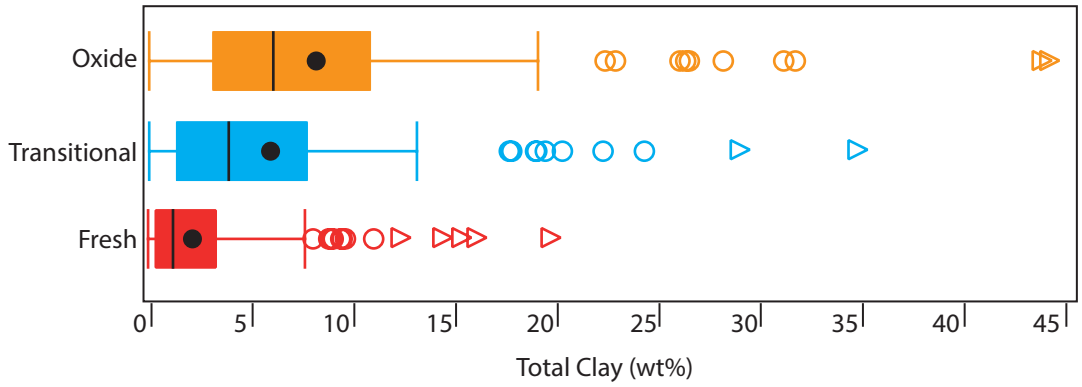

Figure 5.7 Tukey box plot show total clay content of samples logged as oxide, transitional or fresh (logging data from drill hole database provided by Hot Chili Ltd.). Sampels logged by geologists as oxide or transitional have a higher mean clay content than samples logged as fresh. However, fresh samples also have high clay content in some instances - potentially due to hypogene clay alteration. Mean = black dot, median = black horizontal line.

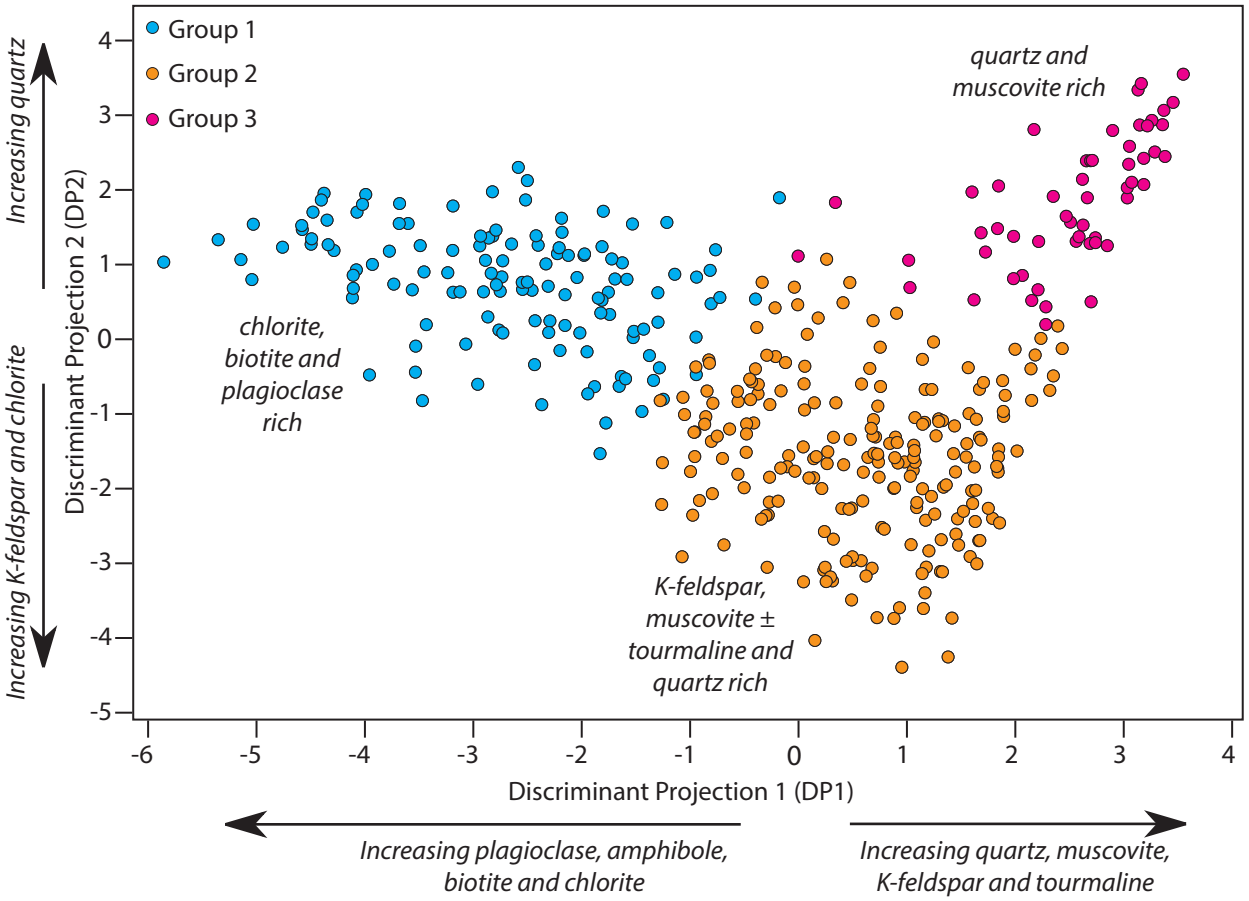

Figure 5.8 Discriminant projection of classified samples. Three clusters were derived from major mineralogy using K-means clustering.

Table 5.8 Summary of the characteristics of the three groups defined by logged weathering and K-means cluster analysis of fresh samples in the training set.

Population/ group	Rock type	Alteration minerals	Mineralogy	Clay content	n
Weathered				Average 7.2 wt% Smectite > Kaolinite	225
Group 1 Distal alteration	Intermediate-mafic; undifferentiated breccia	Albite, sodic-calcic, magnetite-amphibole and background/least altered	Plagioclase, amphibole, chlorite, biotite	Average 1.6 wt% Smectite > Kaolinite	130
Group 2 Deep proximal alteration	Tourmaline-cemented breccias	K-feldspar Sericite-albite	K-feldspar, quartz, tourmaline, chlorite,	Average 2.3 wt% Kaolinite > Smectite	216
Group 3 Shallow proximal alteration	Tourmaline-cemented breccias; felsic intrusive rocks; intermediate volcaniclastic rocks	Sericite K-feldspar	Quartz, muscovite	Average 2.7 wt% Kaolinite >> Smectite	54

intermediate volcaniclastic lithologies that have undergone sericite and K-feldspar alteration – there is generally a higher kaolinite content in these samples.

5.6.3 Discriminant projection analysis

The three clusters described above were identified using WLSQ data available on 625 samples. In order to classify all other samples in the drill hole database into one of the three groups, discriminant functions were calculated. Discriminant functions were calculated from 16 variables in the assay data using ioGAS® version 6.1 'Discriminant Projection Analysis' (DPA) tool. The discriminant functions were then applied to near pit samples (between 6,820,400—6,822,700 mN and 322,600—324,000 mE) through a classification diagram. Both of these methods are detailed in Appendix D8.

Approximately one third of the database was classified as 'weathered' (which included all samples logged as oxide or transitional; Figure 5.9). Another third was categorized in Group 2 (Figure 5.9) and the remainder as Group 1 or Group 3. Group 3 had the smallest population (Figure 5.9). The spatial distribution of the sample groupings (Figure 5.10) indicates that there are more Group 3 samples in the north and east of the deposit. The Group 1 samples are more common on the fringes of Productora, particularly to the north and west. The weathering profile is deeper beyond the planned pit outline but relatively consistent across the width of the deposit (Figure 5.10).

5.6.4 Composition dependant calculated mineralogy by linear programming

In order to most effectively encapsulate mineralogical variability across the deposit, the chemical assay database was divided into compositional groups based on logged weathering features combined with a discriminant projection analysis. A separate linear programming model was developed with variable property values and clay limits (Table 5.9) based on the available training set for each of the compositional groups (Table 5.8). Each model was developed through an iterative process of varying the property values and comparing the results to the training set until the best solution was found. Final models are a compromise, whereby major minerals with geometallurgical implications are prioritised over other minerals which are inherently difficult to model. For example, it was difficult to model amphiboles with carbonate minerals and biotite as over estimate of carbonate minerals did not allow for enough Ca for actinolite or tremolite, and hornblende was created at the expense of biotite. Similarly, in order to generate tourmaline the model did not produce enough chlorite or biotite.

The four linear programming models were applied to the respective chemical assay data sets, as determined by the discriminant project analysis. All results were merged into one database where each assay interval

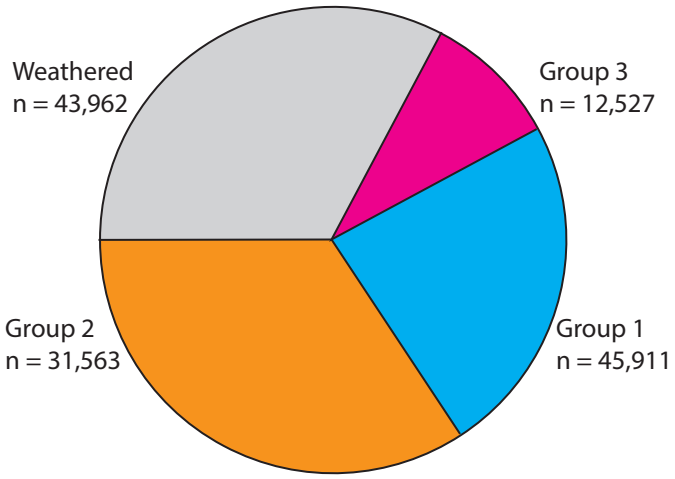

Figure 5.9 Pie chart showing distribution of drill hole database samples between the compositional groups identified by discriminant projection analysis for calculated mineralogy models. Most samples fall into the weathered group or group 2. Group 3 has the smallest population of samples.

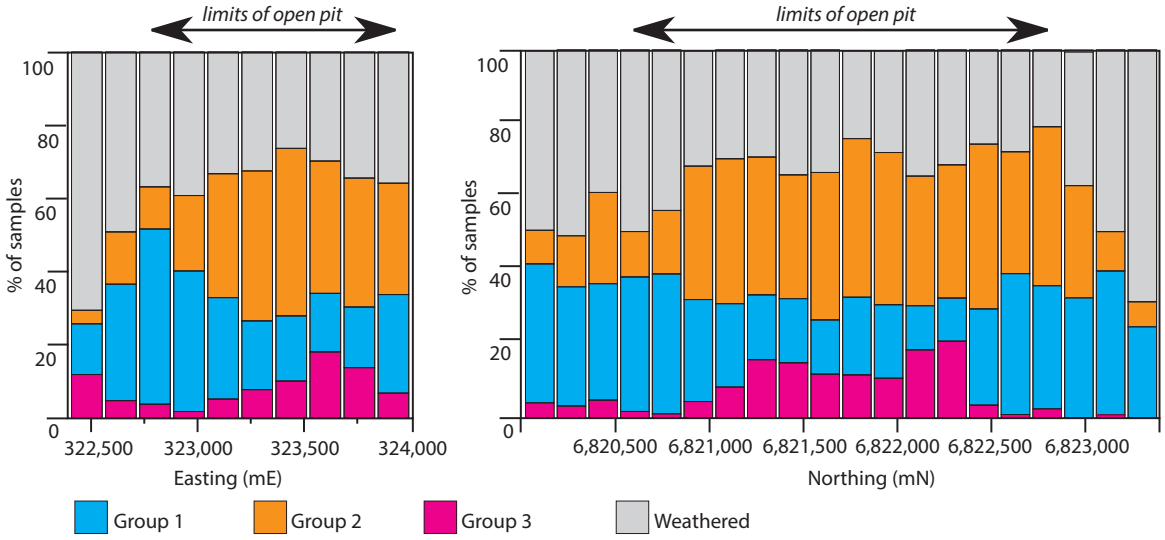

Figure 5.10 Bar graphs to show spatial distribution of compositional groups defined by discriminant projection analysis. Left, percentage of samples by easting. Right, percentage of samples by northing. Limits of the open pit design (March 2014 version) shown by arrows.

has a calculated modal mineralogy. A simpler approach was also tested whereby a single global model was developed and applied to the whole database. Model constraints are outlined in Appendix D9.

5.6.4.1 Results

Comparison against measured mineralogy

A total of 38 minerals were modelled by linear programming using geochemical data for 15 elements analysed by four acid digest and ICP-AES (Figure 5.6, Figure 5.11, Appendix D10). Four separate compositional groups (weathered, group 1, group 2 and group 3) were identified and an individual linear programming model developed for each.

Table 5.9 Property values applied to each mineral and upper threshold limits to calculated clay content for each of the four composition dependant linear programming models for calculated mineralogy.

Phase	Oxide-Transitional	Group 1	Group 2	Group 3
		Property values		
Other (quartz)	7	7	7	7
Ca-Na-albite	5	5	5	5
Na-albite	5	5	5	5
K-feldspar	7	7.5	7	7
K-feldspar (Ba-bearing)	7	7.1	7	7
Plagioclase	3	7	3	3
Calcite	0.3	1.5	0.3	0.3
Ankerite	5.7	5	5.4	5.7
Dolomite	3	0	3	3
Anhydrite/gypsum	1.3	0.5	1.3	1.3
Chlorite (Fe-rich)	10	10	10	10
Chlorite (Mg-rich)	10	10	10	10
Muscovite	7	8.9	7.1	7
Muscovite - phengite	4	9.4	5	4
Biotite (Mg-rich)	9	8.5	9	9
Biotite (Fe-rich)	9	8.5	9.5	9
Actinolite	8	6.9	8	8
Hornblende (Mg-rich)	7.5	6.6	7.5	7.5
Tremolite	6	5.9	6	6
Epidote	4	4	4	4
Epidote (clinozoisite)	3	3	3	3
Magnetite	7	7	7	7
Apatite	10	10	10	10
Chalcopyrite	8	8	8	8
Pyrite	5	5	5	5
Uraninite	10	10	10	10
Arsenopyrite	10	10	10	10
Molybdenite	10	10	10	10
Chalcocite	6	6	6	6
Titanite	2	2	2	2
Rutile	-1	-1	-1	-1
Barite	-1	-1	-1	-1
Kaolinite	7.1	10.8	7.2	7.2
Smectite-montmorillonite	7.2	8.2	7.2	7.2
Jarosite	5.0	5.0	5.0	5.0
Tourmaline (schorl)	7.5	7.5	7.5	7.5
Tourmaline (dravite)	6	6	6	6
Native Cu	-100	-100	-100	-100
Chrysocolla	0	0	0	0
As	-100	-100	-100	-100
Ba	-100	-100	-100	-100

Table 5.9 continued.

Phase	Oxide-Transitional	Group 1	Group 2	Group 3
Ca	-100	-100	-100	-100
K	-100	-100	-100	-100
Mg	-100	-100	-100	-100
Na	-100	-100	-100	-100
Mn	-100	-100	-100	-100
Additional Constraints				
Kaolinite upper limit (%)	7	1	4	7
Smectite upper limit (%)	7	2	4	7

Overall the results of the mineralogy calculations are excellent, with most major minerals, including quartz, K-feldspar, albite, pyrite, iron oxides, chalcopyrite and molybdenite, matching the weighted least squares corrected QXRD (WLSQ) data extremely well (R^2 values greater than 0.8; Figure 5.11 and Table 5.10). The correlation between calculated muscovite, biotite and chlorite results with the WLSQ data is poorer, due to compositional similarities between these minerals, particularly between biotite and chlorite which results in one mineral being made at the expense of the other in the numerical models. Consequently it has proven preferable to interpret the sum of these minerals (total chlorite and micas) rather than the individual minerals (Figure 5.11). Despite these challenges, the numerical modelling results provide a good indication of the range in the abundance of chlorite and mica, which is important for geometallurgical applications, as these phyllosilicate minerals can cause problems for flotation when present in high (> 30 wt%) abundance (Berry et al., 2014).

The clay and carbonate minerals proved the most challenging to model, and produced poor results overall with correlation coefficients of <0.1 (Figure 5.11) and 0.51 (Appendix D10) respectively (Table 5.10). The calculations tend to either radically over-estimate clay content at the expense of feldspars and mica, or under-estimate clay. This problem was addressed by applying upper limits, informed by the measured training dataset, to the amount of each clay mineral allowed in the modelled results (Table 5.9). Carbonate minerals (calcite, ankerite and dolomite) as well as anhydrite-gypsum were also difficult to model due to their similar chemistries and because there are no data available for volatile phases in the ICP-AES database. The results for some minor minerals, specifically apatite and titanite-rutile, have excellent correlations due to their distinctive chemistry compared to other low abundance minerals found at Productora.

Tourmaline, amphibole, epidote and jarosite proved difficult to model. Despite tourmaline being a major mineral, its abundance proved very difficult to predict due to the lack of boron analyses. Apart from boron, the tourmaline major element components are similar to other calcium-iron-magnesium rich phases such as amphibole. Similarly the abundance of epidote and jarosite has proven difficult to

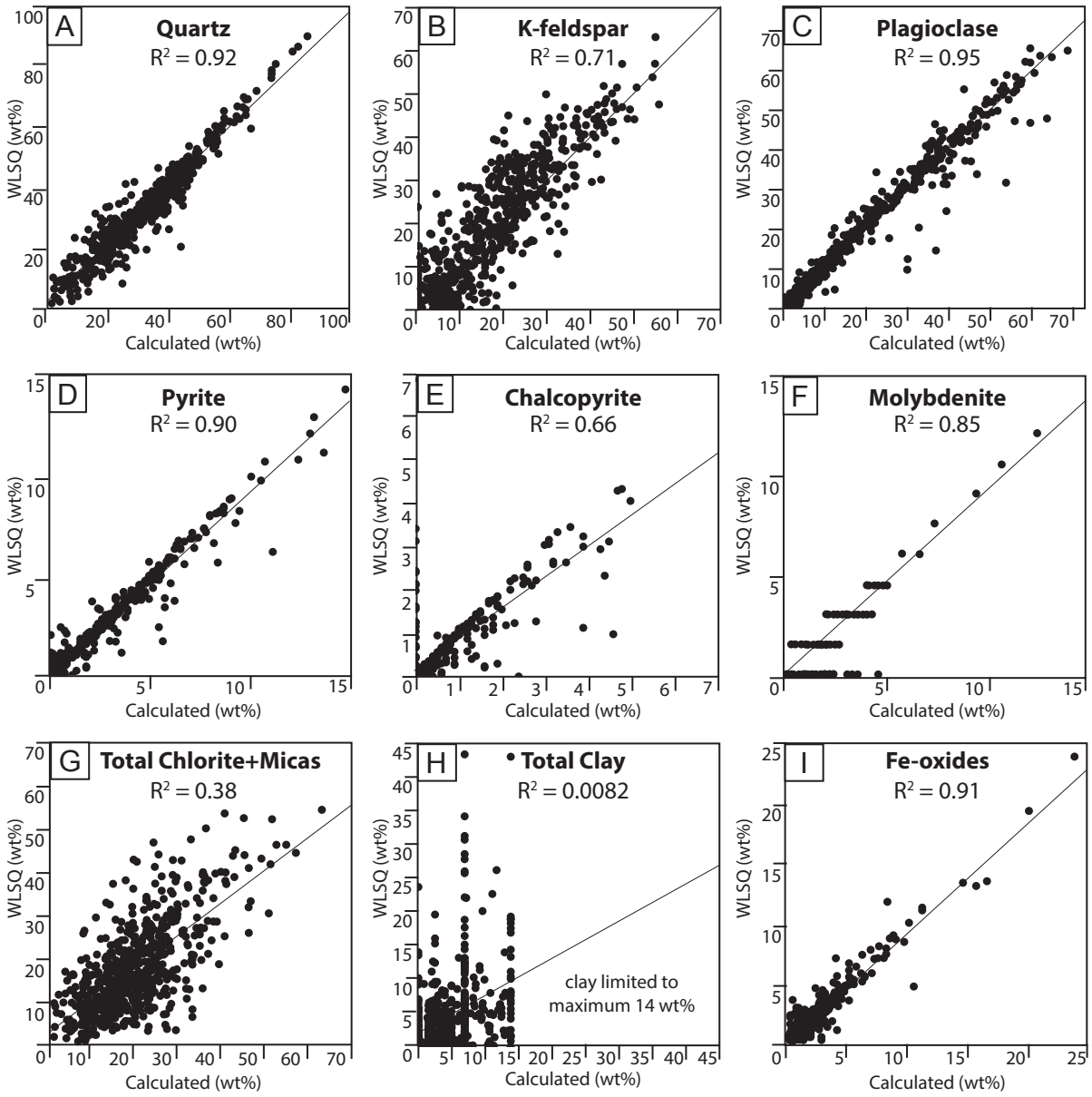

Figure 5.11 Comparison of calculated mineralogy, by composition dependent linear programming, against measured mineralogy, from QXRD data corrected against chemical assay by weighted least squares (WLSQ). Regression line and R^2 also shown. A) Quartz. B) K-feldspar. C) Plagioclase (including sodic and calcic plagioclase). D) Pyrite. E) Chalcopyrite. F) Molybdenite. G) Total chlorite and micas (including chlorite, muscovite, phengite and biotites). H) Total clay (including kaolinite and smectite-montmorillonite). I) Fe-oxides (including magnetite, hematite, goethite). Major minerals, including quartz, feldspars, pyrite and Fe-oxides show excellent correlation between measured (WLSQ) and calculated (linear programming).

model with respect to other aluminium, calcium and/or iron rich minerals and iron, potassium and/or sulphur minerals respectively.

Several pure elements (As, Ba, Ca, K, Mg, Mn and Na) were included in the modelling calculation to permit valid numerical solutions. The number of times these elements are predicted to occur in significant amounts is a good indication of model failure, where by the mineral list does not cover the range of assay data. Of the near-pit samples (n = 133,963) there were 2202 instances of failure, which equate to a failure rate of 1.64 % (Table 5.11). Most failures were due to excess abundances (>0.5 wt%)

Table 5.10 The R^2 and root mean squared error (RMSE) for major minerals and mineral groups, at the Productora deposit, calculated by linear programming compared to QXRD measured values corrected against chemical assays by weighted least squares (WLSQ). Listed in order of decreasing R^2.

Mineral	R^2	RMSE
Quartz	0.92	4.16
Fe-oxides	0.91	0.75
Pyrite	0.9	0.5
Molybdenite	0.85	0
Titanite + rutile	0.82	0.56
Total feldspars	0.81	7.95
Total plagioclase	0.95	3.04
Total K-feldspar	0.71	7.14
Apatite	0.81	0.21
Total amphibole	0.7	4.46
Chalcopyrite	0.66	0.52
Total carbonate	0.51	1.59
Total chlorite + mica	0.38	8.24
Total chlorite	0.64	0.52
Total Mica	0.36	9.16
Total muscovite	0.43	8.62
Total biotite	0.16	5.05
Jarosite	0.37	0.59
Total epidote	0.31	1.64
Anhydrite/gypsum	0.07	0.76
Tourmaline	0.02	3.68
Total clay	0.01	3.12
Kaolinite	0.06	3.52
Montmorillonite	0.11	3.46

Table 5.11 Instances of model failure where pure elements are generated by the model in greater than 0.2 wt % for major and 0.5 wt % for trace elements.

Major elements	Ca	K	Mg	Na
Count >0.2 wt%	1	985	874	283
Maximum	0.6	5.1	3.4	7.5
Trace elements	**As**	**Ba**	**Cu**	**Mn**
Count >0.5 wt%	0	1	11	47
Maximum	0.1	0.7	1.8	1.4

of the major elements K, Mg, or Na. Together these may indicate that the Al data are too low, as there is not sufficient Al to make any reasonable Na, K or Mg mineral in these two thousand samples. Al is one of the more insoluble elements, and may not have been completely dissolved in the four acid digest. Mn was commonly generated in small amounts, indicating that one or more minerals likely contains trace Mn (e.g. chlorite, epidote, calcite) or a minor Mn phase exists .

Table 5.12 Parameters used for modelling calculated mineralogy data in 3D as interpolants using Leapfrog Geo software.

	Min. N (mN)	Max. N (mN)	Min. E (mN)	Max. E (mE)	Min Elv (m)	Max. Elv (m)
Section 6,822,215 mN	6,822,2175	6,822,250	323,200	323,800	300	950
Section 6,822,215 mN	6,820,800	6,820,880	322,700	323,250	350	950
Deposit-wide model	6,820,400	6,822,700	322,600	324,000	300	1,100
Additional parameters						
Resolution:	12 (cross section model)					
	25 adaptive (deposit-wide model)					
Trend[1]:	Direction	Ellipsoid ratio				
Dip	75	2				
Dip azimuth	285	2				
Pitch	0	1				

[1]Trend as recommended by Hot Chili Ltd based on resource variography

Comparison of the R^2 and root mean squared error (RMSE) values for each modelled mineral by compositional groups indicates the group 2 and 3 models performed best, with lowest RMSE. The weathered group performed worst in terms of RMSE, despite better R^2 values (Appendix D12).

A more simplistic approach, whereby a single linear programming model was developed for the whole deposit, was also tested. Results indicate that the composition dependant model provides improved results for total mica and chlorite and small improvement in clay prediction compared to the global model (Appendix D12). In particular, the spatial correlation between measured and calculated results is better from the composition dependant model for total chlorite and micas and total clays. Results of the global model are discussed further in comparison to the composition dependant model results in Appendix D12.

5.6.4.2 Spatial correlation of calculated mineralogy against measured mineralogy

Measured mineralogy (WLSQ corrected QXRD data) and the equivalent calculated mineralogy (from composition dependant modelling) for select minerals were modelled using Leapfrog Geo® version 2.2.1 "interpolant" function (Appendix D13) over narrow section windows (Table 5.12) on each study section (6,822,215 mN and 6,820,850 mN) in order to spatially compare the calculated results directly with the measured mineralogy. Models were generated for major mineral phases including total quartz and feldspar, total chlorite and micas, pyrite and total clays (Figure 5.12 to 16) as these minerals are volumetrically significant and, with the exception of total clays, yielded the most robust mineral estimates from calculated mineralogy (Figure 5.11).

Overall the calculated mineralogy by linear programming results have the same predicted distribution as the WLSQ mineralogy, particularly for total quartz and feldspar, pyrite and total mica and chlorite

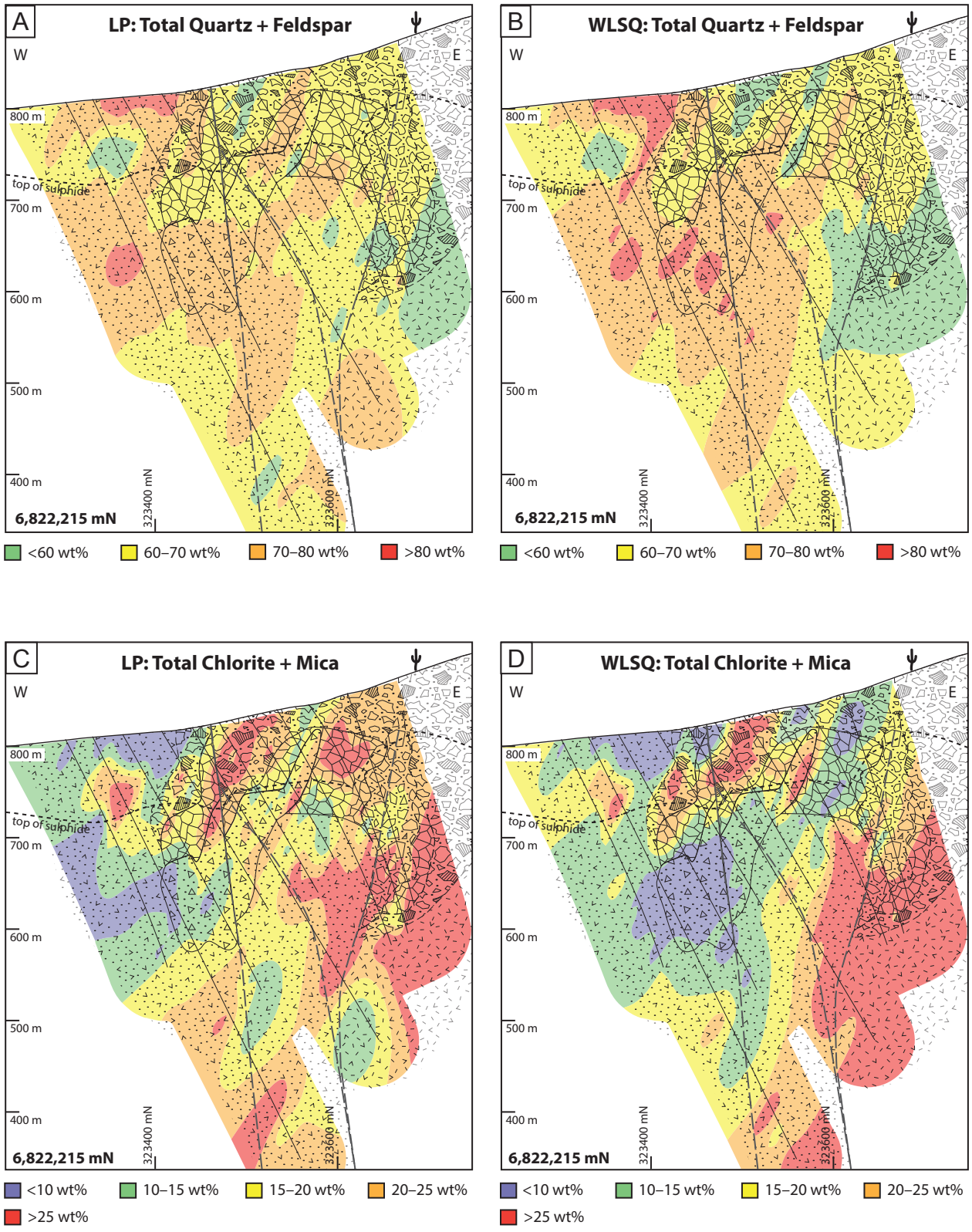

Figure 5.12 Section 6,822,215 mN comparison of calculated mineralogy (by compositional dependant linear programming, LP) against measured mineralogy from weighted least squares corrected QXRD data (WLSQ). A) Calculated total quartz and feldspar. B) Measured total quartz and feldspar. C) Calculated total chlorite and micas. D) Measured total chlorite and micas. The sample by sample difference between measured and modelled are presented on cross section in Appendix D11.

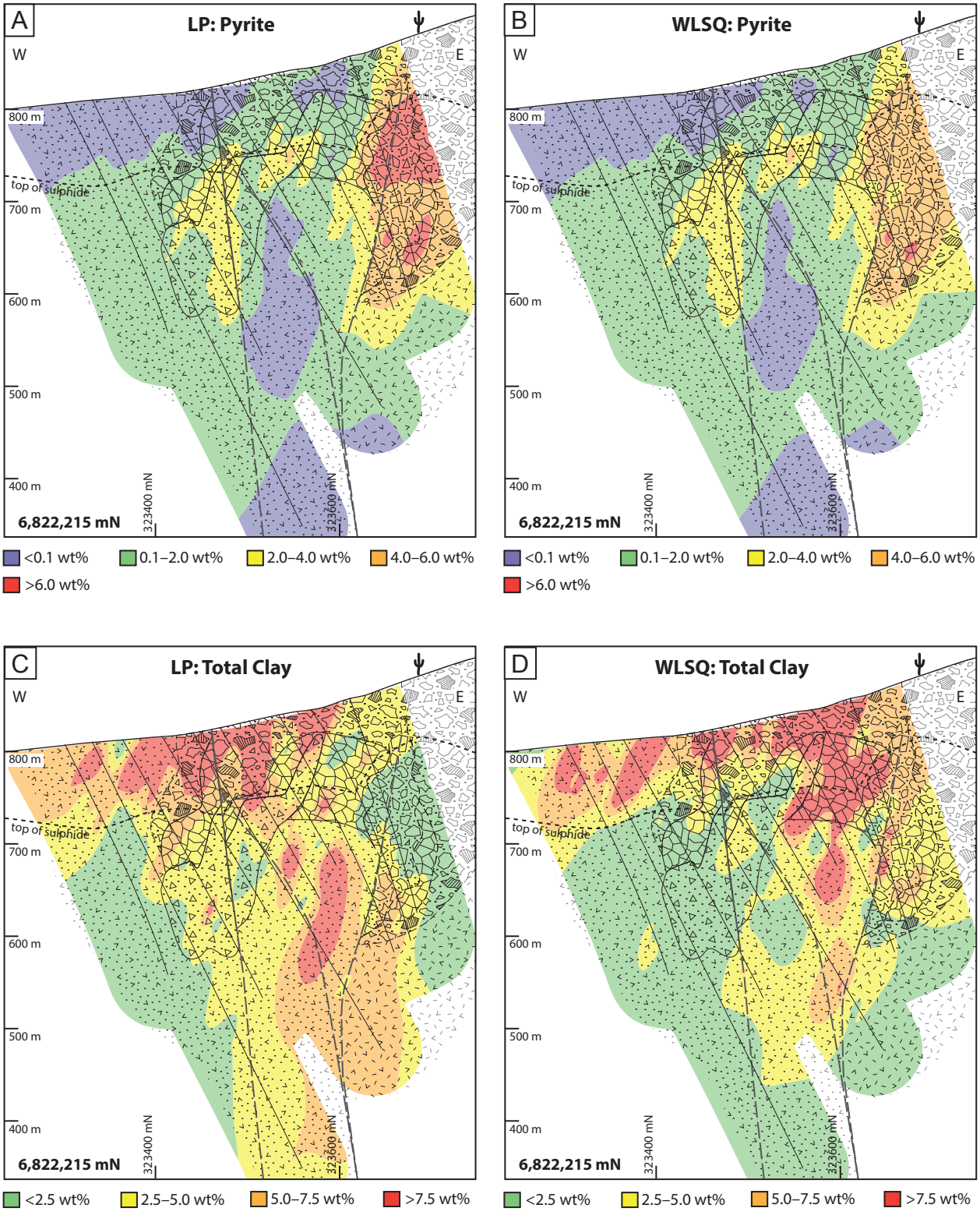

Figure 5.13 Section 6,822,215 mN comparison of calculated mineralogy (by compositional dependant linear programming, LP) against measured mineralogy from weighted least squares corrected QXRD data (WLSQ). A) Calculated pyrite. B) Measured pyrite. C) Calculated total clay. D) Measured total clay. The sample by sample difference between measured and modelled are presented on cross section in Appendix D11.

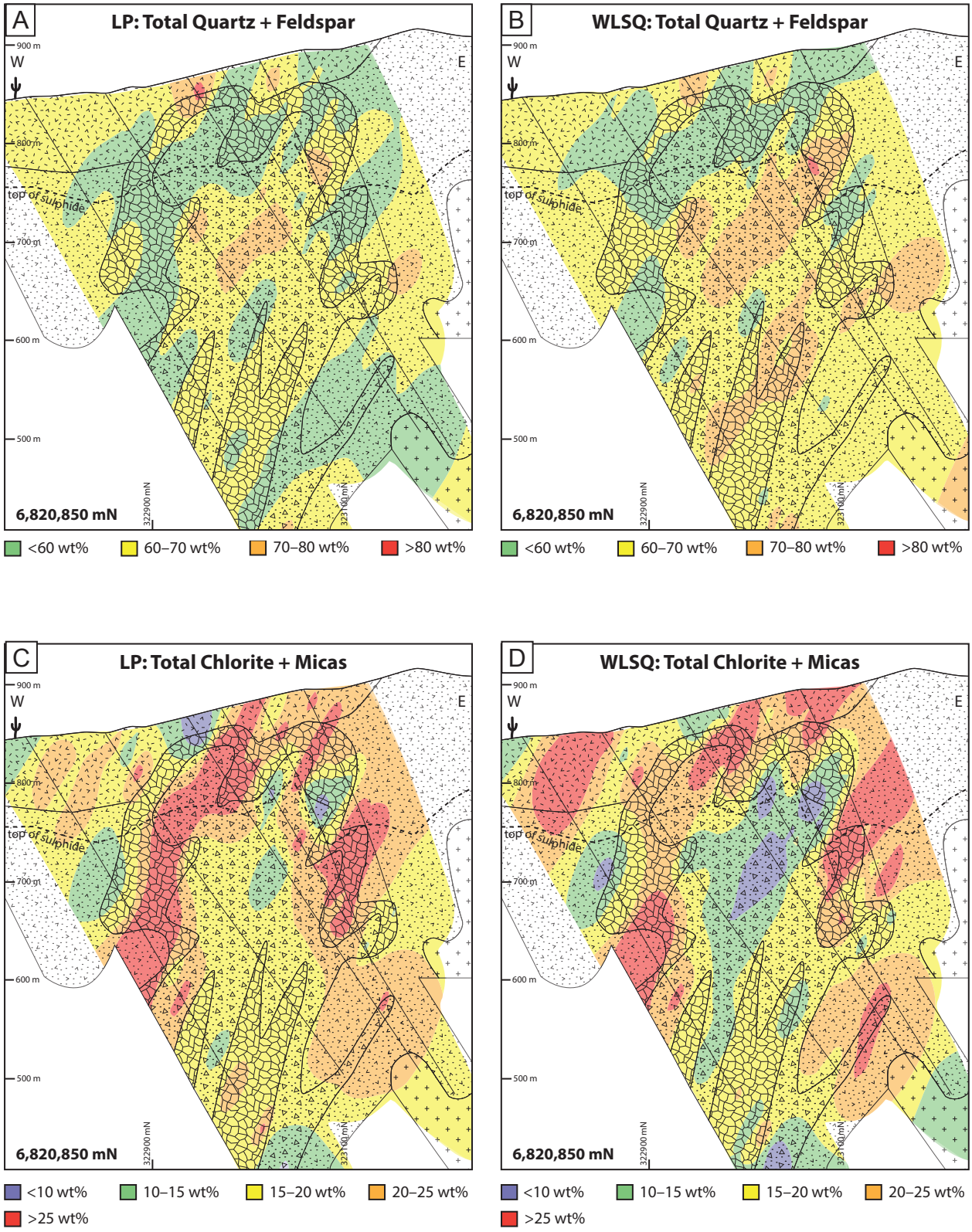

Figure 5.14 Section 6,820,850 mN comparison of calculated mineralogy (by compositional dependant linear programming, LP) against measured mineralogy from weighted least squares corrected QXRD data (WLSQ). A) Calculated total quartz and feldspar. B) Measured total quartz and feldspar. C) Calculated total chlorite and micas. D) Measured total chlorite and micas. The sample by sample difference between measured and modelled are presented on cross section in Appendix D11.

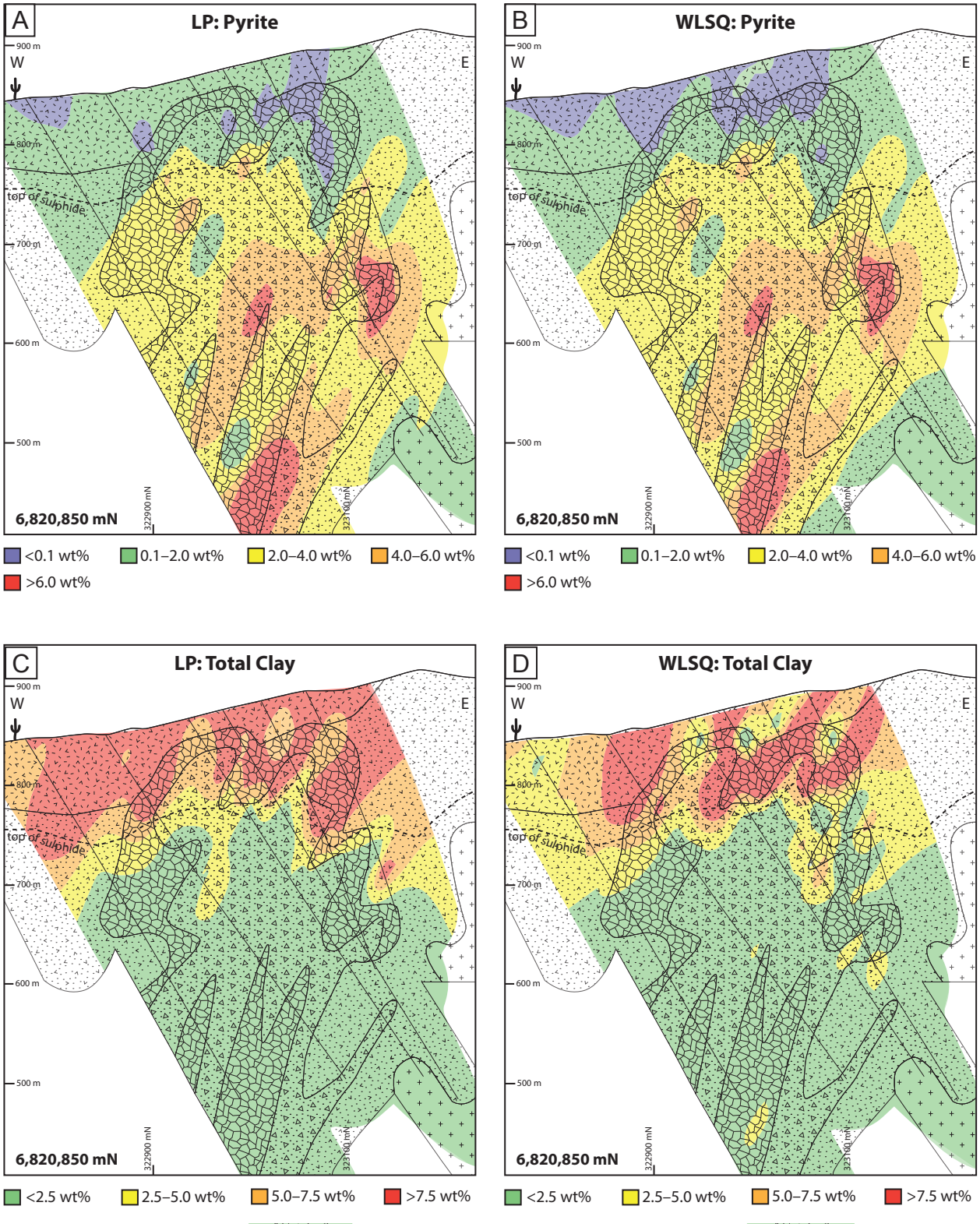

Figure 5.15 Section 6,820,850 mN comparison of calculated mineralogy (by compositional dependant linear programming, LP) against measured mineralogy from weighted least squares corrected QXRD data (WLSQ). A) Calculated pyrite. B) Measured pyrite. C) Calculated total clay. D) Measured total clay. The sample by sample difference between measured and modelled are presented on cross section in Appendix D11.

(Figure 5.12 to 16). Results for total clay are also considered reasonable when taking into account the challenges encountered in calculating the abundance of clay minerals from chemical assays. The calculated mineralogy results are likely to be most accurate on the two study sections, because the training set data are from these sections, and the models are optimised for this sample suite.

The measured mineralogy (WLSQ) across the northern study section (6,822,215 mN) indicates higher values (>70 %) of total quartz and feldspar in the central ore zone, and lower values to the east (Figure 5.12 B). This distribution is reflected clearly in the calculated mineralogy (Figure 5.12 A). The southern study section, (6,820,850 mN) has a central zone with higher measured total quartz and feldspar content, but with lower values closer to the surface (Figure 5.14 B). This measured distribution is also replicated in the calculated mineralogy (Figure 5.14 A). In both cases, the calculated mineralogy appears to present a slightly narrower range in total quartz and feldspar values than the measured mineralogy, but the overall spatial distribution of high and low total quartz and feldspar is analogous.

Comparison of total chlorite and micas against the measured mineralogy (WLSQ) shows very good broad spatial correlation (Figure 5.12 C and D). On the northern section, higher phyllosilicate abundances were defined in the east (Figure 5.12 D) and this trend is also apparent in the calculated mineralogy (Figure 5.12 C). A domain with lower total chlorite and micas in the central-west of the northern section is not as pronounced in the calculated mineralogy results (Figure 5.12 C) compared to the WLSQ estimates, although the broad decrease of total chlorite and micas is reproduced. The calculated mineralogy also reproduced the spatial distribution defined by the WLSQ mineralogy on the southern section, with predicted increased total chlorite and micas to the east, and also in a steeply west-plunging domain (Figure 5.14 C and D).

There is excellent spatial correlation between the calculated and measured pyrite contents (Figure 5.13 A and B, Figure 5.15 A and B). The interpolants of the calculated mineralogy data on the northern section yield a higher pyrite domain (> 6 wt%) to the east (Figure 5.13 A), however on a sample by sample basis the results are very similar to the WLSQ. Only a couple of high values generated the >6 wt% interpolant shell.

For the total clay modelling results, the mineralogy predicted by calculated (linear programming) and measured (WLSQ) are surprisingly similar (Figure 5.13 C and D, Figure 5.15 C and D). Higher total clay contents at shallow levels reflects the weathering profile, whereas a deeper domain of higher clay occurs to the east that is likely hypogene clay alteration (Figure 5.13 C and D). The total clays calculated by linear programming suggest broader domains of abundant clays than the WLSQ data, particularly at

depth (Figure 5.13 C and D, Figure 5.15 C and D). Overall the calculated mineralogy provides a useful indication of significant spatial variations in clay content.

5.6.4.3 Deposit-wide 3D mineralogy interpolant

The deposit-wide distribution of total quartz and feldspar, total chlorite and micas, total clay and pyrite calculated by the linear programming method on each assay interval were modelled as 3D interpolants using Leapfrog Geo® version 2.2.1 interpolant function (Appendix D13), with modelling parameters outlined in Table 5.12. Plan slices from the 3D model are presented in Figure 5.16 and Figure 5.17.

The 3D model of total quartz and feldspar indicates that the north-eastern portion of the open pit design contains higher (significant domains > 70 wt%) total quartz and feldspar than the southern portion (< 70 wt%; Figure 5.16 A). In the northeast, total quartz and feldspar content decreases with depth from predominantly >70 wt% to <70 wt%.

Total chlorite and mica content is extremely variable across the deposit, ranging from <10 wt% to >25 wt% over narrow intervals (10s of meters). The total chlorite and mica content broadly increases toward the south and with depth. Larger domains of >25 wt% total chlorite and mica were modelled by 3D interpolation in the southern end of the pit design. Elevated domains (>20 wt%) of total chlorite and mica are also predicted on the eastern side of the deposit. The distribution of total chlorite and micas is somewhat antithetic to the total quartz and feldspar (Figure 5.12, Figure 5.14 and Figure 5.16).

Pyrite abundances varies widely from <0.1 wt% to > 6wt% across the deposit (Figure 5.17 A). Generally, pyrite content increases with depth and toward the southeast. There are discrete zones where pyrite exceeds 6 wt%. These domains are both laterally and vertically continuous over 100s of meters.

Modelled clay abundance across the deposit generally decrease from >7.5 wt% in the upper 100 m below surface to <2.5 wt% below 120 m depth from surface. This is consistent with the broad weathering profile at Productora (Chapter 4). The interpolant of the modelled total clays indicates that several clay-rich (>7.5 wt %) domains are also predicted at depth (680 m RL) within the pit design, including one in the north-east and one in the south (Figure 5.17 B).

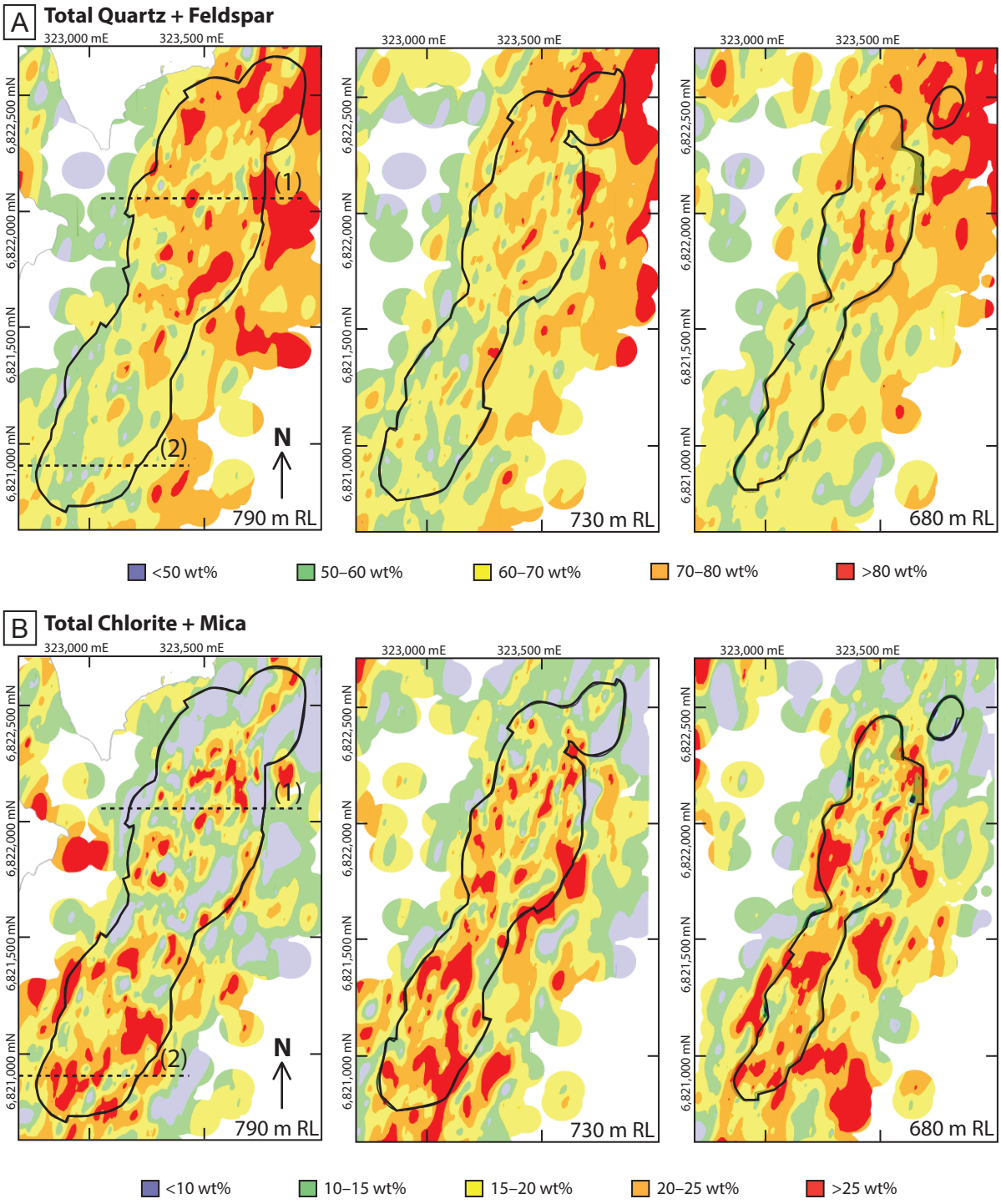

Figure 5.16 Plan slices through 3D interpolant of composition dependant linear programming model for calculated mineralogy for A) total quartz and feldspar and B) total micas and chlorite. Interpolants generated in Leapfrog Geo version 3.1.0 (spheroidal interpolant; global trend with dip 75°, dip azimuth 285°, pitch 0; ellipsoid ratios maximum 2, intermediate 1, minimum 1; resolution 25).Black line = pit design (March, 2014). Dashed lines show study sections, 1 = 6,822,215 mN, 2 = 6,820,850 mN.

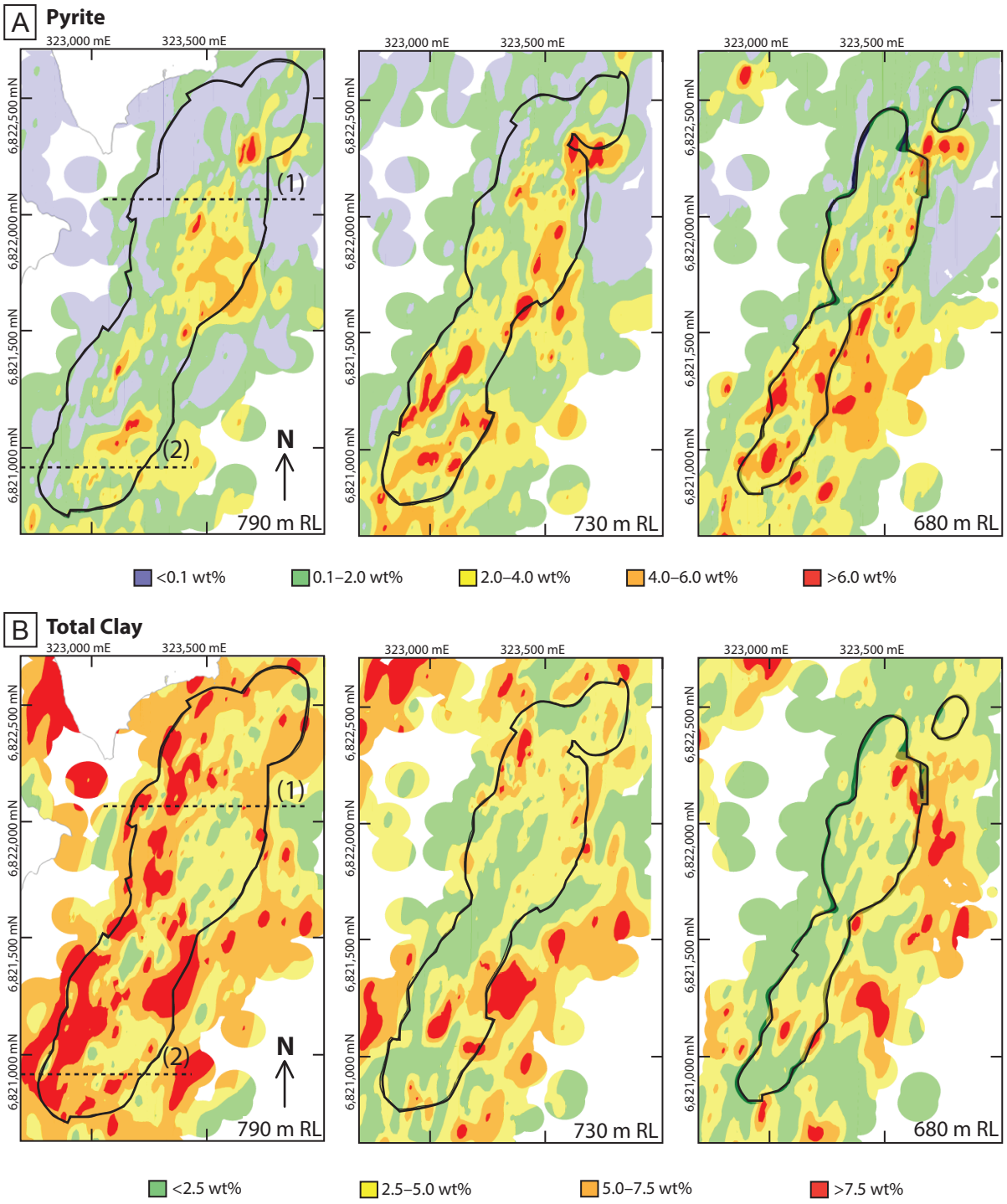

Figure 5.17 Plan slices through 3D interpolant of composition dependant linear programming model for calculated mineralogy for A) pyrite and B) total clay. Interpolants generated in Leapfrog Geo version 3.1.0 (spheroidal interpolant; global trend with dip 75°, dip azimuth 285°, pitch 0; ellipsoid ratios maximum 2, intermediate 1, minimum 1; resolution 25). Black line = pit design (March, 2014). Dashed lines show study sections, 1 = 6,822,215 mN, 2 = 6,820,850 mN.

5.7 Discussion

5.7.1 Application of calculated mineralogy as a method for estimating mineralogy

Results from this study indicate that calculated mineralogy through linear programming using the method of Berry et al. (2011) provides a useful estimation of model mineralogy from chemical assay in quartz-feldspar dominant assemblages. A composition-dependent modelling approach generated results with robust correlations to measured mineralogies for quartz, total feldspars, pyrite, iron oxides and molybdenite with R^2 values greater than 0.8 (Figure 5.11 and Table 5.10). Calculations for muscovite, biotite and chlorite yielded R^2 values between 0.3 and 0.5 against measured mineralogy and provide a useful qualitative indication of the variability of total micas and chlorite.

Calculated mineralogy methods fail to accurately quantify minerals where ambiguity exists due to similarities in chemical composition between minerals, particularly between clay minerals and feldspar (both dominated by Al and Si), carbonates and other Ca-rich minerals, and ferromagnesian minerals (compositions provided in Table 5.7). Carbonate predictions may be improved through inclusion of additional analyses, such as loss on ignition (LOI) data, CO_2 and also SiO_2 (Berry et al., 2015). Tourmaline is a significant phase in this example with relevance to geometallurgy, owing to its hardness and high abrasion characteristics (Dana and Hurlbut, 1971). In the current study, its abundance has been poorly estimated due to the lack of boron assay data and the similar major element composition of tourmaline to amphiboles and other mafic minerals. However there are other geological proxies for tourmaline distribution within the ore body. For example, it is associated with K-feldspar alteration and elemental Cu grades (Chapter 4).

Potentially, the estimated abundance of tourmaline, amphibole, epidote and other challenging minerals may be improved by applying additional limits and constraints to the model that dictate the relative proportions of minerals that have similar chemistry. This would require the definition of appropriate domains where dominant mineral proportions are likely to be consistent. Such definition could be based on a geological model, for example tourmaline-cemented breccia domains would be dominated by tourmaline and varying amounts of biotite depending on the breccia facies (and location; Chapter 4) whereas andesite host rocks (prevalent in the south of the deposit; Chapter 3) would be likely to have higher amphibole. Unfortunately, it was beyond the scope of this study to investigate these adaptations to the linear programming model.

Although calculations for clays did not yield good correlations with measured results, the process of splitting the database into compositional groups through cluster analysis, based on known mineralogy,

and discriminant projection, proved to be a useful step in understanding the variability in clay content across the deposit. Each of the four compositional groups defined for modelling had a different clay content. For example, group 1 had low clay (average 1.6 wt%) with smectite more abundant than kaolinite, whereas group 3 had higher total clay (average 2.7 wt%) with kaolinite dominant over smectite (Table 5.8). Therefore just the classification of samples into compositional groups gives an indication of which are expected to have higher clay contents. Based on the classification information areas can be targeted for further core logging and review, additional QXRD analyses or short wave infra-red (SWIR) data to improve understanding of clay mineralogy and abundance.

A significant limitation of the modelling method is that an appropriate training set of known mineralogy is critical to model success. The model(s) are only accurate for mineral compositions similar to those of the training set used in model development. Mineral compositions falling outside of this range are unlikely to be predicted correctly.

5.7.2 The role of calculated mineralogy in geometallurgy

This research provides a new case study demonstrating the potential to translate chemical assays to mineral proportions on a deposit-wide scale. The calculated mineralogy method enables chemical assay data to be transformed into tangible information about rock character for further modelling, or as a foundation to inform the sampling and test work of a geometallurgy program. The ability to generate quantitative predictions of major mineral proportions on every assay interval is a significant advantage in the field of geometallurgy, as it provides a quick and cost effective method to increase mineralogical data by many orders of magnitude. In this example 625 QXRD analyses have been transformed into 133,963 data points of predicted mineralogy, significantly enhancing the potential for modelling the geometallurgical characteristics of the Productora deposit.

Understanding mineralogy across a deposit is fundamental to any mining feasibility study (e.g. Hoal, 2008). In many hydrothermal ore deposits, particularly porphyry deposits, quartz and the feldspars are the most common hard minerals (7 and 6 – 6.5 on Mohs hardness scale respectively; Dana and Hurlbut, 1971). They are likely to have significant impact on mill throughput when abundant in the ores (e.g. Montoya et al. 2011). Having knowledge of the variability in total quartz and feldspar across a deposit at an early stage, in this case pre-feasibility, ensures comminution sampling covers the range of rock types and thus expected rock strengths (ease of crushing, grinding etc.). This enables samples to be appropriately weighted in process model simulations by how representative they are.

Pyrite is a major contributor to acid rock drainage and in high abundances can cause dilution of any

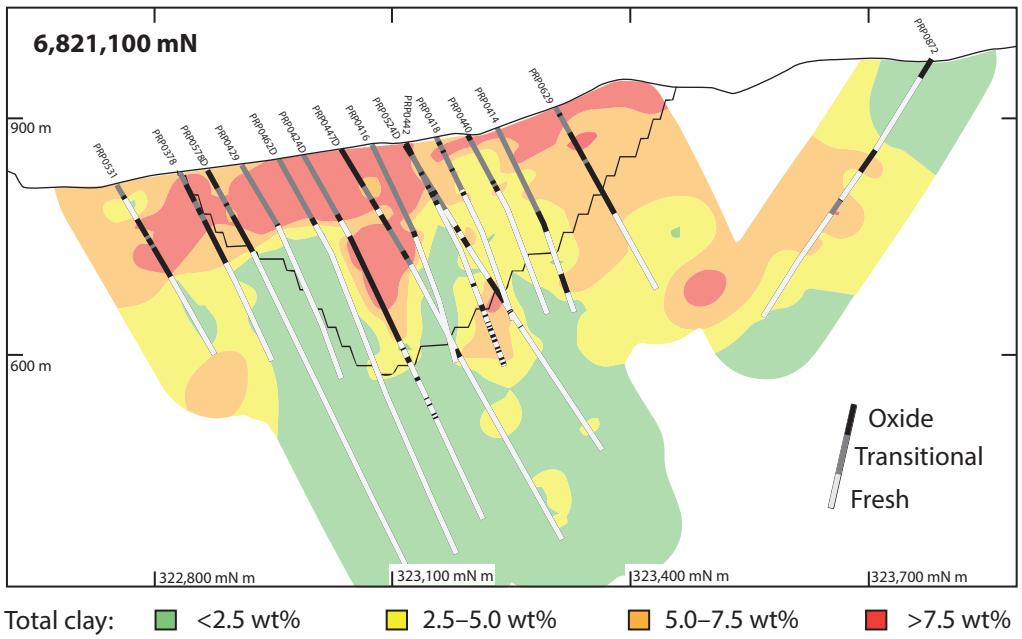

Figure 5.18 Cross section at 6,821,100 mN showing 3D interpolant of calculated total clay (by linear programming) and logged weathering (from drill hole database provided by Hot Chili Ltd). Interpolant generated in Leapfrog Geo version 3.1.0 (spheroidal interpolant; global trend with dip 75°, dip azimuth 285°, pitch 0; ellipsoid ratios maximum 2, intermediate 1, minimum 1; resolution 25).

metal-bearing concentrate produced from the ore. This study has shown (Figure 5.13 A and Figure 5.17 A) that it is possible to make robust predictions of its occurrence and distribution throughout a deposit using calculated mineralogy.

Phyllosilicate phases, including muscovite, biotite, chlorite and clay minerals can have significant impact on milling and flotation when they occur in high abundance (Farrokhpay and Bradshaw, 2012; Cruz et al., 2013; Farrokhpay and Ndlovu, 2013; Appendix D14). Using the calculated mineralogy results it is now possible to broadly estimate areas of high abundance phyllosilicates at Productora. This information enables potential variability in test work, such as flotation, to be rationalised against the mineralogy, and can also be used as a guide to inform further sample locations.

Despite the obvious advantages of using calculated mineralogy for geometallurgy, there are only limited examples available in the literature. Comparable examples of the development, and application of a complex deposit-scale calculated mineralogy were limited in the literature at the time of writing. At the La Colosa deposit, Colombia, calculated mineralogy was used successfully for class-based analysis facilitating the development of predictive proxy support models of comminution indices (Montoya et al., 2011). Clearly there is scope for much greater utilisation of calculated mineralogy in the field of geometallurgy as a method of predicting modal mineralogy, both across a given deposit and for niche applications.

5.7.3 Productora mineralogy conclusions

The 3D model of total quartz and feldspar indicates that the shallow northern half of the open pit contains more quartz and feldspar (locally >80 wt%) than the southern portion (Figure 5.16 A). It is inferred that the rocks are likely to be harder in the near-surface in the north, which will lead to higher blasting and grinding costs, and reduced throughput whilst mining these domains compared to other parts of the deposit. The mineralogical model results provide important information to consider when selecting representative comminution test samples from which mining schedule designs are based.

Significant domains of high (>25 wt%) total chlorite and mica were identified in the south of the pit design (Figure 5.16 B), this is consistent with increased biotite observed in handspecimens of the breccias from this area (Chapter 4). Pyrite abundance increases with depth, particularly in the south, and locally there are discrete zones of >6 wt% pyrite (Figure 5.17 A). These domains of high pyrite and/or phyllosilicates may be problematic in a flotation circuit without an appropriate blending strategy. The calculated pyrite model provides a key dataset to help tackle this issue by being able to predict pyrite content in the ore feed. It is also important to understand how much of the ore is associated with high pyrite domains, and whether flotation test work has appropriately sampled this material to assess accumulation in the concentrate. High pyrite zones within waste rock also require careful consideration to ensure appropriate waste handling and storage measures can be planned to account for the acid rock drainage potential of high pyrite rocks. The robust pyrite model for Productora provides a useful tool to aid in addressing each of these challenges.

The modelled clay abundance across the deposit is higher (>7.5 wt%) within 100 m of the surface (Figure 5.13, Figure 5.15 and Figure 5.17) and generally decreases with depth. This largely corresponds with degree of weathering, as recorded in Hot Chili Ltd.'s drill core logging database. However, there are also several clay-rich domains at depth, including one in the north-east and one in the south (at 680 m RL; Figure 5.17 B). A review of logging results from this area has validated the model. In the north-east the clay domain is associated with hypogene kaolinite observed in the Habanero ore zone (chapter 4). In the south, the clay domain is due to a deep weathering zone which has been logged as transitional where intersected by drill core (Hot Chili Ltd geological logging; Figure 5.18). These examples highlight the potential applications of the calculated mineralogy model, particularly when combined with other available data. This method provides the ability to rapidly assess the deposit for mineralogical variability, and facilitates the identification of discrete zones which are anomalous or require additional test work to ensure that all ore types are characterised.

5.8 Conclusions

The results of the study have shown that mathematical modelling of quantitative mineralogy, specifically the translation of geochemical information into mineral proportions through calculated mineralogy using the linear programming and Simplex method (Press et al. 1968; Berry et al., 2015) can aid geometallurgical studies. The findings are as follows:

- Altered rocks at the Productora deposit are dominated by quartz, K-feldspar, albite and muscovite (Figure 5.3 and Table 5.1). Chalcopyrite is the most common sulphide phase after pyrite and kaolinite is the most abundant clay mineral (Figure 5.3).

- The northern section (6,822,215 mN) has elevated quartz, K-feldspar, muscovite, tourmaline and kaolinite. The southern section (6,820,850 mN) has higher abundances of total plagioclase (albite plus calcic plagioclase) biotite, chlorite, pyrite, amphibole and calcite (Figure 5.3).

- A weighted least squares correction (WLSQ) can be applied to raw QXRD data in order to overcome high detection limits associated with QXRD analysis. This approach provides a more robust estimate of mineralogy for both abundant and minor phases than the raw data (Figure 5.4).

- Cluster analysis of a 625 sample training set defined four discrete compositional groups based on logged weathering and mineralogy (Figure 5.8 and Table 5.8). Classifying the deposit-wide dataset into 4 groups using logging and discriminant function analysis provided a broad indication of variability in mineralogy across the deposit (Figure 5.9 and Figure 5.10).

- Four linear programming models were developed to calculate modal mineralogy for each compositional group using 15 different elements (from chemical assay) to calculate 38 minerals. The training set 625 QXRD analyses and geochemical database were transformed into 133,963 data points of predicted modal mineralogy which enable the spatial variability in mineralogy at the Productora deposit to be understood.

- Overall the results of the linear programming mineralogy calculations are excellent when compared with the measured data. Most of the major minerals, including quartz, K-feldspar, albite, pyrite, iron oxides, chalcopyrite and molybdenite, matched the results from weighted least squares corrected QXRD (WLSQ) data extremely well (Figure 5.11 – 16). The model fail rate was 1.64 % (Table 5.11).

- Minerals with similar chemical compositions proved challenging to model. The major

problem minerals included clays, carbonates, tourmaline, amphibole, epidote and jarosite. It is suggested that the incorporation of additional analytical data (such as B, CO_2, SiO_2 and LOI) into the model along with the existing 15 elements would assist with modelling carbonates, clays and tourmaline. Further investigation into the application of additional model constraints to control the relative proportions of problem minerals based on geological knowledge is recommended.

- Linear programming calculated mineralogy models provide a good indication of the range in abundance and spatial distribution of total chlorite and micas (Figure 5.11 G, Figure 5.12 C and D, Figure 5.14 C and D).

- Results for minor minerals apatite and titanite-rutile are excellent compared to measured data due to their unique chemistry with respect to other minerals found at Productora

- The calculated mineralogy through linear programming using the method of Berry et al. (2011) provides a robust model mineralogy from chemical assay in quartz-feldspar dominant assemblages that can be used to rapidly assess for mineralogical variability across the deposit, and facilitates the identification of discrete zones which are anomalous or require additional test work to ensure that all ore types are appropriately characterised.

- The calculated mineralogy by linear programming results have the same predicted spatial distribution as the WLSQ corrected mineralogy, particularly for total quartz and feldspar, pyrite and total chlorite and micas (Figure 5.12 – 5.16). Results for the distribution of clay are also better than expected considering the challenges in calculating the abundance of clay minerals from chemical assay (Figure 5.13 C and D, Figure 5.15 C and D). Therefore the calculated mineralogy, once verified against the training set, can be used on the entire drill hole database.

- 3D interpolants of the calculated mineralogy indicate:

    - » total quartz and feldspar are higher (> 70 wt %) in altered rocks in the northern half of the pit design than the southern portion (Figure 5.16 A).

    - » total chlorite and mica are variable across the deposit but generally increase to the southeast and with depth (Figure 5.16 B).

    - » pyrite abundances range from 0.1–6 wt% across the deposit, generally increasing with depth and to the south, with discrete zones of pyrite in excess of 6 wt% (Figure 5.17 A).

» clay abundance in the deposit generally decreases from >7.5 wt% to <2.5 wt% with depth. Two high clay domains are predicted at depths (> 7.5 wt% at 680 m RL) in the northeast (Figure 5.15 A) and the south (Figure 5.18).

Chapter 6: Modelling copper speciation

6.1 Introduction

This chapter aims to develop a new methodology for the deposit-wide definition (both spatial and compositional) of oxide, transitional and sulphide material at Productora, using the existing site geochemical database (33 element ICP-AES). At the inception of this research project, Hot Chili Ltd had published a revised resource estimate of 214.3 Mt @ 0.48 % Cu, 0.1 g/t Au and 138 ppm Mo with a reserve of 90.5 Mt @ 0.48 % Cu, 0.11 g/t Au and 172 ppm Mo (Hot Chili Ltd, 2014). This reserve estimate only included non-oxidised, sulphide material. A major objective for the company's pre-feasibility study (PFS; completed in early 2016) was to better define oxide resources at Productora to enable them to be included in the reserve. This could help to reduce overall mining strip ratios and lower pre-strip related start-up capital. This chapter has focussed on developing novel predictive models for copper speciation in order to improve ore body knowledge at the weathering interface between oxide and sulphide domains.

The dominant hypogene Cu-ore minerals at Productura are Cu-sulphides, mostly chalcopyrite (Chapter 4). Weathering of hypogene Cu ore results in oxidation of sulphide minerals to secondary Cu-sulphide and Cu-oxide minerals, a list of the common oxide minerals is provided in Table 6.1. With increased weathering, hypogene ores are converted to transitional ores (containing significant proportions of both sulphide and oxide Cu-minerals) and eventually to oxide, or supergene, ores (dominated by oxide, carbonate and/or silicate Cu-minerals; Chávez, 2000). Typically, Cu is recovered from transitional and oxide ores by heap or dump leaching, where sulphuric acid (often with added ferric iron for leaching secondary sulphides) is used to dissolve the Cu-bearing minerals. The resulting pregnant leach solution is treated by solvent extraction and electrowinning methods to recover the extracted Cu (Benvie et al. 2013). Recovery of Cu by leaching is economically more attractive than by conventional ore milling (Chávez, 2000). Knowledge about the proportions of Cu-oxides and Cu-sulphides is important when considering what the appropriate processing route (leach versus flotation) for ore is, and for estimating

Table 6.1 Minerals commonly found in the oxide zone and leached capping of porphyry copper deposits. This non-exhaustive list was compiled from Schwartz (1933), Ramdohr (1969) and Chávez (2000).

Mineral name	**Chemical Formula**
Antlerite	$Cu_3SO_4(OH)_4$
Atacamite	$Cu_2Cl(OH)_3$
Azurite	$Cu_3(OH)_2(CO_3)_2$ or $2CuCO_3{\cdot}Cu(OH)_2$
Bonattite	$CuSO_4{\cdot}3H_2O$
Brochantite	$Cu_4SO_4{\cdot}OH_6$
Ceruleite	$Cu_2Al_7(AsO_4)_4(OH)_{13}{\cdot}11.5H_2O$
Chalcanthite	$CuSO_4{\cdot}5H_2O$
Chalcosiderite	$CuFe_6(PO_4)_4(OH)_8{\cdot}4H_2O$
Chenevixite	$Cu_2Fe_3^{+2}(AsO_4)_2(OH)_4{\cdot}H_2OCu(Fe,Mn)Ox{\cdot}SiO_2{\cdot}H_2O$
Chrysocolla (mineraloid)	$(Cu_{2-x}Al_x)H_{2-x}Si_2O_5(OH)_4{\cdot}nH_2O$ (Cu content varies from 20–40 wt% Cu)
Copiapite	$Fe_5(SO_4)_6(OH)_2{\cdot}20H_2O$
Copper pitch (Melaconite)	Cu and Fe-bearing manganese oxide/hydroxide
Copper wad	
Coquimbite	$Fe_2(SO_4)_3{\cdot}9H_2O$
Goethite	α-FeOOH
Jarosite	$KFe_3(SO_4)_2(OH)_6$
Kröhnkite	$Na_2Cu(SO_4){\cdot}2H_2O$
Lavendulan	$NaCaCu_2^{+5}(AsO_4)_4Cl{\cdot}5H_2O$
Libethenite	$Cu_2PO_4(OH)$
Malachite	$Cu_2(OH)_2CO_8$ or $CuCO_3{\cdot}Cu(OH)_2$
Native copper	Cu^0
Paramelanconite (tetragonal variety of tenorite)	Cu_4O_3 (see tenorite (CuO) and cuprite (Cu_2O)
Poitevinite	$(Cu,Fe,Zn)SO_4{\cdot}H_2O$
Posnjakite	$Cu_4SO_4(OH)_6{\cdot}H_2O$
Pseudomalachite (see libethenite)	$Cu_5(PO_4)_2(OH)_4$
Scorodite (see chenevixite)	$Fe^{3+}AsO_4{\cdot}2H_2O$
Tenorite (melaconite)	CuO
Turquoise	$CuAl_6(PO_4)_4(OH)_8{\cdot}4H_2O$
Voltaite	$K_2Fe_8Al(SO_4)_{12}{\cdot}18H_2O$
Wroewolfeite (Langite)	$Cu_4SO_4(OH)_6{\cdot}2H_2O$

valuable phase recovery and ultimately resource value.

Current industry practice is to characterise samples in the weathering zone through sequential, or diagnostic, leaching. Due to the expense (currently US$35.70 per sample; ALS, 2016) this is unlikely to be performed comprehensively. It is usually carried out on a suite of samples selected to be representative based on geological logging. This section outlines the development of a novel method of predicting Cu speciation on every sample interval, in terms of oxide, transitional and sulphide, from geochemical assay and logging data. The technique has the potential to increase the number of samples used for

geometallurgical characterisation by several orders of magnitude. A new sample classification scheme based on sequential leach data is presented for the Productora deposit, followed by a model to predict sample classification using multi-element ICP-AES geochemical data.

6.2 Classification based on sequential leaching

6.2.1 Sequential leaching method

Samples from Cu ores can be classified as either oxide, transitional or sulphide, with respect to the dominant Cu minerals present based on sequential (or diagnostic) leach data. Sequential leaching is regarded as an alternative (or proxy) to direct estimates of modal mineralogy such as optical microscopy, scanning electron microscope (SEM), electron microprobe, quantitative X-ray diffraction, and more recently automated SEM-based energy-dispersive X-ray spectroscopy (EDS) systems using MLA and/or QEMSCAN software. Sequential leaching has a larger measurement error but lower sampling error and cost compared to other methods.

Typically, samples have Cu extracted in a series of three leach stages which sequentially dissolve the various Cu-minerals as follows: 1) Sulphuric acid digests all copper oxide minerals and about 70% of the cuprite. 2) Cyanide leach digests chalcocite and bornite and circa 7 % of the chalcopyrite (Parkinson and Bhappu, 1995). 3) A final multi-acid leach digests any residual copper minerals. The residual Cu is typically assumed to be in chalcopyrite. An additional weaker acid leach (typically citric) is also available as a first stage to identify proportions of the copper carbonate minerals azurite and malachite, if required. The method does not account for the variable solubility of other black copper-bearing oxides – commonly called copper wad or neoticite, which can range from 10–80 % (Jansen and Taylor, 2014).

In the pre-existing analytical protocol, samples are classified as either oxide, transitional or fresh based on the relative proportions of Cu-phases. Typically 'oxide' was defined as having >65 % of the total Cu in oxide phases (soluble in the first sulphuric acid leach step), 'sulphide' had >80 % total Cu in sulphide phases (soluble only in the cyanide or multi-acid digest) and all samples inbetween were designated 'transitional'(R. Cantrell, pers. commun., 2014).

At Productora, comparison of the results of this approach against Hot Chili Ltd.'s 33-element ICP-AES chemical database, collected on every 1 m assay interval, identified discrepancies in the calculated chalcopyrite content from the final multi-acid leach step of the sequential leach analysis. It was found that a number of samples did not contain sufficient S to account for all the residual Cu (i.e. Cu only dissolved in the multi-acid leach) residing in a sulphide phase. To investigate this issue, chip trays for

these intervals were examined visually. Where insufficient S was identified, a black (Cu-bearing) oxide was observed – Cu in this oxide was confirmed via a field test using an iron nail and dilute hydrochloric acid (Roseveare, 1966). Copper present in the black oxide formed a precipitate coating the iron nail. At Productora the copper in black oxide is considered unrecoverable through normal processing routes as it will neither float nor readily leach, as demonstrated by the sequential leach analyses. Description and characterisation of this black Cu oxide is detailed in the following section.

6.2.2 Black Cu oxides

Weathering of hypogene sulphide ores leads to a characteristic mineral stratigraphy of copper oxides, iron oxides, and copper sulphides (Chávez, 2000). Near-surface rocks are commonly leached and typified by the occurrence of iron oxides, residual copper and manganese minerals. Late-stage zones of leaching may extend into or below earlier formed supergene copper oxide and copper sulphide zones (Figure 6.1), this is typically controlled by the fracture network in host rocks and climatic evolution. The most reduced copper oxides (native copper and cuprite) form in the lower portions of the oxide horizon, superjacent to zones of in-situ oxidation of sulphide bearing rock.

The Cu-carbonate malachite and Cu-silicate chrysocolla are typically the most abundant copper minerals in the upper zones of geochemically mature copper oxide systems within reactive host rocks, such as K-silicate assemblages (Chávez, 2000). Here sources of low pH solutions (e.g. from oxidation of pyrite) have been consumed or buffered by the host rock and sources of silica and carbonate are available from the rock mass and atmospheric interaction respectively (Chávez, 2000). The black copper oxides tenorite and paramelaconite (Table 6.1), and neotocite (an amorphous, manganese oxide with idealised formula $(Mn,Fe,)SiO_3 \cdot H_2O$; Whelan and Goldich, 1961; Clark and Easton, 1978; Eggleton et al, 1983) also occur, but are volumetrically minor in comparison. The tenorite-paramelaconite-neotocite assemblage is paragenetically late, typically replaces earlier oxides assemblages and indicates the most oxidised zone of weathering.

Confusion exists in the literature over the nomenclature of tenorite. Crystalline prismatic tenorite is considered rare, type examples are associated with volcanic sublimates (Vesuvius; Ramdohr, 1969). The earthy or massive variety of tenorite associated with the oxidation of copper minerals is commonly known as copper pitch. Short (1931) provided the following recommendation:
"*The massive variety, the more common, is melaconite; and the prismatic variety, tenorite. Melaconite commonly has more or less chemically combined manganese oxide and silica. If it contains more than about 5 % of either of these two components the mineral is known as "copper pitch ore"*

Further confusion exists over the definitions of copper-pitch and copper-wad. A non-exhaustive summary of the nomenclature is provided in Table 6.2 and , and summarised below. Literature regarding oxide-Cu occurrences regularly use the term Cu-wad and Cu-pitch less commonly, but rarely provide a definition. It would appear that the terms are commonly used interchangeably for black or dark brown amorphous phases, with similar compositions but differing habit. In general, Cu-pitch is described as black and shiny, colloquially called 'black chrysocolla', with >5–10 wt% Si and is inferred to be an impure tenorite (with Mn and/or Si) or mixture of tenorite and other crystalline phases (Hunt, 1916; Short, 1931; Matthew, 1932; Pignet, 2012, Menzies et al., 2015). Copper-wad is reported to have a similar composition to Cu-

Table 6.2 Definition of Cu-pitch found in the literature.

Definition	Location	Reference
$Cu_2(Si)O_4Cu(OH)_2$	Bisbee, Arizona	Koenig (1902)
Mixture of tenorite, malachite and chrysocolla	Bisbee, Arizona	Hunt (1916)
Tenorite with >5 wt% MnO_2 or Si	unknown	Short (1931)
Impure tenorite (chrysocolla, malachite, chalcocite ± manganese oxide or silica)	Bisbee, Arizona; Kalispell, Montana	Matthew (1932)
Variable Mn, Fe, Cu, Si and Al; similar composition to Cu-wad; Mn-ric or Fe-rich	Mina Sur	Pincheira et al. (2003)
Black and shiny; chrysocolla-like mineraloid associated with atacamite, lebethenite, birnessite and gypsum	Chuquicamata	Pinget (2012)
Silica-rich (>10 wt%) Cu-bearing phase closely associated with chrysocolla, often called 'black chrysocolla'; Cu-pitch; Cu-Mn pitch; ass. with Mg, Al, S, Cl, Ca and Co; numerous subdivisions based on Fe, Ca, S, Si, P and Cl	Unidentified exotic Cu deposits of northern Chile	Menzies et al. (2015)

Table 6.3 Definitions of Cu-wad from the literature, modified from Menzies et al. (2015).

Definition	Location (Chile)	Reference
$CuO{\cdot}MnO_2{\cdot}7H_2O$	Damiana	Rojas and Müller (1994)
Cu-rich Mn-Fe oxides	Mina Sur	Münchmeyer (1996)
$Mn_yCu_xO_z$	El Abra	Moraga (2000)
Cu-rich, K-bearing, Mn oxyhydrates; copper-bearing cryptomelane $[K_{1-2}(Mn^{3+}Mn^{4+})_8O_{16}{\cdot}xH_2O]$ and birnessite $[K_{0.33}Mn_{3.9}{}^{+7}O_{14}{\cdot}7H_2O]$	El Salvador district: Damiana, Quebrada, Turqueza	Mote et al. (2001)
$CuMnO_2$; amorphous; similarities to manganese oxides cryptomelane and crednerite	Radomiro Tomic	Cuadra and Rojas (2001)
Variable Mn, Fe, Cu, Si and Al; similar composition to Cu-pitch; Mn-rich or Fe-rich	Mina Sur	Pincheira et al. (2003)
$2CuO{\cdot}MnO_2$	Huinquintipa, Collahuasi	Garcia et al. (2007)
Dark brown-black, powdery; chrysocolla-like mineraloid associated with atacamite, lebethenite, birnessite and gypsum	Chuquicamata	Pinget (2012)
<10 wt% Si; Cu-Mn wad; Cu-wad; numerous subdivisions based on Fe, Ca, S, Si, P and Cl	Unidentified exotic Cu deposits of northern Chile	Menzies et al. (2015)

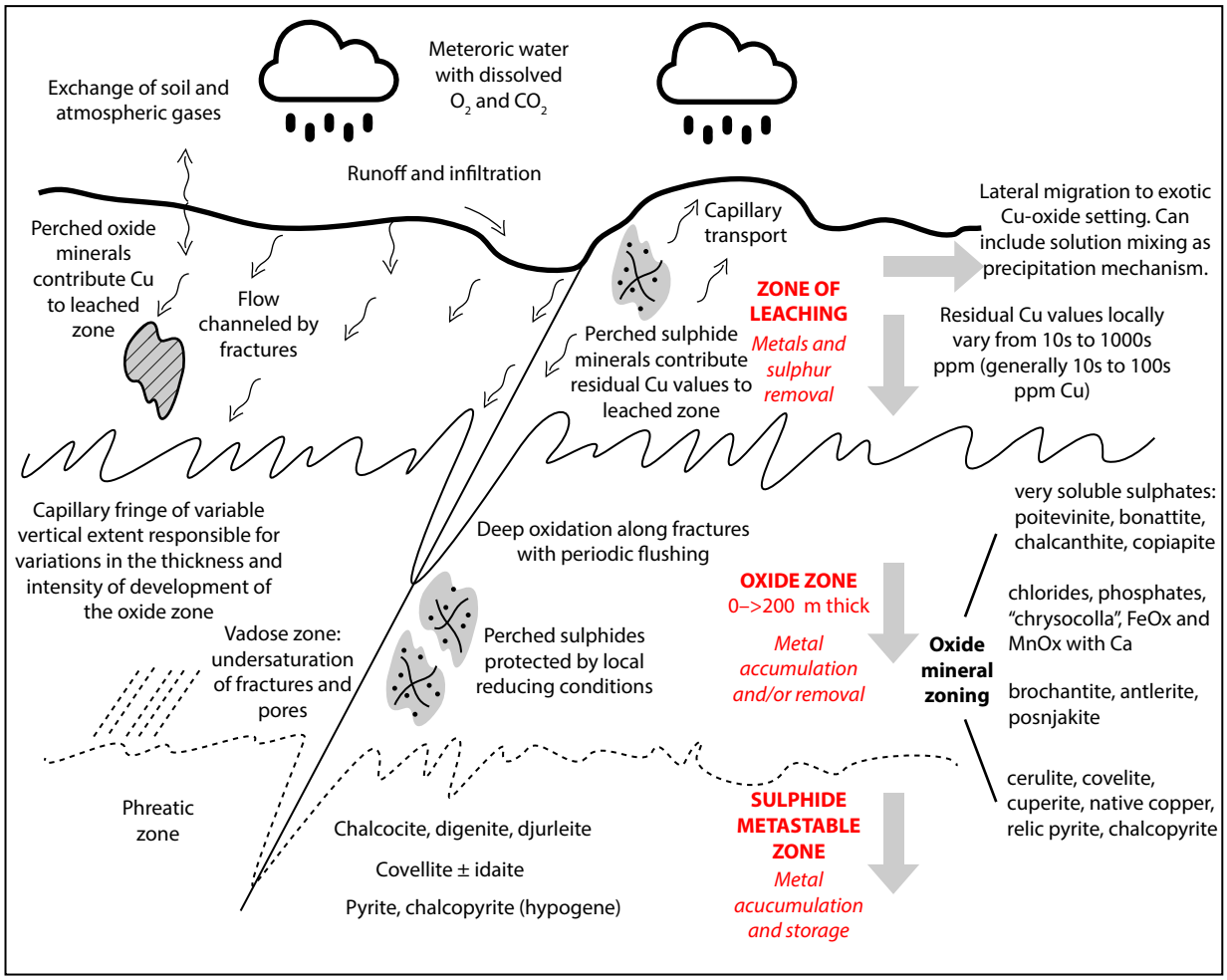

Figure 6.1 Schematic diagram showing the weathering environment of a sulphide-bearing mineral occurrence. Modified from Chávez (2000). The weathering environment at Productora is mature in the north, characterised by leached capping, but shows evidence of continued in-situ weathering in the south (section 4.10.5). Oxide mineralogy is further complicated by neutralisation of acid fluids with migration from source.

pitch, typically between tenorite and manganese oxide (Moraga, 2000; Münchmeyer, 1996; Cuadra and Rojas, 2001; Pincheira et al., 2003; Garcia et al., 2007). Some authors also report Cu-wad as hydrated oxides (Rojas and Müller, 1994; Mote at al. 2001).

6.2.3 Methodology

In this work the term Cu-wad is used to refer to black, earthy, amorphous masses that tested positive for Cu in field tests with an iron nail and dilute hydrochloric acid (Roseveare, 1966). A sample of this Cu-wad was prepared as a polished grain mount. Scanning electron microscopy (SEM) and energy dispersive X-ray spectrometry (EDS) were performed at Central Sciences Laboratory, University of Tasmania on a Hitachi SU-70 field emission SEM fitted with an Oxford AZtec XMax80 EDS system. A series of back scattered electron images, semi-quantitative spot analyses and a semi-quantitative, 148 µm by 215 µm area, element map were collected. Spot analyses were performed at an accelerating voltage of 15 kV and ten second acquisition time. The element map was generated with accelerating voltage of 15 kV, 2.4 ms

dwell time and 0.2 μm pixel size (1024 by 704 pixels). Prior to analysis, the samples were coated with 20 nm of carbon in a Ladd 40000 carbon evaporator.

6.2.4 Results

Backscatter electron images show the wad material is texturally and compositionally complex with apparent colloform banding surrounding silicate crystals with abundant REE-rich phases residing within bands (Figure 6.2). In order of most abundant, the Cu-wad chemistry is dominated by Cu and Mn (typically 13–40 wt%) with lesser Si, Co and Al (typically 2.3–10 wt%), and variable minor Fe, Ca and Mg (0–1 wt%; Figure 6.3 and Appendix E1). Cerium is also a significant component and was measured up to 10 wt%, generally higher close to REE-rich phases. Compositions similar to that of chrysocolla but with additional Fe (up to 33 wt % Cu and 23 wt% Si with mean Fe of 15 wt% and minor Mn and Al; Appendix E1) were also noted in discreet domains within goethite. The mixed composition is inferred to indicate a fine intergrowth of goethite and chrysocolla The colloform banding reflects variations in the major and minor element chemistry of the Cu-wad. A series of analyses across the banding observed in the backscatter electron images indicates that the abundances of Cu, Mn, Si and Ce vary significantly (ranging over 7 wt%). A correlation matrix of dominant chemistry (Cu, Mn, Si, Co, Al and Ce), calculated using the Spearman rank method (Spearman, 1904), indicates moderate correlation exists between several elements. Mn correlates with Si and Co; Si with Al; and Co with Al (Table 6.4). These relationships can also be seen in the point data traversing the colloform banding (Figure 6.2). It was not possible to confidently match the chemistry of the Cu-wad analyses to any mineral in the MinIdent-Win 4 database. This suggests that either the resolution of the analyses was too coarse and all the analyses are mixed compositions, resulting from fine mineral intergrowths, or that the material is amorphous in nature.

The bright REE-rich phases visible in the back scatter image (Figure 6.2) range from <1–5 μm and have a chemistry dominated by Ce (5–45 wt%) with variable Nd, La, P, Ca and S (<1–15 wt%; Appendix E1). The spectra also indicate the presence of Si, Cu, Mn, Al and Co, however it is likely that this may be the result of mixed signal from the local host Cu-wad. The compositions did not confidently match with any mineral in the MinIdent-Win 4 data base but the association of REEs with P suggest monazite or or rhabdophane composition. It was beyond the scope of this work to further investigate the mineralogy.

6.2.5 Revised sequential leach based classification scheme

In order to account for non-recoverable Cu in the black Cu-oxide a new classification scheme has been devised to reconcile the available S against Cu for each sample interval. Sulphur analyses were available in

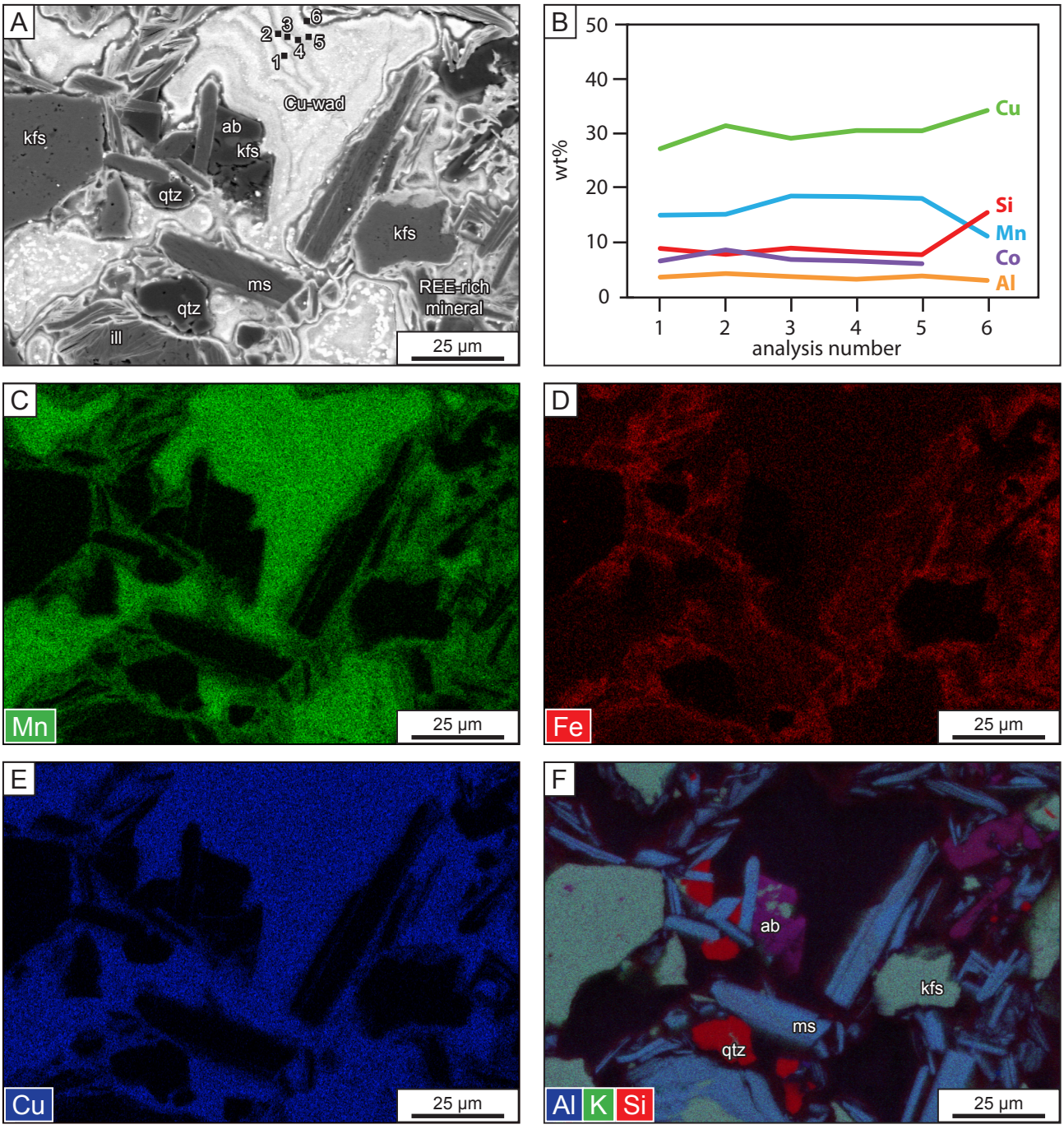

Figure 6.2 Cu-wad sample (PR14AE158, MET015 81.5 m). A) Backscatter electron image with six analysis points across banding. B) Composition of six analysis points. SEM Element map of C) Mn, D) Fe, E) Cu. F) RGB element map for Al, K and Si. The backscatter image shows colloform banding in the Cu-wad and inclusions of REE-rich phases. Analysis of six points traversing the bands indicates variable major element composition, particularly Cu, Mn and Si. Element maps show zoning in Mn Fe and Cu around grains of silicate minerals. The Cu-wad is relatively enriched in Fe but depleted in Mn and Cu adjacent to the silicate grains. The RGB image clearly shows the four types of silicate mineral which occur with the Cu-wad. ab = albite, kfs = K-feldspar, ill = illite, ms = muscovite, qtz = quartz.

the multi-element ICP-AES assay data base with lower detection limit of 0.01 wt% and upper detection limit of 10 wt% (method description provided in Appendix A3). To avoid misclassification of samples approaching typical detection limits in sequential leach data set (0.01 wt%Cu), samples with less than 0.05 wt%Cu were assigned to a class labelled 'barren'. For the remaining samples, the maximum amount

Table 6.4 Spearman rank correlation coefficients for major elements measured in Cu-wad (PR14AE158, MET015 81.5 m) based on 50 SEM analyses.

	Al	**Co**	**Si**	**Mn**	**Cu**	**O**
O	0.13	-0.49	0.13	-0.49	-0.15	1
Cu	0.17	-0.023	-0.21	-0.15	1	
Mn	-0.22	0.38	-0.52	1		
Si	0.36	-0.071	1			
Co	-0.33	1				
Al	1					

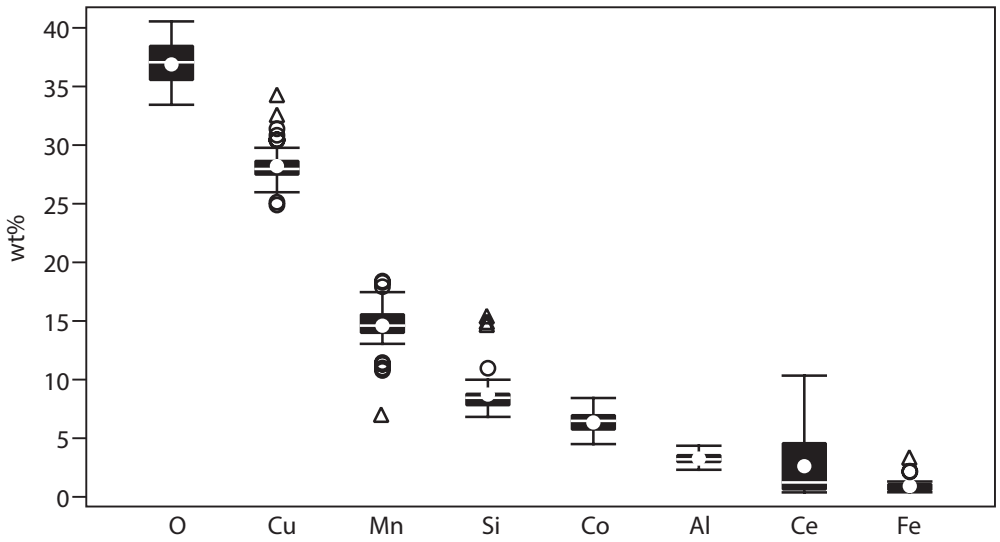

Figure 6.3 Tukey box plot showing composition of Cu-wad based on 50 analyses from sample PR14AE158 (MET015 81.5 m).

of Cu in chalcopyrite (Cu_{MaxCpy}) was calculated by assuming that all the S occurs in chalcopyrite as follows;

- $Cu_{MaxCpy} = (S_{sample}/S_{cpy})*Cu_{cpy}$
- $Cu_{MaxCpy} = (S_{sample} / 34.94)*34.63$

Where Cu_{MaxCpy} is the maximum amount of Cu which can occur as chalcopyrite (wt%), S_{cpy} is the amount of S in chalcopyrite (typically 34.94 wt%), S_{sample} is the amount of S in the sample (wt%) and Cu_{cpy} is the amount of Cu in chalcopyrite (typically 34.63 wt%; calculated from stoichiometry; Appendix E2).

If there was insufficient S for all residual Cu to be present as chalcopyrite, the remaining Cu was attributed to a non-sulphide, weak acid insoluble Cu phase termed 'insoluble' in the output table. The 'insoluble' component corresponds to Cu-wad, chrysocolla and other insoluble Cu minerals. Samples were then classified into five groups based on the relative proportions of oxide, sulphide and insoluble Cu

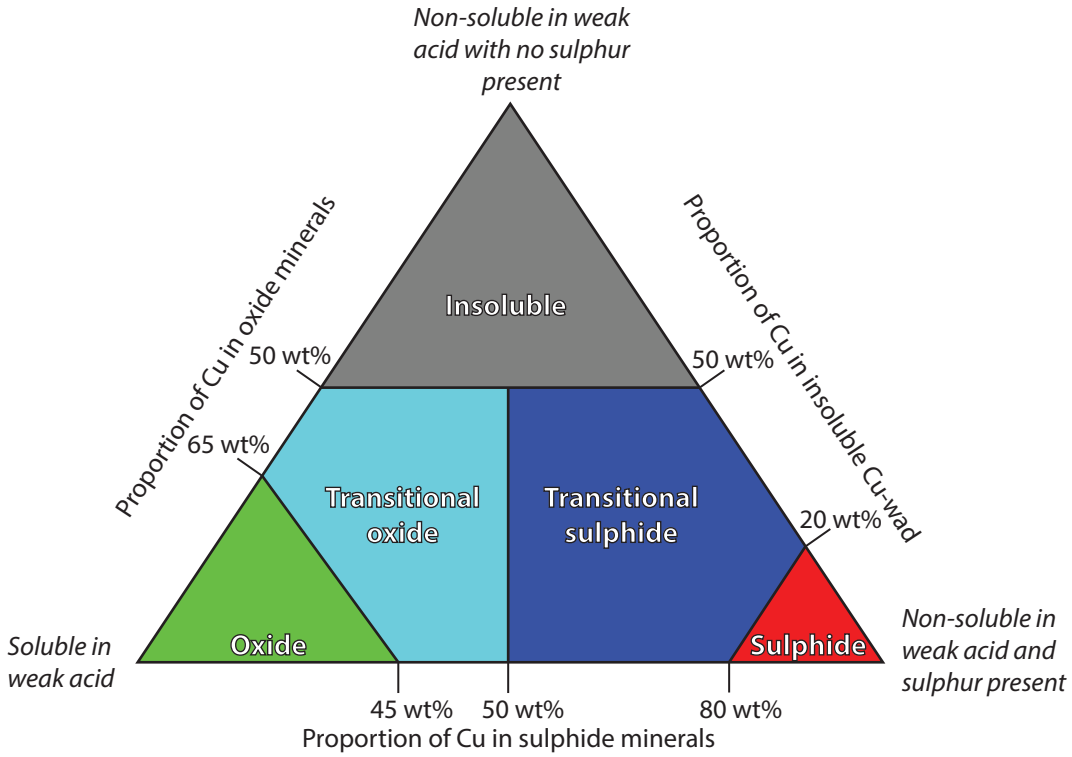

Figure 6.4 Revised Cu-species classification based on sequential leach data and sulphur. Proportion of sulphide minerals is reconciled against available sulphur based on chemical assay data for each sample.

minerals (Figure 6.4); oxide, transitional-oxide, transitional-sulphide, sulphide and insoluble. Samples with greater than 50 % of their contained Cu occurring as the non weak-acid soluble, black copper oxide phase were classified as insoluble.

6.2.6 Results

The new geochemical classification scheme was applied to a dataset of 2326 samples with sequential leach data and geochemical assays, primarily from sections 6,822,215 mN and 6,820,850 mN (Figure 6.5). Samples that contained <0.05 wt%Cu were classified as barren. A total of 347 samples, that were previously classified as sulphide or transitional, were found to actually contain substantial insoluble oxide Cu (Figure 6.6, Figure 6.7 A and B, Figure 6.8 A and B and Figure 6.9). All of the samples previously classified as oxide were classed as oxide by the new method. Some samples previously classified as sulphide were reclassified as insoluble (23 %) and transitional-sulphide (3 %; Figure 6.6). Transitional samples are predominantly split into either transitional-oxide or transitional-sulphide, with 18 % reclassified as insoluble (Figure 6.6).

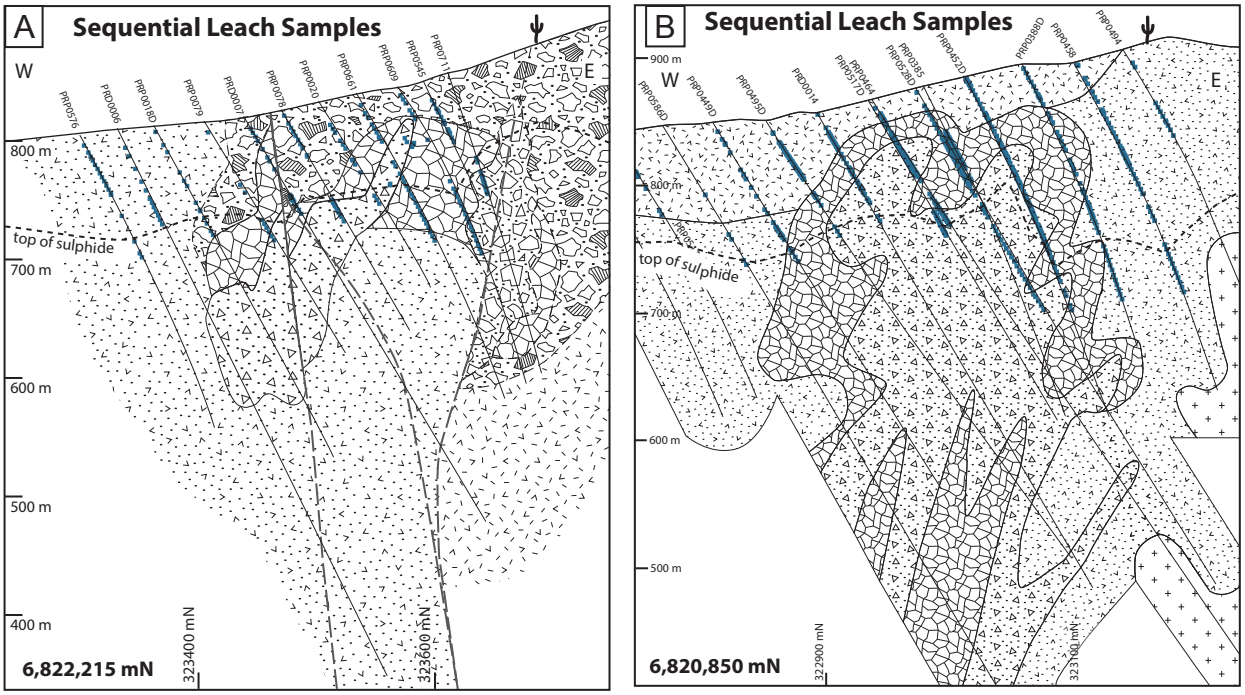

Figure 6.5 Cross sections to show distribution of 384 sequential leach data points on two study sections at A) 6,822,215 mN and B) 6,820,850 mN. Data from an additional 1979 samples, distributed widely throughout the oxide and transitional zone of the deposit were also available. Existing interpreted surface for top of sulphide also shown (provided by Hot Chili Ltd).

6.3 Extrapolation using proxies

A key object of this research was to extrapolate the ore classification across the entire deposit in order to highlight problematic areas, without incurring the cost of sequential leach analysis on every sample. In this study machine learning algorithms (MLAs) were tested in order to predict Cu species classification using sample depth, multi-element geochemistry and a wide range of logging parameters. MLAs are a group of data-driven inference tools which can be applied to high-dimensional data for automated pattern recognition (Witten et al., 2011). Once learned, pattern relationships can be applied to other similar data in order to generate predictions for data-driven classification and regression problems.

There are three major categories of machine learning which reflect the learning system; supervised learning, unsupervised learning and reinforcement learning. Supervised learning indicates that the computer is presented with example inputs and desired outputs with the aim of mapping inputs to outputs (Kotsiantis, 2007; Ripley,1996; Witten and Frank, 2005). During unsupervised learning, only examples are provided and the learning algorithm must find structure in the data — most clustering algorithms fall into this category (Kohavi and Provost, 1998). Reinforcement learning is where the computer interacts with a dynamic environment to achieve a goal, such as playing a game against an opponent.

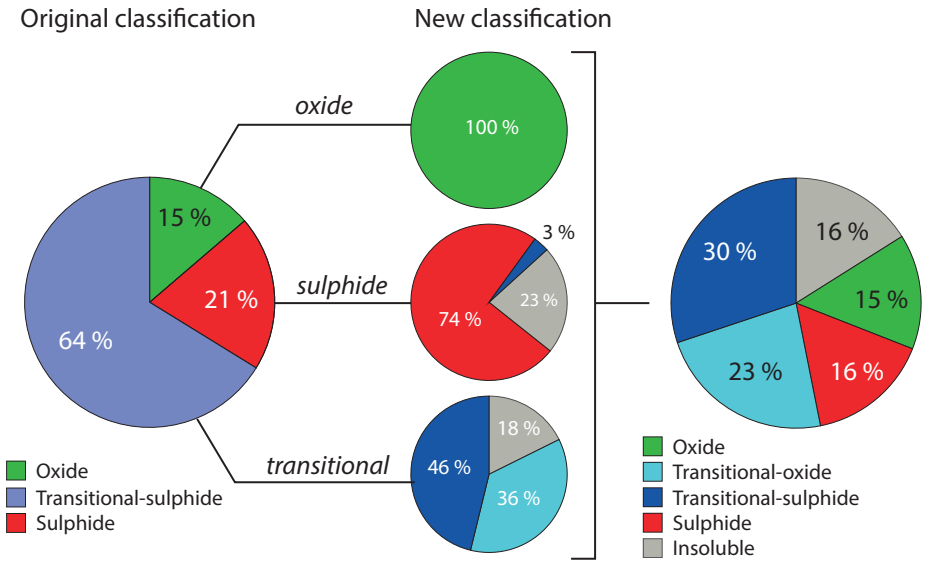

Figure 6.6 Comparison between classification of training set by original method and by revised method where residual Cu is reconciled against sulphur content. All samples previously classified as oxide remain classified as oxide. Some samples previously classified as sulphide are reclassified as insoluble (23 %) and transitional (3 %). Transitional samples are split into transitional oxide and transitional sulphide with 18 % reclassified as insoluble.

In this example a training set of inputs, also known as labelled or classified samples, was available that included all logging and geochemical assay data. The desired outputs, or inference targets, were the sequential leach classification of each sample. Therefore, supervised classification techniques were applied to the problem.

During supervised classification, MLA architecture and the statistical distributions of the observed data (i.e. the training set) guide the development of classification models, typically by minimizing an error function (Kuncheva, 2004; Marsland, 2009). Trained classification models can then be applied to similar input variables to predict the classes defined from the training data (Hastie et al. 2009; Witten and Frank, 2005). Two key requirements of the chosen algorithm were that it should generate a discrete answer (e.g. categorical), as opposed to a continuous, and that the method be transparent and easy to understand. A categorical classification (e.g. oxide, transitional, sulphide etc.) was also preferred to enable future database coding and integration of the data into resource models.

Figure 6.7 Cross sections at 6,822,215 mN showing sample classification and interpretation of Cu-species domains based on A) sequential leach data and original classification scheme. B) Sequential leach data and new classification scheme. C) Model data from machine learning methods with slice through 3D interpolant generated in Leapfrog Geo version 3.1.0 (model settings outlined in section 6.4.1). Also shown are the bottom of complete oxidation and top of sulphide surfaces interpreted from geological logging data (provided by Hot Chili Ltd) and Cu grade interpolants generated using Leapfrog Geo

Figure 6.8 Cross sections at 6,820,850 mN showing sample classification and interpretation of Cu-species domains based on A) sequential leach data and original classification scheme. B) Sequential leach data and new classification scheme. C) Model data from machine learning methods with slice through 3D interpolant generated in Leapfrog Geo version 3.1.0 (model settings outlined in section 6.4.1). Also shown are the bottom of complete oxidation and top of sulphide surfaces interpreted from geological logging data (provided by Hot Chili Ltd) and Cu grade interpolants generated using Leapfrog Geo.

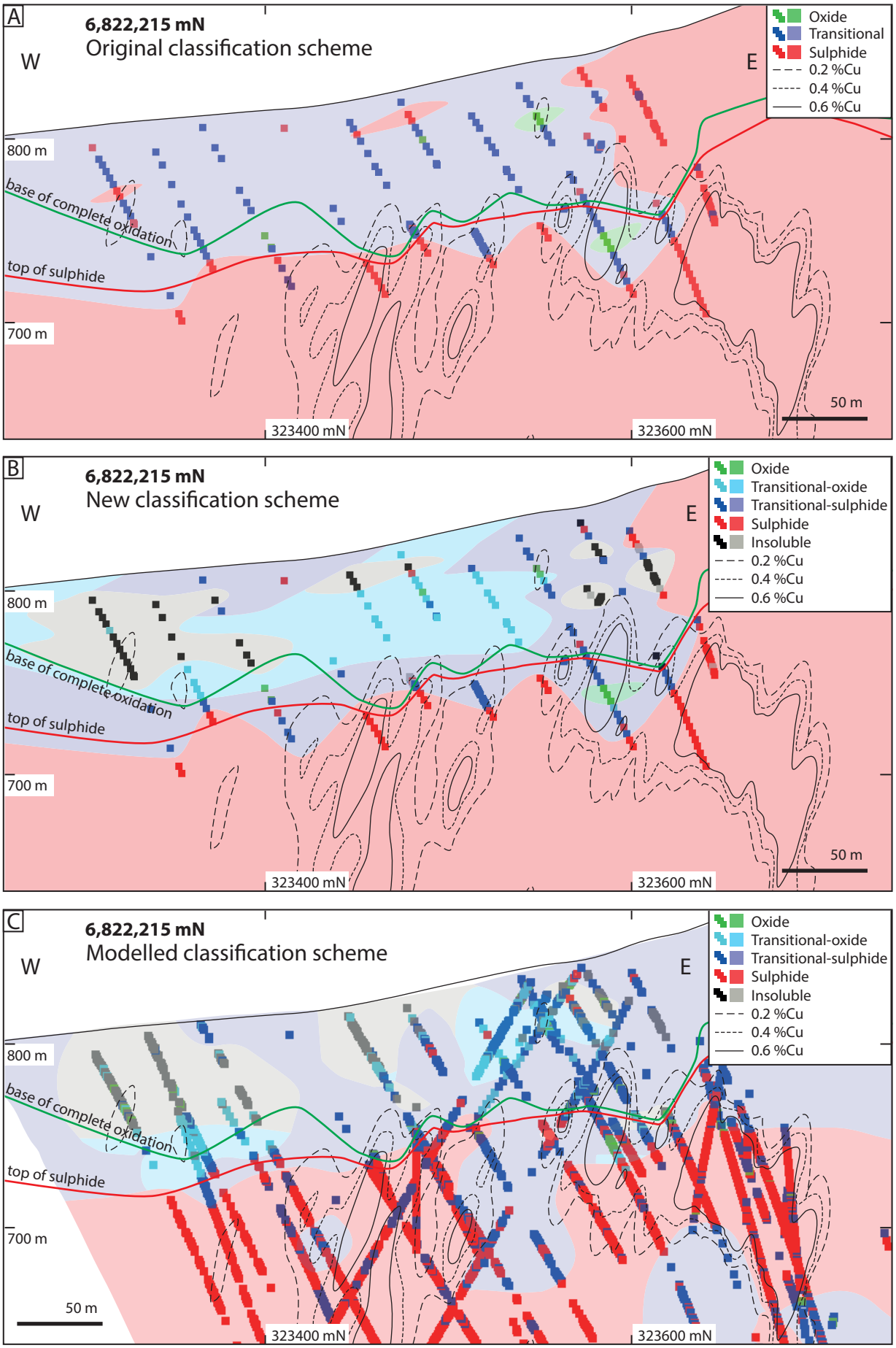
A
6,822,215 mN
Original classification scheme
W
E
Oxide
Transitional
Sulphide
0.2 %Cu
0.4 %Cu
0.6 %Cu
800 m
base of complete oxidation
top of sulphide
700 m
50 m
323400 mN
323600 mN
B
6,822,215 mN
New classification scheme
W
E
Oxide
Transitional-oxide
Transitional-sulphide
Sulphide
Insoluble
0.2 %Cu
0.4 %Cu
0.6 %Cu
800 m
base of complete oxidation
top of sulphide
700 m
50 m
323400 mN
323600 mN
C
6,822,215 mN
Modelled classification scheme
W
E
Oxide
Transitional-oxide
Transitional-sulphide
Sulphide
Insoluble
0.2 %Cu
0.4 %Cu
0.6 %Cu
800 m
base of complete oxidation
top of sulphide
700 m
50 m
323400 mN
323600 mN

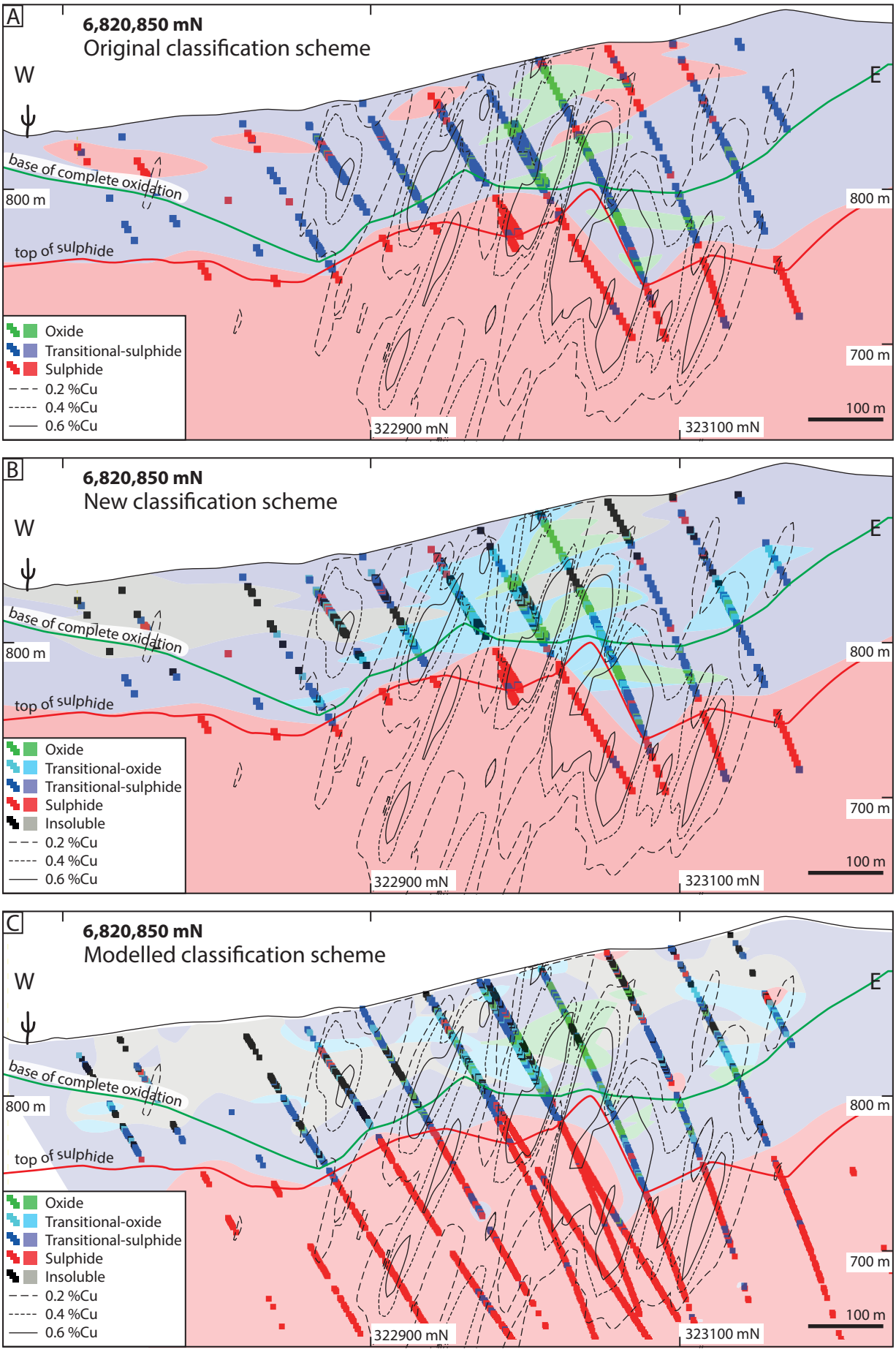
A
6,820,850 mN
Original classification scheme
W
E
base of complete oxidation
top of sulphide
800 m
800 m
700 m
100 m
322900 mN
323100 mN
Oxide
Transitional-sulphide
Sulphide
0.2 %Cu
0.4 %Cu
0.6 %Cu
B
6,820,850 mN
New classification scheme
W
E
base of complete oxidation
top of sulphide
800 m
800 m
700 m
100 m
322900 mN
323100 mN
Oxide
Transitional-oxide
Transitional-sulphide
Sulphide
Insoluble
0.2 %Cu
0.4 %Cu
0.6 %Cu
C
6,820,850 mN
Modelled classification scheme
W
E
base of complete oxidation
top of sulphide
800 m
800 m
700 m
100 m
322900 mN
323100 mN
Oxide
Transitional-oxide
Transitional-sulphide
Sulphide
Insoluble
0.2 %Cu
0.4 %Cu
0.6 %Cu

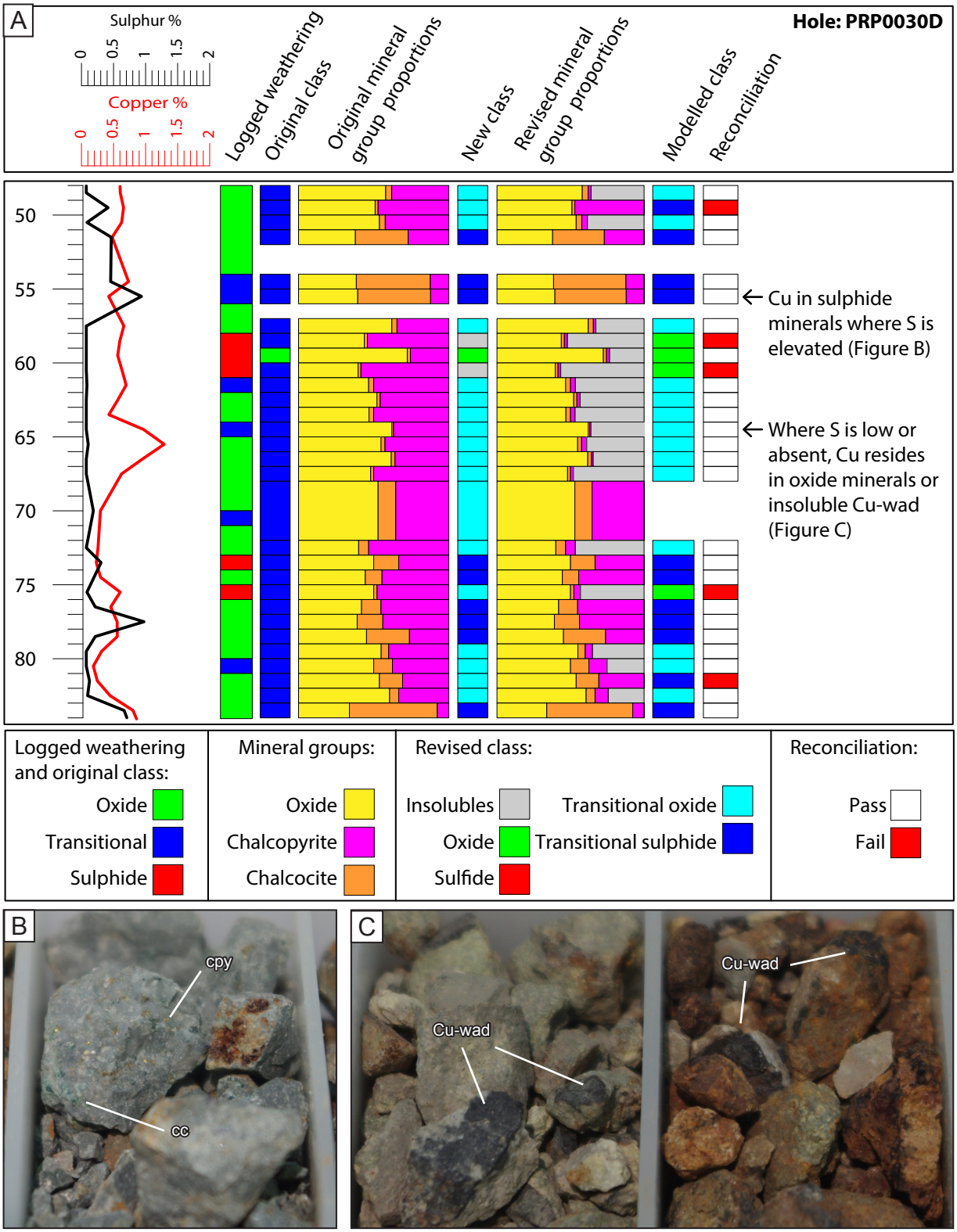

Figure 6.9 A) Log for hole PRP0030D to show Cu wt% and S wt%, logged weathering (from drill hole database provided by Hot Chili Ltd), original and revised Cu-species classification based on sequential leach data with breakdown of model proportions of each mineral group, modelled classification (by machine learning) and reconciliation of modelled classification against sequential leach based classification. Photo of chips trays showing B) sulphide minerals including chalcopyrite and chalcocite at 55 m and C) Cu-wad (insoluble in weak acid) at 65 m. The reconciliation of Cu against S in the new classification scheme indicates the presence of insoluble oxides where chalcopyrite was expected under the original classification scheme. The modelled classification is a good match against the new sequential leach based classification. cc = chalcocite, cpy = chalcopyrite.

Machine learning in geometallurgy

A review of current literature on the application of machine learning to geoscience and mining reveals a wide range of case studies. There are numerous published papers regarding the application of MLAs, especially neural networks (NN) and support vector machines (SVM), to mineral processing applications such as prediction of semiautogenous mill behaviour (Acuna and Curilem 2009) and wear (Ahmadzadeh and Lundberg, 2013), prediction of ball mill power draw (Datta and Mishra, 1999), flotation circuit behaviour (Cortez and Duráo, 1995; Gouws et al., 1996) and mean particle size prediction in blast fragmentation (Kulatilake et al. 2010). Machine learning has also been explored as an alternative to traditional geostatistical grade and resource estimation. This has included both NN (Williams, 1993; Wu and Zhou ,1993; Denby and Burnett, 1995; Yama and Lineberry, 1999; Samanta et al., 2005; Chatterjee et al., 2008; Dutta et al. 2011), SVM (Pozdnoukhov et al., 2002; Dutta et al. 2011) and sequential Gaussian simulation (Oliver and Willingham, 2016). Other examples of MLAs in the wider geoscience industry include the supervised classification of remote sensing data for prediction of land cover and vegetation class (Huang et al.,2002; Foody and Mathur,2004; Ham et al.,2005; Pal, 2005; Waske and Braun, 2009; Song et al.,2012), and for lithology classification (Cracknell and Reading, 2014, 2015). A variety of MLAs have also been applied to mineral prospectivity modelling, including: NN (Singer and Kouda, 1999; Brown et al., 2000; Porwal and Kreuzer, 2010); decision trees (Breiman et al., 1984); SVM (Boser et al., 1992; Cortes and Vapnik, 1995; Zuo and Carranza, 2011); and random forests (Breiman, 2001; Rodriguez-Galiano et al., 2014; Carranza, 2015).

The range of MLA applications in geoscience and mining is broad and likely to become much greater as machine learning continues to gain popularity as a tool for the analysis of large multivariate datasets and 'big data'. Although there are numerous case studies related to mill performance, there are only limited geometallurgy-specific examples. Given the variety and abundance of data typically available to a geometallurgist from the geology and metallurgy disciplines, and obvious benefits of automated pattern recognition, this void is surprising. No published examples were found of geochemical data being utilised for geometallurgy, which is also surprising given that multi-element geochemistry is routinely collected on every assay interval by many companies and provides an obvious deposit-wide data set.

6.3.1 Training set

A dataset of 2066 samples from Productora has been used in this study. The ore classification of each sample was defined from sequential leach data as described above. These data were combined with multi-element geochemistry (33-element ICP-AES) and all available logging data (including lithology, alteration, weathering, regolith, RQD; provided by Hot Chili Ltd) as the training set for machine

learning.

To enable the results to be interpreted and validated more easily, almost half (45 %) of the samples included in the training set were from cross-sections 6,822,215 mN and 6,820,850 mN, as the geology is well constrained on these sections (Chapter 3 and 4). Only samples with greater than 0.05 %Cu were included in the training set. Samples with < 0.05 wt%Cu were classed as 'Barren' (from a mining perspective) on the basis of Cu grade alone, without the need for further sub-categorization. It was also undesirable to include samples with <0.05 wt%Cu as the sequential leach data in these samples approaches detection limits which could cause samples to be misclassified.

6.3.2 Machine learning

The success of MLAs is dependant of the quality of data that they operate on. If these data are inadequate, or contain extraneous and irrelevant information, MLAs may produce poor results that are inaccurate, hard to understand or not useful (Hall, 1998). Associated attributes can be selected using evaluation functions. In this study we used evaluator and search methods, CfsSubsetEva (Hall, 1998) and BestFirst (Witten et al., 2011; Table 6.5), in open source machine learning Java software Waikato Environment for Knowledge Analysis (WEKA) version 3.6.11 to select appropriate attributes in the data set.

The training dataset of 2066 samples is considered limited in comparison to many machine learning problems where datasets may be many orders of magnitude larger. There are two general approaches to dealing with this problem; the holdout method and cross-validation (Witten et al., 2011). The holdout method reserves one third of the data for testing and uses the other two thirds for training. This ensures that the model can be tested on unseen data. In cross-validation, the data is equally partitioned at random into a fixed number (n) of folds. One fold is reserved for testing and the others (n-1) are used to train the model. This is repeated n times until all data has been used for testing once. This is called n-fold cross-validation. In order to maximise the amount of data used for training the classification models in this study, ten-fold cross-validation was adopted. Using this method an error rate is calculated for each fold reserved for testing. The ten error estimates are then averaged to yield an overall error estimate. Using ten folds is widely regarded as an appropriate number of folds for a robust error estimate (Witten et al. 2011).

The program WEKA was also used to develop a classification model based on the attributes selected using evaluator and search algorithms. Thirty four different classification algorithms, all available in the WEKA program, were applied to the training set to determine the optimum classification model in terms of accuracy and complexity (Appendix E3). Each algorithm was tested with ten-fold cross validation.

Table 6.5 Description of elevator and search machine learning algorithms employed to select the attributes most associated with Cu species classification.

Algorithm	Description	Reference
Attribute evaluator:		
CfsSubsetEva	Correlation-based feature subset selection for machine learning which evaluates the worth of a subset of attributes by considering the individual predictive ability of each feature along with the degree of redundancy between them. Subsets of features that are highly correlated with the class while having low inter-correlation.	Hall (1998)
Attribute selector:		
BestFirst	Searches the space of attribute subsets by 'greedy hillclimbing' - a mathematical optimization technique which belongs to the family of local search, Russell and Norvig (2010), augmented with a 'backtracking' search facility.	Witten et al. (2011)

To enable the model to be written as program script in reasonable time for application to unseen data, a simple model was preferred. In addition to this, it was also important that the model be transparent and easy to explain. For these reasons, decision tree (Breiman et al. 1984) and rule learner algorithms (Rakesh et al. 1993) were preferred, although a variety of other types of algorithms were also tested including naïve Bayes, nearest neighbour, support vector machine, clustering, linear logistic regression and locally weighted.

Decision trees have a flowchart-like structure similar to a tree branch where each split, or node, represents an attribute test (Breiman et al. 1984). Each branch is the outcome of that test and each leaf represents a class label (Russell and Norvig, 2010; Figure 6.10). Decision trees can also be combined with the Bagging algorithm (Breiman 1996). Bagging is a method of generating multiple predictions on bootstrap replicas (iterations) of a training set to return an aggregated prediction based on the most common outcome from each of the decision trees (Breiman, 1996). This method has the advantage of reducing variance for improved reliability of the result.

6.3.3 Machine learning results

Using evaluator and search methods, CfsSubsetEva (Hall, 1998) and BestFirst (Witten et al., 2011), on the training set of 2066 samples, nine attributes were found to be most closely associated with the ore classification as determined from sequential leach data. The nine attributes are as follows: sample depth in drill hole, Ca %, Cu %, Fe %, K %, Mn ppm, S %, Ln(Cu/S) and the logged regolith term. Samples where the logged regolith term changed within the assay interval, causing ambiguous parameter values, were omitted from the training set for modelling. After testing a wide range of classification algorithms (results provided in Table 6.6), it was found that the algorithms J48 decision tree (Quinlan, 1993), REPTree decision tree (WEKA, 2014) and Bagging method (Breiman, 1996) with REPTree (Table 6.7),

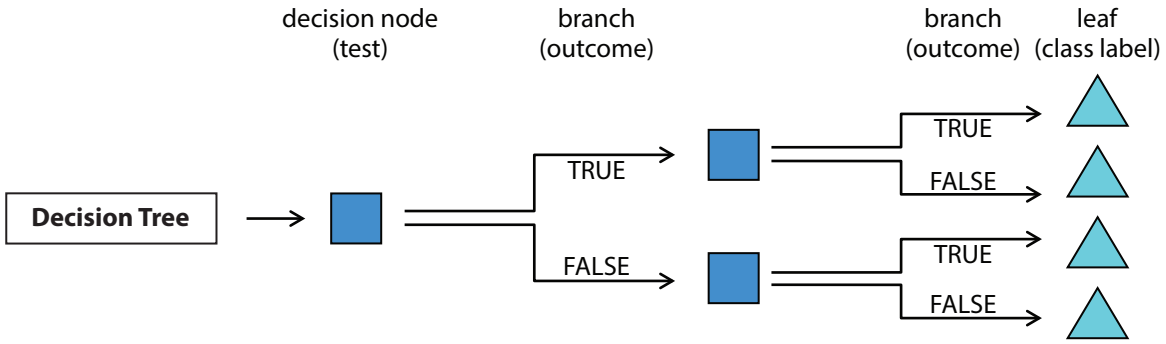

Figure 6.10 Schematic diagram to show basic structure and nomenclature of a decision tree.

all available in the WEKA program, generated accurate results and also satisfied the requirements for transparency and low complexity.

The WEKA Bagging-REPTree algorithm with five iterations was chosen as the optimum model with an accuracy of 67.6 % reported using ten-fold cross validation (Table 6.6 and Table 6.8). It combines the bagging predictor approach with a simple decision tree classifier. The J48 decision tree is similar in accuracy to the REPTree but it is significantly more complex, having double the tree size (number of nodes) in each decision tree. Bagging was trialled with ten and five bootstrap replicates. Bagging improved the accuracy as measured by cross validation using both models. Using five bootstrap replicates was sufficient to gain most of this advantage and it was concluded the additional complexity of ten iterations (i.e. ten different trees) could not be justified by the small gain in accuracy (1.4 % gain for Bagging-REPTree).

The Bagging-REPTree algorithm, with five iterations has a success rate of 82.6 % on the training set and 67.6 % as estimated by ten-fold cross validation (Table 6.8). A matrix of results from this model applied to the training set using ten-fold cross validation is presented in Table 6.9. The model is most successful at recognising sulphide, transitional-sulphide and insoluble samples with accuracy of 70.2 %, 87.5 % and 67.8 % respectively against the training set (Table 6.9). The model performed less effectively when discriminating between transitional-oxide and oxide, commonly confusing the two, with accuracy of 49.8 % and 52.2 % respectively. Figure 6.11 presents the break down of MLA predicted classification for each of the five classes. The most confusion exists between the oxide, transitional-oxide and insoluble classes (Figure 6.11 and Figure 6.9). Most sulphide samples are correctly classified as sulphide, although some additional transitional-sulphide samples are also misclassified as sulphide (Table 6.9 and Figure 6.11). Misclassified samples are widely distributed through the weathering zone on each study section and do not appear to be limited to any particular location, class or geological feature (Figure 6.12).

Table 6.6 Accuracy and root mean square error (RMSE) for the thirty-four algorithms tested to define a Cu-species classification model using the following nine attributes: sample depth, Ca %, Cu %, Fe %, K %, Mn ppm, S %, Ln(Cu/S) and the logged regolith term. Descriptions of each algorithms provided in Appendix E3.

Classifier	Type	Accuracy*	RMSE	Complexity	Comment	Ref.
Rules						
ConjunctiveRule	Rule learner	48.76	0.351	1 rules	Too simplistic, poor accuracy	23
DecisionTable	Decision tree table	58.88	0.332	235 rules	Non transparent	8
DTNB	Decision table/ naive bayes hybrid	61.40	0.322	663 rules	Non transparent	22
Jrip	Rule learner	63.15	0.328	20 rules	OK	6
Nnge	Nearest-neighbour-like	61.01	0.395	453 rules	OK	9, 17
OneR	1R classifier	47.36	0.450	85 rules	Too simplistic (only uses LnCu/S), poor accuracy	4
PART	Rules learner/ decision tree	66.87	0.335	unknown	Non transparent	12
Ridor	Ripple-down rule learner	60.96	0.395	unknown	Non transparent	23
Trees						
BFTree	Decision tree	63.77	0.349	411/206‡	OK	21
DecisionStump	1-level decicion tree	48.81	0.351	3 rules	Too simplistic, poor accuracy	23
FT	Functional tree	66.73	0.335		Includes regression function, too complex	19, 20
J48	Decision tree	66.00	0.340	474/269‡	OK **Preferred**	5
J48graft	Decision tree	66.34	0.339	620/342‡	OK, more complex	14
LADTree	Decision tree	61.84	0.311	15 trees	Non transparent, complex	16
NBTree	Decision tree with Naïve Bayes	63.38	0.326	152/80‡	Non transparent, complex	11
RandomForest	Random forests	69.39	0.2901	10 trees	Non transparent, complex	15
RandomTree	Decision tree	62.71	0.386	1134	OK	23
REPTree	Decision tree	63.87	0.323	153	OK **Preferred**	23
SimpleCart	Decision tree	62.64	0.322	149/75‡	OK	2
Bayes						
NaiveBayes	Naïve Bayes	51.57	0.387		Linear - not suitable	1
NaiveBayesSimple	Naïve Bayes	51.96	0.389		Linear - not suitable	23
BayesNet - Simple Estimator - K2	Naïve Bayes	63.05	0.323		Non transparent, complex	23

*Accuracy = percentage of correctly classified samples using 10-fold cross validation, ‡decision tree complexity = tree size/ number of leaves. Ref = reference. [1]Duda and Hart (1973), [2]Breiman (1984), [3]Aha et al. (1991), [4]Holte (1993), [5]Quinlan (1993), [6]Cohen (1995), [7]Cleary and Trigg (1995), [8]Kohavi (1995), [9]Martin (1995), [10]Freund anbd Schapire (1996), [11]Kohavi (1996), [12]Frank and Witten (1998), [13]Platt (1998), [14]Webb (1999) [15]Breiman (2001), [16]Holmes et al. (2002), [17]Roy (2002), [18]Frank et al. (2003), [19]Gama (2004), [20]Landwehr et al. (2005), [21]Shi (2007), [22]Hall and Frank (2008), [23]Witten et al. (2011).

Table 6.6 continued.

Classifier	Type	Accuracy*	RMSE	Complexity	Comment	Ref.
Functions						
SMO - PolyKernel	Support vector	58.06	0.350		Includes regression function, too complex	12
SimpleLogistic - polyKernel	Linear logistic regression	62.90	0.317		Includes regression function, too complex	20
Lazy						
Kstar	Nearest-neighbour	65.81	0.323		Non transparent, complex	7
LWL	Locally weighted	48.71	0.345		Non transparent, complex	18
IB1	Nearest-neighbour	64.98	0.374		Non transparent, complex	3
Ibk	Nearest-neighbour	64.98	0.374		Non transparent, complex	3
Combinations						
AttributeSelectedClassifier (CfsSubsetEval - BestFirst - J48)	Decision tree	62.51	0.338		OK	23
Bagging - REPTree	Decision tree	69.05	0.290	222	**Preferred**	23
ClassificationViaClustering (SimpleKMeans - EuclideanDistance)	Clustering	36.61	0.535		Poor	23
AdaBoostM1 (DecisionStump)	Decision tree	48.81	0.351	3 rules	Too simplistic, poor accuracy	10
AdaBoostM1 (REPTree)	Decision tree	68.66	0.299	10 trees 189 nodes	Non transparent, complex	10
AttributeSelectedClassifier (CfsSubsetEval - REPTree)	Decision tree	59.51	0.334	151	Too simplistic (only uses From, S%, LnCuonS, Regolith)	23

*Accuracy = percentage of correctly classified samples using 10-fold cross validation, ‡decision tree complexity = tree size/ number of leaves. Ref = reference. [1]Duda and Hart (1973), [2]Breiman (1984), [3]Aha et al. (1991), [4]Holte (1993), [5]Quinlan (1993), [6]Cohen (1995), [7]Cleary and Trigg (1995), [8]Kohavi (1995), [9]Martin (1995), [10]Freund anbd Schapire (1996), [11]Kohavi (1996), [12]Frank and Witten (1998), [13]Platt (1998), [14]Webb (1999) [15]Breiman (2001), [16]Holmes et al. (2002), [17]Roy (2002), [18]Frank et al. (2003), [19]Gama (2004), [20]Landwehr et al. (2005), [21]Shi (2007), [22]Hall and Frank (2008), [23]Witten et al. (2011).

Table 6.7 Description of preferred machine learning classification algorithms employed.

Classifier Algorithm	Description	Ref.
REPTree	Fast decision tree learner. Builds a decision/regression tree using information gain/variance and prunes it using reduced-error pruning (with backfitting). Only sorts values for numeric attributes once. Missing values are dealt with by splitting the corresponding instances into pieces (i.e. as in C4.5 decision tree, Quinlan, 1993).	Witten et al. (2011)
J48	Class for generating a pruned or unpruned C4.5 decision tree. At each node of the tree, C4.5 chooses the attribute of the data that most effectively splits its set of samples into subsets enriched in one class or the other.	Quinlan (1993)
Bagging	Also known as 'bootstrap aggregating', bagging is the use of multiple machine learning algorithms to improve the reliability of the result by reducing variance and over fitting. Can be used for classification and regression depending on the base learner.	Breiman (1996)

Table 6.8 Algorithm specifications used and resulting accuracy.

Classifier	Confidence Factor[1]	Min. number of objects	Min. variance propagation	Folds[2]	Seed[3]	Max. depth[4]	Tree Size[5]	Accuracy
J48	0.25	2	-	3	1	-	474	66.0 %
RepTree	-	2	0.001	3	1	none	153	63.9 %

Classifier	Bag Size[6]	Iterations[7]	Seed[3]	Classifier	Tree Size[5]	Accuracy
Bagging	100	5	1	J48 (as above)	456	67.6 %
Bagging	100	10	1	J48 (as above)	480	69.5 %
Bagging	100	5	1	RepTree (as above)	226	67.6 %
Bagging	100	10	1	RepTree (as above)	222	69.0 %

[1]confidence factor = effectiveness of 'post-pruning' i.e. evaluating the decision error (estimated percent misclassifications) at each decision junction and propagating this error up the tree, [2]folds = refers to the repeated validation steps in k-fold cross validation, [3]seed = collection of information used as a training set, [4]depth = maximum number of decision tree queries before a leaf, in this case class, is reached, [5]tree size = number of nodes, [6]bag size = training set size, [7]iterations = number of bootstrap replicas. min = minimum, max = maximum

Table 6.9 Confusion matrix of results from Bagging-REPTree model with five iterations using 10-fold cross validation against sequential leach based classification for a 2066 sample training set. Overall accuracy is 67.6 % (Table 6.8).

		Modelled classification					
Actual classification	*n*	**Insoluble**	**Oxide**	**Transitional-oxide**	**Transitional-sulphide**	**Sulphide**	**Accuracy**
Insoluble	329	223	29	74	2	1	67.8 %
Oxide	351	29	166	95	28	0	52.2 %
Transitional-Oxide	478	78	92	238	67	3	49.8 %
Transitional- Sulphide	631	2	8	23	552	46	87.5 %
Sulphide	309	0	2	3	87	217	70.2 %

6.3.4 Extrapolation of machine learning model

The five iterations of the REPTree decision tree as reported by the program WEKA were reformatted for the Python programming language (Appendix E4). The bagging component was performed using the 'index' function in Microsoft Excel to choose the most common result. As the results are counted from five trees, ambiguity can occur where three different classes are predicted, e.g. where two classes receive two votes. In this case it is not possible to determine which of the classes with two votes is correct, leading to ambiguity. This situation arose 81 times in the 2065 sample training set, 3.9 % of total predictions. As the index function reports the first pair in the array as the preferred result, this leads to a slight bias toward the results of first three trees.

6.3.5 Results of extrapolation

The decision tree model was applied using Python code to every assay interval with greater than

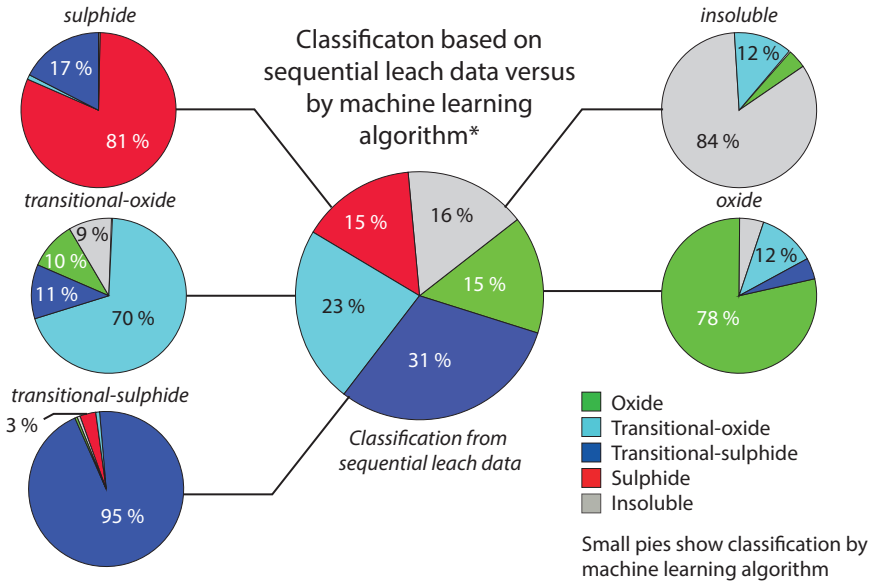

Figure 6.11 Pie charts to show classification of training set by sequential leach data (using new classification scheme; large pie) against predicted classification by machine learning and geochemical assays with logging (small pies). Confusion exists between the classification of oxide, transitional-oxide and insoluble classes where as prediction of sulphide and transitional-sulphide is more accurate. *Data presented from entire training set without cross-validation.

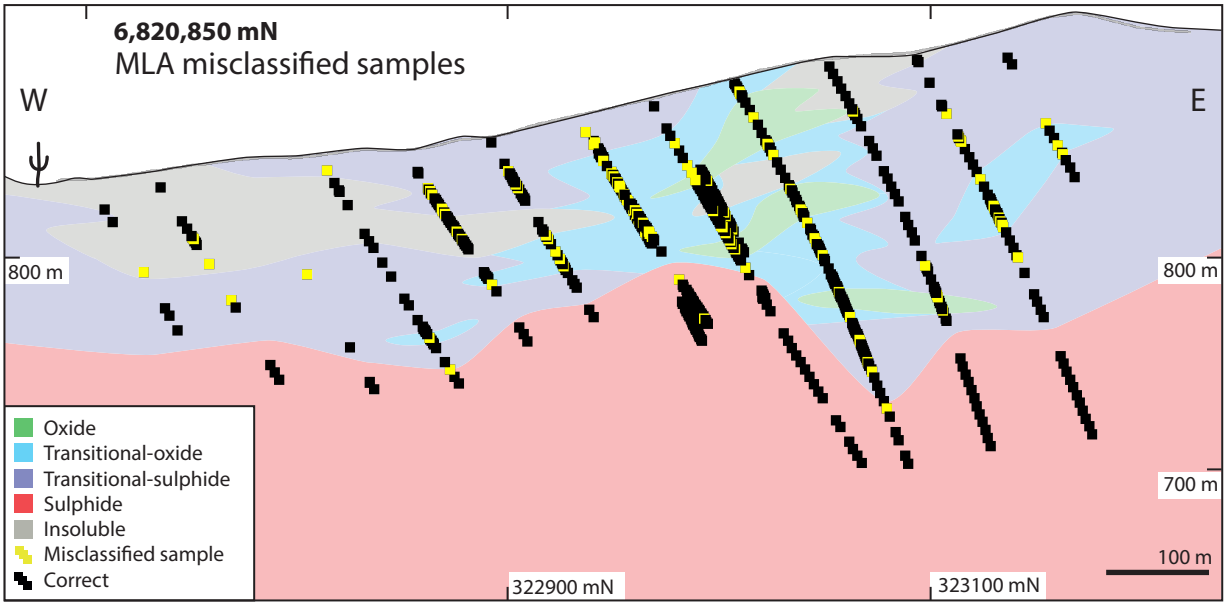

Figure 6.12 Cross section at 6,820,850 mN showing samples which were misclassified by the machine learning algorithm compared to the new sequential leach classification scheme. Interpretation of new sequential leach data also shown by coloured domains.

0.05 wt%Cu (approximately 81,000 assays) in order to generate a predicted ore classification for each assay interval. Over half of the samples with greater than 0.05 wt%Cu were classified as sulphide and a further 25 % as transitional sulphide. Only 2 % were classified as oxide, 6 % as transitional oxide and 8 % as insoluble.

Compared to the original prediction of the weathering surfaces, based largely on manual logging, a more complex interpretation of the predicted class is possible, one which includes domains rather than

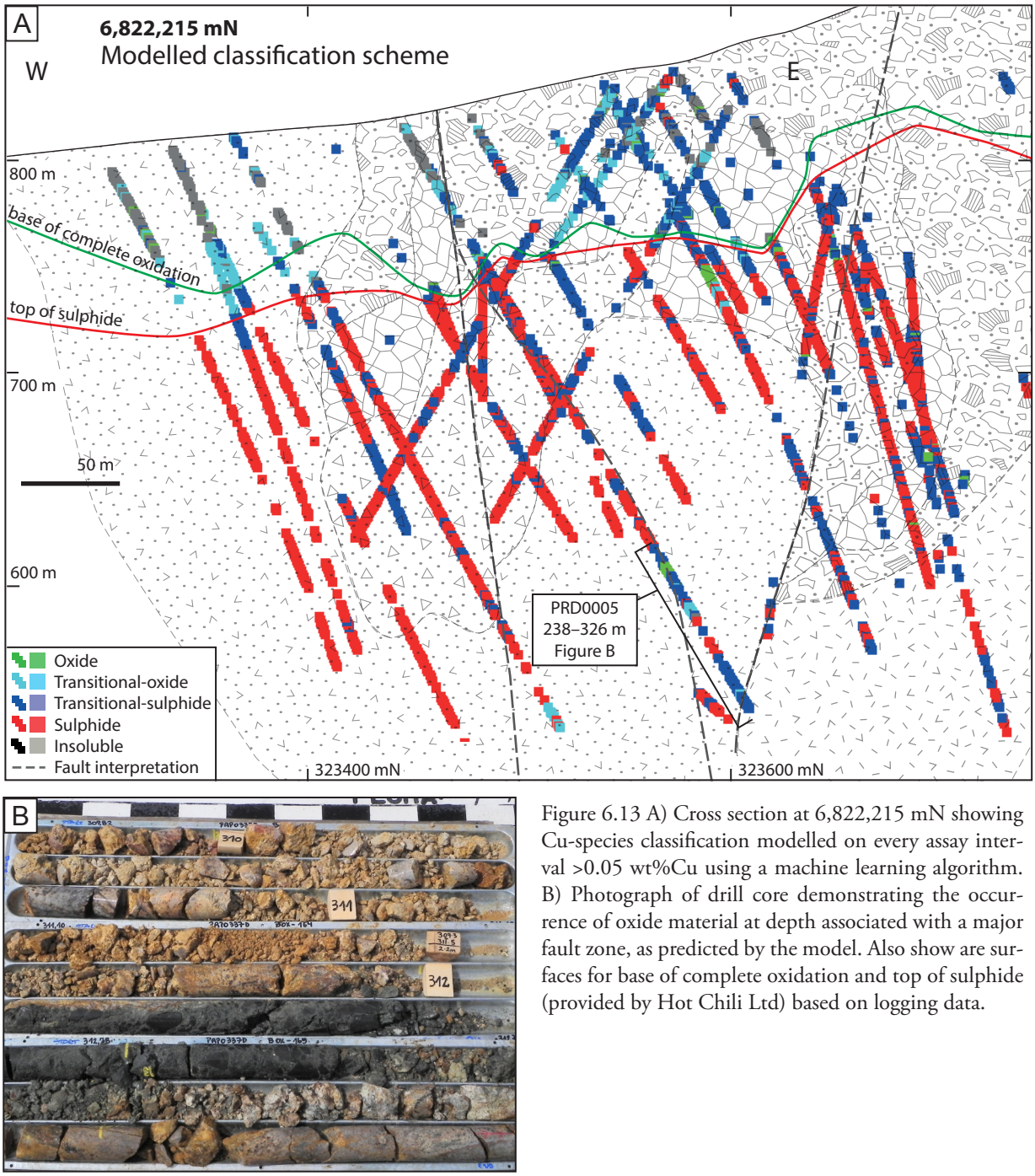

Figure 6.13 A) Cross section at 6,822,215 mN showing Cu-species classification modelled on every assay interval >0.05 wt%Cu using a machine learning algorithm. B) Photograph of drill core demonstrating the occurrence of oxide material at depth associated with a major fault zone, as predicted by the model. Also show are surfaces for base of complete oxidation and top of sulphide (provided by Hot Chili Ltd) based on logging data.

just surfaces (Figure 6.7 C and Figure 6.8 C). The predicted Cu-species class results on every assay interval >0.05 %Cu indicate that across the centre of the deposit, sulphide material locally extends to shallower elevations (>50 m above the top of sulphide surface at 6,821,455 mN and 20 m shallower on section 6,820,850 mN; Figure 6.8 C) than previously thought. Pockets of transitional-sulphide material also occur at shallow depths (<50 m from surface), above the previously interpreted base of complete oxidation (Figure 6.7 C and Figure 6.8 C). Transitional-sulphide material is also predicted at great depths (>400 m from surface). On section 6,822,215 mN the predictions of deep transitional-oxide material coincide with interpretations of fault zones and can be validated by review of core photography

Table 6.10 Rougher recovery at 150 µm and acid soluble Cu content with predicted Cu-species classification for fourteen metallurgy samples tested for flotation. Metallurgical test work data provided by Hot Chili Ltd. Cu-species classification is based on nearest neighbour holes as multi-element geochemical data was not available for metallurgical samples. Samples with high estimated transitional-sulphide and transitional-oxide components generally have lower recovery and higher acid soluble Cu content (FD-2, -3, -4, -5) compared to those predicted as purely sulphide (FD-8, -9, -10, -11, 12). However exceptions also exist which require more detailed investigation (FD-6 and FD-13).

Sample	Total meterage	Contiguous	Proportion transitional-sulphide (%)	Proportion transitional-oxide (%)	Rougher recovery at 150 µm (%)	Acid soluble Cu (%)
FD-1	143	No	9	0	90.2	5
FD-2	138	No	18	19	87.1	9
FD-3	163	No	19	7	79.0	10
FD-4	157	No	0	13	66.5	16
FD-5	36	Yes	58	0	68.6	26
FD-6	16	Yes	0	0	88.0	26
FD-7	9	Yes	0	0	(no data)	27
FD-8	10	Yes	0	0	83.0	6
FD-9	9	Yes	0	0	87.4	6
FD-10	11	Yes	0	0	84.3	4
FD-11	10	Yes	0	0	86.5	5
FD-12	10	Yes	0	0	96.4	5
FD-13	10	No	100	0	86.8	6
FD-14	19	No	53	0	94.3	4

(Figure 6.13). Oxide-dominant material largely occurs at shallow depth (<75 m from surface) except in the south (< 6,820,850 mN) where oxide material is predicted to extend to depths of 150 m from surface — this is consistent with logged weathering and is likely indicative of a steep fault zone (Figure 6.8).

Metallurgical data for flotation response and acid soluble Cu content from 14 samples were compared to the Cu-species classification (Table 6.10). The metallurgical samples consist of a composite of up to 163 m of drill core (both contiguous and non-contiguous). An estimate of the proportion of each composite sample that is transitional-sulphide and transitional-oxide was made based on the MLA modelled Cu-species class of the nearest neighbour interval(s) from the drill hole database. Generally samples that have a significant transitional-sulphide and/or transitional oxide component also have poorer flotation recovery and increased acid soluble Cu content (for example, samples FD-2, -3, -4 and -5; Table 6.10). This data supports the results of the MLA modelled Cu-species classification.

6.4 Modelling predicted ore class in 3D

6.4.1 Method

In order to visualise domains of each mineralogical class, the dataset of predicted Cu-species classes was

modelled in 3D using the Leapfrog Geo version 2.2 implicit 3D modelling approach. Implicit modelling differs from explicit modelling in that models are generated by computer algorithms directly from a combination of measured data and user interpretation (Lane, 2016). Traditional explicit models rely on the modeller/user essentially drawing the geological structures at regular intervals and then joining them up – commonly known as wire framing (Lane, 2016).

The MLA modelled data for oxide, transitional-oxide and insoluble classes are highly variable, in many areas alternating on a meter by meter basis (Figure 6.7 C and Figure 6.8 C). This poses challenges to the implicit 3D modelling approach since domains of mixed class proportions are a more likely scenario. In order to address this issue, the predicted ore classification data was composited to filter out intervals of less than 2 m. The composited data was then modelled in Leapfrog Geo version 2.2 using the intrusion algorithm to simulate the class domains with models clipped to topography and within 80 m of drill holes. A trend surface, approximating the topographic surface (dip = 3.34°, azimuth = 0° and pitch = 0° with ellipse ratio of maximum = 3, intermediate = 3, minimum = 1). was applied to the oxide, transitional-oxide and insoluble models in order to emphasise lateral continuity. Three dimensional models where generated for each class domain with an adaptive resolution of 25.

6.4.2 Results

Cross section slices through the implicit 3D model are presented in Figure 6.7 C and Figure 6.8 C and 3D images in Figure 6.14. The 3D model indicates significant domains of transitional-oxide and oxide occur in the northeast and south of the pit design (Figure 6.14 B). The insoluble class domains are spatially associated with the oxide and transitional-oxide domains. Sulphide was modelled as a continuous domain at depth (> 100 m) with some perched domains modelled at shallower levels (0–50 m; Figure 6.14 C). The 3D model suggests a large volume of transitional-sulphide material in the shallow portions of the deposit (Figure 6.14 D). However, in areas such as the eastern portion of the pit design (Figure 6.14 A), this is an artefact of low sample density where the implicit modelling has extrapolated between few data points. Since the pit area has been drilled on an 80 m by 40 m spacing, low data point density is primarily a result of barren samples which were not classified. Including the barren samples as a 'barren-unknown Cu-species' class may help mitigate this modelling challenge and reduce erroneously large transitional-sulphide domains. Developing more advanced 3D models fell beyond the scope of this study, however it is acknowledged that experimentation with more sophisticated statistical modelling would likely generate improved results.

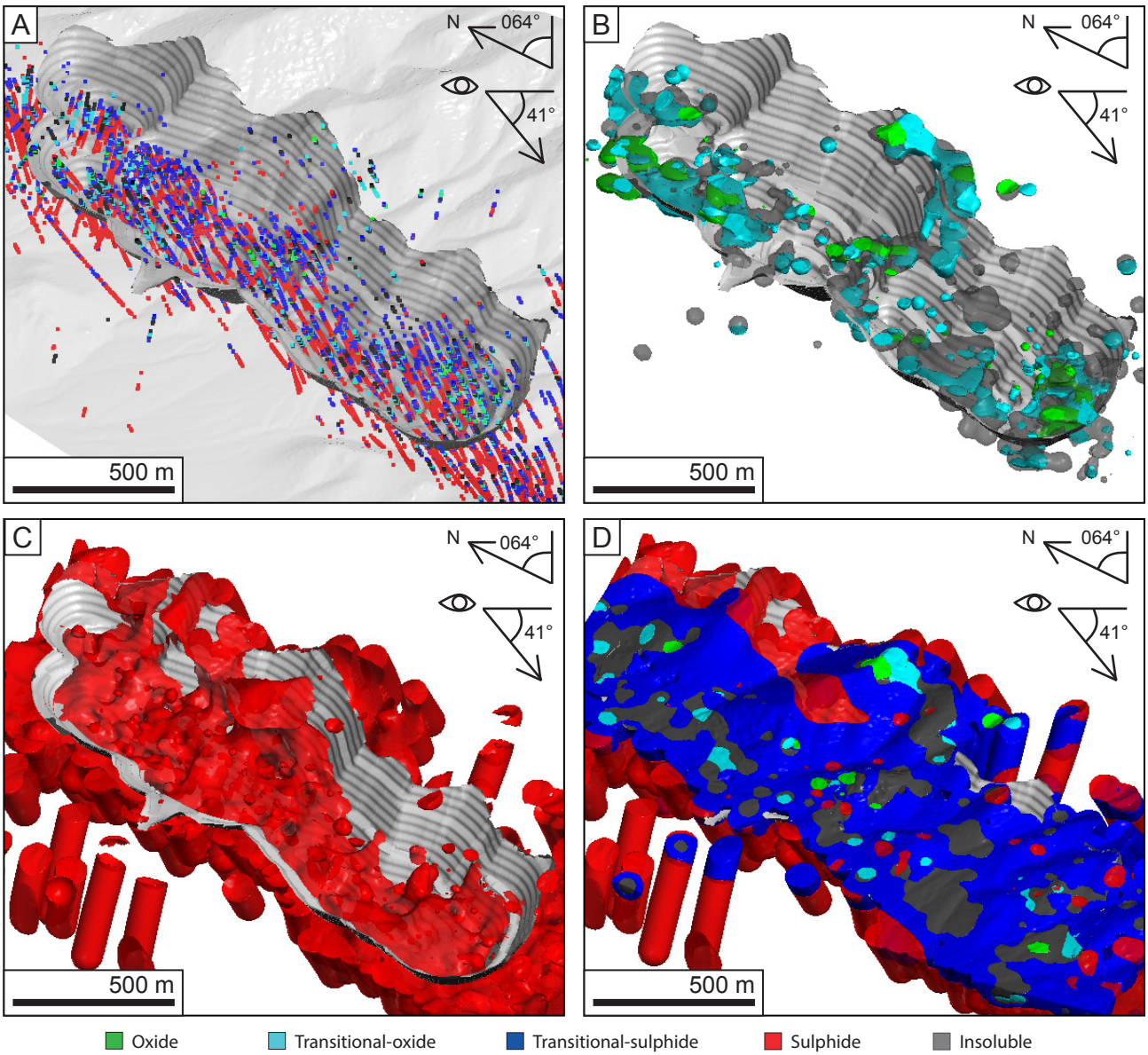

Figure 6.14 Images rendered from Leapfrog Geo to show data points and 3D domain volumes. A) Classified assay intervals >0.05 wt%Cu with pit shell design (March, 2014; provided by Hot Chili Ltd) and transparent topography. Implicit 3D models of Cu-species class domains: B) oxide, transitional-oxide and insoluble, C) sulphide, D) all domains.

6.5 Discussion

6.5.1 New sequential leach classification scheme

The revised classification scheme provides a useful reconciliation of weak acid insoluble Cu against S in order to predict chalcopyrite versus non-sulphide insoluble Cu mineral species, which are inferred to be largely Cu-wad or similar. The original classification scheme did not differentiate chalcopyrite from Cu-wad. In some cases, this resulted in samples that did not contain S being classified as sulphide or transitional. The ability to predict Cu-wad occurrence enables domains of potentially poor recovery to be identified. The revised classification also prevents misidentification of sulphide or transitional domains which actually have high Cu-wad content.

The reclassification of some sulphide and transitional samples to insoluble is significant as these samples are likely to have poorer recovery than previously predicted (Figure 6.6). Where domains of substantial insoluble copper occur within the Productora resource, marginal low grade ore may be reclassified as waste if the revised recovery is below cut off grade. No significant insoluble copper domains were identified within the March 2014 resource wire frames provided by Hot Chili Ltd.

The revised scheme also separates original transitional samples into transitional-sulphide and transitional-oxide based on the dominant Cu-species. This provides a useful guide for the assessment of material for leaching over flotation and visa-versa as it indicates the dominant mineralogy. For example, across section 6,822,215 mN the original ore classification method indicates that all the shallow material is transitional ore (Figure 6.7 A). The revised classification scheme on this section indicates heterogeneity in this material, with a significant domain of oxide dominant material (transitional-oxide) and pockets of insoluble material (Figure 6.7 B). Similarly on section 6,820,850 mN, the revised classification scheme indicates domains of oxide material surrounded by transitional-oxide material grading to transitional-sulphide material (Figure 6.8 B). This distinction defines a larger domain of material suitable for leach recovery than the original classification of transitional indicated, as the former classification did not provide any indication of whether the material was dominated by oxide or sulphide minerals.

In the new classification scheme (version 1; Figure 6.4), it is assumed that all S is associated with chalcopyrite and does not account for S in other phases, such as pyrite or other Cu-sulphides. Consequently, estimates of total insoluble material can be regarded as an optimistic scenario. For example, if pyrite also remains in the rock, then the S budget for chalcopyrite is less. Therefore, where S is insufficient, the Cu associated with Cu-wad will be higher than estimated. Pyrite and molybdenite are the only other major sulphide phases that are not accounted for by the sequential leach data (Chapter 5). In Chapter 5, modal mineralogy calculated from chemical assay via linear programming was shown to provide robust estimates for both pyrite and molybdenite. Including the proportions of pyrite and molybdenite in the classification scheme allows S in these minerals to be reconciled and excluded from estimates of chalcopyrite (section 6.2.5). An amended classification scheme (version 2) that includes pyrite and molybdenite data, which were not available prior to development of the new classification scheme and machine learning phase presented in this chapter, is provided in Appendix E5 with a summary of results. Compared to the classification scheme presented in this chapter, the reconciliation of S in pyrite, molybdenite and chalcocite leads to the reclassification of 14 samples in the training set from transitional-oxide (4) to insoluble, from transitional-sulphide to transitional-oxide (6), and sulphide to transitional-sulphide (4). The low number of reclassified samples indicates that the more simplistic

scheme (version 1) is sufficient to capture the predominant Cu-species variability.

The new classification scheme (version 1) has the most impact on shallow samples (<100 m from surface) where Cu-wad is more prolific (section 4.7). The original classification method predicts perched sulphide domains where no S is present (Figure 6.8 A and Figure 6.9 A). These domains are flagged for high insoluble Cu content under the new scheme. The discrimination of true sulphide material is consistent with the original classification and logged weathering (Figure 6.7, Figure 6.8 and Figure 6.9).

6.5.2 Machine learning modelled classification

The machine learning model developed for Productora ore classification proves most successful at defining transitional-sulphide and sulphide material (87.5 % and 70.2 % accuracy respectively; Table 6.9) compared to the training set (Figure 6.11). In combination with logging and other available data, the MLA modelling results enable a robust interpretation of sulphide-dominant domains (Figure 6.7 C and Figure 6.8 C). The model also proved successful at identifying insoluble Cu dominant material, with 68 % accuracy (Table 6.9). This is particularly significant as there was previously no method of predicting domains dominated by insoluble Cu-wad. Being able to identify areas of abundant insoluble, and essentially unrecoverable Cu, enables these domains to be more critically assessed at an early stage for inclusion in, or rejection from, resource estimates. It also enables poor recoveries from test work to be rationalized and weighted appropriately.

The model was least effective at discriminating between transitional-oxide and oxide (49.8 % and 52.2 % accuracy respectively; Table 6.9), but overall the model successfully identified samples dominated by oxide Cu-species as opposed to sulphide Cu-species (Figure 6.11). This is the most important distinction with respect to the processing route for ore, flotation or leach recovery. The MLA model data on every assay interval >0.05 wt%Cu provides additional information to inform the definition of domains of variable Cu-species at Productora by combining several data sets to generate the best modelling result. A significant advantage of this method is that it allows the identification of appropriate target areas for future sampling.

An important limitation of the machine learning method is that it is very dependent on the training set. It is essential that the training set data be as representative of the deposit as possible. The more representative the training set, the more reliable the model is likely to be. In this case a large proportion of data was taken from two control sections where detailed knowledge of the geology and a high density of data allowed the results to be evaluated. Further sequential leach assays should now be undertaken in order to test the model off-section, and up-date it as necessary.

A major outcome of this research has been an increase in the data available for determining Cu-species classification, particularly at depth, beyond samples with sequential leach data (Figure 6.13). This has the benefit of providing increased deposit knowledge at reduced cost. Traditional approaches rely on an appropriate sample distribution being selected for sequential leaching across the sulphide-transitional-oxide boundaries based on existing geological interpretation. These boundaries are often assumed to be horizontal or parallel to the topographic surface, and can neglect discrete fault zones which may result in extension of oxide material to depth.

The availability of a deposit-wide predicted ore classification at an early stage in a project's life cycle can allow for better sample selection, increased understanding of existing metallurgy samples and potentially finding unrealised resources. Significant cost saving can be made through more efficient sampling and better informed decision making at critical stages in project development.

6.6 Conclusions

In this chapter it has been demonstrated that it is possible to generate robust predictive models of Cu-species classification from an appropriate training set of geochemical and logging data through machine learning methods. Major conclusions are as follows.

- Discrepancies between expected chalcopyrite content, determined from sequential leach data, and sulphur assays led to the identification of weak acid insoluble black Cu-oxides, known as Cu-wad (Figure 6.9).
- Scanning electron microscope analysis indicated that the Cu-wad from Productora consists of predominantly Cu (25–30 wt%) and Mn (14–17 wt%; Figure 6.3). The composition does not match a specific mineral and is probably fine grained intergowths of minerals. Rare earth element-rich inclusions are inferred to be rare earth phosphates.
- A new sequential leach based classification scheme was developed in order to account for non-recoverable Cu-wad by reconciling S against residual Cu from the final leach stage. Samples with sequential leach data and sulphur analyses were classified as either barren (<0.05 %Cu), oxide, transitional-oxide, transitional-sulphide, sulphide or insoluble (Figure 6.4).
- Applying the new classification scheme to a 2326 sample training set identified 347 samples with significant insoluble Cu content. This lead to the reclassification of 23 % of sulphide

samples and 18 % of transitional samples in the training set to insoluble (Figure 6.6). Under the new scheme all original oxide samples remained in the oxide class. Transitional samples were split between transitional-sulphide and transitional-oxide.

- The ability to predict Cu-wad occurrence enables domains of potentially poor recovery to be identified. The new classification also prevents misidentification of sulphide or transitional domains which actually have high Cu-wad content.

- The new scheme also separates original transitional samples into transitional-sulphide and transitional-oxide based on the dominant Cu-species. This provides a useful guide for the assessment of material for leaching over flotation and visa-versa as it indicates the dominant mineralogy (Figure 6.7 and Figure 6.8).

- The revised classification scheme was extrapolated across the assay database using machine learning. Nine attributes associated with ore classification were identified using evaluator and search algorithms; these include sample depth in drill hole, Ca %, Cu %, Fe %, K %, Mn ppm, S %, Ln(Cu/S) and the logged regolith term.

- The best machine learning algorithm, in terms of accuracy and simplicity, was found to be the Bagging-REPTree algorithm with five iterations. This algorithm is a decision tree combined with bagging, a method of generating multiple predictions on bootstrap replicas (iterations) of a training set to return an aggregated prediction. Applied to the training set with ten-fold cross validation, the model is 67.6 % accurate (Table 6.9). The model is most successful at recognising sulphide, transitional-sulphide and insoluble samples with accuracy of 70.2 %, 87.5 % and 67.8 % respectively against the training set. The model performed less effectively when discriminating between transitional-oxide and oxide, commonly confusing the two, with accuracy of 49.8 % and 52.2 % respectively.

- The Bagging-Reptree algorithm was applied to each assay interval with > 0.05 wt%Cu. Over half of the samples were classified as sulphide and a further 25 % as transitional sulphide. Only 2 % were classified as oxide, 6 % as transitional oxide and 8 % as insoluble.

- A major outcome of this research has been an increase in the data available for determining Cu-species classification, particularly at depth, beyond samples with sequential leach data (Figure 6.13). Results indicate that deep (locally >400 m from surface) domains of transitional-sulphide material are associated with steep fault zones that complicate the weathering profile (Figure 6.13).

- Implicit 3D models of the predicted Cu-species classification indicate significant domains of transitional-oxide and oxide occur in the northeast and southern parts of the pit design (Figure 6.14 B). The insoluble class domains are spatially associated with the oxide and transitional-oxide domains. Sulphide was modelled as a continuous domain at depth (> 100 m) with some perched domains modelled at shallower levels (0–50 m; Figure 6.14 C).

- The predictive model for Cu-species classification provides a useful dataset to augment with other available data (both geological, geochemical and metallurgical) in order to inform the definition of domains, rather than just surfaces (Figure 6.7 C and Figure 6.8 C), of variable Cu-species. This information can be used to inform further sampling campaigns, rationalise and weight existing samples, and has application in resource definition, and mine planning.

Chapter 7: Hydrothermal Geochemistry

7.1 Introduction

This chapter presents new stable (S) and radiogenic (Pb, Sr and Nd) isotope data for hydrothermal minerals from the Productora deposit. These data sets are used to inform interpretations of fluid sources and to constrain physiochemical conditions and depositional mechanisms at Productora.

7.2 Sulphur isotopes

7.2.1 Introduction

Sulphur isotopes can be used to understand the geochemistry of sulphur in ore deposits, in terms of sulphur source, transport and precipitation mechanisms (Ohmoto, 1972). Reviews of the controls on sulphur isotope systematics of sulphides in ore deposits are given by Ohmoto and Rye (1979), Ohmoto (1986), Ohmoto and Goldhaber (1997), and Seal (2006). The isotopic composition of sulphur in hydrothermal fluids associated with porphyry-style deposits is largely controlled by the lithological and thermal nature of the deposit's plumbing system (Ohmoto and Goldhaber, 1997). Variable $\delta^{34}S$ signatures of sulphide and sulphate minerals within ore deposits are typically the result of a) temperature-dependant fractionation between fluid and mineral, b) variation in redox state and c) changing source(s) of sulphur (Ohmoto and Goldhaber, 1997).

Porphyry deposits associated with I-type granites generally report a narrow range of $\delta^{34}S$ values, with $\delta^{34}S_{sulphide}$ approximating that of the local igneous rocks and country rocks — this is inferred to indicate that magmatic sulphur is the primary sulphur source (Ohmoto and Goldhaber, 1997). Based on deposits throughout the western U.S. and South America, porphyry deposits have $\delta^{34}S_{sulphide}$ values typically around 0 ± 5 ‰ (Field and Gustafson, 1979; Ohmoto and Rye, 1979; Ohmoto, 1986 and Ohmoto and Goldhaber, 1997). Globally, deposits of the IOCG class have variable $\delta^{34}S$ values which are typically, but not universally, close to 0 ± 5 ‰ (Williams et al. 2005). Notable exceptions from the Andean Mesozoic belt of northern Chile and southern Peru include the Mantoverde and Raul Condestable deposits, where

high $\delta^{34}S_{sulphide}$ values are attributed to involvement of evaporite- and seawater-sourced fluids, respectively (Benavides et al., 2007, de Haller and Fontbote 2009).

7.2.2 Previous Work

A sulphur isotope study of Productora was conducted by Fox (2000) on 19 samples collected during mapping and drill core logging. The sample suite included twelve pyrite samples, six chalcopyrite samples and one chalcocite sample. Sulphide paragenesis for each sample is not provided. Twenty duplicate analyses were also performed, making 39 analyses in total. Results were not quoted with reference to the Canyon Diablo Troilite international standard (although this is assumed to be the frame of reference), but analytical precision of ± 0.2 ‰ is quoted. The results for $\delta^{34}S_{sulphide}$ values ranged broadly between -8.2 and +1.2 ‰ (Figure 7.1 A). Pyrite compositions were from -5.4 to +1.2 ‰ (average -3.5 ‰), chalcopyrite ranges from -6.3 to -1.1 ‰ (average -1.8 ‰), and supergene chalcocite has a value of -8.1 ‰.

7.2.3 Methods

Sulphur isotope compositions in the current study were determined for 48 paragenetically constrained mineral samples from Productora. The sample suite included 25 pyrite samples, 21 chalcopyrite, one molybdenite sample and one anhydrite sample. Samples were predominantly sourced from cross sections 6,822,215 mN (n= 27) and 6,820,850 mN (n = 19), with two from central section 6,821,730 mN. Monomineralic powders (~10 mg) were prepared by hand drilling directly from in-situ coarse grain sulphide minerals using a Dremel Multipro 225 T2 Flex-shaft drill. The drill bit was cleaned between samples using a chalk block. Powders were transferred on clean weighing paper into a vial and weighed to check that the minimum sample requirement had been met. Samples were submitted to Christine Cook at the Central Science Laboratory, University of Tasmania, Australia, for sulphur isotope analysis. Analyses were performed on sub-samples, weighing <1 mg, by conventional isotope ratio mass spectrometry methods using an Isoprime100 mass spectrometer coupled to an Elementar vario PYRO cube elemental analyser. Seven international standards (IAEA-S-1, -2 and -3, IAEA-SO-6 and -7, and NBS127) were also collected and results are reported with reference to the Canyon Diablo Troilite (CDT $\delta^{34}S$ = 0.0‰) international standard.

7.2.4 Results

The $\delta^{34}S$ values for pyrite, chalcopyrite, molybedenite and anhydrite from Productora lie between -8.5 and +2.2 ‰ relative to the Cañon Diablo Troilite (CDT; Table 7.1, Figure 7.1 B). A variety of

Table 7.1 Results from sulphur isotope analysis on paragenetically constrained samples. Sample locations provided in Appendix A4.

SampleID	HoleID	mFrom	Mineral	Paragenesis	Stage	Stage/facies	Northing	Location	$\delta^{34}S_{CDT}$	$\Delta_{py\text{-}cpy}$
PR14AE005	MET007	452.16	py	mt-cpy-py-chl alteration	Cachiyuyito		6822215	North	-5.4	
PR14AE027-1	MET008B	118.1	py	tur-cpy-py veinlet stockwork	Stage 3	Facies 3B-2	6822215	North	-3.4	-0.7
PR14AE027-2	MET008B	118.1	cpy	tur-cpy-py veinlet stockwork	Stage 3	Facies 3B-2	6822215	North	-2.7	
PR14AE031	MET008B	124.2	py	tur-py-breccia cement	Stage 3	Facies 3B-2	6822215	North	-1.6	
PR14AE038	MET007	162.2	py	mt-py-cpy	Stage 3	Facies 3B-2	6822215	North	-2.9	
PR14AE046-1	MET007	375.05	cpy	cpy-py-cal vein	Stage 5		6822215	North	-6.1	2.1
PR14AE046-2	MET007	375.05	py	cpy-py-cal vein	Stage 5		6822215	North	-4.0	
PR14AE053	MET007	400.73	py	ill-py vein	Stage 4	Sub-stage 4C	6822215	North	-5.0	
PR14AE057	MET008	129.8	cpy	chl-cpy vein with kfs selvage	Stage 3	Facies 3B-2	6822215	North	-5.3	
PR14AE060-1	MET007	188.25	cpy	cpy-py-tur-kfs breccia cement	Stage 3	Facies 3B-1	6822215	North	-5.9	4.6
PR14AE060-2	MET007	188.25	py	cpy-py-tur-kfs breccia cement	Stage 3	Facies 3B-1	6822215	North	-1.3	
PR14AE061	MET007	191.8	cpy	qtz-chl-tur-cpy-mt vein	Stage 3	Facies 3B-1	6822215	North	-4.7	
PR14AE066	MET007	277.8	cpy	Diss. cpy in rhyodacite lapilli tuff	Stage 3	Facies 3B-1	6822215	North	-8.0	
PR14AE070	PRP0027D	193.4	cpy	cpy-tur cemented breccia	Stage 3		6822050	North	-6.8	
PR14AE098	PRP0064D	283.2	cpy	kfs-chl-qtz-tur-cpy-mt	Cachiyuyito		6822130	North	-7.8	
PR14AE102	PRP0064D	400.1	py	mt-py vein surrounded by chl alteration	Cachiyuyito		6822130	North	-4.2	
PR14AE119	(surface sample)		py	qtz-py breccia cement	Stage 1	Stage 1	6822215	North	-0.3	
PR14AE123	MET023	79.2	py	py-tur-kfs vein and kln-ms alteration	Stage 3	3B-2 (Hab. vein)	6822215	North	-2.9	
PR14AE124	MET023	81.5	py	Disseminated py	Stage 3	3B-2 (Hab. diss.)	6822215	North	-4.2	
PR14AE125	MET023	84.1	cpy	cpy-cv-tur veins with kfs selvage	Stage 3	3B-2 (Hab. vein)	6822215	North	-5.5	
PR14AE128-1	MET023	171.7	py	py-tur vein	Stage 3	3B-2 (Hab. vein)	6822215	North	-2.3	3.5
PR14AE128-2	MET023	171.7	cpy	Disseminated cpy in kfs vein halo	Stage 3	3B-2 (Hab. vein)	6822215	North	-5.8	
PR14AE129	MET023	119	cpy	Disseminated cpy in ms-kln alteration	Stage 3	3B-2 (Hab. diss.)	6822215	North	-8.5	
PR14AE133	MET023	132	py	Diss. py in ms-kln alteration	Stage 3	3B-2 (Hab. diss.)	6822215	North	-4.8	

anh = anhydrite, bt = biotite, cal = calcite, chl = chlorite, cpy = chalcopyrite, cv = covellite, diss. = disseminated, Hab. = Habanero, ill = illite, kfs = K-feldspar, kln = kaolinite, ms = muscovite, mo = molybdenite, mt = magnetite, py = pyrite, qtz = quartz, tur = tourmaline. mFrom = meters from depth

Table 7.1 continued

SampleID	HoleID	mFrom	Mineral	Paragenesis	Stage	Stage/facies	Northing	Location	$\delta^{34}S_{CDT}$	$\Delta_{py\text{-}cpy}$
PR14AE138	MET023	152.5	cpy	Diss. cpy in ms-kln alteration	Stage 3	3B-2 (Hab. diss.)	6822215	North	-7.0	
PR14AE139	MET023	223.4	py	ill-py-qtz	Stage 4	Sub-stage 4C (Hab.)	6822215	North	-3.1	
PR14AE141	NS5D	191.5	py	py-cpy-mo-chl vein	Stage 3		6820850	South	-2.7	
PR14AE142	NS5D	273.4	py	kfs-py vein	Stage 3		6820850	South	2.2	
PR14AE144-1	PRD0011	177.5	py	py veinlets	Stage 4	Sub-stage 4B	6821730	Central	-0.7	
PR14AE144-2	PRD0011	177.5	cpy	cpy-chl veins	Stage 3		6821730	Central	0.3	
PR14AE148-1	MET014	148.7	cpy	cpy-chl (after bt) breccia cement	Stage 3	Facies 3B-4	6820850	South	-5.8	
PR14AE148-2	MET014	148.7	mo	mo-chl (after bt) breccia cement	Stage 3	Facies 3B-4	6820850	South	-3.5	
PR14AE151-1	MET014	248	cpy	cpy-tur-chl breccia cement	Stage 3	Facies 3B-5	6820850	South	-6.6	
PR14AE151-2	MET014	248	py	tur-py alteration clot	Stage 3	Facies 3B-5	6820850	South	-0.1	
PR14AE151-3	MET014	248	py	late py-veinlet	Stage 4	Sub-stage 4B	6820850	South	1.1	
PR14AE153	MET014	287.8	cpy	cpy-chl (after bt) -tur vein	Stage 3	Facies 3B-5	6820850	South	-1.2	
PR14AE162	MET015	239.6	cpy	cpy-chl (after bt) breccia cement	Stage 3	Facies 3B-4	6820850	South	-3.1	
PR14AE165	MET015	271.8	cpy	mt-cpy-chl (after bt) vein	Stage 3	Facies 3B-4	6820850	South	-2.2	
PR14AE169-1	MET016	151.3	py	qtz-kfs-py-tur-cpy laminated vein	Stage 3	Facies 3B-4	6820850	South	-1.6	-0.4
PR14AE169-2	MET016	151.3	cpy	qtz-kfs-py-tur-cpy laminated vein	Stage 3	Facies 3B-4	6820850	South	-1.2	
PR14AE171	MET016	161	py	tur-chl-py vein	Stage 3	Facies 3B-4	6820850	South	-2.4	
PR14AE174-1	MET016	316.4	anh	anh-tur-py-cpy vein	Stage 3		6820850	South	-4.6	
PR14AE174-2	MET016	316.4	cpy	anh-tur-py-cpy vein	Stage 3		6820850	South	-5.3	
PR14AE180	MET022	117.15	cpy	tur-cpy cemented breccia	Stage 3	Facies 3B-2	6822215	North	-3.0	
PR14AE185	MET018	249.85	py	py-veinlet with chl-py selvage	Stage 4	Sub-stage 4B	6821010	South	-3.8	
PR14AE186	MET018	291.2	py	Diss. py in contact breccia infill	Zapallo		6821010	South	-1.5	
PR14AE187	MET018	294.7	py	py veinlet	Stage 4	Sub-stage 4B	6821010	South	-1.3	
PR14AE189	MET018	297.8	py	py-chl (after bt) vein	Stage 3		6821010	South	1.5	

anh = anhydrite, bt = biotite, cal = calcite, chl = chlorite, cpy = chalcopyrite, cv = covellite, diss. = disseminated, Hab. = Habanero, ill = illite, kfs = K-feldspar, kln = kaolinite, ms = muscovite, mo = molybdenite, mt = magnetite, py = pyrite, qtz = quartz, tur = tourmaline. mFrom = meters from depth

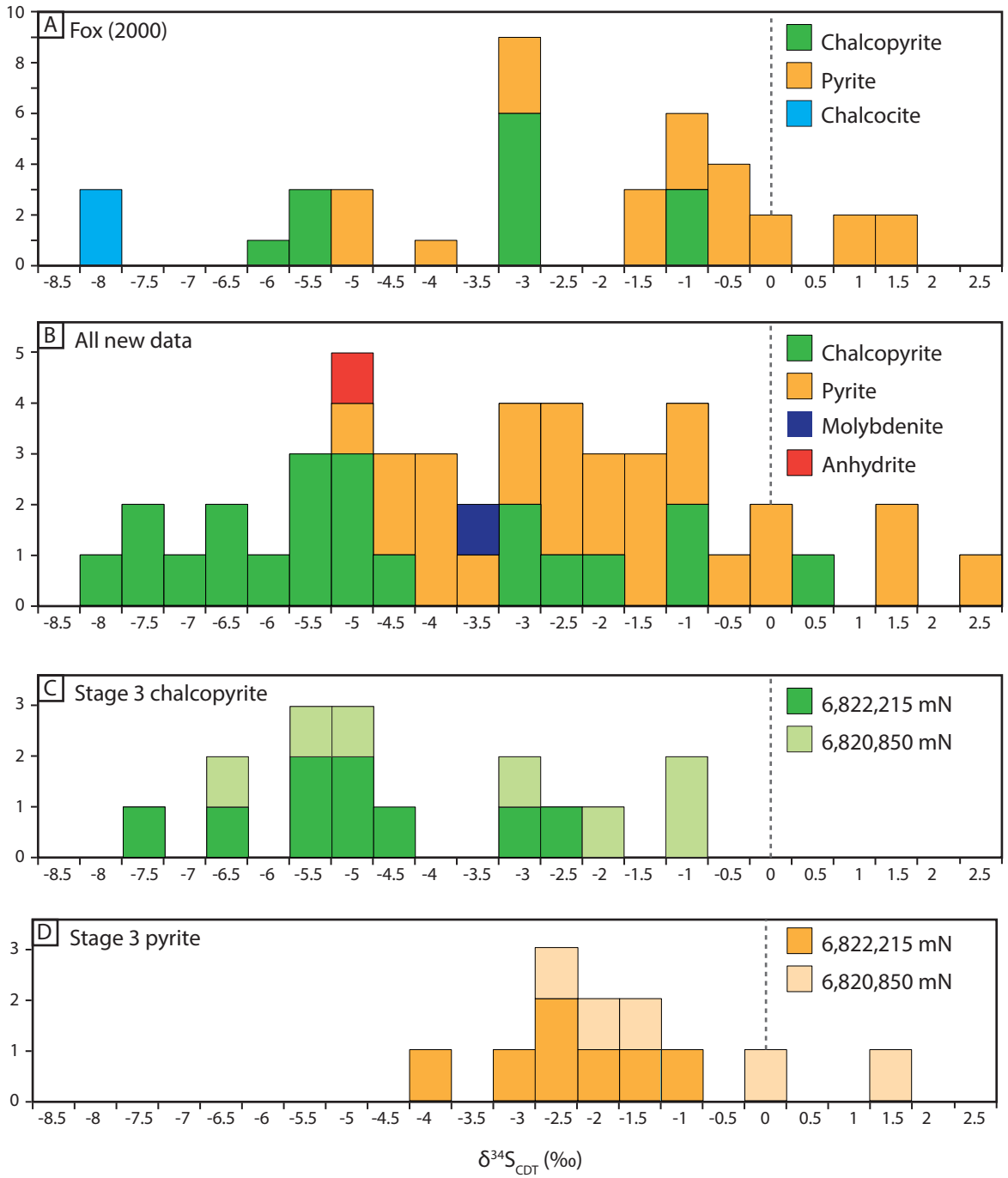

Figure 7.1 Cumulative frequency histograms to show $\delta^{34}S$ data A) from Fox (2000) and B) from this study, including C) stage 3 chalcopyrite, and D) stage 3 pyrite. Data from this study define a similar range to that of Fox (2000). Values for $\delta^{34}S$ from chalcopyrite are more negative than from pyrite. There is a subtle shift in $\delta^{34}S$ toward more negative values from south to north in both the chalcopyrite and pyrite data.

paragenetic stages from the Productora breccia complex (stages 1, 3 and 4), adjacent Cachiyuyito system and Zapallo porphyry were analysed. Overall, the range of results is comparable to that of Fox (2000; Figure 7.1 A and B). Chalcopyrite values range from -8.5 to +0.3 ‰ (average -4.7 ‰) and tend toward more negative values than pyrite, which range from -5.4 to +2.2 ‰ (average -2.2 ‰; Figure 7.1 B). Five pyrite - chalcopyrite mineral pairs were analysed from stage 3 (n = 4) and stage 5 (n = 1). Values for $\Delta_{pyrite\text{-}chalcopyrite}$ range between -0.7 and +4.6 ‰ (Table 7.1). Negative values indicate that isotopic enrichment by fractionation is reversed from what would be expected under equilibrium conditions

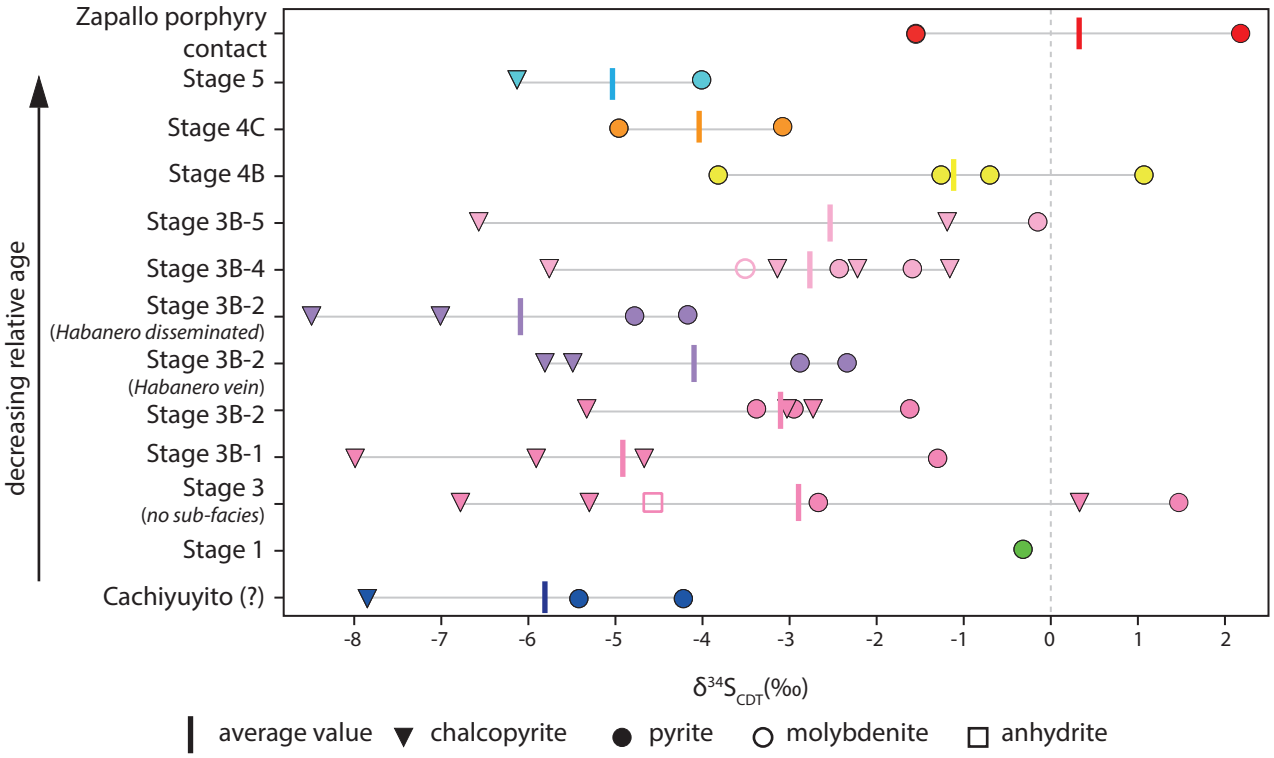

Figure 7.2 Distribution of $\delta^{34}S_{sulphide}$ (pyrite, chalcopyrite and molybdenite) and $\delta^{34}S_{sulphate}$ (anhydrite) values from Productora breccia complex stages 1, 3, 4 and 5, Cachiyuyito magnetite alteration and Zapallo porphyry contact breccia. Cachiyuyito samples have low $\delta^{34}S$ compared to the other events. Stage 1 (pyrite - quartz-cemented breccia) has $\delta^{34}S$ close to 0 ‰. Productora stage 3 samples return a wide range of values and the breccia facies overlap. Stage 3 facies do not show systematic variability, although facies 3B-2 (Habanero disseminated sulphide) has lower $\delta^{34}S$. Sub-stage 4B (chalcopyrite and pyrite veinlets) have higher $\delta^{34}S$ than sub-stage 4C (illite-pyrite veins), whereas stage 5 calcite-sulphide veins have lower $\delta^{34}S$. Pyrite associated with the Zapallo porphyry has higher $\delta^{34}S$ than most of the Productora breccia complex samples. Within each paragenetic group, chalcopyrite has lower $\delta^{34}S$ values than pyrite. Both molybdenite and anhydrite have $\delta^{34}S$ values within the middle of the stage 3 range.

($\Delta_{observed} < \Delta_{equilibrium}$) and that the minerals are not in isotopic equilibrium.

Anhydrite, from a stage 3 anhydrite - chalcopyrite - pyrite - tourmaline vein returned a surprisingly low $\delta^{34}S$ value of -4.6 ‰, which is considered extremely light. Molybdenite, from stage 3 chlorite (after biotite) breccia cement returned a $\delta^{34}S$ value of -3.5 ‰. A shift toward more positive $\delta^{34}S$ values from section 6,822,215 mN to 6,820,850 mN is evident amongst both the stage 3 chalcopyrite and pyrite data (Figure 7.1 C and D).

Results subdivided by paragenetic stage are presented in Figure 7.2. Only one result was obtained from stage 1 pyrite, which returned a $\delta^{34}S$ value of -0.3 ‰. Stage 3 sulphides (n = 34) span a range of values from -8.5 to +1.5 ‰ with an average of -3.5 ‰. Results from the different stage 3 facies overlap and do not show systematic variations between facies, although the 3B-2 facies and 3B-2 (Habanero vein) samples span a narrower range, from -5.8 to -1.6 ‰. Sub-stage 4B (sulphide veinlets; n = 4)) tends toward more positive values, -3.8 to +1.3 ‰, compared to sub-stage 4C (illite ± sulphide veins; n = 2;

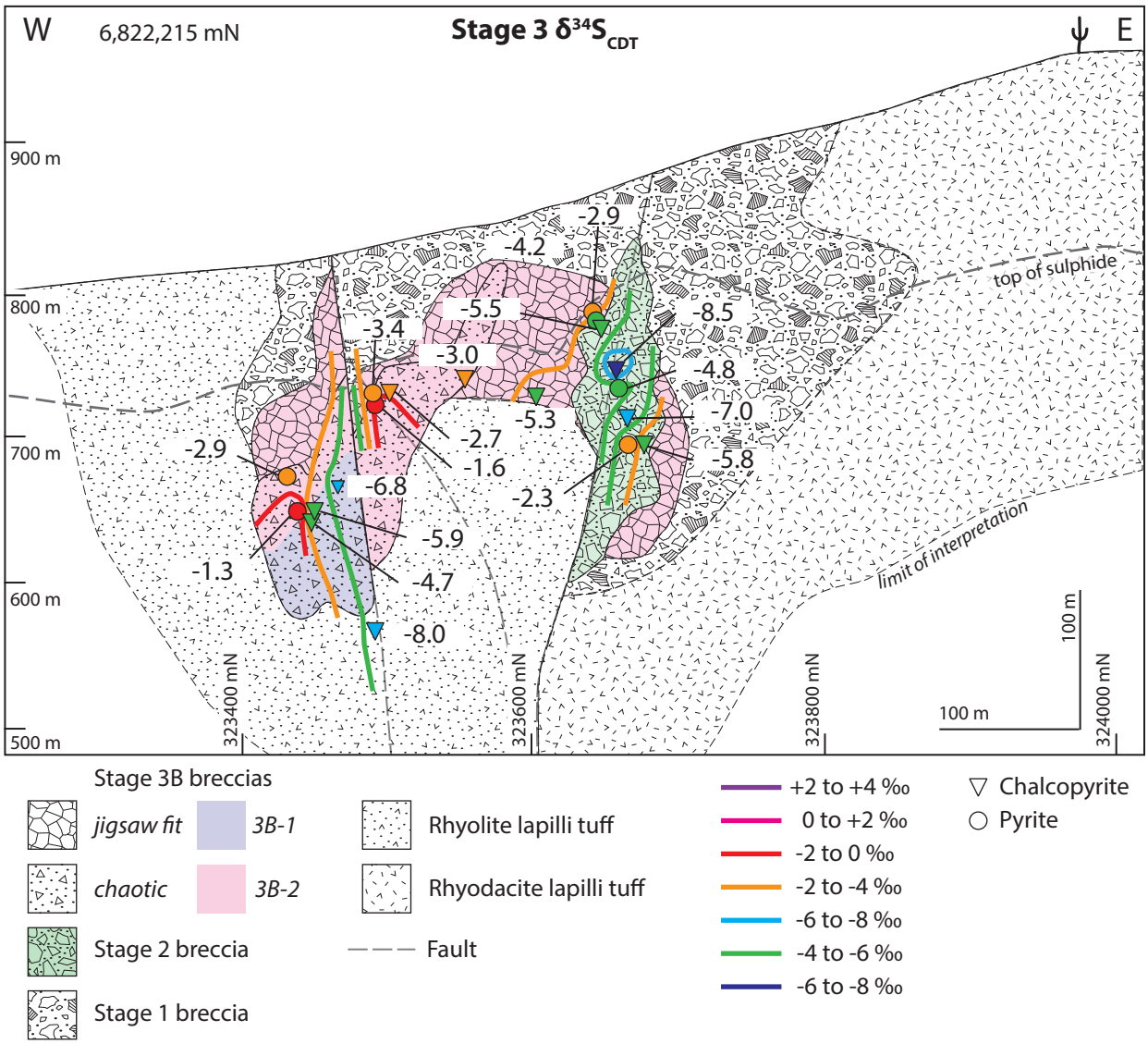

Figure 7.3 Distribution of stage 3 $\delta^{34}S_{sulphide}$ values (‰) from chalcopyrite and pyrite with interpreted contours at 2 ‰ increments on section 6,822,215 mN. Smaller symbols indicate sample position is outside of ±80 m section window. $\delta^{34}S_{sulphide}$ values are increasingly negative toward centre of fault zones. Lithology, breccia facies and fault zones also shown.

-5.0 to -3.0 ‰) and stage 5 (n = 2; -6.1 to -4.0 ‰).

Results from samples interpreted to be associated with the Cachiyuyito system (n = 3), based on their location below the breccia complex and magnetite-chlorite alteration, returned negative $\delta^{34}S$ values between -7.8 and -4.2 ‰. Analysis of pyrite associated with the Zapallo porphyry (n = 2) returned higher $\delta^{34}S$ values, between -1.5 ‰ and 2.2 ‰.

7.2.5 Sulphur isotope zonation

Across section 6,822,215 mN, the $\delta^{34}S_{sulphide}$ values from stage 3 show zonation about major fault zones toward more negative $\delta^{34}S$ values in the centre of the fault zone (Figure 7.3). Despite sparse data, this is clearly evident within the Habanero domain, where stage 3 breccias overprinted stage 2 fault breccias,

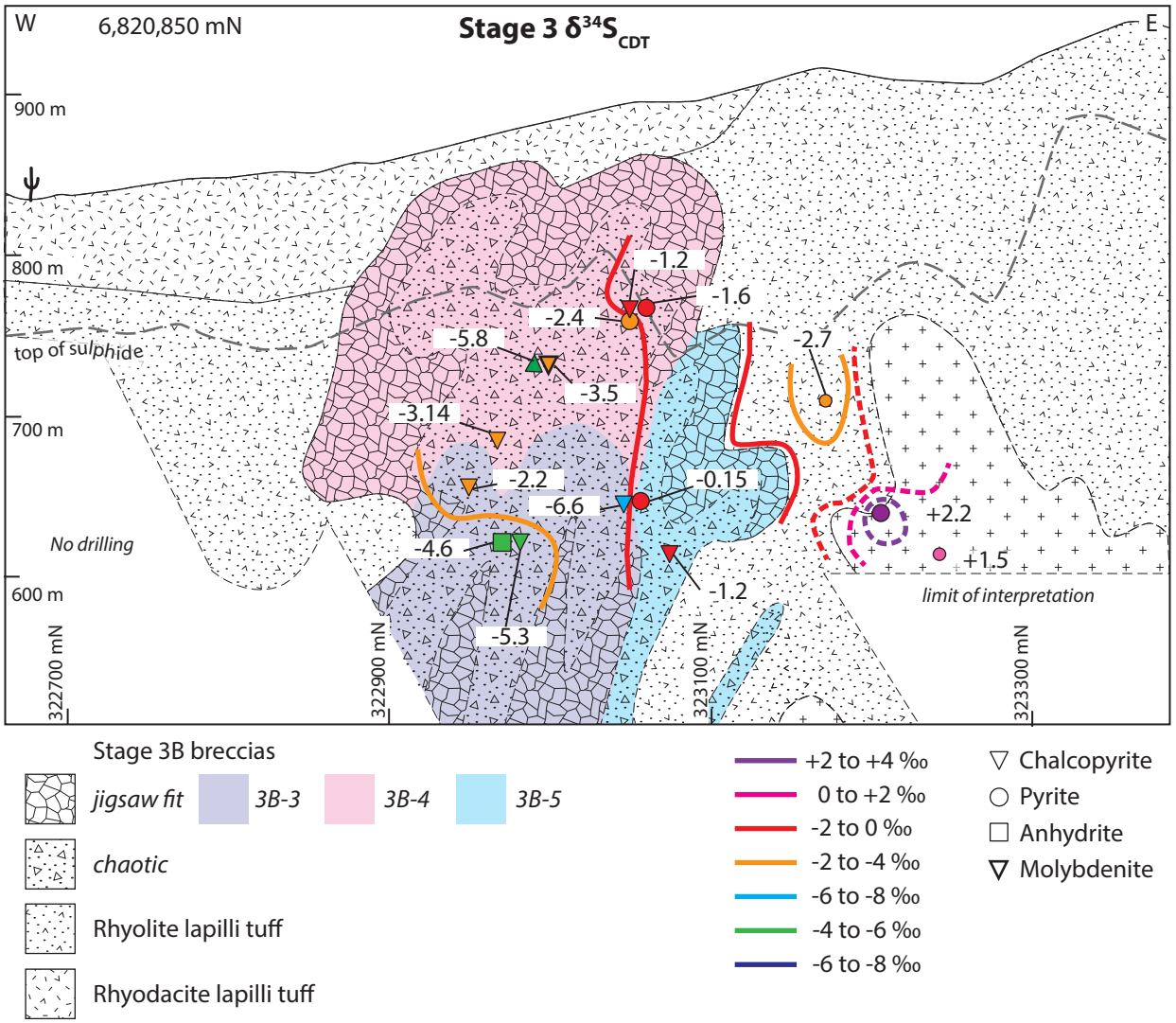

Figure 7.4 Distribution of stage 3 $\delta^{34}S_{sulphide}$ values (‰) from chalcopyrite, pyrite, molybdenite, and $\delta^{34}S_{sulphate}$ value from anhydrite with interpreted contours at 2 ‰ increments on section 6,820,850 mN. Smaller symbols indicate sample position is located outside of ±80 m section window. Dashed contours shown in define zoning around samples associated with Zapallo porphyry intrusion. Lithology and breccia facies also shown.

which were then reactivated and crosscut stage 3. A similar association between lower $\delta^{34}S$ values and fault zone also occurs around the major western most fault of the same section. Values of $\delta^{34}S$ also tend toward more negative values upward and outward from the core of the breccia complex.

The stage 3 values for $\delta^{34}S_{sulphide}$ from section 6,820,850 mN show a lateral gradient, increasing toward the east (Figure 7.4). Sparse data points limit the interpretations of zonation patterns, but it is notable that $\delta^{34}S_{sulphide}$ is higher within the 3B-5 breccia domain on the east of the breccia complex. No other consistent zonation patterns were observed within the breccia complex from the available data. To the east, samples associated with the Zapallo porphyry have positive $\delta^{34}S_{sulphide}$ values.

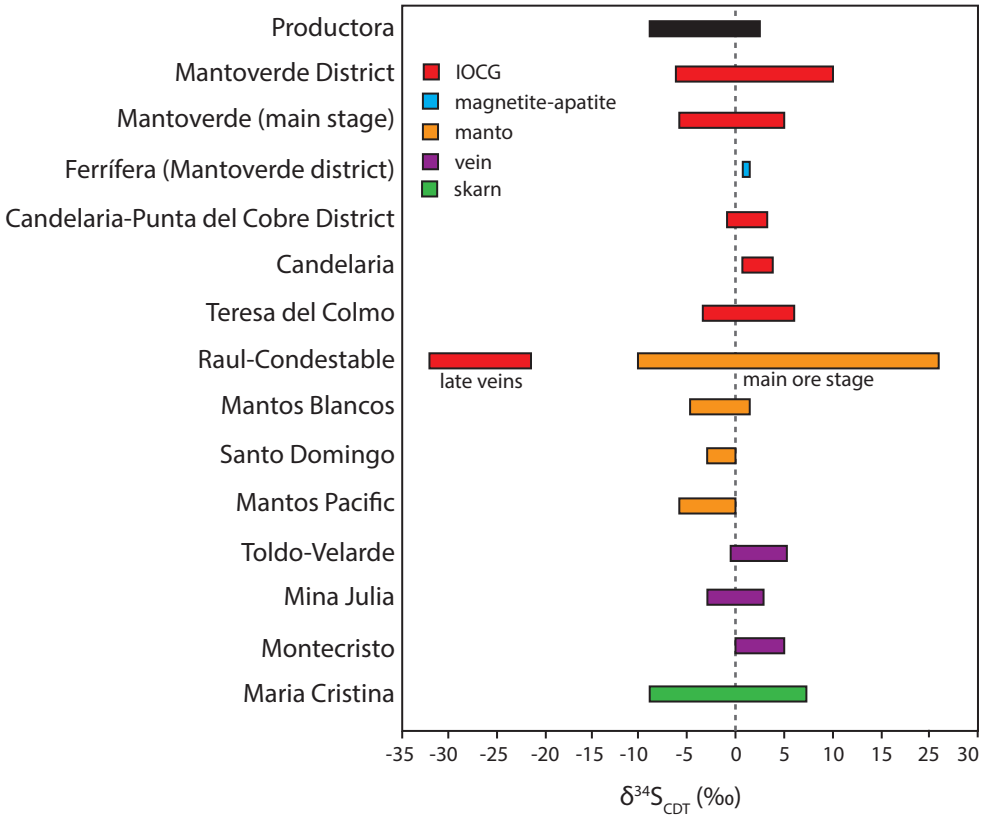

Figure 7.5 Compilation of $\delta^{34}S$ values for sulphide minerals, mostly pyrite and chalcopyrite, from selected IOCG, manto-Cu, vein, skarn and magnetite-apatite deposits in northern Chile and southern Peru. Figure modified from Sillitoe (2003), data from Ripley and Ohmoto (1977), Vivallo and Henriquez (1998), Leidli (1998) in Hopper (2000), Lieben et al. (2000), Marschik & Fontbote (2001), Ramirez et al. (2006), Benavides et al. (2007), de Haller and Fontbote (2009), Reiger (2012). Values are centred close to zero ‰, indicating a predominantly magmatic sulphur source — assuming conditions are relatively reduced and aqueous sulphur is sulphide (H2S, HS^-)-dominated (Barton, 2014). Large deviations at Raul-Condestable are interpreted to indicate reduction of evaporitic or seawater sulphate (Ripley and Ohmoto, 1977; de Haller et al., 2002) and biogenic sulphur (de Haller et al., 2002).

7.2.6 Discussion

The $\delta^{34}S_{sulphide}$ values analysed from the Productora project, by Fox (2000) and in this study, range between -8.5 and +2.2 ‰. This range of $\delta^{34}S$ values overlaps with the range expected for both porphyry or magmatic-hydrothermal IOCG deposits, 0 ± 5‰ (Field and Gustafson, 1979; Ohmoto and Rye, 1979; Ishihara, 1981; Ohmoto, 1986; Ohmoto and Goldhaber, 1997; Williams et al., 2005; Figure 7.5 and Figure 7.6). This suggests that igneous sulphur could have been an important sulphur source at Productora. Magmatic sulphur is inferred based on mineralogy that is consistent with magmatic-hydrothermal fluids (chapter 4). Fluids exsolved from an I-type magma typically have H_2S/SO_2 equal to one. The cooling path taken by the fluid influences the H_2S/SO_2 whereby under oxidising conditions (i.e., $H_2S/SO_4 < 1$), $\delta^{34}S_{sulphide}$ values span a wide, increasingly negative range throughout the cooling history. Under more reduced conditions the $\delta^{34}S_{sulphide}$ values span a narrower range (Rye, 1993). The broad range of $\delta^{34}S_{sulphide}$ values at Productora suggest fluids have evolved under oxidising conditions, although sulphide-sulphate pairs were not available to calculate fluid bulk sulphur composition. This

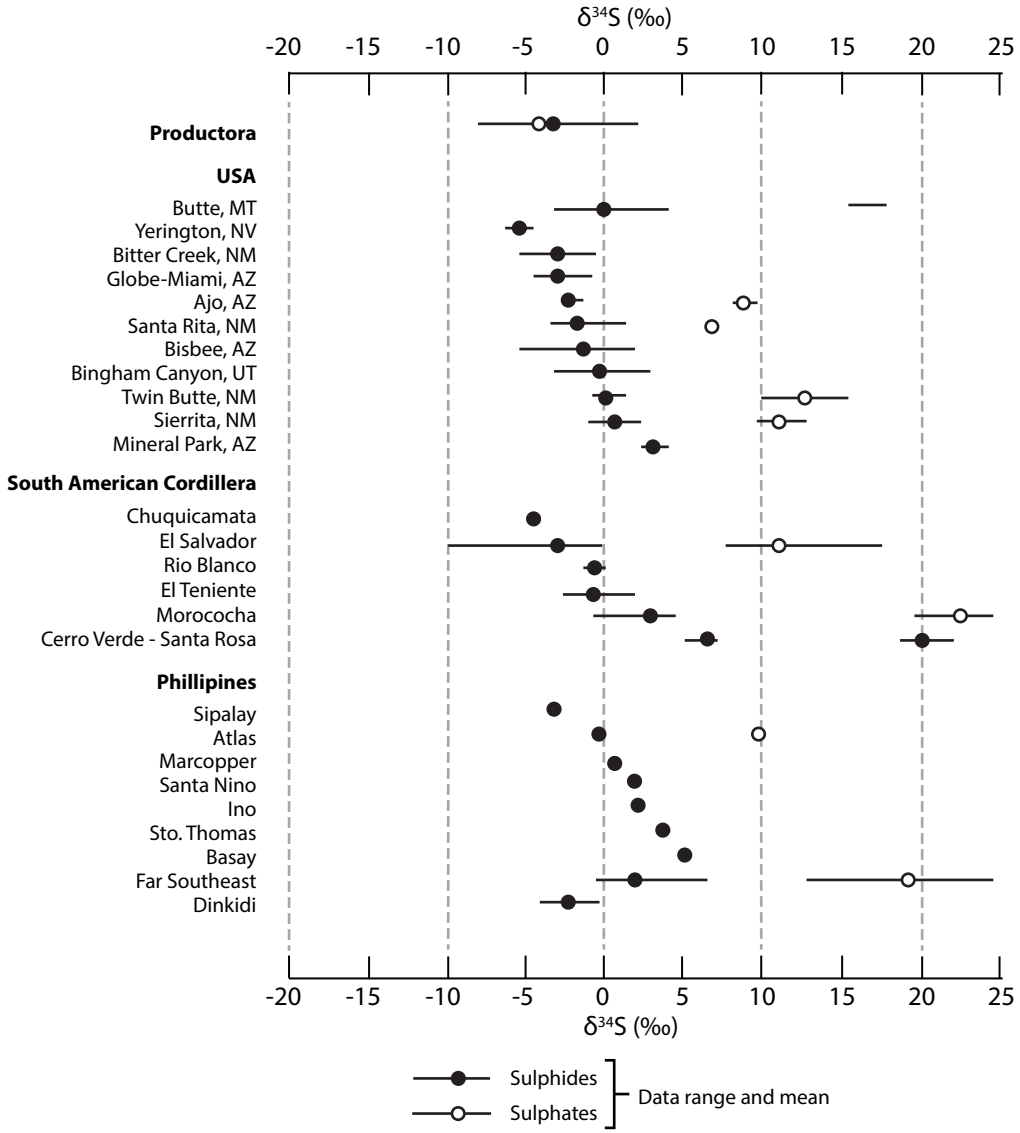

Figure 7.6 Ranges of $\delta^{34}S$ values determined for sulphide and sulphate minerals associated with porphyry Cu deposits. Modified from Wilson et al., 2007. Productora data from this study, other data compiled from Ohmoto and Rye (1979), Taylor (1987), Akira (2000), Wolfe (2001) and Wilson et al. (2007).

is a reasonable assumption in most porphyry settings, where systems are close to the sulphide-sulphate boundary and there is ample sulphur.

Weakly oxidising conditions are inferred from the limited occurrence of sulphate minerals. The absence of high $\delta^{34}S_{sulphide}$ values indicates that there was no significant input of sulphur from evaporite- or seawater-sourced fluids, which have relatively high $\delta^{34}S$ (Triassic– Early Cretaceous seawater had $\delta^{34}S$ ranging from +14 to +15 ‰; Claypool et al., 1980). The observed $\delta^{34}S_{sulphide}$ range is comparable to other global porphyry Cu deposits (Figure 7.6) and Mesozoic IOCG and iron-rich deposits from northern Chile and southern Peru, which typically range between -10 and +10 ‰ (Figure 7.5). The broad similarity in regional deposit sulphur isotope characteristics implies, but does not prove, that these deposits all formed from fluids of similar metal and sulphur chemistry, and by similar depositional mechanisms

(Ohmoto and Goldhaber, 1997).

The $\delta^{34}S_{sulphate}$ value from one anhydrite vein is anomalously low (-4.6 ‰ ; Table 7.1 and Figure 7.1 B). Sulphate with $\delta^{34}S$ this low suggests oxidation of negative $\delta^{34}S$ sulphur from sulphide and precipitation as anhydrite, or a source of negative $\delta^{34}S$ e.g., biogenic. Additional data is required to make robust interpretations from this anomalous result. In addition to this, the possibility of supergene anhydrite should be considered.

Zonation in $\delta^{34}S_{sulphide}$ across section 6,822,215 mN toward more negative values associated with fault zones indicates that sulphides in these areas formed from more oxidised fluids than those in the rest of the breccia complex, although not sufficiently oxidised to form hematite. Increased sulphate content in the mineralising fluid is likely to be the result of a) oxidation of H_2S, sulphide or native sulphur, b) hydrolysis of SO_2; and/or c) mixing with sulphate-rich fluid (e.g., sea water or connate brines; Ohmoto and Goldhaber, 1997). Mixing of sulphate-rich fluid is unlikely, since the involvement of seawater or connate brines would cause a much larger positive shift in $\delta^{34}S$ that is not observed. As sulphate minerals are not observed in these domains, hydrolysis of SO_2 is also unlikely. However, without additional constraints on temperature and bulk sulphur composition this interpretation is somewhat speculative. Fault zones provide enhanced permeability enabling oxygenated meteoric water to permeate downward. Interaction of magmatic H_2S with groundwater could have caused oxidation of H_2S, and may have resulted in the observed shift in $\delta^{34}S$. Other processes are also possible - more detailed sampling laterally and vertically is required to resolve this.

The $\delta^{34}S$ values across section 6,820,850 mN show an eastward trend toward higher values, with facies 3B-5 and the easternmost samples of facies 3B-4 returning values between -1.6 and -0.1 ‰. This zonation suggests higher temperature, or less oxidised, fluids precipitated the sulphides in the east compared to the sulphides in breccia cement to the west. The cement-rich, poorly sorted, chaotic texture of the facies 3B-5 breccias (section 4.4.4.2) is consistent with a fluid pathway created by intense brecciation and high temperature fluid flow. High $\delta^{34}S$ values for sulphides associated with the Zapallo porphyry are also consistent with deposition from a higher temperature fluid, although fluid mixing, water-rock interaction or a less oxidised fluid are alternative explanations.

Disequilibrium between coexisting pyrite and chalcopyrite is indicated by the calculated $\Delta_{pyrite\text{-}chalcopyrite}$. Disequilibrium is greatest in pairs from the north of the deposit. There are several scenarios to consider which could have led to isotopic disequilibrium, including precipitation from multiple fluids, replacement with H_2S input and rapid mineral precipitation (e.g., Eldridge et al., 1983; Ohmoto and Lasaga, 1982;

Rye 1993). However, chalcopyrite is also considered notoriously prone to isotopic disequilibrium (e.g. Ohmoto, 1986). This tendency toward disequilibrium precludes further justified interpretation without additional constraints on bulk sulphur composition.

The values for $\delta^{34}S$ from sulphides associated with the Cachiyuyito system (Figure 7.2) are consistent with the Cachiyuyito mineralisation and alteration having formed from a more oxidised fluid than the Productora breccia complex. This is consistent with the magnetite-apatite model, which involves highly oxidised mineralising fluids (Menard 1995, Oyarzun 2003).

Productora stage 1 has $\delta^{34}S$ values close to 0 ‰, indicating the hydrothermal fluids that generated the stage 1 breccia were not as strongly oxidised as the stage 3 fluids, which have more negative $\delta^{34}S$. Sub-stage 4B chalcopyrite and pyrite stringers trend to higher $\delta^{34}S$ than the stage 3 breccia cement, which is the opposite to what would be expected from cooling of the same fluid. This reversal is therefore interpreted either as a later pulse of either a less oxidised fluid or a higher temperature fluid. The former is favoured on the basis of mineralogy presented in chapter 4 — sub-stage 4B has an assemblage of chalcopyrite, pyrite ± sericite typical of lower temperatures than the K-feldspar-, tourmaline- and magnetite-rich stage 3 assemblages. This is also consistent with decreasing redox state inferred from sulphide and oxide minerals (section 4.10.3). Sub-stage 4C late illite-sulphide veins and stage 5 calcite veins and breccias show increasingly negative $\delta^{34}S$ values (Figure 7.2), which are consistent with the cooling path of an oxidised fluid.

The shift toward positive $\delta^{34}S$ values in the south suggests that sulphides formed from a hotter fluid in this area. This supports interpretations that the core of the breccia complex is in the south of the deposit. This is also consistent with the upward-flaring pyrite distribution discussed in chapter 5.

7.3 Strontium and neodymium isotopes

7.3.1 Introduction

The purpose of the strontium isotope study is to trace hydrothermal fluids involved in mineralisation of the Productora breccia complex, specifically to determine if connate fluids were involved. Strontium isotopes show no temperature or mineral dependent fractionation (Faure and Powell, 1986), consequently the $^{87}Sr/^{86}Sr$ concentrations of hydrothermal minerals are interpreted to be representative of the fluids from which they precipitated. Strontium isotope ratios in hydrothermal minerals can be compared to the contemporaneous Sr isotope compositions of various reservoirs, such as upper mantle, volcanic sequences, batholiths or lower crust, in order to place constraints on possible reservoirs contributing Sr

and other components to mineralisation (King and Kerrich, 1989).

Tourmaline is an ideal mineral for Sr isotope tracer studies of mineralising fluid at Productora for several reasons: a) tourmaline commonly has high Sr and low Rb contents (Taylor and Slack, 1984; King and Kerrich, 1989; Griffin et al., 1996); b) tourmaline coprecipitated with chalcopyrite (chapter 4); c) tourmaline is relatively resistant to alteration and weathering, and is highly retentive, thus acting as a closed system with respect to Rb-Sr isotope systematics (King and Kerrich, 1989).

7.3.2 Previous work

No previous Sr or Nd isotope study has been conducted on rocks or minerals from Productora. A sample from the Ruta Cinco granodiorite batholith, to the east of Productora, was reported by McNutt (1975) to have initial Sr ($^{87}Sr/^{86}Sr_i$) value of 0.7036. No data was available for the Cachiyuyito stock. The strontium isotope character of igneous rocks from northern Chile show a systematic east to west increase in mean Sr isotope ratio from Jurassic to recent times (McNutt et al., 1975; Rogers and Hawkesworth; 1989) from 0.7043 to 0.7059 (McNutt et al., 1975). The systematic change in Sr initial ratios across northern Chile is interpreted to reflect changes in the region of partial melting, and with increasing crustal melting and contamination associated with thickened continental crust (Rogers and Hawkesworth; 1989). The $^{87}Sr/^{86}Sr_i$ values of Phanerozoic seawater have been compiled by Veizer et al. (1999) based on calcitic and phosphatic fossilized shells, with Mesozoic seawater ranging between 0.7067 and 0.7082. At Productora, magmatic sourced fluids are therefore expected to have $^{87}Sr/^{86}Sr_i$ ratios close to that of the local igneous plutons. Connate fluids are expected to have more radiogenic $^{87}Sr/^{86}Sr_i$ values, between those of the volcanic rocks and Mesozoic seawater.

7.3.3 Methods

Tourmaline samples were selected based predominantly on the presence of coarse tourmaline and secondly on the spatial distribution across the deposit. The samples include examples of proximal, distal, shallow and deep tourmaline (Figure 7.8). A pilot study was conducted to determine trace element compositions on one grain mount of tourmaline (PR14AE060; Table 7.2) in order to establish Sr and Nd abundances and potential inclusions. The sample was crushed with a mortar and pestle and sieved for the 250-500 μm size fraction. A strong magnet was used to separate iron rich phases (tourmaline and pyrite), from quartz-feldspar rich grains. Grains were then washed in tap water and dried at 60 degrees for two hours. Using a binocular microscope, grains of tourmaline were separated and prepared as a grain mount in epoxy resin.

The grain mount was analysed by LA-ICP-MS at CODES, University of Tasmania, Australia. Strontium and Nd were measured with a suite of 43 major and trace elements using an Agilent 7900 quadrupole ICPMS equipped with a 193 nm excimer laser and the Resonetics S155 laser ablation system. The instrument drift and mass bias correction factors were calculated using the NIST612 standard, which was analysed twice at the beginning and end of the run and once every 30 min throughout the run. Each analysis began with a 12 s blank gas measurement followed by a further 50 s of analysis while the laser was switched on. Analyses were performed using 43 μm spot diameter using the laser at 5 Hz and fluence of approximately 3.04 J cm^{-2}. The counting time on all elements was 0.01 s. Data reduction for trace elements was performed using similar methods to those outlined in Danyushevsky et al. (2011). Integration intervals were selected based on the major element data that were used to confirm tourmaline was being analysed for the duration of the analysis.

The strontium concentration of tourmaline was 300 ppm, whereas Nd was only 2 ppm. For isotopic characterisation, a total elemental weight of 100 nanograms was required for Sr and Nd respectively (R. Maas, pers. comm., 2016). Approximately 100 mg of mineral would be required at concentrations of 2 ppm for Nd characterisation. This sample (PR14AE060) was the only one selected for Nd isotopic analysis because the Nd concentration was known and a large sample weight was feasible. Trace element analysis of PR14AE060 indicated common zircon inclusions and one apatite inclusion. Most grains were agglomerates of pyrite and tourmaline. Contamination of quartz, pyrite and zircon are not problematic as they have negligible Sr content, whereas apatite inclusions would impact Sr analysis.

Table 7.2 Strontium radiogenic isotope data from tourmaline and epidote mineral separates from the Productora breccia complex. Initial strontium isotope ratios have been calculated using equations from DePaolo and Wasserburg (1976) based on age of mineralisation reported in Chapter 4, 130 Ma. Breccia facies are described in Chapter 4. Whilst it would have aided interpretation, no samples of the Cachiyuyito stock were available to analyse in the current study.

Sample	Mineral	Drill Hole	Depth	Facies	Paragenesis	$^{87}Rb/^{86}Sr$	$^{87}Sr/^{86}Sr$	$^{87}Sr/^{86}Sr_i$
PR14AE060E	Epidote	MET007	188.25	4D	ep-cpy vein	0.209	0.705762	0.70525
PR14AE022	Tourmaline	MET008B	104.20	3B-2	tur breccia cement	0.018	0.704014	0.70397
PR14AE060T	Tourmaline	MET007	188.25	3B-1	tur veins and clots	0.066	0.704137	0.70398
PR14AE062	Tourmaline	MET007	218.45	3B-1	tur-py-cpy-kfs-chl clot	0.045	0.704030	0.70392
PR14AE114	Tourmaline	PRP0066D	188.6	3B	tur-py-cpy-qtz clot	0.081	0.704311	0.70412
PR14AE074	Tourmaline	PRP0027D	258.25	3B-2	chl-tur-kfs-mo vein	0.180	0.704241	0.70380
PR14AE141	Tourmaline	NS5D	191.5	3B	tur-chl-py-cpy-mo vein	0.028	0.704016	0.70395
PR14AE125	Tourmaline	MET023	84.1	3B-2	tur-cpy vein	0.113	0.704244	0.70397
PR14AE128	Tourmaline	MET023	171.7	3B-2	tur-cpy-py breccia cement	0.147	0.704677	0.70432

Precision for Sr ± 0.000040. LA-ICP-MS results for PR14AE062 indicate average Rb 0.639 ppm and average Sr 304 ppm. chl = chlorite, cpy = chalcopyrite, ep = epidote, kfs = K-feldspar, mo = molybdenite, py = pyrite, qtz = quartz, tur = tourmaline

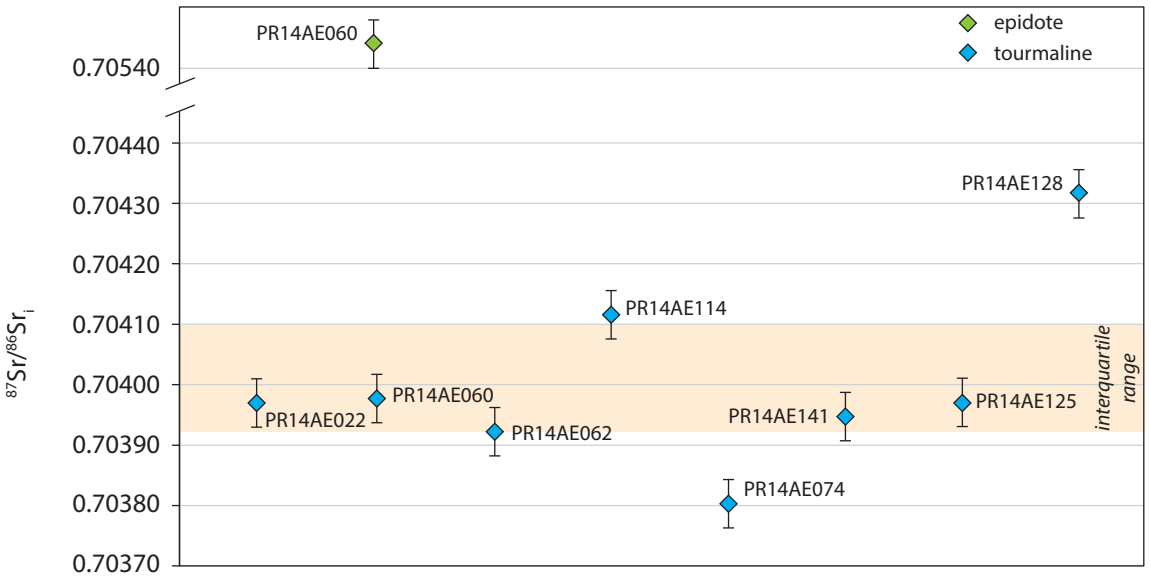

Figure 7.7 Chart to show relative initial Sr ($^{87}Sr/^{86}Sr_i$) values from tourmaline (blue) and epidote (green) mineral separates with error bars to show external precision (2sd) ± 0.000040. Interquartile range of tourmaline shaded in orange, six out of the eight tourmaline samples fall within or with in error of the interquartile range. Sample PR14AE128 is more radiogenic where as PR14AE074 is less radiogenic. The epidote sample is significantly more radiogenic than all the tourmaline samples.

Following the pilot study, samples of tourmaline (n = 8) and epidote (n = 1) grains, weighting 6 mg, were separated following the method outlined above. Mineral separates were submitted to Dr. Roland Maas at University of Melbourne for Sr (n = 9) and Nd analysis (n = 1). Samples were ground to a powder in agate under ethanol, then rinsed in distilled water before being dried overnight. Samples were then treated to an acid leach (HF-HNO_3, 3:1) at high tempertature (160°C), dried, heated with concentrated HNO_3 and returned to the oven with 6 Molar HNO_3. An approximately 9% split of dissolved sample solution was taken for trace element analysis by quadropole ICP-MS. Sample analysed was estimated at 1-3 mg but it was not possible to make an accurate measure of sample weight as it was transferred between vessels in a slurry with water. Trace elements were thus reported in total nanograms. Strontium and Nd extracted using Eichrom ion extraction resins, isotopic analysis performed by MC-ICP-MS with sample uptake via Aridus desolvator. Mass fractionation was corrected by normalising to $^{88}Sr/^{86}Sr = 8.37521$ and $^{146}Nd/^{144}Nd = 0.7219$, and reported relative to SRM987=0.710230 and La Jolla = 0.511860. Epsilon Nd calculated relative to $^{143}Nd/^{144}Nd = 0.512632$ in modern CHUR (Chondritic Uniform Reservoir; Bouvier et al., 2008).

7.3.4 Results

Initial Sr isotopic compositions for tourmaline and epidote from the Productora breccia complex and associated veins range between 0.70380 and 0.70525 (Table 7.2). The $^{87}Sr/^{86}Sr$ ratio of the sub-stage 4D epidote sample is the highest, most radiogenic, in the sample suite and has the highest $^{87}Sr/^{86}Sr_i$ at 0.70525. Tourmaline samples have $^{87}Sr/^{86}Sr_i$ ranging between 0.70380 and 0.70432, five samples fall

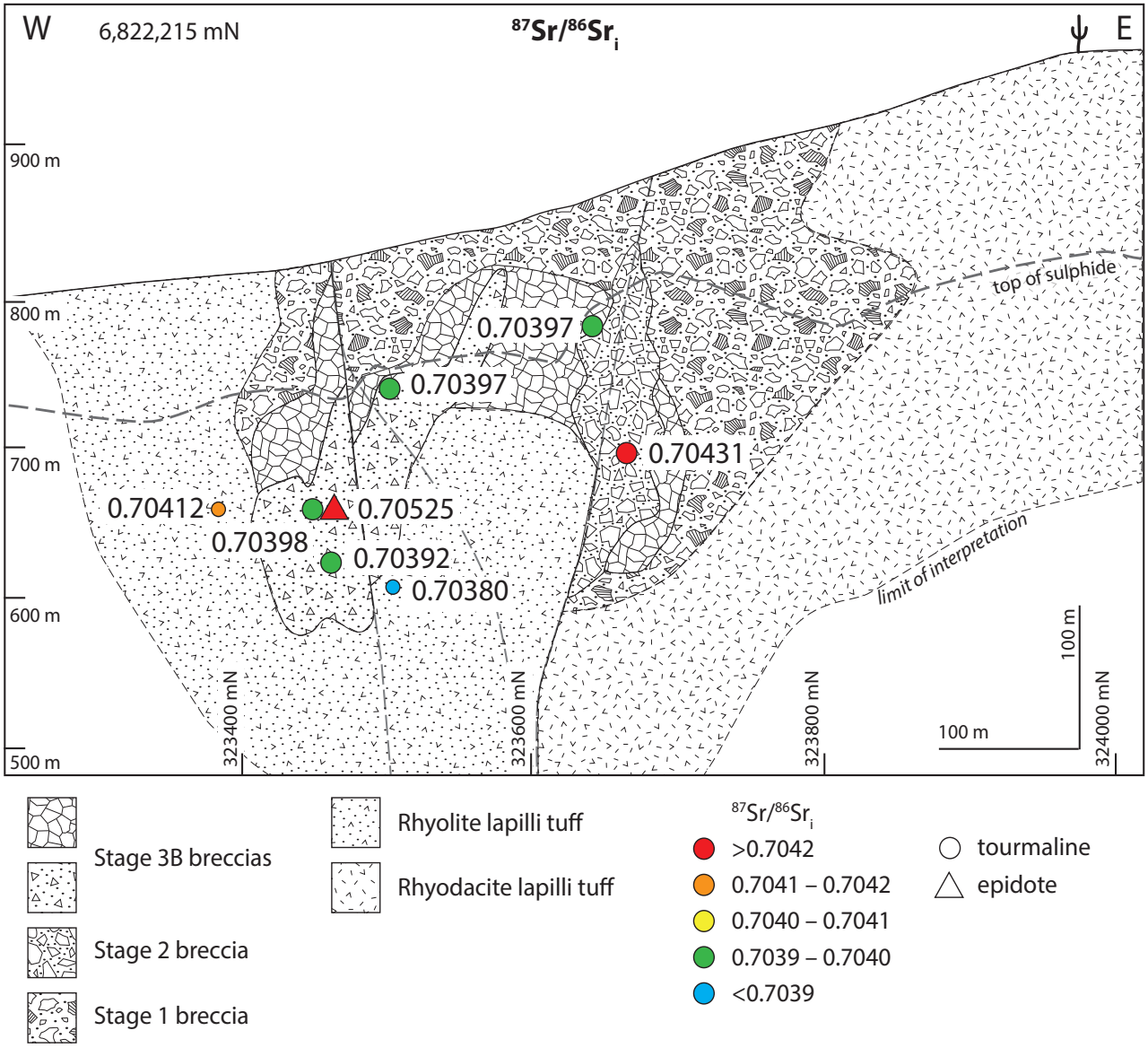

Figure 7.8 Cross section at 6,822,215 mN showing initial Sr isotope ratios of tourmaline and epidote, and sample locations. Small symbols indicate samples lie outside of ± 80 m section window. Epidote returns a significantly more radiogenic ratio than the majority of tourmaline samples.

within error of each other between 0.70392 and 0.70398 (Figure 7.7). Three tourmaline samples fall outside of the interquartile range of the tourmaline sample suite, including two samples from distal veins and clots hosted in volcanic rocks to the west (PR14AE114 and PR14AE074) and one from the Habanero ore zone. One distal sample is more radiogenic (PR14AE114) than the majority of tourmaline samples, and the other less radiogenic (PR14AE074; Figure 7.7 and Figure 7.8). Sample PR14AE128 is the most radiogenic of the tourmaline samples, including sample PR14AE125 which is from the

Table 7.3 Neodymium radiogenic isotope data from tourmaline mineral separate from the Productora breccia complex.

Sample	Mineral	Sm/Nd	$^{147}Sm/^{144}Nd$	$^{143}Nd/^{144}Nd$	$^{143}Nd/^{144}Nd_i$	εNd_i
PR14AE062	Tourmaline	0.128	0.077	0.512799	0.512733	5.2

Precision for Nd ± 0.000020. Initial Nd ratios calculated using equations of Bouvier et al. (2008) based on age on age of mineralisation reported in Chapter 4, 130 Ma. Paragenesis provided in Table 7.2.

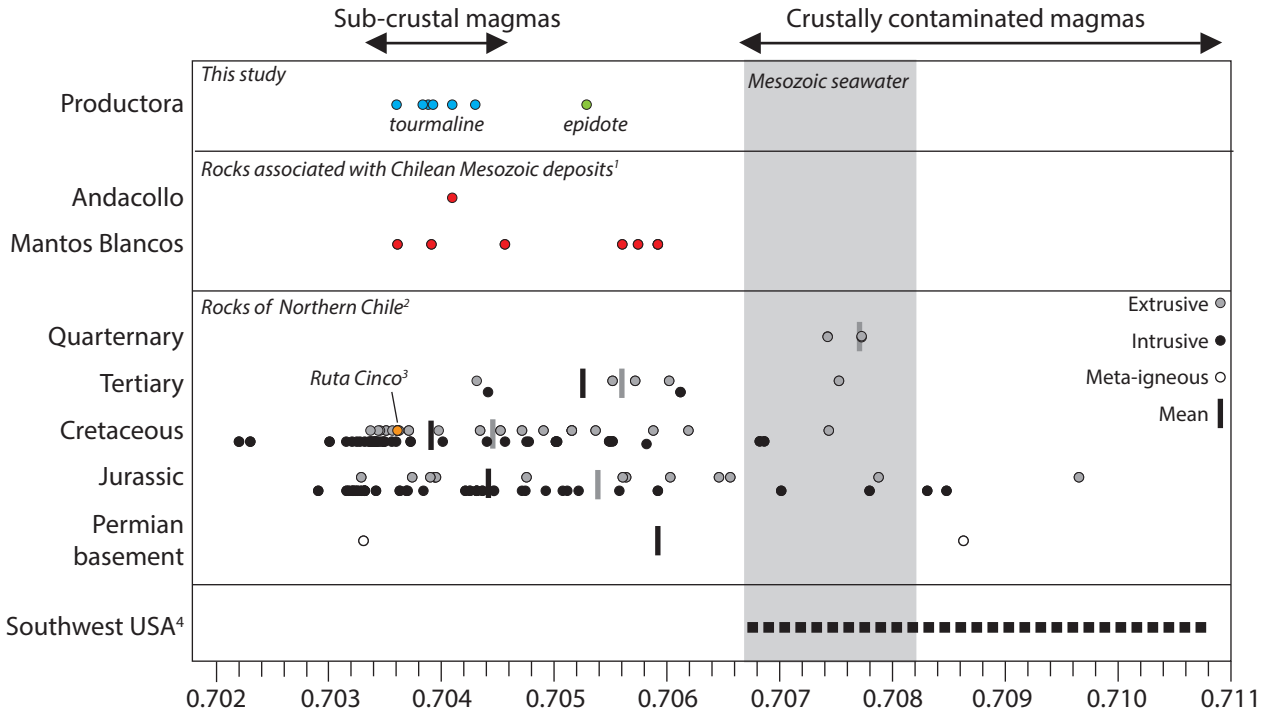

Figure 7.9 Initial $^{87}Sr/^{86}Sr$ isotopic data for tourmaline and epidote from Productora, compared to other Mesozoic deposits in northern Chile, as well as major crustal rocks of northern Chile and Mesozoic sea water (Viezer et al. 1999). Also included are the range of Sr isotope compositions for porphyry deposits from the south-western U.S. continental setting. This diagram is modified from Cooke et al. (2011). Data sourced from [1]Sillitoe (1987), [2]Ramirez et al.(2008), [3]McNutt (1975), Rogers and Hawkesworth (1989), Lucassen et al. (2002), Morata and Aguirre (2003), Morata et al. (2008) and Girardi (2014).

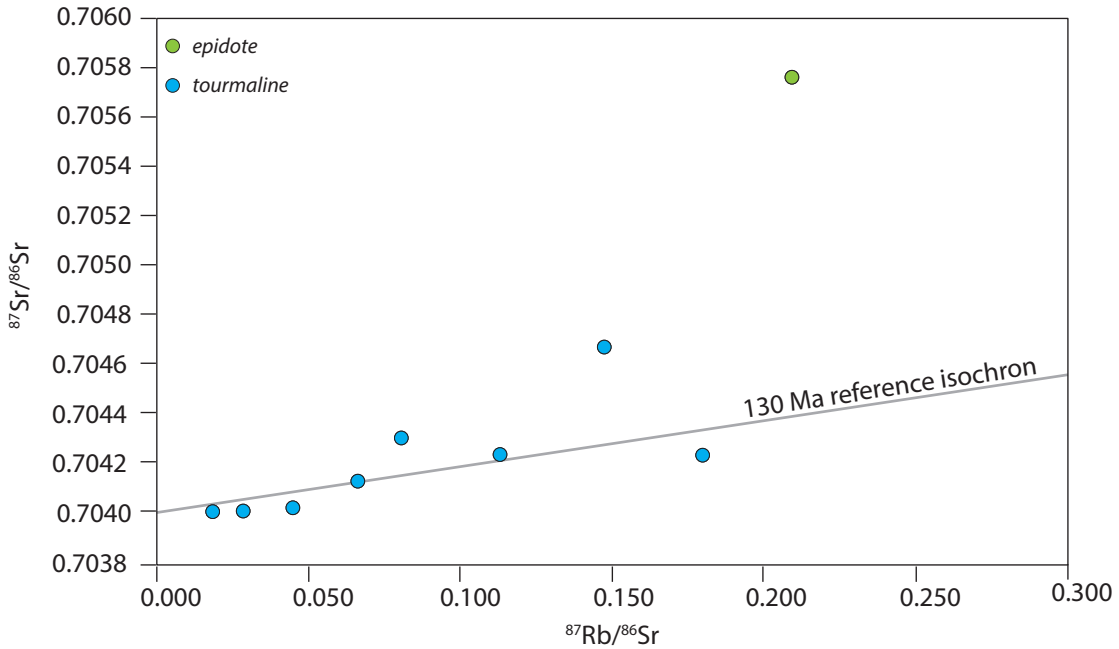

Figure 7.10 Rb-Sr isochron diagram with 130 Ma reference isochron (anchored at $^{87}Sr/^{86}Sr$ 0.704). The epidote sample has a significantly more radiogenic $^{87}Sr/^{86}Sr$ which cannot be rationalised by evolution from the same fluid composition as the tourmaline samples. Similarly, some isotopic heterogeneity exists within the tourmaline samples.

same paragenetic phase and spatial area (Figure 7.8). Samarium and Nd from one tourmaline sample (PR14AE062) were measured and used to calculate an initial epsilon-Nd of +5.2, assuming an age of 130 Ma (Table 7.2).

7.3.5 Discussion

Tourmaline mineral separates from eight samples of sub-stage 3B mineralised breccia from Productora have a mean initial Sr isotope ratio of 0.70397, which corresponds with the mean ratio for Cretaceous intrusive rocks (0.703976; Figure 7.9). The initial Sr ratios are higher than that of the Ruta Cinco batholith (0.7036; McNutt et al. 1975). The epidote mineral separate from a sub-stage 4D epidote-chalcopyrite vein has significantly more radiogenic initial strontium (0.70525) which corresponds to the mean initial Sr ratios for Jurassic extrusive rocks and falls between the mean for Cretaceous extrusive rocks and Mesozoic seawater (Figure 7.9).

The low tourmaline initial Sr ratios coincide with ratios from Cretaceous intrusive rocks and are consistent with a predominantly mantle-derived source of strontium, either by leaching of mantle derived igneous rocks, or exsolution from mantle-derived magma. The significantly higher initial Sr ratio for epidote indicates that it formed from a fluid with a different Sr isotope composition than the fluid that precipitated tourmaline. This is demonstrated by the position of the epidote sample on a Rb-Sr isochron diagram, as it plots above the 130 Ma isochron (Figure 7.10). Geochronology and paragenetic relationships both indicate that the epidote is younger than the tourmaline. The tourmaline is associated with molybdenite that has been dated at 130 ± 0.6 Ma (Chapter 4). The position of the epidote sample on Figure 7.10 indicates that the epidote-Sr did not have the same source as the tourmaline-Sr. Therefore the epidote cannot be explained by deposition from the same fluid as tourmaline. This implies that fluid mixing may have occurred at Productora, if tourmaline- and epidote-stable fluids interacted with each other on the flanks of the breccia complex.

As there is a wide spread of initial Sr values in the Chilean Jurassic and Cretaceous igneous rocks, it is difficult to further constrain the fluid sources at Productora. Additional whole rock Sr data for the local intrusions and stratigraphy would be required. Based on the mean Sr isotope values for Jurassic and Cretaceous rocks, the fluid that precipitated epidote may have been sourced from either Jurassic formation waters or a mixture of Cretaceous magmatic or formation waters and seawater. Calculations for potential seawater contribution, assuming fluids were sourced from Cretaceous volcanic rocks with mean $^{87}Sr/^{86}Sr_i$ of 0.704464 and mixed with seawater of mean Mesozoic contribution indicate the observed initial Sr value of the epidote would require approximately 27 % seawater contamination. Alternatively, the radiogenic Sr value for epidote may be an indication of isotopic exchange between the

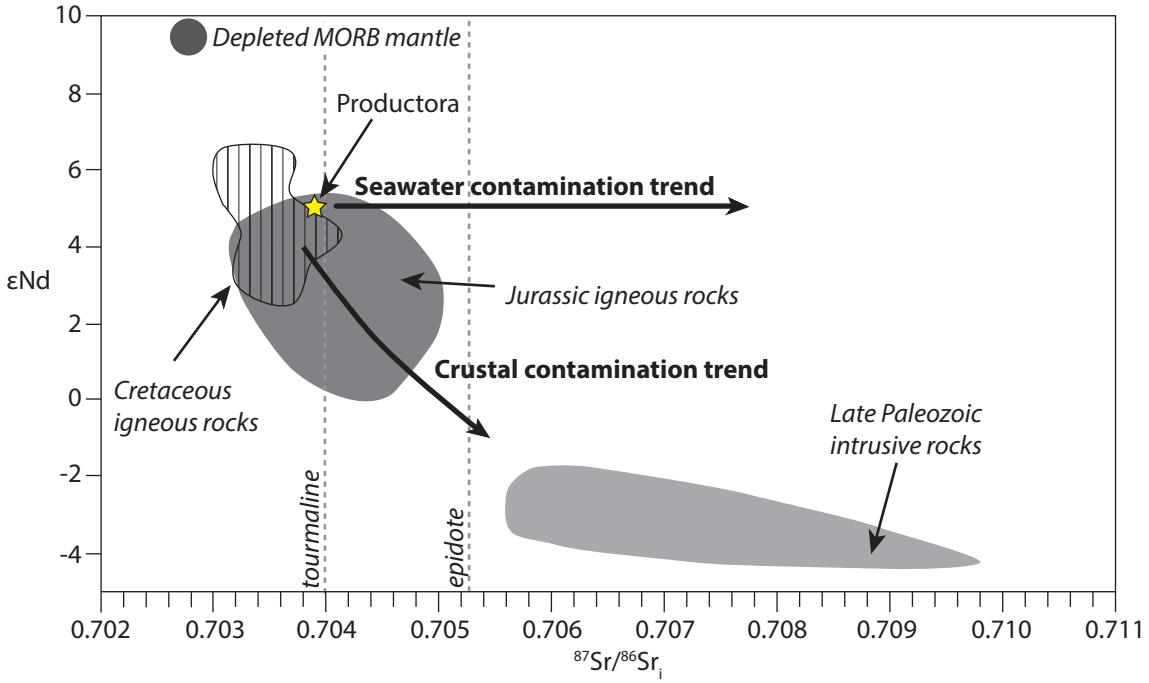

Figure 7.11 εNd vs. initial $^{87}Sr/^{86}Sr$ ratio for sample PR14AE060 (Table 7.3) with Mesozoic rocks from Coastal Cordillera of northern Chile. Dashed lines indicate mean initial $^{87}Sr/^{86}Sr$ ratio for Productora tourmaline and epidote analyses (this study; Table 7.2) . Jurassic igneous rock field and late Paleozoic rock field from Richards et al. (in prep. 2016), Cretaceous igneous rock field based on data from Morata and Aguirre (2003), Morta et al. (2008) and Girardi (2014). Depleted MORB mantle field at ~110 Ma from Pilet et al. (2011).

fluid and wall rocks at low fluid rock ratios (Orovan, 2016), where the Sr isotopic composition of the fluid has partially equilibrated with Mesozoic marine sedimentary rocks resulting in a more radiogenic signature.

A final consideration is whether the epidote has experienced contamination with foreign Sr, potentially by selective migration of radiogenic Sr. Heier (1964) proposed that radiogenic Sr in rubidium sites in mica and K-feldspar would be more mobile than common Sr. During wall-rock reactions this would result in radiogenic Sr enrichment of the fluid, which would be enhanced at low fluid to rock ratios. Additional initial Sr values for epidote distributed across the deposit, and spanning the different alteration assemblages, are required to further constrain the Sr isotopic composition of the fluid which precipitated epidote and any modification of the initial Sr value through radiogenic Sr migration.

The positive εNd value for sample PR14AE060 (Table 7.3) is consistent with Cretaceous and Jurassic igneous rocks (Figure 7.11). Since isotopic fractionation of Nd in the continental crust is minor compared to that of Sr (Hooker et al., 1981), contamination of fluids with initial Sr values in equilibrium with Cretaceous or Jurassic igneous rocks with sea water equilibrated fluids would cause a shift toward more radiogenic Sr with little change in εNd, Figure 7.11. Therefore, determining the εNd value for sub-stage 4D epidote at Productora would assist in resolving the cause of the radiogenic Sr signature and is recommended for future work.

7.4 Lead isotopes

7.4.1 Introduction

Lead isotope compositions of sulphide minerals can be used to inform metal source and fluid pathways in hydrothermal systems (Heyl et al., 1966; Stacey et al., 1968; Gulson, 1986; Sanford, 1992). Geological events lead to the fractionation of U-Th-Pb from typical crustal reservoir compositions (the mantle, lower crust, upper crust; Tosdal et al., 1999). Such fractionations can be measured as deviations of Pb isotope values from average growth curves. In ore deposits, Pb commonly occurs as a trace (or major) element in sulphide minerals whereas U content is intrinsically low (Tosdal et al., 1998). Thus, measured Pb isotope compositions of minerals formed during the Phanerozoic closely approximate the composition of the mineral and fluid at the time of crystallisation, assuming the system remained closed. Comparison of the Pb isotope composition of sulphides against those of potential rock reservoirs through which the hydrothermal fluid flowed or may have been sourced, can provide information on the hydrothermal plumbing system and deposit genesis (Macfarlane et al. 1990; Sanford 1992; Tosdal et al. 1999).

7.4.2 Previous work

No previous Pb isotope studies have been conducted at Productora. A review of Pb sources in a range of Mesozoic and Cenozoic Andean ore deposits between La Serena and Santigo was compiled by Tosdal and Munizaga (2003). Deposits in the district show systematic variation with age, geographic location and basement rocks. Two discrete Pb sources were identified; a high $^{207}Pb/^{204}Pb$ crustal source containing recycled Precambrian Pb and a low $^{207}Pb/^{204}Pb$ reflecting Pb input from subduction related processes.

7.4.3 Method

7.4.3.1 Pyrite etching

Polished 25 mm round mounts were etched using sodium hypochlorite (NaOCl) in order to identify potential zonation patterns and heterogeneity prior to LA-ICP-MS analysis. The NaOCl was applied to the surface of samples which were then and left to stand for two minutes before being dipped in water to remove the solution and air dried. Etched samples were reviewed by reflected light microscopy (Appendix F1). Laser spot targets were chosen to span a range of compositional zones revealed by the etch.

Table 7.4 Paragenesis of eight pyrite samples selected from Pb isotope and trace element (K, Fe, Au, Cu, U, Th, Hg) analysis.

Sample	Breccia facies	Dominant sulphide	Order of precipitation	Types	Occurrence	Size	Etch zoned	Silicate inculsions	Cpy inclusions	Habit	Number of analyses
3B - North (6,822,215 mN)											
PR14AE114	3B	py>>cpy	unkn	py114A	Dissem.	100–500 µm	No	No	No	Euhedral	8
				py114B	Dissem.	50–500 µm	No	Yes	No	Anhedral	2
PR14AE060	3B-1	cpy>py	py, cpy	na	Dissem. on clast margins	50–500 µm	Complex, undulating	Yes	Yes	Subhedral	12
PR14AE022	3B-2	py>cpy	py, cpy	na	Dissem.	<10–300 µm	Simple, 2–3 zones	Yes (patchy)	No	Subhedral	12
3B - Habanero (6,822,215 mN)											
PR14AE125	3B-2 (Habanero)	py>>cpy	py, cpy-py, cv	py125A	Dissem.	50–500 µm	Simple, 2–3 zones	Yes	No	Anhedral - round	12
				py125B	Vein	400 µm	na	No	No	Subhedral	1
PR14AE128	3B-2 (Habanero)	py>>cpy	unkn	na	Dissem., mostly in breccia cement	50–400 µm	Complex, undulating	Yes	No	Subhedral	12
3B - South (6,820,0850 mN)											
PR14AE148	3B-4	py>cpy	py, cpy	na	Dissem., mostly in breccia cement	50–500 µm	Complex, oscillatory	Yes	Yes	Subhedral	13
PR14AE141	3B	py=cpy	py, cpy	na	Dissem. on clast margins	10–400 µm	Complex, oscillatory	Yes	Yes	Subhedral	11
PR14AE162	3B-4	py>cpy	cpy, py, cpy	py162A	Breccia cement	<50–>1000 µm	Simple	No	Yes	Subhedral	11
				py162B	Breccia cement	50–200 µm	Weak, complex, undulating	Yes	Yes	Anhedral	1

cpy = chalcopyrite, py = pyrite, dissem. = disseminated

7.4.3.2 Laser ablation inductively coupled mass spectrometry (LA-ICP-MS)

Pyrite was chosen for Pb isotope characterisation as it occurs ubiquitously with stage 3 mineralised breccias. A total of eight paragenetically constrained samples (Table 7.4) were prepared as polished 25 mm diameter round mounts for lead isotope analysis by laser ablation inductively coupled plasma mass spectrometry (LA-ICP MS) at CODES, University of Tasmania, Australia following the methods of Meffre et al. (2008). For each sample, ten different spot analyses were made. Lead isotopes were measured along with selected trace elements (As, Au, Cu, Fe, K, Hg, U and Th) using an Agilent 7700 quadrupole ICPMS equipped with a 193 nm excimer laser and the Resonetics S155 laser ablation system. Instrument parameters are similar to those outlined by Meffre et al. (2008) and Woodhead et al. (2009). The instrument drift and mass bias correction factors were calculated using the NIST610 standard, which was analysed twice at the beginning and end of the run and once every 30 min throughout the run. Each analysis began with a 12 s blank gas measurement followed by a further 50 s of analysis while the laser was switched on. Pyrite was sampled with either 51 or 74 μm spot diameter, depending on grain size, using the laser at 10 Hz and fluence of approximately 3.5 J cm^{-2}. The counting time on all elements was 0.01 s, except for Au and ^{204}Pb which was counted for 0.1 s to improve on precision and lower the detection limit. Data reduction for trace elements was performed using similar methods to those outlined in Danyushevsky et al. (2011). Integration intervals were selected based on the Fe data which were used to confirm pyrite was being analysed for the duration of the analysis. Correction for radiogenic U did not significantly improve the data and introduced more uncertainty, therefore no radiogenic U correction was applied.

Table 7.5 Mean trace element content (ppm) of laser ablation intervals. Abundance of K correlates with the quantity of K-rich silicate inclusions, noted in Table 7.4. Sample locations provided in Appendix A4.

Sample name	Type	n	^{39}K	^{65}Cu	^{75}As	^{197}Au	Total Pb*	^{232}Th	^{238}U
3B - North (6,822,215 mN)									
PR14AE141		11	199	47.2	161	0.0647	4.67	2.66	4.06
PR14AE060		12	34.4	122	359	0.119	2.78	1.67	2.91
PR14AE022		12	1302	10.7	136	0.0223	1.46	3.97	4.13
3B - Habanero (6,822,215 mN)									
PR14AE125	$Py^{125}A$	12	3134	173	67.9	0.0394	2.35	1.74	1.65
	$Py^{125}B$	1	50.9	71.2	295	0.00885	0.000	0.0767	0.0914
PR14AE128		12	598	119	289	0.00836	0.965	2.93	1.43
3B - South (6,820,0850 mN)									
PR14AE148		13	317	20.2	126	0.0281	4.94	3.59	5.74
PR14AE114	$Py^{114}A$	8	198	42.2	71.8	0.107	0.619	0.145	0.262
	$Py^{114}B$	2	Analyses heavily contaminated with silicate phases						
PR14AE162	$Py^{162}A$	11	33.6	531	52.0	0.0454	0.784	0.0222	0.0874
	$Py^{162}B$	1	414	1432	8.30	0.0117	0.399	0.0054	0.0301

*Total Pb recalculated from ^{208}Pb, ^{207}Pb, ^{206}Pb and ^{204}Pb measurement channels. n = number of analyses, py = pyrite

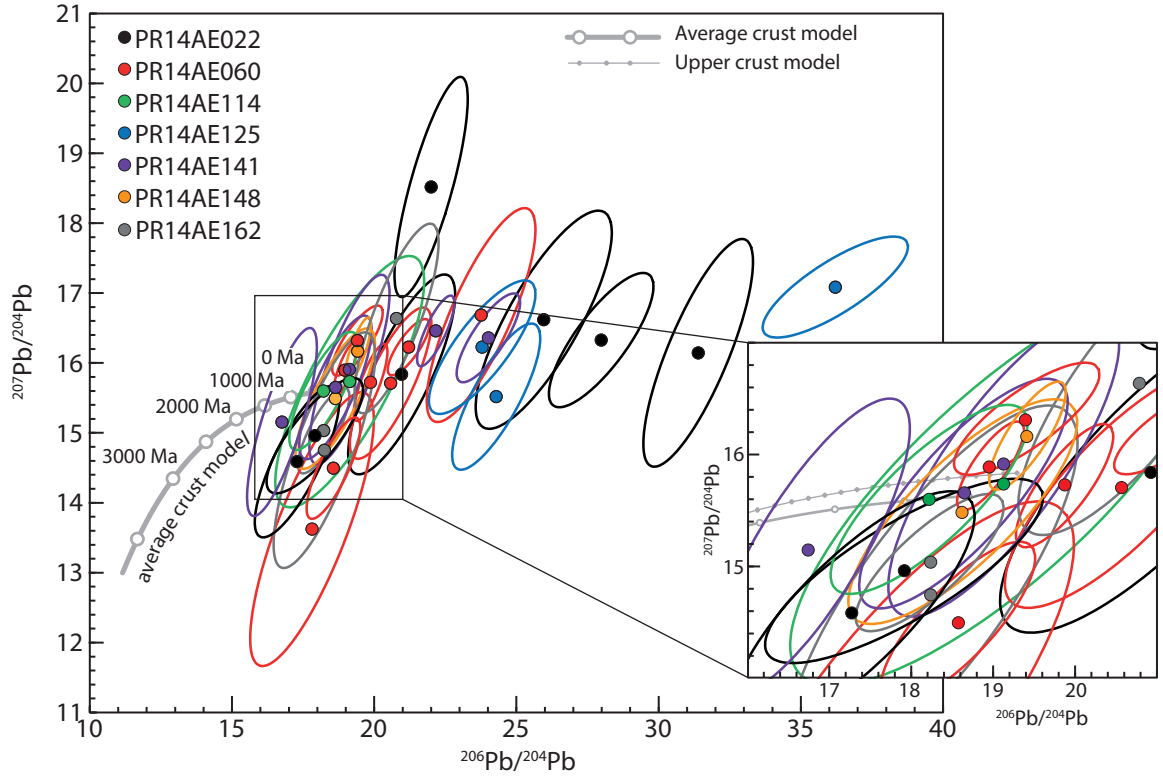

Figure 7.12 Uranogenic ($^{207}Pb/^{204}Pb$ against $^{206}Pb/^{204}Pb$) concordia diagram showing data from seven pyrite samples with 68 % confidence error ellipses. Model growth curves from Stacey and Kramers (1975). Pyrite analyses plot as an array toward increasing $^{206}Pb/^{204}Pb$ values indicating open system behaviour and contamination by radiogenic ^{206}Pb from ^{238}U decay.

7.4.4 Results

The results indicate that total Pb contents of pyrite grains are very low, between 0.75 ppm and 4.67 ppm, with a mean of 1.89 ppm (Table 7.5). The low levels of Pb in most samples poses a significant challenges for isotopic characterisation, particularly in the measurement of the least abundant isotope, ^{204}Pb. The Pb isotopic compositions determined are therefore very imprecise but show variably radiogenic compositions.

Trace element contents vary within each analysis (laser spot; Figure 7.14 to Figure 7.17) and between samples (Table 7.5). Arsenic is the most abundant trace element across all samples, with mean values between 47 and 359 ppm. Copper has mean values in pyrite between 10 and 606 ppm. Higher trace Cu values were noted in samples with disequilibrium textures between pyrite and chalcopyrite. Gold was generally only detected in low quantities (<0.1 ppm), however values of up to 0.38 ppm, 0.47 ppm and 0.52 ppm were measured over short intervals in individual spot analyses from three samples. Uranium and Th concentrations are variable and do not show systematic spatial variations.

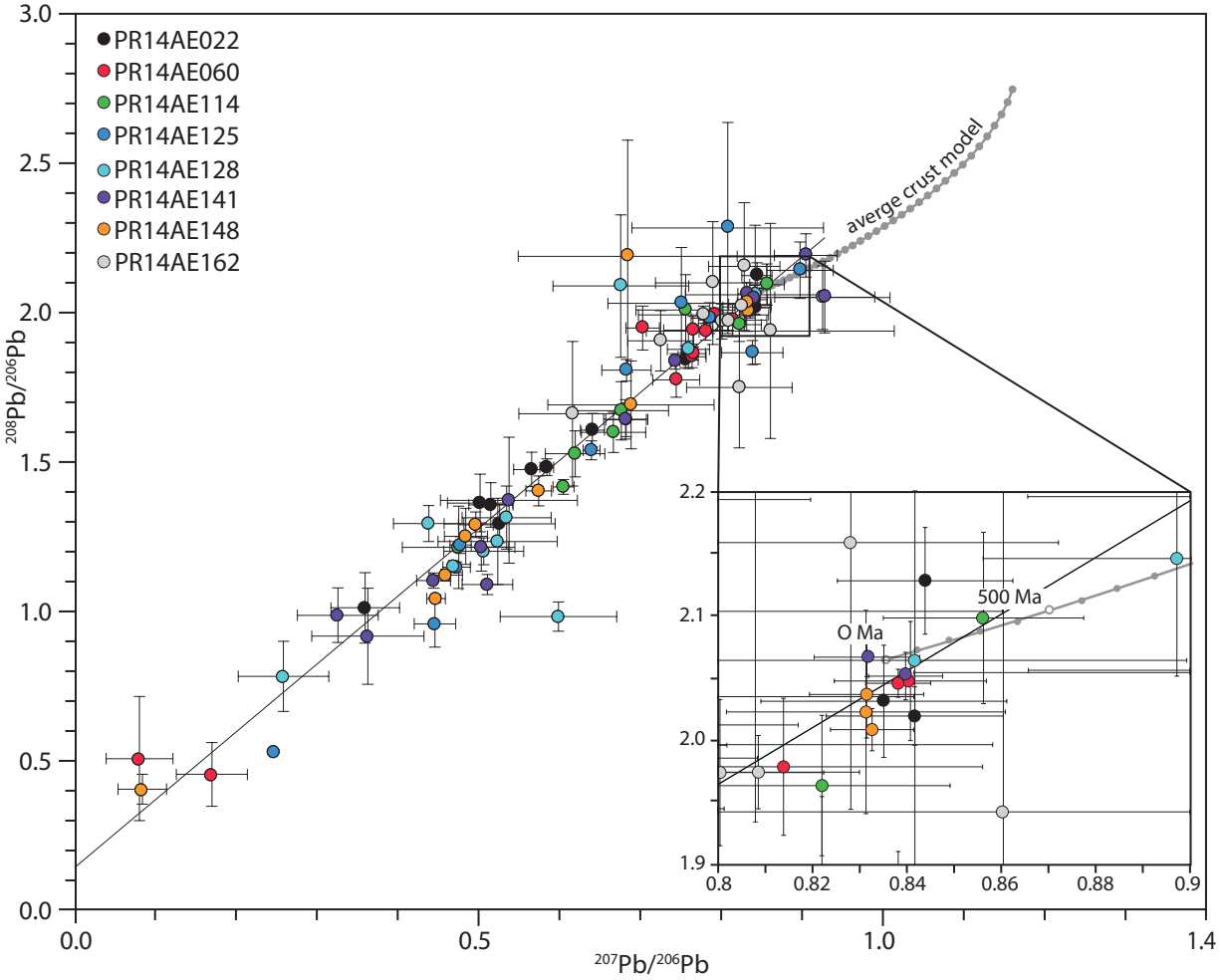

Figure 7.13 Lead isotope diagram ($^{208}Pb/^{206}Pb$ against $^{207}Pb/^{206}Pb$) showing data from seven pyrite samples. Average crust model growth curve (grey line) from Stacey and Kramers (1975) with 100 Ma markers. The model Pb age is 250 Ma. Pyrite data lie in a mixing line toward radiogenic Pb composition, with thorogenic Pb dominant over uranogenic Pb.

7.4.5 Discussion

7.4.5.1 Pb isotopes

The Pb isotope results are adversely affected by low Pb concentrations in pyrite, combined with the influence of a significant component of radiogenic Pb. Plotted on a $^{207}Pb/^{204}Pb$ versus $^{206}Pb/^{204}Pb$ diagram, the pyrite data defines as a wide array far from the crustal Pb growth curve (Figure 7.12). The array toward higher $^{206}Pb/^{204}Pb$ values indicates that the pyrite grains have been contaminated by significant uranogenic Pb. The data also have large uncertainties as a result of the low Pb content in the samples — this is reflected in the large error ellipses in Figure 7.12.

Since the ^{204}Pb data has such large uncertainties, data were plotted on a diagram of $^{208}Pb/^{206}Pb$ and $^{207}Pb/^{206}Pb$ (Figure 7.13). The array of data points trends toward radiogenic compositions, with both thorogenic and uranogenic input. A trend through the data points intersects the average crustal growth

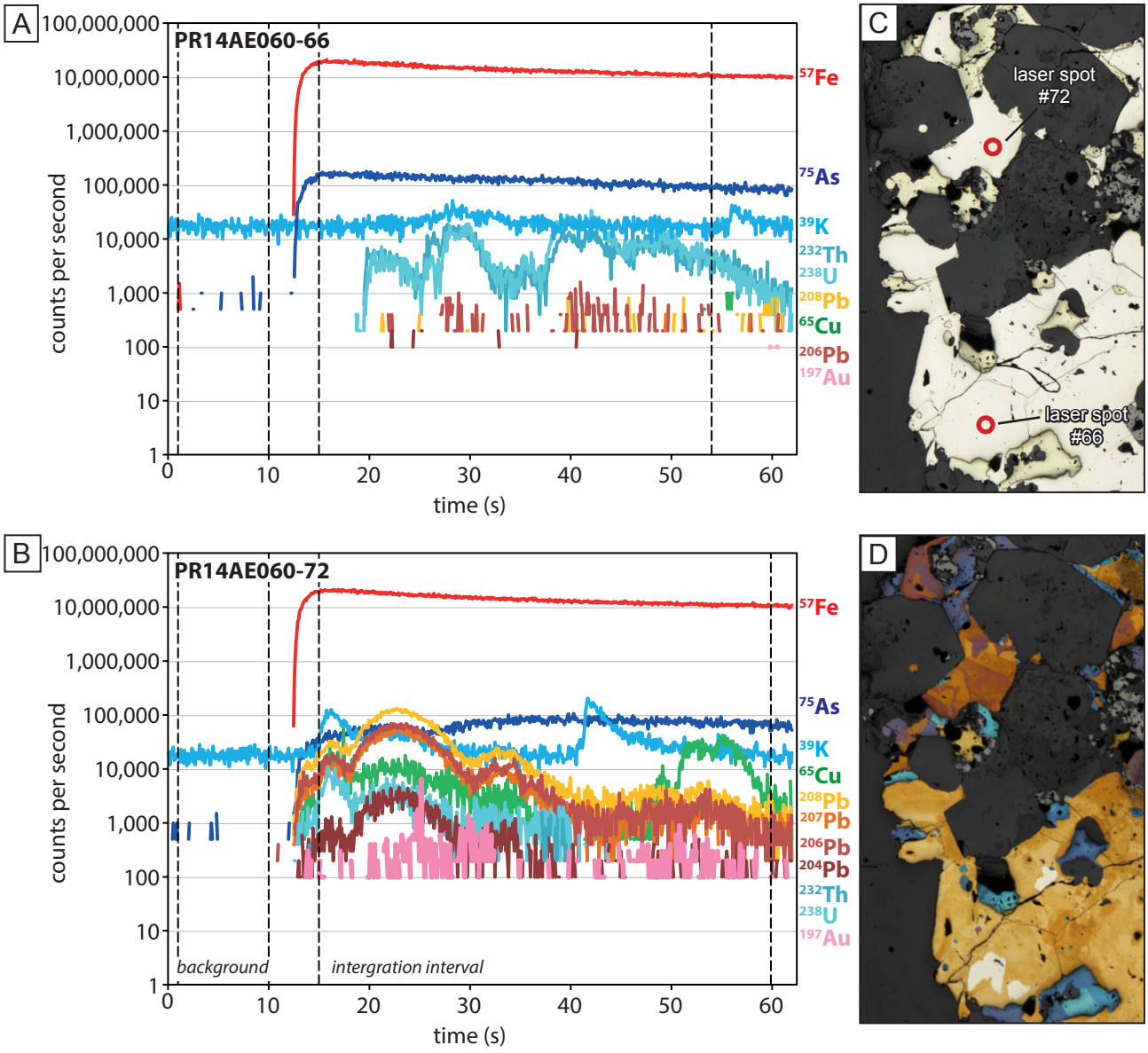

Figure 7.14 Laser spectra from sample PR14AE060 for A) analysis number 66 and B) analysis number 72. C) Analysis locations (spot not to scale) shown on reflected light photomicrograph of sample. D) Same area as C with acid etch. Analysis number 66 is from a grain with simple zoning following crystallographic faces is strongly developed, whereas analysis 72 is from a grain with more complex but weakly developed zonation. The trace element content of analysis number 66 (A) indicates U-Th-rich domains, or inclusions, within the pyrite. The trace element content from analysis number 72 (B) is significantly richer in Pb, Cu and Au compared to analysis number 66 (A), despite appearing to be from the same paragenetic stage (C).

Table 7.6 Spearman correlation coefficients for mean trace element composition of eight pyrite samples.

	Cu	As	Au	Pb	Th	U
U	-0.67	0.45	-0.24	0.62	0.83	1
Th	-0.74	0.57	-0.62	0.31	1	
Pb	0.048	0.6	0.21	1		
Au	0.29	-0.048	1			
As	-0.17	1				
Cu	1					

curve at 250 Ma. This is significantly older than geochronology data presented in Chapter 4 and is discounted on the basis of the low Pb and high uncertainty combined with unquantified radiogenic source(s).

Trace element analysis of the pyrite indicates that U-Th-rich domains, or inclusions, are common in the pyrite (Figure 7.14). Where U-Th-rich inclusions are absent, samples are also devoid of detectable Pb (Figure 7.15). The inclusions are interpreted to be sources of radiogenic Pb. The occurrence of such inclusions suggests that either the fluid that precipitated pyrite must also have been carrying significant U and Th, causing enrichment in pyrite, or that U-Th-rich minerals were present in the rock before pyrite was precipitated.

Many IOCG deposits have anomalous U compared to the expected U-content of their host rocks (Hitzman and Valenta, 2005). In comparison to other districts, the IOCG deposits of northern Chile contain negligable U (Candelaria 3–5 ppm; Marschik and Fontbote, 2001; Marschik et al., 2000 and Williams et al., 2005; and Manto Verde 3 ppm; Hitzman and Valenta, 2005). At Productora the average U content of 1 m interval samples (measured by ICP-AES/MS, section 1.3.3.1) from the two study sections is 17 ppm. Higher average U values (32 ppm with outliers between 400 and 2670 ppm) occur on the northern section and are spatially associated with the stage 2 and breccia facies 3B-2. Elevated U values in IOCG deposits are thought to be related to U-rich magmatic fluids from causative intrusions (Hitzman and Valenta, 2005) or from fluid mixing between the hydrothermal fluid and another U-bearing fluid which may have leached U from the wall rocks (Haynes, 1995). Barton and Johnson (1996) and Barton (2014) also argue for host rock control on U abundance. Hitzman and Valenta (2005) propose that the low U content of the Chilean IOCG deposits reflects the low expected U content of host mafic calc-alkaline volcanic sequences. Review of the U content of local host rocks at Productora would aid interpretation.

Both brannerite and uraninite were identified during SEM analysis of uranium-bearing minerals at Productora (Chapter 4). Interpretation of the Productora Pb isotope data could be improved with additional Pb isotope characterisation of U- and Th-bearing minerals. Orth et al. (2014) were able to identify a mixing trend between the Pb isotope composition of early uraninite and that of pyrite from the Coronation Hill U-Au-PGE deposit, Northern Teritory, Australia. Additional detailed petrography and SEM analyses would be required to better constrain the paragenesis of U-Th-bearing phases at Productora, unfortunately this was beyond the scope of the current study.

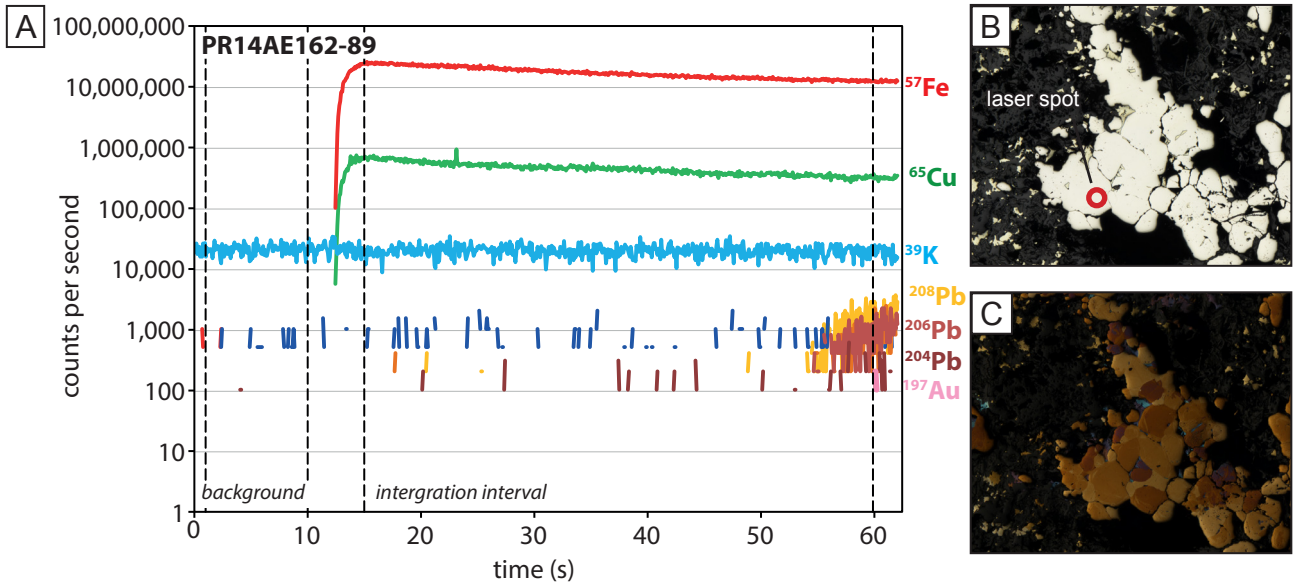

Figure 7.15 Laser spectra (A) from sample PR14AE162 analysis #89 showing relatively clean pyrite crystal with elevated Cu. Reflected light microphotograph of analyses spot before (B) and after (C) etching. Reflected light textures indicate pyrite is replacing chalcopyrite. Etching indicates predominantly homogenous crystals.

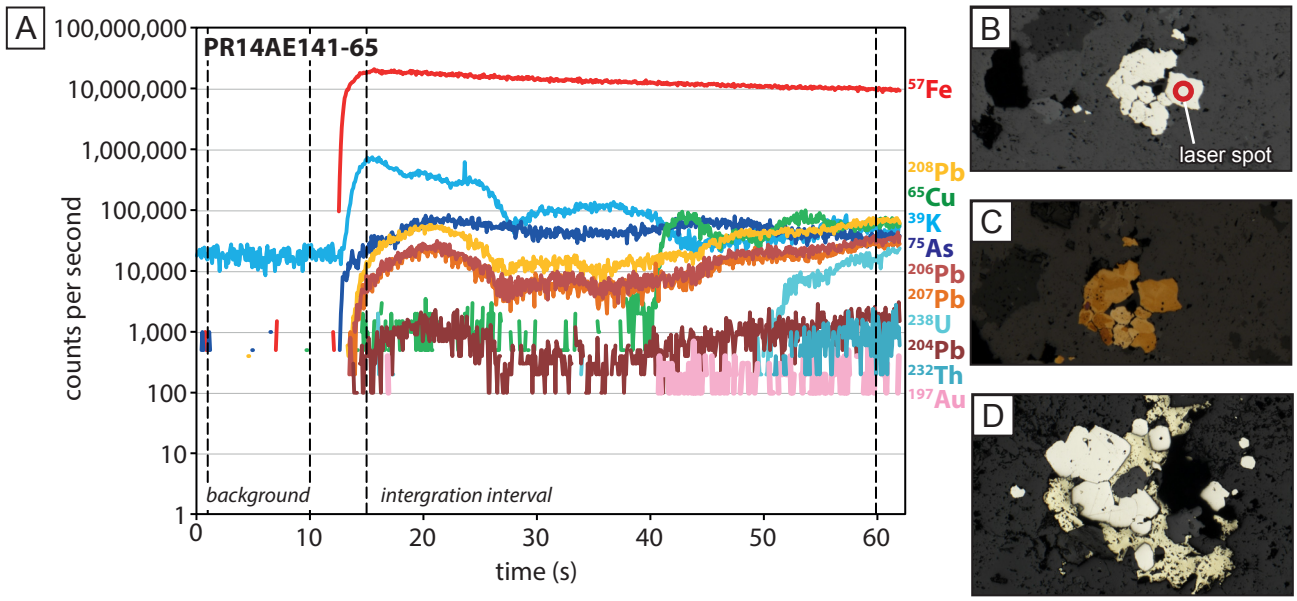

Figure 7.16 Laser spectra (A) from sample PR14AE141 analysis number 65 showing variable Pb, As, Cu, U, Th and Au in pyrite crystal. Variable K indicates silicate inclusions Reflected light microphotograph of analyses spot before (B) and after (C) etching. Etching indicates simple oscillatory zoning. D) Reflected light microphotograph to show pyrite is paragenetically earlier than chalcopyrite, as evidenced by the euhedral pyrite grains surrounded by anhedral chalcopyrite.

7.4.5.2 Pyrite trace element compositions

Uranium and Th are strongly correlated in all pyrite sample analyses (Table 7.6). There are also weak correlations between other elements, including Cu with Th and U, Au with Th, and Pb with As and U (Table 7.6). No systematic patterns in trace element enrichment between breccia facies or sample location could be determined from the limited sample suite. Overall, mean Au and As are higher in pyrite from the section 6,822,215 mN. Mean Cu, Pb and U are higher in pyrite from the southern

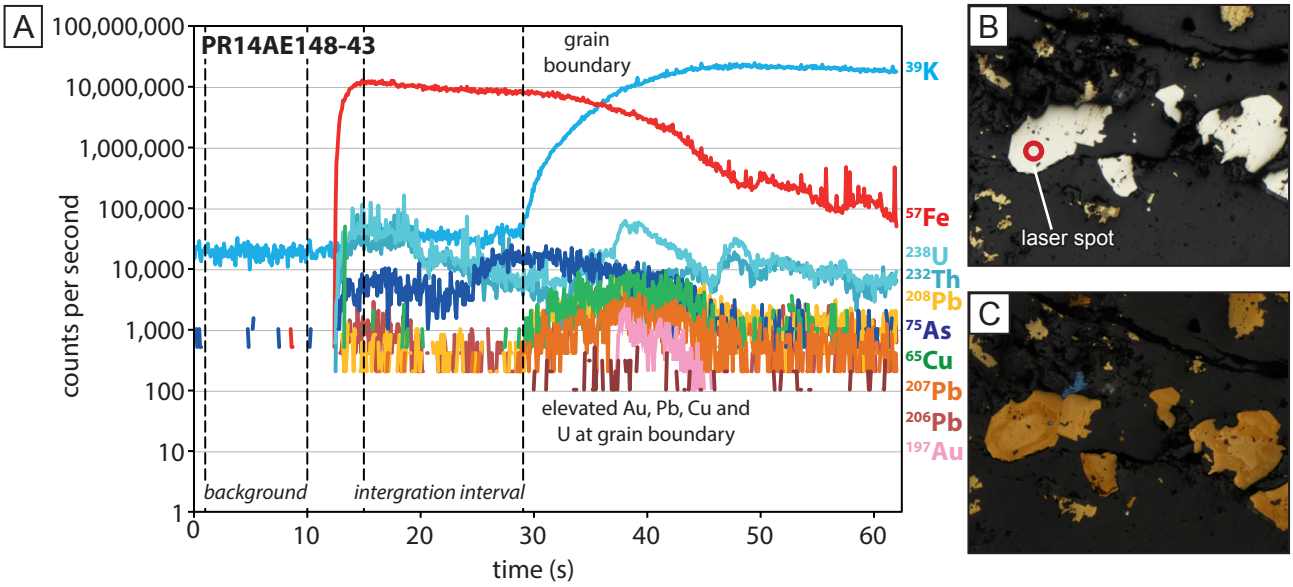

Figure 7.17 Laser spectra (A) from sample PR14AE148 analysis number 43 showing variable U, Th, Pb and As in pyrite crystal, and elevated Au, Pb and Cu on grain boundary with neighbouring K-bearing silicate mineral. Reflected light micro-photograph of analyses spot before (B) and after (C) etching. Etching indicates simple zoning.

section 6,820,850 mN. Compared to other samples from section 6,822,215 mN, the Habanero pyrite samples have higher mean Cu, As and Th but lower Au.

Both As and U are considered deleterious elements. It is noteworthy that they occur in pyrite, with concentrations in excess of 300 ppm and 4 ppm respectively (Table 7.5). Accumulation and concentration of pyrite through mineral processing may lead to higher concentrations of As and U in concentrates and tailings.

The trace element profiles (counts versus time) collected during the laser ablation provide an insight into the variability of trace element contents in the pyrite being ablated (e.g. Figure 7.14 to Figure 7.17). During the 45 second ablation time the laser typically drills to a depth of approximately 140 µm (based on drill rate of 3.07 µm s^{-1}; S. Meffre, pers. commun., 2016). The trace element data from pyrites analysed during the measurement of Pb isotopes reveal a sulphide paragenesis that is more complex than discernible in reflected light microscopy.

Analysis by LA-ICP-MS reveals different trace element patterns in pyrite grains from the same sample (Figure 7.14 A and B). In reflected light, pyrite from a facies 3B-1 breccia facies sample from section 6,822,215 mN appear to be from a single paragenetic stage (Figure 7.14 C). Acid etching indicates subtle differences in the zonation; strong oscillatory zones following crystallographic faces (laser spot #72) versus irregular undulating weak zonation (laser spot #66; Figure 7.14 D). Trace element analysis confirms the zonation pattern. Pyrite with undulating etched zonation has uniform As with variable U

and Th (possibly small inclusions) and low Pb concentrations (Figure 7.14 A), whereas the other has significant Pb, Cu and Au in addition to U, Th and As (Figure 7.14 B). The differences in trace element contents are inferred to indicate two separate pyrite precipitation events. The trace element patterns in analysis #72 show that Pb, Cu, U, Th and Au all co-vary. This suggests that these metals were all elevated in the hydrothermal fluid from which the grain precipitated.

Where pyrite has replaced chalcopyrite there is no evidence for zonation in either the acid etch, or the LA-ICP-MS trace element data (Figure 7.15). Pyrite formed after chalcopyrite also contains significant trace copper ((1270 ppm or 0.127 %; Figure 7.15) A). It is inferred that the fluids responsible for the replacement of chalcopyrite by pyrite did not contain significant Pb, U, Th, As or Au.

Pyrite grains that formed prior to chalcopyrite have variable and elevated Pb, Cu, Au, U and Th (Figure 7.16). Elevated Cu in the early pyrite suggests that fluids also contained varying amounts of Cu, which may not have been sufficient to cause saturation and chalcopyrite precipitation. Laser mapping of pyrite may reveal trends in the evolution of fluid composition.

Where laser ablation intercepted pyrite grain boundaries, increased U, Th, Pb, Cu and Au were commonly detected at the grain boundary (Figure 7.17 A). This is consistent with observations from section 4.8.3 regarding gold deportment as small grains on sulphide surfaces. Calculations for Au particle size are presented in section 7.4.5.3.

Trace element variability within and between pyrite from a limited suite of stage 3 breccia facies samples indicates a more complex hydrothermal history and sulphide paragenesis than previously recognised. The composition of pyrite across the deposit is heterogenous with respect to the trace elements analysed by LA-ICP-MS. It is likely that more could be learned about the mineralising fluids at Productora

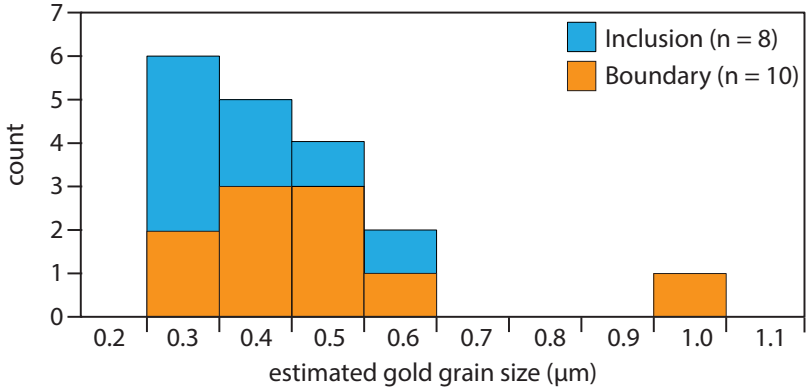

Figure 7.18 Histogram of estimated gold grain size from LA-ICP-MS analyses on pyrite where gold grains were identified on the grain boundaries and as inclusions. Grains on boundaries are slightly larger than the inclusions..

Table 7.7 Estimated Au grain size.

Sample ID	Analysis #	Type	Size (μm)
Section 6,822,215 mN			
PR14AE060	71	Inclusion	0.47
PR14AE060	72	Inclusion	0.22
PR14AE060	73	Boundary	0.26
PR14AE060	76	Inclusion	0.36
PR14AE060	77	Inclusion	0.28
PR14AE114	30	Inclusion	0.54
Section 6,822,215 mN (Habanero)			
PR14AE125	14	Boundary	0.31
PR14AE125	15	Boundary	0.90
PR14AE125	16	Boundary	0.51
PR14AE128	107	Boundary	0.34
PR14AE128	108	Boundary	0.42
PR14AE128	118	Boundary	0.43
Section 6,820 850 mN			
PR14AE141	61	Inclusion	0.37
PR14AE148	40	Boundary	0.30
PR14AE148	43	Boundary	0.44
PR14AE162	86	Inclusion	0.22
PR14AE162	91	Boundary	0.37
PR14AE162	101	Inclusion	0.23

if full trace element characterisation across a wider range of paragenetically and spatially constrained samples and minerals, including chalcopyrite, were conducted. Determining the detailed deportment of deleterious elements would enable potential downstream processing issues to be realised ahead of time. Such work is beyond the scope of this study.

7.4.5.3 Gold particle size estimation

Gold inclusions were intercepted by laser ablation in 18 out of 97 analyses (18.5 % of analyses), in 7 of the 8 samples analysed. Ten of the grains identified were on pyrite grain boundaries and eight as inclusions within pyrite. Grain size was estimated following the methods of Goemann et al. (2015) and Meffre (pers. commun., 2016) based on Au concentration (ppm; extracted from integration of Au peak data from laser profile), pyrite density (5.02 g/cm3; Dana and Hurlbut, 1971), and known ablation interval, ablation speed (calculated from typical pit depth and ablation time). Particles were assumed to be pure Au as no Ag data was collected. Since pure Au is denser than a Au-Ag alloy, this is likely to result in a slight underestimate of grain size.

Calculations indicate that the 18 gold grains identified in the laser profiles range in size between 0.22 μm

and 0.90 μm, (Figure 7.18). Gold grains that occur on sulphide grain boundaries are slightly larger than those that occur as inclusions, mean sizes are 0.43 μm and 0.33 μm respectively. Gold grains were only found on pyrite grain boundaries in samples from the Habanero ore zone. The Habanero grains have a larger mean grain size (0.49 μm) than the other samples. These data are consistent with results from the Au deportment study in section 4.8.3.

Individual laser sweep data were converted from counts per second (cps) to ppm in order to determine potential Au solubility in pyrite as a function of As (Reich et al., 2005). Gold values range between 0.001 ppm and 41 ppm – this is below detection limit for the synchrotron XRF analyses (section 4.8.3). Arsenic values range between 0.15 ppm and 31,000 ppm. Gold plotted against As data reveals that most individual sweep points plot below the Au solubility line (Appendix F2), indicating Au solid solution in pyrite. Data points from samples PR14AE114, PR14AE148 and PR14AE116 plot above the solid solution line indicating Au inclusions present – this is consistent with the interpretation of laser profiles. Data points from sample PR14AE125 contain high As and Au, and plot as an array below the solubility curve. This suggests that intervals of high Au in sample PR14AE125, interpreted as an inclusion, may actually be solid solution. Further characterisation of the Au deportment at Productora would be beneficial in order to determine variability in deportment with alteration facies and to make inferences on recoverability. If significant Au occurs as particles attached to pyrite, a pyrite concentrate for gold extraction may be economic.

7.5 Conclusions

- The $\delta^{34}S$ values of sulphides from Productora range between -8.5 and +2.2 ‰. The range of $\delta^{34}S_{sulphide}$ values overlaps with the range expected for both porphyry or IOCG deposits, 0 ± 5‰. This suggests that magmatic sulphur was an important sulphur source at Productora.
- The broad range of $\delta^{34}S_{sulphide}$ values at Productora indicate fluids have evolved under oxidising conditions, and the absence of high $\delta^{34}S_{sulphide}$ values indicates there was no significant input from evaporite- or seawater-sourced fluids.
- The $\delta^{34}S_{sulphide}$ values at Productora are comparable to other deposits regionally (Figure 7.5 and Figure 7.6), suggesting formation from fluids of similar metal and sulphur source, and by similar depositional mechanisms (Figure 7.5).
- Zonation toward more negative $\delta^{34}S_{sulphide}$ values (-8.5 to -4.8) associated with fault zones is inferred to indicate oxidation of H_2S (Figure 7.3).

- Low $\delta^{34}S_{sulphide}$ values associated with the Cachiyuyito system (-7.8 to -4.2) indicate that the Cachiyuyito mineralisation and alteration formed from a more oxidised fluid than the Productora breccia complex (Figure 7.2).

- The trend toward positive $\delta^{34}S_{sulphide}$ values in the south is consistent with sulphides being precipitated from a hotter fluid in this area, which supports interpretations from Chapter 4 that the roots of the breccia complex are in the southern part of Productora (Figure 7.1).

- One εNd value +5.2 (Table 7.3), that was obtained from tourmaline, is consistent with Cretaceous and Jurassic igneous rocks (Figure 7.11), and implies magmatic input of Nd.

- The mean initial Sr isotope ratios from eight tourmaline mineral separates (0.70397) corresponds with the mean ratio for Cretaceous intrusive rocks (Figure 7.9) which is consistent with a predominantly mantle derived source of Sr.

- The initial Sr value for one epidote mineral separate is more radiogenic than the tourmaline (0.70525) and falls between the mean Cretaceous extrusive rocks and Mesozoic seawater (Figure 7.9). This is interpreted to indicate that epidote precipitated from a fluid with more radiogenic Sr than the fluid which precipitated tourmaline. This may be the result of fluid mixing or isotopic exchange between fluid and wall rocks. Additional analyses of εNd may assist in resolving these conflicting hypotheses.

- Trace element analysis of sulphides indicates that sulphide paragenesis is more complex than previously recognised. Early pyrite grains have elevated Pb, Cu, U, Th and Au (Figure 7.16) which also all co-vary (Figure 7.14). Pyrite that replaced chalcopyrite does not contain significant Pb, U, Th, As or Au, but does have elevated Cu (Figure 7.15).

- Pyrite grains contain abundant U-rich inclusions (Figure 7.13). High U at Productra (17 ppm) and inclusions of U in pyrite may be problematic in ore concentrates .

- Eighteen gold inclusions were intercepted by laser ablation in seven out of the eight samples analysed. Ten of the grains were on pyrite grain boundaries and eight as inclusions within pyrite. Grains that occur on grain boundaries are slightly larger than those that occur as inclusions, mean sizes are 0.43 μm and 0.33 μm respectively (Figure 7.18). This is consistent with observations from section 4.8.3 regrading gold deportment. A pyrite concentrate for Au recovery should be investigated at Productora.

- Gold also occurs in solid solution in pyrite between 0.001 ppm and 41 ppm.

Chapter 8: Conclusions

8.1 Introduction

The aims of this thesis were two fold: 1) increase the geological understanding of the Productora deposit in order to revise the genetic model. 2) advance the knowledge of deposit-wide mineralogy and Cu-speciation for the purposes of understanding processing characteristics. The preceding chapters documented the geology, hydrothermal breccias, alteration and mineralisation of the Productora Cu-Au-Mo deposit and provided insights into its hydrothermal evolution. Deposit-wide models for mineralogy and Cu-speciation have also been presented. This chapter synthesises the geological results of the current study and those of previous workers into a new genetic model. Features that are consistent with the porphyry and IOCG models are outlined with a short discussion regarding how Productora compares to both deposit classes, and the challenges that ambiguity causes regarding unequivocal classification of the deposit. Conclusions from the geometallurgical modelling are summarised and processing implications highlighted. The chapter concludes with recommendations for future work and exploration implications.

8.2 Genetic model

8.2.1 Tectonic setting, volcanism and plutonism

During the Mesozoic, the present day Coastal Cordillera was an active magmatic arc characterised by volcanism and plutonism related to Mariana-style steep subduction. A range of deposit types formed within a convergent tectonic regime where evolving subduction style, magmatic arcs and associated back-arc basin stratigraphy, plutonic complexes and the crustal scale syn-arc strike-slip Atacama Fault Zone evolved in response to prevailing geodynamic conditions.

The Productora Cu-Au-Mo deposit is hosted by the Bandurrias Group, part of the Jurassic-early Cretaceous magmatic arc (Segerstrom 1960; Moscoco et al., 1982; Charrier et al., 2007). The Bandurrias Group is a thick package of predominantly andesite volcanic rocks with intercalations of clastic volcanic rocks

(tuff and breccia), siliclastic and calcareous marine rocks, which are lateral facies variations of the backarc Chañacillo Group limestones (Moscoco et al., 1982). Locally at Productora, the Bandurrias Group stratigraphy consists of early andesite-dacite tuffs succeeded by rhyodacite lapilli tuff and rhyodacite monomict breccias, rhyolite welded lapilli tuff and rhyolite lapilli tuff, and unconformably overlain by basalt and basalt-andesite flows (Fox, 2000; this study, Figure 8.1 A). Volcanic textures observed at Productora are consistent with an explosive sub-aerial magmatic arc environment that generated thick pyroclastic deposits and lavas flows and/or domes. U-Pb_{zircon} geochronology reveal that the volcanic stratigraphy was deposited approximately 128 ± 1 Ma (rhyodacite lapilli tuff and rhyolite welded lapilli tuff; Table 3.3).

Emplacement of the major Mesozoic plutonic complexes that comprise the Chilean Coastal Batholith, were broadly contemporaneous with the volcanic stratigraphy (Sillitoe, 2003). The four significant intrusions recognised at Productora have been dated using the U-Pb_{zircon} method. From oldest to youngest, they are: Cachiyuyito tonalite-diorite (130 Ma; Fox, 2000), Alice granodiorite porphyry (121 ± 2 Ma), Zapallo porphyry (119 ± 1 Ma) and Ruta Cinco batholith (quartz-monzonite border = 96 Ma; Fox 2000; granodiorite core = 92 ± 1 Ma, this study). The Cachiyuyito stock and host volcanic sequence are interpreted to be contemporaneous (almost within error). The Cachiyuyito stock is similar in age to the mineralised productora breccia complex (130 to 128 Ma; Marquardt et al., 2015; this study). Field relations indicate the Cachiyuyito tonalite pre-dates mineralisation at Productora (Fox, 2000). Absolute age constraints indicate that the Alice porphyry intrusion post-dates the Productora breccia complex. The Zapallo porphyry and Ruta Cinco batholith post-date both the Productora breccia complex and Alice porphyry Figure 8.1 B and C.

8.2.2 Brecciation and main-stage mineralisation

The Productora hydrothermal system produced a sequence of hydrothermal breccias, tectonic breccias, veins and alteration assemblages that have been separated into five paragenetic stages: stage 1 quartz-pyrite-cemented breccia; stage 2 chaotic matrix-supported breccia; stage 3 tourmaline breccias; stage 4 phyllic and propylitic veins; and stage 5 propylitic veins (Figure 4.3; Table 4.4). The Productora breccia complex formed via at least two stages of hydraulic fragmentation (stages 1 and 3) and one tectonic-hydrothermal brecciation event (stage 2). The tectonic breccia shows evidence for multiple episodes of reactivation that resulted in polyphase breccia textures (Table 4.11). Mineralisation is associated with the stage 3 hydrothermal breccia and stage 2 tectonic-hydrothermal breccia (at Habanero).

Hydraulic brecciation is inferred to be the result of hydrostatic pressure exceeding lithostatic load and tensile strength of the overlying rock mass resulting in brittle failure (e.g., Burnham, 1979, 1985).

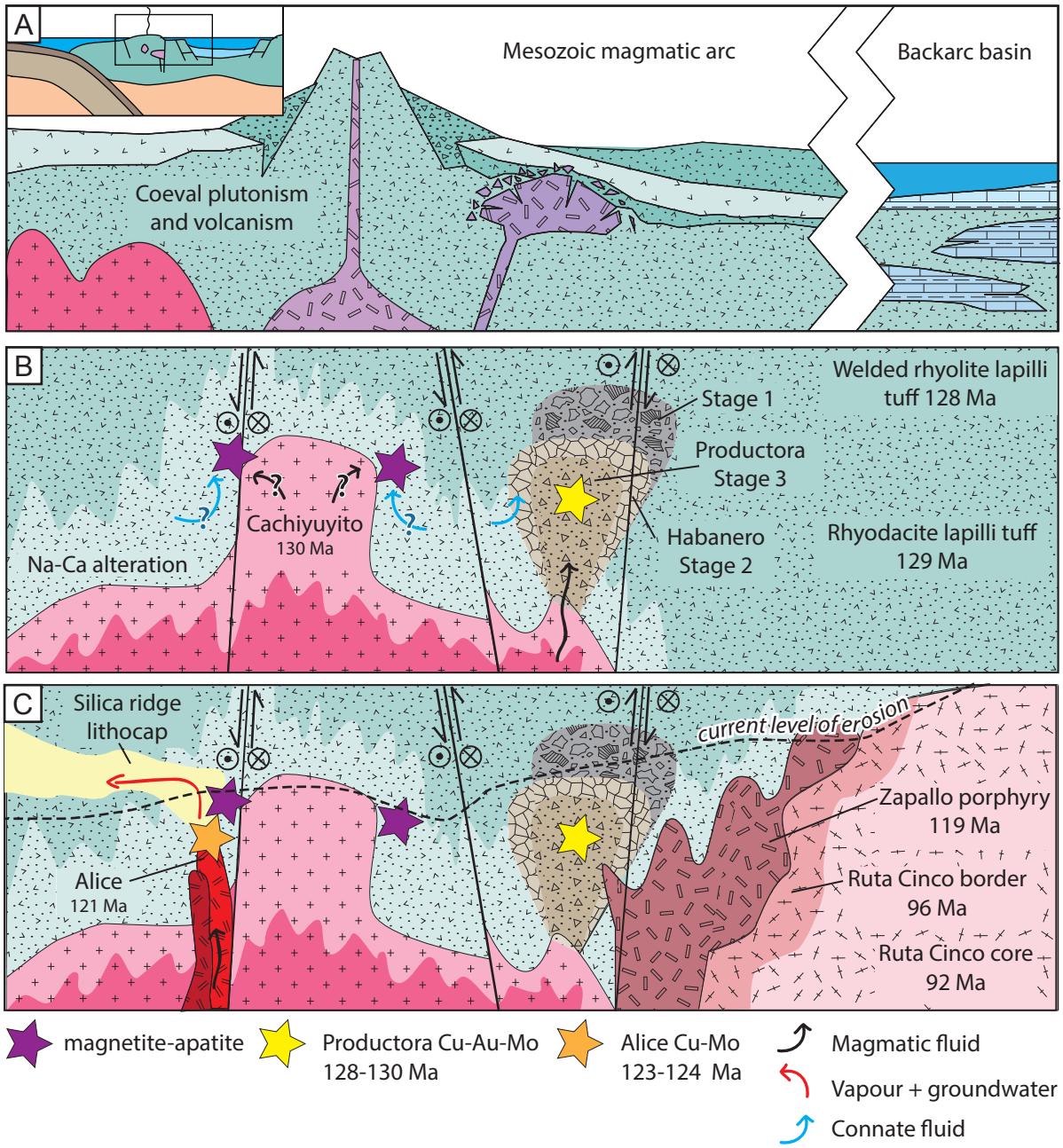

Figure 8.1 Schematic cross sections illustrating key aspects of the genetic model for Productora. A) Regionally, thick sequences of subaerial volcanic rocks were deposited in the Mesozoic magmatic arc under extensional to transtenional conditions with coeval plutonism. B) Locally, intrusion of the Cachiyuyito stock is spatially and temporally associated with large-scale sodic-calcic alteration, magnetite-apatite mineralisation (fluid source and evolution unconstrained) and emplacement of the Productora magmatic-hydrothermal breccia complex and Cu-Au-Mo mineralisation. Local faults associated with the regional Atacama Fault Zone were active throughout. C) Emplacement of the Alice porphyry and associated porphyry Cu-Mo mineralisation and advanced argillic lithocap (absolute age undetermined). Intrusion of barren Zapallo porphyry and Ruta Cinco batholith. Current erosion level indicated.

The dyke-like geometry of the breccia complex suggests that pre-existing north-northeast striking faults provided domains of weakness that were favourable to breccia propagation. Brecciation provided permeability for hydrothermal fluids that subsequently migrated through the rock mass, leading to clast comminution, matrix generation, cementation and alteration.

Stage 1 breccias have textures consistent with high energy, explosive hydraulic ± seismic rupture-driven fragmentation (massive, chaotic, poorly sorted angular clasts; Table 4.11) involving weakly acidic, low to moderate temperature fluids (<300°–400°C) that cemented the breccia with quartz-pyrite. The stage 2 tectonic breccia was generated by seismic rupture driven fragmentation and attrition during faulting, as evidenced by abundant rock flour and matrix, lack of hydrothermal cement, and rounded and stratified clasts. Clast textures suggest multiple phases of reactivation. Stage 2 breccias were altered (possibly at a later stage) by low temperature (<300°C), strongly acidic fluids that generated pervasive kaolinite - muscovite - pyrite alteration. Stage 3 breccia textures are consistent with non-explosive hydraulic ± seismic rupture-driven fragmentation (minor matrix, clast supported, jigsaw fit) involving high temperature (>400°C), alkaline magmatic-hydrothermal fluids that precipitated tourmaline, magnetite, biotite, chalcopyrite and pyrite and caused widespread, intense K-feldspar alteration. Stage 3 breccia cement mineralogy varies vertically and laterally through the breccia complex. At depth (>200 m), magnetite-bearing assemblages indicate precipitation from high temperature fluids (425°–500°C; Figure 4.40). Magnetite-bearing assemblages transition upward and outward to tourmaline-chalcopyrite dominant. High grade (>1 % Cu) mineralisation formed where stage 3 overprinted the stage 2 tectonic breccia. Breccia textures and mineralogy as an indicator of paleo-temperature, indicate a temperature gradient and increased intensity of brecciation to the south. This is suspected to be near the root zone of the breccia complex. The absolute age of stage 3 brecciation and mineralisation was determined by $Re\text{-}Os_{molybdenite}$ to be 130 to 128 Ma (Marquardt et al., 2015; this study).

On cooling, stage 3 fluids evolved to become weakly acidic and sericite stable, as evidenced by 4B (sulphide-sericite) and 4C veins (illite). Incursion of alkaline fluids is inferred to have formed veins during sub-stage 4A (chlorite), sub-stage 4D (epidote) and stage 5 (calcite).

The Alice porphyry intruded approximately 4 to 9 m.y. after emplacement of the Cachiyuyito stock and Productora breccia complex. Mineralisation primarily occurs as fine grained, disseminated chalcopyrite and pyrite, plus sulphide stringers and quartz-sulphide veins. Alice porphyry mineralisation is dated at 124 to 123 Ma ($Re\text{-}Os_{molybdenite}$). Remnants of an advanced argillic lithocap, consisting of massive textureless quartz above alunite and pyrophyllite-dickite assemblages, occurs above the Alice porphyry (Figure 4.28). The lithocap outcrops are disjointed and offset to the southwest, suggesting that they are remnants of a larger, shallow level domain of advanced argillic and silicic alteration (Figure 4.1 and

Figure 4.28). Absolute timing relationships for the lithocap have not been established, but are inferred to be coeval with the Alice porphyry.

8.2.3 Metals and fluid sources

The $\delta^{34}S$ values of sulphides from Productora range between -8.5 and +2.2 ‰. The range of $\delta^{34}S_{sulphide}$ values overlaps with the range expected for both porphyry or IOCG deposits (0 ± 5 ‰; Figure 7.5 and Figure 7.6). Magmatic sulphur is interpreted to be the dominant sulphur source at Productora, assuming a sulphide dominant system. The broad range of $\delta^{34}S_{sulphide}$values indicate fluids evolved under oxidising conditions. The absence of high $\delta^{34}S_{sulphide}$ values indicates there was no significant input from an external brine. A shift toward positive $\delta^{34}S_{sulphide}$ values in the south (Figure 7.1) suggests that sulphides formed from a hotter fluid in this area, which supports interpretations that the roots of the breccia complex are in the south of the deposit.

The mean initial Sr isotope ratios of stage 3 tourmaline (0.704) corresponds with the mean ratio for Cretaceous intrusive rocks (Figure 7.9). This is consistent with a predominantly magmatic derived source of Sr in fluids that cemented the stage 3 breccia with tourmaline - magnetite - chalcopyrite - pyrite. One εNd value (+5.2; Table 7.3) from tourmaline supported this interpretation (Figure 7.11). The initial Sr value for one sub-stage 4D epidote sample (0.705) falls between the mean Sr value for Cretaceous extrusive rocks and Mesozoic seawater (Figure 7.9). The fluid from which sub-stage 4D epidote formed was more radiogenic than that which stage 3 tourmaline precipitated from. This may be the result of fluid mixing of magmatic hydrothermal water with seawater or some other crustal fluid, or isotopic exchange between fluid and crustal wall rocks.

Lead isotope analysis on pyrite grains indicate contamination by significant thorogenic and uranogenic Pb, which are inferred to be sourced from abundant U-rich inclusions in pyrite (Figure 7.13). Heterogeneous pyrite trace element compositions (As, Au, Pb, U, Th) suggest a complex sulphide paragenesis that has not been fully resolved. Gold occurs as sub micron to7 μm grains, on pyrite and chalcopyrite surfaces, and in solid solution in pyrite (up to 41 ppm).

Stable (S) and radiogenic isotope (Sr, Nd) evidence and mineralogy suggest that magmatic fluids contributed to hydraulic brecciation, alteration and mineralisation at Productora. The preferred model for magmatic-hydrothermal breccia formation is that of Burham (1979, 1985), who invoke fluid liberation from high-level hydrous magma chambers during second boiling (water saturated melt → crystals + aqueous fluid) followed by decompression of the released fluids and fluid expansion. Intrusion-related magmatic hydrothermal breccias are commonly located in the upper parts, or immediately

above, plutons or stocks, or are distributed around their sloping margins. Porphyry-related magmatic-hydrothermal breccias may be centrally or asymmetrically positioned relative to the pophyry (Sillitoe, 1985; 2010). Based on the close agreement of $Re\text{-}Os_{molybdenite}$ and $U\text{-}Pb_{zircon}$ dating results, the Cachiyuyito stock is proposed as the likely source for magmatic fluids that caused brecciation and mineralisation at Productora. The breccia complex crops out on the eastern flank of the stock but is potentially more intimately associated with the stock at depth. Deeper drilling is required, possibly coupled with geophysical surveys, to determine the extent of the intrusion at depth and to test whether it is part of the Cachiyuyito stock.

8.2.4 Features consistent with porphyry model

Productora is a controversial deposit in terms of ore deposit classification. Features consistent with the porphyry Cu model include:

- **Tourmaline**-rich breccias, which are widespread in magmatic-hydrothermal systems of the Andes, particularly the porphyry Cu and epithermal deposits (Sillitoe and Sawkins, 1971; Sillitoe, 1985; Warners et al., 1985). Whilst tourmaline is observed in IOCG deposits globally, it typically only occurs as an accessory phase (e.g., Ernest Henry, Williams et al., 2005; Contact Lake Belt, Mumin, 2007). Tornos (2010 and 2011) described abundant tourmaline in Andean IOCG deposits, where it occurs as coarse grained breccia cement (e.g., Silivita and Tropezón) or fine grain replacments (e.g., Candelaria and Carola). Tornos et al. (2010) argued that Tropezón demonstrated a link between porphyry Cu and IOCG deposits based on the intrusive host rocks and mineralogical similar Cu-(Au)-Mo mineralisation.

- **Molybdenum** is noted as part of the anomalous metal suite associated with IOCG deposits (Williams, 2005) but is not typically economic, whereas porphyry Cu deposits supply half of the world's Mo (Sillitoe, 2010). Molybdenum in porphyry systems is thought to be enriched due to contamination of melts by lower crustal rocks in areas of thickened crust (Stein and Hannah, 1985; Klemm et al., 2008). Thus, high Mo grades at Productora are consistent with derivation from more evolved felsic melts (e.g., Tornos et al., 2010). However, the Early Cretaceous crust in the Coastal Cordillera is interpreted to have been hot and thin (Lucassen and Thirlwall, 1998), which contradicts this mechanism.

- **Magnetite** is common but not abundant in the Productora deposit, typically <2 wt% but locally up to 11 wt% in magnetite-rich breccia facies (3B-1 and 3B-3; Figure 4.4 and Figure 4.5). In Cu-ore zones at Productora, Fe content typically ranges between 1 and 8 wt%.

The highest measured Fe content on the study sections is 22.5 wt%. Iron concentrations in Cu-rich IOCGs range between 15–25 wt% Fe in Cu ore zones, this is significantly more than observed at Productora. Magnetite is common in porphyry-related breccias, potassic alteration assemblages (particularly Au-rich pophyryies; Sillitoe, 1979) and early veins (Cu-Au-porphyries; Sillitoe, 2003) but is typically present in low concentrations of a few wt.% at best.

- **Acid alteration assemblages** are generally not well developed in IOCGs systems owing to their lower sulphur content and low sulphidation state. Where acid alteration occurs, it is typically less voluminous than other Na-Ca-K(-Fe) alteration assemblages, and consists of sericite- hematite - quartz assemblages in felsic rocks (Barton, 2014). Although advanced argillic alteration has been noted in 15 ICOG systems (Kreiner, 2011), it is typically accompanied by specular hematite and a near-absence of sulphides and sulphates. Argillic and phyllic assemblages at Productora are associated with significant pyrite and no hematite, which is more typical of porphyry-associated advanced argillic assemblages (e.g., Chang et al., 2011). The Silica Ridge lithocap remnants overlie advanced argillic alteration with abundant alunite. Absolute timing relationships between the lithocap, Productora and Alice have not been established.

- **Elevated sulphur content** indicated by the abundance of sulphide minerals (pyrite, chalcopyrite and molybdenite) and late stage anhydrite veins. Porphyry deposits are huge sulphur anomalies, typically with more sulphur than metals (e.g., Williams-Jones and Heinrich, 2005) whereas IOCGs are sulphur-starved, resulting in abundant iron oxides and minor sulphides (e.g., Williams et al., 2005).

- **No evidence for connate fluid** involvement in mineralisation was found during stable and radiogenic isotope studies. Connate fluids are common in IOCG deposits (e.g., Barton 1996, 2000) but have only rarely been reported in porphyry deposits (e.g. Bowman et al., 1987) Although magmatic-dominant IOCG end members are recognised (Barton and Johnson, 2004) the influx of non-magmatic, oxidized, saline, and relatively Cu-rich solutions has been proposed as critical to IOCG formation (Hitzman, 1992, Barton and Johnson 2000).

- **The Alice porphyry** has spatial and broad temporal association with the Productora complex. This is provides compelling evidence that locally fertile intrusions were capable of generating porphyritic apotheoses and mineralisation around the time the Productora breccia complex was emplaced.

- **Coeval magmatism** - although an intimate association with a causative intrusion has not

been proven, the absolute age of mineralisation of Productora is coeval with emplacement of the Cachiyuyito stock. Based on the absolute ages and the magmatic nature of the mineralising fluid, determined from stable and radiogenic isotopes, mineralisation at Productora is interpretted to be genetically related to the Cahciyuyito stock. All porphyry deposits are magmatic-hydrothermal in origin (e.g., Seedorf et al., 2005; Sillitoe, 2010), whereas IOCGs can be hybrid, or in some cases (e.g., Tennant Creek, Australia) produced entirely by non-magmatic saline fluids (e.g., Wedekind, 1990).

8.2.5 Features consistent with IOCG model

- **Uranium minerals** are observed as accessory phases at Productora and are common in deposits of the IOCG clan. Andean IOCGs typically contain low U compared to other IOCG deposits (3–5 ppm; Marschik and Fontbote, 2001; Marschik et al., 2000; Hitzman and Valenta, 2005; Williams et al., 2005). Uranium contents at Productora average 17 ppm on the study sections. These values are anomalously high with respect to both Andean IOCG deposits and typical porphyry deposits, and requires further investigation to fully understand the U deportment and timing.

- **Structural controls** on the formation of Productora are inferred from its location in a zone of structural complexity, with displaced mineralisation and proximity to the Atacama Fault Zone. Strong structural controls are a characteristic feature of IOCG deposits, which are typically localized along high- to low-angle faults which are generally splays off major, crustal-scale faults (Hitzman, 1992; Williams et al., 2005). In northern Chile, the Atacama Fault Zone was active during arc magmatism and basin formation, and had a strong influence on the distribution of both IOCG and magnetite-apatite mineralisation (e.g., Atherton and Aguirre, 1992; Brown et al., 1993; Sillitoe, 2003).

- **Local magnetite-apatite mineralisation** occurs at the Productora project on the flanks of the Cachiyuyito stock (Figure 4.1). A broad spatial and temporal relationship exists between magnetite-apatite and IOCG deposits (Barton and Johnson, 2000). Where deposits are adjacent, a crude zonal relationship has been proposed (e.g., Manto Verde and Manto Ruso, Rieger et al., 2012). Genetic links have been inferred based on vertical zonation from deep magnetite-apatite to shallow IOCG mineralisation (Espinoza et al., 1996; Sillitoe, 2003) and potentially similar mineralising fluids (Hitzman, 1992).

- **Large scale sodic-calcic alteration** occurs at the Productora project where it is spatially associated with the Cachiyuyito stock and overprinted by the Productora system (Fox,

2000; Ray and Dick 2002). Extensive, regional scale, sodic-calcic alteration is a widely recognised feature of IOCG deposits, whereas in porphyry systems Na-rich alteration is typically smaller in volume, or superimposed and related to external fluids (Dilles et al., 1995).

- **IOCG deposits** are known to occur in the Mesozoic metallogenic belt of northern Chile, Candelaria and Mantoverde are the most notable examples although they are younger than Productora (Candelaria-Punta del Cobre district 116–114 Ma, Marschik et al., 1997; Mantoverde 117–121 Ma; Benavides et al., 2007). The regional temporal and spatial association of deposits indicates that geodynamic conditions were favourable for IOCG deposit formation. In contrast, porphyry Cu deposits are less common in the Mesozoic metallogenic belts of central and northern Chile.

- **No progenitor intrusion** has been confirmed for the Productora breccia complex, although an association with the Cachiyuyito stock is inferred based on current evidence (geochronology, map relationships, stable and radiogenic isotopes). A major characteristic of the IOCG clan is the absence of intimately associated intrusions (Williams et al., 2005).

8.2.6 Genetic model summary

Genesis of the Productora Cu-Au-Mo deposit is interpreted to be the result of a series of catastrophic magmatic-hydrothermal brecciation event. Mineralising fluids, and by inference metals, were predominantly sourced from a crystallising magma chamber. The Productora deposit shares characteristics with porphyry systems (including abundant tourmaline and Mo, low magnetite, acid alteration assemblages, and magmatic fluid signature) and deposits of the IOCG clan (anomalous U, structural control, spatially and temporally coincident magnetite-apatite and large scale sodic-calcic alteration). Previous authors have interpreted Productora to be a magnetite-dominant IOCG deposit similar to Candelaria, in that Candelaria also has significant sulphide mineralisation associated with potassic alteration (Fox, 2000). Based on the available evidence Productora is considered here to show stronger affinities with porphyry rather than IOCG deposits. The most compelling evidence toward this conclusion includes the tourmaline-dominant mineralogy, high Mo content, low magnetite (relative to IOCGs) and high sulphur content — evidenced by acid alteration assemblages and abundant sulphide minerals. In addition, a magmatic-hydrothermal origin is consistent with the porphyry model. However, the high uranium content observed at Productora is inconsistent with the porphyry model and requires further investigation. Whilst other features, such as structural control, large scale sodic-calcic alteration and temporally and spatially associated magnetite-apatite mineralisation, are characteristic of the IOCG

clan they are not mutually exclusive of porphyry systems (e.g., Dilles et al., 1995).

The conclusion of the current study is that the Productora deposit remains somewhat enigmatic. This in part due to the wide range of defining features at Productora which correspond to both deposit classes, and in part due to the poor definition of the IOCG class and genetic model. Current IOCG literature presents a plethora of characteristic features and environments of formation that promote confusion and ambiguity. Fundamental similarities in the genetic mechanisms of porphyry-related magmatic-hydrothermal breccias and magmatic end-member IOCG deposits results in considerable overlap between these models and deposit classes. Productora presents an example of a deposit which sits firmly within this overlap.

8.3 Exploration implications

- The most significant exploration implication from this study is the potential for a mineralised progenitor porphyry at depth beneath Productora. Mineralogy and isotope evidence indicate the breccia root zones lie to the south and hence exploration should be focussed in this area in order to test this hypothesis.

- If the Productora complex is porphyry-related as opposed to IOCG, additional exploration potential exists on the project area, because porphyry systems typically occur in clusters (Sillitoe, 2010).

- The size of the Productora breccia complex is large (>2 km strike, 400 m width) which suggests a large, volatile-rich system, which may have been capable of multiple mineralising events.

- The close spatial association of the Alice porphyry with magnetite-apatite mineralisation on the flanks of the Cachiyuyito stock should be used as an exploration model to test other local magnetite-apatite occurrences for their porphyry potential.

8.4 Geometallurgy considerations

8.4.1 Modelling mineralogy

- The results of the current study have shown that mathematical modelling of modal mineralogy can aid geometallurgical studies.

- Applying a weighted least squares correction (WLSQ) to raw QXRD data can be used to overcome high detection limits associated with QXRD analysis. This approach provides

a more robust estimate of mineralogy for both abundant and minor phases than the raw QXRD data (Figure 5.4).

- Calculated mineralogy through linear programming and the Simplex method (Press et al. 1968; Berry et al., 2015) provides a practical modal mineralogy from chemical assay in quartz-feldspar dominant assemblages. Results for major minerals, including quartz, K-feldspar, albite, pyrite, iron oxides, chalcopyrite and molybdenite, matched measured mineralogy data QXRD-WLSQ extremely well (R^2 = >0.8).

- Minerals with similar chemical compositions proved challenging to model by calculated mineralogy. The major problem minerals included clays, carbonates, tourmaline, amphibole, epidote and jarosite. Incorporation of additional analytical data (such as B, CO_2, SiO_2 and LOI) into the model along with the existing 15 elements would assist with carbonates, clays and tourmaline but significantly increase the cost.

- Modal mineralogy estimates can be used to rapidly assess mineralogical variability across a deposit, and facilitate the identification of discrete zones which are anomalous or require additional test work to ensure that all ore types are appropriately characterised.

8.4.2 Predicting Cu-speciation

- A new sequential leach based Cu-species classification scheme was developed in order to account for non-recoverable Cu-wad by reconciling S against Cu. Samples with sequential leach data and sulphur analyses were classified as either barren (<0.05 %Cu), oxide, transitional-oxide, transitional-sulphide, sulphide or insoluble (Figure 6.4).

- The ability to predict Cu-wad occurrence enables domains of potentially poor recovery to be identified. The new classification also prevents misidentification of sulphide or transitional domains that actually have high Cu-wad content.

- Robust predictive models of Cu-species classification on every sample interval can be generated from an appropriate training set of multi-element geochemical assay and logging data through machine learning methods. Cu-species classification data at Productora were extended to the full assay database using this approach.

- The predictive model for Cu-species classification provides a useful dataset to augment with other available data (both geological, geochemical and metallurgical) in order to inform the definition of domains of variable Cu-species. This information can be used to inform further sampling campaigns, rationalise and weight existing samples, and has application in

resource definition, and mine planning.

8.4.3 Processing implications at Productora

- **Model mineralogy**

  - » Total quartz and feldspar are higher (> 70 wt %) in altered rocks in the northern half of the planned open pit design than in the southern portion (Figure 5.16 A). Harder comminution indexes can be expected in the north and this is expected to lead to higher comminution energy requirements in the north.

  - » Total chlorite and mica contents are variable across the deposit but generally increase to the southeast and with depth (Figure 5.16 B). Domains with high chlorite and mica may show reduced flotation performance.

  - » Pyrite abundances range from 0.1–6 wt% across the deposit, generally increasing with depth and to the south, with discrete zones of pyrite in excess of 6 wt % (Figure 5.17 A). A blending strategy may be required to manage high pyrite ore domains and waste rock with high pyrite will require ARD consideration.

  - » Clay abundance in the deposit generally decreases from >7.5 wt % with depth. In addition, two anomalously high clay domains are predicted at depths (> 7.5 wt % at 680 m RL) in the northeast (Figure 5.15 A) and the south (Figure 5.18). High clay sulphide domains may show reduced flotation performance.

- **Cu-species classification**

  - » Insoluble Cu-wad from Productora consists of predominantly Cu (25 – 30 wt %) and Mn (14 – 17 wt %; Figure 6.3) as oxides.

  - » The insoluble class domains are spatially associated with the oxide and transitional-oxide domains. No significant insoluble copper domains were identified within the March 2014 resource wire frames provided by Hot Chili Ltd.

  - » Deep (locally >400m below surface) domains of transitional-sulphide material were recognised in association with steep fault zones (Figure 6.13).

- **Gold deportment** studies indicate the at Au occurs as fine particles on sulphide surfaces and as solid solution in pyrite. A pyrite concentrate may capture most of the recoverable Au in the deposit.

- **Anomalous U** grades (typically >17 ppm) are present in mineralised domains at Productora and U-bearing inclusions were observed in pyrite grains. If U-bearing inclusions also occur in chalcopyrite or molybdenite, accumulation of this deleterious element may occur in ore concentrates.

8.5 Future research

- **Geometallurgy**
  - » More detailed characterisation of the Au paragenesis and deportment is required in order to determine deportment variability between ore zones, improve predictions of gold recovery and assess viability of pyrite concentrate to maximise Au recovery.
  - » Determination of the U deportment and U-mineral paragenesis is required in order to predict potential U accumulation in ore concentrates or tailings.
  - » Combine calculated mineralogy with other data sets (SWIR, geological logging) to improve modal mineralogy predictions. Analysis of RC chips using SWIR would provide a useful dataset that could be integrated with calculated mineralogy.
  - » When sufficient comminution and recovery data becomes available attempts can be made to develop models for bond work index (BWi), A*b and recovery using calculated mineralogy (insufficient data point were available during the current study).
- **Economic geology**
  - » Radiometric dating of alunite from Silica Ridge lithocap in order to determine whether the lithocap was generated by Productora, Alice or an undiscovered system.
  - » Date apatite (U-Pb) from the magnetite-apatite mineralisation in order to determine its timing relationship to the Cachiyuyito stock and Productora breccia complex.
  - » Investigate relationships between district-scale sodic-calcic alteration and the local Productora potassic assemblages to determine if the Productora system generated or overprinted sodic-calcic alteration.
  - » Detailed sulphide paragenesis and LA-ICP-MS trace-element studies in order to improve understanding of mineralising fluid evolution.

The Productora project presents significant opportunities to advance the fields of Economic Geology and geometallurgy, and to deliver undiscovered resources. The close spatial and temporal association

of a magmatic-hydrothermal breccia complex with porphyry and magnteite-apatite mineralisation at Productora provides great opportunity to learn about the relationships between these deposits styles both locally and regionally. The extensive geochemical and mineralogical datasets now available for Productora are an excellent resource for geometallurgists bridging the gap between geologists and metallurgists or engineers. It is hoped that the current study will be of assistance to future geologists working in research, exploration or mining at the project.

References

Abdioğlu, E., Arslan, M., Kadir, S., and Temizel, İ., 2015, Alteration mineralogy, lithochemistry and stable isotope geochemistry of the Murgul (Artvin, NE Turkey) volcanic hosted massive sulfide deposit: Implications for the alteration age and ore forming fluids: Ore Geology Reviews, v. 66, p. 219–242.

Åberg, G., Aguirre, L., Levi, B., and Nyström, J., 1984, Spreading-subsidence and generation of ensialic marginal basins: An example from the early Cretaceous of central Chile: Geological Society, London, Special Publications, v. 16, p. 185–193.

Acuña, G., and Curilem, M., 2009, Comparison of neural networks and support vector machine dynamic models for state estimation in semiautogenous mills, in Aguirre, A.H., Borja, R.M., and Garciá, C.A.R., eds., Advances in artificial intelligence: Mexican International Conference on Artificial Intelligence, 8th, Guanajuato, Mexico, 2009, p. 478–487.

Agrawal, R., Imieli, T., and Swami, A., 1993, Mining association rules between sets of items in large databases: Association for Computing Machinery Special Interest Group on Management of Data Record, v. 22, p. 207–216.

Aguirre, L., Levi, B., and Nystrom, J.O., 1989, The link between metamorphism, volcanism and geotectonic setting during the evolution of the Andes: Geological Society Special Publications, v. 43, p. 223–232.

Aha, D.W., Kibler, D., and Albert, M.K., 1991, Instance-based learning algorithms: Machine Learning, v. 6, p. 37–66.

Ahmadzadeh, F., and Lundberg, J., 2013, Remaining useful life prediction of grinding mill liners using an artificial neural network: Minerals Engineering, v. 53, p. 1–8.

ALS Geochemistry, 2015a, Schedule of Services and Fees 2015 AUD (http://www.alsglobal.com/en/

our-services/minerals/geochemistry/service-schedule)

ALS, 2015b, Quantitative automated mineralogical analysis conducted on nineteen composites from the SC-100 Productora Project, Chile for Hot Chili Ltd: Unpublished report, p. 1-26.

Ardila, R., 1993, Génesis de los yacimientos de cobre tipo skarn en el distrito minero de San Antonio y el yacimiento Panulcillo: Unpublished PhD thesis, Santiago, Chile, Universidad de Chile, 361 p.

Arif, J., and Baker, T., 2004, Gold paragenesis and chemistry at Batu Hijau, Indonesia: Implications for gold-rich porphyry copper deposits: Mineralium Deposita, v. 39, p. 523–535.

Atherton, M.P., and Aguirre, L., 1992, Thermal and geotectonic setting of Cretaceous volcanic rocks near Ica, Peru, in relation to Andean crustal thinning: Journal of South American Earth Sciences, v. 5, p. 47–69.

Avchenko, O.V., 2014, Genesis of garnet-bearing rocks at the Berezitovoe deposit, Upper Amur Region, Russia: Geology of Ore Deposits, v. 56, p. 15–34.

Bahlburg, H., and Hervé, F., 1997, Geodynamic evolution and tectonostratigraphic terranes of northwestern Argentina and northern Chile: Geological Society of America Bulletin, v. 109, p. 869–884.

Baker, E.M., Kirwin, D.J., and Taylor, R.G., 1986, Hydrothermal breccia pipes, James Cook University of North Queensland, Dept. of Geology, Economic Geology Research Unit Contribuion 12, Townsville, 45p.

Baldwin, J., Swain, H., and Clark, G., 1978, Geology and grade distribution of the Panguna porphyry copper deposit, Bougainville, Papua New Guinea: Economic Geology, v. 73, p. 690–702.

Ballantyne, G.H., Smith, T.W., and Redmond, P.B., 1997, Distribution and mineralogy of gold and silver in the Bingham Canyon porphyry copper deposit, Utah, in John, D.A., and Ballantyne, G.H., eds., Geology and Ore Deposits of the Oquirrh and Wasatch Mountains, Utah: Maps, v. 29, Society of Economic Geologists Guidebook, p. 147–153.

Bancroft, G., and Hyland, M., 1990, Spectroscopic studies of adsorption/reduction reactions of aqueous metal complexes on sulphide surfaces: Reviews in Mineralogy and Geochemistry, v. 23, p. 511–558.

Barazangi, M., and Isacks, B.L., 1979, Subduction of the Nazca Plate beneath Peru; evidence from

spatial distribution of earthquakes: Geophysical Journal of the Royal Astronomical Society, v. 57, p. 537–555.

Barra, F., Reich, M., Selby, D., Rojas, P., Simon, A., Salazar, E., and Palma, G., 2017, Unravelling the origin of the Andean IOCG clan: A Re-Os isotope approach: Ore Geology Reviews, v. 81, Part 1, p. 62–78.

Barton, M.D., 2014, Iron Oxide(-Cu-Au-REE-P-Ag-U-Co) Systems, Treatise on Geochemistry, Elsevier, v. 13, p. 515–541.

Barton, M.D., and Johnson, D.A., 1996, Evaporitic-source model for igneous-related Fe oxide-(REE-Cu-Au-U) mineralization: Geology, v. 24, p. 259–262.

Barton, M.D., and Johnson, D.A., 2000, Alternative brine sources for Fe-oxide (-Cu-Au) systems: Implications for hydrothermal alteration and metals, in Porter, T.M., ed., Hydrothermal iron oxide copper-gold & related deposits: A global perspective: Adelaide, Porter Geological Publishing, p. 43–60.

Beck, S.L., Zandt, G., Myers, S.C., Wallace, T.C., Silver, P.G., and Drake, L., 1996, Crustal-thickness variations in the central Andes: Geology, v. 24, p. 407–410.

Beeson, J., Noble, M., Outhwaite, M., McCormack, B., and Halley, S., 2012, Geology of the Productora project, Republic of Chile: Unpublished confidential report to Hot Chili Limited, Jigsaw Geoscience, 75p.

Benavides, J., Kyser, T.K., Clark, A.H., Oates, C.J., Zamora, R., Tarnovschi, R., and Castillo, B., 2007, The Mantoverde iron oxide-copper-gold district, III Región, Chile: The role of regionally derived, nonmagmatic fluids in chalcopyrite mineralization: Economic Geology, v. 102, p. 415–440.

Benvie, B., Kuhar, L.L., Jeffrey, M., and Botsis, N.M., 2013, GeM (Amira P843A) - Technical Report 11: Theme 5: Determination of copper and gold deportment by diagnostic leaching, 35p.

Berg, K., Breitkreuz, C., Damm, K.W., Pichowiak, S., and Zeil, W., 1983, The North-Chilean Coast Range—an example for the development of an active continental margin: Geologische Rundschau, v. 72, p. 715–731.

Berry, R., Hunt, J., and McKnight, S., 2011, Estimating mineralogy in bulk samples: AusIMM International Geometallurgy Conference, 1st, Brisbane, Australia, 2011, p. 153–156.

Berry, R., O'Conner, L., Hunt, J., and Bradshaw, D., 2013, Theme Four: Texture-based liberation and recovery modelling, GeM (AMIRA P843A) - Technical Report 11, 82p.

Berry, R., Hunt, J., Parbhakar-Fox, A., and Lottermoser, B., 2015, Prediction of acid rock drainage (ARD) from calculated mineralogy: International Conference on Acid Rock Drainage and IMWA Annual Conference, 10th, Santiago, 2015, p. 1–10.

Blackwell, J.L., 2010, Characteristics and origins of breccias in a volcanic hosted alkalic epithermal gold deposit, Ladolam, Lihir Island, Papua New Guinea: Unpublished PhD thesis, Hobart, Australia, University of Tasmania, p.

Bodnar, R., 1995, Fluid inclusion evidence for a magmatic source for metals in porphyry copper deposits: Mineralogical Association of Canada short course series, v. 23, p. 139–152.

Bogdanic, T., Doebel, R., Laubacher, G., Olivier, R.A., and Vatin-Perigonon, N., 1990, Cretaceous and early Tertiary in northern Chile between 21° and 23°S: Colloques et Seminaires - Institut de Recherche Scientifique pour le Developement en Cooperation: Paris, editions de l'Office de la Recherche Scientifique et Technique d'Outre-mer, p. 245–248.

Bookstrom, A.A., 1977, The magnetite deposits of El Romeral, Chile: Economic Geology, v. 72, p. 1101–1130.

Boric, R., 2002, Geology, mineral zoning, and lithochemistry of the el Soldado manto type copper deposit, Chile: Unpublished M.Sc. thesis, Halifax, Canada, Dalhousie University, 378p.

Boric, P.R., Díaz, F.F., Maksaev, J.V., 1990, Geología y yacimientos metalíferos de la región de Antofagasta: Servicio Nacional de Geología y Minería Boletín, v. 40, 246p.

Boser, B.E., Guyon, I.M., and Vapnik, V.N., 1992, A training algorithm for optimal margin classifiers: Proceedings of the fifth annual workshop on Computational learning theory, Pittsburgh, USA, 1992, p. 144–152.

Bouvier, A., Vervoort, J.D., and Patchett, P.J., 2008, The Lu–Hf and Sm–Nd isotopic composition of CHUR: Constraints from unequilibrated chondrites and implications for the bulk composition of terrestrial planets: Earth and Planetary Science Letters, v. 273, p. 48–57.

Bowman, J.R., Parry, W.T., Kropp, W.P., and Kruer, S.A., 1987, Chemical and isotopic evolution of hydrothermal solutions at Bingham, Utah: Economic Geology, v. 82, p. 395–428.

Breiman, L., 1996, Bagging predictors: Machine Learning, v. 24, p. 123–140.

Breiman, L., 2001, Random forests: Machine Learning, v. 45, p. 5–32.

Breiman, L., Friedman, J., Olshen, R.A., and Stone, C.J., 1984, Classification and regression trees: Monterey, CA, Wadsworth.

Breiman, L., Friedman, J., Stone, C.J., and Olshen, R.A., 1984, Classification and regression trees, CRC press.

Brown, M., Diáz, F., and Grocott, J., 1993, Displacement history of the Atacama fault system 25°00 S – 27° 0S, northern Chile: Geological Society of America Bulletin, v. 105, p. 1165–1174.

Brown, W.M., Gedeon, T.D., Groves, D.I., and Barnes, R.G., 2000, Artificial neural networks: A new method for mineral prospectivity mapping: Australian Journal of Earth Sciences, v. 47, p. 757–770.

Browne, P.R.L., 1978, Hydrothermal alteration in active geothermal fields: Annual Review of Earth and Planetary Sciences, v. 6, p. 229–248.

Bryan, W.B., Finger, L.W., and Chayes, F., 1969, Estimating proportions in petrographic mixing equations by least-squares approximation: Science, v. 163, p. 926–927.

Bryner, L., 1968, Proposed terminology for hydrothermal breccias and conglomerates: Economic Geology, v. 63, p. 692.

Burnham, C.W., 1979, Magmas and hydrothermal fluids, in Barnes, H., ed., Geochemistry of Hydrothermal Ore Deposits: New York, John Wiley, p. 71–136.

Burnham, C.W., 1985, Energy release in subvolcanic environments; implications for breccia formation, Economic Geology, v. 80, p. 1515–1522.

Camus, F. and Drummond, A.D., 1979, The Chivato gold prospect: Unpublished report, v. 18, p.1

Camus, F. and Duhalde, A., 1981, Evaluacion geologica del distrito minero de Chancon, VI Region, Chile: Unpublished report, 20p.

Camus, F., 1982, Evaluacion geologica-economica de los yacimientos de oro El Bronce y Pedro de Valdivia: Unpublished internal report, Compania Minera E1 Bronce, 72p.

Camus, F., Boric, R. and Skewes, A., 1986, E1 distrito de oro El Bronce y su relacion con la caldera Morro Hediondo, region de Valparaiso: Andean Geology, v. 28–29, p. 95–101.

Camus, F. and Reichhard, E., 1987, Evaluacion geologica preliminar del yacimiento de oro Las Vacas, IV region, Sociedad Minera Las Vacas: Upublished internal report, 24p.

Camus, F., 2002, The Andean porphyry systems: Centre for Ore Deposit and Exploration Studies (CODES), Special publication no. 4, p. 5–21.

Carranza, E.J.M., 2015, Data-driven evidential belief modeling of mineral potential using few prospects and evidence with missing values: Natural Resources Research, v. 24, p. 291–304.

Cembrano, J., González, G., Arancibia, G., Ahumada, I., Olivares, V., and Herrera, V., 2005, Fault zone development and strain partitioning in an extensional strike-slip duplex: A case study from the Mesozoic Atacama fault system, Northern Chile: Tectonophysics, v. 400, p. 105–125.

Chang, Z., Hedenquist, J.W., White, N.C., Cooke, D.R., Roach, M., Deyell, C.L., Garcia, J., Gemmell, J.B., McKnight, S., and Cuison, A.L., 2011, Exploration tools for linked porphyry and epithermal deposits: Example from the Mankayan intrusion-centered Cu-Au district, Luzon, Philippines: Economic Geology, v. 106, p. 1365–1398.

Charrier, R., and Muñoz, N., 1994, Jurassic Cretaceous palaeogeographic evolution of the Chilean Andes at 23°S – 24°S latitude and 34°S – 35°S latitude; a comprehensive analysis, in Reutter, K.J., Scheuber, E., and Wigger, P.J., eds., Tectonics of the Southern Central Andes: Berlin, Springer-Verlag, p. 233–242.

Charrier, R., Pinto, L., and Rodríguez, M.P., 2007, Tectonostratigraphic evolution of the Andean Orogen in Chile, in Moreno, T., and Gibbons, W., eds., The Geology of Chile: London, The Geological Society, p. 21–114.

Chatterjee, S., Bandopadhyay, S., and Rai, P., 2008, Genetic algorithm-based neural network learning parameter selection for ore grade evaluation of limestone deposit: Mining Technology, v. 117, p. 178–190.

Chávez, W.X., 2000, Supergene oxidation of copper deposits: Zoning and distribution of copper oxide minerals: SEG Newsletter, v. 41, p. 1, 10–21.

Chen, H., 2010, Mesozoic IOCG mineralisation in the Central Andes: An updated review, in Porter,

T.M., ed., Hydrothermal iron oxide copper-gold and related deposits; a global perspective: Adelaide, PGC Publishing, p. 14.

Clark, A.H., Farrar, K., Caelles, J.C., Haynes, S.J., Lortie, R.B., McBride, S.L., Quirt, C.S., Robertson, R.C.R., and Zentilli, M., 1976, Longitudinal variations in the metallogenic evolution of the central Andes: A progress report: Geological Association of Canada Special Paper 14, p. 23–58.

Clark, A.M., Easton, A.J., and Jones, G., 1978, A study of the neotocite group: Mineral Magazine, v. 42, p. 279–280.

Claypool, G.E., Holser, W.T., Kaplan, I.R., Sakai, H., and Zak, I., 1980, The age curves of sulfur and oxygen isotopes in marine sulfate and their mutual interpretation: Chemical Geology, v. 28, p. 199–260.

Cleary, J.G., and Trigg, L.E., 1995, K*: An instance-based learner using an entropic distance measure: International Conference on Machine learning, 12th, Tahoe City, USA, 1995, p. 108–114.

Cohen, W.W., 1995, Fast effective rule induction: International Conference on Machine Learning, 12th, Tahoe, USA, 1995, p. 115–123.

Coira, B., Davidson, J., Mpodozis, C., and Ramos, V., 1982, Tectonic and magmatic evolution of the Andes of northern Argentina and Chile: Earth Science Reviews, v. 18, p. 303–332.

Cooke, D.R, and McPhail, D., 1996, Telluride mineralisation in low sulfidation epithermal veins–contributions of magmatic volatiles: Australian Geological Convention, 13th, Canberra, Australia, 1996, p. 96.

Cooke, D.R., and Simmons, S.F., 2000, Characteristics and genesis of epithermal gold deposits: Reviews in Economic Geology, v. 13, p. 221–244.

Cooke, D.R., Deyell, C.L., Waters, P.J., Gonzales, R.I., and Zaw, K., 2011, Evidence for magmatic-hydrothermal fluids and ore-forming processes in epithermal and porphyry deposits of the Baguio district, Philippines: Economic Geology v. 106, p. 1399-1424.

Corbett, G.J., and Leach, T.M., 1998, Chapter 4 Controls on Hydrothermal Alteration and Mineralisation, in Corbett, G.J., and Leach, T.M., eds., Southwest Pacific Rim Gold-Copper Systems: Structure, Alteration, and Mineralization, Special Publication: Littleton, Colorado, Society of Economic Geologists, 236p.

Cortes, C., and Vapnik, V., 1995, Support-vector networks: Machine Learning, v. 20, p. 273–297.

Cortez, L., and Duráo, F., 1995, An Expert Neural Network to Control a Mineral Flotation Process: APCOM, 25th, Brisbane, Australia, p. 431–436.

Cracknell, M.J., and Reading, A.M., 2015, Spatial-contextual supervised classifiers explored: A challenging example of lithostratigraphy classification: IEEE Journal of Selected Topics in Applied Earth Observations and Remote Sensing, v. 8, p. 1371–1384.

Cross, T.A., and Pilger, R.H., 1982, Controls of subduction geometry, location of magmatic arcs, and tectonics of arc and back-arc regions: Geological Society of America Bulletin, v. 93, p. 545–562.

Cruz, N., Peng, Y., Farrokhpay, S., and Bradshaw, D., 2013, Interactions of clay minerals in copper–gold flotation: Part 1 – Rheological properties of clay mineral suspensions in the presence of flotation reagents: Minerals Engineering, v. 50–51, p. 30–37.

Cuadra, W.A., and Dunkerley, P.M., 1991, A history of gold in Chile: Economic Geology, v. 86, p. 1155–1173.

Cuddy, A., and Kesler, S., 1982, Gold in the Granisle and Bell porphyry copper deposits, in Levinson, A., ed., Precious metals in the Northern Cordillera: Association of Exploration Geochemists Special Publication 2, p. 139–155.

Dallmeyer, R.D., Brown, M., Grocott, J., Taylor, G.K., and Treloar, P.J., 1996, Mesozoic magmatic and tectonic events within the Andean plate boundary zone, 26°–27°30'S, North Chile: Constraints from mineral ages: Geology, v. 104, p. 19–40.

Dana, J.D., and Hurlbut, C.S., 1971, Dana's Manual of mineralogy: New York, Wiley.

Danyushevsky, L., Robinson, P., Gilbert, S., Norman, M., Large, R., McGoldrick, P., and Shelley, M., 2011, Routine quantitative multi-element analysis of sulphide minerals by laser ablation ICP-MS: Standard development and consideration of matrix effects: Geochemistry: Exploration, Environment, Analysis, v. 11, p. 51–60.

Datta, A., and Mishra, B.K., 1999, Power draw estimation of ball mills using neural networks: Minerals and Metallurgical Processing, v. 16, p. 57–60.

Davies, A.G.S., 2002, Geology and genesis of the Kelian gold deposit, East Kalimantan, Indonesia: Unpublished PhD thesis, University of Tasmania, 405 p.

Davies, A.G.S., Cooke, D.R., Gemmell, J.B., and Simpson, K.A., 2008, Diatreme Breccias at the Kelian Gold Mine, Kalimantan, Indonesia: Precursors to Epithermal Gold Mineralization: Economic Geology, v. 103, p. 689–716.

de Haller, A., and Fontboté, L., 2009, The Raúl-Condestable Iron Oxide Copper-Gold Deposit, Central Coast of Peru: Ore and Related Hydrothermal Alteration, Sulfur Isotopes, and Thermodynamic Constraints: Economic Geology, v. 104, p. 365–384.

de Haller, A., Zúñiga, A., Corfu, F., and Fontboté, L., 2002, The iron oxide-Cu-Au deposit of Raúl-Condestable: Mala, Lima, Peru [abs.]: Congreso Geológico Peruano, 11th, Resúmenes, 2002, p. 80.

Denby, B., and Burnett, C.C.H., 1995, GEMNet - Using Neural Networks to Approximate the Location-Grade Relationship in Mineral Deposits, APCOM XXV: Brisbane, QLD, The Australasian Institute of Mining and Metallurgy.

Denis, C.M.M., Alard, O., and Demouchy, S., 2015, Water content and hydrogen behaviour during metasomatism in the uppermost mantle beneath Ray Pic volcano (Massif Central, France): Lithos, v. 236–237, p. 256–274.

DePaolo, D.J., and Wasserburg, G.J., 1976, Nd isotopic variations and petrogenetic models: Geophysical Research Letters, v. 3, p. 249–252.

Dephaine, Q., and Filippov, L.O., 2015, From Plant to Mine: a Reverse Approach to Help Resource Estimation and Geometallurgical Modelling: 13th Biennial SGA Meeting, Nancy, France, 24–27 August 2015, 2015, p. 1399–1402.

Dick, L.A., and Ray, G.E., 2000, Iron oxide-Cu-Au-U-REE-apatite mineralisation at the Productora property, north-central Chile, Iron oxide copper-gold deposits: Seperating fact from fantasy: Vancouver, British Columbia, Vancouver Mining Exploration and Britich Columbia and Yukon Chamber of Mines, p. E19–E33.

Dilles, J.H., Farmer, G.L., and Field, C.W., 1995, Sodium-calcium alteration by non-magmatic saline fluids in porphyry copper deposits: Results from Yerington, Nevada: Mineralogical Association of Canada Short Course, v. 23, p. 309–338.

Domeyko, I., 1876, Ensayo sobre los dépositos metalíferos de Chile: Santiago, Imprenta Nacional, p. 140

Donskoi, E., Suthers, S.P., Campbell, J.J., and Raynlyn, T., 2008, Modelling and optimization of hydrocyclone for iron ore fines beneficiation — using optical image analysis and iron ore texture classification: International Journal of Mineral Processing, v. 87, p. 106–119.

Donskoi, E., Suthers, S.P., Fradd, S.B., Young, J.M., Campbell, J.J., Raynlyn, T.D., and Clout, J.M.F., 2007, Utilization of optical image analysis and automatic texture classification for iron ore particle characterisation: Minerals Engineering, v. 20, p. 461–471.

Duan, X., 2014, Melt–peridotite interaction in the shallow lithospheric mantle of the North China Craton: evidence from melt inclusions in the quartz-bearing orthopyroxene-rich websterite from Hannuoba: International geology review, v. 56, p. 448–472.

Duda, R.O., and Hart, P.E., 1973, Pattern classification and scene analysis: New York, Wiley

Dutta, S., Bandopadhyay, S., Ganguli, R., and Misra, D., 2011, Critical Assessment of Machine Learning Algorithms as Estimation Techniques for a Polymetallic Ore Deposit, 35th APCOM Symposium: Wollongong, NSW.

Dyl, K.A., Cleverley, J.S., Bland, P.A., Ryan, C.G., Fisher, L.A., and Hough, R.M., 2014, Quantified, whole section trace element mapping of carbonaceous chondrites by Synchrotron X-ray Fluorescence Microscopy: 1. CV meteorites: Geochimica et Cosmochimica Acta, v. 134, p. 100–119.

Eastoe, C., 1978, A fluid inclusion study of the Panguna porphyry copper deposit, Bougainville, Papua New Guinea: Economic Geology, v. 73, p. 721–748.

Eggleton, R., Pennington, J., Freeman, R., and Threadgold, I., 1983, Structural aspects of the hisingerite-neotocite series: Clay Minerals, v. 18, p. 21–31.

Eldridge, C.S., Barton, P., and Ohmoto, H., 1983, Mineral textures and their bearing on formation of the Kuroko orebodies: Economic Geology Monograph, v. 5, p. 241–281.

Escolme, A., Halley, S., and Potma, W., 2015a, The Productora Cu-Au-Mo Deposit, Chile. SGA Biennial Meeting 2015, Nancy, France. Extended abstracts, vol 1, p. 287–290.

Escolme, A., Berry, R., Hunt, J., 2015b, Using geochemistry to inform geometallurgy at the Productora Cu-Au-Mo deposit, Chile. SEG 2015: World-Class Ore Deposits: Discovery to Recovery, Hobart, Australia

Escolme, A., Berry, R., and Hunt, J., 2016, Predicting Cu-species classification using geochemistry at the Productora Cu-Au-Mo deposit, Chile, AusIMM International Geometallurgy Conference: Perth, Australia, AusIMM p. 113–117.

Espinoza Reyes, S., Veliz, G.H., Esquivel L.J., Arias Farias, J., Moraga, B.A., Camus, F., Sillitoe, R.M., and Petersen, R., 1996, The cupriferous province of the Coastal Range, northern Chile: Society of Economic Geologists Special Publication No. 5, p. 19–32.

Eugster, H.P., and Chou, I.M., 1979, A model for the deposition of Cornwall-type magnetite deposits: Economic Geology, v. 74, p. 763–774.

Fandrich, R., Gu, Y., Burrows, D., and Moeller, K., 2007, Modern SEM-based mineral liberation analysis: International Journal of Mineral Processing, v. 84, p. 310–320.

Farrokhpay, S., and Bradshaw, D.J., 2012, Effect of clay minerals on froth stability in mineral flotation: a review: 26th International Mineral Processing Congress, IMPC 2012: Innovative Processing for Sustainable Growth-Conference Proceedings, New Delhi, India, 2012, p. 4601–4611.

Farrokhpay, S., and Ndlovu, B., 2013, Effect of phyllosilicate minerals on the rheology, colloidal and flotation behaviour of chalcopyrite mineral, Chemeca 2013: Australasian Conference on Chemical Engineering: Brisbane, QLD, Australia, Institution of Engineers, Australia, p. 1–7.

Field, C., and Gustafson, L., 1976, Sulfur isotopes in the porphyry copper deposit at El Salvador, Chile: Economic Geology, v. 71, p. 1533–1548.

Fisher, L.A., Fougerouse, D., Cleverley, J.S., Ryan, C.G., Micklethwaite, S., Halfpenny, A., Hough, R.M., Gee, M., Paterson, D., Howard, D.L., and Spiers, K., 2015, Quantified, multi-scale X-ray fluorescence element mapping using the Maia detector array: application to mineral deposit studies: Mineralium Deposita, v. 50, p. 665–674.

Fisher, R.V., 1961, Proposed classification of volcaniclastic sediments and rocks: Geological Society of America Bulletin, v. 72, p. 1409–1414.

Fleet, M., and Mumin, A., 1997, Gold-bearing arsenian pyrite abd marcasite and arsenopyrite from Carlin Trend gold deposits abd laboratory synthesis: American Mineralogist, v. 82, p. 182–193.

Flint, S., Turner, P., Jolley, E.J., and Hartley, A.J., 1993, Extensional tectonics in convergent margin basins; an example from the Salar de Atacama, Chilean Andes: Geological Society of America

Bulletin, v. 105, p. 603–617.

Flores, H., 1943, Informe sobre el mineral de Capote aurifero de Freirina, Instituto de Investigaciones Geologicas, Internal Report, p. 8

Flores, H., 1948, Informe geologico sobre los yacimientos de la sociedad Aurifera de Alhue, Direccion de Minas y Petroleo, Internal Report, p. 8

Flores, H. and Ruiz, C., 1946, Estudio geologico del distrito de Inca de Oro, provincia de Atacama, Chile. In: 2nd Congr. Panam. Ing. Geol., v. 2, p. 243–273.

Foody, G.M., and Mathur, A., 2004, A relative evaluation of multiclass image classification by support vector machines: IEEE Transactions on Geoscience and Remote Sensing, v. 42, p. 1335–1343.

Forrest, M., 2009, Geometallurgy for mine data: Materials World, v. 17, p. 48–50.

Foster, A.R., Williams, P.J., and Ryan, C.G., 2007, Distribution of Gold in Hypogene Ore at the Ernest Henry Iron Oxide Copper-Gold Deposit, Cloncurry District, NW Queensland: Exploration and Mining Geology, v. 16, p. 125–143.

Fox, K.A., 2000, Fe-Oxide (Cu-U-Au-REE) Mineralisation and Alteration at the Productora Prospect, Colorado School of Mines, 114 p.

Frank, M., Inostroza, C. and Mattheus, F., 1985, Evaluacion geologica del distrito aurifero de E1 Capote de Freirina Compania Minera E1 Bronce, Internal Report, p. 52

Frank, E., Hall, M., and Pfahringer, B., 2003, Locally weighted Naive Bayes: 19th Conference on Uncertainty in Artificial Intelligence, Acapulco, 2003, p. 249–256.

Frank, E., and Witten, I.H., 1998, Generating accurate rule sets without global optimization. Department of Computer Science: Hamilton, New Zealand, University of Waikato.

Franz, G., Lucassen, F., Kramer, W., Trumbull, R.B., Romer, R.L., Wilke, H.-G., Viramonte, J.G., Becchio, R., and Siebel, W., 2006, Crustal evolution of the Central Andean continental margin: a geochemical record of crustal growth, recyscling and destruction, in Oncken, O., Chong, G., Franz, G., Giese, P., Gotze, H.-J., Ramos, V.A., Strecker, M. R., and Wigger, P.J., eds., The Andes Active Subduction Orogeny: Berlin, Springer-Verlag, p. 45–64.

Freund, Y., and Schapire, R.E., 1996, Experiments with a new boosting algorithm: 13th International

Conference on Machine Learning, Bari, Italy, 1996, p. 148–156.

Frietsch, R., 1978, On the magmatic origin of iron ores of the Kiruna type: Economic Geology, v. 73, p. 478–485.

Frikken, P.H., Cooke, D.R., Walshe, J.L., Archibald, D., Skarmeta, J., Serrano, L., and Vargas, R., 2005, Mineralogical and Isotopic Zonation in the Sur-Sur Tourmaline Breccia, Río Blanco-Los Bronces Cu-Mo Deposit, Chile: Implications for Ore Genesis: Economic Geology, v. 100, p. 935–961.

Galán, G., and Oliveras, V., 2014, Melting and metasomatism in the lithospheric mantle of NE Spain: Geochemical and SrNd isotopic characteristics: Chemical Geology, v. 366, p. 75–89.

Galay, I., 1974, Inventario geologico minero de la Hoja Ovalle, Instituto de Investigaciones Geologicas. Unpublished Report, p. 21–31.

Gálvez Soto, P.A., 2013, Caracterización geológico-geotécnica de Mina Carmen, Región de Atacama: Departmento de Geologia, Universidad de Chile, p. 112.

Gama, J., 2004, Functional Trees: Machine Learning, v. 55, p. 219–250.

Gammons, C.H., and William-Jones, A.E., 1997, Chemical mobility of gold in the porphyry-epithermal environment: Economic Geology, v. 92, p. 45–59.

Garcia, C., Garcés, J., Rojas, C., and Zárate, G., 2007, Efecto sinérgico del tratamiento de mezclas de minerales conteniendo copper wad y sulfuros secundarios, Hydrocopper 2007: Viña del Mar, Chile.

Gelcich, S., Davis, D.W., and Spooner, E.T.C., 2005, Testing the apatite-magnetite geochronometer: U-Pb and $^{40}Ar/^{39}Ar$ geochronology of plutonic rocks, massive magnetite-apatite tabular bodies, and IOCG mineralization in Northern Chile: Geochimica et Cosmochimica Acta, v. 69, p. 3367–3384.

Gentili, S., Comodi, P., Bonadiman, C., and Coltorti, M., 2015, Mass balance vs Rietveld refinement to determine the modal composition of ultramafic rocks: The case study of mantle peridotites from Northern Victoria Land (Antarctica): Tectonophysics, v. 650, p. 144–155.

Giggenbach, W.F., 1992, Magma degassing and mineral deposition in hydrothermal systems along convergent plate boundaries: Economic Geology, v. 87, p. 1927–1944.

Goemann, K., Stepanox, A.S., Meffre, S., and Large, R.R., 2015, Gold and arsenopyrite exsolution and limits of arsenic solubility in pyrite investigated by SEM, EPMA, and LA-ICPMS, 13th biennial Australian Microbeam Analysis Symposium, 3: Hobart, TAS, Microscopy Society of America, p. 1229–1230.

Gouws, F.S., Aldrich, C., and Schmitz, G.P.J., 1996, The Use of Machine Learning Techniques for the Extraction of Process Knowledge from Industrial Flotation Plants, in Ramani, R. V., ed., APCOM XXVI Pennsylvania State University, Pennsylvania, Society for Mining, Metallurgy & Exploration, p. 315–321.

Griffin, W.L., Slack, J.F., Ramsden, A. R., Win, T.T., and Ryan, C.G., 1996, Trace elements in tourmalines from massive sulfides deposits and tourmalinites; geochemical controls and exploration applications: Economic Geology, v. 91, p. 657–675.

Grocott, J., Brown, M., Dallmeyer, R.D., Taylor, G.K., and Treloar, P.J., 1994, Mechanisms of continental growth in extensional arcs: An example from the Andean plate-boundary zone: Geology, v. 22, p. 391–394.

Grocott, J., and Taylor, G.K., 2002, Magmatic arc fault systems, deformation partitioning and emplacement of granitic complexes in the Coastal Cordillera, north Chilean Andes (25°30'S to 27°00'S): Journal of the Geological Society, v. 159, p. 425–442.

Gu, Y., 2003, Automated scanning electron microscope based mineral liberation analysis: Journal of Minerals and Materials Characterization and Engineering, v. 2, p. 33–41.

Gulson, B.L., 1986, Lead isotopes in mineral exploration: Amsterdam, Elsevier, p. 245

Gustafson, L.B., and Hunt, J.P., 1975, The porphyry copper deposit at El Salvador, Chile: Economic Geology, v. 70, p. 857–912.

Gutscher, M.-A., Spakman, W., Bijwaard, H., and Engdahl, E.R., 2000, Geodynamics of flat subduction: Seismicity and tomographic constraints from the Andean margin: Tectonics, v. 19, p. 814–833.

Hales, L.B., and Ynchausti, R.A., 2000, History and use of expert control systems in minerals processing: Control 2000: Mineral and Metallurgical Processing, Littleton, 2000, p. 93–98.

Hall, M.A., and Frank, E., 2008, Combining Naive Bayes and Decision Tables: 21st Florida Artificial Intelligence Research Society Conference, Miami, 2008, p. 318–319.

Hall, M.A., and Smith, L.A., 1998, Practical feature subset selection for machine learning: Singapore, Springer-Verlag Singapore Pte Ltd, p. 181–191

Ham, J., Yangchi, C., Crawford, M.M., and Ghosh, J., 2005, Investigation of the random forest framework for classification of hyperspectral data: IEEE Transactions on Geoscience and Remote Sensing, v. 43, p. 492–501.

Haschke, M., Scheuber, E., Günther, A., and Reutter, K.J., 2002, Evolutionary cycles during the Andean orogeny: repeated slab breakoff and flat subduction?: Terra nova, v. 14, p. 49–55.

Hastie, T., Tibshirani, R., and Friedman, J.H., 2009, The elements of statistical learning: data mining, inference and prediction: New York, USA, Springer.

Haynes, D.W., Cross, K.C., Bills, R.T., and Reed, M.H., 1995, Olympic Dam ore genesis; a fluid-mixing model: Economic Geology, v. 90, p. 281–307.

Hedenquist, J., and Houghton, B., 1987, Epithermal gold mineralisation and its volcanic enviroments: Sydney, University of Sydney, p. 15–21

Hedenquist, J.W., 1987, Mineralization associated with volcanic-related hydrothermal systems in the Circum-Pacific basin: Transactions of the Circum-Pacific Energy and Mineral Resources Conference, v. 4, p. 513–524.

Hedenquist, J.W., and Arribas, R., 2000, Exploration for epithermal gold deposits: Reviews in Economic Geology, v. 13, p. 245.

Hedenquist, J.W., Arribas, R.A., and Gonzalez-Urien, E., 2000, Exploration for epithermal gold deposits: Reviews in Economic Geology, v. 13, p. 245–277.

Heier, K. S., 1964, Rubidium/Strontium and Strontium87/Strontium86 Ratios in Deep Crustal Material: Nature, v. 202, p. 477–478.

Helle, S., Kelm, U., Barrientos, A., Rivas, P., and Reghezza, A., 2005, Improvement of mineralogical and chemical characterization to predict the acid laching of geometallurgical units from Mina Sur, Chuquicamata, Chile: Minerals Engineering, v. 18, p. 1334–1336.

Hemley, J.J., Montoya, J.W., Marinenko, J.W., and Luce, R.W., 1980, Equilibria in the system Al2O3 -SiO2-H2O and some general implications for alteration/mineralization processes: Economic Geology, v. 75, p. 210–228.

Henley, R.W., and Ellis, A.J., 1983, Geothermal systems ancient and modern: a geochemical review: Earth-Science Reviews, v. 19, p. 1–50.

Herrmann, W., and Berry, R. F., 2002, MINSQ - a least squares spreadsheet method for calcuating mineral proportions from whole rock major element analyses: Geochemistry: Exploration, Environment, Analysis v. 2, p. 361–368.

Hervé, F., Munizaga, F., Parada, M., Brook, M., Pankhurst, R., Snelling, N., and Drake, R., 1988, Granitoids of the Coast Range of central Chile: geochronology and geologic setting: Journal of South American Earth Sciences, v. 1, p. 185–194.

Hervé, M., 1987a, Movimiento normal de la falla Paposo, zona de Falla Atacama, en el Mioceno, Chile: Andean Geology, p. 31–36.

Hervé, M., 1987b, Movimiento sinistral en el Cretácico Inferior de la Zona de Falla de Atacama al Norte de Paposo (24ºS), Chile: Andean Geology, p. 37–42.

Heyl, A.V., Delevaux, M.H., Zartman, R.E., and Brock, M.R., 1966, Isotopic study of galenas from the upper Mississippi Valley, the Illinois-Kentucky, and some Appalachian Valley mineral districts: Economic Geology, v. 61, p. 933–961.

Hildebrand, R.S., 1986, Kiruna-type deposits; their origin and relationship to intermediate subvolcanic plutons in the Great Bear magmatic zone, Northwest Canada: Economic Geology, v. 81, p. 640–659.

Hitzman, M.W., 2000, Iron oxide-Cu-Au deposits: What, where, when, and why, in Porter, T. M., ed., Hydrothermal iron oxide copper-gold and related deposits: A global perspective, 1: Adelaide, PGC Publishing, p. 9–25.

Hitzman, M.W., Oreskes, N., and Einaudi, M.T., 1992, Geological characteristics and tectonic setting of proterozoic iron oxide (Cu-U-Au-REE) deposits: Precambrian Research, v. 58, p. 241–287.

Hitzman, M.W., and Valenta, R.K., 2005, Uranium In Iron Oxide-Copper-Gold (Iocg) Systems: Economic Geology, v. 100, p. 1657–1661.

Hoal, K.O., 2008, Getting the geo into geomet: SEG Newsletter, Society of Economic Geologists, v. 73, p. 11–15.

Hoal, K.O., Appleby, S. K., Stammer, J.G., and Palmer, C., 2009, SEM-based quantitative mineralogical

analysis of peridotite, kimberlite, and concentrate: Lithos, v. 112, Supplement 1, p. 41–46.

Holmes, G., Pfahringer, B., Kirkby, R., Frank, E., and Hall, M., 2002, Multiclass alternating decision trees: 13th European Conference on Machine Learning, Helsinki, Finland, August 2002, 2002, p. 161–172.

Holte, R.C., 1993, Very Simple Classification Rules Perform Well on Most Commonly Used Datasets: Machine Learning, v. 11, p. 63–90.

Hopf, S., 1987, Petrographische, Mineralogische und Geochemische Beobachtungen an der Cu-Lagerstätte Agustina/Distrikt Punta del Cobre/Chile: Unpublished Diplomarbeit, Heidelberg, Universität Heidelberg, p. 144

Hopper, D., and Correa, A., 2000, The Panulcillo and Teresa de Colmo copper deposits: Two contrasting examples of Fe-ox Cu-Au miineralisation from the Coastal Cordillera of Chile, in Porter, T. M., ed., Hydrothermal Iron Oxide Copper-Gold and Related Deposits: A Global Perspective, 1: Adelaide, PGC Publishing, p. 177–189.

Hot Chili Ltd, 2013, Quarterley Report: Period Ending September 30th 2013.

Hot Chili Ltd, 2014a, ASX announcement: Friday 21st November 2014, More strong drilling results highlight potential of Alice copper discovery at Productora.

Hot Chili Ltd, 2014b, ASX announcement: Monday 31st March 2014, Maiden ore reserve at Productora.

Hot Chili Ltd, 2016, ASX announcement: Wednesday 2nd March 2016, Hot Chili delivers PFS and near doubles reserves at Productora.

Huang, C., Davis, L.S., and Townshend, J.R.G., 2002, An assessment of support vector machines for land cover classification: International Journal of Remote Sensing, v. 23, p. 725–749.

Hunt, J., Berry, R., Walters, S., Bonnici, N., Kamenetsky, M., Nguyen, K., and Evans, C., 2008, A new look at mineral maps and the potential relationships of extracted data to mineral processing behaviours: Australasian Institute of Mining and Metallurgy Publication Series, 2008, p. 429–432.

Hunt, W. F., and Kraus, E.H., 1916, Note on the variable composition of melanochalcite: American Journal of Science, v. Series 4 Vol. 41, p. 211–214.

Huston, D.L., Bolger, C., and Cozens, G., 1993, A comparison of mineral deposits at the Gecko and

White Devil deposits; implications for ore genesis in the Tennant Creek District, Northern Territory, Australia: Economic Geology, v. 88, p. 1198–1225.

Ireland, T., 2011, Geological Framework of the Mineral Deposits of the Collahuasi district, Región de Tarapacá, Chile: Unpublished PhD thesis, Hobart, Australia, University of Tasmania.

Jansen, M., and Taylor, A., 2014, Overview of gangue mineralogy issues in oxide copper heap leaching, p. 1–18.

Jean, G.E., and G. Michael, B., 1985, An XPS and SEM study of gold deposition at low temperatures on sulphide mineral surfaces: Concentration of gold by adsorption/reduction: Geochimica et Cosmochimica Acta, v. 49, p. 979–987.

Johnson, L.J., Chu, C.H., and Hussey, G.A., 1985, Quantitative clay mineral analysis using simultaneous linear-equations: Clays and Clay Minerals, v. 33, p. 107–117.

Jordan, T.E., Isacks, B.L., Allmendinger, R.W., Brewer, J.A., Ramos, V.A., and Ando, C.J., 1983, Andean tectonics related to geometry of subducted Nazca plate: Geological Society of America Bulletin, v. 94, p. 341–361.

Kesler, S.E., 1973, Copper, molybdenum and gold abundances in porphyry copper deposits: Economic Geology, v. 68, p. 106–112.

Kesler, S.E., Chryssoulis, S.L., and Simon, G., 2002, Gold in porphyry copper deposits: Its abundance and fate: Ore Geology Reviews, v. 21, p. 103–124.

King, R.W., and Kerrich, R.W., 1989, Strontium isotope compositions of tourmaline from lode gold deposits of the Archean Abitibi Greenstone belt (Ontario-Quebec, Canada): Implications for source reservoirs: Chemical Geology: Isotope Geoscience section, v. 79, p. 225–240.

Kirkham, R., Dunn, P.A., Kuczewski, A.J., Siddons, D.P., Dodanwela, R., Moorhead, G.F., Ryan, C.G., De Geronimo, G., Beuttenmuller, R., Pinelli, D., Pfeffer, M., Davey, P., Jensen, M., Paterson, D. J., de Jonge, M.D., Howard, D.L., Küsel, M., and McKinlay, J., 2010, The Maia Spectroscopy Detector System: Engineering for Integrated Pulse Capture, Low-Latency Scanning and Real-Time Processing: 10th International Conference on Radiation Instrumentation, AIP Conference Proceedings, Melbourne, Australia, p. 240–243.

Kley, J., Monaldi, C.R., and Salfity, J.A., 1999, Along-strike segmentation of the Andean foreland;

causes and consequences: Tectonophysics, v. 301, p. 75–94.

Knipping, J.L., Bilenker, L.D., Simon, A.C., Reich, M., Barra, F., Deditius, A.P., Wille, M., Heinrich, C.A., Holtz, F., and Munizaga, R., 2015a, Trace elements in magnetite from massive iron oxide-apatite deposits indicate a combined formation by igneous and magmatic-hydrothermal processes: Geochimica et Cosmochimica Acta, v. 171, p. 15–38.

Knipping, J. L., Bilenker, L. D., Simon, A. C., Reich, M., Barra, F., Deditius, A. P., Lundstrom, C., Bindeman, I., and Munizaga, R., 2015b, Giant Kiruna-type deposits form by efficient flotation of magmatic magnetite suspensions: Geology, v. 43, p. 591-594.

Knorr, K., 2010, Advances in quantitative x-ray mineralogy: Process Mineralogy, v. 10, p. 10–12.

Koenig, G. A., 1902, On the new species melanochalcite and keweenawite; with notes on some other known species: American Journal of Science, ser. 4, vol. 14, p. 404–416.

Kohavi, R., 1995, The power of decision tables: 8th European Conference on Machine Learning, Heraclion, Greece, 1995, p. 174–189.

Kohavi, R., 1996, Scaling up the accuracy of Naive-Bayes classifiers: A decision-tree hybrid: Second International Conference on Knowledge Discovery and Data Mining, Portland, USA, 1996, p. 202–207.

Kohavi, R., and Provost, F., 1998, Glossary of Terms: Machine Learning, v. 30, p. 271–274.

Kojovic, K., Michaux, S., and Walters, S., 2010, Development of new comminution testing methodologies for geometallurgical mapping of ore hardness and throughput: XXV International Mineral Processing Congresss, Brisbane, Australia, 2010, p. 891–899.

Kotsiantis, S.B., Zaharakis, I., and Pintelas, P., 2007, Supervised machine learning: A review of classification techniques: Informatica 31, p. 249–268.

Kreiner, D., 2011, Epithermal style iron oxide(–Cu–Au) (=IOCG) vein systems and related alteration: Unpublished PhD thesis, Tuscon, Arizona, University of Arizona, 659 p.

Kulatilake, P.H.S.W., Qiong, W., Hudaverdi, T., and Kuzu, C., 2010, Mean particle size prediction in rock blast fragmentation using neural networks: Engineering Geology, v. 114, p. 298–311.

Kuncheva, L.I., 2004, Combining pattern classifiers: methods and algorithms, John Wiley & Sons.

Lamberg, P., 2011, Particles–the bridge between geology and metallurgy: Proceedings of the Conference in Minerals Engineering, Luleå, Sweden, 2011, p. 8–9.

Landwehr, N., Hall, M., and Frank, E., 2005, Logistic Model Trees: Machine Learning, v. 59, p. 161–205.

Lane, G.R., Martin, C., and Pirard, E., 2008, Techniques and applications for predictive metallurgy and ore characterization using optical image analysis: Minerals Engineering, v. 21, p. 568–577.

Lane, R., 2016, Why implicit modelling, 2016.

Lang, J., Stanley, C., and Thompson, J., 1995, Porphyry copper-gold deposits related to alkalic igneous rocks in the Triassic-Jurassic arc terranes of British Columbia, in Pierce, F. W., and Bolm, J. G., eds., Porphyry Copper Deposits of the America Cordillera, Digest 20, Arizona Geological Society p. 219–236.

Lang, J.R., Stanley, C.R., Thompson, J.F., and Dunne, K.P., 1995, Na-K-Ca magmatic-hydrothermal alteration in alkalic porphyry Cu-Au deposits, British Columbia, in Thompson, J. F. H., ed., Magmas, Fluids and Ore Deposits, 23. Mineralogical Association of Canada Short Course Series: Victoria, BC, p. 339–366.

Larson, R.L., and Pitman, W.C., 1972, World-wide correlation of Mesozoic magnetic anomalies, and its implications: Geological Society of America Bulletin, v. 83, p. 3645–3662.

Laznicka, P., 1988, Breccias and coarse fragmentites: petrology, environments, associations, ores: New York, Elsevier

Le Maitre, R.W., 1981, GENMIX - a generalized petrological mixing model program: Computers & Geosciences, v. 7, p. 229–247.

Lebedeva, E., 2014, Qualitative Clay X-Ray Diffraction Analysis, Genalysis Laboratory Services Pty Ltd, p. 1–23.

Leinonen, O., 1998, Use of chromite microstructure image analysis to estimate concentration characteristics in the Kemi chrome ore: Acta-universitatis ouluensis series a scientiae rerum naturalium.

Lepeltier, C., 1964, Geochemical prospecting for mercury at Los Mantos de Punitaqui: Instituto de Investigaciones Geologicas, Unpubl. Rep, p. 56–83.

Lieben, F., Moritz, R., and Fontboté, L., 2000, Mineralogy, Geochemistry, and Age Constraints on the Zn-Pb Skarn Deposit of Maria Cristina, Quebrada Galena, Northern Chile: Economic Geology, v. 95, p. 1185–1196.

Liipo, J., Lamberg, P., Turunen, J., and Pitkäjärvi, J., 2004, Grain Size and Liberation of Chromite in Ground Chrome Ore from Kemi Mine, Finland, ICAM 2004 - The 8thInternational Congress on Applied Mineralogy: Aquas de Lindoia, Brazil.

Little, J.M., 1926, The geology and metal deposits of Chile: New York, The Branwell Company, 188 p.

Llaumett, C., 1980. Antecedentes sobre produccion recursos y expectativas de la mineria del oro en Chile. Minerales, v. 35(150), p. 9–20.

Llaumett, C., Olcay, L., Marín, C., Marquardt, J.C., and Reyes, R., 1975, El yacimiento cobre porfídico "Andacollo", Provincia de Coquimbo, Chile: Revista Geologica de Chile v. 2, p. 56–66.

Losada-Calderón, A., McPhail, D., Camus, F., Sillitoe, R., and Petersen, R., 1996, Porphyry and high-sulfidation epithermal mineralization in the Nevados del Famatina mining district, Argentina, Andean copper deposits: new discoveries, mineralization, styles and metallogeny, 5. Society Economic Geology Special Publication: Littleton, CO, Society Economic Geology, p. 91–118.

Losert, J., 1974, The formation of stratiform copper deposits in relation to alteration of volcanic series (on North-Chilean examples): Rozpravy Ceskoslovenske Akademie Ved, v. 84, p. 77.

Lowell, J.D. and Aspillaga, J., 1987, Deposito de mineral de oro diseminado San Cristobal, Mineria Chilena, v. 80, p. 5–9.

Lucassen, F., Escayola, M., Romer, R.L., Viramonte, J., 2002, Isotopic composition of Late Mesozoic basic and ultrabasic rocks from the Andes (23–32 degrees S) - Implications for the Andean mantle: Contributions to Mineralogy and Petrology, v. 143, p. 336–349.

Lucassen, F., and Thirlwall, M.F., 1998, Sm-Nd ages of mafic rocks from the Coastal Cordillera at 24 degrees S, northern Chile: Geologische Rundschau, v. 86, p. 767–774.

Lund, C., Lamberg, P., and Lindberg, T., 2013, Practical way to quantify minerals from chemical assays at Malmberget iron ore operations – An important tool for the geometallurgical program: Minerals Engineering, v. 49, p. 7–16.

Lund, C., and Martinsson, O., 2008, A characterising of the ore minerals due to mineralogical, chemical

and textural properties in Malmberget: Conference in Minerals Engineering, 2008, p. 71–80.

Lund, C., Martinsson, O., and Lindberg, T., 2010, Mineralogical-textural characterisation of different apatite-iron ore bodies, Malmberget deposit, Sweden, treated in a sorting process in laboratory scale, Process Mineralogy'10: Cape Town, South Africa.

Macfarlane, A.W., Marcet, P., LeHuray, A.P., and Petersen, U., 1990, Lead isotope provinces of the Central Andes inferred from ores and crustal rocks: Economic Geology, v. 85, p. 1857–1880.

Maddox, L., Bancrost, G., Scani, M., and Lorimer, J., 1998, Invisible gold: Comparison of Au deposition on pyrite and arsenopyrite: American Mineralogist, v. 83, p. 1240–1245.

Maksaev, V., Townley, B., Palacios, C., and Camus, F., 2007, Metallic ore deposits, in Moreno, T., and Gibbons, W., eds., The Geology of Chile:, The Geological Society, London, p. 179–199.

Maksaev, V., and Zentilli, M., 2002, Chilean strata-bound Cu-(Au) deposits: An overview, in Porter, T.M., ed., Hydrothermal iron oxide copper-gold and related deposits; a global perspective, 2: Adelaide, PGC Publishing, p. 22.

Mark, G., Oliver, N.H.S., and Williams, P.J., 2006, Mineralogical and chemical evolution of the Ernest Henry Fe oxide–Cu–Au ore system, Cloncurry district, northwest Queensland, Australia: Mineralium Deposita, v. 40, p. 769.

Markey, R.J., Stein H.J., and Morgan, J.W., 1998, Highly precise Re-Os dating for molybdenite using alkaline fusion and NTIMS. Talanta, v. 45, p. 935–946.

Markey, R.J., Stein, H.J., Hannah, J.L., Selby, D., and Creaser, R.A., 2007 Standardizing Re-Os geochronology: A new molybdenite Reference Material (Henderson, USA) and the stoichiometry of Os salts. Chemical Geology, v. 244, p. 74–87.

Marquardt, M., Cembrano, J., Bissig, T., and Vásquez, C., 2015, Mid Cretaceous Cu-Au (Mo) mineralization in the Vallenar district: new Re-Os age constraints from Productora deposit, northern Chile, XIV Congreso Geológico Chileno: La Serena, Sociedad Geologica de Chile.

Marschik, R., Chiaradia, M., and Fontbote, L., 2003, Implications of Pb isotope signatures of rocks and iron oxide Cu-Au ores in the Candelaria-Punta del Cobre district, Chile: Mineralium Deposita, v. 38, p. 900–912.

Marschik, R., and Fontboté, L., 1996, Copper(-iron) mineralization and superposition of alteration

events in the Punta del Cobre Belt, northern Chile: Society of Economic Geologists Special Publication No. 5, p. 171–190.

Marschik, R., and Fontboté, L., 2001, The Candelaria-Punta del Cobre iron oxide Cu-Au(-Zn-Ag) deposits, Chile: Economic Geology, v. 96, p. 1799–1826.

Marschik, R., Leveille, R., and Martin, W., 2000, La Candelaria and the Punta del Cobre district, Chile: Early Cretaceous iron oxide Cu-Au(-Zn-Ag) mineralization, in Porter, T. M., ed., Hydrothermal iron oxide cooper–gold and related deposits: a global perspective Austral Miner Fund, Adelaide, 1: Adelaide, Australian Mineral Foundation, p. 163–176.

Marschik, R., Singer, B.S., Munizaga, F., Tassinari, C., Moritz, R., and Fontboté, L., 1997, Age of Cu(-Fe)-Au mineralization and thermal evolution of the Punta del Cobre district, Chile: Mineralium Deposita, v. 32, p. 531–546.

Marschik, R., and Sollner, F., 2006, Early cretaceous U-Pb zircon ages for the Copiapo plutonic complex and implications for the IOCG mineralization at Candelaria, Atacama Region, Chile: Mineralium Deposita, v. 41, p. 785–801.

Marslund, S., 2009, Machine learning: An algorithm perspective, Chapman & Hall/CRC.

Martin, B., 1995, Instance-based learning: nearest neighbour with generalisation: Hamilton, New Zealand, University of Waikato, Department of Computer Science.

Masterman, G., 2003, Structural and geochemical evolution of the Rosario Cu-Mo porphyry deposit and related Cu-Ag veins, Collahuasi district, northern Chile: Unpublished PhD thesis, Hobart, Australia,University of Tasmania, p. 253.

Mathur, R., Marschik, R., Ruiz, J., Munizaga, F., Leveille, R.A., and Martin, W., 2002, Age of mineralization of the Candelaria Fe Oxide Cu-Au deposit and the origin of the Chilean Iron Belt, based on Re-Os isotopes: Economic Geology, v. 97, p. 59–71.

Matthew, R., 1932, Some notes on the composition of “copper pitch”: Unpublished B.Sc. thesis, 1928–1970, Montana Tech.

McLemore, V., Sweeney, D., Dunbar, N., Heizler, L., and Writer, E., 2009, Determining quantitative mineralogy using a modified modan approach on the Questa rock pile materials, New Mexico: SME Annual Meeting, Denver, USA, 2009.

McNutt, R.H., Crocket, J.H., Clark, A.H., Caelles, J.C., Farrar, E., Haynes, S.J., and Zentilli, M., 1975, Initial 87Sr/86Sr ratios of plutonic and volcanic rocks of the Central Andes between latitudes 26° and 29° south: Earth and Planetary Science Letters, v. 27, p. 305–313.

McPhie, J., Doyle, M., and Allen, R., 1993, Volcanic textures: a guide to the interpretation of textures in volcanic rocks: Hobart, Centre of Excellence in Ore Deposits, University of Tasmania, 198 p.

McQuiston, F.W., Jr., and Bechaud, L.J., Jr., 1968, Metallurgical sampling and testing, surface mining. New York: The American Institute of Mining, Metallurgical, and Petroleum Engineers, p. 103–121.

Meffre, S., Large, R.R., Scott, R., Woodhead, J., Chang, Z., Gilbert, S.E., Danyushevsky, L.V., Maslennikov, V., and Hergt, J.M., 2008, Age and pyrite Pb-isotopic composition of the giant Sukhoi Log sediment-hosted gold deposit, Russia: Geochimica et Cosmochimica Acta, v. 72, p. 2377–2391.

Meinert, L.D., 1984, Mineralogy and petrology of iron skarns in western British Columbia, Canada: Economic Geology, v. 79, p. 869–882.

Meinert, L.D., Dipple, G.M., and Nicolescu, S., 2005, World skarn deposits: Economic Geology 100th Anniversary Volume, p. 299–336.

Ménard, J.J., 1995, Relationship between altered pyroxene diorite and the magnetite mineralization in the Chilean Iron Belt, with emphasis on the El Algarrobo iron deposits (Atacama region, Chile): Mineralium Deposita, v. 30, p. 268–274.

Menzies, A., Campos, E., Hernández, V., Sola, S., Riquelme, R., and Barraza, M., 2015, Understanding Exotic-Cu Mineralisation: Part II-Characterisation of Black Copper ("Cobre Negro") ore: 13th Biennial SGA Meeting, Nancy, France, 2015.

Meyer, C., and Hemley, J.J., 1967, Wall rock alteration, in Barnes, H.L., ed., Geochemistry of hydrothermal ore deposits: New York, Wiley, p. 166–232.

Möller, P., and Kersten, G., 1994, Electrochemical accumulation of visible gold on pyrite and arsenopyrite surfaces: Mineralium Deposita, v. 29, p. 404–413.

Montoya, P., Keeney, L., Jahoda, R., Hunt, J., Berry, R., Drews, U., Chamberlain, V., and Leichliter, S., 2011, Geometallurgical modelling techniques applicable to prefeasability projects-La Colosa case

study: Geomet 2011 -The First AusIMM International Geometallurgical Conferenece, Brisbane, Australia, 2011, p. 103–112.

Montecinos, P., 1985, Pétrologie des roches intrusives associées au gisement de fer El Algarrobo (Chile): Unpublished PhD thesis, Paris, France, Université de Paris-Sud, 191 p.

Moraga, A., 2000, Un modelo mineralógico en el yacimiento El Abra, tipo pórfido cuprífero: IX Congreso Geológico Chileno, Puerto Varas, Chile, 2000, p. 298–302.

Mort, K., and Woodcock, N.H., 2008, Quantifying fault breccia geometry: Dent Fault, NW England: Journal of Structural Geology, v. 30, p. 701–709.

Moscoso, R., Nasi, C., and Salinas, P., 1982, Hojo Vallenar y parte norte de La Serena, regiones de Atacama y Coquimbo, Carta Geológica de Chile, Servicio Nacional de Geología y Minería (Chile), p. 1–100.

Mote, T.I., Becker, T.A., Renne, P., and Brimhall, G.H., 2001, Chronology of exotic mineralization at El Salvador, Chile, by 40Ar/39Ar dating of copper wad and supergene alunite: Economic Geology, v. 96, p. 351–366.

Mpodozis, C., and Allmendinger, R.W., 1993, Extensional tectonics, Cretaceous Andes, northern Chile (27 degrees S): Geological Society of America Bulletin, v. 105, p. 1462–1477.

Mpodozis, C., and Ramos, V.A., 1990, The Andes of Chile and Argentina: Earth Science Series, v. 11, p. 59–90.

Mumin, A.H., Corriveau, L., Somarin, A.K., and Ootes, L., 2007, Iron oxide copper-gold-type polymetallic mineralization in the Contact Lake Belt, Great Bear Magmatic Zone, Northwest Territories, Canada: Exploration and Mining Geology, v. 16, p. 187–208.

Münchmeyer, C., 1996, Exotic deposits-products of lateral migration of supergene solutions from porphyry copper deposits, in Camus, F., Sillitoe, R., and Petersen, R., eds., Andean Copper Deposits: New discoveries, mineralization, styles and metallogeny: Littleton, Society of Economic Geology, p. 43–58.

Munizaga, F., Huete, C., and Hervé, F., 1985, Geocronologia K-Ar y razones iniciales Sr87/Sr86 de la "Faja Pacífica" de "Desarrollos Hidrotermales", 4th Congreso Geologico Chileno, 3: Antofagasta, p. 357–379.

Mycroft, J.R., 1993, Electroless reduction of gold (III) on pyrite from chloride electrolytes: Unpublished PhD thesis, London, Canada, University of Western Ontario, 350 p.

Mycroft, J.R., Bancroft, G.M., McIntyre, N.S., and Lorimer, J.W., 1995, Spontaneous deposition of gold on pyrite from solutions containing Au (III) and Au (I) chlorides. Part I: A surface study: Geochimica et Cosmochimica Acta, v. 59, p. 3351–3365.

Nash, J.T., 1976, Fluid-inclusion petrology-data from porphyry copper deposits and applications to exploration: U.S. Geological Survey Professional Papern 907-D.

Naslund, H.R., Henriquez, F., Nystrom, J.O., Vivallo, W., and Dobbs, F.M., 2002, Magmatic iron ores and associated mineralisation; examples from the Chilean High Andes and Coastal Cordillera, in Porter, T.M., ed., Hydrothermal iron oxide copper-gold and related deposits; a global perspective, 2: Adelaide, PGC Publishing, p. 207–226.

Ness, S., 2014, Quantitative X-ray diffraction analysis, Genalysis Laboratory Services Pty Ltd, p. 1–6.

Novoselov, A.A., and de Souza Filho, C.R., 2015, Potassium metasomatism of Precambrian paleosols: Precambrian Research, v. 262, p. 67–83

Nyström, J.O., and Henríquez, F., 1994, Magmatic features of iron ores of the Kiruna type in Chile and Sweden; ore textures and magnetite geochemistry: Economic Geology, v. 89, p. 820–839.

Oghazi, P., Pålsson, B., and Tano, K., 2009, Applying traceability to grinding circuits by using particle texture analysis (PTA): Minerals Engineering, v. 22, p. 710–718.

Ohmoto, H., 1972, Systematics of sulfur and carbon isotopes in hydrothermal ore deposits: Economic Geology, v. 67, p. 551–578.

Ohmoto, H., 1986, Stable isotope geochemistry of ore deposits: Reviews in Mineralogy and Geochemistry, v. 16, p. 491–559.

Ohmoto, H., and Goldharber, M.B., 1997, Sulfur and Carbon Isotopes, in Barnes, H.L., ed., Geochemistry of hydrothermal ore deposits, New York, John Wiley and Sons, p. 517–600.

Ohmoto, H., and Lasaga, A.C., 1982, Kinetics of reactions between aqueous sulfates and sulfides in hydrothermal systems: Geochimica Et Cosmochimica Acta, v. 46, p. 1727–1745.

Ohmoto, H., and Rye, R.O., 1979, Isotopes of sulfur and carbon, in Barnes, H.L., ed., Geochemistry

of hydrothermal ore deposits, New York, John Wiley and Sons.

Oliver, S., and Willingham, D., 2016, Maximise Orebody value through the automation of resource model development using machine learning: AusIMM international geometallurgy conference, 3rd, Perth, Western Australia, 2016, Extended Abstracts, p. 295–301.

Oliveros, V., Féraud, G., Aguirre, L., Fornari, M., and Morata, D., 2006, The early Andean magmatic province (EAMP): 40Ar/39Ar dating on Mesozoic volcanic and plutonic rocks from the Coastal Cordillera, northern Chile: Journal of Volcanology and Geothermal Research, v. 157, p. 311–330.

Omotoso, O., McCarty, D.K., Hillier, S., and Kleeberg, R., 2006, Some successful approaches to quantitative mineral analysis as revealed by the 3rd Reynolds Cup contest: Clays and Clay Minerals, v. 54, p. 748–760.

Orovan, E.A, 2016, Geology, geochemistry and genesis of the Namosi porphyry Cu-Au deposits, Fiji, Unpublished PhD thesis, Hobart, Tasmania, University of Tasmania, 295 p.

Orth, K., Meffre, S., and Davidson, G., 2014, Age and paragenesis of mineralisation at Coronation Hill uranium deposit, Northern Territory, Australia: Mineralium Deposita, v. 49, p. 595–623.

Oyarzun, J., and Frutos, J., 1984, Tectonic and Petrological Frame of the Cretaceous Iron Deposits of North Chile: Mining Geology, v. 34, p. 21–31.

Oyarzun, R., Oyarzún, J., Ménard, J.J., and Lillo, J., 2003, The Cretaceous iron belt of northern Chile: role of oceanic plates, a superplume event, and a major shear zone: Mineralium Deposita, v. 38, p. 640–646.

Paktunc, A.D., 1998, MODAN: an interactive computer program for estimating mineral quantities based on bulk composition: Computers & Geosciences, v. 24, p. 425–431.

Paktunc, A.D., 1999, Mineralogical constraints on the determination of neutralization potential and prediction of acid mine drainage: Environmental Geology, v. 39, p. 103–112.

Paktunc, A.D., 2001, MODAN - a computer program for estimating mineral quantities based on bulk composition: windows version: Computers & Geosciences, v. 27, p. 883–886.

Pal, M., 2005, Random forest classifier for remote sensing classification: International Journal of Remote Sensing, v. 26, p. 217–222.

Palacios, C.M., 1990, Geology of the Buena Esperanza Copper-Silver Deposit, northern Chile, in Fontboté, L., Amstutz, G. C., Cardozo, M., Cedillo, E., and Frutos, J., eds., Stratabound Ore Deposits in the Andes: Special Publication No.8 of the Society for Geology Applied to Mineral Deposits, Berlin, Springer-Verlag, p. 313–318.

Parada, M., and Larrondo, P., 1999, Thermocronology of the Lower Cretaceous Caleu pluton in the Coast Range of central Chile: tectono-stratigraphic implications, International Symposium on Andean Geodynamics, 4th, Göttingen, Germany, 1999, Extended Abstracts p. 563–566.

Parada, M.A., López-Escobar, L., Oliveros, V., Fuentes, F., Morata, D., Calderón, M., Aguirre, L., Féraud, G., Espinoza, F., Moreno, H., Figueroa, O., Bravo, J.M., Vásquez, R.T., and Stern, C.R., 2007, Andean Magmatism, in Moreno, T., and Gibbons, W., eds., The Geology of Chile, London, The Geological Society, p. 115–146.

Parian, M., Lamberg, P., Möckel, R., and Rosenkranz, J., 2015, Analysis of mineral grades for geometallurgy: Combined element-to-mineral conversion and quantitative X-ray diffraction: Minerals Engineering, v. 82, p. 25–35.

Park, C.F., 1961, A magnetite "flow" in northern Chile: Economic Geology, v. 56, p. 431–436.

Parkison, G., and Bhappu, R., 1995, The sequential copper analysis method-geological, mineralogical, and metallurgical implications: annual meeting of Society of mining engineers of AIME, 90th, Denver, Colorado, 1995, Extended Abstracts.

Pass, H.E., 2010, Breccia-hosted chemical and mineralogical zonation patterns of the Northeast Zone, Mt. Polly Cu-Ag-Au alkalic porphyry deposit, British Columbia, Canada: Unpublished PhD thesis, Hobart, Tasmania, University of Tasmania, 276 p.

Paterson, D., De Jonge, M., Howard, D., Lewis, W., McKinlay, J., Starritt, A., Kusel, M., Ryan, C., Kirkham, R., Moorhead, G., and Siddons, D., 2011, The X-ray fluorescence microscopy beamline at the Australian synchrotron: International Conference on X-ray Microscopy, 10th, Chicago, Illinois, 2010, Extended Abstracts, p. 219.

Pilger, R.H., 1981, Plate reconstructions, aseismic ridges, and low-angle subduction beneath the Andes: Geological Society of America Bulletin, v. 92, p. 448–456.

Pincheira, M., Dagnino, A., Kelm, U., and Helle, S., 2003, "Copper pitch y copper wad": contraste entre las fases presentes en las cabezas y en los ripios en pruebas de lixiviación de materiales

de Mina Sur, Chuquicamata: Congreso Geológico Chileno, 10th, Concepcion, Chile, 2003, Extended Abstracts

Pinget, M., Dold, B., and Fontboté, L., 2012, Exotic mineralization at Chuquicamata, Chile: focus on the copper wad enigma, Swiss Geoscience Meeting, 10th, Bern, Switzerland, 2013, Extended Abstracts, p. 88–89.

Platt, J.C., 1998, Fast training of support vector machines using sequential minimal optimization, in Scholkopf, B., Burges, C., and Smola, A., eds., Advances in kernel methods: Support vector learning: Cambridge, Massachusetts, MIT Press, p. 185–208.

Pollard, P., 2006, An intrusion-related origin for Cu–Au mineralization in iron oxide–copper–gold (IOCG) provinces: Mineralium Deposita, v. 41, p. 179–187.

Pollard, P.J., 2001, Sodic(–calcic) alteration in Fe-oxide–Cu–Au districts: an origin via unmixing of magmatic H_2O-CO_2-NaCl ± $CaCl_2$-KCl fluids: Mineralium Deposita, v. 36, p. 93–100.

Porwal, A.K., and Kreuzer, O.P., 2010, Introduction to the Special Issue: Mineral prospectivity analysis and quantitative resource estimation: Ore Geology Reviews, v. 38, p. 121–127.

Pozdnukhov, A., Kanevski, M., Maignan, M., and Canu, S., 2002, Robust mapping of spatial data with Support Vector Regression: IBRAE, 2002, Nuclear Safety Institute RAS, p. 15.

Press, W.H., Flannery, B.P., Teukolsky, S.A., and Vetterling, W.T., 1986, Numerical Recipes: The art of scientific computing, Cambridge, Cambridge University Press, p. 818.

Prinz, P., Wilke, H.-G., and von Hillebrant, A., 1994, Sediment accumulation and subsidence history in the Mesozoic marginal basin of northern Chile, in Reutter, K.J., Scheuber, E., and Wigger, P.J., eds., Tectonics of the Southern Central Andes: Berlin, Springer-Verlag.

Quinlan, J.R., 1993, C4.5 : Programs for machine learning: San Fransico, Morgan Kaufmann Publishers,

Ramdohr, P., 1969, The ore minerals and their intergrowths. International series of monographs on earth sciences, Oxford, New York, Pergamon Press

Ramírez, L.E., Palacios, C., Townley, B., Parada, M.A., Sial, A.N., Fernandez-turiel, J.L., Gimeno, D., Garcia-valles, M., and Lehmann, B., 2006, The Mantos Blancos copper deposit: an upper Jurassic breccia-style hydrothermal system in the Coastal Range of Northern Chile: Mineralium Deposita, v. 41, p. 246–258.

Ramos, V.A., 1999, Plate tectonic setting of the Andean Cordillera: Episodes, v. 22, p. 183–190.

Ramos, V.A., and Folguera, A., 2009, Andean flat-slab subduction through time: Geological Society Special Publications, v. 327, p. 31–54.

Ray, G.E., and Dick, L.A., 2002, The Productora prospect in north-central Chile: An example of an intrusion-related, Candelaria type Fe-Cu-Au hydrothermal system, in Porter, T. M., ed., Hydrothermal Iron Oxide, Copper-Gold & Related Deposits: A Global Perspective, 2: Adelaide, PGC Publishing, p. 131–151.

Ramírez, L.E., Palacios, C., Townley, B., Parada, M.A., Sial, A.N., Fernandez-turiel, J.L., Gimeno, D., Garcia-valles, M., and Lehmann, B., 2006, The Mantos Blancos copper deposit: an upper Jurassic breccia-style hydrothermal system in the Coastal Range of Northern Chile: Mineralium Deposita, v. 41, p. 246–258.

Ramos, V.A., 1999, Plate tectonic setting of the Andean Cordillera: Episodes, v. 22, p. 183–190.

Ramos, V.A., and Folguera, A., 2009, Andean flat-slab subduction through time: Geological Society Special Publications, v. 327, p. 31–54.

Ray, G.E., and Dick, L.A., 2002, The Productora prospect in north-central Chile: An example of an intrusion-related, Candelaria type Fe-Cu-Au hydrothermal system, in Porter, T.M., ed., Hydrothermal Iron Oxide, Copper-Gold & Related Deposits: A Global Perspective, 2: Adelaide, PGC Publishing, p. 131–151.

Reich, M., Kesler, S.E., Utsunomiya, S., Palenik, C.S., Chryssoulis, S.L., and Ewing, R.C., 2005, Solubility of gold in arsenian pyrite: Geochimica et Cosmochimica Acta, v. 69, p. 2781–2796.

Reich, M., Simon, A.C., Deditius, A., Barra, F., Chryssoulis, S., Lagas, G., Tardani, D., Knipping, J., Bilenker, L., and Sánchez-Alfaro, P., 2016, Trace element signature of pyrite from the Los Colorados iron oxide-apatite (IOA) deposit, Chile: a missing link between Andean IOA and iron oxide copper-gold systems: Economic Geology, v. 111, p. 743–761.

Reyes, A. G., 1990, Petrology of Philippine geothermal systems and the application of alteration mineralogy to their assessment: Journal of Volcanology and Geothermal Research, v. 43, p. 279–309.

Reyes, M., 1991, The Andacollo strata bound gold deposit, Chile, and its position in a porphyry copper-

gold system: Economic Geology, v. 86, p. 1301–1316.

Rhodes, A.L., Oreskes, N., and Sheets, S., 1999, Geology and rare earth element geochemistry of magnetic deposits at El Laco, Chile: Society of Economic Geologists Special Publication No. 7, p. 299–332.

Rieger, A.A., Marschik, R., and Díaz, M., 2012, The evolution of the hydrothermal IOCG system in the Mantoverde district, northern Chile: new evidence from microthermometry and stable isotope geochemistry: Mineralium Deposita, v. 47, p. 359–369.

Ripley, B.D., 1996, Pattern recognition and neural networks: Cambridge, UK, Cambridge University Press, 416 p.

Ripley, E.M., and Ohmoto, H., 1977, Mineralogic, sulfur isotope, and fluid inclusion studies of the stratabound copper deposits at the Raul Mine, Peru: Economic Geology, v. 72, p. 1017–1041.

Rivera, S., 1984, Esquema de distribucion de vetas y tipos de clavos mineralizados en el distrito aurifero San Cristobal, II region, Chile. In: IV Congr. Ing. Minas, Copiapo, Chile, p. 209–213.

Rodriguez-Galiano, V.F., Chica-Olmo, M., and Chica-Rivas, M., 2014, Predictive modelling of gold potential with the integration of multisource information based on random forest: a case study on the Rodalquilar area, Southern Spain: International Journal of Geographical Information Science, v. 28, p. 1336–1354.

Roedder, E., 1971, Fluid inclusion studies on the porphyry-type ore deposits at Bingham, Utah, Butte, Montana, and Climax, Colorado: Economic Geology, v. 66, p. 98–118.

Rogers, G., and Hawkesworth, C.J., 1989, A geochemical traverse across the North Chilean Andes: Evidence for crust generation from the mantle wedge: Earth and Planetary Science Letters, v. 91, p. 271–285.

Rojas, P., Barra, F., Uribe, F., Reich, M., Palma, G., and Salazar, E., 2015, Eventos de Mineralización en el Depósito de Magnetita-Apatito El Romeral, IV Región de Coquimbo: XIV Congreso Geológico Chileno, La Serena, 2015.

Rojas, R., and Müller, G., 1994, "Damiana": uno de los yacimientos tipo "exóticos" de El Salvador, VII Congreso Geológico Chileno, 2: Concepción, p. 892–896.

Roseveare, G.H., 1966, Field tests for the common mineral elements: Tucsan, University of Arizona

Press, 43 p.

Roy, S., 2002, Nearest neighbor with generalization: Christchurch, New Zealand.

Rubin, J.N., and Kyle, J.R., 1997, Precious metal mineralogy in porphyry-, skarn-, and replacement-type ore deposits of the Ertsberg (Gunung Bijih) District, Irian Jaya, Indonesia: Economic Geology, v. 92, p. 535–550.

Ruiz, C., Aguirre, L., Corvalan, J., Klohn, C., Klohn, E., and Levi, B., 1965, Geología y Yacimientos Metalíferos de Chile: Instituto de Investigaciones Geológicas de Chile: Santiago, v. 1.

Ruiz, C., and Ericksen, G.E., 1962, Metallogenetic provinces of Chile, S.A: Economic Geology, v. 57, p. 91–106.

Ruiz, F.C., and Peebles, L.F., 1988, Geología, distribución y génesis de los yacimientos metalíferos Chilenos: Unpublished PhD thesis, Santiago, Chile, Editorial Universitaria, 334 p.

Rusk, B. G., Reed, M. H., and Dilles, J. H., 2008, Fluid inclusion evidence for magmatic-hydrothermal fluid evolution in the porphyry copper-molybdenum deposit at Butte, Montana: Economic Geology, v. 103, p. 307–334.

Russell, S.J., and Novig, P., 2010, Artificial intelligence: A modern approach: Upper Saddle River, NJ, Prentice Hall, 1132 p.

Ryan, P.J., Lawrence, A.L., Jenkins, R.A., Matthews, J.P., Zamora, J.C., Marino, E., and Urqueta, I., 1995, The Candelaria copper-gold deposit, Chile: Arizona Geological Society Digest, v. 20, p. 625–645.

Ryan, C., Kirkham, R., Hough, R., Moorhead, G., Siddons, D., De Jonge, M., Paterson, D., De Geronimo, G., Howard, D., and Cleverley, J., 2010, Elemental X-ray imaging using the Maia detector array: the benefits and challenges of large solid-angle: Nuclear Instruments and Methods in Physics Research Section A: Accelerators, Spectrometers, Detectors and Associated Equipment, v. 619, p. 37–43.

Ryan, C., Siddons, D., Kirkham, R., Dunn, P., Kuczewski, A., Moorhead, G., De Geronimo, G., Paterson, D., De Jonge, M., Hough, R., Lintern, M., Hoard, D., Kappen, P., and Cleverley, J., 2010, The new Maia detector system: methods for high definition trace element imaging of natural material: X-Ray Optics and Microanalysis, 2010, p. 9–17.

Ryan, C., Siddons, D., Kirkham, R., Li, Z., De Jonge, M., Paterson, D., Cleverley, J., Kuczewski, A., Dunn, P., and Jensen, M., 2013, The Maia detector array and X-ray fluorescence imaging system: locating rare precious metal phases in complex samples: Proceedings SPIE 8851, X-Ray Nanoimaging: Instruments and Methods, 88510Q (September 26, 2013)

Rye, R.O., 1993, The evolution of magmatic fluids in the epithermal environment; the stable isotope perspective: Economic Geology, v. 88, p. 733–752.

Salinas, M., 1975, Yacimientos auriferos de la provincia de Atacama. Instituto de Investigaciones Geologicas, Unpublished Report, p. 216

Samanta, B., Bandopadhyay, S., Ganguli, R., and Dutta, S., 2005, A comparative study of the performance of single neural network vs. adaboost algorithm based combination of multiple neural networks for mineral resource estimation: Journal of South African institute of mining and metallurgy, v. 105, p. 237–246.

Sanford, R.F., 1992, Lead isotopic compositions and paleohydrology of caldera-related epithermal veins, Lake City, Colorado: Geological Society of America Bulletin, v. 104, p. 1236–1245.

Sato, T., 1984, Manto type copper deposits in Chile; a review: Bulletin of the Geological Survey of Japan, v. 35, p. 565–582.

Scaini, M., Bancroft, G., and Knipe, S., 1998, Reactions of aqueous Au^{1+} sulfide species with pyrite as a function of pH and temperature: American Mineralogist, v. 83, p. 316–322.

Scheuber, E., and Andriessen, P.A.M., 1990, The kinematic and geodynamic significance of the Atacama fault zone, northern Chile: Journal of Structural Geology, v. 12, p. 243–257.

Scheuber, E., and Gonzalez, G., 1999, Tectonics of the Jurassic-Early Cretaceous magmatic arc of the North Chilean Coastal Cordillera (22 degrees –26 degrees S); a story of crustal deformation along a convergent plate boundary: Tectonics, v. 18, p. 895–910.

Scheuber, E., Hammerschmidt, K., and Friedrichsen, H., 1995, $^{40}Ar/^{39}Ar$ and Rb/Sr analyses from ductile shear zones from the Atacama Fault Zone, northern Chile: the age of deformation: Tectonophysics, v. 250, p. 61–87.

Scheuber, E., and Reutter, K.-J., 1992, Magmatic arc tectonics in the Central Andes between 21° and 25°S: Tectonophysics, v. 205, p. 127–140.

Schmitz, M., 1994, A balanced model of the southern Central Andes: Tectonics, v. 13, p. 484–492.

Seal, R.R., 2006, Sulfur isotope geochemistry of sulfide minerals: Washington, D.C., Mineralogical Society of America, p. 633–677.

Seedorff, E., Dilles, J., Proffett, J., Einaudi, M., Zurcher, L., Stavast, W., Johnson, D., and Barton, M., 2005, Porphyry deposits: Characteristics and origin of hypogene features: Economic Geology 100th Anniversary Volume, p. 251–298.

Segerstrom, K., 1960, Erosion and related phenomena at Paricutin in 1957, USGS.

Selby D., and Creaser R.A., 2004, Macroscale NTIMS and microscale LA-MC-ICP-MS Re-Os isotopic analysis of molybdenite: Testing spatial restrictions for reliable Re-Os age determinations, and implications for the decoupling of Re and Os within molybdenite, Geochimica et Cosmochimica Acta, v. 68, p. 3897–3908.

Selby, D., Creaser, R. A., Stein, H. J., Markey, R. J., and Hannah, J. L., 2007, Assessment of the 187Re decay constant by cross calibration of Re–Os molybdenite and U–Pb zircon chronometers in magmatic ore systems: Geochimica et Cosmochimica Acta, v. 71, p. 1999–2013.

Shi, H., 2007, Best-first decision tree learning: Unpublished M.Sc. thesis, Hillcrest, New Zealand, The University of Waikato, 199 p.

Short, M.N., 1931, Microscopic determination of the ore minerals, U. S. Geological Survey.

Sillitoe, R., 1995, Exploration of porphyry copper lithocaps: Proceedings of Pacific Rim Congress, Auckland, New Zealand, 1995, p. 527–532.

Sillitoe, R., and Clark, A., 1969, Copper and copper-iron sulfides as initial products of supergene oxidation, Copiapo mining district, northern Chile: American Mineralogist, v. 54, p. 1684–1710.

Sillitoe, R.H., 1979, Some thoughts on gold-rich porphyry copper deposits: Mineralium Deposita, v. 14, p. 161–174.

Sillitoe, R.H., 1981, Regional aspects of the Andean porphyry copper belt in Chile and Argentina: Transactions of the Institute of Mining and Metallurgy Section B, v. 90, p. 15–36.

Sillitoe, R.H., 1985, Ore-related breccias in volcanoplutonic arcs: Economic Geology, v. 80, p. 1467–1514.

Sillitoe, R.H., 1988, Epochs of intrusion-related copper mineralization in the Andes: Journal of South American Earth Sciences, v. 1, p. 89–108.

Sillitoe, R.H., 1992, Gold and copper metallogeny of the Central Andes; past, present, and future exploration objectives: Economic Geology, v. 87, p. 2205–2206.

Sillitoe, R.H., 1997, Characteristics and controls of the largest porphyry copper-gold and epithermal gold deposits in the circum-Pacific region: Australian Journal of Earth Sciences, v. 44, p. 373–388.

Sillitoe, R.H., 2003, Iron oxide-copper-gold deposits: An Andean view: Mineralium Deposita, v. 38, p. 787–812.

Sillitoe, R.H., 2010, Porphyry Copper Systems: Economic Geology, v. 105, p. 3–41.

Sillitoe, R.H., 2015, A report prepared for Hot Chili Limited: Comments on the Alice and Productora copper-gold-molybdenum deposits, Región III, Chile.

Sillitoe, R.H., and Burrows, D.R., 2002, New field evidence bearing on the origin of the El Laco magnetite deposit, northern Chile: Economic Geology, v. 97, p. 1101–1109.

Sillitoe, R.H., and Perelló, J., 2005, Andean copper province: Tectonomagmatic settings, deposit types, metallogeny, exploration, and discovery: Economic Geology 100th Anniversary Volume, p. 845–890.

Sillitoe, R.H., and Sawkins, F.J., 1971, Geologic, Mineralogic and Fluid Inclusion Studies Relating to the Origin of Copper-bearing Tourmaline Breccia Pipes, Chile: Economic Geology, v. 66, p. 1028–1041.

Simon, G., Kesler, S.E., Essene, E.J., and Chryssoulis, S.L., 2000, Gold in porphyry copper deposits: Experimental determination of the distribution of gold in the Cu-Fe-S system at 400° to 700°C: Economic Geology, v. 95, p. 259–270.

Simpson, K.A., Davies, A.G.S., Cooke, D.R., and Gemmell, B.J., 2007, Description before interpretation: a suggested framework for consistent description of subsurface fragmental rocks: Breccia Symposium, Townsville, Australia, 2007, EGRU Contribution 65, p. 27.

Singer, D.A., and Kouda, R., 1999, A comparison of the weights-of-evidence method and probabilistic neural networks: Natural Resources Research, v. 8, p. 287–298.

Slack, J.F., 1996, Tourmaline associations with hydrothermal ore deposits, in Grew, E., and Anovitz, L., eds., Boron: Mineralogy, Petrology and Geochemistry, 33: Washington, D.C., Mineralogical Society of America, p. 559–643.

Song, X., Duan, Z., and Jiang, X., 2012, Comparison of artificial neural networks and support vector machine classifiers for land cover classification in Northern China using a SPOT-5 HRG image: International Journal of Remote Sensing, v. 33, p. 3301–3320.

Spear, F.S., 1993, Metamorphic phase equilibria and pressure-temperature-time paths: Washington, D.C., Mineralogical Society of America, 799 p.

Spearman, C., 1904, The proof and measurement of association between two things: The American Journal of Psychology, v. 15, p. 72–101.

Stacey, J.S., and Kramers, J.D., 1975, Approximation of terrestrial lead isotope evolution by a 2-stage model: Earth and Planetary Science Letters, v. 26, p. 207–221.

Stacey, J.S., Zartman, R.E., and Komo, I.T., 1968, A lead isotope study of galenas and selected feldspars from mining districts in Utah: Economic Geology, v. 63, p. 796–814.

Streckeisen, A., 1979, Classification and nomenclature of volcanic rocks, lamprophyres, carbonatites, and melilitic rocks: Recommendations and suggestions of the IUGS Subcommission on the Systematics of Igneous Rocks: Geology, v. 7, p. 331-335.

Sugaki, A., Campos, E., and Kojima, S., 2000, Mineralogy of the Panulcillo skarn copper deposit, Coquimbo Region, Chile: Revista geológica de Chile, v. 27, p. 139–155.

Sverjensky, D.A., Hemley, J.J., and D'Angelo, W.M., 1991, Thermodynamic assessment of hydrothermal alkali feldspar-mica-aluminosilicate equilibria: Geochimica et Cosmochimica Acta, v. 55, p. 989–1004.

Swayne, W.H., 1949, Reconnaissance report on the Las Vacas gold property near Los Vilos, Departament of Ulapel, Province of Coquimbo, Chile, Internal Report, p. 4.

Tarkian, M., and Koopmann, G., 1995, Platinum-group minerals in the Santo Tomas II (Philex) porphyry copper-gold deposit, Luzon Island, Philippines: Mineralium Deposita, v. 30, p. 39–47.

Taylor, B.E., and Slack, J.F., 1984, Tourmalines from Appalachian-Caledonian massive sulfide deposits; textural, chemical, and isotopic relationships: Economic Geology, v. 79, p. 1703–1726.

Taylor, G.K., Grocott, J., Pope, A., and Randall, D.E., 1998, Mesozoic fault systems, deformation and fault block rotation in the Andean forearc: a crustal scale strike-slip duplex in the Coastal Cordillera of northern Chile: Tectonophysics, v. 299, p. 93–109.

Taylor, H.P., and Pollard, P.J., 1993, Mineralised breccia systems: methods of recognition and interpretation, Townsville, Australia, 1993, EGRU Contribution 46, p. 31.

Teck Resources Limited, 2016, Reserves and resources, 2016 (http://www.teck.com/investors/reserves-&-resources/).

Tolosana-Delgado, R., and van den Boogaart, K.G., 2011, Linear models with compositions in R: Compositional data analysis: Theory and Applications, p. 356–371.

Tolosana-Delgado, R., von Eynatten, H., and Karius, V., 2011, Constructing modal mineralogy from geochemical composition: A geometric-Bayesian approach: Computers & Geosciences, v. 37, p. 677–691.

Tomlinson, A., Cornejo, P., and Mpodozis, C., 1999, Hoja Potrerillos, Región de Atacama, Servicio Nacional de Geología y Minería: Santiago, Mapas Geológicos.

Tornos, F., and Velasco, F., 2010, Magmatic-hydrothermal Evolution of the IOCG Deposits of Central Chile: Townsville, James Cook University, 662–664 p.

Tornos, F., Velasco, F., Barra, F., and Morata, D., 2010, The Tropezón Cu–Mo–(Au) deposit, Northern Chile: the missing link between IOCG and porphyry copper systems?: Mineralium Deposita, v. 45, p. 313–321.

Tosdal, R., Cline, J., Hofstra, A., Peters, S., Wooden, J., and Young-Mitchell, M., 1998, Mixed sources of Pb in sedimentary-rock-hosted Au deposits, northern Nevada: Contributions to the Au metallogeny of northern Nevada: US Geological Survey Open-File Report, p. 98–338.

Tosdal, R., Wooden, J., and Bouse, R., 1999, Pb isotopes, ore deposits, and metallogenic terranes: Reviews in Economic Geology, v. 12, p. 1–25.

Tosdal, R.M., Dilles, J.H., and Cooke, D.R., 2009, From source to sinks in auriferous magmatic-hydrothermal porphyry and epithermal deposits: Elements, v. 5, p. 289–295.

Tosdal, R.M., and Munizaga, F., 2003, Lead sources in Mesozoic and Cenozoic Andean ore deposits, north-central Chile (30–34 degrees S): Mineralium Deposita, v. 38, p. 234–250.

Travisany, V., Henriquez, F., and Nystroem, J.O., 1995, Magnetite lava flows in the Pleito-Melon District of the Chilean iron belt: Economic Geology, v. 90, p. 438–444.

Ullrich, T.D., and Clark, A.H., 1999, The Candelaria copper-gold deposit, Region III, Chile; paragenesis, geochronology and fluid composition: Proceedings of the 5th Biennial SGA Meeting and 10th Quadren IAGOD Symposium, London, United Kingdom, p. 201–204.

Uribe, F., 1987, Emplazamiento sintectonico del pluton Cerro Varillas con transcurrencia en el cretacico inferior de la Zona de Falla Atacama, Chile: Andean Geology, p. 101–106.

Vásquez, P., Franz, G., Glodny, J., Romer, R.L., and Frei, D., 2011, Early Mesozoic plutonism of the Cordillera de la Costa (34°–37°S), Chile: Constraints on the onset of the Andean Orogeny: Journal of Geology, v. 119, p. 159–184.

Veizer, J., Ala, D., Azmy, K., Bruckschen, P., Buhl, D., Bruhn, F., Carden, G.A.F., Diener, A., Ebneth, S., Godderis, Y., Jasper, T., Korte, C., Pawellek, F., Podlaha, O.G., and Strauss, H., 1999, 87Sr/86Sr, $\delta^{13}C$ and $\delta^{18}O$ evolution of Phanerozoic seawater: Chemical Geology, v. 161, p. 59–88.

Vergara, M., Levi, B., Nystrom, J.O., and Cancino, A., 1995, Jurassic and Early Cretaceous island arc volcanism, extension, and subsidence in the Coast Range of Central Chile: Geological Society of America Bulletin, v. 107, p. 1427–1440.

Villaroel, P., 1972, Informe geologico de lamina Rhodesia, Instituto de Investigaciones Geologicas, Unpublished Report, p. 12.

Vivallo, W., and Henríquez, F., 1998, Génesis común de los yacimientos estratoligados y vetiformes de cobre del Jurásico Medio a Superior en la Cordillera de la Costa, Región de Antofagasta, Chile: Revista geológica de Chile, v. 25, p. 199–228.

Walters, S., 2008, An overview of new integrated geometallurgical research: Ninth International Congress for Applied Mineralogy, Brisbane, Australia, 2008, p. 79–82.

Warnaars, F.W., Holmgren, D.C., and Barassi, F.S., 1985, Porphyry copper and tourmaline breccias at Los Bronces-Rio Blanco, Chile: Economic Geology, v. 80, p. 1544–1565.

Waske, B., and Braun, M., 2009, Classifier ensembles for land cover mapping using multitemporal SAR imagery: ISPRS Journal of Photogrammetry and Remote Sensing, v. 64, p. 450–457.

Webb, G.I., 1999, Decision tree grafting from the all-tests-but-one partition: Proceedings of the 16th

International Joint Conference on Artificial Intelligence, Stockholm, Sweden, 1999, p. 702–707.

Wedekind, M.R., 1990, Geology and geochemistry of the Warrego Au-Cu-Bi mine, Tennant Creek, Northern Territory, Australia: Unpublished PhD thesis, Hobart, Australia, University of Tasmania, 324 p.

Wentworth, C.K., 1922, A scale of grade and class terms for clastic sediments: The Journal of Geology, v. 30, p. 377–392.

Whelan, J., and Goldich, S., 1961, New data for hisingerite and neotocite: American Mineralogist, v. 46, p. 1412–1423.

Williams, P.J., Barton, M.D., Johnson, D.A., Fontboté, L., De Haller, A., Mark, G., Oliver, N.H., and Marschik, R., 2005, Iron oxide copper-gold deposits: geology, space-time distribution, and possible modes of origin, Economic Geology 100th Anniversary Volume, p. 371–405.

Williams, P.M., 1993, Improved generalization and network pruning using adaptive Laplace regularization: Third International Conference on Artificial Neural Networks, Brighton, UK, 1993, p. 76–80.

Williams, S., and Richardson, J., 2004, Geometallurgical mapping: A new approach that reduces technical risk: Proceedings of the 36th Annual Meeting of the Canadian Mineral Processors, Ottawa, Ontario, Canada, 2004, p. 241–268.

Williams-Jones, A.E., and Heinrich, C.A., 2005, Vapor transport of metals and the formation of magmatic-hydrothermal ore deposits: Economic Geology 100th Anniversary Volume, p. 1287–1312.

Witten, I.H., and Frank, E., 2005, Data mining: Practical machine learning tools and techniques: San Francisco, Morgan Kaufmann, 524 p.

Witten, I.H., Frank, E., and Hall, M.A., 2011, Data mining: Practical machine learning tools and techniques: Burlington, Morgan Kaufmann, 629 p.

Wolf, F.B., Fontboté, L., and Amstutz, G.C., 1990, The Susana copper (-silver) deposit in northern Chile hydrothermal mineralization associated with a Jurassic volcanic arc: Special Publication of the Society for Geology Applied to Mineral Deposits, v. 8, p. 319–338.

Woodcock, N.H., and Daly, M.C., 1986, The role of strike-slip fault systems at plate boundaries: Philosophical Transactions of the Royal Society of London, ser. A, v. 317, p. 13–29.

Woodcock, N.H., and Richards, B., 2003, Transpressive duplex and flower structure: Dent Fault System, NW England: Journal of Structural Geology, v. 25, p. 1981–1992.

Woodhead, J., Hergt, J., Meffre, S., Large, R.R., Danyushevsky, L., and Gilbert, S., 2009, In situ Pb-isotope analysis of pyrite by laser ablation (multi-collector and quadrupole) ICPMS: Chemical Geology, v. 262, p. 344–354.

Wu, X., and Zhou, Y., 1993, Reserve estimation using neural network techniques: Computers & Geosciences, v. 19, p. 567–575.

Yama, B., and Lineberry, G., 1999, Artificial neural network application for a predictive task in mining: Mining engineering, v. 51, p. 59–64.

Zaw, K., Huston, D.L., Large, R.R., Mernagh, T., and Hoffmann, C.F., 1994, Microthermometry and geochemistry of fluid inclusions from the Tennant Creek gold-copper deposits: implications for ore deposition and exploration: Mineralium Deposita, v. 29, p. 288–300.

Zentilli, M., 1974, Geological evolution and metallogenetic relationships in the Andes of Northern Chile between 26° and 29° South: Unpublished PhD thesis, Kingston, Canada, Queen's University, 340 p.

Zuo, R., and Carranza, E.J.M., 2011, Support vector machine: A tool for mapping mineral prospectivity: Computers & Geosciences, v. 37, p. 1967–1975.